Scattering, Absorption, and Emission of Light by Small Particles

Michael I. Mishchenko
Larry D. Travis
Andrew A. Lacis

CAMBRIDGE

Scattering, Absorption, and Emission of Light by Small Particles

This volume provides a thorough and up-to-date treatment of electromagnetic scattering by small particles. First, the general formalism of scattering, absorption, and emission of light and other electromagnetic radiation by arbitrarily shaped and arbitrarily oriented particles is introduced, and the relation of radiative transfer theory to single-scattering solutions of Maxwell's equations is discussed. Then exact theoretical methods and computer codes for calculating scattering, absorption, and emission properties of arbitrarily shaped particles are described in detail. Further chapters demonstrate how the scattering and absorption characteristics of small particles depend on particle size, refractive index, shape, and orientation. The work illustrates how the high efficiency and accuracy of existing theoretical and experimental techniques and the availability of fast scientific workstations result in advanced physically based applications of electromagnetic scattering to noninvasive particle characterization and remote sensing. This book will be valuable for science professionals, engineers, and graduate students in a wide range of disciplines including optics, electromagnetics, remote sensing, climate research, and biomedicine.

MICHAEL I. MISHCHENKO is a Senior Scientist at the NASA Goddard Institute for Space Studies in New York City. After gaining a Ph.D. in physics in 1987, he has been project scientist and principal investigator on several NASA and DoD projects and has served as editor, topical editor, and editorial board member of leading scientific journals such as the *Journal of Quantitative Spectroscopy and Radiative Transfer*, *Applied Optics*, *Journal of the Atmospheric Sciences*, *Waves in Random and Complex Media*, *Journal of Electromagnetic Waves and Applications*, and *Kinematics and Physics of Celestial Bodies.* Dr. MISHCHENKO is a recipient of the Henry G. Houghton Award of the American Meteorological Society and an elected Fellow of the American Geophysical Union, the Optical Society of America, the American Meteorological Society, and The Institute of Physics. His research interests include electromagnetic scattering, radiative transfer in planetary atmospheres and particulate surfaces, and remote sensing.

LARRY D. TRAVIS is presently Associate Chief of the NASA Goddard Institute for Space Studies. He gained a Ph.D. in astronomy at Pennsylvania State University in 1971. Dr. TRAVIS has acted as principal investigator on several NASA projects and was awarded a NASA Exceptional Scientific Achievement Medal. His research interests include the theoretical interpretation of remote sensing measurements of polarization, planetary atmospheres, atmospheric dynamics, and radiative transfer.

ANDREW A. LACIS is a Senior Scientist at the NASA Goddard Institute for Space Studies, and teaches radiative transfer at Columbia University. He gained a Ph.D. in physics at the University of Iowa in 1970 and has acted as principal investigator on numerous NASA and DoE projects. His research interests include radiative transfer in planetary atmospheres, the absorption of solar radiation by the Earth's atmosphere, and climate modeling.

M. I. MISHCHENKO, L. D. TRAVIS, and A. A. LACIS also authored a book on *Multiple Scattering of Light by Particles: Radiative Transfer and Coherent Backscattering* published in 2006 by Cambridge University Press. M. I. MISHCHENKO and L. D. TRAVIS co-edited a monograph on *Light Scattering by Nonspherical Particles: Theory, Measurements, and Applications* published in 2000 by Academic Press.

Scattering, Absorption, and Emission of Light by Small Particles

Third electronic release

Michael I. Mishchenko
Larry D. Travis
Andrew A. Lacis

NASA Goddard Institute for Space Studies, New York

CAMBRIDGE
UNIVERSITY PRESS

The first hardcopy edition of this book was published in 2002 by

CAMBRIDGE UNIVERSITY PRESS
The Edinburgh Building
Cambridge CB2 2RU
UK
http://www.cambridge.org

A catalogue record for this book is available from the British Library

ISBN 0 521 78252 X hardback

© NASA 2002

The first and second electronic editions of this book were published in 2004 and 2005, respectively, by

NASA Goddard Institute for Space Studies
2880 Broadway
New York, NY 10025
USA
http://www.giss.nasa.gov

The current electronic version is available at the following Internet site:

http://www.giss.nasa.gov/~crmim/books.html

This book is in copyright, except in the jurisdictional territory of the United States of America. The moral rights of the authors have been asserted. Single copies of the book may be printed from the Internet site http://www.giss.nasa.gov/~crmim/books.html for personal use as allowed by national copyright laws. Unless expressly permitted by law, no reproduction of any part may take place without the written permission of NASA.

Contents

Preface to the electronic edition xi
Preface to the original hardcopy edition xiii
Acknowledgments xvii

Part I **Basic Theory of Electromagnetic Scattering, Absorption, and Emission** 1

Chapter 1 **Polarization characteristics of electromagnetic radiation** 8

1.1 Maxwell's equations, time-harmonic fields, and the Poynting vector 8
1.2 Plane-wave solution 12
1.3 Coherency matrix and Stokes parameters 15
1.4 Ellipsometric interpretation of Stokes parameters 19
1.5 Rotation transformation rule for Stokes parameters 24
1.6 Quasi-monochromatic light and incoherent addition of Stokes parameters 26
Further reading 30

Chapter 2 **Scattering, absorption, and emission of electromagnetic radiation by an arbitrary finite particle** 31

2.1 Volume integral equation 31
2.2 Scattering in the far-field zone 35
2.3 Reciprocity 38
2.4 Reference frames and particle orientation 42
2.5 Poynting vector of the total field 46

2.6 Phase matrix 49
2.7 Extinction matrix 54
2.8 Extinction, scattering, and absorption cross sections 56
2.9 Radiation pressure and radiation torque 60
2.10 Thermal emission 63
2.11 Translations of the origin 66
Further reading 67

Chapter 3 Scattering, absorption, and emission by collections of independent particles 68

3.1 Single scattering, absorption, and emission by a small volume element comprising randomly and sparsely distributed particles 68
3.2 Ensemble averaging 72
3.3 Condition of independent scattering 74
3.4 Radiative transfer equation and coherent backscattering 74
Further reading 82

Chapter 4 Scattering matrix and macroscopically isotropic and mirror-symmetric scattering media 83

4.1 Symmetries of the Stokes scattering matrix 84
4.2 Macroscopically isotropic and mirror-symmetric scattering medium 87
4.3 Phase matrix 88
4.4 Forward-scattering direction and extinction matrix 91
4.5 Backward scattering 94
4.6 Scattering cross section, asymmetry parameter, and radiation pressure 95
4.7 Thermal emission 97
4.8 Spherically symmetric particles 98
4.9 Effects of nonsphericity and orientation 99
4.10 Normalized scattering and phase matrices 100
4.11 Expansion in generalized spherical functions 103
4.12 Circular-polarization representation 105
4.13 Radiative transfer equation 108

Part II Calculation and Measurement of Scattering and Absorption Characteristics of Small Particles 111

Chapter 5 *T*-matrix method and Lorenz–Mie theory 115

5.1 *T*-matrix ansatz 116
5.2 General properties of the *T* matrix 119
5.2.1 Rotation transformation rule 119

5.2.2 Symmetry relations 121
5.2.3 Unitarity 122
5.2.4 Translation transformation rule 125
5.3 Extinction matrix for axially oriented particles 127
5.4 Extinction cross section for randomly oriented particles 132
5.5 Scattering matrix for randomly oriented particles 133
5.6 Scattering cross section for randomly oriented particles 138
5.7 Spherically symmetric scatterers (Lorenz–Mie theory) 139
5.8 Extended boundary condition method 142
5.8.1 General formulation 142
5.8.2 Scale invariance rule 147
5.8.3 Rotationally symmetric particles 148
5.8.4 Convergence 150
5.8.5 Lorenz–Mie coefficients 153
5.9 Aggregated and composite particles 154
5.10 Lorenz–Mie code for homogeneous polydisperse spheres 158
5.10.1 Practical considerations 158
5.10.2 Input parameters of the Lorenz–Mie code 162
5.10.3 Output information 163
5.10.4 Additional comments and illustrative example 164
5.11 *T*-matrix code for polydisperse, randomly oriented, homogeneous, rotationally symmetric particles 165
5.11.1 Computation of the *T* matrix for an individual particle 167
5.11.2 Particle shapes and sizes 171
5.11.3 Orientation and size averaging 172
5.11.4 Input parameters of the code 173
5.11.5 Output information 175
5.11.6 Additional comments and recipes 176
5.11.7 Illustrative examples 178
5.12 *T*-matrix code for a homogeneous, rotationally symmetric particle in an arbitrary orientation 180
5.13 Superposition *T*-matrix code for randomly oriented two-sphere clusters 186
Further reading 189

Chapter 6 **Miscellaneous exact techniques** 191

6.1 Separation of variables method for spheroids 192
6.2 Finite-element method 193
6.3 Finite-difference time-domain method 195
6.4 Point-matching method 196
6.5 Integral equation methods 197
6.6 Superposition method for compounded spheres and spheroids 201

6.7 Comparison of methods, benchmark results, and computer codes 202
Further reading 205

Chapter 7 **Approximations** 206

7.1 Rayleigh approximation 206
7.2 Rayleigh–Gans approximation 209
7.3 Anomalous diffraction approximation 210
7.4 Geometrical optics approximation 210
7.5 Perturbation theories 221
7.6 Other approximations 222
Further reading 223

Chapter 8 **Measurement techniques** 224

8.1 Measurements in the visible and infrared 224
8.2 Microwave measurements 230

Part III **Scattering and Absorption Properties of Small Particles and Illustrative Applications** 235

Chapter 9 **Scattering and absorption properties of spherical particles** 238

9.1 Monodisperse spheres 238
9.2 Effects of averaging over sizes 250
9.3 Optical cross sections, single-scattering albedo, and asymmetry parameter 252
9.4 Phase function $a_1(\Theta)$ 258
9.5 Backscattering 267
9.6 Other elements of the scattering matrix 271
9.7 Optical characterization of spherical particles 273
Further reading 278

Chapter 10 **Scattering and absorption properties of nonspherical particles** 279

10.1 Interference and resonance structure of scattering patterns for nonspherical particles in a fixed orientation; the effects of orientation and size averaging 279
10.2 Randomly oriented, polydisperse spheroids with moderate aspect ratios 282
10.3 Randomly oriented, polydisperse circular cylinders with moderate aspect ratios 299
10.4 Randomly oriented spheroids and circular cylinders with extreme aspect ratios 307
10.5 Chebyshev particles 319

10.6 Regular polyhedral particles 320
10.7 Irregular particles 322
10.8 Statistical approach 334
10.9 Clusters of spheres 337
10.10 Particles with multiple inclusions 347
10.11 Optical characterization of nonspherical particles 350
Further reading 359

Appendix A Spherical wave expansion of a plane wave in the far-field zone 360
Appendix B Wigner functions, Jacobi polynomials, and generalized spherical functions 362
Appendix C Scalar and vector spherical wave functions 370
Appendix D Clebsch–Gordan coefficients and Wigner 3*j* symbols 380
Appendix E Système International units 384

Abbreviations and symbols 385
References 396
Index 441
Color plate section 449

Preface to the electronic edition

This book was originally published by Cambridge University Press in June of 2002. The entire print run was sold out in less than 16 months, and the book has been officially out of print since October of 2003. By agreement with Cambridge University Press, this electronic edition is intended to make the book continually available via the Internet at the World Wide Web site

http://www.giss.nasa.gov/~crmim/books.html

No significant revision of the text has been attempted; the pagination and the numbering of equations follow those of the original hardcopy edition. However, almost all illustrations have been improved, several typos have been corrected, some minor improvements of the text have been made, and a few recent references have been added.

We express sincere gratitude to Andrew Mishchenko for excellent typesetting and copy-editing work and to Nadia Zakharova and Lilly Del Valle for help with graphics. The preparation of this electronic edition was sponsored by the NASA Radiation Sciences Program managed by Donald Anderson.

We would greatly appreciate being informed of any typos and/or factual inaccuracies that you may find either in the original hardcopy edition of the book or in this electronic release. Please communicate them to Michael Mishchenko at

crmim@giss.nasa.gov

Michael I. Mishchenko
Larry D. Travis
Andrew A. Lacis

New York
November 2006

Preface to the original hardcopy edition

The phenomena of scattering, absorption, and emission of light and other electromagnetic radiation by small particles are ubiquitous and, therefore, central to many science and engineering disciplines. Sunlight incident on the earth's atmosphere is scattered by gas molecules and suspended particles, giving rise to blue skies, white clouds, and various optical displays such as rainbows, coronae, glories, and halos. By scattering and absorbing the incident solar radiation and the radiation emitted by the underlying surface, cloud and aerosol particles affect the earth's radiation budget. The strong dependence of the scattering interaction on particle size, shape, and refractive index makes measurements of electromagnetic scattering a powerful noninvasive means of particle characterization in terrestrial and planetary remote sensing, biomedicine, engineering, and astrophysics. Meaningful interpretation of laboratory and field measurements and remote sensing observations and the widespread need for calculations of reflection, transmission, and emission properties of various particulate media require an understanding of the underlying physics and accurate quantitative knowledge of the electromagnetic interaction as a function of particle physical parameters.

This volume is intended to provide a thorough updated treatment of electromagnetic scattering, absorption, and emission by small particles. Specifically, the book

- introduces a general formalism for the scattering, absorption, and emission of light and other electromagnetic radiation by arbitrarily shaped and arbitrarily oriented particles;
- discusses the relation of radiative transfer theory to single-scattering solutions of Maxwell's equations;
- describes exact theoretical methods and computer codes for calculating the scat-

tering, absorption, and emission properties of arbitrarily shaped small particles;

- demonstrates how the scattering and absorption characteristics of small particles depend on particle size, refractive index, shape, and orientation; and
- illustrates how the high efficiency and accuracy of existing theoretical and experimental techniques and the availability of fast scientific workstations can result in advanced physically based applications.

The book is intended for science professionals, engineers, and graduate students working or specializing in a wide range of disciplines: optics, electromagnetics, optical and electrical engineering, biomedical optics, atmospheric radiation and remote sensing, climate research, radar meteorology, planetary physics, oceanography, and astrophysics. We assume that the reader is familiar with the fundamentals of classical electromagnetics, optics, and vector calculus. Otherwise the book is sufficiently self-contained and provides explicit derivations of all important results. Although not formally a textbook, this volume can be a useful supplement to relevant graduate courses.

The literature on electromagnetic scattering is notorious for discrepancies and inconsistencies in the definition and usage of terms. Among the commonly encountered differences are the use of right-handed as opposed to left-handed coordinate systems, the use of the time-harmonic factor $\exp(-\mathrm{i}\omega t)$ versus $\exp(\mathrm{i}\omega t)$, and the way an angle of rotation is defined. Because we extensively employ mathematical techniques of the quantum theory of angular momentum and because we wanted to make the book self-consistent, we use throughout only right-handed (spherical) coordinate systems and always consider an angle of rotation positive if the rotation is performed in the *clockwise* direction when one is looking in the positive direction of the rotation axis (or in the direction of light propagation). Also, we adopt the time-harmonic factor $\exp(-\mathrm{i}\omega t)$, which seems to be the preferred choice in the majority of publications and implies a non-negative imaginary part of the relative refractive index.

Because the subject of electromagnetic scattering crosses the boundaries between many disciplines, it was very difficult to develop a clear and unambiguous notation system. In many cases we found that the conventional symbol for a quantity in one discipline was the same as the conventional symbol for a different quantity in another discipline. Although we have made an effort to reconcile tradition and simplicity with the desire of having a unique symbol for every variable, some symbols ultimately adopted for the book still represent more than one variable. We hope, however, that the meaning of all symbols is clear from the context. We denote vectors using the Times bold font and matrices using the Arial bold or bold italic font. Unit vectors are denoted by a caret, whereas tensors, dyads, and dyadics are denoted by the dyadic symbol $\leftrightarrow$. The Times italic font is usually reserved for scalar variables. However, the square root of minus one, the base of natural logarithms, and the differential sign are denoted by Times roman (upright) characters i, e, and d, respectively.

A table containing the symbols used, their meaning and dimension, and the section where they first appear is provided at the end of the book, to assist the reader.

We have not attempted to compile a comprehensive list of relevant publications and often cite a book or a review article where further references can be found. In this regard, two books deserve to be mentioned specifically. The monograph by Kerker (1969) provides a list of nearly a thousand papers on light scattering published prior to 1970, while the recent book edited by Mishchenko *et al*. (2000a) lists nearly 1400 publications on all aspects of electromagnetic scattering by nonspherical and heterogeneous particles.

We provide references to many relevant computer programs developed by various research groups and individuals, including ourselves, and made publicly available through the Internet. Easy accessibility of these programs can be beneficial both to individuals who are mostly interested in applications and to those looking for sources of benchmark results for testing their own codes. Although the majority of these programs have been extensively tested and are expected to generate reliable results in most cases provided that they are used as instructed, it is not inconceivable that some of them contain errors or idiosyncrasies. Furthermore, input parameters can be used that are outside the range of values for which results can be computed accurately. For these reasons the authors of this book and the publisher disclaim all liability for any damage that may result from the use of the programs. In addition, although the publisher and the authors have used their best endeavors to ensure that the URLs for the external websites referred to in this book are correct and active at the time of going to press, the publisher and the authors have no responsibility for the websites and can make no guarantee that a site will remain live or that the content is or will remain appropriate.

Michael I. Mishchenko
Larry D. Travis
Andrew A. Lacis

New York
November 2001

Acknowledgments

Our efforts to understand electromagnetic scattering and its role in remote sensing and atmospheric radiation better have been generously funded over the years by research grants from the United States Government. We thankfully acknowledge the continuing support from the NASA Earth Observing System Program and the Department of Energy Atmospheric Radiation Measurement Program. The preparation of this book was sponsored by a grant from the NASA Radiation Sciences Program managed by Donald Anderson.

We have greatly benefited from extensive discussions with Oleg Bugaenko, Brian Cairns, Barbara Carlson, Helmut Domke, Kirk Fuller, James Hansen, Joop Hovenier, Vsevolod Ivanov, Kuo-Nan Liou, Kari Lumme, Andreas Macke, Daniel Mackowski, Alexander Morozhenko, William Rossow, Kenneth Sassen, Cornelis van der Mee, Bart van Tiggelen, Gorden Videen, Tõnu Viik, Hester Volten, Ping Yang, Edgard Yanovitskij, and many other colleagues.

We thank Cornelis van der Mee and Joop Hovenier for numerous comments which resulted in a much improved manuscript. Our computer codes have benefited from comments and suggestions made by Michael Wolff, Raphael Ruppin, and many other individuals using the codes in their research. We thank Lilly Del Valle for contributing excellent drawings and Zoe Wai and Josefina Mora for helping to find papers and books that were not readily accessible.

We acknowledge with many thanks the fine cooperation that we received from the staff of Cambridge University Press. We are grateful to Matt Lloyd, Jacqueline Garget, and Jane Aldhouse for their patience, encouragement, and help and to Susan Parkinson for careful copy-editing work.

Our gratitude is deepest, however, to Nadia Zakharova who provided invaluable

assistance at all stages of preparing this book and contributed many numerical results and almost all the computer graphics.

Part I

Basic Theory of Electromagnetic Scattering, Absorption, and Emission

A parallel monochromatic beam of light propagates in a vacuum without any change in its intensity or polarization state. However, interposing a small particle into the beam, as illustrated in panel (a) of the diagram on the next page, causes several distinct effects. First, the particle may convert some of the energy contained in the beam into other forms of energy such as heat. This phenomenon is called *absorption*. Second, it extracts some of the incident energy and scatters it in all directions at the frequency of the incident beam. This phenomenon is called *elastic scattering* and, in general, gives rise to light with a polarization state different from that of the incident beam. As a result of absorption and scattering, the energy of the incident beam is reduced by an amount equal to the sum of the absorbed and scattered energy. This reduction is called *extinction*. The extinction rates for different polarization components of the incident beam can be different. This phenomenon is called *dichroism* and may cause a change in the polarization state of the beam after it passes the particle. In addition, if the absolute temperature of the particle is not equal to zero, then the particle also emits radiation in all directions and at all frequencies, the distribution by frequency being dependent on the temperature. This phenomenon is called *thermal emission*.

In electromagnetic terms, the parallel monochromatic beam of light is an oscillating plane electromagnetic wave, whereas the particle is an aggregation of a large number of discrete elementary electric charges. The oscillating electromagnetic field of the incident wave excites the charges to oscillate with the same frequency and thereby radiate secondary electromagnetic waves. The superposition of the secondary waves gives the total elastically scattered field. If the charges do not oscillate exactly in phase or exactly in anti-phase with the incident field then there is dissipation of electromagnetic energy into the object. This means that the object is absorbing and scatters less total energy than it extracts from the incident wave. The combined effect of scattering and absorption is to reduce the amount of energy contained in the incident wave. If the absolute temperature of the particle differs from zero, electron transitions from a higher to a lower energy level cause thermal emission of electromagnetic energy at specific frequencies. For complex systems of molecules with a large number of degrees of freedom, many different transitions produce spectral emission lines so closely spaced that the resulting radiation spectrum becomes effectively continuous and includes emitted energy at all frequencies.

Electromagnetic scattering is a complex phenomenon because the secondary waves generated by each oscillating charge also stimulate oscillations of all other charges forming the particle. Furthermore, computation of the total scattered field by superposing the secondary waves must take account of their phase differences, which change every time the incidence and/or scattering direction is changed. Therefore, the total scattered radiation depends on the way the charges are arranged to form the particle with respect to the incident and scattered directions.

Since the number of elementary charges forming a micrometer-sized particle is extremely large, solving the scattering problem directly by computing and superposing all secondary waves is impracticable even with the aid of modern computers. Fortunately, however, the same problem can be solved using the concepts of macro-

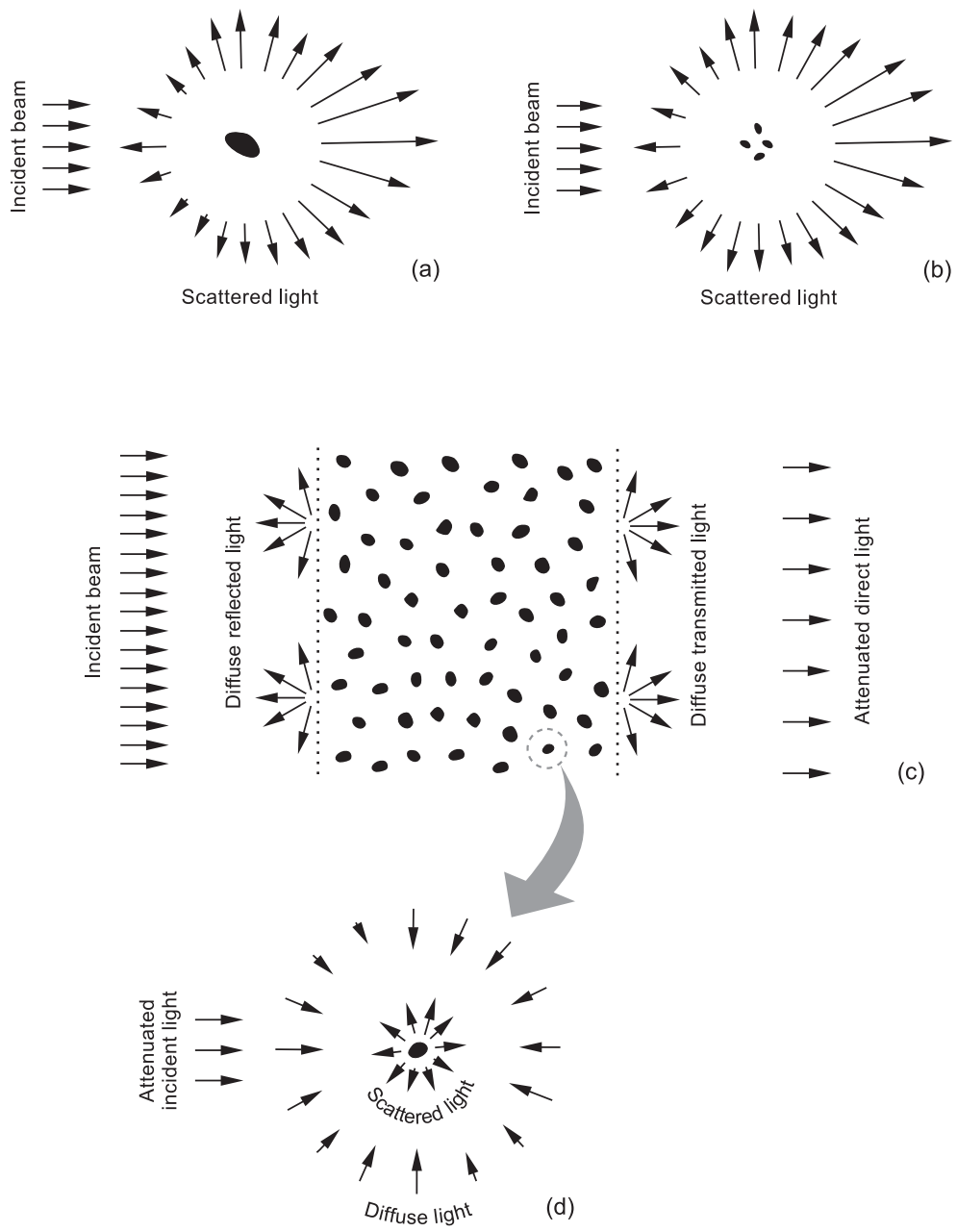

In (a), (b), and (c) a parallel beam of light is incident from the left. (a) Far-field electromagnetic scattering by an individual particle in the form of a single body or a fixed cluster. (b) Far-field scattering by a small volume element composed of randomly positioned, widely separated particles. (c) Multiple scattering by a layer of randomly and sparsely distributed particles. On the left of the layer, diffuse reflected light; on the right of the layer, diffuse transmitted light. On the far right, the attenuated incident beam. (d) Each individual particle in the layer receives and scatters both light from the incident beam, somewhat attenuated, and light diffusely scattered from the other particles.

scopic electromagnetics, which treat the large collection of charges as a macroscopic body with a specific distribution of the refractive index. In this case the scattered field can be computed by solving the Maxwell equations for the macroscopic electromagnetic field subject to appropriate boundary conditions. This approach appears to be quite manageable and forms the basis of the modern theory of electromagnetic scattering by small particles.

We do not aim to cover all aspects of electromagnetic scattering and absorption by a small particle and limit our treatment by imposing several well-defined restrictions, as follows.

- We consider only the scattering of time-harmonic, monochromatic or quasi-monochromatic light in that we assume that the amplitude of the incident electric field is either constant or fluctuates with time much more slowly than the time factor $\exp(-\mathrm{i}\omega t)$, where ω is the angular frequency and t is time.
- It is assumed that electromagnetic scattering occurs without frequency redistribution, i.e., the scattered light has the same frequency as the incident light. This restriction excludes inelastic scattering phenomena such as Raman and Brillouin scattering and fluorescence.
- We consider only finite scattering particles and exclude such peculiar two-dimensional scatterers as infinite cylinders.
- It is assumed that the unbounded host medium surrounding the scatterer is homogeneous, linear, isotropic, and nonabsorbing.
- We study only scattering in the far-field zone, where the propagation of the scattered wave is away from the particle, the electric field vector vibrates in the plane perpendicular to the propagation direction, and the scattered field amplitude decays inversely with distance from the particle.

By directly solving the Maxwell equations, one can find the field scattered by an object in the form of a single body or a fixed cluster consisting of a limited number of components. However, one often encounters situations in which light is scattered by a very large group of particles forming a constantly varying spatial configuration. A typical example is a cloud of water droplets or ice crystals in which the particles are constantly moving, spinning, and even changing their shapes and sizes due to oscillations of the droplet surface, evaporation, condensation, sublimation, and melting. Although such a particle collection can be treated at each given moment as a fixed cluster, a typical measurement of light scattering takes a finite amount of time, over which the spatial configuration of the component particles and their sizes, orientations, and/or shapes continuously and randomly change. Therefore, the registered signal is in effect a statistical average over a large number of different cluster realizations.

A logical way of modeling the measurement of light scattering by a random collection of particles would be to solve the Maxwell equations for a statistically representative range of fixed clusters and then take the average. However, this approach becomes prohibitively time consuming if the number of cluster components is large and is impractical for objects such as clouds in planetary atmospheres, oceanic hydro-

sols, or stellar dust envelopes. Moreover, in the traditional far-field scattering formalism a cluster is treated as a single scatterer and it is assumed that the distance from the cluster to the observation point is much larger than any linear dimension of the cluster. This assumption may well be violated in laboratory and remote sensing measurements, thereby making necessary explicit computations of the scattered light in the near-field zone of the cluster as a whole.

Fortunately, particles forming a random group can often be considered as independent scatterers. This means that the electromagnetic response of each particle in the group can be calculated using the extinction and phase matrices that describe the scattering of a plane electromagnetic wave by the same particle but placed in an infinite homogeneous space in complete isolation from all other particles (panel (a) of the diagram). In general, this becomes possible when (i) each particle resides in the far-field zones of all the other particles forming the group, and (ii) scattering by individual particles is incoherent, i.e., there are no systematic phase relations between partial waves scattered by individual particles during the time interval necessary to take the measurement. As a consequence of condition (ii), the intensities (or, more generally, the Stokes parameters) of the partial waves can be added without regard to phase. An important exception is scattering in the exact forward direction, which is always coherent and causes attenuation of the incident wave.

The assumption of independent scattering greatly simplifies the problem of computing light scattering by groups of randomly positioned, widely separated particles. Consider first the situation when a plane wave illuminates a small volume element containing a tenuous particle collection, as depicted schematically in panel (b) of the diagram. Each particle is excited by the external field and the secondary fields scattered by all other particles. However, if the number of particles is sufficiently small and their separation is sufficiently large then the contribution of the secondary waves to the field exciting each particle is much smaller than the external field. Therefore, the total scattered field can be well approximated by the sum of the fields generated by the individual particles in response to the external field in isolation from the other particles. This approach is called the single-scattering approximation. By assuming also that particle positions are sufficiently random, one can show that the optical cross sections and the extinction and phase matrices of the volume element are obtained by simply summing the respective characteristics of all constituent particles.

When the scattering medium contains very many particles, the single-scattering approximation is no longer valid. Now one must explicitly take into account that each particle is illuminated by light scattered by other particles as well as by the (attenuated) incident light, as illustrated in panels (c) and (d) of the diagram. This means that each particle scatters light that has already been scattered by other particles, so that the light inside the scattering medium and the light leaving the medium have a significant *multiply scattered* (or *diffuse*) component. A traditional approach in this case is to find the intensity and other Stokes parameters of the diffuse light by solving the so-called radiative transfer equation. This technique still assumes that particles forming the scattering medium are randomly positioned and widely separated and that the extinction and phase matrices of each small volume element can be obtained by inco-

herently adding the respective characteristics of the constituent particles.

Thus, the treatment of light scattering by a large group of randomly positioned, widely separated particles can be partitioned into three consecutive steps:

- computation of the far-field scattering and absorption properties of an individual particle by solving the Maxwell equations;
- computation of the scattering and absorption properties of a small volume element containing a tenuous particle collection by using the single-scattering approximation; and
- computation of multiple scattering by the entire particle group by solving the radiative transfer equation supplemented by appropriate boundary conditions.

Although the last two steps are inherently approximate, they are far more practicable than attempting to solve the Maxwell equations for large particle collections and usually provide results accurate enough for many applications. A notable exception is the exact backscattering direction, where so-called self-avoiding reciprocal multiple-scattering paths in the particle collection always interfere constructively and cause a coherent intensity peak. This phenomenon is called coherent backscattering (or weak photon localization) and is not explicitly described by the standard radiative transfer theory.

When a group of randomly moving and spinning particles is illuminated by a monochromatic, spatially coherent plane wave (e.g., laser light), the random constructive and destructive interference of the light scattered by individual particles generates in the far-field zone a speckle pattern that fluctuates in time and space. In this book we eliminate the effect of fluctuations by assuming that the Stokes parameters of the scattered light are averaged over a period of time much longer than the typical period of the fluctuations. In other words, we deal with the average, *static* component of the scattering pattern. Therefore, the subject of the book could be called static light scattering. Although explicit measurements of the spatial and temporal fluctuations of the speckle pattern are more complicated than measurements of the averages, they can contain useful information about the particles complementary to that carried by the mean Stokes parameters. Statistical analyses of light scattered by systems of suspended particles are the subject of the discipline called photon correlation spectroscopy (or dynamic light scattering) and form the basis of many well established experimental techniques. For example, instruments for the measurement of particle size and dispersity and laser Doppler velocimeters and transit anemometers have been commercially available for many years. More recent research has demonstrated the application of polarization fluctuation measurements to particle shape characterization (Pitter *et al*. 1999; Jakeman 2000). Photon correlation spectroscopy is not discussed in this volume; the interested reader can find the necessary information in the books by Cummins and Pike (1974, 1977), Pecora (1985), Brown (1993), Pike and Abbiss (1997), and Berne and Pecora (2000) as well as in the recent feature issues of *Applied Optics* edited by Meyer *et al.* (1997, 2001).

Chapter 1

Polarization characteristics of electromagnetic radiation

The analytical and numerical basis for describing scattering properties of media composed of small discrete particles is formed by the classical electromagnetic theory. Although there are several excellent textbooks outlining the fundamentals of this theory, it is convenient for our purposes to begin with a summary of those concepts and equations that are central to the subject of this book and will be used extensively in the following chapters.

We start by formulating Maxwell's equations and constitutive relations for time-harmonic macroscopic electromagnetic fields and derive the simplest plane-wave solution, which underlies the basic optical idea of a monochromatic parallel beam of light. This solution naturally leads to the introduction of such fundamental quantities as the refractive index and the Stokes parameters. Finally, we define the concept of a quasi-monochromatic beam of light and discuss its implications.

1.1 Maxwell's equations, time-harmonic fields, and the Poynting vector

The mathematical description of all classical optics phenomena is based on the set of Maxwell's equations for the macroscopic electromagnetic field at interior points in matter, which in SI units are as follows (Jackson 1998):

$$\nabla \cdot \mathbf{D} = \rho, \tag{1.1}$$

$$\nabla \times \mathbf{E} = -\frac{\partial \mathbf{B}}{\partial t}, \tag{1.2}$$

$$\nabla \cdot \mathbf{B} = 0, \tag{1.3}$$

$$\nabla \times \mathbf{H} = \mathbf{J} + \frac{\partial \mathbf{D}}{\partial t}, \tag{1.4}$$

where t is time, **E** the electric and **H** the magnetic field, **B** the magnetic induction, **D** the electric displacement, and ρ and **J** the macroscopic (free) charge density and current density, respectively. All quantities entering Eqs. (1.1)–(1.4) are functions of time and spatial coordinates. Implicit in the Maxwell equations is the continuity equation

$$\frac{\partial \rho}{\partial t} + \nabla \cdot \mathbf{J} = 0, \tag{1.5}$$

which can be derived by combining the time derivative of Eq. (1.1) with the divergence of Eq. (1.4). The vector fields entering Eqs. (1.1)–(1.4) are related by

$$\mathbf{D} = \varepsilon_0 \mathbf{E} + \mathbf{P}, \tag{1.6}$$

$$\mathbf{H} = \frac{1}{\mu_0} \mathbf{B} - \mathbf{M}, \tag{1.7}$$

where **P** is the electric polarization (average electric dipole moment per unit volume), **M** is the magnetization (average magnetic dipole moment per unit volume), and ε_0 and μ_0 are the electric permittivity and the magnetic permeability of free space. Equations (1.1)–(1.7) are insufficient for a unique determination of the electric and magnetic fields from a given distribution of charges and currents and must be supplemented with so-called constitutive relations:

$$\mathbf{J} = \sigma \mathbf{E}, \tag{1.8}$$

$$\mathbf{B} = \mu \mathbf{H}, \tag{1.9}$$

$$\mathbf{P} = \varepsilon_0 \chi \mathbf{E}, \tag{1.10}$$

where σ is the conductivity, μ the permeability, and χ the electric susceptibility. For linear and isotropic media, σ, μ, and χ are scalars independent of the fields. The microphysical derivation and the range of validity of the macroscopic Maxwell equations are discussed in detail by Jackson (1998).

The Maxwell equations are strictly valid only for points in whose neighborhood the physical properties of the medium, as characterized by σ, μ, and χ, vary continuously. Across an interface separating one medium from another the field vectors **E**, **D**, **B**, and **H** may be discontinuous. The boundary conditions at such an interface can be derived from the integral equivalents of the Maxwell equations (Jackson 1998) and are as follows:

1. There is a discontinuity in the normal component of **D**:

$$(\mathbf{D}_2 - \mathbf{D}_1) \cdot \hat{\mathbf{n}} = \rho_S, \tag{1.11}$$

where $\hat{\mathbf{n}}$ is the unit vector directed along the local normal to the interface separating media 1 and 2 and pointing toward medium 2 and ρ_S is the surface charge density (the charge per unit area).

2. There is a discontinuity in the tangential component of **H**:

$$\hat{\mathbf{n}}\times(\mathbf{H}_2-\mathbf{H}_1)=\mathbf{J}_S, \tag{1.12}$$

where $\mathbf{J}_S$ is the surface current density. However, media with finite conductivity cannot support surface currents, so that

$$\hat{\mathbf{n}}\times(\mathbf{H}_2-\mathbf{H}_1)=0 \quad \text{(finite conductivity)}. \tag{1.13}$$

3. The normal component of **B** and the tangential component of **E** are continuous:

$$(\mathbf{B}_2-\mathbf{B}_1)\cdot\hat{\mathbf{n}}=0, \tag{1.14}$$

$$\hat{\mathbf{n}}\times(\mathbf{E}_2-\mathbf{E}_1)=0. \tag{1.15}$$

The boundary conditions (1.11)–(1.15) are useful in solving the Maxwell equations in different adjacent regions with continuous physical properties and then linking the partial solutions to determine the fields throughout all space.

We assume that all fields and sources are time-harmonic and adopt the standard practice of representing real time-dependent fields as real parts of the respective complex fields, viz.,

$$\mathbf{E}(\mathbf{r},t)=\mathrm{Re}\,\mathbf{E}_{\mathrm{c}}(\mathbf{r},t)=\mathrm{Re}[\mathbf{E}(\mathbf{r})\mathrm{e}^{-\mathrm{i}\omega t}]\equiv\tfrac{1}{2}[\mathbf{E}(\mathbf{r})\mathrm{e}^{-\mathrm{i}\omega t}+\mathbf{E}^*(\mathbf{r})\mathrm{e}^{\mathrm{i}\omega t}], \tag{1.16}$$

where **r** is the position (radius) vector, ω the angular frequency, $\mathrm{i}=\sqrt{-1}$, and the asterisk denotes a complex-conjugate value. Then we can derive from Eqs. (1.1)–(1.10)

$$\nabla\cdot\mathbf{D}(\mathbf{r})=\rho(\mathbf{r}) \quad \text{or} \quad \nabla\cdot[\varepsilon\mathbf{E}(\mathbf{r})]=0, \tag{1.17}$$

$$\nabla\times\mathbf{E}(\mathbf{r})=\mathrm{i}\omega\mu\mathbf{H}(\mathbf{r}), \tag{1.18}$$

$$\nabla\cdot[\mu\mathbf{H}(\mathbf{r})]=0, \tag{1.19}$$

$$\nabla\times\mathbf{H}(\mathbf{r})=\mathbf{J}(\mathbf{r})-\mathrm{i}\omega\mathbf{D}(\mathbf{r})=-\mathrm{i}\omega\varepsilon\mathbf{E}(\mathbf{r}), \tag{1.20}$$

where

$$\varepsilon=\varepsilon_0(1+\chi)+\mathrm{i}\frac{\sigma}{\omega} \tag{1.21}$$

is the (complex) permittivity. Under the complex time-harmonic representation, the constitutive coefficients σ, μ, and χ can be frequency dependent and are not restricted to be real (Jackson 1998). For example, a complex permeability implies a difference in phase between the real time-harmonic magnetic field **H** and the corresponding real time-harmonic magnetic induction **B**. We will show later that complex ε and/or μ results in a non-zero imaginary part of the refractive index, Eq. (1.44),

thereby causing the absorption of electromagnetic energy, Eq. (1.45), by converting it into other forms of energy such as heat.

Note that the scalar or the vector product of two real vector fields is not equal to the real part of the respective product of the corresponding complex vector fields. Instead we have

$$\begin{aligned} c(\mathbf{r},t) &= \mathbf{a}(\mathbf{r},t)\cdot\mathbf{b}(\mathbf{r},t) \\ &= \tfrac{1}{4}[\mathbf{a}(\mathbf{r})\mathrm{e}^{-\mathrm{i}\omega t}+\mathbf{a}^*(\mathbf{r})\mathrm{e}^{\mathrm{i}\omega t}]\cdot[\mathbf{b}(\mathbf{r})\mathrm{e}^{-\mathrm{i}\omega t}+\mathbf{b}^*(\mathbf{r})\mathrm{e}^{\mathrm{i}\omega t}] \\ &= \tfrac{1}{2}\mathrm{Re}[\mathbf{a}(\mathbf{r})\cdot\mathbf{b}^*(\mathbf{r})+\mathbf{a}(\mathbf{r})\cdot\mathbf{b}(\mathbf{r})\mathrm{e}^{-2\mathrm{i}\omega t}] \end{aligned} \tag{1.22}$$

and similarly for a vector product. A common situation in practice is that the angular frequency ω is so high that a measuring instrument is not capable of following the rapid oscillations of the instantaneous product values but rather responds to a time average

$$\langle c(\mathbf{r})\rangle = \frac{1}{\Delta t}\int_t^{t+\Delta t}\mathrm{d}t' c(\mathbf{r},t'), \tag{1.23}$$

where Δt is a time interval long compared with $1/\omega$. Therefore, it follows from Eq. (1.22) that for time averages of products, one must take the real part of the product of one complex field with the complex conjugate of the other, e.g.,

$$\langle c(\mathbf{r})\rangle = \tfrac{1}{2}\mathrm{Re}[\mathbf{a}(\mathbf{r})\cdot\mathbf{b}^*(\mathbf{r})]. \tag{1.24}$$

The flow of the electromagnetic energy is described by the so-called Poynting vector **S**. The expression for **S** can be derived by considering the conservation of energy and taking into account that the magnetic field can do no work and that for a local charge q the rate of doing work by the electric field is $q(\mathbf{r})\mathbf{v}(\mathbf{r})\cdot\mathbf{E}(\mathbf{r},t)$, where **v** is the velocity of the charge. Accordingly, consider the integral

$$\frac{1}{2}\int_V \mathrm{d}V\,\mathbf{J}^*(\mathbf{r})\cdot\mathbf{E}(\mathbf{r}) \tag{1.25}$$

over a finite volume V, whose real part gives the time-averaged rate of work done by the electromagnetic field and which must be balanced by the corresponding rate of decrease of the electromagnetic energy within V. Using Eqs. (1.18) and (1.20) and the vector identity

$$\nabla\cdot(\mathbf{a}\times\mathbf{b}) = \mathbf{b}\cdot(\nabla\times\mathbf{a})-\mathbf{a}\cdot(\nabla\times\mathbf{b}), \tag{1.26}$$

we derive

$$\begin{aligned} \frac{1}{2}\int_V \mathrm{d}V\,\mathbf{J}^*(\mathbf{r})\cdot\mathbf{E}(\mathbf{r}) &= \frac{1}{2}\int_V \mathrm{d}V\,\mathbf{E}(\mathbf{r})\cdot[\nabla\times\mathbf{H}^*(\mathbf{r})-\mathrm{i}\omega\mathbf{D}^*(\mathbf{r})] \\ &= \frac{1}{2}\int_V \mathrm{d}V\{-\nabla\cdot[\mathbf{E}(\mathbf{r})\times\mathbf{H}^*(\mathbf{r})]-\mathrm{i}\omega[\mathbf{E}(\mathbf{r})\cdot\mathbf{D}^*(\mathbf{r})-\mathbf{B}(\mathbf{r})\cdot\mathbf{H}^*(\mathbf{r})]\}. \end{aligned} \tag{1.27}$$

If we now define the complex Poynting vector

$$\mathbf{S}(\mathbf{r}) = \tfrac{1}{2}[\mathbf{E}(\mathbf{r}) \times \mathbf{H}^*(\mathbf{r})] \tag{1.28}$$

and the harmonic electric and magnetic energy densities

$$w_{\mathrm{e}}(\mathbf{r}) = \tfrac{1}{4}[\mathbf{E}(\mathbf{r}) \cdot \mathbf{D}^*(\mathbf{r})], \qquad w_{\mathrm{m}}(\mathbf{r}) = \tfrac{1}{4}[\mathbf{B}(\mathbf{r}) \cdot \mathbf{H}^*(\mathbf{r})], \tag{1.29}$$

and use the Gauss theorem, we have instead of Eq. (1.27)

$$\frac{1}{2}\int_V \mathrm{d}V\, \mathbf{J}^*(\mathbf{r}) \cdot \mathbf{E}(\mathbf{r}) + \int_S \mathrm{d}S\, \mathbf{S}(\mathbf{r}) \cdot \hat{\mathbf{n}} + 2\mathrm{i}\omega \int_V \mathrm{d}V [w_{\mathrm{e}}(\mathbf{r}) - w_{\mathrm{m}}(\mathbf{r})] = 0, \tag{1.30}$$

where the closed surface S bounds the volume V and $\hat{\mathbf{n}}$ is a unit vector in the direction of the local outward normal to the surface. The real part of Eq. (1.30) manifests the conservation of energy for the time-averaged quantities by requiring that the rate of the total work done by the fields on the sources within the volume, the electromagnetic energy flowing out through the volume boundary per unit time, and the time rate of change of the electromagnetic energy within the volume add up to zero. The time-averaged Poynting vector $\langle \mathbf{S}(\mathbf{r}) \rangle$ is equal to the real part of the complex Poynting vector,

$$\langle \mathbf{S}(\mathbf{r}) \rangle = \mathrm{Re}[\mathbf{S}(\mathbf{r})],$$

and has the dimension of [energy/(area$\times$ time)]. The net rate W at which the electromagnetic energy crosses the surface S is

$$W = -\int_S \mathrm{d}S\, \langle \mathbf{S}(\mathbf{r}) \rangle \cdot \hat{\mathbf{n}}. \tag{1.31}$$

The rate is positive if there is a net transfer of electromagnetic energy into the volume V and is negative otherwise.

1.2 Plane-wave solution

A fundamental feature of the Maxwell equations is that they allow for a simple traveling-wave solution, which represents the transport of electromagnetic energy from one point to another and embodies the concept of a perfectly monochromatic parallel beam of light. This solution is a plane electromagnetic wave propagating in a *homogeneous* medium without sources and is given by

$$\mathbf{E}_{\mathrm{c}}(\mathbf{r}, t) = \mathbf{E}_0 \exp(\mathrm{i}\mathbf{k} \cdot \mathbf{r} - \mathrm{i}\omega t), \qquad \mathbf{H}_{\mathrm{c}}(\mathbf{r}, t) = \mathbf{H}_0 \exp(\mathrm{i}\mathbf{k} \cdot \mathbf{r} - \mathrm{i}\omega t), \tag{1.32}$$

where $\mathbf{E}_0$ and $\mathbf{H}_0$ are constant complex vectors. The wave vector $\mathbf{k}$ is also constant and may, in general, be complex:

$$\mathbf{k} = \mathbf{k}_{\mathrm{R}} + \mathrm{i}\mathbf{k}_{\mathrm{I}}, \tag{1.33}$$

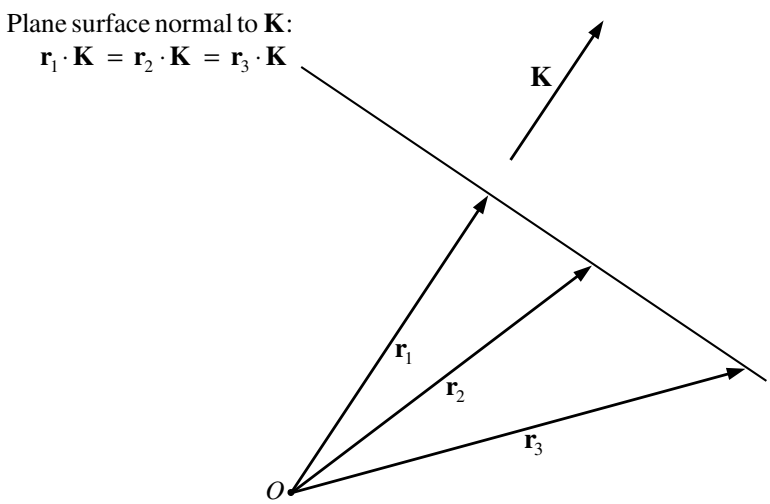

Figure 1.1. Plane surface normal to a real vector **K**.

where $\mathbf{k}_\mathrm{R}$ and $\mathbf{k}_\mathrm{I}$ are real vectors. We thus have

$$\mathbf{E}_\mathrm{c}(\mathbf{r}, t) = \mathbf{E}_0 \exp(-\mathbf{k}_\mathrm{I} \cdot \mathbf{r}) \exp(\mathrm{i}\mathbf{k}_\mathrm{R} \cdot \mathbf{r} - \mathrm{i}\omega t), \tag{1.34}$$

$$\mathbf{H}_\mathrm{c}(\mathbf{r}, t) = \mathbf{H}_0 \exp(-\mathbf{k}_\mathrm{I} \cdot \mathbf{r}) \exp(\mathrm{i}\mathbf{k}_\mathrm{R} \cdot \mathbf{r} - \mathrm{i}\omega t). \tag{1.35}$$

$\mathbf{E}_0 \exp(-\mathbf{k}_\mathrm{I} \cdot \mathbf{r})$ and $\mathbf{H}_0 \exp(-\mathbf{k}_\mathrm{I} \cdot \mathbf{r})$ are the amplitudes of the electric and magnetic waves, respectively, while $\mathbf{k}_\mathrm{R} \cdot \mathbf{r} - \omega t$ is their phase. Obviously, $\mathbf{k}_\mathrm{R}$ is normal to the surfaces of constant phase, whereas $\mathbf{k}_\mathrm{I}$ is normal to the surfaces of constant amplitude. (A plane surface normal to a real vector **K** is defined as $\mathbf{r} \cdot \mathbf{K} = \text{constant}$, where **r** is the radius vector drawn from the origin of the reference frame to any point in the plane; see Fig. 1.1.) Surfaces of constant phase propagate in the direction of $\mathbf{k}_\mathrm{R}$ with the phase velocity $v = \omega/|\mathbf{k}_\mathrm{R}|$. The electromagnetic wave is called homogeneous when $\mathbf{k}_\mathrm{R}$ and $\mathbf{k}_\mathrm{I}$ are parallel (including the case $\mathbf{k}_\mathrm{I} = 0$); otherwise it is called inhomogeneous. When $\mathbf{k}_\mathrm{R} \| \mathbf{k}_\mathrm{I}$, the complex wave vector can be written as $\mathbf{k} = (k_\mathrm{R} + \mathrm{i}k_\mathrm{I})\hat{\mathbf{n}}$, where $\hat{\mathbf{n}}$ is a real unit vector in the direction of propagation and both k_R and k_I are real and non-negative.

The Maxwell equations for the plane wave take the form

$$\mathbf{k} \cdot \mathbf{E}_0 = 0, \tag{1.36}$$

$$\mathbf{k} \cdot \mathbf{H}_0 = 0, \tag{1.37}$$

$$\mathbf{k} \times \mathbf{E}_0 = \omega\mu\mathbf{H}_0, \tag{1.38}$$

$$\mathbf{k} \times \mathbf{H}_0 = -\omega\varepsilon\mathbf{E}_0. \tag{1.39}$$

The first two equations indicate that the plane electromagnetic wave is transverse: both $\mathbf{E}_0$ and $\mathbf{H}_0$ are perpendicular to **k**. Furthermore, it is evident from Eq. (1.38) or (1.39) that $\mathbf{E}_0$ and $\mathbf{H}_0$ are mutually perpendicular: $\mathbf{E}_0 \cdot \mathbf{H}_0 = 0$. Since $\mathbf{E}_0$, $\mathbf{H}_0$, and $\mathbf{k}$ are, in general, complex vectors, the physical interpretation of these facts can be far from obvious. It becomes most transparent when ε, μ, and $\mathbf{k}$ are real. The

reader can verify that in this case the real field vectors **E** and **H** are mutually perpendicular and lie in a plane normal to the direction of wave propagation.

Equations (1.32) and (1.38) yield $\mathbf{H}_{\mathrm{c}}(\mathbf{r},t)=(\omega\mu)^{-1}\,\mathbf{k}\times\mathbf{E}_{\mathrm{c}}(\mathbf{r},t)$. Therefore, a plane electromagnetic wave can always be considered in terms of only the electric (or only the magnetic) field.

By taking the vector product of both sides of Eq. (1.38) with **k** and using Eq. (1.39) and the vector identity

$$\mathbf{a}\times(\mathbf{b}\times\mathbf{c})=\mathbf{b}(\mathbf{a}\cdot\mathbf{c})-\mathbf{c}(\mathbf{a}\cdot\mathbf{b}), \tag{1.40}$$

together with Eq. (1.36), we derive

$$\mathbf{k}\cdot\mathbf{k}=\omega^2\varepsilon\mu. \tag{1.41}$$

In the practically important case of a homogeneous plane wave, we obtain from Eq. (1.41)

$$k=k_{\mathrm{R}}+\mathrm{i}k_{\mathrm{I}}=\omega\sqrt{\varepsilon\mu}=\frac{\omega m}{c}, \tag{1.42}$$

where k is the wave number,

$$c=\frac{1}{\sqrt{\varepsilon_0\mu_0}} \tag{1.43}$$

is the speed of light in a vacuum, and

$$m=m_{\mathrm{R}}+\mathrm{i}m_{\mathrm{I}}=\sqrt{\frac{\varepsilon\mu}{\varepsilon_0\mu_0}}=c\sqrt{\varepsilon\mu} \tag{1.44}$$

is the complex refractive index with non-negative real part m_{R} and non-negative imaginary part m_{I}. Thus, the plane homogeneous wave has the form

$$\mathbf{E}_{\mathrm{c}}(\mathbf{r},t)=\mathbf{E}_0\exp\left(-\frac{\omega}{c}m_{\mathrm{I}}\hat{\mathbf{n}}\cdot\mathbf{r}\right)\exp\left(\mathrm{i}\frac{\omega}{c}m_{\mathrm{R}}\hat{\mathbf{n}}\cdot\mathbf{r}-\mathrm{i}\omega t\right). \tag{1.45}$$

If the imaginary part of the refractive index is non-zero, then it determines the decay of the amplitude of the wave as it propagates through the medium, which is thus absorbing. The real part of the refractive index determines the phase velocity of the wave: $v=c/m_{\mathrm{R}}$. For a vacuum, $m=m_{\mathrm{R}}=1$ and $v=c$.

As follows from Eqs. (1.28), (1.32), (1.38), and (1.40), the time-averaged Poynting vector of a plane wave is

$$\begin{aligned}\langle\mathbf{S}(\mathbf{r})\rangle&=\tfrac{1}{2}\mathrm{Re}[\mathbf{E}(\mathbf{r})\times\mathbf{H}^*(\mathbf{r})]\\&=\mathrm{Re}\left\{\frac{\mathbf{k}^*[\mathbf{E}(\mathbf{r})\cdot\mathbf{E}^*(\mathbf{r})]-\mathbf{E}^*(\mathbf{r})[\mathbf{k}^*\cdot\mathbf{E}(\mathbf{r})]}{2\omega\mu^*}\right\}.\end{aligned} \tag{1.46}$$

If the wave is homogeneous, then $\mathbf{k}\cdot\mathbf{E}=0$ and so $\mathbf{k}^*\cdot\mathbf{E}=0$, and

$$\langle \mathbf{S}(\mathbf{r})\rangle = \tfrac{1}{2}\mathrm{Re}\left\{\sqrt{\frac{\varepsilon}{\mu}}\right\}|\mathbf{E}_0|^2 \exp\left(-2\frac{\omega}{c}m_{\mathrm{I}}\hat{\mathbf{n}}\cdot\mathbf{r}\right)\hat{\mathbf{n}}. \tag{1.47}$$

Thus, $\langle \mathbf{S}(\mathbf{r})\rangle$ is in the direction of propagation and its absolute value $I(\mathbf{r}) = |\langle \mathbf{S}(\mathbf{r})\rangle|$, usually called the intensity (or irradiance), is exponentially attenuated provided that the medium is absorbing:

$$I(\mathbf{r}) = I_0 \mathrm{e}^{-\alpha\hat{\mathbf{n}}\cdot\mathbf{r}}, \tag{1.48}$$

where I_0 is the intensity at $\mathbf{r} = 0$. The absorption coefficient α is

$$\alpha = 2\frac{\omega}{c}m_{\mathrm{I}} = \frac{4\pi m_{\mathrm{I}}}{\lambda}, \tag{1.49}$$

where

$$\lambda = \frac{2\pi c}{\omega} \tag{1.50}$$

is the free-space wavelength. The intensity has the dimension of monochromatic energy flux: [energy/(area$\times$ time)].

The reader can verify that the choice of the time dependence $\exp(\mathrm{i}\omega t)$ rather than $\exp(-\mathrm{i}\omega t)$ in the complex representation of time-harmonic fields in Eq. (1.16) would have led to $m = m_{\mathrm{R}} - \mathrm{i}m_{\mathrm{I}}$ with a non-negative m_{I}. The $\exp(-\mathrm{i}\omega t)$ time-factor convention adopted here has been used in many other books on optics and light scattering (e.g., Born and Wolf 1999; Bohren and Huffman 1983; Barber and Hill 1990) and is a nearly standard choice in electromagnetics (e.g., Stratton 1941; Tsang *et al.* 1985; Kong 1990; Jackson 1998) and solid-state physics. However, van de Hulst (1957) and Kerker (1969) used the time factor $\exp(\mathrm{i}\omega t)$, which implies a non-positive imaginary part of the complex refractive index. It does not matter in the final analysis which convention is chosen because all measurable quantities of practical interest are always real. However, it is important to remember that once a choice of the time factor has been made, its consistent use throughout all derivations is essential.

1.3 Coherency matrix and Stokes parameters

Most photometric and polarimetric optical instruments cannot measure the electric and magnetic fields associated with a beam of light; rather, they measure quantities that are time averages of real-valued linear combinations of products of field vector components and have the dimension of intensity. Important examples of such observable quantities are so-called Stokes parameters. In order to define them, we will use the spherical coordinate system associated with a local right-handed Cartesian coordinate system having its origin at the observation point, as shown in Fig. 1.2. The direction of propagation of a plane electromagnetic wave in a homogeneous nonab-

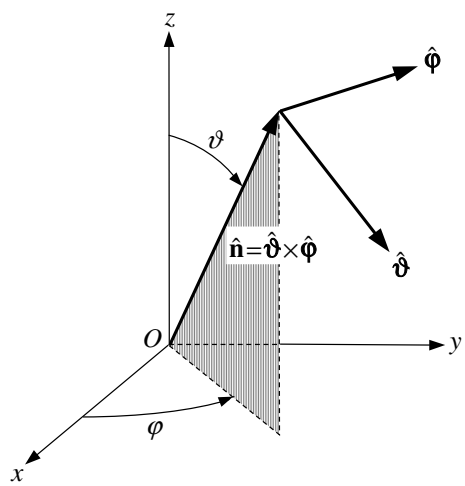

Figure 1.2. Coordinate system used to describe the direction of propagation and the polarization state of a plane electromagnetic wave.

sorbing medium is specified by a unit vector $\hat{\mathbf{n}}$ or, equivalently, by a couplet (ϑ, φ), where $\vartheta \in [0, \pi]$ is the polar (zenith) angle measured from the positive z-axis and $\varphi \in [0, 2\pi)$ is the azimuth angle measured from the positive x-axis in the clockwise direction when looking in the direction of the positive z-axis. Since the medium is assumed to be nonabsorbing, the component of the electric field vector along the direction of propagation $\hat{\mathbf{n}}$ is equal to zero, so that the electric field at the observation point is given by $\mathbf{E} = \mathbf{E}_\vartheta + \mathbf{E}_\varphi$, where $\mathbf{E}_\vartheta$ and $\mathbf{E}_\varphi$ are the ϑ- and φ-components of the electric field vector. The component $\mathbf{E}_\vartheta = E_\vartheta \hat{\boldsymbol{\vartheta}}$ lies in the meridional plane (i.e., plane through $\hat{\mathbf{n}}$ and the z-axis), whereas the component $\mathbf{E}_\varphi = E_\varphi \hat{\boldsymbol{\varphi}}$ is perpendicular to this plane; $\hat{\boldsymbol{\vartheta}}$ and $\hat{\boldsymbol{\varphi}}$ are the corresponding unit vectors such that $\hat{\mathbf{n}} = \hat{\boldsymbol{\vartheta}} \times \hat{\boldsymbol{\varphi}}$. Note that in the microwave remote sensing literature, $\mathbf{E}_\vartheta$ and $\mathbf{E}_\varphi$ are often denoted as $\mathbf{E}_\mathrm{v}$ and $\mathbf{E}_\mathrm{h}$ and called the vertical and horizontal electric field vector components, respectively (e.g., Tsang *et al.* 1985; Ulaby and Elachi 1990).

The specification of a unit vector $\hat{\mathbf{n}}$ uniquely determines the meridional plane of the propagation direction except when $\hat{\mathbf{n}}$ is oriented along the positive or negative direction of the z-axis. Although it may seem redundant to specify φ in addition to ϑ when $\vartheta = 0$ or π, the unit ϑ and φ vectors and, thus, the electric field vector components $\mathbf{E}_\vartheta$ and $\mathbf{E}_\varphi$ still depend on the orientation of the meridional plane. Therefore, we will always assume that the specification of $\hat{\mathbf{n}}$ implicitly includes the specification of the appropriate meridional plane in cases when $\hat{\mathbf{n}}$ is parallel to the z-axis. To minimize confusion, we often will specify explicitly the direction of propagation using the angles ϑ and φ; the latter uniquely defines the meridional plane when $\vartheta = 0$ or π.

Consider a plane electromagnetic wave propagating in a medium with constant real ε, μ, and k and given by

$$\mathbf{E}_{\mathrm{c}}(\mathbf{r}, t) = \mathbf{E}_0 \exp(\mathrm{i}k\hat{\mathbf{n}} \cdot \mathbf{r} - \mathrm{i}\omega t). \tag{1.51}$$

The simplest complete set of linearly independent quadratic combinations of the electric field vector components with non-zero time averages consists of the following four quantities:

$$E_{\mathrm{c}\vartheta}E^*_{\mathrm{c}\vartheta} = E_{0\vartheta}E^*_{0\vartheta}, \quad E_{\mathrm{c}\vartheta}E^*_{\mathrm{c}\varphi} = E_{0\vartheta}E^*_{0\varphi}, \quad E_{\mathrm{c}\varphi}E^*_{\mathrm{c}\vartheta} = E_{0\varphi}E^*_{0\vartheta}, \quad E_{\mathrm{c}\varphi}E^*_{\mathrm{c}\varphi} = E_{0\varphi}E^*_{0\varphi}.$$

The products of these quantities and $\frac{1}{2}\sqrt{\varepsilon/\mu}$ have the dimension of monochromatic energy flux and form the 2×2 so-called coherency (or density) matrix $\boldsymbol{\rho}$:

$$\boldsymbol{\rho} = \begin{bmatrix} \rho_{11} & \rho_{12} \\ \rho_{21} & \rho_{22} \end{bmatrix} = \frac{1}{2}\sqrt{\frac{\varepsilon}{\mu}} \begin{bmatrix} E_{0\vartheta}E^*_{0\vartheta} & E_{0\vartheta}E^*_{0\varphi} \\ E_{0\varphi}E^*_{0\vartheta} & E_{0\varphi}E^*_{0\varphi} \end{bmatrix}. \tag{1.52}$$

The completeness of the set of the four coherency matrix elements means that any plane-wave characteristic directly observable with a traditional optical instrument is a real-valued linear combination of these quantities.

Since ρ_{12} and ρ_{21} are, in general, complex, it is convenient to introduce an alternative complete set of four real, linearly independent quantities called Stokes parameters. Let us first group the elements of the 2×2 coherency matrix into a 4×1 coherency column vector (O'Neill 1992):

$$\mathbf{J} = \begin{bmatrix} \rho_{11} \\ \rho_{12} \\ \rho_{21} \\ \rho_{22} \end{bmatrix} = \frac{1}{2}\sqrt{\frac{\varepsilon}{\mu}} \begin{bmatrix} E_{0\vartheta}E^*_{0\vartheta} \\ E_{0\vartheta}E^*_{0\varphi} \\ E_{0\varphi}E^*_{0\vartheta} \\ E_{0\varphi}E^*_{0\varphi} \end{bmatrix}. \tag{1.53}$$

The Stokes parameters I, Q, U, and V are then defined as the elements of a 4×1 column vector $\mathbf{I}$, otherwise known as the Stokes column vector, as follows:

$$\mathbf{I} = \begin{bmatrix} I \\ Q \\ U \\ V \end{bmatrix} = \mathbf{DJ} = \frac{1}{2}\sqrt{\frac{\varepsilon}{\mu}} \begin{bmatrix} E_{0\vartheta}E^*_{0\vartheta} + E_{0\varphi}E^*_{0\varphi} \\ E_{0\vartheta}E^*_{0\vartheta} - E_{0\varphi}E^*_{0\varphi} \\ -E_{0\vartheta}E^*_{0\varphi} - E_{0\varphi}E^*_{0\vartheta} \\ \mathrm{i}(E_{0\varphi}E^*_{0\vartheta} - E_{0\vartheta}E^*_{0\varphi}) \end{bmatrix} = \frac{1}{2}\sqrt{\frac{\varepsilon}{\mu}} \begin{bmatrix} E_{0\vartheta}E^*_{0\vartheta} + E_{0\varphi}E^*_{0\varphi} \\ E_{0\vartheta}E^*_{0\vartheta} - E_{0\varphi}E^*_{0\varphi} \\ -2\,\mathrm{Re}(E_{0\vartheta}E^*_{0\varphi}) \\ 2\mathrm{Im}(E_{0\vartheta}E^*_{0\varphi}) \end{bmatrix}, \tag{1.54}$$

where

$$\mathbf{D} = \begin{bmatrix} 1 & 0 & 0 & 1 \\ 1 & 0 & 0 & -1 \\ 0 & -1 & -1 & 0 \\ 0 & -\mathrm{i} & \mathrm{i} & 0 \end{bmatrix}. \tag{1.55}$$

The converse relationship is

$$\mathbf{J} = \mathbf{D}^{-1}\mathbf{I}, \tag{1.56}$$

where the inverse matrix $\mathbf{D}^{-1}$ is given by

$$\mathbf{D}^{-1} = \frac{1}{2}\begin{bmatrix} 1 & 1 & 0 & 0 \\ 0 & 0 & -1 & \mathrm{i} \\ 0 & 0 & -1 & -\mathrm{i} \\ 1 & -1 & 0 & 0 \end{bmatrix}. \tag{1.57}$$

Since the Stokes parameters are real-valued and have the dimension of monochromatic energy flux, they can be measured directly with suitable optical instruments. Furthermore, they form a complete set of quantities needed to characterize a plane electromagnetic wave, inasmuch as it is subject to practical analysis. This means that (i) any other observable quantity is a linear combination of the four Stokes parameters, and (ii) it is impossible to distinguish between two plane waves with the same values of the Stokes parameters using a traditional optical device (the so-called principle of optical equivalence). Indeed, the two complex amplitudes $E_{0\vartheta} = a_\vartheta \exp(\mathrm{i}\Delta_\vartheta)$ and $E_{0\varphi} = a_\varphi \exp(\mathrm{i}\Delta_\varphi)$ are characterized by four real numbers: the non-negative amplitudes a_ϑ and a_φ and the phases Δ_ϑ and $\Delta_\varphi = \Delta_\vartheta - \Delta$. The Stokes parameters carry information about the amplitudes and the phase difference Δ, but not about Δ_ϑ. The latter is the only quantity that could be used to distinguish different waves with the same a_ϑ, a_φ, and Δ (and thus the same Stokes parameters), but it vanishes when a field vector component is multiplied by the complex conjugate value of the same or another field vector component; cf. Eqs. (1.52) and (1.54).

The first Stokes parameter, I, is the intensity introduced in the previous section; the explicit definition given in Eq. (1.54) is applicable to a homogeneous, nonabsorbing medium. The Stokes parameters Q, U, and V describe the polarization state of the wave. The ellipsometric interpretation of the Stokes parameters will be the subject of the following section. The reader can easily verify that the Stokes parameters of a plane monochromatic wave are not completely independent but rather are related by the quadratic identity

$$I^2 \equiv Q^2 + U^2 + V^2. \tag{1.58}$$

We will see later, however, that this identity may not hold for a quasi-monochromatic beam of light. Because one usually must deal with relative rather than absolute intensities, the constant factor $\frac{1}{2}\sqrt{\varepsilon/\mu}$ is often unimportant and will be omitted in all cases where this does not generate confusion.

The coherency matrix and the Stokes column vector are not the only representations of polarization and not always the most convenient ones. Two other frequently used representations are the real so-called modified Stokes column vector given by

$$\mathbf{I}^{\mathrm{MS}} = \begin{bmatrix} I_{\mathrm{v}} \\ I_{\mathrm{h}} \\ U \\ V \end{bmatrix} = \mathbf{B}\mathbf{I} = \begin{bmatrix} \frac{1}{2}(I+Q) \\ \frac{1}{2}(I-Q) \\ U \\ V \end{bmatrix} \tag{1.59}$$

and the complex circular-polarization column vector defined as

$$\mathbf{I}^{\mathrm{CP}} = \begin{bmatrix} I_2 \\ I_0 \\ I_{-0} \\ I_{-2} \end{bmatrix} = \mathbf{A}\mathbf{I} = \frac{1}{2}\begin{bmatrix} Q + \mathrm{i}U \\ I + V \\ I - V \\ Q - \mathrm{i}U \end{bmatrix}, \tag{1.60}$$

where

$$\mathbf{B} = \begin{bmatrix} 1/2 & 1/2 & 0 & 0 \\ 1/2 & -1/2 & 0 & 0 \\ 0 & 0 & 1 & 0 \\ 0 & 0 & 0 & 1 \end{bmatrix}, \tag{1.61}$$

$$\mathbf{A} = \frac{1}{2}\begin{bmatrix} 0 & 1 & \mathrm{i} & 0 \\ 1 & 0 & 0 & 1 \\ 1 & 0 & 0 & -1 \\ 0 & 1 & -\mathrm{i} & 0 \end{bmatrix}. \tag{1.62}$$

It is easy to verify that

$$\mathbf{I} = \mathbf{B}^{-1}\mathbf{I}^{\mathrm{MS}} \tag{1.63}$$

and

$$\mathbf{I} = \mathbf{A}^{-1}\mathbf{I}^{\mathrm{CP}}, \tag{1.64}$$

where

$$\mathbf{B}^{-1} = \begin{bmatrix} 1 & 1 & 0 & 0 \\ 1 & -1 & 0 & 0 \\ 0 & 0 & 1 & 0 \\ 0 & 0 & 0 & 1 \end{bmatrix} \tag{1.65}$$

and

$$\mathbf{A}^{-1} = \begin{bmatrix} 0 & 1 & 1 & 0 \\ 1 & 0 & 0 & 1 \\ -\mathrm{i} & 0 & 0 & \mathrm{i} \\ 0 & 1 & -1 & 0 \end{bmatrix}. \tag{1.66}$$

1.4 Ellipsometric interpretation of Stokes parameters

In this section we show how the Stokes parameters can be used to derive the ellipsometric characteristics of the plane electromagnetic wave given by Eq. (1.51).

Writing

$$E_{0\vartheta} = a_\vartheta \exp(\mathrm{i}\Delta_\vartheta), \tag{1.67}$$

$$E_{0\varphi} = a_\varphi \exp(\mathrm{i}\Delta_\varphi) \tag{1.68}$$

with real non-negative amplitudes a_ϑ and a_φ and real phases Δ_ϑ and Δ_φ, using Eq. (1.54), and omitting the factor $\frac{1}{2}\sqrt{\varepsilon/\mu}$ we obtain for the Stokes parameters

$$I = a_\vartheta^2 + a_\varphi^2, \tag{1.69}$$

$$Q = a_\vartheta^2 - a_\varphi^2, \tag{1.70}$$

$$U = -2a_\vartheta a_\varphi \cos\Delta, \tag{1.71}$$

$$V = 2a_\vartheta a_\varphi \sin\Delta, \tag{1.72}$$

where

$$\Delta = \Delta_\vartheta - \Delta_\varphi. \tag{1.73}$$

Substituting Eqs. (1.67) and (1.68) in Eq. (1.51), we have for the real electric vector

$$E_\vartheta(\mathbf{r}, t) = a_\vartheta \cos(\delta_\vartheta - \omega t), \tag{1.74}$$

$$E_\varphi(\mathbf{r}, t) = a_\varphi \cos(\delta_\varphi - \omega t), \tag{1.75}$$

where

$$\delta_\vartheta = \Delta_\vartheta + k\hat{\mathbf{n}}\cdot\mathbf{r}, \qquad \delta_\varphi = \Delta_\varphi + k\hat{\mathbf{n}}\cdot\mathbf{r}. \tag{1.76}$$

At any fixed point O in space, the endpoint of the real electric vector given by Eqs. (1.74)–(1.76) describes an ellipse with specific major and minor axes and orientation (see the top panel of Fig. 1.3). The major axis of the ellipse makes an angle ζ with the positive direction of the φ-axis such that $\zeta \in [0, \pi)$. By definition, this orientation angle is obtained by rotating the φ-axis in the *clockwise* direction when looking in the direction of propagation, until it is directed along the major axis of the ellipse. The ellipticity is defined as the ratio of the minor to the major axes of the ellipse and is usually expressed as $|\tan\beta|$, where $\beta \in [-\pi/4, \pi/4]$. By definition, β is positive when the real electric vector at O rotates clockwise, as viewed by an observer looking in the direction of propagation. The polarization for positive β is called right-handed, as opposed to the left-handed polarization corresponding to the anti-clockwise rotation of the electric vector.

To express the orientation ζ of the ellipse and the ellipticity $|\tan\beta|$ in terms of the Stokes parameters, we first write the equations representing the rotation of the real electric vector at O in the form

$$E_q(\mathbf{r}, t) = a\sin\beta\sin(\delta - \omega t), \tag{1.77}$$

$$E_p(\mathbf{r}, t) = a\cos\beta\cos(\delta - \omega t), \tag{1.78}$$

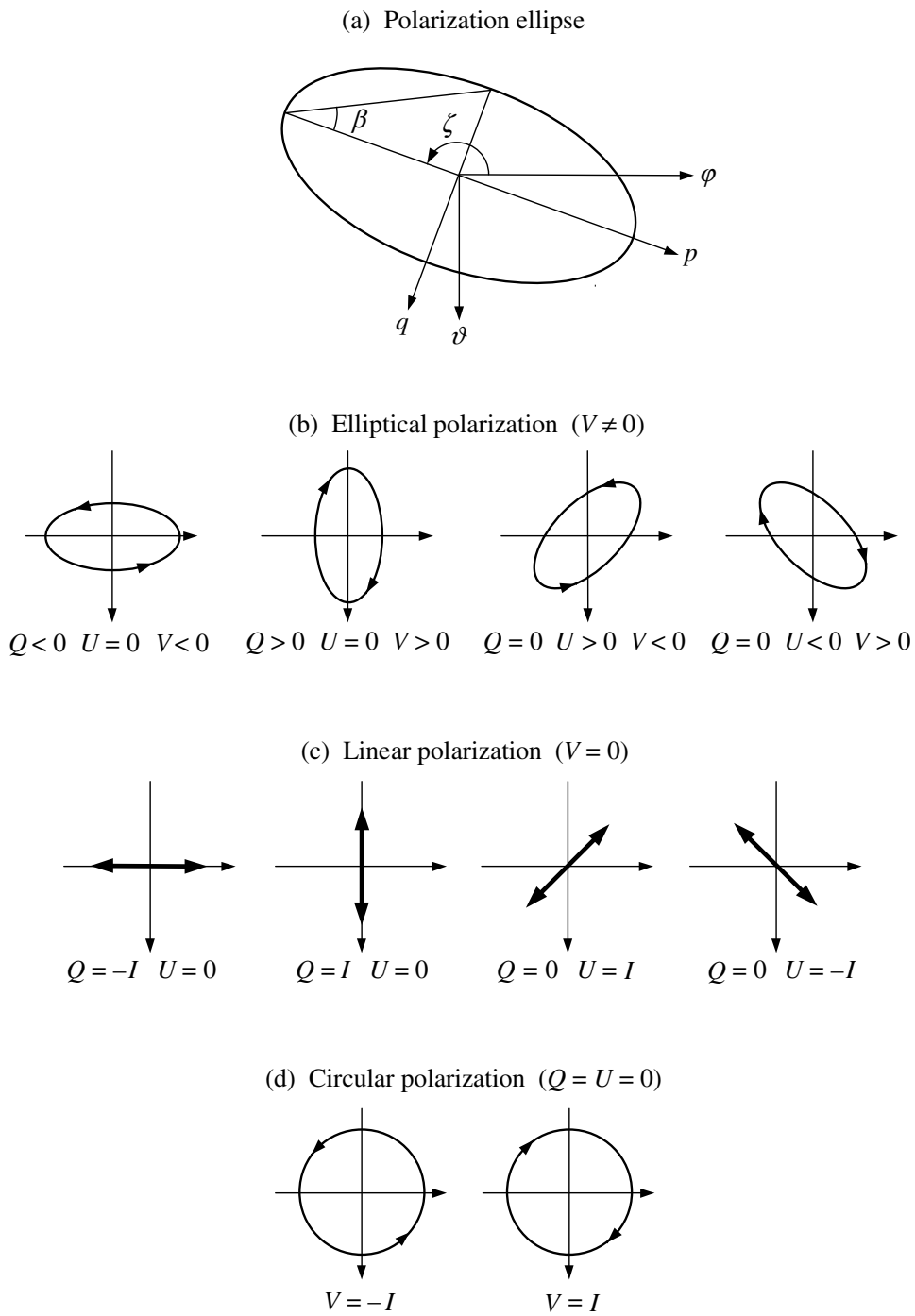

Figure 1.3. Ellipse described by the tip of the real electric vector at a fixed point O in space (upper panel) and particular cases of elliptical, linear, and circular polarization. The plane electromagnetic wave propagates in the direction $\hat{\boldsymbol{\vartheta}} \times \hat{\boldsymbol{\varphi}}$ (i.e., towards the reader).

where E_p and E_q are the electric field components along the major and minor axes of the ellipse, respectively (Fig. 1.3). One easily verifies that a positive (negative) β

indeed corresponds to the right-handed (left-handed) polarization. The connection between Eqs. (1.74)–(1.75) and Eqs. (1.77)–(1.78) can be established by using the simple transformation rule for rotation of a two-dimensional coordinate system:

$$E_\vartheta(\mathbf{r}, t) = -E_q(\mathbf{r}, t)\cos\zeta + E_p(\mathbf{r}, t)\sin\zeta, \tag{1.79}$$

$$E_\varphi(\mathbf{r}, t) = -E_q(\mathbf{r}, t)\sin\zeta - E_p(\mathbf{r}, t)\cos\zeta. \tag{1.80}$$

By equating the coefficients of $\cos\omega t$ and $\sin\omega t$ in the expanded Eqs. (1.74) and (1.79) and those in the expanded Eqs. (1.75) and (1.80), we obtain

$$a_\vartheta \cos\delta_\vartheta = -a\sin\beta\sin\delta\cos\zeta + a\cos\beta\cos\delta\sin\zeta, \tag{1.81}$$

$$a_\vartheta \sin\delta_\vartheta = a\sin\beta\cos\delta\cos\zeta + a\cos\beta\sin\delta\sin\zeta, \tag{1.82}$$

$$a_\varphi \cos\delta_\varphi = -a\sin\beta\sin\delta\sin\zeta - a\cos\beta\cos\delta\cos\zeta, \tag{1.83}$$

$$a_\varphi \sin\delta_\varphi = a\sin\beta\cos\delta\sin\zeta - a\cos\beta\sin\delta\cos\zeta. \tag{1.84}$$

Squaring and adding Eqs. (1.81) and (1.82) and Eqs. (1.83) and (1.84) gives

$$a_\vartheta^2 = a^2(\sin^2\beta\cos^2\zeta + \cos^2\beta\sin^2\zeta), \tag{1.85}$$

$$a_\varphi^2 = a^2(\sin^2\beta\sin^2\zeta + \cos^2\beta\cos^2\zeta). \tag{1.86}$$

Multiplying Eqs. (1.81) and (1.83) and Eqs. (1.82) and (1.84) and adding yields

$$a_\vartheta a_\varphi \cos\Delta = -\tfrac{1}{2}a^2\cos 2\beta\sin 2\zeta. \tag{1.87}$$

Similarly, multiplying Eqs. (1.82) and (1.83) and Eqs. (1.81) and (1.84) and subtracting gives

$$a_\vartheta a_\varphi \sin\Delta = -\tfrac{1}{2}a^2\sin 2\beta. \tag{1.88}$$

Comparing Eqs. (1.69)–(1.72) with Eqs. (1.85)–(1.88), we finally derive

$$I = a^2, \tag{1.89}$$

$$Q = -I\cos 2\beta\cos 2\zeta, \tag{1.90}$$

$$U = I\cos 2\beta\sin 2\zeta, \tag{1.91}$$

$$V = -I\sin 2\beta. \tag{1.92}$$

The parameters of the polarization ellipse are thus expressed in terms of the Stokes parameters as follows. The major and minor axes are given by $\sqrt{I}\cos\beta$ and $\sqrt{I}\,|\sin\beta|$, respectively (cf. Eqs. (1.77) and (1.78)). Equations (1.90) and (1.91) yield

$$\tan 2\zeta = -\frac{U}{Q}. \tag{1.93}$$

Because $|\beta| \le \pi/4$, we have $\cos 2\beta \ge 0$ so that $\cos 2\zeta$ has the same sign as $-Q$.

Therefore, from the different values of ζ that satisfy Eq. (1.93) but differ by $\pi/2$, we must choose the one that makes the sign of $\cos 2\zeta$ the same as that of $-Q$. The ellipticity and handedness follow from

$$\tan 2\beta = -\frac{V}{\sqrt{Q^2+U^2}}. \tag{1.94}$$

Thus, the polarization is left-handed if V is positive and right-handed if V is negative (Fig. 1.3).

The electromagnetic wave becomes linearly polarized when $\beta = 0$; then the electric vector vibrates along a line making an angle ζ with the φ-axis (cf. Fig. 1.3) and $V = 0$. Furthermore, if $\zeta = 0$ or $\zeta = \pi/2$ then U vanishes as well. This explains the usefulness of the modified Stokes representation of polarization given by Eq. (1.59) in situations involving linearly polarized light, as follows. The modified Stokes vector then has only one non-zero element and is equal to $[I\ \ 0\ \ 0\ \ 0]^{\mathrm{T}}$ if $\zeta = \pi/2$ (the electric vector vibrates along the ϑ-axis, i.e., in the meridional plane) or to $[0\ \ I\ \ 0\ \ 0]^{\mathrm{T}}$ if $\zeta = 0$ (the electric vector vibrates along the φ-axis, i.e., in the plane perpendicular to the meridional plane), where T indicates the transpose of a matrix.

If, however, $\beta = \pm\pi/4$, then both Q and U vanish, and the electric vector describes a circle either in the clockwise direction $(\beta = \pi/4,\ V = -I)$ or the anticlockwise direction $(\beta = -\pi/4,\ V = I)$, as viewed by an observer looking in the direction of propagation (Fig. 1.3). In this case the electromagnetic wave is circularly polarized; the circular-polarization vector $\mathbf{I}^{\mathrm{CP}}$ has only one non-zero element and takes the values $[0\ \ 0\ \ I\ \ 0]^{\mathrm{T}}$ and $[0\ \ I\ \ 0\ \ 0]^{\mathrm{T}}$, respectively (see Eq. (1.60)).

The polarization ellipse, along with a designation of the rotation direction (right- or left-handed), fully describes the temporal evolution of the real electric vector at a fixed point in space. This evolution can also be visualized by plotting the curve, in (ϑ, φ, t) coordinates, described by the tip of the electric vector as a function of time. For example, in the case of an elliptically polarized plane wave with right-handed polarization the curve is a right-handed helix with an elliptical projection onto the $\vartheta\varphi$-plane centered around the t-axis (Fig. 1.4(a)). The pitch of the helix is simply $2\pi/\omega$, where ω is the angular frequency of the wave. Another way to visualize a plane wave is to fix a moment in time and draw a three-dimensional curve in (ϑ, φ, s) coordinates described by the tip of the electric vector as a function of a spatial coordinate $s = \mathbf{r}\cdot\hat{\mathbf{n}}$ oriented along the direction of propagation $\hat{\mathbf{n}}$. According to Eqs. (1.74)–(1.76), the electric field is the same for all position–time combinations with constant $ks - \omega t$. Therefore, at any instant of time (say, $t = 0$) the locus of the points described by the tip of the electric vector originating at different points on the s-axis is also a helix, with the same projection onto the $\vartheta\varphi$-plane as the respective helix in the (ϑ, φ, t) coordinates but with opposite handedness. For example, for the wave with right-handed elliptical polarization shown in Fig. 1.4(a), the respective curve in the (ϑ, φ, s) coordinates is a left-handed elliptical helix, shown in Fig.

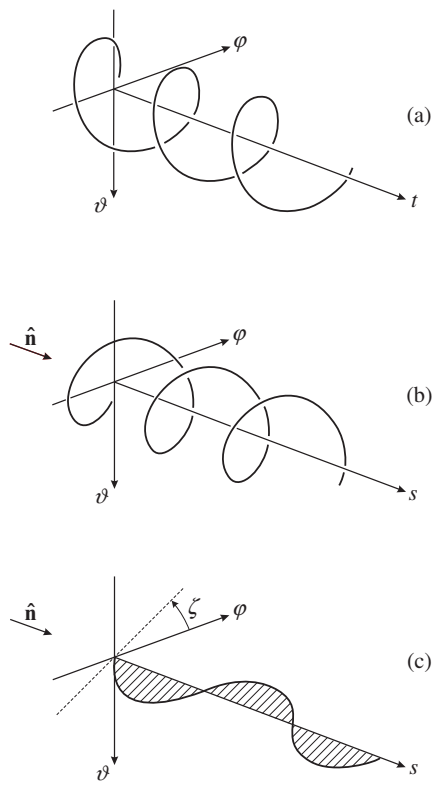

Figure 1.4. (a) The helix described by the tip of the real electric vector of a plane electromagnetic wave with right-handed polarization in (ϑ, φ, t) coordinates at a fixed point in space. (b) As in (a), but in (ϑ, φ, s) coordinates at a fixed moment in time. (c) As in (b), but for a linearly polarized wave.

1.4(b). The pitch of this helix is the wavelength λ. It is now clear that the propagation of the wave in time and space can be represented by progressive movement in time of the helix shown in Fig. 1.4(b) in the direction of $\hat{\mathbf{n}}$ with the speed of light. With increasing time, the intersection of the helix with any plane s = constant describes a right-handed vibration ellipse. In the case of a circularly polarized wave, the elliptical helix becomes a helix with a circular projection onto the $\vartheta\varphi$-plane. If the wave is linearly polarized, then the helix degenerates into a simple sinusoidal curve in the plane making an angle ζ with the φ-axis (Fig. 1.4(c)).

1.5 Rotation transformation rule for Stokes parameters

The Stokes parameters of a plane electromagnetic wave are always defined with respect to a reference plane containing the direction of wave propagation. If the reference plane is rotated about the direction of propagation then the Stokes parameters are modified according to a rotation transformation rule, which can be derived as follows. Consider a rotation of the coordinate axes ϑ and φ through an angle $0 \le \eta < 2\pi$ in

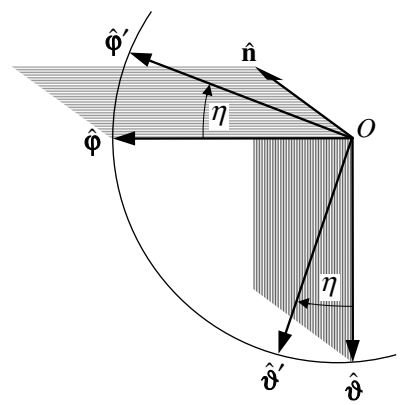

Figure 1.5. Rotation of the ϑ- and φ-axes through an angle $\eta \geq 0$ around $\hat{\mathbf{n}}$ in the clockwise direction when looking in the direction of propagation.

the *clockwise* direction when looking in the direction of propagation (Fig. 1.5). The transformation rule for rotation of a two-dimensional coordinate system yields

$$E'_{0\vartheta} = E_{0\vartheta}\cos\eta + E_{0\varphi}\sin\eta, \tag{1.95}$$

$$E'_{0\varphi} = -E_{0\vartheta}\sin\eta + E_{0\varphi}\cos\eta, \tag{1.96}$$

where the primes denote the electric field vector components with respect to the new reference frame. It then follows from Eq. (1.54) that the rotation transformation rule for the Stokes parameters is

$$\mathbf{I}' = \begin{bmatrix} I' \\ Q' \\ U' \\ V' \end{bmatrix} = \mathbf{L}(\eta)\mathbf{I} = \begin{bmatrix} 1 & 0 & 0 & 0 \\ 0 & \cos 2\eta & -\sin 2\eta & 0 \\ 0 & \sin 2\eta & \cos 2\eta & 0 \\ 0 & 0 & 0 & 1 \end{bmatrix} \begin{bmatrix} I \\ Q \\ U \\ V \end{bmatrix}, \tag{1.97}$$

where $\mathbf{L}(\eta)$ is called the Stokes rotation matrix for angle η. It is obvious that a $\eta = \pi$ rotation does not change the Stokes parameters.

Because

$$(\mathbf{I}^{\mathrm{MS}})' = \mathbf{B}\mathbf{I}' = \mathbf{B}\mathbf{L}(\eta)\mathbf{I} = \mathbf{B}\mathbf{L}(\eta)\mathbf{B}^{-1}\mathbf{I}^{\mathrm{MS}}, \tag{1.98}$$

the rotation matrix for the modified Stokes column vector is given by

$$\mathbf{L}^{\mathrm{MS}}(\eta) = \mathbf{B}\mathbf{L}(\eta)\mathbf{B}^{-1} = \begin{bmatrix} \cos^2\eta & \sin^2\eta & -\frac{1}{2}\sin 2\eta & 0 \\ \sin^2\eta & \cos^2\eta & \frac{1}{2}\sin 2\eta & 0 \\ \sin 2\eta & -\sin 2\eta & \cos 2\eta & 0 \\ 0 & 0 & 0 & 1 \end{bmatrix}. \tag{1.99}$$

Similarly, for the circular polarization representation,

$$(\mathbf{I}^{\mathrm{CP}})' = \mathbf{A}\mathbf{I}' = \mathbf{A}\mathbf{L}(\eta)\mathbf{I} = \mathbf{A}\mathbf{L}(\eta)\mathbf{A}^{-1}\mathbf{I}^{\mathrm{CP}}, \tag{1.100}$$

and the corresponding rotation matrix is diagonal (Hovenier and van der Mee 1983):

$$\mathbf{L}^{\mathrm{CP}}(\eta) = \mathbf{A}\mathbf{L}(\eta)\mathbf{A}^{-1} = \begin{bmatrix} \exp(\mathrm{i}2\eta) & 0 & 0 & 0 \\ 0 & 1 & 0 & 0 \\ 0 & 0 & 1 & 0 \\ 0 & 0 & 0 & \exp(-\mathrm{i}2\eta) \end{bmatrix}. \tag{1.101}$$

1.6 Quasi-monochromatic light and incoherent addition of Stokes parameters

The definition of a monochromatic plane electromagnetic wave given by Eqs. (1.51) and (1.67)–(1.68) implies that the complex amplitude $\mathbf{E}_0$ and, therefore, the quantities a_ϑ, a_φ, Δ_ϑ, and Δ_φ are constant. In reality, these quantities often fluctuate in time. Although the typical frequency of these fluctuations is much smaller than the angular frequency ω, it is still so high that most optical devices are incapable of tracing the instantaneous values of the Stokes parameters but rather measure averages of the Stokes parameters over a relatively long period of time. Therefore, we must modify the definition of the Stokes parameters for such *quasi-monochromatic* beam of light as follows:

$$I = \langle E_{0\vartheta}E_{0\vartheta}^*\rangle + \langle E_{0\varphi}E_{0\varphi}^*\rangle = \langle a_\vartheta^2\rangle + \langle a_\varphi^2\rangle, \tag{1.102}$$

$$Q = \langle E_{0\vartheta}E_{0\vartheta}^*\rangle - \langle E_{0\varphi}E_{0\varphi}^*\rangle = \langle a_\vartheta^2\rangle - \langle a_\varphi^2\rangle, \tag{1.103}$$

$$U = -\langle E_{0\vartheta}E_{0\varphi}^*\rangle - \langle E_{0\varphi}E_{0\vartheta}^*\rangle = -2\langle a_\vartheta a_\varphi \cos\Delta\rangle, \tag{1.104}$$

$$V = \mathrm{i}\langle E_{0\varphi}E_{0\vartheta}^*\rangle - \mathrm{i}\langle E_{0\vartheta}E_{0\varphi}^*\rangle = 2\langle a_\vartheta a_\varphi \sin\Delta\rangle, \tag{1.105}$$

where we have omitted the common factor $\frac{1}{2}\sqrt{\varepsilon/\mu}$ and

$$\langle f\rangle = \frac{1}{T}\int_t^{t+T} \mathrm{d}t' f(t') \tag{1.106}$$

denotes the average over a time interval T long compared with the typical period of fluctuation.

The identity (1.58) is not valid, in general, for a quasi-monochromatic beam. Indeed, now we have

$$\begin{aligned} & I^2 - Q^2 - U^2 - V^2 \\ & = 4[\langle a_\vartheta^2\rangle\langle a_\varphi^2\rangle - \langle a_\vartheta a_\varphi \cos\Delta\rangle^2 - \langle a_\vartheta a_\varphi \sin\Delta\rangle^2] \\ & = \frac{4}{T^2}\int_t^{t+T}\mathrm{d}t' \int_t^{t+T}\mathrm{d}t''\{[a_\vartheta(t')]^2[a_\varphi(t'')]^2 \\ & \qquad -a_\vartheta(t')a_\varphi(t')\cos[\Delta(t')]a_\vartheta(t'')a_\varphi(t'')\cos[\Delta(t'')] \\ & \qquad -a_\vartheta(t')a_\varphi(t')\sin[\Delta(t')]a_\vartheta(t'')a_\varphi(t'')\sin[\Delta(t'')]\} \end{aligned}$$

$$
\begin{aligned}
&= \frac{4}{T^2}\int_t^{t+T} \mathrm{d}t' \int_t^{t+T} \mathrm{d}t''\{[a_\vartheta(t')]^2[a_\varphi(t'')]^2 \\
&\qquad\qquad -a_\vartheta(t')a_\varphi(t')a_\vartheta(t'')a_\varphi(t'')\cos[\Delta(t')-\Delta(t'')]\} \\
&= \frac{2}{T^2}\int_t^{t+T} \mathrm{d}t' \int_t^{t+T} \mathrm{d}t''\{[a_\vartheta(t')]^2[a_\varphi(t'')]^2+[a_\vartheta(t'')]^2[a_\varphi(t')]^2 \\
&\qquad\qquad -2a_\vartheta(t')a_\varphi(t')a_\vartheta(t'')a_\varphi(t'')\cos[\Delta(t')-\Delta(t'')]\} \\
&\geq \frac{2}{T^2}\int_t^{t+T} \mathrm{d}t' \int_t^{t+T} \mathrm{d}t''\{[a_\vartheta(t')]^2[a_\varphi(t'')]^2+[a_\vartheta(t'')]^2[a_\varphi(t')]^2 \\
&\qquad\qquad -2a_\vartheta(t')a_\varphi(t')a_\vartheta(t'')a_\varphi(t'')\} \\
&= \frac{2}{T^2}\int_t^{t+T} \mathrm{d}t' \int_t^{t+T} \mathrm{d}t''[a_\vartheta(t')a_\varphi(t'')-a_\vartheta(t'')a_\varphi(t')]^2 \\
&\geq 0\,,
\end{aligned}
$$

thereby yielding

$$I^2 \geq Q^2+U^2+V^2. \tag{1.107}$$

The equality holds only if the ratio $a_\vartheta(t)/a_\varphi(t)$ of the real amplitudes and the phase difference $\Delta(t)$ are independent of time, which means that $E_{0\vartheta}(t)$ and $E_{0\varphi}(t)$ are completely correlated. In this case the beam is said to be fully (or completely) polarized. This definition includes a monochromatic wave, but is, of course, more general. However, if $a_\vartheta(t)$, $a_\varphi(t)$, $\Delta_\vartheta(t)$, and $\Delta_\varphi(t)$ are totally uncorrelated and $\langle a_\vartheta^2\rangle = \langle a_\varphi^2\rangle$, then $Q = U = V = 0$, and the quasi-monochromatic beam of light is said to be unpolarized (or natural). This means that the parameters of the vibration ellipse traced by the endpoint of the electric vector fluctuate in such a way that there is no preferred vibration ellipse.

When two or more quasi-monochromatic beams propagating in the same direction are mixed incoherently (i.e., there is no permanent phase relationship between the separate beams), the Stokes vector of the mixture is equal to the sum of the Stokes vectors of the individual beams:

$$\mathbf{I} = \sum_n \mathbf{I}_n, \tag{1.108}$$

where n numbers the beams. Indeed, inserting Eqs. (1.67) and (1.68) in Eq. (1.54), we obtain for the total intensity

$$
\begin{aligned}
I &= \sum_n\sum_m \langle a_{\vartheta n}\, a_{\vartheta m}\exp[\mathrm{i}(\Delta_{\vartheta n}-\Delta_{\vartheta m})]+a_{\varphi n}\, a_{\varphi m}\exp[\mathrm{i}(\Delta_{\varphi n}-\Delta_{\varphi m})]\rangle \\
&= \sum_n I_n + \sum_n\sum_{m\neq n} \langle a_{\vartheta n}\, a_{\vartheta m}\exp[\mathrm{i}(\Delta_{\vartheta n}-\Delta_{\vartheta m})]+a_{\varphi n}\, a_{\varphi m}\exp[\mathrm{i}(\Delta_{\varphi n}-\Delta_{\varphi m})]\rangle.
\end{aligned} \tag{1.109}
$$

Since the phases of different beams are uncorrelated, the second term on the right-

hand side of the relation above vanishes. Hence

$$I = \sum_n I_n, \tag{1.110}$$

and similarly for Q, U, and V. Of course, this additivity rule also applies to the coherency matrix $\boldsymbol{\rho}$, the modified Stokes vector $\mathbf{I}^{\mathrm{MS}}$, and the circular-polarization vector $\mathbf{I}^{\mathrm{CP}}$. An important example demonstrating the application of Eq. (1.108) is the scattering of light by a small volume element containing randomly positioned particles. The phases of the individual waves scattered by the particles depend on the positions of the particles. Therefore, if the distribution of the particles is sufficiently random then the individual scattered waves will be incoherent and the Stokes vectors of the individual waves will add. The additivity of the Stokes parameters allows us to generalize the principle of optical equivalence (Section 1.3) to quasi-monochromatic light as follows: it is impossible by means of a traditional optical instrument to distinguish between various incoherent mixtures of quasi-monochromatic beams that form a beam with the same Stokes parameters (I, Q, U, V). For example, there is only one kind of unpolarized light, although it can be composed of quasi-monochromatic beams in an infinite variety of optically indistinguishable ways.

In view of the general inequality (1.107), it is always possible *mathematically* to decompose any quasi-monochromatic beam into two parts, one unpolarized, with a Stokes vector

$$[I - \sqrt{Q^2 + U^2 + V^2} \quad 0 \quad 0 \quad 0]^{\mathrm{T}},$$

and one fully polarized, with a Stokes vector

$$[\sqrt{Q^2 + U^2 + V^2} \quad Q \quad U \quad V]^{\mathrm{T}}.$$

Thus, the intensity of the fully polarized component is $\sqrt{Q^2 + U^2 + V^2}$, so that the degree of (elliptical) polarization of the quasi-monochromatic beam is

$$P = \frac{\sqrt{Q^2 + U^2 + V^2}}{I}. \tag{1.111}$$

We further define the degree of linear polarization as

$$P_{\mathrm{L}} = \frac{\sqrt{Q^2 + U^2}}{I} \tag{1.112}$$

and the degree of circular polarization as

$$P_{\mathrm{C}} = \frac{V}{I}. \tag{1.113}$$

P vanishes for unpolarized light and is equal to unity for fully polarized light. For a partially polarized beam $(0 < P < 1)$ with $V \neq 0$, the sign of V indicates the preferen-

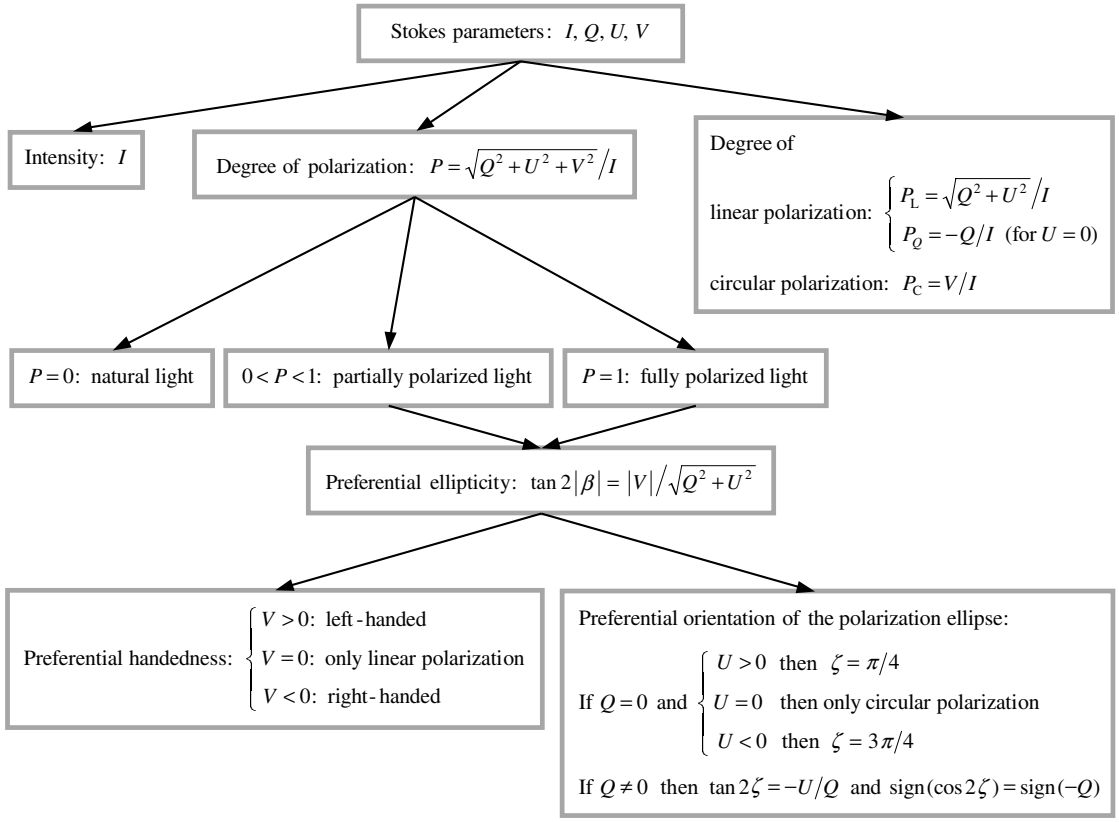

Figure 1.6. Analysis of a quasi-monochromatic beam with Stokes parameters I, Q, U, and V.

tial handedness of the vibration ellipses described by the endpoint of the electric vector: a positive V indicates left-handed polarization and a negative V indicates right-handed polarization. By analogy with Eqs. (1.93) and (1.94), the quantities $-U/Q$ and $|V|/\sqrt{Q^2+U^2}$ may be interpreted as specifying the preferential orientation and ellipticity of the vibration ellipse. Unlike the Stokes parameters, these quantities are not additive. In view of the rotation transformation rule (1.97), P, P_L, and P_C are invariant with respect to rotations of the reference frame around the direction of propagation. When $U = 0$, the ratio

$$P_Q = -\frac{Q}{I} \tag{1.114}$$

is also called the degree of linear polarization (or the *signed* degree of linear polarization). P_Q is positive when the vibrations of the electric vector in the φ-direction (i.e., the direction perpendicular to the meridional plane of the beam) dominate those in the ϑ-direction and is negative otherwise. The standard polarimetric analysis of a general quasi-monochromatic beam with Stokes parameters I, Q, U, and V is summarized in Fig. 1.6 (after Hovenier *et al*. 2004).

Further reading

Excellent treatments of classical electrodynamics and optics are provided by Stratton (1941), Kong (1990), Jackson (1998), and Born and Wolf (1999). The optical properties of bulk matter and their measurement are discussed in Chapters 9 and 10 of Bohren and Huffman (1983) as well as in the comprehensive handbook edited by Palik and Ghosh (1997). Several books are entirely devoted to polarization, for example Shurcliff (1962), Clarke and Grainger (1971), Azzam and Bashara (1977), Kliger *et al*. (1990), Collett (1992), and Brosseau (1998). In Pye (2001), numerous manifestations of polarization in science and nature are discussed.

Chapter 2

Scattering, absorption, and emission of electromagnetic radiation by an arbitrary finite particle

The presence of an object with a refractive index different from that of the surrounding medium changes the electromagnetic field that would otherwise exist in an unbounded homogeneous space. The difference of the total field in the presence of the object and the original field that would exist in the absence of the object can be thought of as the field *scattered* by the object. In other words, the total field is equal to the vector sum of the *incident* (original) field and the *scattered* field.

The angular distribution and polarization of the scattered field depend on the polarization and directional characteristics of the incident field as well as on such properties of the scatterer as its size relative to the wavelength and its shape, composition, and orientation. Therefore, in practice one usually must solve the scattering problem anew every time some or all of these input parameters change. It is appropriate, however, to consider first the general mathematical description of the scattering process without making any detailed assumptions about the scattering object except that it is composed of a linear and isotropic material. Hence the goal of this chapter is to establish a basic theoretical framework underlying more specific problems discussed in the following chapters.

2.1 Volume integral equation

Consider a finite scattering object in the form of a single body or a fixed aggregate embedded in an infinite, homogeneous, linear, isotropic, and nonabsorbing medium (Fig. 2.1(a)). Mathematically, this is equivalent to dividing all space into two mutually disjoint regions, the finite interior region V_{INT} occupied by the scattering object and the infinite exterior region V_{EXT}. The region V_{INT} is filled with an isotropic, linear, and possibly inhomogeneous material.

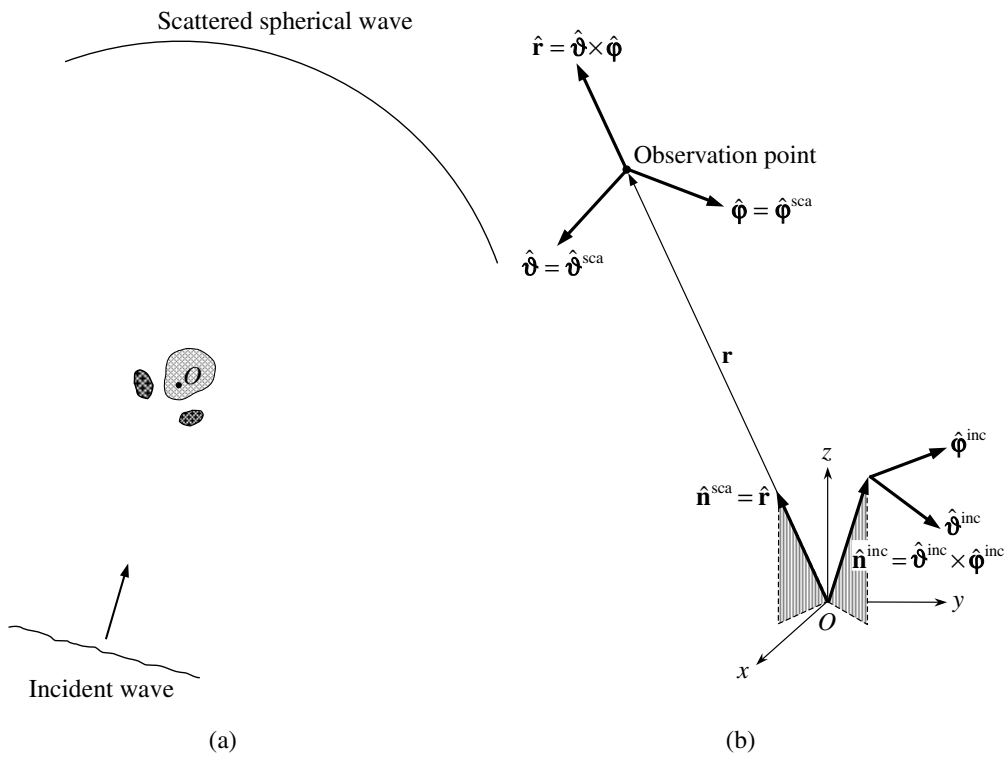

Figure 2.1. Schematic representation of the electromagnetic scattering problem. The unshaded exterior region V_{EXT} is unbounded in all directions and the shaded areas collectively constitute the interior region V_{INT}.

It is well known that optical properties of bulk substances in solid or liquid phase are qualitatively different from those of their constituent atoms and molecules when the latter are isolated. This may cause a problem when one applies the concept of bulk optical constants to a very small particle because either the optical constants determined for bulk matter provide an inaccurate estimate or the particle is so small that the entire concept of optical constants loses its validity. We will therefore assume that the individual bodies forming the scattering object are sufficiently large that they can still be characterized by optical constants appropriate to bulk matter. According to Huffman (1988), this implies that each body is larger than approximately 50 Å.

The monochromatic Maxwell curl equations (1.18) and (1.20) describing the scattering problem can be rewritten as follows:

$$\left.\begin{aligned} \nabla \times \mathbf{E}(\mathbf{r}) &= \mathrm{i}\omega\mu_1 \mathbf{H}(\mathbf{r}) \\ \nabla \times \mathbf{H}(\mathbf{r}) &= -\mathrm{i}\omega\varepsilon_1 \mathbf{E}(\mathbf{r}) \end{aligned}\right\} \qquad \mathbf{r} \in V_{\mathrm{EXT}}, \tag{2.1}$$

$$\left.\begin{aligned} \nabla \times \mathbf{E}(\mathbf{r}) &= \mathrm{i}\omega\mu_2(\mathbf{r}) \mathbf{H}(\mathbf{r}) \\ \nabla \times \mathbf{H}(\mathbf{r}) &= -\mathrm{i}\omega\varepsilon_2(\mathbf{r}) \mathbf{E}(\mathbf{r}) \end{aligned}\right\} \qquad \mathbf{r} \in V_{\mathrm{INT}}, \tag{2.2}$$

where the subscripts 1 and 2 refer to the exterior and interior regions, respectively. Since the first relations in Eqs. (2.1) and (2.2) yield the magnetic field provided that

the electric field is known everywhere, we will look for the solution of Eqs. (2.1) and (2.2) in terms of only the electric field. Assuming that the host medium and the scattering object are nonmagnetic, i.e., $\mu_2(\mathbf{r}) \equiv \mu_1 = \mu_0$, where μ_0 is the permeability of a vacuum, we easily derive the following vector wave equations:

$$\nabla\times\nabla\times\mathbf{E}(\mathbf{r}) - k_1^2\mathbf{E}(\mathbf{r}) = 0, \qquad \mathbf{r}\in V_{\mathrm{EXT}}, \tag{2.3}$$

$$\nabla\times\nabla\times\mathbf{E}(\mathbf{r}) - k_2^2(\mathbf{r})\mathbf{E}(\mathbf{r}) = 0, \qquad \mathbf{r}\in V_{\mathrm{INT}}, \tag{2.4}$$

where $k_1 = \omega\sqrt{\varepsilon_1\mu_0}$ and $k_2(\mathbf{r}) = \omega\sqrt{\varepsilon_2(\mathbf{r})\mu_0}$ are the wave numbers of the exterior and interior regions, respectively. The permittivity for the interior region is regarded as a function of $\mathbf{r}$, to provide for the general case where the scattering object is inhomogeneous. Equations (2.3) and (2.4) can be rewritten as the single inhomogeneous differential equation

$$\nabla\times\nabla\times\mathbf{E}(\mathbf{r}) - k_1^2\mathbf{E}(\mathbf{r}) = \mathbf{j}(\mathbf{r}), \qquad \mathbf{r}\in V_{\mathrm{EXT}}\cup V_{\mathrm{INT}}, \tag{2.5}$$

where

$$\mathbf{j}(\mathbf{r}) = k_1^2[\tilde{m}^2(\mathbf{r}) - 1]\,\mathbf{E}(\mathbf{r}), \tag{2.6a}$$

$$\tilde{m}(\mathbf{r}) = \begin{cases} 1, & \mathbf{r}\in V_{\mathrm{EXT}}, \\ m(\mathbf{r}) = k_2(\mathbf{r})/k_1 = m_2(\mathbf{r})/m_1, & \mathbf{r}\in V_{\mathrm{INT}}, \end{cases} \tag{2.6b}$$

and $m(\mathbf{r})$ is the refractive index of the interior relative to that of the exterior. The forcing function $\mathbf{j}(\mathbf{r})$ obviously vanishes everywhere outside the interior region.

Any solution of an inhomogeneous linear differential equation can be divided into two parts: (i) a solution of the respective homogeneous equation with the right-hand side identically equal to zero and (ii) a particular solution of the inhomogeneous equation. Thus, the first part satisfies the equation

$$\nabla\times\nabla\times\mathbf{E}^{\mathrm{inc}}(\mathbf{r}) - k_1^2\mathbf{E}^{\mathrm{inc}}(\mathbf{r}) = 0, \qquad \mathbf{r}\in V_{\mathrm{EXT}}\cup V_{\mathrm{INT}}, \tag{2.7}$$

and describes the field that would exist in the absence of the scattering object, i.e., the *incident field.* The physically appropriate particular solution of Eq. (2.5) must give the *scattered field* $\mathbf{E}^{\mathrm{sca}}(\mathbf{r})$ generated by the forcing function $\mathbf{j}(\mathbf{r})$. Obviously, of all possible particular solutions of Eq. (2.5) we must choose the one that vanishes at large distances from the scattering object and ensures energy conservation.

To find $\mathbf{E}^{\mathrm{sca}}(\mathbf{r})$, we first introduce the free space dyadic Green's function $\overleftrightarrow{G}(\mathbf{r},\mathbf{r}')$ as a dyadic (Cartesian tensor) satisfying the differential equation

$$\nabla\times\nabla\times\overleftrightarrow{G}(\mathbf{r},\mathbf{r}') - k_1^2\overleftrightarrow{G}(\mathbf{r},\mathbf{r}') = \overleftrightarrow{I}\delta(\mathbf{r}-\mathbf{r}'), \tag{2.8}$$

where $\overleftrightarrow{I}$ is the identity dyadic and $\delta(\mathbf{r}-\mathbf{r}') = \delta(x-x')\delta(y-y')\delta(z-z')$ is the three-dimensional Dirac delta function. Note that the result of a dyadic operating on a vector is another vector (see, e.g., Appendix 3 of Van Bladel 1964). This operation may be thought of as a 3×3 matrix representing the dyadic multiplying a column matrix consisting of the initial vector components, thereby producing another column matrix consisting of the resulting vector components. The components of both vectors must

be specified in the same coordinate system. From a coordinate-free standpoint, a dyadic can be introduced as a sum of so-called dyads, each dyad being the result of a dyadic product of two vectors $\mathbf{a}\otimes\mathbf{b}$ such that the operation $(\mathbf{a}\otimes\mathbf{b})\cdot\mathbf{c}$ yields the vector $\mathbf{a}(\mathbf{b}\cdot\mathbf{c})$ and the operation $\mathbf{c}\cdot(\mathbf{a}\otimes\mathbf{b})$ yields the vector $(\mathbf{c}\cdot\mathbf{a})\mathbf{b}$. Any dyadic can be represented as a sum of at most nine dyads. The vector product $(\mathbf{a}\otimes\mathbf{b})\times\mathbf{c}$ is defined as a dyad $\mathbf{a}\otimes(\mathbf{b}\times\mathbf{c})$, and $\mathbf{c}\times(\mathbf{a}\otimes\mathbf{b})$ yields $(\mathbf{c}\times\mathbf{a})\otimes\mathbf{b}$. The dot product of dyads $\mathbf{a}\otimes\mathbf{b}$ and $\mathbf{c}\otimes\mathbf{d}$ yields the dyad $(\mathbf{b}\cdot\mathbf{c})(\mathbf{a}\otimes\mathbf{d})$.

Taking into account that

$$\nabla\times[\overleftrightarrow{G}(\mathbf{r},\mathbf{r}')\cdot\mathbf{j}(\mathbf{r}')]=[\nabla\times\overleftrightarrow{G}(\mathbf{r},\mathbf{r}')]\cdot\mathbf{j}(\mathbf{r}'),$$

we get

$$\nabla\times\nabla\times[\overleftrightarrow{G}(\mathbf{r},\mathbf{r}')\cdot\mathbf{j}(\mathbf{r}')]-k_1^2[\overleftrightarrow{G}(\mathbf{r},\mathbf{r}')\cdot\mathbf{j}(\mathbf{r}')]=\overleftrightarrow{I}\cdot\mathbf{j}(\mathbf{r}')\delta(\mathbf{r}-\mathbf{r}'). \tag{2.9}$$

We integrate both sides of this equation over the entire space to obtain

$$(\nabla\times\nabla\times\overleftrightarrow{I}-k_1^2\overleftrightarrow{I})\cdot\int_{V_{\mathrm{INT}}\cup V_{\mathrm{EXT}}}\mathrm{d}\mathbf{r}'\overleftrightarrow{G}(\mathbf{r},\mathbf{r}')\cdot\mathbf{j}(\mathbf{r}')=\mathbf{j}(\mathbf{r}). \tag{2.10}$$

Comparison with Eq. (2.5) now shows that

$$\mathbf{E}^{\mathrm{sca}}(\mathbf{r})=\int_{V_{\mathrm{INT}}}\mathrm{d}\mathbf{r}'\overleftrightarrow{G}(\mathbf{r},\mathbf{r}')\cdot\mathbf{j}(\mathbf{r}'),\qquad \mathbf{r}\in V_{\mathrm{INT}}\cup V_{\mathrm{EXT}}, \tag{2.11}$$

where we have taken into account that $\mathbf{j}(\mathbf{r})$ vanishes everywhere outside V_{INT}. We will see in the following section that this particular solution of Eq. (2.5) indeed vanishes at infinity and ensures energy conservation and is therefore the physically appropriate particular solution. Hence, the complete solution of Eq. (2.5) is

$$\mathbf{E}(\mathbf{r})=\mathbf{E}^{\mathrm{inc}}(\mathbf{r})+\int_{V_{\mathrm{INT}}}\mathrm{d}\mathbf{r}'\overleftrightarrow{G}(\mathbf{r},\mathbf{r}')\cdot\mathbf{j}(\mathbf{r}'),\qquad \mathbf{r}\in V_{\mathrm{INT}}\cup V_{\mathrm{EXT}}. \tag{2.12}$$

To find the free space dyadic Green's function $\overleftrightarrow{G}(\mathbf{r},\mathbf{r}')$, we first express it in terms of a scalar Green's function $g(\mathbf{r},\mathbf{r}')$ as follows:

$$\overleftrightarrow{G}(\mathbf{r},\mathbf{r}')=\left(\overleftrightarrow{I}+\frac{1}{k_1^2}\nabla\otimes\nabla\right)g(\mathbf{r},\mathbf{r}'). \tag{2.13}$$

Inserting Eq. (2.13) into Eq. (2.8) and noticing that

$$\nabla\times[\nabla\times(\nabla\otimes\nabla)]=\nabla\times[(\nabla\times\nabla)\otimes\nabla]=\overleftrightarrow{0},$$
$$\nabla\times\nabla\times(\overleftrightarrow{I}g)=\nabla\otimes\nabla g-\overleftrightarrow{I}\,\nabla^2 g,$$

where $\overleftrightarrow{0}$ is a zero dyad, we obtain the following differential equation for g:

$$(\nabla^2+k_1^2)g(\mathbf{r},\mathbf{r}')=-\delta(\mathbf{r}-\mathbf{r}'). \tag{2.14}$$

The well-known solution of this equation representing so-called *outgoing* waves (i.e., satisfying the condition $\lim_{k_1|\mathbf{r}-\mathbf{r}'|\to\infty}g(\mathbf{r},\mathbf{r}')=0$) is

$$g(\mathbf{r}, \mathbf{r}') = \frac{\mathrm{e}^{\mathrm{i}k_1|\mathbf{r}-\mathbf{r}'|}}{4\pi|\mathbf{r}-\mathbf{r}'|} \tag{2.15}$$

(e.g., Jackson 1998, p. 427). Hence, Eqs. (2.6), (2.12), (2.13), and (2.15) finally yield (Shifrin 1968; Saxon 1955b)

$$\begin{aligned}\mathbf{E}(\mathbf{r}) &= \mathbf{E}^{\mathrm{inc}}(\mathbf{r}) + k_1^2 \int_{V_{\mathrm{INT}}} \mathrm{d}\mathbf{r}' \overleftrightarrow{G}(\mathbf{r}, \mathbf{r}') \cdot \mathbf{E}(\mathbf{r}') [m^2(\mathbf{r}') - 1] \\ &= \mathbf{E}^{\mathrm{inc}}(\mathbf{r}) + k_1^2 \left(\overleftrightarrow{I} + \frac{1}{k_1^2} \nabla \otimes \nabla \right) \cdot \int_{V_{\mathrm{INT}}} \mathrm{d}\mathbf{r}' [m^2(\mathbf{r}') - 1] \, \mathbf{E}(\mathbf{r}') \frac{\mathrm{e}^{\mathrm{i}k_1|\mathbf{r}-\mathbf{r}'|}}{4\pi|\mathbf{r}-\mathbf{r}'|}, \\ &\qquad \mathbf{r} \in V_{\mathrm{INT}} \cup V_{\mathrm{EXT}}.\end{aligned} \tag{2.16}$$

Equation (2.16) expresses the total electric field everywhere in space in terms of the incident field and the total field inside the scattering object. Since the latter is not known in general, one must solve Eq. (2.16) either numerically or analytically. As a first step, the internal field can be approximated by the incident field. This is the gist of the so-called Rayleigh–Gans approximation otherwise known as the Rayleigh–Debye or Born approximation (van de Hulst 1957; Ishimaru 1997). The total field computed in the Rayleigh-Gans approximation can be substituted in the integral on the right-hand side of Eq. (2.16) in order to compute an improved approximation, and this iterative process can be continued until the total field converges within a given numerical accuracy. Although this procedure can be rather involved, it shows that in the final analysis the total electric field can be expressed in terms of the incident field as follows:

$$\mathbf{E}(\mathbf{r}) = \mathbf{E}^{\mathrm{inc}}(\mathbf{r}) + \int_{V_{\mathrm{INT}}} \mathrm{d}\mathbf{r}' \overleftrightarrow{G}(\mathbf{r}, \mathbf{r}') \cdot \int_{V_{\mathrm{INT}}} \mathrm{d}\mathbf{r}'' \overleftrightarrow{T}(\mathbf{r}', \mathbf{r}'') \cdot \mathbf{E}^{\mathrm{inc}}(\mathbf{r}''), \qquad \mathbf{r} \in V_{\mathrm{INT}} \cup V_{\mathrm{EXT}}, \tag{2.17}$$

where $\overleftrightarrow{T}$ is the so-called dyadic transition operator (Tsang *et al*. 1985). Substituting Eq. (2.17) in Eq. (2.16), we derive the following integral equation for $\overleftrightarrow{T}$:

$$\begin{aligned}\overleftrightarrow{T}(\mathbf{r}, \mathbf{r}') &= k_1^2 [m^2(\mathbf{r}) - 1] \delta(\mathbf{r} - \mathbf{r}') \overleftrightarrow{I} \\ &\quad + k_1^2 [m^2(\mathbf{r}) - 1] \int_{V_{\mathrm{INT}}} \mathrm{d}\mathbf{r}'' \overleftrightarrow{G}(\mathbf{r}, \mathbf{r}'') \cdot \overleftrightarrow{T}(\mathbf{r}'', \mathbf{r}'), \qquad \mathbf{r}, \mathbf{r}' \in V_{\mathrm{INT}}.\end{aligned} \tag{2.18}$$

Equations of this type appear in the quantum theory of scattering and are called Lippmann-Schwinger equations (Lippmann and Schwinger 1950; Newton 1966).

2.2 Scattering in the far-field zone

Let us now choose an arbitrary point O close to the geometrical center of the scattering object as the common origin of all position (radius) vectors (Figs. 2.1(a), (b)). Usually one is interested in calculating the scattered field in the so-called far-field

zone. Specifically, let us assume that $k_1 r \gg 1$ and that r is much greater than any linear dimension of the scattering object ($r \gg r'$ for any $\mathbf{r}' \in V_{\mathrm{INT}}$). Since

$$|\mathbf{r}-\mathbf{r}'| = r\sqrt{1-2\frac{\hat{\mathbf{r}}\cdot\mathbf{r}'}{r}+\frac{r'^2}{r^2}} \approx r-\hat{\mathbf{r}}\cdot\mathbf{r}'+\frac{r'^2}{2r}, \tag{2.19}$$

where $\hat{\mathbf{r}} = \mathbf{r}/r$ is the unit vector in the direction of $\mathbf{r}$ (Fig. 2.1(b)), we have

$$g(\mathbf{r},\mathbf{r}') \approx \frac{\mathrm{e}^{\mathrm{i}k_1 r}}{4\pi r}\mathrm{e}^{-\mathrm{i}k_1\hat{\mathbf{r}}\cdot\mathbf{r}'},$$

where it is also assumed that $k_1 r'^2/2r \ll 1$. Therefore,

$$\overleftrightarrow{G}(\mathbf{r},\mathbf{r}') \approx (\overleftrightarrow{I}-\hat{\mathbf{r}}\otimes\hat{\mathbf{r}})\frac{\mathrm{e}^{\mathrm{i}k_1 r}}{4\pi r}\mathrm{e}^{-\mathrm{i}k_1\hat{\mathbf{r}}\cdot\mathbf{r}'}. \tag{2.20}$$

In deriving Eq. (2.20), we have taken into account that in spherical coordinates, defined in Section 1.3, centered at the origin,

$$\nabla = \hat{\mathbf{r}}\frac{\partial}{\partial r}+\hat{\boldsymbol{\vartheta}}\frac{1}{r}\frac{\partial}{\partial\vartheta}+\hat{\boldsymbol{\varphi}}\frac{1}{r\sin\vartheta}\frac{\partial}{\partial\varphi}, \tag{2.21}$$

where the order of operator components relative to the unit basis vectors is essential because $\hat{\mathbf{r}}$, $\hat{\boldsymbol{\vartheta}}$, and $\hat{\boldsymbol{\varphi}}$ depend on ϑ and φ. Hence,

$$\mathbf{E}^{\mathrm{sca}}(\mathbf{r}) \approx \frac{\mathrm{e}^{\mathrm{i}k_1 r}}{r}\frac{k_1^2}{4\pi}(\overleftrightarrow{I}-\hat{\mathbf{r}}\otimes\hat{\mathbf{r}})\cdot\int_{V_{\mathrm{INT}}}\mathrm{d}\mathbf{r}'[m^2(\mathbf{r}')-1]\,\mathbf{E}(\mathbf{r}')\mathrm{e}^{-\mathrm{i}k_1\hat{\mathbf{r}}\cdot\mathbf{r}'}. \tag{2.22}$$

This important formula shows that the scattered field at a large distance from the object behaves as an outgoing transverse spherical wave. Specifically, since the identity dyadic in the spherical coordinate system centered at the origin is given by

$$\overleftrightarrow{I} = \hat{\mathbf{r}}\otimes\hat{\mathbf{r}}+\hat{\boldsymbol{\vartheta}}\otimes\hat{\boldsymbol{\vartheta}}+\hat{\boldsymbol{\varphi}}\otimes\hat{\boldsymbol{\varphi}},$$

the factor $\overleftrightarrow{I}-\hat{\mathbf{r}}\otimes\hat{\mathbf{r}} = \hat{\boldsymbol{\vartheta}}\otimes\hat{\boldsymbol{\vartheta}}+\hat{\boldsymbol{\varphi}}\otimes\hat{\boldsymbol{\varphi}}$ ensures that the scattered wave in the far-field zone is transverse, i.e., the electric field vector is always perpendicular to the direction of propagation $\hat{\mathbf{r}}$:

$$\hat{\mathbf{r}}\cdot\mathbf{E}^{\mathrm{sca}}(\mathbf{r}) = 0. \tag{2.23}$$

Hence, only the ϑ- and φ-components of the electric vector of the scattered field are non-zero. Furthermore, the scattered field decays inversely with distance r from the scattering object. Equation (2.22) can be rewritten in the form

$$\mathbf{E}^{\mathrm{sca}}(\mathbf{r}) = \frac{\mathrm{e}^{\mathrm{i}k_1 r}}{r}\mathbf{E}_1^{\mathrm{sca}}(\hat{\mathbf{r}}), \qquad \hat{\mathbf{r}}\cdot\mathbf{E}_1^{\mathrm{sca}}(\hat{\mathbf{r}}) = 0, \tag{2.24}$$

where the vector $\mathbf{E}_1^{\mathrm{sca}}(\hat{\mathbf{r}})$ is independent of r and describes the angular distribution of the scattered radiation in the far-field zone. Obviously, this solution also obeys the

energy conservation law by making the total energy flux across a spherical surface of radius r independent of r.

Assuming that the incident field is a plane electromagnetic wave given by

$$\mathbf{E}^{\text{inc}}(\mathbf{r}) = \mathbf{E}_0^{\text{inc}} \exp(\mathrm{i}k_1\hat{\mathbf{n}}^{\text{inc}} \cdot \mathbf{r}) \tag{2.25}$$

and using Eq. (2.17), we derive for the far-field zone

$$\mathbf{E}^{\text{sca}}(r\hat{\mathbf{n}}^{\text{sca}}) = \frac{\mathrm{e}^{\mathrm{i}k_1 r}}{r} \overleftrightarrow{A}(\hat{\mathbf{n}}^{\text{sca}}, \hat{\mathbf{n}}^{\text{inc}}) \cdot \mathbf{E}_0^{\text{inc}}, \tag{2.26}$$

where $\hat{\mathbf{n}}^{\text{sca}} = \hat{\mathbf{r}}$ (Fig. 2.1(b)) and the scattering dyadic $\overleftrightarrow{A}$ is given by

$$\overleftrightarrow{A}(\hat{\mathbf{n}}^{\text{sca}}, \hat{\mathbf{n}}^{\text{inc}}) = \frac{1}{4\pi}(\overleftrightarrow{I} - \hat{\mathbf{n}}^{\text{sca}} \otimes \hat{\mathbf{n}}^{\text{sca}}) \cdot \int_{V_{\text{INT}}} \mathrm{d}\mathbf{r}' \exp(-\mathrm{i}k_1\hat{\mathbf{n}}^{\text{sca}} \cdot \mathbf{r}')$$
$$\times \int_{V_{\text{INT}}} \mathrm{d}\mathbf{r}'' \overleftrightarrow{T}(\mathbf{r}', \mathbf{r}'') \exp(\mathrm{i}k_1\hat{\mathbf{n}}^{\text{inc}} \cdot \mathbf{r}''). \tag{2.27}$$

The elements of the scattering dyadic have the dimension of length.

Equation (2.17) shows that if $\mathbf{E}_1^{\text{inc}}(\mathbf{r})$ and $\mathbf{E}_2^{\text{inc}}(\mathbf{r})$ are two different incident fields and $\mathbf{E}_1^{\text{sca}}(\mathbf{r})$ and $\mathbf{E}_2^{\text{sca}}(\mathbf{r})$ are the corresponding scattered fields, then $\mathbf{E}_1^{\text{sca}}(\mathbf{r}) + \mathbf{E}_2^{\text{sca}}(\mathbf{r})$ is the scattered field corresponding to the incident field $\mathbf{E}_1^{\text{inc}}(\mathbf{r}) + \mathbf{E}_2^{\text{inc}}(\mathbf{r})$. This result is, of course, a consequence of the linearity of Maxwell's equations (2.1) and (2.2) and constitutive relations (1.8)–(1.10) and a manifestation of the well-known principle of superposition: if two electromagnetic fields satisfy the Maxwell equations, then their sum also satisfies these equations. Therefore, although the scattering dyadic $\overleftrightarrow{A}$ describes the scattering of a plane electromagnetic wave, it can be used to compute the scattering of any incident field as long as the latter can be expanded in elementary plane waves.

It follows from Eqs. (2.23) and (2.27) that

$$\hat{\mathbf{n}}^{\text{sca}} \cdot \overleftrightarrow{A}(\hat{\mathbf{n}}^{\text{sca}}, \hat{\mathbf{n}}^{\text{inc}}) = 0. \tag{2.28}$$

However, because the incident field given by Eq. (2.25) is a transverse wave with electric vector perpendicular to the direction of propagation, the dot product $\overleftrightarrow{A}(\hat{\mathbf{n}}^{\text{sca}}, \hat{\mathbf{n}}^{\text{inc}}) \cdot \hat{\mathbf{n}}^{\text{inc}}$ is not defined by Eq. (2.26). To complete the definition, we take this product to be zero:

$$\overleftrightarrow{A}(\hat{\mathbf{n}}^{\text{sca}}, \hat{\mathbf{n}}^{\text{inc}}) \cdot \hat{\mathbf{n}}^{\text{inc}} = 0, \tag{2.29}$$

which means that one must retain only the part of the expression on the right-hand side of Eq. (2.27) that is transverse to the incidence direction. As a consequence of Eqs. (2.28) and (2.29), only four out of the nine components of the scattering dyadic are independent. It is therefore convenient to formulate the scattering problem in the spherical coordinate system centered at the origin and to introduce the 2×2 so-called amplitude scattering matrix $\mathbf{S}$, which describes the transformation of the ϑ- and φ-components of the incident plane wave into the ϑ- and φ-components of the scattered spherical wave:

$$\begin{bmatrix} E_{\vartheta}^{\text{sca}}(r\hat{\mathbf{n}}^{\text{sca}}) \\ E_{\varphi}^{\text{sca}}(r\hat{\mathbf{n}}^{\text{sca}}) \end{bmatrix} = \frac{\mathrm{e}^{\mathrm{i}k_1 r}}{r} \mathbf{S}(\hat{\mathbf{n}}^{\text{sca}}, \hat{\mathbf{n}}^{\text{inc}}) \begin{bmatrix} E_{0\vartheta}^{\text{inc}} \\ E_{0\varphi}^{\text{inc}} \end{bmatrix}. \tag{2.30}$$

The amplitude scattering matrix depends on the directions of incidence and scattering as well as on the size, morphology, composition, and orientation of the scattering object with respect to the coordinate system. As will be discussed in Section 2.11, it also depends on the choice of origin of the coordinate system inside the scattering object. If known, the amplitude scattering matrix gives the scattered and thus the total field, thereby providing a complete description of the scattering pattern in the far-field zone. The elements of the amplitude scattering matrix have the dimension of length and are expressed in terms of the scattering dyadic as follows:

$$S_{11} = \hat{\boldsymbol{\vartheta}}^{\text{sca}} \cdot \overleftrightarrow{A} \cdot \hat{\boldsymbol{\vartheta}}^{\text{inc}}, \tag{2.31}$$

$$S_{12} = \hat{\boldsymbol{\vartheta}}^{\text{sca}} \cdot \overleftrightarrow{A} \cdot \hat{\boldsymbol{\varphi}}^{\text{inc}}, \tag{2.32}$$

$$S_{21} = \hat{\boldsymbol{\varphi}}^{\text{sca}} \cdot \overleftrightarrow{A} \cdot \hat{\boldsymbol{\vartheta}}^{\text{inc}}, \tag{2.33}$$

$$S_{22} = \hat{\boldsymbol{\varphi}}^{\text{sca}} \cdot \overleftrightarrow{A} \cdot \hat{\boldsymbol{\varphi}}^{\text{inc}}. \tag{2.34}$$

We have pointed out in Section 1.3 that when a wave propagates along the z-axis, the ϑ- and φ-components of the electric field vector are determined by the specific choice of meridional plane. Therefore, the amplitude scattering matrix explicitly depends on φ^{inc} and φ^{sca} even when $\vartheta^{\text{inc}} = 0$ or π and/or $\vartheta^{\text{sca}} = 0$ or π.

2.3 Reciprocity

A fundamental property of the scattering dyadic is the reciprocity relation, which is a manifestation of the symmetry of the scattering process with respect to an inversion of time (Saxon 1955a). To derive the reciprocity relation, we first consider the scattering of a spherical incoming wave by an arbitrary finite object embedded in an infinite, homogeneous, nonabsorbing medium. In the far-field zone of the object, the total electric field is the sum of the incoming and scattered spherical waves:

$$\mathbf{E}(r\hat{\mathbf{r}}) = \frac{\mathrm{e}^{-\mathrm{i}k_1 r}}{r} \mathbf{E}^{\text{inc}}(\hat{\mathbf{r}}) + \frac{\mathrm{e}^{\mathrm{i}k_1 r}}{r} \mathbf{E}^{\text{sca}}(\hat{\mathbf{r}}), \tag{2.35}$$

where $\mathbf{E}^{\text{inc}}(\hat{\mathbf{r}})$ and $\mathbf{E}^{\text{sca}}(\hat{\mathbf{r}})$ are independent of r and

$$\hat{\mathbf{r}} \cdot \mathbf{E}^{\text{inc}}(\hat{\mathbf{r}}) = 0, \tag{2.36}$$

$$\hat{\mathbf{r}} \cdot \mathbf{E}^{\text{sca}}(\hat{\mathbf{r}}) = 0. \tag{2.37}$$

Equation (2.37) follows from Eq. (2.24), whereas Eq. (2.36) follows from the divergence condition

$$\nabla \cdot \mathbf{E}(\mathbf{r}) = 0 \tag{2.38}$$

(Eq. (1.17) with $\varepsilon_1 = \text{constant}$) and the following relations:

$$\nabla \cdot (f\mathbf{a}) = f\nabla \cdot \mathbf{a} + (\nabla f) \cdot \mathbf{a}, \tag{2.39}$$

$$\nabla \frac{\mathrm{e}^{\pm \mathrm{i}k_1 r}}{r} = -\left(\frac{1}{r} \mp \mathrm{i}k_1\right) \frac{\mathrm{e}^{\pm \mathrm{i}k_1 r}}{r} \hat{\mathbf{r}}, \tag{2.40}$$

$$\nabla \cdot \left[\frac{\mathrm{e}^{-\mathrm{i}k_1 r}}{r} \mathbf{E}^{\mathrm{inc}}(\hat{\mathbf{r}})\right] = \frac{\mathrm{e}^{-\mathrm{i}k_1 r}}{r} \nabla \cdot \mathbf{E}^{\mathrm{inc}}(\hat{\mathbf{r}}) - \left(\frac{1}{r} + \mathrm{i}k_1\right) \frac{\mathrm{e}^{-\mathrm{i}k_1 r}}{r} \hat{\mathbf{r}} \cdot \mathbf{E}^{\mathrm{inc}}(\hat{\mathbf{r}}) = 0, \tag{2.41}$$

$$\nabla \cdot \mathbf{E}^{\mathrm{inc}}(\hat{\mathbf{r}}) = O(r^{-1}). \tag{2.42}$$

The latter is a consequence of Eq. (2.21) and the fact that $\mathbf{E}^{\mathrm{inc}}(\hat{\mathbf{r}})$ is independent of r.

Because of the linearity of the Maxwell equations and by analogy with Eq. (2.26), the outgoing spherical wave must be linearly related to the incoming spherical wave. Following Saxon (1955a), we express this relationship in terms of the so-called scattering tensor $\overleftrightarrow{S}$ as follows:

$$\mathbf{E}^{\mathrm{sca}}(\hat{\mathbf{r}}) = -\int_{4\pi} \mathrm{d}\hat{\mathbf{r}}' \overleftrightarrow{S}(\hat{\mathbf{r}}, \hat{\mathbf{r}}') \cdot \mathbf{E}^{\mathrm{inc}}(-\hat{\mathbf{r}}'), \tag{2.43}$$

where

$$\int_{4\pi} \mathrm{d}\hat{\mathbf{r}}' = \int_0^{2\pi} \mathrm{d}\varphi' \int_0^{\pi} \mathrm{d}\vartheta' \sin\vartheta'. \tag{2.44}$$

In view of Eq. (2.37), we have

$$\hat{\mathbf{r}} \cdot \overleftrightarrow{S}(\hat{\mathbf{r}}, \hat{\mathbf{r}}') = 0. \tag{2.45}$$

Since $\mathbf{E}^{\mathrm{inc}}(\hat{\mathbf{r}})$ is transverse, the product $\overleftrightarrow{S}(\hat{\mathbf{r}}, \hat{\mathbf{r}}') \cdot \hat{\mathbf{r}}'$ remains undefined by Eq. (2.43). Therefore, we will complete the definition of the scattering tensor by taking this product to be zero:

$$\overleftrightarrow{S}(\hat{\mathbf{r}}, \hat{\mathbf{r}}') \cdot \hat{\mathbf{r}}' = 0. \tag{2.46}$$

As a consequence of Eqs. (2.45) and (2.46), $\overleftrightarrow{S}$ has only four independent components.

The derivation of the reciprocity relation for the scattering tensor starts from the fact that if $\mathbf{E}_1$ and $\mathbf{E}_2$ are any two solutions of the source-free Maxwell equations (but with the same harmonic time dependence) then

$$r^2 \int_{4\pi} \mathrm{d}\hat{\mathbf{r}}\, \hat{\mathbf{r}} \cdot \{\mathbf{E}_2(r\hat{\mathbf{r}}) \times [\nabla \times \mathbf{E}_1(r\hat{\mathbf{r}})] - \mathbf{E}_1(r\hat{\mathbf{r}}) \times [\nabla \times \mathbf{E}_2(r\hat{\mathbf{r}})]\} \underset{r\to\infty}{=} 0. \tag{2.47}$$

Indeed, using Eqs. (1.26), (2.1), and (2.2), it can easily be established that $\nabla \cdot (\mathbf{E}_2 \times \mathbf{H}_1 - \mathbf{E}_1 \times \mathbf{H}_2)$ vanishes identically everywhere in space. Integrating $\nabla \cdot (\mathbf{E}_2 \times \mathbf{H}_1 - \mathbf{E}_1 \times \mathbf{H}_2)$ over all space and applying the Gauss theorem then yields Eq. (2.47). We now take $\mathbf{E}_1$ and $\mathbf{E}_2$ at infinity to be superpositions of incoming and outgoing spherical waves:

$$\mathbf{E}_j(r\hat{\mathbf{r}}) = \frac{e^{-ik_1 r}}{r}\mathbf{E}_j^{\text{inc}}(\hat{\mathbf{r}}) + \frac{e^{ik_1 r}}{r}\mathbf{E}_j^{\text{sca}}(\hat{\mathbf{r}}), \qquad j = 1, 2. \tag{2.48}$$

Taking into account Eq. (1.40), (2.36), (2.37), and (2.40) and the formulas

$$\nabla\times(f\mathbf{a}) = (\nabla f)\times\mathbf{a} + f(\nabla\times\mathbf{a}), \tag{2.49}$$

$$\nabla\times\mathbf{E}_{1,2}^{\text{inc,sca}}(\hat{\mathbf{r}}) = O(r^{-1}), \tag{2.50}$$

cf. Eq. (2.21), we derive the following after some algebra:

$$\int_{4\pi} d\hat{\mathbf{r}}\,[\mathbf{E}_2^{\text{inc}}(\hat{\mathbf{r}})\cdot\mathbf{E}_1^{\text{sca}}(\hat{\mathbf{r}}) - \mathbf{E}_1^{\text{inc}}(\hat{\mathbf{r}})\cdot\mathbf{E}_2^{\text{sca}}(\hat{\mathbf{r}})] = 0. \tag{2.51}$$

Using Eq. (2.43) to express the outgoing waves in terms of the incoming waves, we then have

$$\int_{4\pi} d\hat{\mathbf{r}} \int_{4\pi} d\hat{\mathbf{r}}'[\mathbf{E}_2^{\text{inc}}(\hat{\mathbf{r}})\cdot\overleftrightarrow{S}(\hat{\mathbf{r}},\hat{\mathbf{r}}')\cdot\mathbf{E}_1^{\text{inc}}(-\hat{\mathbf{r}}') - \mathbf{E}_1^{\text{inc}}(\hat{\mathbf{r}})\cdot\overleftrightarrow{S}(\hat{\mathbf{r}},\hat{\mathbf{r}}')\cdot\mathbf{E}_2^{\text{inc}}(-\hat{\mathbf{r}}')] = 0. \tag{2.52}$$

Replacing $\hat{\mathbf{r}}$ by $-\hat{\mathbf{r}}'$ and $\hat{\mathbf{r}}'$ by $-\hat{\mathbf{r}}$ in the last term and transposing the tensor product according to the identity

$$\mathbf{a}\cdot\overleftrightarrow{B}\cdot\mathbf{c} = \mathbf{c}\cdot\overleftrightarrow{B}^{\text{T}}\cdot\mathbf{a}$$

we derive

$$\int_{4\pi} d\hat{\mathbf{r}} \int_{4\pi} d\hat{\mathbf{r}}'\mathbf{E}_2^{\text{inc}}(\hat{\mathbf{r}})\cdot[\overleftrightarrow{S}(\hat{\mathbf{r}},\hat{\mathbf{r}}') - \overleftrightarrow{S}^{\text{T}}(-\hat{\mathbf{r}}',-\hat{\mathbf{r}})]\cdot\mathbf{E}_1^{\text{inc}}(-\hat{\mathbf{r}}') = 0, \tag{2.53}$$

where T denotes the transposed tensor:

$$(\overleftrightarrow{S}^{\text{T}})_{ij} = \overleftrightarrow{S}_{ji}. \tag{2.54}$$

Since $\mathbf{E}_1^{\text{inc}}$ and $\mathbf{E}_2^{\text{inc}}$ are arbitrary, we finally have

$$\overleftrightarrow{S}(\hat{\mathbf{r}},\hat{\mathbf{r}}') = \overleftrightarrow{S}^{\text{T}}(-\hat{\mathbf{r}}',-\hat{\mathbf{r}}). \tag{2.55}$$

This is the reciprocity condition for the scattering tensor.

It should be remarked that in deriving Eq. (2.47) we assumed, as almost everywhere else in this book, that the permeability, permittivity, and conductivity are scalars. However, it is easily checked that Eq. (2.47) and thus the reciprocity condition (2.55) remain valid even when the permeability, permittivity, and conductivity of the scattering object are tensors, provided that all these tensors are symmetric. If any of these tensors is not symmetric, then Eq. (2.55) may become invalid (Dolginov *et al.* 1995; Lacoste and van Tiggelen 1999).

We now use Eq. (2.55) to derive the reciprocity relation for the scattering dyadic $\overleftrightarrow{A}$ by considering the case in which the scattering object is illuminated by a plane wave incident along the direction $\hat{\mathbf{n}}^{\text{inc}}$. As follows from Eqs. (2.24) and (2.25), the total electric field in the far-field zone is given by

$$\mathbf{E}(r\hat{\mathbf{n}}^{\text{sca}}) = \mathbf{E}_0^{\text{inc}} \exp(\mathrm{i}k_1 r\hat{\mathbf{n}}^{\text{inc}} \cdot \hat{\mathbf{n}}^{\text{sca}}) + \mathbf{E}_1^{\text{sca}}(\hat{\mathbf{n}}^{\text{sca}}) \frac{\mathrm{e}^{\mathrm{i}k_1 r}}{r}. \tag{2.56}$$

Representing the incident plane wave as a superposition of incoming and outgoing spherical waves,

$$\exp(\mathrm{i}k_1 r\hat{\mathbf{n}}^{\text{inc}} \cdot \hat{\mathbf{n}}^{\text{sca}}) \underset{k_1 r\to\infty}{=} \frac{\mathrm{i}2\pi}{k_1}\left[\delta(\hat{\mathbf{n}}^{\text{inc}} + \hat{\mathbf{n}}^{\text{sca}})\frac{\mathrm{e}^{-\mathrm{i}k_1 r}}{r} - \delta(\hat{\mathbf{n}}^{\text{inc}} - \hat{\mathbf{n}}^{\text{sca}})\frac{\mathrm{e}^{\mathrm{i}k_1 r}}{r}\right] \tag{2.57}$$

(see Appendix A), where

$$\delta(\hat{\mathbf{n}}^{\text{inc}} \pm \hat{\mathbf{n}}^{\text{sca}}) = \delta(\cos\vartheta^{\text{inc}} \pm \cos\vartheta^{\text{sca}})\,\delta(\varphi^{\text{inc}} \pm \varphi^{\text{sca}}) \tag{2.58}$$

is the solid-angle Dirac delta function, we derive

$$\begin{aligned}\mathbf{E}(r\hat{\mathbf{n}}^{\text{sca}}) \underset{k_1 r\to\infty}{=} & \frac{\mathrm{i}2\pi}{k_1}\mathbf{E}_0^{\text{inc}}\,\delta(\hat{\mathbf{n}}^{\text{inc}} + \hat{\mathbf{n}}^{\text{sca}})\frac{\mathrm{e}^{-\mathrm{i}k_1 r}}{r} \\ & + \left[\mathbf{E}_1^{\text{sca}}(\hat{\mathbf{n}}^{\text{sca}}) - \frac{\mathrm{i}2\pi}{k_1}\delta(\hat{\mathbf{n}}^{\text{inc}} - \hat{\mathbf{n}}^{\text{sca}})\mathbf{E}_0^{\text{inc}}\right]\frac{\mathrm{e}^{\mathrm{i}k_1 r}}{r}.\end{aligned} \tag{2.59}$$

Considering this a special form of Eq. (2.35) and recalling the definition of the scattering tensor, Eq. (2.43), we have

$$\mathbf{E}_1^{\text{sca}}(\hat{\mathbf{n}}^{\text{sca}}) = \frac{\mathrm{i}2\pi}{k_1}[\delta(\hat{\mathbf{n}}^{\text{inc}} - \hat{\mathbf{n}}^{\text{sca}})\mathbf{E}_0^{\text{inc}} - \overleftrightarrow{S}(\hat{\mathbf{n}}^{\text{sca}}, \hat{\mathbf{n}}^{\text{inc}}) \cdot \mathbf{E}_0^{\text{inc}}]. \tag{2.60}$$

It now follows from the definition of the scattering dyadic, Eqs. (2.26), (2.28), and (2.29), that

$$\overleftrightarrow{A}(\hat{\mathbf{n}}^{\text{sca}}, \hat{\mathbf{n}}^{\text{inc}}) = \frac{\mathrm{i}2\pi}{k_1}[(\overleftrightarrow{I} - \hat{\mathbf{n}}^{\text{inc}} \otimes \hat{\mathbf{n}}^{\text{inc}})\,\delta(\hat{\mathbf{n}}^{\text{inc}} - \hat{\mathbf{n}}^{\text{sca}}) - \overleftrightarrow{S}(\hat{\mathbf{n}}^{\text{sca}}, \hat{\mathbf{n}}^{\text{inc}})]. \tag{2.61}$$

Finally, from Eqs. (2.55) and (2.61) we derive the reciprocity relation for the scattering dyadic:

$$\overleftrightarrow{A}(-\hat{\mathbf{n}}^{\text{inc}}, -\hat{\mathbf{n}}^{\text{sca}}) = \overleftrightarrow{A}^{\mathrm{T}}(\hat{\mathbf{n}}^{\text{sca}}, \hat{\mathbf{n}}^{\text{inc}}). \tag{2.62}$$

The reciprocity relation for the amplitude scattering matrix follows from Eqs. (2.31)–(2.34) and (2.62) and the unit vector identities

$$\hat{\boldsymbol{\vartheta}}(-\hat{\mathbf{n}}) = \hat{\boldsymbol{\vartheta}}(\hat{\mathbf{n}}), \qquad \hat{\boldsymbol{\varphi}}(-\hat{\mathbf{n}}) = -\hat{\boldsymbol{\varphi}}(\hat{\mathbf{n}}). \tag{2.63}$$

Simple algebra gives

$$\mathbf{S}(-\hat{\mathbf{n}}^{\text{inc}}, -\hat{\mathbf{n}}^{\text{sca}}) = \begin{bmatrix} S_{11}(\hat{\mathbf{n}}^{\text{sca}}, \hat{\mathbf{n}}^{\text{inc}}) & -S_{21}(\hat{\mathbf{n}}^{\text{sca}}, \hat{\mathbf{n}}^{\text{inc}}) \\ -S_{12}(\hat{\mathbf{n}}^{\text{sca}}, \hat{\mathbf{n}}^{\text{inc}}) & S_{22}(\hat{\mathbf{n}}^{\text{sca}}, \hat{\mathbf{n}}^{\text{inc}}) \end{bmatrix}. \tag{2.64}$$

An interesting consequence of reciprocity is the so-called backscattering theorem, which directly follows from Eq. (2.64) after substituting $\hat{\mathbf{n}}^{\text{inc}} = \hat{\mathbf{n}}$ and $\hat{\mathbf{n}}^{\text{sca}} = -\hat{\mathbf{n}}$:

$$S_{21}(-\hat{\mathbf{n}}, \hat{\mathbf{n}}) = -S_{12}(-\hat{\mathbf{n}}, \hat{\mathbf{n}}) \tag{2.65}$$

(van de Hulst 1957, Section 5.32).

Because of the universal nature of reciprocity, Eqs. (2.62), (2.64), and (2.65) are important tests in computations or measurements of light scattering by small particles; violation of reciprocity means that the computations or measurements are incorrect or inaccurate. Alternatively, the use of reciprocity can substantially shorten the required computer time or reduce the measurement effort because one may calculate or measure light scattering for only half of the scattering geometries and then use Eqs. (2.62) and (2.64) for the reciprocal geometries. Reciprocity plays a fundamental role in the phenomenon of coherent backscattering of light from discrete random media discussed in Section 3.4 (e.g., Mishchenko 1992b; van Tiggelen and Maynard 1997).

2.4 Reference frames and particle orientation

It is often convenient to specify the orientation of the scattering object using the same fixed reference frame that is used to specify the directions and states of polarization of the incident and scattered waves. In what follows, we will refer to this reference frame as the laboratory coordinate system and denote it by L. Although the spatial orientation of the laboratory coordinate system is, in principle, arbitrary, it can often be chosen in such a way that it most adequately represents the geometry of the scattering medium or the physical mechanism of particle orientation. In order to describe the orientation of the scattering object with respect to the laboratory reference frame, we introduce a right-handed coordinate system P affixed to the particle and having the same origin inside the particle as L. This coordinate system will be called the particle reference frame. The orientation of the particle with respect to L is specified by three Euler angles of rotation, α, β, and γ, which transform the laboratory coordinate system $L\{x, y, z\}$ into the particle coordinate system $P\{x', y', z'\}$, as shown in Fig. 2.2. The three consecutive Euler rotations are performed as follows:

- rotation of the laboratory coordinate system about the z-axis through an angle $\alpha \in [0, 2\pi)$, reorienting the y-axis in such a way that it coincides with the line of nodes (i.e., the line formed by the intersection of the xy- and $x'y'$- planes);
- rotation about the new y-axis through an angle $\beta \in [0, \pi]$;
- rotation about the z'- axis through an angle $\gamma \in [0, 2\pi)$.

An angle of rotation is positive if the rotation is performed in the *clockwise* direction when one is looking in the positive direction of the rotation axis.

As we will see in Chapters 5 and 6, most of the available analytical and numerical techniques assume that (or become especially efficient when) the scattering problem is solved in the particle reference frame with coordinate axes directed along the axes of particle symmetry. This implies that the incidence and scattering directions and polarization reference planes must also be specified with respect to the particle refer-

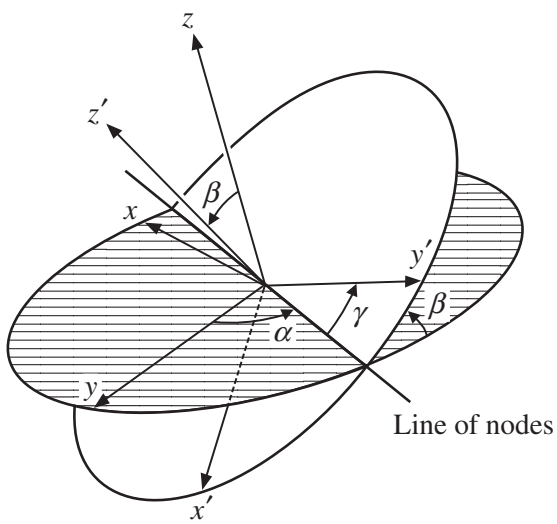

Figure 2.2. Euler angles of rotation α, β, and γ transforming the laboratory coordinate system $L\{x, y, z\}$ into the particle coordinate system $P\{x', y', z'\}$.

ence frame. Therefore, in order to solve the scattering problem with respect to the laboratory reference frame, one must first determine the illumination and scattering directions with respect to the particle reference frame for a given orientation of the particle relative to the laboratory reference frame, then solve the scattering problem in the particle reference frame, and finally perform the backward transition to the laboratory reference frame. In this section we derive general formulas describing this procedure (Mishchenko 2000).

Consider a monochromatic plane electromagnetic wave with electric field vector

$$\mathbf{E}^{\text{inc}}(\mathbf{r}) = (E_{0\vartheta L}^{\text{inc}}\hat{\boldsymbol{\vartheta}}_L^{\text{inc}} + E_{0\varphi L}^{\text{inc}}\hat{\boldsymbol{\varphi}}_L^{\text{inc}})\exp(\mathrm{i}k_1\hat{\mathbf{n}}^{\text{inc}}\cdot\mathbf{r}) \tag{2.66}$$

incident upon a nonspherical particle in a direction $\hat{\mathbf{n}}^{\text{inc}}$, where $\mathbf{r}$ is the position (radius) vector connecting the origin of the laboratory coordinate system and the observation point and the index L labels unit vectors and electric field vector components computed in the laboratory reference frame. In the far-field region, the scattered field vector components are given by

$$\begin{bmatrix} E_{\vartheta L}^{\text{sca}}(r\hat{\mathbf{n}}^{\text{sca}}) \\ E_{\varphi L}^{\text{sca}}(r\hat{\mathbf{n}}^{\text{sca}}) \end{bmatrix} = \frac{\exp(\mathrm{i}k_1 r)}{r}\mathbf{S}^L(\hat{\mathbf{n}}^{\text{sca}}, \hat{\mathbf{n}}^{\text{inc}}; \alpha, \beta, \gamma)\begin{bmatrix} E_{0\vartheta L}^{\text{inc}} \\ E_{0\varphi L}^{\text{inc}} \end{bmatrix}, \tag{2.67}$$

where $\mathbf{S}^L$ is the 2×2 amplitude scattering matrix in the laboratory reference frame. The amplitude scattering matrix depends on the directions of incidence and scattering as well as on the orientation of the scattering particle with respect to the laboratory reference frame as specified by the Euler angles of rotation α, β, and γ.

Assume now that one of the available analytical or numerical techniques can be efficiently used to find the amplitude scattering matrix with respect to the particle

reference frame. This matrix will be denoted by $\mathbf{S}^P$ and relates the incident and scattered field vector components computed in the particle reference frame for the same incidence and scattering directions:

$$\begin{bmatrix} E_{\vartheta P}^{\text{sca}}(r\hat{\mathbf{n}}^{\text{sca}}) \\ E_{\varphi P}^{\text{sca}}(r\hat{\mathbf{n}}^{\text{sca}}) \end{bmatrix} = \frac{\exp(\mathrm{i}k_1 r)}{r}\mathbf{S}^P(\hat{\mathbf{n}}^{\text{sca}}, \hat{\mathbf{n}}^{\text{inc}}) \begin{bmatrix} E_{0\vartheta P}^{\text{inc}} \\ E_{0\varphi P}^{\text{inc}} \end{bmatrix}. \tag{2.68}$$

The amplitude scattering matrix with respect to the laboratory reference frame can be expressed in terms of the matrix $\mathbf{S}^P$ as follows. Denote by $\mathbf{t}$ a 2×2 matrix that transforms the electric field vector components of a transverse electromagnetic wave computed in the laboratory reference frame into those computed in the particle reference frame:

$$\begin{bmatrix} E_{\vartheta P}(\vartheta_P, \varphi_P) \\ E_{\varphi P}(\vartheta_P, \varphi_P) \end{bmatrix} = \mathbf{t}(\hat{\mathbf{n}}; \alpha, \beta, \gamma) \begin{bmatrix} E_{\vartheta L}(\vartheta_L, \varphi_L) \\ E_{\varphi L}(\vartheta_L, \varphi_L) \end{bmatrix}, \tag{2.69}$$

where $\hat{\mathbf{n}}$ is a unit vector in the direction of light propagation; (ϑ_L, φ_L) and (ϑ_P, φ_P) specify this direction with respect to the laboratory and particle reference frames, respectively. The $\mathbf{t}$ matrix depends on $\hat{\mathbf{n}}$ as well as on the orientation of the particle relative to the laboratory reference frame, specified by the Euler angles α, β, and γ. The inverse transformation is

$$\begin{bmatrix} E_{\vartheta L}(\vartheta_L, \varphi_L) \\ E_{\varphi L}(\vartheta_L, \varphi_L) \end{bmatrix} = \mathbf{t}^{-1}(\hat{\mathbf{n}}; \alpha, \beta, \gamma) \begin{bmatrix} E_{\vartheta P}(\vartheta_P, \varphi_P) \\ E_{\varphi P}(\vartheta_P, \varphi_P) \end{bmatrix}, \tag{2.70}$$

where

$$\mathbf{t}(\hat{\mathbf{n}}; \alpha, \beta, \gamma)\,\mathbf{t}^{-1}(\hat{\mathbf{n}}; \alpha, \beta, \gamma) = \begin{bmatrix} 1 & 0 \\ 0 & 1 \end{bmatrix}. \tag{2.71}$$

We then easily derive

$$\mathbf{S}^L(\vartheta_L^{\text{sca}}, \varphi_L^{\text{sca}}; \vartheta_L^{\text{inc}}, \varphi_L^{\text{inc}}; \alpha, \beta, \gamma) = \mathbf{t}^{-1}(\hat{\mathbf{n}}^{\text{sca}}; \alpha, \beta, \gamma) \times \mathbf{S}^P(\vartheta_P^{\text{sca}}, \varphi_P^{\text{sca}}; \vartheta_P^{\text{inc}}, \varphi_P^{\text{inc}})\,\mathbf{t}(\hat{\mathbf{n}}^{\text{inc}}; \alpha, \beta, \gamma). \tag{2.72}$$

To determine the matrix $\mathbf{t}$, we proceed as follows. Denote by $\boldsymbol{\alpha}$ a 3×2 matrix that transforms the ϑ and φ components of the electric field vector into its x, y, and z components,

$$\begin{bmatrix} E_x \\ E_y \\ E_z \end{bmatrix} = \boldsymbol{\alpha}(\vartheta, \varphi) \begin{bmatrix} E_\vartheta \\ E_\varphi \end{bmatrix}, \tag{2.73}$$

and by $\boldsymbol{\beta}$ a 3×3 matrix that expresses the x, y, and z components of a vector in the particle coordinate system in terms of the x, y, and z components of the same vector in the laboratory coordinate system,

$$\begin{bmatrix} E_{xP} \\ E_{yP} \\ E_{zP} \end{bmatrix} = \boldsymbol{\beta}(\alpha, \beta, \gamma) \begin{bmatrix} E_{xL} \\ E_{yL} \\ E_{zL} \end{bmatrix}. \tag{2.74}$$

We then have

$$\mathbf{t}(\hat{\mathbf{n}}; \alpha, \beta, \gamma) = \boldsymbol{\alpha}^{-1}(\vartheta_P, \varphi_P)\, \boldsymbol{\beta}(\alpha, \beta, \gamma)\, \boldsymbol{\alpha}(\vartheta_L, \varphi_L), \tag{2.75}$$

where $\boldsymbol{\alpha}^{-1}(\vartheta_P, \varphi_P)$ is a suitable left inverse of $\boldsymbol{\alpha}(\vartheta_P, \varphi_P)$.

The matrices entering the right-hand side of Eq. (2.75) are as follows (Arfken and Weber 1995, pp. 118 and 189):

$$\boldsymbol{\alpha}(\vartheta, \varphi) = \begin{bmatrix} \cos\vartheta\cos\varphi & -\sin\varphi \\ \cos\vartheta\sin\varphi & \cos\varphi \\ -\sin\vartheta & 0 \end{bmatrix}, \tag{2.76}$$

$$\boldsymbol{\alpha}^{-1}(\vartheta, \varphi) = \begin{bmatrix} \cos\vartheta\cos\varphi & \cos\vartheta\sin\varphi & -\sin\vartheta \\ -\sin\varphi & \cos\varphi & 0 \end{bmatrix}, \tag{2.77}$$

$$\boldsymbol{\beta}(\alpha, \beta, \gamma) = \begin{bmatrix} \cos\alpha\cos\beta\cos\gamma - \sin\alpha\sin\gamma & \sin\alpha\cos\beta\cos\gamma + \cos\alpha\sin\gamma & -\sin\beta\cos\gamma \\ -\cos\alpha\cos\beta\sin\gamma - \sin\alpha\cos\gamma & -\sin\alpha\cos\beta\sin\gamma + \cos\alpha\cos\gamma & \sin\beta\sin\gamma \\ \cos\alpha\sin\beta & \sin\alpha\sin\beta & \cos\beta \end{bmatrix}. \tag{2.78}$$

To express the angles ϑ_P and φ_P in terms of the angles ϑ_L and φ_L, we rewrite Eq. (2.74) as

$$\begin{bmatrix} \sin\vartheta_P\cos\varphi_P \\ \sin\vartheta_P\sin\varphi_P \\ \cos\vartheta_P \end{bmatrix} = \boldsymbol{\beta}(\alpha, \beta, \gamma) \begin{bmatrix} \sin\vartheta_L\cos\varphi_L \\ \sin\vartheta_L\sin\varphi_L \\ \cos\vartheta_L \end{bmatrix}, \tag{2.79}$$

where (ϑ_L, φ_L) and (ϑ_P, φ_P) are spherical angular coordinates of an arbitrary unit vector in the laboratory and particle reference frames, respectively. Equations (2.78) and (2.79) and simple algebra then give

$$\cos\vartheta_P = \cos\vartheta_L\cos\beta + \sin\vartheta_L\sin\beta\cos(\varphi_L - \alpha), \tag{2.80}$$

$$\begin{aligned} \cos\varphi_P = \frac{1}{\sin\vartheta_P}[&\cos\beta\cos\gamma\sin\vartheta_L\cos(\varphi_L - \alpha) \\ &+ \sin\gamma\sin\vartheta_L\sin(\varphi_L - \alpha) - \sin\beta\cos\gamma\cos\vartheta_L], \end{aligned} \tag{2.81}$$

$$\begin{aligned} \sin\varphi_P = \frac{1}{\sin\vartheta_P}[&-\cos\beta\sin\gamma\sin\vartheta_L\cos(\varphi_L - \alpha) \\ &+ \cos\gamma\sin\vartheta_L\sin(\varphi_L - \alpha) + \sin\beta\sin\gamma\cos\vartheta_L]. \end{aligned} \tag{2.82}$$

One easily verifies that if $\alpha = 0$, $\beta = 0$, and $\gamma = 0$ (i.e., the particle reference

frame coincides with the laboratory reference frame), then $\vartheta_P = \vartheta_L$, $\varphi_P = \varphi_L$,

$$\mathbf{t}(\hat{\mathbf{n}}; \alpha = 0, \beta = 0, \gamma = 0) \equiv \begin{bmatrix} 1 & 0 \\ 0 & 1 \end{bmatrix}, \tag{2.83}$$

and

$$\mathbf{S}^L(\vartheta_L^{\text{sca}}, \varphi_L^{\text{sca}}; \vartheta_L^{\text{inc}}, \varphi_L^{\text{inc}}; 0, 0, 0) = \mathbf{S}^P(\vartheta_P^{\text{sca}}, \varphi_P^{\text{sca}}; \vartheta_P^{\text{inc}}, \varphi_P^{\text{inc}}). \tag{2.84}$$

For rotationally symmetric particles, it is often advantageous to choose the particle coordinate system such that its z-axis is directed along the axis of particle symmetry. In this case the orientation of the particle with respect to the laboratory coordinate system is independent of the Euler angle γ, so that we can set $\gamma = 0$ and get instead of Eqs. (2.78), (2.81), and (2.82)

$$\boldsymbol{\beta}(\alpha, \beta, \gamma = 0) = \begin{bmatrix} \cos\alpha\cos\beta & \sin\alpha\cos\beta & -\sin\beta \\ -\sin\alpha & \cos\alpha & 0 \\ \cos\alpha\sin\beta & \sin\alpha\sin\beta & \cos\beta \end{bmatrix}, \tag{2.85}$$

$$\cos\varphi_P = \frac{1}{\sin\vartheta_P}[\cos\beta\sin\vartheta_L\cos(\varphi_L - \alpha) - \sin\beta\cos\vartheta_L], \tag{2.86}$$

$$\sin\varphi_P = \frac{\sin\vartheta_L\sin(\varphi_L - \alpha)}{\sin\vartheta_P}. \tag{2.87}$$

In summary, the numerical scheme for computing the amplitude scattering matrix for given ϑ_L^{inc}, φ_L^{inc}, ϑ_L^{sca}, φ_L^{sca}, α, β, and γ is as follows:

- calculation of ϑ_P^{inc}, φ_P^{inc}, ϑ_P^{sca}, and φ_P^{sca} via Eqs. (2.80)–(2.82);
- calculation of the matrix $\boldsymbol{\beta}(\alpha, \beta, \gamma)$ via Eq. (2.78);
- calculation of the matrices $\boldsymbol{\alpha}(\vartheta_L^{\text{inc}}, \varphi_L^{\text{inc}})$, $\boldsymbol{\alpha}(\vartheta_L^{\text{sca}}, \varphi_L^{\text{sca}})$, $\boldsymbol{\alpha}^{-1}(\vartheta_P^{\text{inc}}, \varphi_P^{\text{inc}})$, and $\boldsymbol{\alpha}^{-1}(\vartheta_P^{\text{sca}}, \varphi_P^{\text{sca}})$ via Eqs. (2.76) and (2.77);
- calculation of the matrices $\mathbf{t}(\hat{\mathbf{n}}^{\text{inc}}; \alpha, \beta, \gamma)$ and $\mathbf{t}^{-1}(\hat{\mathbf{n}}^{\text{sca}}; \alpha, \beta, \gamma)$ via Eq. (2.75);
- calculation of the matrix $\mathbf{S}^P(\vartheta_P^{\text{sca}}, \varphi_P^{\text{sca}}; \vartheta_P^{\text{inc}}, \varphi_P^{\text{inc}})$ using one of the available analytical or numerical techniques;
- calculation of the matrix $\mathbf{S}^L(\vartheta_L^{\text{sca}}, \varphi_L^{\text{sca}}; \vartheta_L^{\text{inc}}, \varphi_L^{\text{inc}}; \alpha, \beta, \gamma)$ via Eq. (2.72).

We finally remark that because the particle reference frame can, in principle, be chosen arbitrarily, Eq. (2.72) can be considered as a general rotation transformation law expressing the amplitude scattering matrix in the original coordinate system in terms of the amplitude scattering matrix computed in a rotated coordinate system.

2.5 Poynting vector of the total field

Although the knowledge of the amplitude scattering matrix provides a complete de-

scription of the monochromatic scattering process in the far-field zone, measurement of the amplitude scattering matrix is a very complicated experimental problem involving the determination of both the amplitude and the phase of the incident and scattered waves. Measuring the phase is especially difficult, and only a handful of such experiments have been performed, all using the microwave analog technique (Gustafson 2000). The majority of other experiments have dealt with quasi-monochromatic rather than monochromatic light and involved measurements of derivative quantities having the dimension of energy flux rather than the electric field itself. It is therefore useful to characterize the scattering process using quantities that are easier to measure and are encountered more often, even though they may provide a less complete description of the scattering pattern in some cases. These quantities will be introduced in this and the following sections.

We begin by writing the time-averaged Poynting vector $\langle \mathbf{S}(\mathbf{r})\rangle$ at any point in the far-field zone as the sum of three terms:

$$\langle \mathbf{S}(\mathbf{r})\rangle = \tfrac{1}{2}\mathrm{Re}[\mathbf{E}(\mathbf{r})\times\mathbf{H}^*(\mathbf{r})] = \langle \mathbf{S}^{\mathrm{inc}}(\mathbf{r})\rangle + \langle \mathbf{S}^{\mathrm{sca}}(\mathbf{r})\rangle + \langle \mathbf{S}^{\mathrm{ext}}(\mathbf{r})\rangle, \tag{2.88}$$

where

$$\langle \mathbf{S}^{\mathrm{inc}}(\mathbf{r})\rangle = \tfrac{1}{2}\mathrm{Re}\{\mathbf{E}^{\mathrm{inc}}(\mathbf{r})\times[\mathbf{H}^{\mathrm{inc}}(\mathbf{r})]^*\} \tag{2.89}$$

and

$$\langle \mathbf{S}^{\mathrm{sca}}(\mathbf{r})\rangle = \tfrac{1}{2}\mathrm{Re}\{\mathbf{E}^{\mathrm{sca}}(\mathbf{r})\times[\mathbf{H}^{\mathrm{sca}}(\mathbf{r})]^*\} \tag{2.90}$$

are Poynting vectors associated with the incident and the scattered fields, respectively, whereas

$$\langle \mathbf{S}^{\mathrm{ext}}(\mathbf{r})\rangle = \tfrac{1}{2}\mathrm{Re}\{\mathbf{E}^{\mathrm{inc}}(\mathbf{r})\times[\mathbf{H}^{\mathrm{sca}}(\mathbf{r})]^* + \mathbf{E}^{\mathrm{sca}}(\mathbf{r})\times[\mathbf{H}^{\mathrm{inc}}(\mathbf{r})]^*\} \tag{2.91}$$

can be interpreted as a term caused by interaction between the incident and the scattered fields. Let us consider a scattering object illuminated by a plane electromagnetic wave. Recalling Eqs. (1.36), (1.38), (1.42), (2.25), and (2.57), we have for the incident wave in the far-field zone of the scattering particle

$$\begin{aligned}\mathbf{E}^{\mathrm{inc}}(\mathbf{r}) &= \mathbf{E}_0^{\mathrm{inc}}\exp(\mathrm{i}k_1\hat{\mathbf{n}}^{\mathrm{inc}}\cdot\mathbf{r})\\ &\underset{k_1r\to\infty}{=} \frac{\mathrm{i}2\pi}{k_1}\left[\delta(\hat{\mathbf{n}}^{\mathrm{inc}}+\hat{\mathbf{r}})\frac{\mathrm{e}^{-\mathrm{i}k_1r}}{r} - \delta(\hat{\mathbf{n}}^{\mathrm{inc}}-\hat{\mathbf{r}})\frac{\mathrm{e}^{\mathrm{i}k_1r}}{r}\right]\mathbf{E}_0^{\mathrm{inc}}, \qquad \mathbf{E}_0^{\mathrm{inc}}\cdot\hat{\mathbf{n}}^{\mathrm{inc}} = 0,\end{aligned} \tag{2.92}$$

$$\begin{aligned}\mathbf{H}^{\mathrm{inc}}(\mathbf{r}) &= \sqrt{\frac{\varepsilon_1}{\mu_0}}\exp(\mathrm{i}k_1\hat{\mathbf{n}}^{\mathrm{inc}}\cdot\mathbf{r})\,\hat{\mathbf{n}}^{\mathrm{inc}}\times\mathbf{E}_0^{\mathrm{inc}}\\ &\underset{k_1r\to\infty}{=} \frac{\mathrm{i}2\pi}{k_1}\left[\delta(\hat{\mathbf{n}}^{\mathrm{inc}}+\hat{\mathbf{r}})\frac{\mathrm{e}^{-\mathrm{i}k_1r}}{r} - \delta(\hat{\mathbf{n}}^{\mathrm{inc}}-\hat{\mathbf{r}})\frac{\mathrm{e}^{\mathrm{i}k_1r}}{r}\right]\sqrt{\frac{\varepsilon_1}{\mu_0}}\,\hat{\mathbf{n}}^{\mathrm{inc}}\times\mathbf{E}_0^{\mathrm{inc}},\end{aligned} \tag{2.93}$$

where $\mathbf{r} = r\hat{\mathbf{r}}$ is the radius vector connecting the particle and the observation point. The first relation of Eq. (2.1) and Eqs. (2.23), (2.24), (2.40), and (2.49)–(2.50) give for the scattered wave:

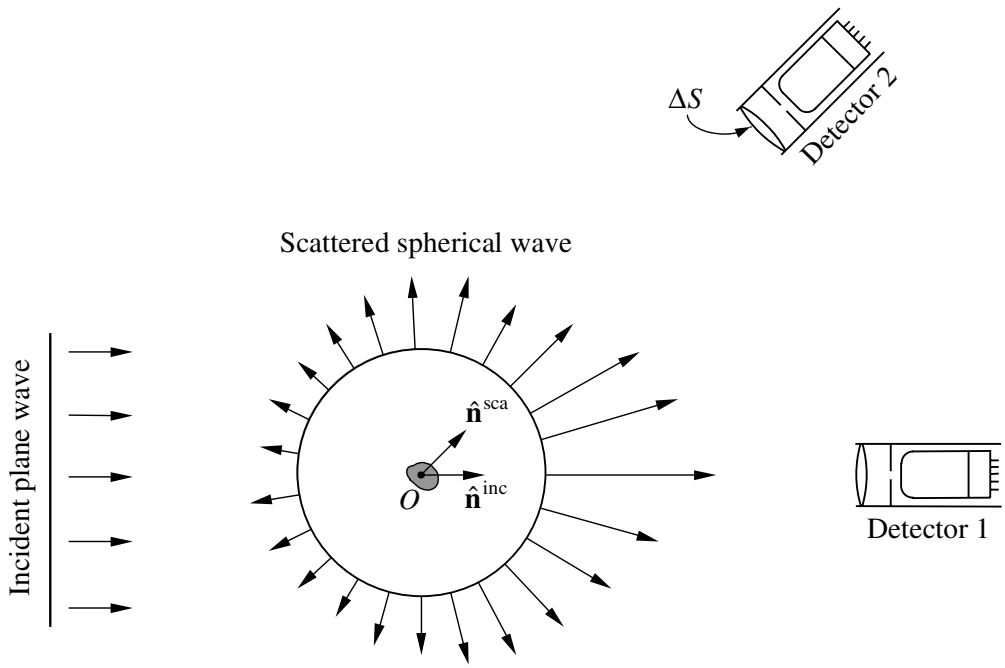

Figure 2.3. The response of the collimated detector depends on the line of sight.

$$\mathbf{E}^{\text{sca}}(\mathbf{r}) \underset{k_1 r \to \infty}{=} \frac{\mathrm{e}^{\mathrm{i}k_1 r}}{r} \mathbf{E}_1^{\text{sca}}(\hat{\mathbf{r}}), \qquad \mathbf{E}_1^{\text{sca}}(\hat{\mathbf{r}}) \cdot \hat{\mathbf{r}} = 0, \tag{2.94}$$

$$\mathbf{H}^{\text{sca}}(\mathbf{r}) \underset{k_1 r \to \infty}{=} \sqrt{\frac{\varepsilon_1}{\mu_0}} \frac{\mathrm{e}^{\mathrm{i}k_1 r}}{r} \hat{\mathbf{r}} \times \mathbf{E}_1^{\text{sca}}(\hat{\mathbf{r}}). \tag{2.95}$$

Consider now a well-collimated detector of electromagnetic radiation placed at a distance r from the particle in the far-field zone, with its surface ΔS aligned normal to and centered on the straight line extending from the particle in the direction of the unit vector $\hat{\mathbf{r}}$ (Fig. 2.3). We assume that the dimension of the detector surface is much greater than any dimension of the scattering object and the wavelength but much smaller than r. Furthermore, we assume that $\Delta S/r^2$ is smaller than the detector solid-angle field of view Ω so that all radiation scattered by the particle and impinging on ΔS is detected. Obviously, the term $\langle \mathbf{S}^{\text{inc}}(\mathbf{r}) \rangle$ does not contribute to the detected signal unless $\hat{\mathbf{r}} = \hat{\mathbf{n}}^{\text{inc}}$. From Eqs. (2.88)–(2.95), it is straightforward to show that the total electromagnetic power received by the detector is

$$\begin{aligned} W_{\Delta S}(\hat{\mathbf{n}}^{\text{sca}}) &= \int_{\Delta S} \mathrm{d}S \hat{\mathbf{n}}^{\text{sca}} \cdot \langle \mathbf{S}(\mathbf{r}) \rangle \\ &\approx \Delta S \frac{1}{2} \sqrt{\frac{\varepsilon_1}{\mu_0}} \frac{1}{r^2} |\mathbf{E}_1^{\text{sca}}(\hat{\mathbf{n}}^{\text{sca}})|^2 \end{aligned} \tag{2.96}$$

when $\hat{\mathbf{n}}^{\text{sca}} \neq \hat{\mathbf{n}}^{\text{inc}}$, whereas for the exact forward-scattering direction

$$
\begin{aligned}
W_{\Delta S}(\hat{\mathbf{n}}^{\text{inc}}) &= \int_{\Delta S} \mathrm{d}S\,\hat{\mathbf{n}}^{\text{inc}} \cdot \langle \mathbf{S}(\mathbf{r}) \rangle \\
&= \Delta S \frac{1}{2}\sqrt{\frac{\varepsilon_1}{\mu_0}}\,|\mathbf{E}_0^{\text{inc}}|^2 + \int_{\Delta S} \mathrm{d}S\,\hat{\mathbf{n}}^{\text{inc}} \cdot [\langle \mathbf{S}^{\text{sca}}(\mathbf{r}) \rangle + \langle \mathbf{S}^{\text{ext}}(\mathbf{r}) \rangle] \\
&\approx \Delta S \frac{1}{2}\sqrt{\frac{\varepsilon_1}{\mu_0}}\left[|\mathbf{E}_0^{\text{inc}}|^2 + \frac{1}{r^2}|\mathbf{E}_1^{\text{sca}}(\hat{\mathbf{n}}^{\text{inc}})|^2\right] + r^2 \int_{\Delta\Omega} \mathrm{d}\hat{\mathbf{r}}\,\hat{\mathbf{n}}^{\text{inc}} \cdot \langle \mathbf{S}^{\text{ext}}(r\mathbf{r}) \rangle \\
&\approx \Delta S \frac{1}{2}\sqrt{\frac{\varepsilon_1}{\mu_0}}\left[|\mathbf{E}_0^{\text{inc}}|^2 + \frac{1}{r^2}|\mathbf{E}_1^{\text{sca}}(\hat{\mathbf{n}}^{\text{inc}})|^2\right] - \frac{2\pi}{k_1}\sqrt{\frac{\varepsilon_1}{\mu_0}}\,\mathrm{Im}[\mathbf{E}_1^{\text{sca}}(\hat{\mathbf{n}}^{\text{inc}}) \cdot \mathbf{E}_0^{\text{inc}*}] \\
&= \Delta S \frac{1}{2}\sqrt{\frac{\varepsilon_1}{\mu_0}}\,|\mathbf{E}_0^{\text{inc}}|^2 - \frac{2\pi}{k_1}\sqrt{\frac{\varepsilon_1}{\mu_0}}\,\mathrm{Im}[\mathbf{E}_1^{\text{sca}}(\hat{\mathbf{n}}^{\text{inc}}) \cdot \mathbf{E}_0^{\text{inc}*}] + O(r^{-2}), \qquad (2.97)
\end{aligned}
$$

where $\Delta\Omega = \Delta S/r^2$ is the solid angle element centered at the direction $\hat{\mathbf{n}}^{\text{inc}}$ and formed by the detector surface at the distance r from the particle. The term $\frac{1}{2}\Delta S\sqrt{\varepsilon_1/\mu_0}\,|\mathbf{E}_0^{\text{inc}}|^2$ on the right-hand side of Eq. (2.97) is proportional to the detector area ΔS and is equal to the electromagnetic power that would be received by detector 1 in the absence of the scattering particle, whereas $-(2\pi/k_1)\sqrt{\varepsilon_1/\mu_0}\,\mathrm{Im}[\mathbf{E}_1^{\text{sca}}(\hat{\mathbf{n}}^{\text{inc}}) \cdot \mathbf{E}_0^{\text{inc}*}]$ is an attenuation term independent of ΔS, caused by interposing the particle between the light source and the detector. Thus, a well-collimated detector located in the far-field zone and having its surface ΔS aligned normal to the exact forward-scattering direction (i.e., $\hat{\mathbf{n}}^{\text{sca}} = \hat{\mathbf{n}}^{\text{inc}}$, detector 1 in Fig. 2.3) measures the power of the incident light attenuated by interference of the incident and the scattered fields plus a relatively small contribution from the scattered light, whereas a detector with surface aligned normal to any other scattering direction (i.e., $\hat{\mathbf{n}}^{\text{sca}} \neq \hat{\mathbf{n}}^{\text{inc}}$, detector 2 in Fig. 2.3) "sees" only the scattered light. These are two fundamental features of electromagnetic scattering by a small particle. Equation (2.97) is a representation of the so-called optical theorem and will be further discussed in Section 2.8.

2.6 Phase matrix

In the thought experiment described in the previous section and shown schematically in Fig. 2.3, it is assumed that the detectors can measure only the total electromagnetic power and that they make no distinction between electromagnetic waves with different states of polarization. Many detectors of electromagnetic energy are indeed polarization-insensitive. However, by interposing a polarizer between the source of light and the scattering particle one can generate incident light with a specific state of polarization, whereas interposing a polarizer between the scattering particle and the detector enables the detector to measure the power corresponding to a particular polarization component of the scattered light. By repeating the measurement for a num-

ber of different combinations of the polarizers one can, in principle, determine the specific prescription for the transformation of a complete set of polarization characteristics of the incident light into that of the scattered light, *provided that both sets of characteristics have the same dimension of energy flux* (Section 8.1). As we saw in Chapter 1, convenient complete sets of polarization characteristics having the dimension of monochromatic energy flux are the coherency and the Stokes vectors. So we will now assume that the device shown schematically in Fig. 2.3 can (i) generate incident light with different (but physically realizable) combinations of coherency or Stokes vector components, and (ii) measure the electromagnetic power associated with any component of the coherency vector or the Stokes vector and equal to the integral of the component over the surface ΔS of the collimated detector aligned normal to the direction of propagation $\hat{\mathbf{r}}$. The component itself is then found by dividing the measured power by ΔS.

To derive the relationship between the polarization characteristics of the incident and the scattered waves for scattering directions *away from the incidence direction* ($\hat{\mathbf{r}} \neq \hat{\mathbf{n}}^{\text{inc}}$), we first define the respective coherency vectors (cf. Eqs. (1.53), (2.24), and (2.25)):

$$\mathbf{J}^{\text{inc}} = \frac{1}{2}\sqrt{\frac{\varepsilon_1}{\mu_0}} \begin{bmatrix} E_{0\vartheta}^{\text{inc}} E_{0\vartheta}^{\text{inc}*} \\ E_{0\vartheta}^{\text{inc}} E_{0\varphi}^{\text{inc}*} \\ E_{0\varphi}^{\text{inc}} E_{0\vartheta}^{\text{inc}*} \\ E_{0\varphi}^{\text{inc}} E_{0\varphi}^{\text{inc}*} \end{bmatrix}, \tag{2.98}$$

$$\begin{aligned} \mathbf{J}^{\text{sca}}(r\hat{\mathbf{n}}^{\text{sca}}) &= \frac{1}{2}\sqrt{\frac{\varepsilon_1}{\mu_0}} \begin{bmatrix} E_{\vartheta}^{\text{sca}}(r\hat{\mathbf{n}}^{\text{sca}})[E_{\vartheta}^{\text{sca}}(r\hat{\mathbf{n}}^{\text{sca}})]^* \\ E_{\vartheta}^{\text{sca}}(r\hat{\mathbf{n}}^{\text{sca}})[E_{\varphi}^{\text{sca}}(r\hat{\mathbf{n}}^{\text{sca}})]^* \\ E_{\varphi}^{\text{sca}}(r\hat{\mathbf{n}}^{\text{sca}})[E_{\vartheta}^{\text{sca}}(r\hat{\mathbf{n}}^{\text{sca}})]^* \\ E_{\varphi}^{\text{sca}}(r\hat{\mathbf{n}}^{\text{sca}})[E_{\varphi}^{\text{sca}}(r\hat{\mathbf{n}}^{\text{sca}})]^* \end{bmatrix} \\ &= \frac{1}{r^2}\frac{1}{2}\sqrt{\frac{\varepsilon_1}{\mu_0}} \begin{bmatrix} E_{1\vartheta}^{\text{sca}}(\hat{\mathbf{n}}^{\text{sca}})[E_{1\vartheta}^{\text{sca}}(\hat{\mathbf{n}}^{\text{sca}})]^* \\ E_{1\vartheta}^{\text{sca}}(\hat{\mathbf{n}}^{\text{sca}})[E_{1\varphi}^{\text{sca}}(\hat{\mathbf{n}}^{\text{sca}})]^* \\ E_{1\varphi}^{\text{sca}}(\hat{\mathbf{n}}^{\text{sca}})[E_{1\vartheta}^{\text{sca}}(\hat{\mathbf{n}}^{\text{sca}})]^* \\ E_{1\varphi}^{\text{sca}}(\hat{\mathbf{n}}^{\text{sca}})[E_{1\varphi}^{\text{sca}}(\hat{\mathbf{n}}^{\text{sca}})]^* \end{bmatrix}. \end{aligned} \tag{2.99}$$

Equation (2.30) and simple algebra lead to the following formula describing the transformation of the coherency column vector of the incident wave into that of the scattered wave:

$$\mathbf{J}^{\text{sca}}(r\hat{\mathbf{n}}^{\text{sca}}) = \frac{1}{r^2}\mathbf{Z}^J(\hat{\mathbf{n}}^{\text{sca}}, \hat{\mathbf{n}}^{\text{inc}})\mathbf{J}^{\text{inc}}, \tag{2.100}$$

where the elements of the coherency phase matrix $\mathbf{Z}^J(\hat{\mathbf{n}}^{\text{sca}}, \hat{\mathbf{n}}^{\text{inc}})$ are quadratic combinations of the elements of the amplitude scattering matrix $\mathbf{S}(\hat{\mathbf{n}}^{\text{sca}}, \hat{\mathbf{n}}^{\text{inc}})$:

$$\mathbf{Z}^J = \begin{bmatrix} |S_{11}|^2 & S_{11}S_{12}^* & S_{12}S_{11}^* & |S_{12}|^2 \\ S_{11}S_{21}^* & S_{11}S_{22}^* & S_{12}S_{21}^* & S_{12}S_{22}^* \\ S_{21}S_{11}^* & S_{21}S_{12}^* & S_{22}S_{11}^* & S_{22}S_{12}^* \\ |S_{21}|^2 & S_{21}S_{22}^* & S_{22}S_{21}^* & |S_{22}|^2 \end{bmatrix}. \tag{2.101}$$

Analogously, the Stokes phase matrix $\mathbf{Z}$ describes the transformation of the Stokes column vector of the incident wave into that of the scattered wave,

$$\mathbf{I}^{\text{sca}}(r\hat{\mathbf{n}}^{\text{sca}}) = \frac{1}{r^2}\mathbf{Z}(\hat{\mathbf{n}}^{\text{sca}}, \hat{\mathbf{n}}^{\text{inc}})\mathbf{I}^{\text{inc}}, \tag{2.102}$$

and is given by

$$\mathbf{Z}(\hat{\mathbf{n}}^{\text{sca}}, \hat{\mathbf{n}}^{\text{inc}}) = \mathbf{D}\mathbf{Z}^J(\hat{\mathbf{n}}^{\text{sca}}, \hat{\mathbf{n}}^{\text{inc}})\mathbf{D}^{-1}, \tag{2.103}$$

where

$$\mathbf{I}^{\text{inc}} = \mathbf{D}\mathbf{J}^{\text{inc}} = \frac{1}{2}\sqrt{\frac{\varepsilon_1}{\mu_0}} \begin{bmatrix} E_{0\vartheta}^{\text{inc}}E_{0\vartheta}^{\text{inc}*} + E_{0\varphi}^{\text{inc}}E_{0\varphi}^{\text{inc}*} \\ E_{0\vartheta}^{\text{inc}}E_{0\vartheta}^{\text{inc}*} - E_{0\varphi}^{\text{inc}}E_{0\varphi}^{\text{inc}*} \\ -E_{0\vartheta}^{\text{inc}}E_{0\varphi}^{\text{inc}*} - E_{0\varphi}^{\text{inc}}E_{0\vartheta}^{\text{inc}*} \\ \mathrm{i}(E_{0\varphi}^{\text{inc}}E_{0\vartheta}^{\text{inc}*} - E_{0\vartheta}^{\text{inc}}E_{0\varphi}^{\text{inc}*}) \end{bmatrix} \tag{2.104}$$

and

$$\mathbf{I}^{\text{sca}}(r\hat{\mathbf{n}}^{\text{sca}}) = \mathbf{D}\mathbf{J}^{\text{sca}}(r\hat{\mathbf{n}}^{\text{sca}}) = \frac{1}{r^2}\frac{1}{2}\sqrt{\frac{\varepsilon_1}{\mu_0}} \begin{bmatrix} E_{1\vartheta}^{\text{sca}}E_{1\vartheta}^{\text{sca}*} + E_{1\varphi}^{\text{sca}}E_{1\varphi}^{\text{sca}*} \\ E_{1\vartheta}^{\text{sca}}E_{1\vartheta}^{\text{sca}*} - E_{1\varphi}^{\text{sca}}E_{1\varphi}^{\text{sca}*} \\ -E_{1\vartheta}^{\text{sca}}E_{1\varphi}^{\text{sca}*} - E_{1\varphi}^{\text{sca}}E_{1\vartheta}^{\text{sca}*} \\ \mathrm{i}(E_{1\varphi}^{\text{sca}}E_{1\vartheta}^{\text{sca}*} - E_{1\vartheta}^{\text{sca}}E_{1\varphi}^{\text{sca}*}) \end{bmatrix} \tag{2.105}$$

(cf. Eq. (1.54)); the matrices $\mathbf{D}$ and $\mathbf{D}^{-1}$ were defined by Eqs. (1.55) and (1.57), respectively. Explicit formulas for the elements of the Stokes phase matrix in terms of the amplitude scattering matrix elements follow from Eqs. (2.101) and (2.103):

$$Z_{11} = \tfrac{1}{2}(|S_{11}|^2 + |S_{12}|^2 + |S_{21}|^2 + |S_{22}|^2), \tag{2.106}$$

$$Z_{12} = \tfrac{1}{2}(|S_{11}|^2 - |S_{12}|^2 + |S_{21}|^2 - |S_{22}|^2), \tag{2.107}$$

$$Z_{13} = -\mathrm{Re}(S_{11}S_{12}^* + S_{22}S_{21}^*), \tag{2.108}$$

$$Z_{14} = -\mathrm{Im}(S_{11}S_{12}^* - S_{22}S_{21}^*), \tag{2.109}$$

$$Z_{21} = \tfrac{1}{2}(|S_{11}|^2 + |S_{12}|^2 - |S_{21}|^2 - |S_{22}|^2), \tag{2.110}$$

$$Z_{22} = \tfrac{1}{2}(|S_{11}|^2 - |S_{12}|^2 - |S_{21}|^2 + |S_{22}|^2), \tag{2.111}$$

$$Z_{23} = -\mathrm{Re}(S_{11}S_{12}^* - S_{22}S_{21}^*), \tag{2.112}$$

$$Z_{24} = -\mathrm{Im}(S_{11}S_{12}^* + S_{22}S_{21}^*), \tag{2.113}$$

$$Z_{31} = -\mathrm{Re}(S_{11}S_{21}^* + S_{22}S_{12}^*), \tag{2.114}$$

$$Z_{32} = -\mathrm{Re}(S_{11}S_{21}^* - S_{22}S_{12}^*), \tag{2.115}$$

$$Z_{33} = \mathrm{Re}(S_{11}S_{22}^* + S_{12}S_{21}^*), \tag{2.116}$$

$$Z_{34} = \mathrm{Im}(S_{11}S_{22}^* + S_{21}S_{12}^*), \tag{2.117}$$

$$Z_{41} = -\mathrm{Im}(S_{21}S_{11}^* + S_{22}S_{12}^*), \tag{2.118}$$

$$Z_{42} = -\mathrm{Im}(S_{21}S_{11}^* - S_{22}S_{12}^*), \tag{2.119}$$

$$Z_{43} = \mathrm{Im}(S_{22}S_{11}^* - S_{12}S_{21}^*), \tag{2.120}$$

$$Z_{44} = \mathrm{Re}(S_{22}S_{11}^* - S_{12}S_{21}^*). \tag{2.121}$$

Finally, the modified Stokes and circular-polarization phase matrices are given by

$$\mathbf{Z}^{\mathrm{MS}}(\hat{\mathbf{n}}^{\mathrm{sca}}, \hat{\mathbf{n}}^{\mathrm{inc}}) = \mathbf{B}\mathbf{Z}(\hat{\mathbf{n}}^{\mathrm{sca}}, \hat{\mathbf{n}}^{\mathrm{inc}})\mathbf{B}^{-1} \tag{2.122}$$

and

$$\mathbf{Z}^{\mathrm{CP}}(\hat{\mathbf{n}}^{\mathrm{sca}}, \hat{\mathbf{n}}^{\mathrm{inc}}) = \mathbf{A}\mathbf{Z}(\hat{\mathbf{n}}^{\mathrm{sca}}, \hat{\mathbf{n}}^{\mathrm{inc}})\mathbf{A}^{-1}, \tag{2.123}$$

respectively (see Eqs. (1.59)–(1.66)). The elements of all phase matrices have the same dimension of area. The matrices $\mathbf{Z}$ and $\mathbf{Z}^{\mathrm{MS}}$ are real-valued. Like the amplitude scattering matrix, the phase matrices explicitly depend on φ^{inc} and φ^{sca} even when the incident and/or scattered light propagates along the z-axis.

Up to this point we have considered the scattering of only monochromatic plane waves. However, it is obvious that Eqs. (2.100) and (2.102) remain valid even when the incident radiation is a parallel quasi-monochromatic beam of light, provided that the coherency and Stokes vectors entering these equations are averages over a time interval long compared with the period of fluctuations (Section 1.6). Hence, the phase matrix concept is quite useful even in the more general situations involving quasi-monochromatic light.

In general, all 16 elements of any of the phase matrices introduced above are nonzero. However, the phase matrix elements of a single particle are expressed in terms of only seven independent real numbers resulting from the four moduli $|S_{ij}|$ $(i, j = 1,2)$ and three differences in phase between the S_{ij}. Therefore, only seven of the phase matrix elements are actually independent, and there must be nine unique relations among the 16 phase matrix elements. Furthermore, the specific mathematical structure of the phase matrix can also be used to derive many useful linear and quadratic inequalities for the phase matrix elements. Two important inequalities are $Z_{11} \geq 0$ (this property follows directly from Eq. (2.106)) and $|Z_{ij}| \leq Z_{11}$ $(i, j = 1, \ldots, 4)$. The reader is referred to Hovenier *et al*. (1986), Cloude and Pottier (1996), and Hovenier and van der Mee (1996, 2000) for a review of this subject and a discussion of how the general properties of the phase matrix can be used for testing the results of theoretical computations and laboratory measurements.

From Eqs. (2.106)–(2.121) and (2.64) we derive the reciprocity relation for the Stokes phase matrix:

$$\mathbf{Z}(-\hat{\mathbf{n}}^{\text{inc}}, -\hat{\mathbf{n}}^{\text{sca}}) = \mathbf{\Delta}_3[\mathbf{Z}(\hat{\mathbf{n}}^{\text{sca}}, \hat{\mathbf{n}}^{\text{inc}})]^{\text{T}}\mathbf{\Delta}_3, \tag{2.124}$$

where

$$\mathbf{\Delta}_3 = \mathbf{\Delta}_3^{\text{T}} = \mathbf{\Delta}_3^{-1} = \begin{bmatrix} 1 & 0 & 0 & 0 \\ 0 & 1 & 0 & 0 \\ 0 & 0 & -1 & 0 \\ 0 & 0 & 0 & 1 \end{bmatrix} \tag{2.125}$$

and T denotes the transpose of a matrix, as before. The reciprocity relations for other phase matrices can be obtained easily from Eqs. (2.103), (2.122), and (2.123):

$$\begin{aligned} \mathbf{Z}^J(-\hat{\mathbf{n}}^{\text{inc}}, -\hat{\mathbf{n}}^{\text{sca}}) &= \mathbf{D}^{-1}\mathbf{Z}(-\hat{\mathbf{n}}^{\text{inc}}, -\hat{\mathbf{n}}^{\text{sca}})\mathbf{D} \\ &= \mathbf{D}^{-1}\mathbf{\Delta}_3[\mathbf{Z}(\hat{\mathbf{n}}^{\text{sca}}, \hat{\mathbf{n}}^{\text{inc}})]^{\text{T}}\mathbf{\Delta}_3\mathbf{D} \\ &= \mathbf{D}^{-1}\mathbf{\Delta}_3[\mathbf{D}\mathbf{Z}^J(\hat{\mathbf{n}}^{\text{sca}}, \hat{\mathbf{n}}^{\text{inc}})\mathbf{D}^{-1}]^{\text{T}}\mathbf{\Delta}_3\mathbf{D} \\ &= \mathbf{D}^{-1}\mathbf{\Delta}_3[\mathbf{D}^{-1}]^{\text{T}}[\mathbf{Z}^J(\hat{\mathbf{n}}^{\text{sca}}, \hat{\mathbf{n}}^{\text{inc}})]^{\text{T}}\mathbf{D}^{\text{T}}\mathbf{\Delta}_3\mathbf{D} \\ &= \mathbf{\Delta}_{23}[\mathbf{Z}^J(\hat{\mathbf{n}}^{\text{sca}}, \hat{\mathbf{n}}^{\text{inc}})]^{\text{T}}\mathbf{\Delta}_{23}, \end{aligned} \tag{2.126}$$

$$\begin{aligned} \mathbf{Z}^{\text{MS}}(-\hat{\mathbf{n}}^{\text{inc}}, -\hat{\mathbf{n}}^{\text{sca}}) &= \mathbf{B}\mathbf{Z}(-\hat{\mathbf{n}}^{\text{inc}}, -\hat{\mathbf{n}}^{\text{sca}})\mathbf{B}^{-1} \\ &= \mathbf{B}\mathbf{\Delta}_3[\mathbf{Z}(\hat{\mathbf{n}}^{\text{sca}}, \hat{\mathbf{n}}^{\text{inc}})]^{\text{T}}\mathbf{\Delta}_3\mathbf{B}^{-1} \\ &= \mathbf{B}\mathbf{\Delta}_3[\mathbf{B}^{-1}\mathbf{Z}^{\text{MS}}(\hat{\mathbf{n}}^{\text{sca}}, \hat{\mathbf{n}}^{\text{inc}})\mathbf{B}]^{\text{T}}\mathbf{\Delta}_3\mathbf{B}^{-1} \\ &= \mathbf{B}\mathbf{\Delta}_3\mathbf{B}^{\text{T}}[\mathbf{Z}^{\text{MS}}(\hat{\mathbf{n}}^{\text{sca}}, \hat{\mathbf{n}}^{\text{inc}})]^{\text{T}}[\mathbf{B}^{-1}]^{\text{T}}\mathbf{\Delta}_3\mathbf{B}^{-1} \\ &= \mathbf{\Delta}^{\text{MS}}[\mathbf{Z}^{\text{MS}}(\hat{\mathbf{n}}^{\text{sca}}, \hat{\mathbf{n}}^{\text{inc}})]^{\text{T}}[\mathbf{\Delta}^{\text{MS}}]^{-1}, \end{aligned} \tag{2.127}$$

$$\begin{aligned} \mathbf{Z}^{\text{CP}}(-\hat{\mathbf{n}}^{\text{inc}}, -\hat{\mathbf{n}}^{\text{sca}}) &= \mathbf{A}\mathbf{\Delta}_3\mathbf{A}^{\text{T}}[\mathbf{Z}^{\text{CP}}(\hat{\mathbf{n}}^{\text{sca}}, \hat{\mathbf{n}}^{\text{inc}})]^{\text{T}}[\mathbf{A}^{-1}]^{\text{T}}\mathbf{\Delta}_3\mathbf{A}^{-1} \\ &= [\mathbf{Z}^{\text{CP}}(\hat{\mathbf{n}}^{\text{sca}}, \hat{\mathbf{n}}^{\text{inc}})]^{\text{T}}, \end{aligned} \tag{2.128}$$

where

$$\mathbf{\Delta}_{23} = \mathbf{\Delta}_{23}^{\text{T}} = \mathbf{\Delta}_{23}^{-1} = \begin{bmatrix} 1 & 0 & 0 & 0 \\ 0 & -1 & 0 & 0 \\ 0 & 0 & -1 & 0 \\ 0 & 0 & 0 & 1 \end{bmatrix}, \tag{2.129}$$

$$\mathbf{\Delta}^{\text{MS}} = [\mathbf{\Delta}^{\text{MS}}]^{\text{T}} = \begin{bmatrix} 1/2 & 0 & 0 & 0 \\ 0 & 1/2 & 0 & 0 \\ 0 & 0 & -1 & 0 \\ 0 & 0 & 0 & 1 \end{bmatrix}, \quad [\mathbf{\Delta}^{\text{MS}}]^{-1} = \begin{bmatrix} 2 & 0 & 0 & 0 \\ 0 & 2 & 0 & 0 \\ 0 & 0 & -1 & 0 \\ 0 & 0 & 0 & 1 \end{bmatrix}. \tag{2.130}$$

The backscattering theorem, Eq. (2.65), along with Eqs. (2.106), (2.111), (2.116), and (2.121), leads to the following general property of the backscattering Stokes phase

matrix (Mishchenko *et al.* 2000b):

$$Z_{11}(-\hat{\mathbf{n}}, \hat{\mathbf{n}}) - Z_{22}(-\hat{\mathbf{n}}, \hat{\mathbf{n}}) + Z_{33}(-\hat{\mathbf{n}}, \hat{\mathbf{n}}) - Z_{44}(-\hat{\mathbf{n}}, \hat{\mathbf{n}}) = 0. \tag{2.131}$$

Electromagnetic scattering most typically produces light with polarization characteristics different from those of the incident beam. If the incident beam is unpolarized, i.e., $\mathbf{I}^{\text{inc}} = [I^{\text{inc}}\ 0\ 0\ 0]^{\text{T}}$, the scattered light generally has at least one non-zero Stokes parameter other than intensity:

$$I^{\text{sca}} = Z_{11} I^{\text{inc}}, \quad Q^{\text{sca}} = Z_{21} I^{\text{inc}}, \quad U^{\text{sca}} = Z_{31} I^{\text{inc}}, \quad V^{\text{sca}} = Z_{41} I^{\text{inc}}. \tag{2.132}$$

This phenomenon is traditionally called "polarization" and results in scattered light with non-zero degree of polarization, see Eq. (1.111),

$$P = \frac{\sqrt{Z_{21}^2 + Z_{31}^2 + Z_{41}^2}}{Z_{11}}. \tag{2.133}$$

Obviously, if the incident light is unpolarized, then the element Z_{11} determines the angular distribution of the scattered intensity. When the incident beam is linearly polarized, i.e., $\mathbf{I}^{\text{inc}} = [I^{\text{inc}}\ Q^{\text{inc}}\ U^{\text{inc}}\ 0]^{\text{T}}$, the scattered light may become elliptically polarized ($V^{\text{sca}} \neq 0$). Conversely, when the incident light is circularly polarized, i.e., $\mathbf{I}^{\text{inc}} = [I^{\text{inc}}\ 0\ 0\ V^{\text{inc}}]^{\text{T}}$, the scattered light may become partially linearly polarized ($Q^{\text{sca}} \neq 0$ and/or $U^{\text{sca}} \neq 0$). A general feature of scattering by a single particle is that if the incident beam is fully polarized ($P^{\text{inc}} = 1$) then the scattered light is also fully polarized. Hovenier *et al.* (1986) gave a proof of this property based on the general mathematical structure of the Stokes phase matrix. Thus, a single particle does not depolarize fully polarized incident light. We will see later, however, that single scattering by a collection of non-identical nonspherical particles (including particles of the same kind but with different orientations) can result in depolarization of the incident polarized light, and this is another important property of electromagnetic scattering.

2.7 Extinction matrix

Let us now consider the special case of the *exact forward-scattering direction* ($\hat{\mathbf{r}} = \hat{\mathbf{n}}^{\text{inc}}$). As in Section 2.6, we begin by defining the coherency vector of the total field for $\hat{\mathbf{r}}$ very close to $\hat{\mathbf{n}}^{\text{inc}}$ as

$$\mathbf{J}(r\hat{\mathbf{r}}) = \frac{1}{2}\sqrt{\frac{\varepsilon_1}{\mu_0}} \begin{bmatrix} E_\vartheta(r\hat{\mathbf{r}})[E_\vartheta(r\hat{\mathbf{r}})]^* \\ E_\vartheta(r\hat{\mathbf{r}})[E_\varphi(r\hat{\mathbf{r}})]^* \\ E_\varphi(r\hat{\mathbf{r}})[E_\vartheta(r\hat{\mathbf{r}})]^* \\ E_\varphi(r\hat{\mathbf{r}})[E_\varphi(r\hat{\mathbf{r}})]^* \end{bmatrix}, \tag{2.134}$$

where the total electric field is

$$\mathbf{E}(r\hat{\mathbf{r}}) = \mathbf{E}^{\text{inc}}(r\hat{\mathbf{r}}) + \mathbf{E}^{\text{sca}}(r\hat{\mathbf{r}}). \tag{2.135}$$

Integrating the elements of $\mathbf{J}(r\hat{\mathbf{r}})$ over the surface of the collimated detector aligned normal to $\hat{\mathbf{n}}^{\text{inc}}$ and using Eqs. (2.92), (2.94), and (2.98), we derive after rather lengthy algebraic manipulations

$$\Delta S\mathbf{J}(r\hat{\mathbf{n}}^{\text{inc}}) = \Delta S\mathbf{J}^{\text{inc}} - \mathbf{K}^{J}(\hat{\mathbf{n}}^{\text{inc}})\mathbf{J}^{\text{inc}} + O(r^{-2}), \tag{2.136}$$

where the elements of the 4×4 so-called coherency extinction matrix $\mathbf{K}^{J}(\vartheta^{\text{inc}}, \varphi^{\text{inc}})$ are expressed in terms of the elements of the forward-scattering amplitude matrix $\mathbf{S}(\vartheta^{\text{inc}}, \varphi^{\text{inc}}; \vartheta^{\text{inc}}, \varphi^{\text{inc}})$ as follows:

$$\mathbf{K}^{J} = \frac{\mathrm{i}2\pi}{k_1}\begin{bmatrix} S_{11}^{*} - S_{11} & S_{12}^{*} & -S_{12} & 0 \\ S_{21}^{*} & S_{22}^{*} - S_{11} & 0 & -S_{12} \\ -S_{21} & 0 & S_{11}^{*} - S_{22} & S_{12}^{*} \\ 0 & -S_{21} & S_{21}^{*} & S_{22}^{*} - S_{22} \end{bmatrix}. \tag{2.137}$$

Switching again to Stokes parameters, we have

$$\Delta S\mathbf{I}(r\hat{\mathbf{n}}^{\text{inc}}) = \Delta S\mathbf{I}^{\text{inc}} - \mathbf{K}(\hat{\mathbf{n}}^{\text{inc}})\mathbf{I}^{\text{inc}} + O(r^{-2}), \tag{2.138}$$

where $\mathbf{I}(r\hat{\mathbf{n}}^{\text{inc}}) = \mathbf{D}\mathbf{J}(r\hat{\mathbf{n}}^{\text{inc}})$. The Stokes extinction matrix is given by

$$\mathbf{K}(\hat{\mathbf{n}}^{\text{inc}}) = \mathbf{D}\mathbf{K}^{J}(\hat{\mathbf{n}}^{\text{inc}})\mathbf{D}^{-1}. \tag{2.139}$$

The explicit formulas for the elements of this matrix in terms of the elements of the matrix $\mathbf{S}(\vartheta^{\text{inc}}, \varphi^{\text{inc}}; \vartheta^{\text{inc}}, \varphi^{\text{inc}})$ are as follows:

$$K_{jj} = \frac{2\pi}{k_1}\operatorname{Im}(S_{11} + S_{22}), \qquad j = 1, ..., 4, \tag{2.140}$$

$$K_{12} = K_{21} = \frac{2\pi}{k_1}\operatorname{Im}(S_{11} - S_{22}), \tag{2.141}$$

$$K_{13} = K_{31} = -\frac{2\pi}{k_1}\operatorname{Im}(S_{12} + S_{21}), \tag{2.142}$$

$$K_{14} = K_{41} = \frac{2\pi}{k_1}\operatorname{Re}(S_{21} - S_{12}), \tag{2.143}$$

$$K_{23} = -K_{32} = \frac{2\pi}{k_1}\operatorname{Im}(S_{21} - S_{12}), \tag{2.144}$$

$$K_{24} = -K_{42} = -\frac{2\pi}{k_1}\operatorname{Re}(S_{12} + S_{21}), \tag{2.145}$$

$$K_{34} = -K_{43} = \frac{2\pi}{k_1}\operatorname{Re}(S_{22} - S_{11}). \tag{2.146}$$

Thus, only seven elements of the Stokes extinction matrix are independent. It is easy to verify that this is also true of the coherency extinction matrix. The elements of both matrices have the dimension of area and explicitly depend on $\varphi^{\rm inc}$ even when the incident wave propagates along the z-axis.

Equations (2.136) and (2.138) represent the most general form of the optical theorem. They show that the presence of the scattering particle changes not only the total power of the electromagnetic radiation received by the detector facing the incident wave (detector 1 in Fig. 2.3) but also, perhaps, its state of polarization. This phenomenon is called dichroism and results from different attenuation rates for different polarization components of the incident wave. Obviously, Eqs. (2.136) and (2.138) remain valid if the incident radiation is a parallel quasi-monochromatic beam of light rather than a monochromatic plane wave.

From Eqs. (2.64) and (2.140)–(2.146) we obtain the reciprocity relation for the Stokes extinction matrix:

$$\mathbf{K}(-\hat{\mathbf{n}}^{\rm inc}) = \mathbf{\Delta}_3[\mathbf{K}(\hat{\mathbf{n}}^{\rm inc})]^{\rm T}\mathbf{\Delta}_3, \tag{2.147a}$$

where the matrix $\mathbf{\Delta}_3$ is given by Eq. (2.125). It is also easy to derive a related symmetry property:

$$\mathbf{K}(-\hat{\mathbf{n}}^{\rm inc}) = \begin{bmatrix} K_{11}(\hat{\mathbf{n}}^{\rm inc}) & K_{12}(\hat{\mathbf{n}}^{\rm inc}) & -K_{13}(\hat{\mathbf{n}}^{\rm inc}) & K_{14}(\hat{\mathbf{n}}^{\rm inc}) \\ K_{21}(\hat{\mathbf{n}}^{\rm inc}) & K_{22}(\hat{\mathbf{n}}^{\rm inc}) & K_{23}(\hat{\mathbf{n}}^{\rm inc}) & -K_{24}(\hat{\mathbf{n}}^{\rm inc}) \\ -K_{31}(\hat{\mathbf{n}}^{\rm inc}) & K_{32}(\hat{\mathbf{n}}^{\rm inc}) & K_{33}(\hat{\mathbf{n}}^{\rm inc}) & K_{34}(\hat{\mathbf{n}}^{\rm inc}) \\ K_{41}(\hat{\mathbf{n}}^{\rm inc}) & -K_{42}(\hat{\mathbf{n}}^{\rm inc}) & K_{43}(\hat{\mathbf{n}}^{\rm inc}) & K_{44}(\hat{\mathbf{n}}^{\rm inc}) \end{bmatrix}. \tag{2.147b}$$

In other words, the only effect of reversing the direction of propagation is to change the sign of four elements of the Stokes extinction matrix. The modified Stokes and circular-polarization extinction matrices are given by

$$\mathbf{K}^{\rm MS}(\hat{\mathbf{n}}^{\rm inc}) = \mathbf{B}\mathbf{K}(\hat{\mathbf{n}}^{\rm inc})\mathbf{B}^{-1}, \tag{2.148}$$

$$\mathbf{K}^{\rm CP}(\hat{\mathbf{n}}^{\rm inc}) = \mathbf{A}\mathbf{K}(\hat{\mathbf{n}}^{\rm inc})\mathbf{A}^{-1}. \tag{2.149}$$

Reciprocity relations for the matrices $\mathbf{K}^J(\hat{\mathbf{n}}^{\rm inc})$, $\mathbf{K}^{\rm MS}(\hat{\mathbf{n}}^{\rm inc})$, and $\mathbf{K}^{\rm CP}(\hat{\mathbf{n}}^{\rm inc})$ can be derived from Eq. (2.147a) by analogy with Eqs. (2.126)–(2.128):

$$\mathbf{K}^J(-\hat{\mathbf{n}}^{\rm inc}) = \mathbf{\Delta}_{23}[\mathbf{K}^J(\hat{\mathbf{n}}^{\rm inc})]^{\rm T}\mathbf{\Delta}_{23}, \tag{2.150}$$

$$\mathbf{K}^{\rm MS}(-\hat{\mathbf{n}}^{\rm inc}) = \mathbf{\Delta}^{\rm MS}[\mathbf{K}^{\rm MS}(\hat{\mathbf{n}}^{\rm inc})]^{\rm T}[\mathbf{\Delta}^{\rm MS}]^{-1}, \tag{2.151}$$

$$\mathbf{K}^{\rm CP}(-\hat{\mathbf{n}}^{\rm inc}) = [\mathbf{K}^{\rm CP}(\hat{\mathbf{n}}^{\rm inc})]^{\rm T}. \tag{2.152}$$

2.8 Extinction, scattering, and absorption cross sections

Knowledge of the total electromagnetic field in the far-field zone also allows us to calculate such important optical characteristics of the scattering object as the total

scattering, absorption, and extinction cross sections. These optical cross sections are defined as follows. The product of the scattering cross section C_{sca} and the incident monochromatic energy flux gives the total monochromatic power removed from the incident wave as a result of scattering of the incident radiation in all directions. Analogously, the product of the absorption cross section C_{abs} and the incident monochromatic energy flux gives the total monochromatic power removed from the incident wave as a result of absorption of light by the object. Of course, the absorbed electromagnetic energy does not disappear but, rather, is converted into other forms of energy. Finally, the extinction cross section C_{ext} is the sum of the scattering and absorption cross sections and, when multiplied by the incident monochromatic energy flux, gives the total monochromatic power removed from the incident light by the combined effect of scattering and absorption.

To determine the total optical cross sections, we surround the object by an imaginary sphere of radius r large enough to be in the far-field zone. Since the surrounding medium is assumed to be nonabsorbing, the net rate at which the electromagnetic energy crosses the surface S of the sphere is always non-negative and is equal to the power absorbed by the particle:

$$W^{\text{abs}} = -\int_S \mathrm{d}S \langle \mathbf{S}(\mathbf{r}) \rangle \cdot \hat{\mathbf{r}} = -r^2 \int_{4\pi} \mathrm{d}\hat{\mathbf{r}} \langle \mathbf{S}(\mathbf{r}) \rangle \cdot \hat{\mathbf{r}} \tag{2.153}$$

(see Eq. (1.31)). According to Eq. (2.88), W^{abs} can be written as a combination of three terms:

$$W^{\text{abs}} = W^{\text{inc}} - W^{\text{sca}} + W^{\text{ext}}, \tag{2.154}$$

where

$$W^{\text{inc}} = -r^2 \int_{4\pi} \mathrm{d}\hat{\mathbf{r}} \langle \mathbf{S}^{\text{inc}}(\mathbf{r}) \rangle \cdot \hat{\mathbf{r}}, \qquad W^{\text{sca}} = r^2 \int_{4\pi} \mathrm{d}\hat{\mathbf{r}} \langle \mathbf{S}^{\text{sca}}(\mathbf{r}) \rangle \cdot \hat{\mathbf{r}},$$

$$W^{\text{ext}} = -r^2 \int_{4\pi} \mathrm{d}\hat{\mathbf{r}} \langle \mathbf{S}^{\text{ext}}(\mathbf{r}) \rangle \cdot \hat{\mathbf{r}}. \tag{2.155}$$

W^{inc} vanishes identically because the surrounding medium is nonabsorbing and $\mathbf{S}^{\text{inc}}(\mathbf{r})$ is a constant vector independent of $\mathbf{r}$, whereas W^{sca} is the rate at which the scattered energy crosses the surface S in the outward direction. Therefore, W^{ext} is equal to the sum of the energy scattering rate and the energy absorption rate:

$$W^{\text{ext}} = W^{\text{sca}} + W^{\text{abs}}. \tag{2.156}$$

Inserting Eqs. (2.90)–(2.95) in Eq. (2.155) and recalling the definitions of the extinction and scattering cross sections, we derive after some algebra

$$C_{\text{ext}} = \frac{W^{\text{ext}}}{\frac{1}{2}\sqrt{\varepsilon_1/\mu_0}\,|\mathbf{E}_0^{\text{inc}}|^2} = \frac{4\pi}{k_1|\mathbf{E}_0^{\text{inc}}|^2}\,\mathrm{Im}[\mathbf{E}_1^{\text{sca}}(\hat{\mathbf{n}}^{\text{inc}}) \cdot \mathbf{E}_0^{\text{inc}*}], \tag{2.157}$$

$$C_{\rm sca} = \frac{W^{\rm sca}}{\frac{1}{2}\sqrt{\varepsilon_1/\mu_0}\,|\mathbf{E}_0^{\rm inc}|^2} = \frac{1}{|\mathbf{E}_0^{\rm inc}|^2}\int_{4\pi} {\rm d}\hat{\mathbf{r}}\,|\mathbf{E}_1^{\rm sca}(\hat{\mathbf{r}})|^2. \tag{2.158}$$

In view of Eqs. (2.24), (2.30), (2.102), (2.104), (2.105), and (2.140)–(2.143), Eqs. (2.157) and (2.158) can be rewritten as

$$C_{\rm ext} = \frac{1}{I^{\rm inc}}[K_{11}(\hat{\mathbf{n}}^{\rm inc})I^{\rm inc} + K_{12}(\hat{\mathbf{n}}^{\rm inc})Q^{\rm inc} + K_{13}(\hat{\mathbf{n}}^{\rm inc})U^{\rm inc} + K_{14}(\hat{\mathbf{n}}^{\rm inc})V^{\rm inc}], \tag{2.159}$$

$$\begin{aligned} C_{\rm sca} &= \frac{r^2}{I^{\rm inc}}\int_{4\pi} {\rm d}\hat{\mathbf{r}}\, I^{\rm sca}(r\hat{\mathbf{r}}) \\ &= \frac{1}{I^{\rm inc}}\int_{4\pi} {\rm d}\hat{\mathbf{r}}[Z_{11}(\hat{\mathbf{r}},\hat{\mathbf{n}}^{\rm inc})I^{\rm inc} + Z_{12}(\hat{\mathbf{r}},\hat{\mathbf{n}}^{\rm inc})Q^{\rm inc} \\ &\qquad + Z_{13}(\hat{\mathbf{r}},\hat{\mathbf{n}}^{\rm inc})U^{\rm inc} + Z_{14}(\hat{\mathbf{r}},\hat{\mathbf{n}}^{\rm inc})V^{\rm inc}]. \end{aligned} \tag{2.160}$$

The absorption cross section is equal to the difference of the extinction and scattering cross sections:

$$C_{\rm abs} = C_{\rm ext} - C_{\rm sca} \geq 0. \tag{2.161}$$

The single-scattering albedo is defined as the ratio of the scattering and extinction cross sections:

$$\varpi = \frac{C_{\rm sca}}{C_{\rm ext}} \leq 1. \tag{2.162}$$

This quantity is widely used in radiative transfer theory and is interpreted as the probability that a photon interacting with the particle will be scattered rather than absorbed. Obviously, $\varpi = 1$ for nonabsorbing particles. Equations (2.159) and (2.160) (and thus Eqs. (2.161) and (2.162)) also hold for quasi-monochromatic incident light provided that the elements of the Stokes vector entering these equations are averages over a time interval long compared with the period of fluctuations. All cross sections are inherently real-valued positive quantities and have the dimension of area. They depend on the direction, polarization state, and wavelength of the incident light as well as on the particle size, morphology, relative refractive index, and orientation with respect to the reference frame.

Equation (2.159) is another representation of the optical theorem and, along with Eqs. (2.140)–(2.143), shows that although extinction is the combined effect of absorption and scattering in all directions by the particle, it is determined only by the amplitude scattering matrix in the exact forward direction. This is a direct consequence of the fact that extinction results from interference between the incident and scattered light, Eq. (2.91), and the presence of delta-function terms in Eqs. (2.92) and (2.93). Having derived Eq. (2.157), we can now rewrite Eq. (2.97) in the form

$$W_{\Delta S}(\hat{\mathbf{n}}^{\rm inc}) = (\Delta S - C_{\rm ext})\frac{1}{2}\sqrt{\frac{\varepsilon_1}{\mu_0}}\,|\mathbf{E}_0^{\rm inc}|^2 + O(r^{-2}). \tag{2.163}$$

This shows that the extinction cross section is a well-defined, observable quantity and can be determined by measuring $W_{\Delta S}(\hat{\mathbf{n}}^{\text{inc}})$ with and without the particle interposed between the source of light and the detector. The net effect of the particle is to reduce the detector area by "casting a shadow" of area C_{ext}. Of course, this does not mean that C_{ext} is merely given by the area G of the particle geometrical projection on the detector surface. However, this geometrical interpretation of the extinction cross section illustrates the rationale for introducing the dimensionless efficiency factor for extinction as the ratio of the extinction cross section to the geometrical cross section:

$$Q_{\text{ext}} = \frac{C_{\text{ext}}}{G}. \tag{2.164}$$

We will see in later chapters that Q_{ext} can be considerably greater or much less than unity. The efficiency factors for scattering and absorption are defined analogously:

$$Q_{\text{sca}} = \frac{C_{\text{sca}}}{G}, \qquad Q_{\text{abs}} = \frac{C_{\text{abs}}}{G}. \tag{2.165}$$

The quantity

$$\begin{aligned}\frac{\mathrm{d}C_{\text{sca}}}{\mathrm{d}\Omega} &= \frac{I^{\text{sca}}(r\hat{\mathbf{r}})r^2}{I^{\text{inc}}} \\ &= \frac{1}{I^{\text{inc}}}[Z_{11}(\hat{\mathbf{r}},\hat{\mathbf{n}}^{\text{inc}})I^{\text{inc}} + Z_{12}(\hat{\mathbf{r}},\hat{\mathbf{n}}^{\text{inc}})Q^{\text{inc}} + Z_{13}(\hat{\mathbf{r}},\hat{\mathbf{n}}^{\text{inc}})U^{\text{inc}} + Z_{14}(\hat{\mathbf{r}},\hat{\mathbf{n}}^{\text{inc}})V^{\text{inc}}]\end{aligned} \tag{2.166}$$

also has the dimension of area and is called the differential scattering cross section; it describes the angular distribution of the scattered light and specifies the electromagnetic power scattered into unit solid angle about a given direction per unit incident intensity. (Note that the symbol $\mathrm{d}C_{\text{sca}}/\mathrm{d}\Omega$ should not be interpreted as the derivative of a function of Ω.) The differential scattering cross section depends on the polarization state of the incident light as well as on the incidence and scattering directions. Clearly,

$$C_{\text{sca}} = \int_{4\pi} \mathrm{d}\hat{\mathbf{r}} \frac{\mathrm{d}C_{\text{sca}}}{\mathrm{d}\Omega}$$

(cf. Eqs. (2.160) and (2.166)). A quantity related to the differential scattering cross section is the phase function $p(\hat{\mathbf{r}},\hat{\mathbf{n}}^{\text{inc}})$ defined as

$$p(\hat{\mathbf{r}},\hat{\mathbf{n}}^{\text{inc}}) = \frac{4\pi}{C_{\text{sca}}}\frac{\mathrm{d}C_{\text{sca}}}{\mathrm{d}\Omega}. \tag{2.167}$$

The convenience of the phase function is that it is dimensionless and normalized:

$$\frac{1}{4\pi}\int_{4\pi} \mathrm{d}\hat{\mathbf{r}}\, p(\hat{\mathbf{r}},\hat{\mathbf{n}}^{\text{inc}}) = 1. \tag{2.168}$$

The asymmetry parameter $\langle\cos\Theta\rangle$ is defined as the average cosine of the scattering angle $\Theta = \arccos(\hat{\mathbf{r}}\cdot\hat{\mathbf{n}}^{\text{inc}})$ (i.e., the angle between the incidence and scattering directions):

$$\langle\cos\Theta\rangle = \frac{1}{4\pi}\int_{4\pi} \mathrm{d}\hat{\mathbf{r}}\, p(\hat{\mathbf{r}}, \hat{\mathbf{n}}^{\text{inc}})\hat{\mathbf{r}}\cdot\hat{\mathbf{n}}^{\text{inc}} = \frac{1}{C_{\text{sca}}}\int_{4\pi} \mathrm{d}\hat{\mathbf{r}}\,\frac{\mathrm{d}C_{\text{sca}}}{\mathrm{d}\Omega}\hat{\mathbf{r}}\cdot\hat{\mathbf{n}}^{\text{inc}}. \tag{2.169}$$

The asymmetry parameter is positive if the particle scatters more light toward the forward direction $(\Theta = 0)$, is negative if more light is scattered toward the backscattering direction $(\Theta = \pi)$, and vanishes if the scattering is symmetric with respect to the plane perpendicular to the incidence direction. Obviously, $\langle\cos\Theta\rangle \in [-1, +1]$. The limiting values correspond to the phase functions $4\pi\delta(\hat{\mathbf{r}} + \hat{\mathbf{n}}^{\text{inc}})$ and $4\pi\delta(\hat{\mathbf{r}} - \hat{\mathbf{n}}^{\text{inc}})$, respectively.

2.9 Radiation pressure and radiation torque

The scattering and absorption of an electromagnetic wave cause the transfer of momentum from the electromagnetic field to the scattering object. The resulting force, called radiation pressure, is used in laboratories to levitate and size small particles (Ashkin and Dziedzic 1980; Chýlek *et al*. 1992; Ashkin 2000) and affects the spatial distribution of interplanetary and interstellar dust grains (Il'in and Voshchinnikov 1998; Landgraf *et al*. 1999). If the amplitudes of the incident and scattered fields do not change in time, the force due to radiation pressure averaged over the period $2\pi/\omega$ of the time-harmonic incident wave is

$$\mathbf{F} = \int_S \mathrm{d}S\,\langle\overleftrightarrow{T}_{\text{M}}(\mathbf{r})\rangle\cdot\hat{\mathbf{n}} \tag{2.170}$$

(Stratton 1941, Section 2.5; Jackson 1998, Section 6.7), where $\overleftrightarrow{T}_{\text{M}}$ is the so-called Maxwell stress tensor, the integration is performed over a closed surface S surrounding the scattering object, and $\hat{\mathbf{n}}$ is the unit vector in the direction of the local outward normal to S. Assume, for simplicity, that the scattering object is surrounded by a vacuum. Then the instantaneous value of the Maxwell stress tensor is

$$\begin{aligned}\overleftrightarrow{T}_{\text{M}} &= \varepsilon_0[\mathbf{E}\otimes\mathbf{E} + c^2\mathbf{B}\otimes\mathbf{B} - \tfrac{1}{2}(\mathbf{E}\cdot\mathbf{E} + c^2\mathbf{B}\cdot\mathbf{B})\overleftrightarrow{I}] \\ &= \varepsilon_0\mathbf{E}\otimes\mathbf{E} + \mu_0\mathbf{H}\otimes\mathbf{H} - \tfrac{1}{2}(\varepsilon_0\mathbf{E}\cdot\mathbf{E} + \mu_0\mathbf{H}\cdot\mathbf{H})\overleftrightarrow{I},\end{aligned} \tag{2.171}$$

where $c = 1\big/\sqrt{\varepsilon_0\mu_0}$ is the speed of light in a vacuum. By analogy with Eq. (1.24), we have for the time average of the Maxwell stress tensor

$$\langle\overleftrightarrow{T}_{\text{M}}(\mathbf{r})\rangle = \tfrac{1}{2}\mathrm{Re}[\varepsilon_0\mathbf{E}(\mathbf{r})\otimes\mathbf{E}^*(\mathbf{r}) + \mu_0\mathbf{H}(\mathbf{r})\otimes\mathbf{H}^*(\mathbf{r}) - \tfrac{1}{2}(\varepsilon_0|\mathbf{E}(\mathbf{r})|^2 + \mu_0|\mathbf{H}(\mathbf{r})|^2)\overleftrightarrow{I}]. \tag{2.172}$$

It is convenient to choose for S a sphere centered at the scattering object and having a radius r large enough to be in the far-field zone. Then Eq. (2.170) becomes

$$\mathbf{F} = r^2 \int_{4\pi} \mathrm{d}\hat{\mathbf{r}} \langle \overleftrightarrow{T}_{\mathrm{M}}(r\hat{\mathbf{r}}) \rangle \cdot \hat{\mathbf{r}}. \tag{2.173}$$

The total electric and magnetic fields are vector sums of the respective incident and scattered fields given by Eqs. (2.92)–(2.95). Because the incident and scattered fields are transverse, the first and second terms in square brackets on the right-hand side of Eq. (2.172) do not contribute to the integral in Eq. (2.173). We thus have

$$\begin{aligned}\mathbf{F} = &-\frac{\varepsilon_0 r^2}{4} \mathrm{Re} \int_{4\pi} \mathrm{d}\hat{\mathbf{r}}\, \hat{\mathbf{r}} \{ |\mathbf{E}^{\mathrm{inc}}(\mathbf{r})|^2 + |\mathbf{E}^{\mathrm{sca}}(\mathbf{r})|^2 + \mathbf{E}^{\mathrm{inc}}(\mathbf{r}) \cdot [\mathbf{E}^{\mathrm{sca}}(\mathbf{r})]^* \\ &\qquad + \mathbf{E}^{\mathrm{sca}}(\mathbf{r}) \cdot [\mathbf{E}^{\mathrm{inc}}(\mathbf{r})]^* \} \\ &-\frac{\mu_0 r^2}{4} \mathrm{Re} \int_{4\pi} \mathrm{d}\hat{\mathbf{r}}\, \hat{\mathbf{r}} \{ |\mathbf{H}^{\mathrm{inc}}(\mathbf{r})|^2 + |\mathbf{H}^{\mathrm{sca}}(\mathbf{r})|^2 + \mathbf{H}^{\mathrm{inc}}(\mathbf{r}) \cdot [\mathbf{H}^{\mathrm{sca}}(\mathbf{r})]^* \\ &\qquad + \mathbf{H}^{\mathrm{sca}}(\mathbf{r}) \cdot [\mathbf{H}^{\mathrm{inc}}(\mathbf{r})]^* \}.\end{aligned} \tag{2.174}$$

The terms $|\mathbf{E}^{\mathrm{inc}}(\mathbf{r})|^2$ and $|\mathbf{H}^{\mathrm{inc}}(\mathbf{r})|^2$ are constants independent of $\mathbf{r}$, so their contribution to $\mathbf{F}$ is simply zero. The contribution of the remaining terms follows from Eqs. (2.92)–(2.95) and the vector identity $(\mathbf{a}\times\mathbf{b})\cdot(\mathbf{c}\times\mathbf{d}) = (\mathbf{a}\cdot\mathbf{c})(\mathbf{b}\cdot\mathbf{d}) - (\mathbf{a}\cdot\mathbf{d})(\mathbf{b}\cdot\mathbf{c})$:

$$\mathbf{F} = \frac{2\pi\varepsilon_0}{k_1} \hat{\mathbf{n}}^{\mathrm{inc}} \, \mathrm{Im}\{\mathbf{E}_1^{\mathrm{sca}}(\hat{\mathbf{n}}^{\mathrm{inc}}) \cdot \mathbf{E}_0^{\mathrm{inc}*}\} - \frac{\varepsilon_0}{2} \int_{4\pi} \mathrm{d}\hat{\mathbf{r}}\, \hat{\mathbf{r}} |\mathbf{E}_1^{\mathrm{sca}}(\hat{\mathbf{r}})|^2 \tag{2.175}$$

or, in view of Eqs. (2.102), (2.104), (2.105), (2.157), and (2.166),

$$\begin{aligned}\mathbf{F} &= \frac{1}{c} \hat{\mathbf{n}}^{\mathrm{inc}} C_{\mathrm{ext}} I^{\mathrm{inc}} - \frac{1}{c} \int_{4\pi} \mathrm{d}\hat{\mathbf{r}}\, \hat{\mathbf{r}} [Z_{11}(\hat{\mathbf{r}}, \hat{\mathbf{n}}^{\mathrm{inc}}) I^{\mathrm{inc}} + Z_{12}(\hat{\mathbf{r}}, \hat{\mathbf{n}}^{\mathrm{inc}}) Q^{\mathrm{inc}} \\ &\qquad + Z_{13}(\hat{\mathbf{r}}, \hat{\mathbf{n}}^{\mathrm{inc}}) U^{\mathrm{inc}} + Z_{14}(\hat{\mathbf{r}}, \hat{\mathbf{n}}^{\mathrm{inc}}) V^{\mathrm{inc}}] \\ &= \frac{1}{c} \hat{\mathbf{n}}^{\mathrm{inc}} C_{\mathrm{ext}} I^{\mathrm{inc}} - \frac{1}{c} I^{\mathrm{inc}} \int_{4\pi} \mathrm{d}\hat{\mathbf{r}}\, \hat{\mathbf{r}} \frac{\mathrm{d}C_{\mathrm{sca}}}{\mathrm{d}\Omega}\end{aligned} \tag{2.176}$$

(Mishchenko 2001).

Although the first term on the right-hand side of Eq. (2.176) represents a force in the direction of $\hat{\mathbf{n}}^{\mathrm{inc}}$, the direction of the total radiation force is different, in general, from the direction of propagation of the incident beam and depends on its polarization state because of the second term. The projection of the total force on any direction $\hat{\mathbf{n}}$ is simply the dot product $\mathbf{F}\cdot\hat{\mathbf{n}}$. In particular, the component of the force in the direction of propagation of the incident light is

$$\begin{aligned}\mathbf{F}\cdot\hat{\mathbf{n}}^{\mathrm{inc}} &= \frac{1}{c} C_{\mathrm{ext}} I^{\mathrm{inc}} - \frac{1}{c} I^{\mathrm{inc}} \int_{4\pi} \mathrm{d}\hat{\mathbf{r}}\, \hat{\mathbf{r}} \cdot \hat{\mathbf{n}}^{\mathrm{inc}} \frac{\mathrm{d}C_{\mathrm{sca}}}{\mathrm{d}\Omega} \\ &= \frac{1}{c} I^{\mathrm{inc}} (C_{\mathrm{ext}} - C_{\mathrm{sca}} \langle \cos\Theta \rangle)\end{aligned}$$

$$= \frac{1}{c} I^{\text{inc}} C_{\text{pr}} \tag{2.177}$$

(see Eq. (2.169)), where the quantity

$$C_{\text{pr}} = C_{\text{ext}} - C_{\text{sca}} \langle \cos \Theta \rangle \tag{2.178}$$

is called the radiation-pressure cross section. By analogy with Eqs. (2.164) and (2.165), we can define the radiation-pressure efficiency factor as

$$Q_{\text{pr}} = \frac{C_{\text{pr}}}{G}. \tag{2.179}$$

Although being the result of a lengthy rigorous derivation, Eq. (2.177) allows a transparent physical interpretation. A beam of light carries linear momentum as well as energy. The direction of the momentum is that of propagation, while the absolute value of the momentum is energy/(speed of light). Since the total momentum of the electromagnetic field and the scattering object must be constant, the radiation force exerted on the object is equal to the momentum removed from the total electromagnetic field per unit time. Consider the component of the force in the direction of incidence. The momentum removed from the incident beam per unit time is $C_{\text{ext}} I^{\text{inc}} / c$. Of this amount, the part proportional to C_{abs} is not replaced, whereas the part proportional to C_{sca} is to some extent replaced by the contribution due to the projection of the moment of the scattered light on the direction of incidence. This contribution is equal to the integral of $I^{\text{sca}} \cos \Theta / c$ over all scattering directions, or $I^{\text{inc}} C_{\text{sca}} \langle \cos \Theta \rangle / c$. Note that van de Hulst (1957) used similar arguments as an heuristic derivation of Eq. (2.177).

If the absolute temperature of the particle is above zero then light emitted by the particle in all directions causes an additional component of the radiation force. This component will be discussed in Section 2.10.

The radiation pressure is accompanied by the radiation torque exerted on the particle and given by

$$\begin{aligned} \mathbf{\Gamma} &= -\int_S \mathrm{d}S\, r \hat{\mathbf{r}} \cdot [\langle \overleftrightarrow{T}_{\text{M}}(\mathbf{r}) \rangle \times \hat{\mathbf{r}}] \\ &= -r^3 \int_{4\pi} \mathrm{d}\hat{\mathbf{r}}\, \hat{\mathbf{r}} \cdot [\langle \overleftrightarrow{T}_{\text{M}}(\mathbf{r}) \rangle \times \hat{\mathbf{r}}] \end{aligned} \tag{2.180}$$

(cf. p. 288 of Jackson 1998), where r is the radius of a sphere S centered inside the scattering particle and having its surface in the far-field zone. Since $\hat{\mathbf{r}} \cdot \overleftrightarrow{I} \times \hat{\mathbf{r}}$ vanishes identically, only the first two terms in square brackets on the right-hand side of Eq. (2.172) contribute to the integrals in Eq. (2.180). The evaluation of this contribution is complicated because it requires the knowledge of not only the transverse component of the scattered electric and magnetic fields but also of the longitudinal component, which we have so far neglected because it decays faster than $1/r$. Marston and

Crichton (1984) computed $\mathbf{\Gamma}$ for homogeneous and isotropic spherical particles, whereas Draine and Weingartner (1996) derived a formula for $\mathbf{\Gamma}$ in the framework of the so-called discrete dipole approximation (see Section 6.5).

2.10 Thermal emission

If the particle's absolute temperature T is above zero, it can emit as well as scatter and absorb electromagnetic radiation. The emitted radiation in the far-field zone of the particle propagates in the radial direction, i.e., along the unit vector $\hat{\mathbf{r}} = \mathbf{r}/r$, where $\mathbf{r}$ is the position vector of the observation point with origin inside the particle. The energetic and polarization characteristics of the emitted radiation are described by a four-component Stokes emission column vector $\mathbf{K}_{\mathrm{e}}(\hat{\mathbf{r}}, T, \omega)$ defined in such a way that the net rate at which the emitted energy crosses a surface element ΔS normal to $\hat{\mathbf{r}}$ at a distance r from the particle at angular frequencies from ω to $\omega + \Delta\omega$ is

$$W^{\mathrm{e}} = \frac{1}{r^2} K_{\mathrm{e}1}(\hat{\mathbf{r}}, T, \omega)\Delta S \Delta\omega. \tag{2.181}$$

$K_{\mathrm{e}1}(\hat{\mathbf{r}}, T, \omega)$, the first component of the column vector, can also be interpreted as the amount of electromagnetic energy emitted by the particle in the direction $\hat{\mathbf{r}}$ per unit solid angle per unit frequency interval per unit time.

In order to calculate $\mathbf{K}_{\mathrm{e}}(\hat{\mathbf{r}}, T, \omega)$, let us assume that the particle is placed inside an opaque cavity of dimensions large compared with the particle and any wavelength under consideration (Fig. 2.4a). If the cavity and the particle are maintained at the constant absolute temperature T, then the equilibrium electromagnetic radiation inside the cavity is isotropic, homogeneous, and unpolarized (Mandel and Wolf 1995). This radiation can be represented as a collection of quasi-monochromatic, unpolarized, incoherent beams propagating in all directions and characterized by the Planck black-body energy distribution $I_{\mathrm{b}}(T, \omega)$. Specifically, at any point inside the cavity the amount of radiant energy per unit frequency interval, confined to a small solid angle $\Delta\Omega$ about any direction, which crosses an area ΔS normal to this direction in unit time is given by

$$I_{\mathrm{b}}(T, \omega)\Delta S \Delta\Omega = \frac{\hbar\omega^3}{4\pi^3 c^2 \left[\exp\left(\dfrac{\hbar\omega}{k_{\mathrm{B}}T}\right) - 1\right]} \Delta S \Delta\Omega, \tag{2.182}$$

where $\hbar = h/2\pi$, h is Planck's constant, c is the speed of light in a vacuum, and k_{B} is Boltzmann's constant.

Consider an imaginary collimated, polarization-sensitive detector of electromagnetic radiation with surface ΔS and small solid-angle field of view $\Delta\Omega$, placed at a distance r from the particle (Fig. 2.4(a)). The dimension of the detector surface is much greater than any dimension of the particle and r is large enough to be in the far-

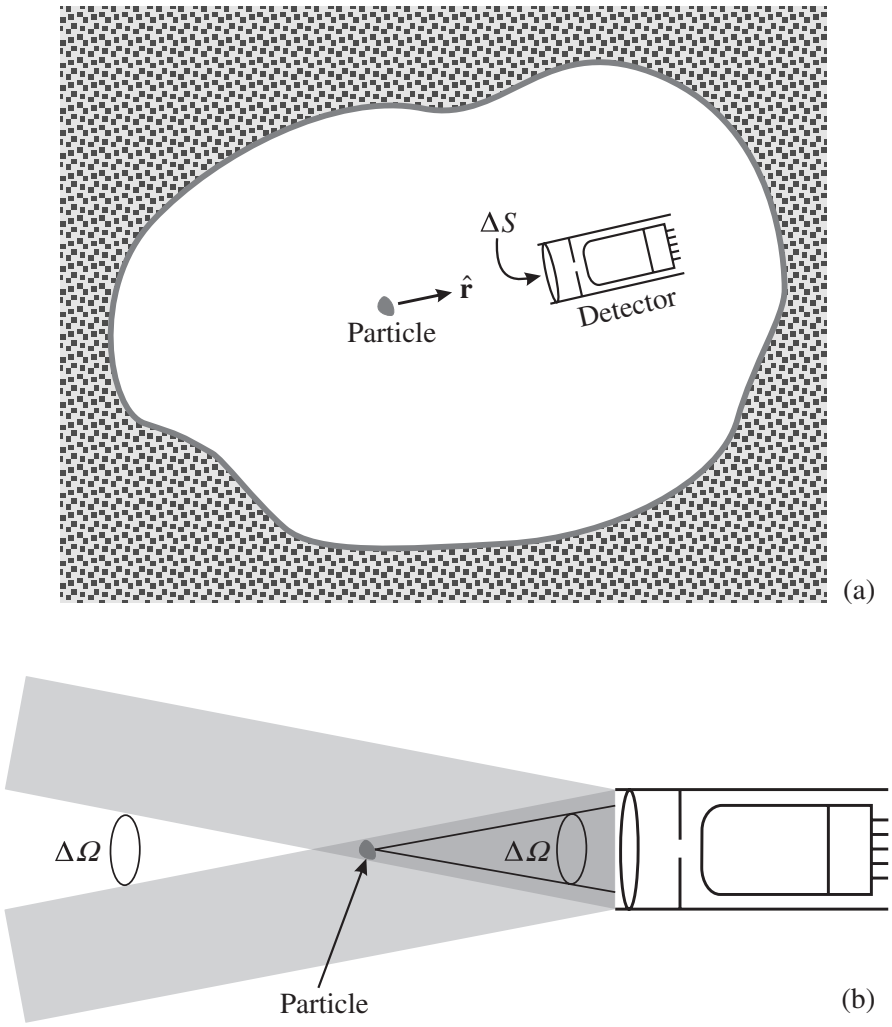

Figure 2.4. (a) Cavity, particle, and electromagnetic radiation field in thermal equilibrium. (b) Illumination geometry.

field zone of the particle but smaller than $\sqrt{\Delta S/\Delta\Omega}$. The latter condition ensures that all plane wave fronts incident on the detector in directions falling into its solid-angle field of view $\Delta\Omega$ are equally attenuated by the particle (Fig. 2.4(b)). The surface ΔS is aligned normal to and centered on $\hat{\mathbf{r}}$, where $\hat{\mathbf{r}}$ is the unit vector originating inside the particle and pointing toward the detector.

In the absence of the particle, the polarized signal per unit frequency interval measured by the detector would be given by

$$\mathbf{I}_{\mathrm{b}}(T,\omega)\Delta S\Delta\Omega, \tag{2.183}$$

where

$$\mathbf{I}_{\mathrm{b}}(T,\omega)=\begin{bmatrix} I_{\mathrm{b}}(T,\omega) \\ 0 \\ 0 \\ 0 \end{bmatrix} \tag{2.184}$$

is the blackbody Stokes column vector. The particle attenuates the incident blackbody radiation, emits radiation, and scatters the blackbody radiation coming from all directions in the direction of the detector. Taking into account that only the radiation emitted and scattered by the particle within the solid-angle field of view $\Delta\Omega$ is detected (Fig. 2.4(b)), we conclude that the polarized signal measured by the detector in the presence of the particle is

$$\mathbf{I}_{\mathrm{b}}(T,\omega)\Delta S\Delta\Omega-\mathbf{K}(\hat{\mathbf{r}},\omega)\mathbf{I}_{\mathrm{b}}(T,\omega)\Delta\Omega+\mathbf{K}_{\mathrm{e}}(\hat{\mathbf{r}},T,\omega)\Delta\Omega+\Delta\Omega\int_{4\pi}\mathrm{d}\hat{\mathbf{r}}'\,\mathbf{Z}(\hat{\mathbf{r}},\hat{\mathbf{r}}',\omega)\mathbf{I}_{\mathrm{b}}(T,\omega) \tag{2.185}$$

(see Eqs. (2.138) and (2.102)). However, in thermal equilibrium the presence of the particle does not change the distribution of radiation. Therefore, we can equate expressions (2.183) and (2.185) and finally derive for the ith component of $\mathbf{K}_{\mathrm{e}}$

$$K_{\mathrm{e}i}(\hat{\mathbf{r}},T,\omega)=I_{\mathrm{b}}(T,\omega)K_{i1}(\hat{\mathbf{r}},\omega)-I_{\mathrm{b}}(T,\omega)\int_{4\pi}\mathrm{d}\hat{\mathbf{r}}'Z_{i1}(\hat{\mathbf{r}},\hat{\mathbf{r}}',\omega),\qquad i=1,\ldots,4. \tag{2.186}$$

This important relation expresses the Stokes emission vector in terms of the leftmost columns of the extinction and phase matrices and the Planck energy distribution. Although our derivation assumed that the particle was in thermal equilibrium with the surrounding radiation field, emissivity is a property of the particle only. Therefore, Eq. (2.186) is valid for any particle, in equilibrium or in nonequilibrium. A more detailed derivation of this formula based on the so-called fluctuation-dissipation theorem is given by Tsang *et al.* (2000).

As we pointed out in Section 2.9, the emitted radiation contributes to the total radiation force exerted on the particle. The emitted radiation is incoherent and does not interact with the incident and scattered radiation, thereby generating an independent component of the radiation force. Furthermore, emission is analogous to scattering in that it generates radiation propagating radially in all directions. Therefore, we can write the emission component of the radiation force by analogy with the scattering component given by the second term on the right-hand side of Eq. (2.176):

$$\mathbf{F}_{\mathrm{e}}(T)=-\frac{1}{c}\int_0^{\infty}\mathrm{d}\omega\int_{4\pi}\mathrm{d}\hat{\mathbf{r}}\hat{\mathbf{r}}K_{\mathrm{e}1}(\hat{\mathbf{r}},T,\omega). \tag{2.187}$$

Unlike the extinction and scattering components of the radiation force, the emission component depends on the particle temperature. Another effect of emission is to pro-

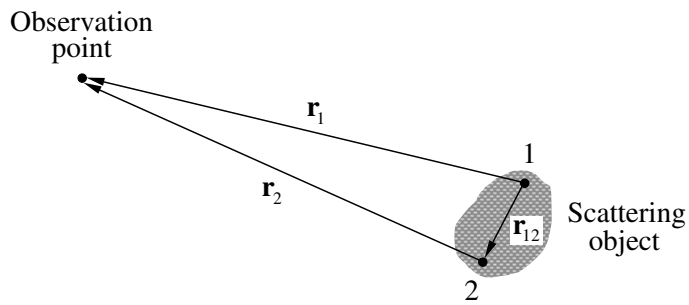

Figure 2.5. The amplitude matrix changes when the origin is shifted. The position vectors $\mathbf{r}_1$ and $\mathbf{r}_2$ originate at points 1 and 2, respectively.

duce a component of the radiation torque independent of that caused by scattering and absorption.

2.11 Translations of the origin

We began Section 2.2 by choosing the origin of the coordinate system close to the geometrical center of the scattering object, and that step was essential in deriving the formulas describing electromagnetic scattering in the far-field zone. Although the origin can be chosen arbitrarily, in general, the amplitude scattering matrix will change if the origin is moved, even if the orientation of the particle with respect to the reference frame remains the same. It is, therefore, important to supplement the rotation transformation law of Eq. (2.72) by a translation law describing the transformation of the amplitude scattering matrix upon a shift in the origin.

Let us consider two reference frames with origins 1 and 2 inside a scattering particle (Fig. 2.5). We assume that both reference frames have the same spatial orientation and denote the respective amplitude scattering matrices as $\mathbf{S}_1$ and $\mathbf{S}_2$. Let the particle be illuminated by a plane electromagnetic wave

$$\mathbf{E}^{\text{inc}}(\mathbf{r}_1) = \mathbf{E}_0^{\text{inc}} \exp(\mathrm{i}k_1\hat{\mathbf{n}}^{\text{inc}} \cdot \mathbf{r}_1), \tag{2.188}$$

where $\mathbf{r}_1$ is the position vector originating at origin 1. Let $\mathbf{r}_2$ be the position vector of the same observation point but originating at origin 2. Since $\mathbf{r}_1 = \mathbf{r}_2 + \mathbf{r}_{12}$, where $\mathbf{r}_{12}$ connects origins 1 and 2, the incident electric field at the same observation point can also be written as

$$\mathbf{E}^{\text{inc}}(\mathbf{r}_2) = \mathbf{E}_0^{\text{inc}} \exp(\mathrm{i}k_1\hat{\mathbf{n}}^{\text{inc}} \cdot \mathbf{r}_2) \exp(\mathrm{i}k_1\hat{\mathbf{n}}^{\text{inc}} \cdot \mathbf{r}_{12}). \tag{2.189}$$

The scattered field at an observation point does not depend on how we choose the origin of the coordinate system as long as the incident field remains the same. Therefore, we have in the far-field zone

$$\frac{\mathrm{e}^{\mathrm{i}k_1 r_1}}{r_1}\mathbf{S}_1\left(\frac{\mathbf{r}_1}{r_1},\hat{\mathbf{n}}^{\mathrm{inc}}\right)\begin{bmatrix}E_{0\vartheta}^{\mathrm{inc}}\\ E_{0\varphi}^{\mathrm{inc}}\end{bmatrix}=\frac{\mathrm{e}^{\mathrm{i}k_1 r_2}}{r_2}\exp(\mathrm{i}k_1\hat{\mathbf{n}}^{\mathrm{inc}}\cdot\mathbf{r}_{12})\,\mathbf{S}_2\left(\frac{\mathbf{r}_2}{r_2},\hat{\mathbf{n}}^{\mathrm{inc}}\right)\begin{bmatrix}E_{0\vartheta}^{\mathrm{inc}}\\ E_{0\varphi}^{\mathrm{inc}}\end{bmatrix}. \tag{2.190}$$

Taking the limits $k_1 r_1 \to \infty$ and $k_1 r_2 \to \infty$ and using the law of cosines,

$$r_2^2 = r_1^2 + r_{12}^2 - 2\mathbf{r}_1\cdot\mathbf{r}_{12},$$

we finally obtain

$$\mathbf{S}_1(\hat{\mathbf{n}}^{\mathrm{sca}},\hat{\mathbf{n}}^{\mathrm{inc}}) = \mathrm{e}^{\mathrm{i}\Delta}\mathbf{S}_2(\hat{\mathbf{n}}^{\mathrm{sca}},\hat{\mathbf{n}}^{\mathrm{inc}}), \tag{2.191}$$

where $\hat{\mathbf{n}}^{\mathrm{sca}} = \mathbf{r}_1/r_1$,

$$\Delta = k_1\,\mathbf{r}_{12}\cdot(\hat{\mathbf{n}}^{\mathrm{inc}} - \hat{\mathbf{n}}^{\mathrm{sca}}), \tag{2.192}$$

and we have assumed that

$$\frac{r_{12}}{r_1} \ll 1 \qquad \text{and} \qquad \frac{k_1\,r_{12}^2}{2r_1} \ll 1. \tag{2.193}$$

Equation (2.191) is the sought translation transformation law for the amplitude scattering matrix. It remains valid even if either origin lies outside the scattering particle, as long as the asymptotic far-field conditions of Eq. (2.193) are satisfied.

Despite the fact that the amplitude scattering matrix changes when the origin is shifted, the extinction and phase matrices remain invariant. Indeed, the factor $\mathrm{e}^{\mathrm{i}\Delta}$ is common to all elements of the amplitude scattering matrix and disappears when multiplied by its complex-conjugate counterpart, whereas the phase Δ vanishes identically in the exact forward-scattering direction (cf. Eqs. (2.106)–(2.121) and (2.140)–(2.146)). It is straightforward to verify that all optical cross sections and efficiency factors, the single-scattering albedo, the phase function, the asymmetry parameter, the emission vector, and the radiation force also remain unchanged.

Further reading

The books by Colton and Kress (1983), Varadan *et al*. (1991) and de Hoop (1995) provide a thorough theoretical introduction to the propagation and scattering of electromagnetic, acoustic, and elastodynamic waves. Appendix 3 of Van Bladel (1964) and chapter 6 of Varadan *et al*. (1991) list important formulas from vector and dyadic algebra and vector and dyadic calculus. The use of dyadics and dyadic Green's functions in electromagnetics is described by Tai (1993).

Chapter 3

Scattering, absorption, and emission by collections of independent particles

The formalism developed in the preceding chapter strictly applies only to the far-field scattering and absorption of monochromatic or quasi-monochromatic light by an isolated particle in the form of a single body or a fixed finite aggregate (Fig. 2.1) and to the thermal emission from such a particle. We will now describe how this formalism can be extended to single and multiple scattering, absorption, and emission by collections of independently scattering particles under certain simplifying assumptions.

3.1 Single scattering, absorption, and emission by a small volume element comprising randomly and sparsely distributed particles

Consider first a small volume element having a linear dimension l, comprising a number N of randomly positioned particles, and illuminated by a plane electromagnetic wave. Although the volume element is assumed to be macroscopically small, its size must still be much larger than the size of the constituent particles and the wavelength of the incident light. We assume that N is sufficiently small that the mean distance between the particles is also much larger than the incident wavelength and the average particle size. We also assume that N is sufficiently small that the main contribution to the total scattered radiation exiting the volume element comes from light scattered only once. In other words, the contribution to the total scattered signal of light scattered two and more times by particles inside the volume element is assumed to be negligibly small. This is equivalent to requiring that the "scattering efficiency"

$N\langle C_{\text{sca}}\rangle l^{-2}$ of the volume element (i.e., the ratio of the total scattering cross section of the particles contained in the volume element to the volume element's geometrical cross section) be much smaller than unity; $\langle C_{\text{sca}}\rangle$ is the average scattering cross section per particle. Finally, we assume that the positions of the particles during the measurement are sufficiently random that there are no systematic phase relations between individual waves scattered by different particles.

Let the incident electric field be given by

$$\mathbf{E}^{\text{inc}}(\mathbf{r}) = \mathbf{E}_0^{\text{inc}} \exp(\mathrm{i}k_1\hat{\mathbf{n}}^{\text{inc}}\cdot\mathbf{r}), \tag{3.1}$$

where the position vector $\mathbf{r}$ originates at the geometrical center of the volume element O. The total electric field scattered by the volume element at a large distance r from O can be written as the vector sum of the partial fields scattered by the component particles:

$$\mathbf{E}^{\text{sca}}(\mathbf{r}) = \sum_{n=1}^{N} \mathbf{E}_n^{\text{sca}}(\mathbf{r}), \tag{3.2}$$

where the position vector $\mathbf{r}$ of the observation point originates at O, and the index n numbers the particles. Since we ignore multiple scattering, we assume that each particle is excited only by the external incident field but not by the secondary fields scattered by other particles. Furthermore, because the particles are widely separated, each of them scatters the incident wave in exactly the same way as if all other particles did not exist. Therefore, according to Section 2.11, the partial scattered fields are given by

$$\begin{bmatrix} [\mathbf{E}_n^{\text{sca}}(\mathbf{r})]_\vartheta \\ [\mathbf{E}_n^{\text{sca}}(\mathbf{r})]_\varphi \end{bmatrix} = \frac{\mathrm{e}^{\mathrm{i}k_1 r}}{r}\mathrm{e}^{\mathrm{i}\Delta_n}\mathbf{S}_n(\hat{\mathbf{r}}, \hat{\mathbf{n}}^{\text{inc}}) \begin{bmatrix} E_{0\vartheta}^{\text{inc}} \\ E_{0\varphi}^{\text{inc}} \end{bmatrix}, \tag{3.3}$$

where $\hat{\mathbf{r}} = \mathbf{r}/r$, $\mathbf{S}_n(\hat{\mathbf{r}}, \hat{\mathbf{n}}^{\text{inc}})$ is the amplitude scattering matrix of the nth particle, centered inside that particle, the phase Δ_n is given by

$$\Delta_n = k_1\mathbf{r}_{On}\cdot(\hat{\mathbf{n}}^{\text{inc}} - \hat{\mathbf{r}}), \tag{3.4}$$

and the vector $\mathbf{r}_{On}$ connects the origin of the volume element O with the nth particle's origin. As in Section 2.11, we have assumed that

$$\frac{r_{On}}{r} \ll 1 \quad\text{and}\quad \frac{k_1 r_{On}^2}{2r} \ll 1, \qquad n = 1, \ldots, N, \tag{3.5}$$

or, equivalently,

$$\frac{l}{r} \ll 1 \quad\text{and}\quad \frac{k_1 l^2}{2r} \ll 1. \tag{3.6}$$

These conditions explicitly indicate that the observation point is in the far-field zone of the small volume element as a whole and that the latter is treated as a single scatterer. We thus have

$$\begin{bmatrix} E_{\vartheta}^{\text{sca}}(\mathbf{r}) \\ E_{\varphi}^{\text{sca}}(\mathbf{r}) \end{bmatrix} = \frac{\mathrm{e}^{\mathrm{i}k_1 r}}{r} \mathbf{S}(\hat{\mathbf{r}}, \hat{\mathbf{n}}^{\text{inc}}) \begin{bmatrix} E_{0\vartheta}^{\text{inc}} \\ E_{0\varphi}^{\text{inc}} \end{bmatrix}, \tag{3.7}$$

where the total amplitude scattering matrix of the small volume element centered at O is

$$\mathbf{S}(\hat{\mathbf{r}}, \hat{\mathbf{n}}^{\text{inc}}) = \sum_{n=1}^{N} \mathrm{e}^{\mathrm{i}\Delta_n} \mathbf{S}_n(\hat{\mathbf{r}}, \hat{\mathbf{n}}^{\text{inc}}). \tag{3.8}$$

Since the Δ_n vanish in the exact forward-scattering direction, substituting Eq. (3.8) in Eqs. (2.140)–(2.146) yields the total extinction matrix of the small volume element:

$$\mathbf{K} = \sum_{n=1}^{N} \mathbf{K}_n = N\langle \mathbf{K} \rangle, \tag{3.9}$$

where $\langle \mathbf{K} \rangle$ is the average extinction matrix per particle. Equation (2.159) then gives the total extinction cross section:

$$C_{\text{ext}} = \sum_{n=1}^{N} (C_{\text{ext}})_n = N\langle C_{\text{ext}} \rangle, \tag{3.10}$$

where $\langle C_{\text{ext}} \rangle$ is the average extinction cross section per particle. Analogously, by substituting Eq. (3.8) in Eqs. (2.106)–(2.121) and assuming that particle positions are sufficiently random that

$$\left| \mathrm{Re} \sum_{n} \sum_{n' \neq n} [\mathbf{S}_n(\hat{\mathbf{r}}, \hat{\mathbf{n}}^{\text{inc}})]_{ij} [\mathbf{S}_{n'}(\hat{\mathbf{r}}, \hat{\mathbf{n}}^{\text{inc}})]_{kl}^{*} \exp[\mathrm{i}(\Delta_n - \Delta_{n'})] \right|$$
$$\ll \left| \mathrm{Re} \sum_{n} [\mathbf{S}_n(\hat{\mathbf{r}}, \hat{\mathbf{n}}^{\text{inc}})]_{ij} [\mathbf{S}_n(\hat{\mathbf{r}}, \hat{\mathbf{n}}^{\text{inc}})]_{kl}^{*} \right|, \qquad i, j, k, l = 1, 2 \tag{3.11a}$$

and, if $i \neq k$ or $j \neq l$,

$$\left| \mathrm{Im} \sum_{n} \sum_{n' \neq n} [\mathbf{S}_n(\hat{\mathbf{r}}, \hat{\mathbf{n}}^{\text{inc}})]_{ij} [\mathbf{S}_{n'}(\hat{\mathbf{r}}, \hat{\mathbf{n}}^{\text{inc}})]_{kl}^{*} \exp[\mathrm{i}(\Delta_n - \Delta_{n'})] \right|$$
$$\ll \left| \mathrm{Im} \sum_{n} [\mathbf{S}_n(\hat{\mathbf{r}}, \hat{\mathbf{n}}^{\text{inc}})]_{ij} [\mathbf{S}_n(\hat{\mathbf{r}}, \hat{\mathbf{n}}^{\text{inc}})]_{kl}^{*} \right|, \tag{3.11b}$$

it is straightforward to show that the total phase matrix of the volume element is given by

$$\mathbf{Z} = \sum_{n=1}^{N} \mathbf{Z}_n = N\langle \mathbf{Z} \rangle, \tag{3.12}$$

where $\langle \mathbf{Z} \rangle$ is the average phase matrix per particle. Equations (2.160) and (2.161) then give the total scattering and absorption cross sections of the volume element:

$$C_{\text{sca}} = \sum_{n=1}^{N} (C_{\text{sca}})_n = N\langle C_{\text{sca}}\rangle, \tag{3.13}$$

$$C_{\text{abs}} = \sum_{n=1}^{N} (C_{\text{abs}})_n = N\langle C_{\text{abs}}\rangle, \tag{3.14}$$

where $\langle C_{\text{sca}}\rangle$ is the average scattering cross section and $\langle C_{\text{abs}}\rangle$ the average absorption cross section per particle. Finally, Eqs. (2.166), (2.169), (2.178), and (2.186) yield

$$C_{\text{pr}} = \sum_{n=1}^{N} (C_{\text{pr}})_n = N\langle C_{\text{pr}}\rangle, \tag{3.15}$$

$$\mathbf{K}_{\text{e}} = \sum_{n=1}^{N} (\mathbf{K}_{\text{e}})_n = N\langle \mathbf{K}_{\text{e}}\rangle, \tag{3.16}$$

where $\langle C_{\text{pr}}\rangle$ is the average radiation-pressure cross section and $\langle \mathbf{K}_{\text{e}}\rangle$ the average emission vector per particle. Thus, the optical cross sections, the phase and extinction matrices, and the emission vector of the small volume element comprising randomly positioned, widely separated particles are obtained by adding the respective optical characteristics of the individual particles. Obviously, this property of additivity also holds when the incident light is a parallel quasi-monochromatic beam rather than a plane electromagnetic wave.

It should be recognized that at any given moment, the particles filling the volume element form a certain spatial configuration, and the individual waves scattered by different particles have a specific phase relation and interfere. However, even a minute displacement of the particles or a slight change in the scattering geometry during the measurement may change the phase differences entirely. Therefore, in almost all practical situations the light singly scattered by a collection of randomly positioned particles and measured by a real detector appears to be incoherent, and the optical characteristics of individual particles must be added without regard to phase.

Because the total phase matrix of the volume element is the sum of the phase matrices of the constituent particles, the nine independent quadratic relations between the elements of the single-particle phase matrix as well as some quadratic inequalities (see Section 2.6) generally no longer hold. Still, there are a number of linear and quadratic inequalities that can be used for testing the elements of theoretically or experimentally obtained phase matrices of particle collections (Hovenier and van der Mee 2000). The simplest and most important of them are

$$Z_{11} \geq 0 \tag{3.17}$$

(cf. Eqs. (2.106) and (3.12)) and

$$|Z_{ij}| \leq Z_{11}, \qquad i, j = 1, \ldots, 4. \tag{3.18}$$

Obviously, the reciprocity and symmetry relations (2.124) and (2.147a,b) remain valid for the phase and extinction matrices of the volume element.

3.2 Ensemble averaging

Scattering media encountered in practice are usually mixtures of particles with different sizes, shapes, orientations, and refractive indices. Equations (3.9)–(3.16) imply that theoretical computations of single scattering of light by a small volume element consisting of such particles must include averaging the optical cross sections, the phase and extinction matrices, and the emission vector over a representative particle ensemble. The computation of ensemble averages is, in principle, rather straightforward. For example, for homogeneous ellipsoids with semi-axes $a \in [a_{\min}, a_{\max}]$, $b \in [b_{\min}, b_{\max}]$, and $c \in [c_{\min}, c_{\max}]$ and the same refractive index, the ensemble-averaged phase matrix per particle is

$$\langle \mathbf{Z}(\hat{\mathbf{n}}, \hat{\mathbf{n}}') \rangle = \int_{a_{\min}}^{a_{\max}} \mathrm{d}a \int_{b_{\min}}^{b_{\max}} \mathrm{d}b \int_{c_{\min}}^{c_{\max}} \mathrm{d}c \int_0^{2\pi} \mathrm{d}\alpha \int_0^{\pi} \mathrm{d}\beta \sin\beta \int_0^{2\pi} \mathrm{d}\gamma p(\alpha, \beta, \gamma; a, b, c) \times \mathbf{Z}(\hat{\mathbf{n}}, \hat{\mathbf{n}}'; \alpha, \beta, \gamma; a, b, c), \tag{3.19}$$

where the Euler angles α, β, and γ specify particle orientations with respect to the laboratory reference frame, and $p(\alpha, \beta, \gamma; a, b, c)$ is a probability density function satisfying the normalization condition:

$$\int_{a_{\min}}^{a_{\max}} \mathrm{d}a \int_{b_{\min}}^{b_{\max}} \mathrm{d}b \int_{c_{\min}}^{c_{\max}} \mathrm{d}c \int_0^{2\pi} \mathrm{d}\alpha \int_0^{\pi} \mathrm{d}\beta \sin\beta \int_0^{2\pi} \mathrm{d}\gamma p(\alpha, \beta, \gamma; a, b, c) = 1. \tag{3.20}$$

The integrals in Eq. (3.19) are usually evaluated numerically by using appropriate quadrature formulas. Some theoretical techniques (e.g., the T-matrix method) allow analytical averaging over particle orientations, thereby bypassing time-consuming integration over the Euler angles.

It is often assumed that the shape and size distribution and the orientation distribution are statistically independent. The total probability density function can then be simplified by representing it as a product of two functions, one of which, $p_{\mathrm{s}}(a, b, c)$, describes the particle shape and size distribution and the other of which, $p_{\mathrm{o}}(\alpha, \beta, \gamma)$, describes the distribution of particle orientations:

$$p(\alpha, \beta, \gamma; a, b, c) = p_{\mathrm{s}}(a, b, c) p_{\mathrm{o}}(\alpha, \beta, \gamma). \tag{3.21}$$

Each is normalized to unity:

$$\int_{a_{\min}}^{a_{\max}} \mathrm{d}a \int_{b_{\min}}^{b_{\max}} \mathrm{d}b \int_{c_{\min}}^{c_{\max}} \mathrm{d}c p_{\mathrm{s}}(a, b, c) = 1, \tag{3.22}$$

$$\int_0^{2\pi} \mathrm{d}\alpha \int_0^{\pi} \mathrm{d}\beta \sin\beta \int_0^{2\pi} \mathrm{d}\gamma p_{\mathrm{o}}(\alpha, \beta, \gamma) = 1. \tag{3.23}$$

In consequence, the problems of computing the shape and size and the orientation averages are separated. Similarly, it is often convenient to separate averaging over

shapes and sizes by assuming that particle shapes and sizes are statistically independent. For example, the shape of a spheroidal particle can be specified by its aspect ratio ε (the ratio of the largest to the smallest axes) along with the designation of either prolate or oblate, whereas the size of the particle can be specified by an equivalent-sphere radius a. Then the shape and size probability density function $p_{\mathrm{s}}(\varepsilon, a)$ can be represented as a product

$$p_{\mathrm{s}}(\varepsilon, a) = p(\varepsilon) n(a), \tag{3.24}$$

where $p(\varepsilon)$ describes the distribution of spheroid aspect ratios and $n(a)$ is the distribution of equivalent-sphere radii. Again, both $p(\varepsilon)$ and $n(a)$ are normalized to unity:

$$\int_{\varepsilon_{\min}}^{\varepsilon_{\max}} \mathrm{d}\varepsilon p(\varepsilon) = 1, \tag{3.25}$$

$$\int_{a_{\min}}^{a_{\max}} \mathrm{d}a n(a) = 1. \tag{3.26}$$

In the absence of external forces such as magnetic, electrostatic, or aerodynamical forces, all orientations of a nonspherical particle are equiprobable. In this practically important case of randomly oriented particles, the orientation distribution function is uniform with respect to the Euler angles of rotation, and we have

$$p_{\mathrm{o,random}}(\alpha, \beta, \gamma) \equiv \frac{1}{8\pi^2}. \tag{3.27}$$

An external force can make the orientation distribution axially symmetric, the axis of symmetry being given by the direction of the force. For example, interstellar dust grains can be axially oriented by a cosmic magnetic field (Martin 1978), whereas nonspherical hydrometeors can be axially oriented by the aerodynamical force resulting from their non-zero falling velocity (Liou 1992). In this case it is convenient to choose the laboratory reference frame with the z-axis along the external force direction so that the orientation distribution is uniform with respect to the Euler angles α and γ:

$$p_{\mathrm{o,axial}}(\alpha, \beta, \gamma) \equiv \frac{1}{4\pi^2} p_{\mathrm{o}}(\beta). \tag{3.28}$$

Particular details of the particle shape can also simplify the orientation distribution function. For example, for rotationally symmetric bodies it is convenient to direct the z-axis of the particle reference frame along the axis of rotation, in which case the orientation distribution function in the laboratory reference frame becomes independent of the Euler angle γ:

$$p_{\mathrm{o}}(\alpha, \beta, \gamma) \equiv \frac{1}{2\pi} p_{\mathrm{o}}(\alpha, \beta). \tag{3.29}$$

3.3 Condition of independent scattering

The inequalities (3.11a) and (3.11b) require the assumption that scattering is incoherent and that the positions of the particles filling the volume element are uncorrelated during the time necessary to make the measurement. However, it is rather difficult to give general and definitive criteria under which the inequalities (3.11a) and (3.11b) are satisfied. Also, there is no obvious prescription for specifying the minimal interparticle separation that allows the use of the concept of the single-particle amplitude scattering matrix in Eq. (3.3) and makes particles effectively independent scatterers. Exact computations for a few specific cases can perhaps provide qualitative guidance. Figure 3.1 shows the results of exact T-matrix computations (Chapter 5) of the ratios

$$\frac{Z_{22}(\vartheta^{\rm sca}, \varphi^{\rm sca}=0; \vartheta^{\rm inc}=0, \varphi^{\rm inc}=0)}{Z_{11}(\vartheta^{\rm sca}, \varphi^{\rm sca}=0; \vartheta^{\rm inc}=0, \varphi^{\rm inc}=0)},$$
$$-\frac{Z_{21}(\vartheta^{\rm sca}, \varphi^{\rm sca}=0; \vartheta^{\rm inc}=0, \varphi^{\rm inc}=0)}{Z_{11}(\vartheta^{\rm sca}, \varphi^{\rm sca}=0; \vartheta^{\rm inc}=0, \varphi^{\rm inc}=0)} \tag{3.30}$$

versus $\vartheta^{\rm sca}$ for randomly oriented two-sphere clusters with touching or separated components (Mishchenko *et al*. 1995). The relative refractive index is 1.5 + i0.005, the size parameter of the component spheres is $k_1 a = 5$, where k_1 is the wave number in the surrounding medium and a is the sphere radius, and the distance d between the centers of the cluster components varies from $2a$ for touching spheres to $8a$. For comparison, in the lower panel the thin solid curve depicts the results for single scattering by independent spheres with $k_1 a = 5$ (regarding the upper panel, note that in this case $Z_{22}/Z_{11} \equiv 1$; see Section 4.8). Obviously, the results for $d = 8a$ are hardly distinguishable from those for the independently scattering spheres. Even as small a distance between the component sphere centers as four times their radii combined with averaging over cluster orientations is already sufficient to reduce greatly the near-field and interference effects and produce scattering patterns very similar to those for the independent particles. For still larger spheres, with $k_1 a = 15$, the comparisons that can be made from Fig. 3.2 suggest qualitative independence at even smaller separations. While these results with separation measured in terms of particle size may be expected to become inapplicable for particles significantly smaller than a wavelength, they suggest a simple approximate condition of independent scattering by particles comparable to and larger than a wavelength.

3.4 Radiative transfer equation and coherent backscattering

Let us now relax the requirement that the scattering medium be macroscopically small and optically thin and be viewed from a distance much larger than its size. We thus assume that N is so large that the condition $N\langle C_{\rm sca}\rangle l^{-2} \ll 1$ is violated, and the

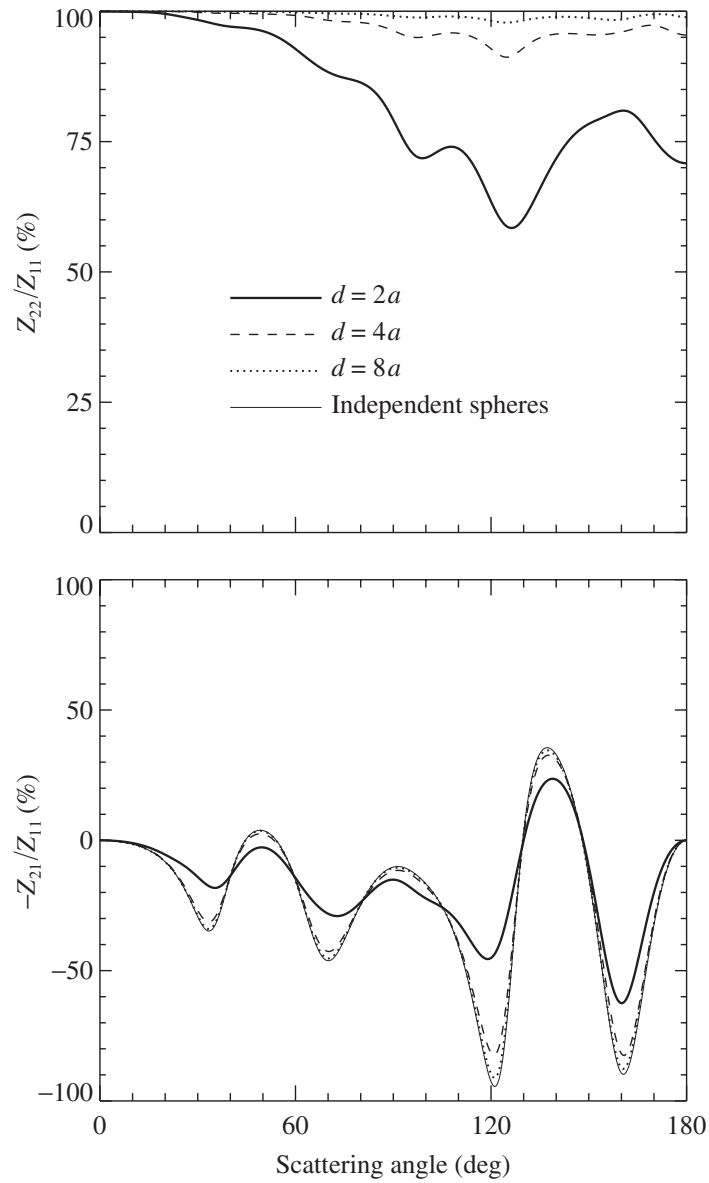

Figure 3.1. The ratios Z_{22}/Z_{11} and $-Z_{21}/Z_{11}$ (%) for randomly oriented two-sphere clusters with touching $(d = 2a)$ and separated components and independently scattering spheres. The component sphere size parameter $k_1 a$ is 5 and the relative refractive index is 1.5 + i0.005.

contribution of multiply scattered light to the total signal scattered by the medium can no longer be ignored. Furthermore, although the observation point is assumed to be in the far-field zone of each constituent particle, it is not necessarily in the far-field zone of the scattering medium as a whole, so that the observer may see scattered light coming from different directions. A traditional approach in such cases is to assume that scattering by different particles is still independent (which implies that the particles are randomly positioned and widely separated) and compute the characteristics of multiply scattered radiation by solving the so-called radiative transfer equation

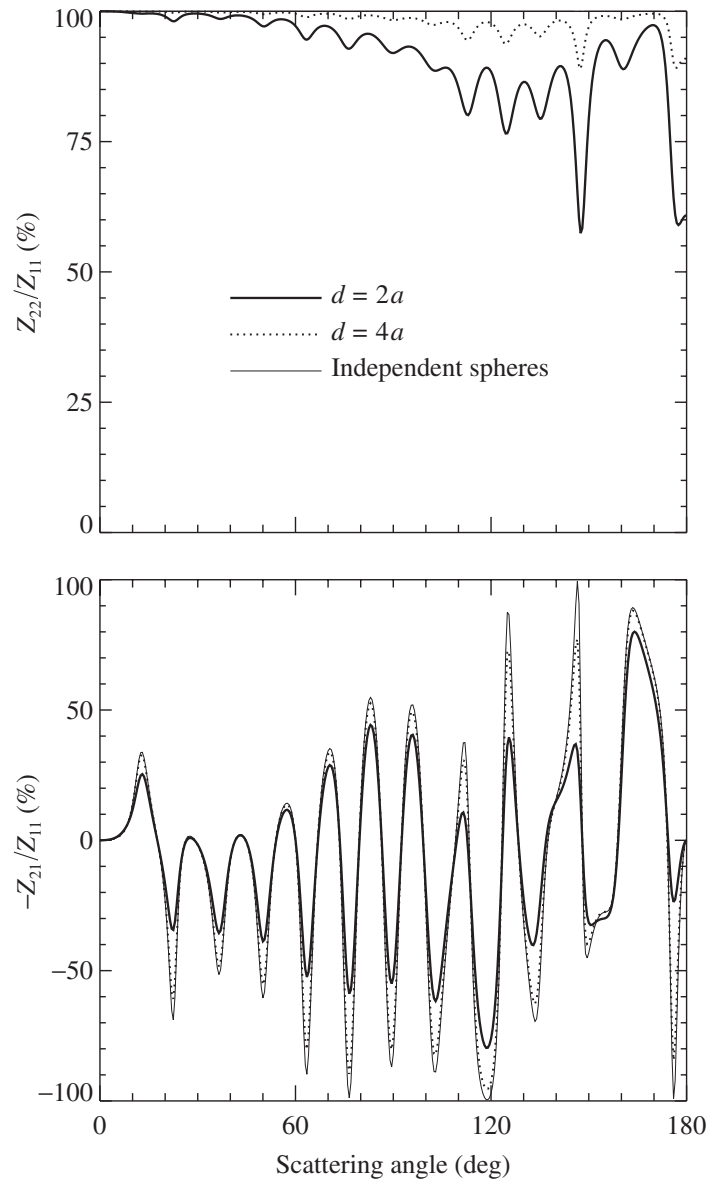

Figure 3.2. As in Fig. 3.1, but for $k_1 a = 15$.

(RTE).

Radiative transfer theory originated as a phenomenological approach based on considering the transport of energy through a medium filled with a large number of particles and ensuring energy conservation (e.g., Chandrasekhar 1960; Sobolev 1974; van de Hulst 1980; Apresyan and Kravtsov 1996; Lagendijk and van Tiggelen 1996; Ishimaru 1997). It has been demonstrated, however, that the RTE can in fact be derived from the electromagnetic theory of multiple wave scattering in discrete random media under certain simplifying assumptions (Mishchenko, 2002, 2003). This deriva-

tion has clarified the physical meaning of the quantities entering the RTE and their relation to single-scattering solutions of the Maxwell equations.

Instead of going into the details of this derivation, we will simply summarize the main concepts of the phenomenological radiative transfer theory, present the conventional form of the RTE, and explain the meaning of the quantities appearing in this equation. The electromagnetic radiation field at each point $\mathbf{r}$ inside the scattering medium is approximated by a collection of quasi-monochromatic beams with a continuous distribution of propagation directions $\hat{\mathbf{n}}$ and angular frequencies ω and is characterized by the local four-component monochromatic specific intensity column vector

$$\mathbf{I}(\mathbf{r}, \hat{\mathbf{n}}, \omega) = \begin{bmatrix} I(\mathbf{r}, \hat{\mathbf{n}}, \omega) \\ Q(\mathbf{r}, \hat{\mathbf{n}}, \omega) \\ U(\mathbf{r}, \hat{\mathbf{n}}, \omega) \\ V(\mathbf{r}, \hat{\mathbf{n}}, \omega) \end{bmatrix}. \tag{3.31}$$

It is assumed that the elementary beams are incoherent and make independent contributions to $\mathbf{I}(\mathbf{r}, \hat{\mathbf{n}}, \omega)$. The elements $Q(\mathbf{r}, \hat{\mathbf{n}}, \omega)$, $U(\mathbf{r}, \hat{\mathbf{n}}, \omega)$, and $V(\mathbf{r}, \hat{\mathbf{n}}, \omega)$ describe the polarization state of light propagating in the direction $\hat{\mathbf{n}}$ at the observation point specified by the position vector $\mathbf{r}$, and the monochromatic specific intensity (or radiance) $I(\mathbf{r}, \hat{\mathbf{n}}, \omega)$ is defined such that

$$I(\mathbf{r}, \hat{\mathbf{n}}, \omega)\, \mathrm{d}\omega\, \mathrm{d}t\, \mathrm{d}S\, \mathrm{d}\Omega \tag{3.32}$$

is the amount of electromagnetic energy in an angular frequency interval $(\omega, \omega + \mathrm{d}\omega)$ which is transported in a time interval $\mathrm{d}t$ through a surface element $\mathrm{d}S$ normal to $\hat{\mathbf{n}}$ and centered at $\mathbf{r}$ in directions confined to a solid angle element $\mathrm{d}\Omega$ centered at the direction of propagation $\hat{\mathbf{n}}$. All elements of the specific intensity vector have the dimension of monochromatic radiance: energy per unit frequency interval per unit time per unit area per unit solid angle.

In the phenomenological radiative transfer theory, a medium filled with a large number of discrete, sparsely and randomly distributed particles is treated as continuous and locally homogeneous. The concept of single scattering and absorption by an individual particle is thus replaced with the concept of single scattering and absorption by a small homogeneous volume element. Furthermore, it is assumed that the result of scattering is not the transformation of a plane incident wave into a spherical scattered wave but, rather, the transformation of the specific intensity vector of the incident light into the specific intensity vector of the scattered light:

$$\mathbf{I}(\mathbf{r}, \hat{\mathbf{n}}^{\mathrm{sca}}, \omega) \propto \mathbf{Z}(\mathbf{r}, \hat{\mathbf{n}}^{\mathrm{sca}}, \hat{\mathbf{n}}^{\mathrm{inc}}, \omega)\, \mathbf{I}(\mathbf{r}, \hat{\mathbf{n}}^{\mathrm{inc}}, \omega),$$

where $\mathbf{Z}(\mathbf{r}, \hat{\mathbf{n}}^{\mathrm{sca}}, \hat{\mathbf{n}}^{\mathrm{inc}}, \omega)$ is the phase matrix of the small volume element.

An informal way to justify this assumption is to note that the product $\mathbf{Z}(\hat{\mathbf{n}}^{\mathrm{sca}}, \hat{\mathbf{n}}^{\mathrm{inc}})\mathbf{I}^{\mathrm{inc}}$ in Eq. (2.102) may be interpreted as the scattered polarized power per unit solid angle.

Specifically, the polarized energy flow across a surface element ΔS normal to $\hat{\mathbf{n}}^{\mathrm{sca}}$ at a distance r from the particle is given by $\Delta S r^{-2}\mathbf{Z}(\hat{\mathbf{n}}^{\mathrm{sca}}, \hat{\mathbf{n}}^{\mathrm{inc}})\mathbf{I}^{\mathrm{inc}}$ and is, at the same time, equal to the polarized power scattered within the solid angle element $\Delta\Omega = \Delta S r^{-2}$ centered at $\hat{\mathbf{n}}^{\mathrm{sca}}$.

Another assumption in the phenomenological radiative transfer theory is that the scattering, absorption, and emission characteristics of the small volume element follow from the Maxwell equations and are given by the incoherent sums of the respective characteristics of the constituent particles according to Eqs. (3.9), (3.10), (3.12)–(3.14), and (3.16).

The change in the specific intensity vector along the direction of propagation $\hat{\mathbf{n}}$ in a medium containing sparsely and randomly distributed, arbitrarily oriented particles is described by the following classical RTE (Rozenberg 1977; Tsang *et al.* 1985; Mishchenko 2002):

$$\begin{aligned}\frac{\mathrm{d}}{\mathrm{d}s}\mathbf{I}(\mathbf{r}, \hat{\mathbf{n}}, \omega) &= -n_0(\mathbf{r})\langle\mathbf{K}(\mathbf{r}, \hat{\mathbf{n}}, \omega)\rangle\mathbf{I}(\mathbf{r}, \hat{\mathbf{n}}, \omega)\\ &\quad + n_0(\mathbf{r})\int_{4\pi}\mathrm{d}\hat{\mathbf{n}}'\langle\mathbf{Z}(\mathbf{r}, \hat{\mathbf{n}}, \hat{\mathbf{n}}', \omega)\rangle\mathbf{I}(\mathbf{r}, \hat{\mathbf{n}}', \omega)\\ &\quad + n_0(\mathbf{r})\langle\mathbf{K}_{\mathrm{e}}[\mathbf{r}, \hat{\mathbf{n}}, T(\mathbf{r}), \omega]\rangle,\end{aligned} \tag{3.33}$$

where the path-length element $\mathrm{d}s$ is measured along the unit vector $\hat{\mathbf{n}}$, $n_0(\mathbf{r})$ is the local particle number density, and $\langle\mathbf{K}(\mathbf{r}, \hat{\mathbf{n}}, \omega)\rangle$, $\langle\mathbf{Z}(\mathbf{r}, \hat{\mathbf{n}}, \hat{\mathbf{n}}', \omega)\rangle$, and $\langle\mathbf{K}_{\mathrm{e}}[\mathbf{r}, \hat{\mathbf{n}}, T(\mathbf{r}), \omega]\rangle$ are the local ensemble-averaged extinction and phase matrices and emission vector per particle, respectively. The first term on the right-hand side of Eq. (3.33) describes the change in the specific intensity vector over the distance $\mathrm{d}s$ caused by extinction and dichroism, the second term describes the contribution of light illuminating a small volume element centered at $\mathbf{r}$ from all directions $\hat{\mathbf{n}}'$ and scattered into the direction $\hat{\mathbf{n}}$, and the third term describes the contribution of the emitted light.

The radiative transfer equation must be supplemented by boundary conditions appropriate for a given physical problem. In particular, the boundary conditions must correspond to the macroscopic geometry of the scattering medium and specify the direction, polarization state, and frequency distribution of the external incident light. For example, in the case of light scattering by the atmosphere, a standard model is a plane-parallel particulate medium illuminated from above by a parallel beam representing solar radiation and bounded from below by a reflecting surface. The solution of the RTE yields the specific intensity vector of the outgoing radiation at each boundary point and, thereby, the angular distribution and polarization state of light multiply scattered (reflected and transmitted) by the medium. It also provides the specific intensity vector of the internal radiation field. General solutions of Eq. (3.33) have been discussed by, e.g., Mishchenko (1990a) and Haferman (2000).

Despite the approximate character of the standard radiative transfer theory, it pro-

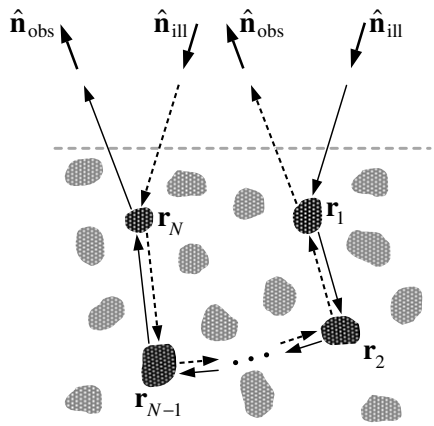

Figure 3.3. Schematic explanation of coherent backscattering.

vides a powerful and reasonably general prescription for the treatment of the interaction of light with particulate media and is accordingly applicable to a broad range of practical situations. However, owing to some of the basic assumptions in the development of the classical RTE, there are circumstances for which it is not sufficient. For example, since the classical RTE does not take full account of interference effects it does not describe directly the so-called coherent backscattering of light (otherwise known as weak photon localization) (Watson 1969). To explain the physical origin of this phenomenon, let us consider a layer composed of discrete, randomly positioned scattering particles and illuminated by a parallel beam of light incident in the direction $\hat{\mathbf{n}}_{\text{ill}}$ (Fig. 3.3). The distant observer measures the intensity of light reflected by the layer in the direction $\hat{\mathbf{n}}_{\text{obs}}$. The reflected signal is composed of the contributions made by waves scattered along various paths inside the layer involving different combinations of particles. Let us consider the two conjugate scattering paths shown in Fig. 3.3 by solid and broken lines. These paths go through the same group of N particles, denoted by their positions $\mathbf{r}_1, \mathbf{r}_2, \ldots, \mathbf{r}_N$, but in opposite directions. The waves scattered along the two conjugate paths interfere, the interference being constructive or destructive depending on the phase difference

$$\Delta = k_1(\mathbf{r}_N - \mathbf{r}_1)\cdot(\hat{\mathbf{n}}_{\text{ill}} + \hat{\mathbf{n}}_{\text{obs}}), \tag{3.34}$$

where k_1 is the wave number in the surrounding medium. If the observation direction is far from the exact backscattering direction given by $-\hat{\mathbf{n}}_{\text{ill}}$, then the waves scattered along conjugate paths involving different groups of particles interfere in different ways, and the average effect of the interference is zero owing to the randomness of particle positions. Consequently, the observer measures some average, incoherent intensity that is well described by the classical radiative transfer theory. However, at exactly the backscattering direction $(\hat{\mathbf{n}}_{\text{obs}} = -\hat{\mathbf{n}}_{\text{ill}})$, the phase difference between conjugate paths involving any group of particles is identically equal to zero, Eq. (3.34), and the interference is always constructive, thereby resulting in a coherent

backscattering intensity peak superposed on the incoherent background (Tsang *et al*. 1985; Barabanenkov *et al.* 1991; Sheng 1995). The scattering paths involving only one particle do not have conjugate counterparts and do not contribute to the coherent intensity peak. Kuga and Ishimaru (1984) were the first to detect coherent backscattering in a controlled laboratory experiment, although it may have been unknowingly observed by Lyot (1929) in the form of the so-called coherent polarization opposition effect (Mishchenko *et al*. 2000e).

An exact computation of the coherent backscattering effect based on solving the Maxwell equations is feasible only for few-component clusters and is complicated by several factors. First, the scattering pattern for a monodisperse cluster in a fixed orientation is always heavily burdened by multiple maxima and minima resulting from the interference of partial waves scattered by the cluster components and by the intricate resonance structure of the single-scattering contribution (Section 9.1). Second, the scattering pattern can be further affected by near-field effects that result from the close proximity of the component particles. Third, simple trigonometry shows that the angular width of the coherent backscattering intensity peak is of the order $1/k_1\langle d\rangle = \lambda_1/2\pi\langle d\rangle$, where $\langle d\rangle$ is the average distance between the cluster components and λ_1 is the wavelength in the surrounding medium. Therefore, the peak may be too broad to be identified reliably unless the cluster components are widely separated. However, increasing the distance between the cluster components diminishes the contribution of multiple scattering and, thus, the amplitude of the coherent backscattering peak, thereby making it difficult to detect.

To smooth out the effect of the first factor and make the backscattering peak detectable, one must compute a scattering pattern that is averaged over particle sizes, cluster orientations, and distances between the components. Furthermore, the average distance between the cluster components must be much larger than the size of the components and the wavelength but yet small enough that the multiple-scattering contribution to the total signal is still significant.

Ismagilov and Kravtsov (1993) studied analytically the simplest case, two widely separated spheres with diameters much smaller than the wavelength, but found that the amplitude of the coherent backscattering intensity peak was extremely small because of the weakness of the multiple-scattering contribution to the total scattered signal. Mishchenko (1996a) used the exact superposition *T*-matrix method (Section 5.9) to compute far-field scattering by polydisperse, randomly oriented clusters composed of two equal wavelength-sized spheres with varying center-to-center distances. He computed the ratio of the intensity scattered by the clusters to the intensity scattered by two independent polydisperse spheres of the same average size, assuming unpolarized incident light. Figure 3.4 shows this ratio versus scattering angle (the angle between the incidence and scattering directions) calculated for $k_1\langle d\rangle = 25$, average component sphere size parameter $k_1\langle a\rangle = 5$, and relative refractive index m = 1.2. The curve clearly exhibits a backscattering enhancement with an angular width comparable to $1/k_1\langle d\rangle$ and an amplitude of about 1.03. Mishchenko (1996a) found

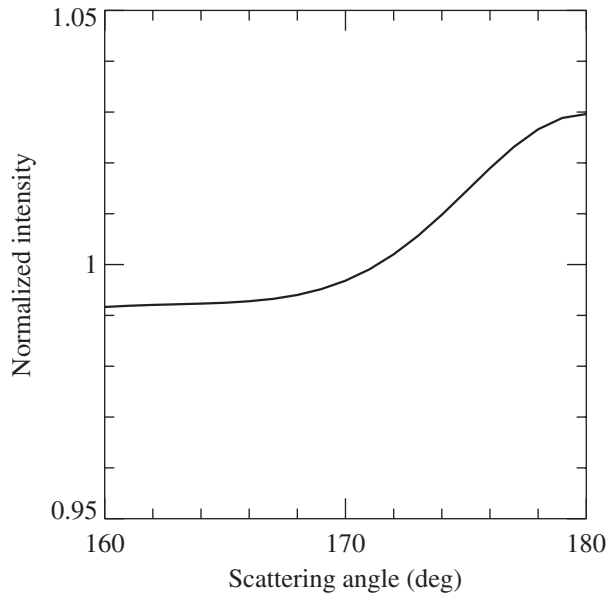

Figure 3.4. Coherent backscattering by polydisperse, randomly oriented two-sphere clusters.

that this feature persisted when $k_1\langle d\rangle$, $k_1\langle a\rangle$, and m were varied, thereby indicating that it was indeed caused by coherent backscattering.

The amplitude of the coherent backscattering peak (the ratio of the intensity in the center of the peak to the background value) can be significantly greater for very large collections of particles because of the much stronger contribution of multiple scattering (van Albada and Lagendijk 1985; Wolf *et al*. 1988; Labeyrie *et al*. 2000). For example, the measurement results depicted in Fig. 3.5 show an amplitude of almost 1.8. Unfortunately, the exact theory of coherent backscattering for large particle collections is extremely complicated and has been developed only for the case of reflection of light by a semi-infinite layer composed of nonabsorbing particles with sizes much smaller than the wavelength (Ozrin 1992; Amic *et al.* 1997). An exact result was obtained by Mishchenko (1992b), who used the reciprocity relation of Eq. (2.124) to show that the photometric and polarization characteristics of coherent backscattering at exactly the backscattering direction as well as outside the backscattering peak can be expressed in terms of the solution of the classical RTE. Other theoretical approaches are based on the so-called diffusion approximation (Stephen and Cwilich 1986) and the Monte Carlo technique (van Albada and Lagendijk 1987; Martinez and Maynard 1994; Iwai *et al*. 1995).

Because the angular width of the intensity peak caused by coherent backscattering from optically thick layers is proportional to the ratio of the wavelength to the photon mean free path, it is negligibly small for sparse particle collections and does not affect the results of remote sensing observations of such tenuous objects as clouds, aerosols, and precipitation. However, measurements of coherent backscattering have proved to

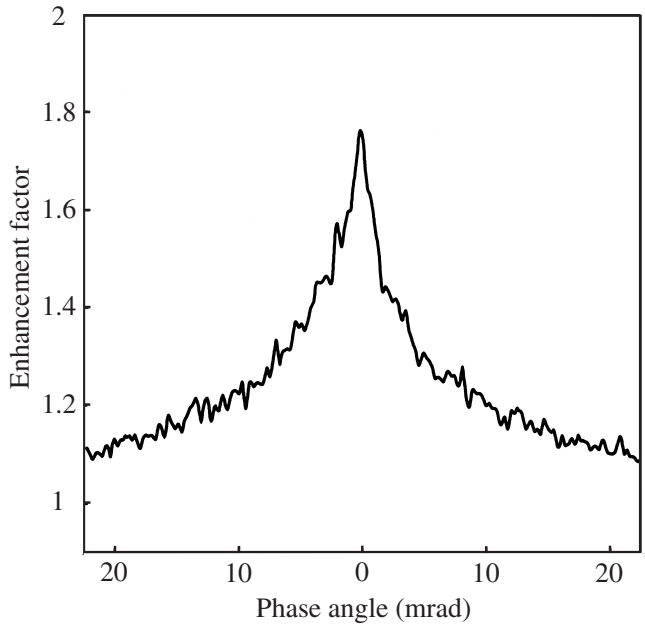

Figure 3.5. Angular profile of the coherent backscattering peak produced by a 1500-μm-thick slab of 9.6 vol% of 0.215-μm-diameter polystyrene spheres suspended in water. The slab was illuminated by a linearly polarized laser beam $(\lambda_1 = 633\ \text{nm})$ incident normally to the slab surface. The scattering plane (i.e., the plane through the vectors $\hat{\mathbf{n}}_{\text{ill}}$ and $\hat{\mathbf{n}}_{\text{obs}}$, Fig. 3.3) was fixed in such a way that the electric vector of the incident beam vibrated in this plane. The detector measured the component of the backscattered intensity polarized parallel to the scattering plane. The curve shows the profile of the backscattered intensity normalized by the intensity of the incoherent background as a function of the phase angle. The latter is defined as the angle between the vectors $\hat{\mathbf{n}}_{\text{obs}}$ and $-\hat{\mathbf{n}}_{\text{ill}}$. (After van Albada *et al.* 1987.)

be a valuable characterization tool in laboratory and remote sensing studies of layers composed of more closely spaced particles, such as particle suspensions and natural and artificial particulate surfaces (e.g., Muinonen 1993; Shkuratov 1994; Mishchenko 1996b; POAN Research Group 1998; Lenke and Maret 2000).

Further reading

A detailed discussion of the concept of single scattering by a small volume element was recently presented by Mishchenko *et al*. (2004a).

Chapter 4

Scattering matrix and macroscopically isotropic and mirror-symmetric scattering media

By definition, the phase matrix relates the Stokes parameters of the incident and scattered beams, defined relative to their respective meridional planes. In contrast to the phase matrix, the scattering matrix $\mathbf{F}$ relates the Stokes parameters of the incident and scattered beams defined with respect to the scattering plane, that is, the plane through the unit vectors $\hat{\mathbf{n}}^{\text{inc}}$ and $\hat{\mathbf{n}}^{\text{sca}}$ (van de Hulst 1957).

A simple way to introduce the scattering matrix is to direct the z-axis of the reference frame along the incident beam and superpose the meridional plane with $\varphi = 0$ and the scattering plane (Fig. 4.1). Then the scattering matrix $\mathbf{F}$ can be defined as

$$\mathbf{F}(\vartheta^{\text{sca}}) = \mathbf{Z}(\vartheta^{\text{sca}}, \varphi^{\text{sca}} = 0; \vartheta^{\text{inc}} = 0, \varphi^{\text{inc}} = 0). \tag{4.1}$$

In general, all 16 elements of the scattering matrix are non-zero and depend on the particle orientation with respect to the incident and scattered beams.

The choice of laboratory reference frame, with z-axis along the incidence direction and the xz-plane with $x \geq 0$ coinciding with the scattering plane, can often be inconvenient because any change in the incidence direction and/or orientation of the scattering plane also changes the orientation of the scattering particle with respect to the coordinate system. However, we will show in this chapter that the concept of the scattering matrix can be very useful in application to so-called macroscopically isotropic and mirror-symmetric scattering media, because the scattering matrix of such a particle collection becomes independent of incidence direction and orientation of the scattering plane, depends only on the angle $\Theta = \arccos(\hat{\mathbf{n}}^{\text{inc}} \cdot \hat{\mathbf{n}}^{\text{sca}})$ between the incidence and scattering directions, and has a simple block-diagonal structure.

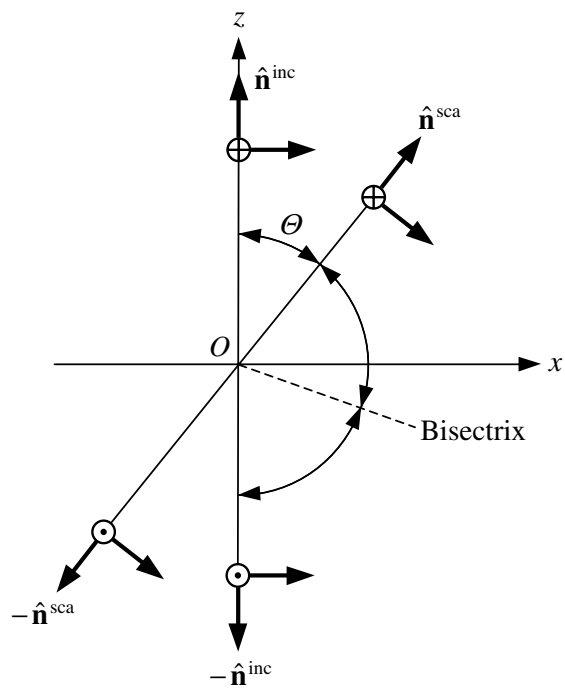

Figure 4.1. The *xz*-plane of the reference frame acts as the scattering plane. The arrows perpendicular to the unit $\hat{\mathbf{n}}$ - vectors show the corresponding unit $\hat{\boldsymbol{\vartheta}}$ - vectors. The symbols $\oplus$ and $\odot$ indicate the corresponding unit $\hat{\boldsymbol{\varphi}}$ - vectors, which are directed into and out of the paper, respectively.

4.1 Symmetries of the Stokes scattering matrix

We begin by considering special symmetry properties of the amplitude scattering matrix that exist when both the incidence and the scattering directions lie in the *xz*-plane (van de Hulst 1957). For the particle shown schematically in Fig. 4.2(a), let

$$\begin{bmatrix} S_{11} & S_{12} \\ S_{21} & S_{22} \end{bmatrix} \tag{4.2a}$$

be the amplitude scattering matrix that corresponds to the directions of incidence and scattering given by $\hat{\mathbf{n}}^{\text{inc}}$ and $\hat{\mathbf{n}}^{\text{sca}}$, respectively (Fig. 4.1). Rotating this particle by 180° about the bisectrix (i.e., the line in the scattering plane that bisects the angle $\pi - \Theta$ between the unit vectors $-\hat{\mathbf{n}}^{\text{inc}}$ and $\hat{\mathbf{n}}^{\text{sca}}$ in Fig. 4.1) puts it in the orientation schematically shown in Fig. 4.2(b). It is clear that the amplitude scattering matrix (4.2a) is also the amplitude scattering matrix for this rotated particle when the directions of incidence and scattering are given by $-\hat{\mathbf{n}}^{\text{sca}}$ and $-\hat{\mathbf{n}}^{\text{inc}}$, respectively. Therefore, the reciprocity relation (2.64) implies that the amplitude scattering matrix of the

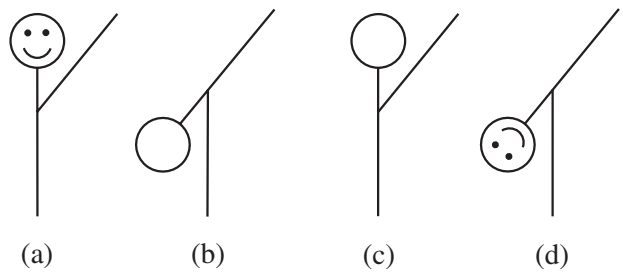

Figure 4.2. Two orientations of an arbitrary particle and two orientations of its mirror-symmetric particle that give rise to certain symmetries in scattering patterns. (After van de Hulst 1957.)

particle shown in Fig. 4.2(b) that corresponds to the original directions of incidence and scattering, $\hat{\mathbf{n}}^{\text{inc}}$ and $\hat{\mathbf{n}}^{\text{sca}}$, is simply

$$\begin{bmatrix} S_{11} & -S_{21} \\ -S_{12} & S_{22} \end{bmatrix}. \tag{4.2b}$$

Mirroring the original particle, Fig. 4.2(a), with respect to the scattering plane gives the particle shown in Fig. 4.2(c). If we also reversed the direction of the unit vectors $\hat{\boldsymbol{\varphi}}^{\text{inc}}$ and $\hat{\boldsymbol{\varphi}}^{\text{sca}}$ in Fig. (4.1), then we would have the same scattering problem as for the particle shown in Fig. 4.2(a). We may thus conclude that the amplitude scattering matrix for the particle shown in Fig. 4.2(c) that corresponds to the directions of incidence and scattering $\hat{\mathbf{n}}^{\text{inc}}$ and $\hat{\mathbf{n}}^{\text{sca}}$ is

$$\begin{bmatrix} S_{11} & -S_{12} \\ -S_{21} & S_{22} \end{bmatrix}. \tag{4.2c}$$

Finally, mirroring the original particle with respect to the bisectrix plane (i.e., the plane through the bisectrix and the y-axis) gives the particle shown in Fig. 4.2(d). Since this particle is simply the mirror-symmetric counterpart of the particle shown in Fig. 4.2(b), its amplitude scattering matrix corresponding to the directions of incidence and scattering $\hat{\mathbf{n}}^{\text{inc}}$ and $\hat{\mathbf{n}}^{\text{sca}}$ is

$$\begin{bmatrix} S_{11} & S_{21} \\ S_{12} & S_{22} \end{bmatrix}. \tag{4.2d}$$

It can be seen that any two of the three transformations shown in Figs. 4.2(b)–4.2(d) give the third.

We will now discuss the implications of Eqs. (4.2a)–(4.2d) for Stokes scattering matrices of collections of independently scattering particles, by considering the following four examples (van de Hulst 1957).

(1) Let us first assume that a small volume element contains only one kind of particle and that each particle in a specific orientation, say Fig. 4.2(a), is accompanied by a particle in the reciprocal orientation, Fig. 4.2(b). It then follows from Eqs. (2.106)–

(2.121), (3.12), (4.1), (4.2a), and (4.2b) that the scattering matrix of the small volume element has the following symmetry:

$$\begin{bmatrix} F_{11} & F_{12} & F_{13} & F_{14} \\ F_{12} & F_{22} & F_{23} & F_{24} \\ -F_{13} & -F_{23} & F_{33} & F_{34} \\ F_{14} & F_{24} & -F_{34} & F_{44} \end{bmatrix}. \tag{4.3}$$

The number of independent matrix elements is 10.

(2) As a second example, let us assume that the volume element contains particles and their mirror-symmetric counterparts such that for each particle in orientation (a) a mirror-symmetric particle in orientation (c) is present (Fig. 4.2). This excludes, for example, scattering media composed of only right-handed or only left-handed helices. It is easy to verify that the resulting scattering matrix involves eight independent elements and has the following structure:

$$\begin{bmatrix} F_{11} & F_{12} & 0 & 0 \\ F_{21} & F_{22} & 0 & 0 \\ 0 & 0 & F_{33} & F_{34} \\ 0 & 0 & F_{43} & F_{44} \end{bmatrix}. \tag{4.4}$$

(3) As a third example, consider a volume element containing particles and their mirror-symmetric counterparts and assume that any particle in orientation (a) is accompanied by a mirror-symmetric particle in orientation (d), Fig. 4.2. The scattering matrix becomes

$$\begin{bmatrix} F_{11} & F_{12} & F_{13} & F_{14} \\ F_{12} & F_{22} & F_{23} & F_{24} \\ F_{13} & F_{23} & F_{33} & F_{34} \\ -F_{14} & -F_{24} & -F_{34} & F_{44} \end{bmatrix} \tag{4.5}$$

and has 10 independent elements.

(4) Finally, consider a volume element containing particles and their mirror-symmetric counterparts and make any two of the preceding assumptions. The third assumption follows automatically, so that there are equal numbers of particles in orientations (a), (b), (c), and (d). The resulting scattering matrix is

$$\begin{bmatrix} F_{11} & F_{12} & 0 & 0 \\ F_{12} & F_{22} & 0 & 0 \\ 0 & 0 & F_{33} & F_{34} \\ 0 & 0 & -F_{34} & F_{44} \end{bmatrix} \tag{4.6}$$

and has eight non-zero elements, of which only six are independent.

4.2 Macroscopically isotropic and mirror-symmetric scattering medium

Now we are ready to consider scattering by a small volume element containing *randomly oriented* particles. This means that there are many particles of each type and their orientation distribution is uniform (see Eq. (3.27)). In this case the assumptions of example (1) from the previous section are satisfied, and the total scattering matrix is given by Eq. (4.3). Furthermore, if particles and their mirror-symmetric counterparts are present in equal numbers or each particle has a plane of symmetry, then the assumptions of example 4 are satisfied, and the resulting scattering matrix is given by Eq. (4.6).

As a consequence of random particle orientation, the scattering medium is *macroscopically isotropic* (i.e., there is no preferred propagation direction and no preferred plane through the incidence direction). Therefore, the scattering matrix becomes independent of the incidence direction and the orientation of the scattering plane and depends only on the angle between the incidence and scattering directions, that is, the scattering angle

$$\Theta = \arccos(\hat{\mathbf{n}}^{\text{inc}} \cdot \hat{\mathbf{n}}^{\text{sca}}), \qquad \Theta \in [0, \pi].$$

Furthermore, the assumptions of example (4) ensure that the scattering medium is *macroscopically mirror-symmetric* with respect to any plane and make the structure of the scattering matrix especially simple. Therefore, scattering media composed of equal numbers of randomly oriented particles and their mirror-symmetric counterparts and/or randomly oriented particles having a plane of symmetry can be called *macroscopically isotropic and mirror-symmetric*. Although this type of scattering medium might be thought to be a rather special case, it nonetheless provides a very good numerical description of the scattering properties of many particle collections encountered in practice and is by far the most often used theoretical model. To emphasize that the scattering matrix of a macroscopically isotropic and mirror-symmetric scattering medium depends only on the scattering angle, we rewrite Eq. (4.6) as

$$\mathbf{F}(\Theta) = \begin{bmatrix} F_{11}(\Theta) & F_{12}(\Theta) & 0 & 0 \\ F_{12}(\Theta) & F_{22}(\Theta) & 0 & 0 \\ 0 & 0 & F_{33}(\Theta) & F_{34}(\Theta) \\ 0 & 0 & -F_{34}(\Theta) & F_{44}(\Theta) \end{bmatrix} = N\langle \mathbf{F}(\Theta)\rangle, \tag{4.7}$$

where N is the number of particles in the volume element and $\langle \mathbf{F}(\Theta)\rangle$ is the ensemble-averaged scattering matrix per particle.

As a direct consequence of Eqs. (3.17) and (3.18) we have the inequalities

$$F_{11} \geq 0, \tag{4.8}$$

$$|F_{ij}| \leq F_{11}, \qquad i, j = 1, \ldots, 4. \tag{4.9}$$

Additional general inequalities for the elements of the scattering matrix (4.7) are

$$(F_{33}+F_{44})^2+4F_{34}^2 \le (F_{11}+F_{22})^2-4F_{12}^2, \tag{4.10}$$

$$|F_{33}-F_{44}| \le F_{11}-F_{22}, \tag{4.11}$$

$$|F_{22}-F_{12}| \le F_{11}-F_{12}, \tag{4.12}$$

$$|F_{22}+F_{12}| \le F_{11}+F_{12}. \tag{4.13}$$

The proof of these and other useful inequalities is given in Hovenier *et al.* (1986).

4.3 Phase matrix

Knowledge of the matrix $\mathbf{F}(\Theta)$ can be used to calculate the Stokes phase matrix for a macroscopically isotropic and mirror-symmetric scattering medium. Assume that $0<\varphi^{\text{sca}}-\varphi^{\text{inc}}<\pi$ and consider phase matrices $\mathbf{Z}(\vartheta^{\text{sca}},\varphi^{\text{sca}};\vartheta^{\text{inc}},\varphi^{\text{inc}})$ and $\mathbf{Z}(\vartheta^{\text{sca}},\varphi^{\text{inc}};\vartheta^{\text{inc}},\varphi^{\text{sca}})$. The second matrix involves the same zenith angles of the incident and scattered beams as the first, but the azimuth angles are switched, as indicated in their respective scattering geometries; these are shown in Figs. 4.3(a), (b). The phase matrix links the Stokes vectors of the incident and scattered beams, specified relative to their respective meridional planes. Therefore, to compute the Stokes vector of the scattered beam with respect to its meridional plane, we must

- calculate the Stokes vector of the incident beam with respect to the scattering plane;
- multiply it by the scattering matrix, thereby obtaining the Stokes vector of the scattered beam with respect to the scattering plane; and finally
- compute the Stokes vector of the scattered beam with respect to its meridional plane (Chandrasekhar 1960).

This procedure involves two rotations of the reference plane, as shown in Figs. 4.3(a), (b), and yields

$$\mathbf{Z}(\vartheta^{\text{sca}},\varphi^{\text{sca}};\vartheta^{\text{inc}},\varphi^{\text{inc}})=\mathbf{L}(-\sigma_2)\mathbf{F}(\Theta)\mathbf{L}(\pi-\sigma_1)$$

$$=\begin{bmatrix} F_{11}(\Theta) & C_1F_{12}(\Theta) & S_1F_{12}(\Theta) & 0 \\ C_2F_{12}(\Theta) & C_1C_2F_{22}(\Theta)-S_1S_2F_{33}(\Theta) & S_1C_2F_{22}(\Theta)+C_1S_2F_{33}(\Theta) & S_2F_{34}(\Theta) \\ -S_2F_{12}(\Theta) & -C_1S_2F_{22}(\Theta)-S_1C_2F_{33}(\Theta) & -S_1S_2F_{22}(\Theta)+C_1C_2F_{33}(\Theta) & C_2F_{34}(\Theta) \\ 0 & S_1F_{34}(\Theta) & -C_1F_{34}(\Theta) & F_{44}(\Theta) \end{bmatrix}, \tag{4.14}$$

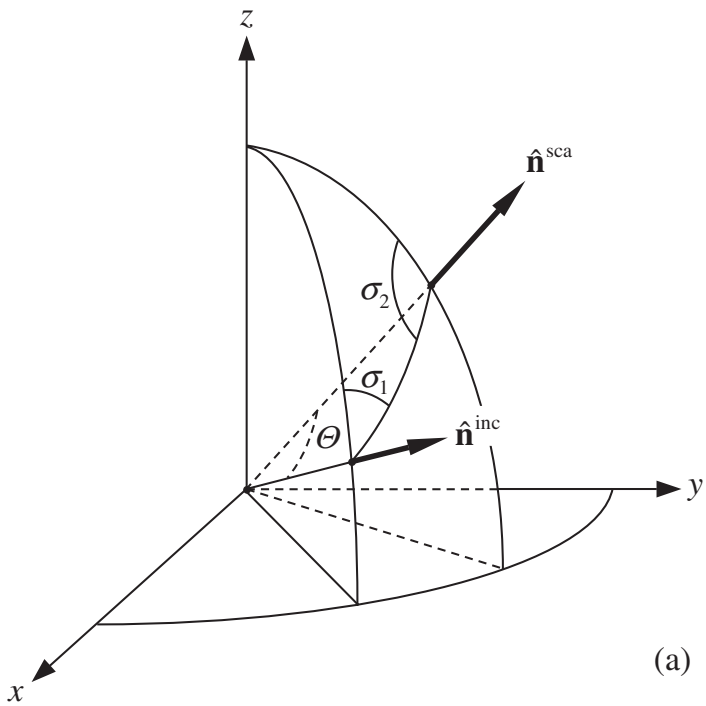

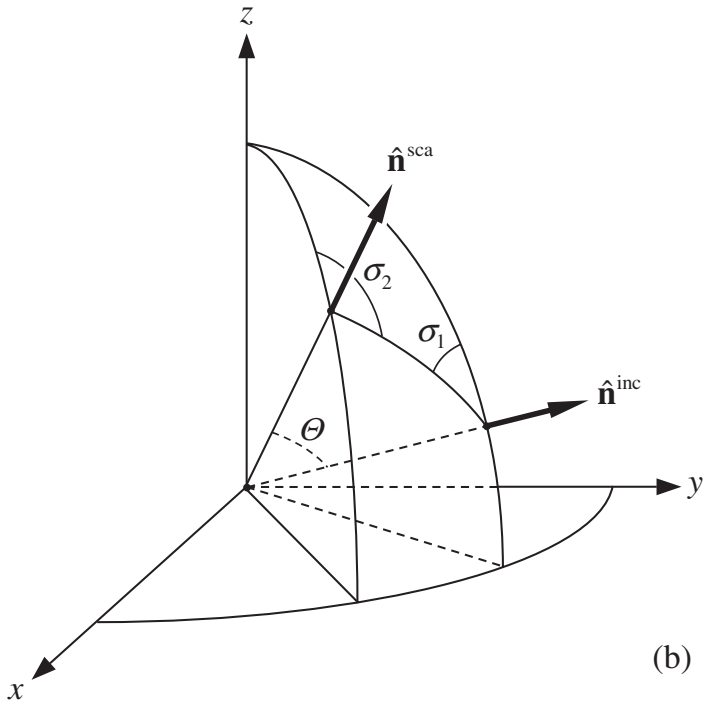

Figure 4.3. Illustration of the relationship between the phase and scattering matrices.

$$\mathbf{Z}(\vartheta^{\rm sca}, \varphi^{\rm inc}; \vartheta^{\rm inc}, \varphi^{\rm sca}) = \mathbf{L}(\sigma_2 - \pi)\mathbf{F}(\Theta)\mathbf{L}(\sigma_1)$$

$$= \begin{bmatrix} F_{11}(\Theta) & C_1F_{12}(\Theta) & -S_1F_{12}(\Theta) & 0 \\ C_2F_{12}(\Theta) & C_1C_2F_{22}(\Theta) - S_1S_2F_{33}(\Theta) & -S_1C_2F_{22}(\Theta) - C_1S_2F_{33}(\Theta) & -S_2F_{34}(\Theta) \\ S_2F_{12}(\Theta) & C_1S_2F_{22}(\Theta) + S_1C_2F_{33}(\Theta) & -S_1S_2F_{22}(\Theta) + C_1C_2F_{33}(\Theta) & C_2F_{34}(\Theta) \\ 0 & -S_1F_{34}(\Theta) & -C_1F_{34}(\Theta) & F_{44}(\Theta) \end{bmatrix}, \tag{4.15}$$

where

$$C_i = \cos 2\sigma_i, \quad S_i = \sin 2\sigma_i, \quad i = 1, 2, \tag{4.16}$$

and the rotation matrix $\mathbf{L}$ is defined by Eq. (1.97). (Recall that a rotation angle is positive if the rotation is performed in the clockwise direction when one is looking in the direction of propagation; see Section 1.5.) The scattering angle Θ and the angles σ_1 and σ_2 can be calculated from $\vartheta^{\rm sca}$, $\vartheta^{\rm inc}$, $\varphi^{\rm sca}$, and $\varphi^{\rm inc}$ using spherical trigonometry:

$$\cos\Theta = \cos\vartheta^{\rm sca}\cos\vartheta^{\rm inc} + \sin\vartheta^{\rm sca}\sin\vartheta^{\rm inc}\cos(\varphi^{\rm sca} - \varphi^{\rm inc}), \tag{4.17}$$

$$\cos\sigma_1 = \frac{\cos\vartheta^{\rm sca} - \cos\vartheta^{\rm inc}\cos\Theta}{\sin\vartheta^{\rm inc}\sin\Theta}, \tag{4.18}$$

$$\cos\sigma_2 = \frac{\cos\vartheta^{\rm inc} - \cos\vartheta^{\rm sca}\cos\Theta}{\sin\vartheta^{\rm sca}\sin\Theta}. \tag{4.19}$$

Equations (4.14)–(4.19) demonstrate the obvious fact that the phase matrix of a macroscopically isotropic and mirror-symmetric medium depends only on the difference between the azimuthal angles of the scattered and incident beams rather than on their specific values. Comparison of Eqs. (4.14) and (4.15) yields the symmetry relation (Hovenier 1969):

$$\mathbf{Z}(\vartheta^{\rm sca}, \varphi^{\rm inc}; \vartheta^{\rm inc}, \varphi^{\rm sca}) = \mathbf{\Delta}_{34}\mathbf{Z}(\vartheta^{\rm sca}, \varphi^{\rm sca}; \vartheta^{\rm inc}, \varphi^{\rm inc})\mathbf{\Delta}_{34}, \tag{4.20}$$

where

$$\mathbf{\Delta}_{34} = \mathbf{\Delta}_{34}^{\rm T} = \mathbf{\Delta}_{34}^{-1} = \begin{bmatrix} 1 & 0 & 0 & 0 \\ 0 & 1 & 0 & 0 \\ 0 & 0 & -1 & 0 \\ 0 & 0 & 0 & -1 \end{bmatrix}. \tag{4.21}$$

It is also easy to see from either Eq. (4.14) or Eq. (4.15) that (Hovenier 1969)

$$\mathbf{Z}(\pi - \vartheta^{\rm sca}, \varphi^{\rm sca}; \pi - \vartheta^{\rm inc}, \varphi^{\rm inc}) = \mathbf{\Delta}_{34}\mathbf{Z}(\vartheta^{\rm sca}, \varphi^{\rm sca}; \vartheta^{\rm inc}, \varphi^{\rm inc})\mathbf{\Delta}_{34}, \tag{4.22}$$

which is a manifestation of symmetry with respect to the *xy*-plane. Finally, we can verify that

$$\mathbf{Z}(\pi - \vartheta^{\rm inc}, \varphi^{\rm inc} + \pi; \pi - \vartheta^{\rm sca}, \varphi^{\rm sca} + \pi) = \mathbf{\Delta}_3[\mathbf{Z}(\vartheta^{\rm sca}, \varphi^{\rm sca}; \vartheta^{\rm inc}, \varphi^{\rm inc})]^{\rm T}\mathbf{\Delta}_3, \tag{4.23}$$

where the matrix $\mathbf{\Delta}_3$ is given by Eq. (2.125). Obviously, this is the reciprocity relation (2.124). Other symmetry relations can be derived by forming combinations of Eqs. (4.20), (4.22), and (4.23). For example, combining Eqs. (4.20) and (4.22) yields

$$\mathbf{Z}(\pi - \vartheta^{\text{sca}}, \varphi^{\text{inc}}; \pi - \vartheta^{\text{inc}}, \varphi^{\text{sca}}) = \mathbf{Z}(\vartheta^{\text{sca}}, \varphi^{\text{sca}}; \vartheta^{\text{inc}}, \varphi^{\text{inc}}). \tag{4.24}$$

Although Eq. (4.14) is valid only for $0 < \varphi^{\text{sca}} - \varphi^{\text{inc}} < \pi$, combining it with Eq. (4.20) yields the phase matrix for all possible incidence and scattering directions. The symmetry relations (4.22) and (4.23) further reduce the range of independent scattering geometries and can be very helpful in theoretical calculations or consistency checks on measurements.

4.4 Forward-scattering direction and extinction matrix

By virtue of spatial isotropy, the extinction matrix of a macroscopically isotropic and mirror-symmetric medium is independent of the direction of light propagation and orientation of the reference plane used to define the Stokes parameters. It also follows from Eqs. (2.142)–(2.145), (3.9), and (4.2a)–(4.2d) that $K_{13} = K_{14} = K_{23} = K_{24} = K_{31} = K_{32} = K_{41} = K_{42} = 0$. Furthermore, we are about to show that the remaining off-diagonal elements of the extinction matrix also vanish.

We will assume for simplicity that light is incident along the positive direction of the z-axis of the laboratory reference frame and will use the xz-plane with $x \geq 0$ as the meridional plane of the incident beam. We will also assume that the initial orientation of a particle is such that the particle reference frame coincides with the laboratory reference frame. The forward-scattering amplitude matrix of the particle in the initial orientation computed in the laboratory reference frame is thus equal to the forward-scattering amplitude matrix computed in the particle reference frame. We will denote the latter as $\mathbf{S}_P$. Let us now rotate the particle through an Euler angle α about the z-axis in the clockwise direction as viewed in the positive z-direction (Figs. 2.2 and 4.4) and denote the forward-scattering amplitude matrix of this rotated particle with respect to the laboratory reference frame as $\mathbf{S}_L^{\alpha}$. This matrix relates the column of the electric field vector components of the incident field to that of the field scattered in the exact forward direction:

$$\begin{bmatrix} E_{\vartheta L}^{\text{sca}} \\ E_{\varphi L}^{\text{sca}} \end{bmatrix} \propto \mathbf{S}_L^{\alpha} \begin{bmatrix} E_{\vartheta L}^{\text{inc}} \\ E_{\varphi L}^{\text{inc}} \end{bmatrix}, \tag{4.25}$$

where the subscript L indicates that all field components are computed in the laboratory reference frame. Figure 4.4 shows the directions of the respective unit $\hat{\boldsymbol{\vartheta}}$- and $\hat{\boldsymbol{\varphi}}$- vectors for the incident and the forward-scattered beams. Simple trigonometry allows us to express the column of the electric vector components in the particle reference frame in terms of that in the laboratory reference frame by means of a trivial

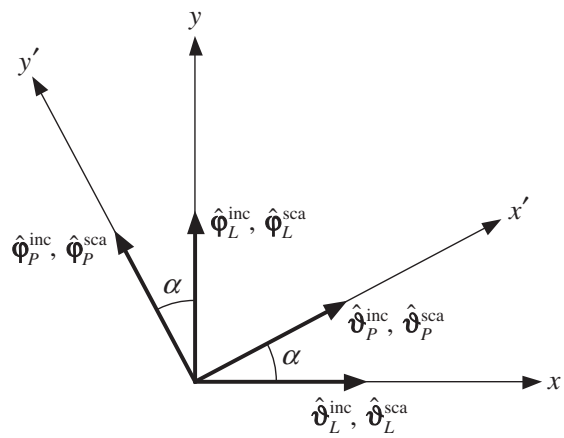

Figure 4.4. Rotation of the particle through an Euler angle α about the z-axis transforms the laboratory reference frame $L\{x, y, z\}$ into the particle reference frame $P\{x', y', z\}$. Since both the incident and the scattered beams propagate in the positive z-direction, their respective unit $\hat{\boldsymbol{\vartheta}}$- and $\hat{\boldsymbol{\varphi}}$- vectors are the same.

matrix multiplication (cf. Fig. 4.4):

$$\begin{bmatrix} E_{\vartheta P}^{\text{inc}} \\ E_{\varphi P}^{\text{inc}} \end{bmatrix} = \begin{bmatrix} C & S \\ -S & C \end{bmatrix} \begin{bmatrix} E_{\vartheta L}^{\text{inc}} \\ E_{\varphi L}^{\text{inc}} \end{bmatrix}, \tag{4.26}$$

where $C = \cos\alpha$ and $S = \sin\alpha$. Conversely,

$$\begin{bmatrix} E_{\vartheta L}^{\text{sca}} \\ E_{\varphi L}^{\text{sca}} \end{bmatrix} = \begin{bmatrix} C & -S \\ S & C \end{bmatrix} \begin{bmatrix} E_{\vartheta P}^{\text{sca}} \\ E_{\varphi P}^{\text{sca}} \end{bmatrix}. \tag{4.27}$$

Rewriting Eq. (4.25) in the particle reference frame,

$$\begin{bmatrix} E_{\vartheta P}^{\text{sca}} \\ E_{\varphi P}^{\text{sca}} \end{bmatrix} \propto \mathbf{S}_P \begin{bmatrix} E_{\vartheta P}^{\text{inc}} \\ E_{\varphi P}^{\text{inc}} \end{bmatrix}, \tag{4.28}$$

and using Eqs. (4.26) and (4.27), we finally derive

$$\begin{aligned} \mathbf{S}_L^{\alpha} &= \begin{bmatrix} C & -S \\ S & C \end{bmatrix} \mathbf{S}_P \begin{bmatrix} C & S \\ -S & C \end{bmatrix} \\ &= \begin{bmatrix} C^2 S_{11P} - SCS_{12P} - SCS_{21P} + S^2 S_{22P} & SCS_{11P} + C^2 S_{12P} - S^2 S_{21P} - SCS_{22P} \\ SCS_{11P} - S^2 S_{12P} + C^2 S_{21P} - SCS_{22P} & S^2 S_{11P} + SCS_{12P} + SCS_{21P} + C^2 S_{22P} \end{bmatrix}. \end{aligned} \tag{4.29}$$

For $\alpha = 0$ and $\alpha = \pi/2$,

$$\mathbf{S}_L^0 = \begin{bmatrix} S_{11P} & S_{12P} \\ S_{21P} & S_{22P} \end{bmatrix}, \tag{4.30}$$

$$\mathbf{S}_L^{\pi/2} = \begin{bmatrix} S_{22P} & -S_{21P} \\ -S_{12P} & S_{11P} \end{bmatrix}. \tag{4.31}$$

Because we are assuming random orientation of the particles in the small volume element, for each particle in the initial orientation, $\alpha = 0$, there is always a particle of the same type but in the orientation corresponding to $\alpha = \pi/2$. It, therefore, follows from Eqs. (2.141), (2.146), (3.9), (4.30), and (4.31) that $K_{12} = K_{21} = K_{34} = K_{43} = 0$. Finally, recalling Eq. (2.159), we conclude that the extinction matrix of a small volume element containing equal numbers of randomly oriented particles and their mirror-symmetric counterparts and/or randomly oriented particles having a plane of symmetry is diagonal:

$$\mathbf{K}(\hat{\mathbf{n}}) \equiv \mathbf{K} = C_{\text{ext}}\mathbf{\Delta} = N\langle C_{\text{ext}}\rangle\mathbf{\Delta}, \tag{4.32}$$

where

$$\mathbf{\Delta} = \begin{bmatrix} 1 & 0 & 0 & 0 \\ 0 & 1 & 0 & 0 \\ 0 & 0 & 1 & 0 \\ 0 & 0 & 0 & 1 \end{bmatrix}$$

is the 4×4 unit matrix, N is the number of particles in the volume element, and $\langle C_{\text{ext}}\rangle$ is the average extinction cross section per particle, which is now independent of the direction of propagation and polarization state of the incident light. This significant simplification is useful in many practical circumstances.

The scattering matrix also becomes simpler when $\Theta = 0$. From Eqs. (2.107), (2.110), (2.117), (2.120), (4.30), and (4.31), we find that $F_{12}(0) = F_{21}(0) = F_{34}(0) = F_{43}(0) = 0$. Equation (4.29) gives for $\alpha = \pi/4$:

$$\mathbf{S}_L^{\pi/4} = \frac{1}{2}\begin{bmatrix} S_{11P} - S_{12P} - S_{21P} + S_{22P} & S_{11P} + S_{12P} - S_{21P} - S_{22P} \\ S_{11P} - S_{12P} + S_{21P} - S_{22P} & S_{11P} + S_{12P} + S_{21P} + S_{22P} \end{bmatrix}. \tag{4.33}$$

Equations (2.111), (2.116), (4.30), and (4.33) and a considerable amount of algebra yield $F_{22}(0) = F_{33}(0)$. Thus, recalling Eq. (4.7), we find that the forward-scattering matrix for a macroscopically isotropic and mirror-symmetric medium is diagonal and has only three independent elements:

$$\mathbf{F}(0) = \begin{bmatrix} F_{11}(0) & 0 & 0 & 0 \\ 0 & F_{22}(0) & 0 & 0 \\ 0 & 0 & F_{22}(0) & 0 \\ 0 & 0 & 0 & F_{44}(0) \end{bmatrix} \tag{4.34}$$

(van de Hulst 1957).

Rotationally-symmetric particles are obviously mirror-symmetric with respect to the plane through the direction of propagation and the axis of symmetry. Choosing this plane as the $x'z'$-plane of the particle reference frame, we see from Eq. (4.2c) that $S_{12P} = S_{21P} = 0$. This simplifies the amplitude scattering matrices (4.30) and (4.33) and ultimately yields

$$F_{44}(0) = 2F_{22}(0) - F_{11}(0), \qquad 0 \le F_{22}(0) \le F_{11}(0) \tag{4.35}$$

(Mishchenko and Travis 1994c; Hovenier and Mackowski 1998).

4.5 Backward scattering

Equation (4.1) provides an unambiguous definition of the scattering matrix in terms of the phase matrix, except for the exact backscattering direction. Indeed, the backscattering direction for an incidence direction $(\vartheta^{\text{inc}}, \varphi^{\text{inc}})$ is given by $(\pi - \vartheta^{\text{inc}}, \varphi^{\text{inc}} + \pi)$. Therefore, the complete definition of the scattering matrix should be as follows:

$$\mathbf{F}(\vartheta^{\text{sca}}) = \begin{cases} \mathbf{Z}(\vartheta^{\text{sca}}, 0; 0, 0) & \text{for } \vartheta^{\text{sca}} \in [0, \pi), \\ \mathbf{Z}(\pi, \pi; 0, 0) & \text{for } \vartheta^{\text{sca}} = \pi, \end{cases}$$

which seems to be different from Eq. (4.1). It is easy to see, however, that $\mathbf{Z}(\pi, 0; 0, 0) = \mathbf{L}(\pi)\mathbf{Z}(\pi, \pi; 0, 0) \equiv \mathbf{Z}(\pi, \pi; 0, 0)$, cf. Eq. (1.97), which demonstrates the equivalence of the two definitions.

We are ready now to consider the case of scattering in the exact backward direction, using the complete definition of the scattering matrix and the backscattering theorem derived in Section 2.3. Let us assume that light is incident along the positive z-axis of the laboratory coordinate system and is scattered in the opposite direction; we use the xz-plane with $x \ge 0$ as the meridional plane of the incident beam. As in the previous section, we consider two particle orientations relative to the laboratory reference frame: (i) the initial orientation, when the particle reference frame coincides with the laboratory reference frame, and (ii) the orientation obtained by rotating the particle about the z-axis through a positive Euler angle α. Figure 4.5 shows the respective unit $\hat{\boldsymbol{\vartheta}}$- and $\hat{\boldsymbol{\varphi}}$- vectors for the incident and the backscattered beams. Denote the backscattering amplitude matrix in the particle reference frame as $\mathbf{S}_P$ and the backscattering amplitude matrix in the laboratory reference frame for the rotated particle as $\mathbf{S}_L^{\alpha}$. A derivation similar to that in the previous section gives

$$\begin{aligned} \mathbf{S}_L^{\alpha} &= \begin{bmatrix} C & S \\ -S & C \end{bmatrix} \mathbf{S}_P \begin{bmatrix} C & S \\ -S & C \end{bmatrix} \\ &= \begin{bmatrix} C^2 S_{11P} - SCS_{12P} + SCS_{21P} - S^2 S_{22P} & SCS_{11P} + C^2 S_{12P} + S^2 S_{21P} + SCS_{22P} \\ -SCS_{11P} + S^2 S_{12P} + C^2 S_{21P} - SCS_{22P} & -S^2 S_{11P} - SCS_{12P} + SCS_{21P} + C^2 S_{22P} \end{bmatrix}. \end{aligned} \tag{4.36}$$

This formula can be simplified, because the backscattering theorem (2.65) yields $S_{21P} = -S_{12P}$. Assuming that particles are randomly oriented and considering the cases $\alpha = 0$ and $\alpha = \pi/2$, we find that $F_{12}(\pi) = F_{21}(\pi) = F_{34}(\pi) = F_{43}(\pi) = 0$. Similarly, considering the cases $\alpha = 0$ and $\alpha = \pi/4$ yields $F_{33}(\pi) = -F_{22}(\pi)$. Finally, recalling Eqs. (2.131) and (4.7), we conclude that the backscattering matrix for

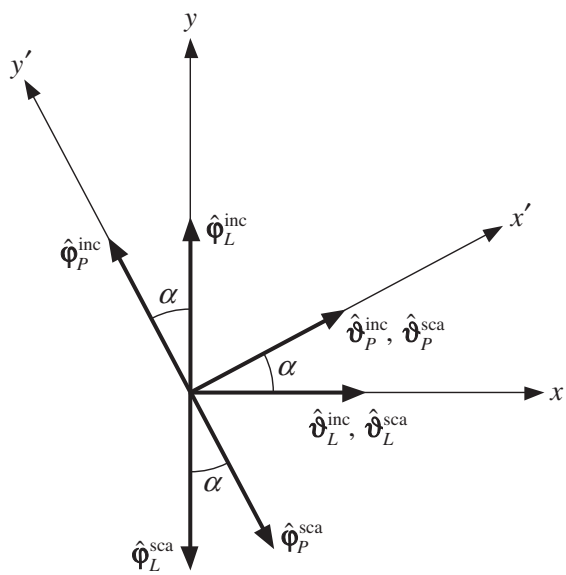

Figure 4.5. As in Fig. 4.4, but for the case of scattering in the exact backward direction.

a macroscopically isotropic and mirror-symmetric medium is diagonal and has only two independent elements:

$$\mathbf{F}(\pi) = \begin{bmatrix} F_{11}(\pi) & 0 & 0 & 0 \\ 0 & F_{22}(\pi) & 0 & 0 \\ 0 & 0 & -F_{22}(\pi) & 0 \\ 0 & 0 & 0 & F_{11}(\pi) - 2F_{22}(\pi) \end{bmatrix} \tag{4.37}$$

(Mishchenko and Hovenier 1995). According to Eq. (4.9) $F_{44} \leq F_{11}$, so we always have

$$F_{22}(\pi) \geq 0. \tag{4.38}$$

4.6 Scattering cross section, asymmetry parameter, and radiation pressure

Like all other macroscopic scattering characteristics, the average scattering cross section per particle for a macroscopically isotropic and mirror-symmetric medium is independent of the direction of illumination. Therefore, we will evaluate the integral on the right-hand side of Eq. (2.160) assuming that the incident light propagates along the positive z-axis of the laboratory reference frame and that the xz-plane with $x \geq 0$ is the meridional plane of the incident beam. Figure 4.6 shows that in order to compute the Stokes vector of the scattered beam with respect to its own meridional plane, we must rotate the reference frame of the incident beam by the angle φ, thereby modifying the Stokes vector of the incident light according to Eq. (1.97) with $\eta = \varphi$,

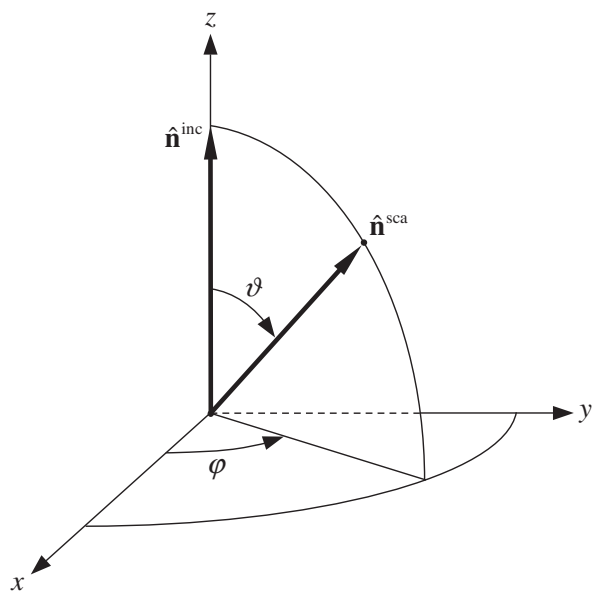

Figure 4.6. Illustration of the relationship between the phase and scattering matrices when the incident light propagates along the positive z-axis.

and then multiply the new Stokes vector of the incident light by the scattering matrix. Therefore, the average phase matrix per particle is simply

$$\langle \mathbf{Z}(\hat{\mathbf{n}}^{\text{sca}}, \hat{\mathbf{n}}^{\text{inc}})\rangle = \langle \mathbf{F}(\vartheta)\rangle \mathbf{L}(\varphi)$$
$$= \begin{bmatrix} \langle F_{11}(\vartheta)\rangle & \langle F_{12}(\vartheta)\rangle \cos 2\varphi & -\langle F_{12}(\vartheta)\rangle \sin 2\varphi & 0 \\ \langle F_{12}(\vartheta)\rangle & \langle F_{22}(\vartheta)\rangle \cos 2\varphi & -\langle F_{22}(\vartheta)\rangle \sin 2\varphi & 0 \\ 0 & \langle F_{33}(\vartheta)\rangle \sin 2\varphi & \langle F_{33}(\vartheta)\rangle \cos 2\varphi & \langle F_{34}(\vartheta)\rangle \\ 0 & -\langle F_{34}(\vartheta)\rangle \sin 2\varphi & -\langle F_{34}(\vartheta)\rangle \cos 2\varphi & \langle F_{44}(\vartheta)\rangle \end{bmatrix}. \tag{4.39}$$

Substituting this formula in Eq. (2.160), we find that the average scattering cross section per particle is independent of the polarization state of the incident light and is given by

$$\langle C_{\text{sca}}\rangle = 2\pi \int_0^{\pi} \mathrm{d}\vartheta \sin\vartheta \langle F_{11}(\vartheta)\rangle. \tag{4.40}$$

The ensemble-averaged asymmetry parameter must also be independent of $\hat{\mathbf{n}}^{\text{inc}}$, and Eqs. (2.166), (2.169), and (4.39) yield

$$\langle \cos\Theta\rangle = \frac{2\pi}{\langle C_{\text{sca}}\rangle} \int_0^{\pi} \mathrm{d}\vartheta \sin\vartheta \cos\vartheta \langle F_{11}(\vartheta)\rangle. \tag{4.41}$$

Obviously, $\langle \cos\Theta\rangle$ is polarization-independent. Equations (2.176), (4.39), and (4.41) show that the average radiation force per particle is now directed along $\hat{\mathbf{n}}^{\text{inc}}$:

$$\langle \mathbf{F} \rangle = \frac{1}{c} \hat{\mathbf{n}}^{\text{inc}} I^{\text{inc}} [\langle C_{\text{ext}} \rangle - \langle C_{\text{sca}} \rangle \langle \cos \Theta \rangle]$$
$$= \frac{1}{c} \hat{\mathbf{n}}^{\text{inc}} I^{\text{inc}} \langle C_{\text{pr}} \rangle, \tag{4.42}$$

where

$$\langle C_{\text{pr}} \rangle = \langle C_{\text{ext}} \rangle - \langle C_{\text{sca}} \rangle \langle \cos \Theta \rangle \tag{4.43}$$

is the polarization- and direction-independent average radiation-pressure cross section per particle. The average absorption cross section per particle,

$$\langle C_{\text{abs}} \rangle = \langle C_{\text{ext}} \rangle - \langle C_{\text{sca}} \rangle, \tag{4.44}$$

and the average single-scattering albedo,

$$\varpi = \frac{\langle C_{\text{sca}} \rangle}{\langle C_{\text{ext}} \rangle}, \tag{4.45}$$

are also independent of the direction and polarization of the incident beam. The same, of course, is true of the extinction, scattering, absorption, and radiation pressure efficiency factors, defined as

$$Q_{\text{ext}} = \frac{\langle C_{\text{ext}} \rangle}{\langle G \rangle}, \quad Q_{\text{sca}} = \frac{\langle C_{\text{sca}} \rangle}{\langle G \rangle}, \quad Q_{\text{abs}} = \frac{\langle C_{\text{abs}} \rangle}{\langle G \rangle}, \quad Q_{\text{pr}} = \frac{\langle C_{\text{pr}} \rangle}{\langle G \rangle}, \tag{4.46}$$

respectively, where $\langle G \rangle$ is the average projection area per particle.

4.7 Thermal emission

Because the ensemble-averaged emission vector for a macroscopically isotropic and mirror-symmetric medium must be independent of the emission direction, we will calculate the integral on the right-hand side of Eq. (2.186) for light emitted in the positive direction of the z-axis and will use the meridional plane $\varphi = 0$ as the reference plane for defining the emission Stokes vector. It is then obvious from Fig. 4.7 that the corresponding average phase matrix per particle can be calculated as

$$\langle \mathbf{Z}(\hat{\mathbf{n}}, \hat{\mathbf{n}}') \rangle = \mathbf{L}(-\varphi') \langle \mathbf{F}(\vartheta') \rangle$$
$$= \begin{bmatrix} \langle F_{11}(\vartheta') \rangle & \langle F_{12}(\vartheta') \rangle & 0 & 0 \\ \langle F_{12}(\vartheta') \rangle \cos 2\varphi' & \langle F_{22}(\vartheta') \rangle \cos 2\varphi' & \langle F_{33}(\vartheta') \rangle \sin 2\varphi' & \langle F_{34}(\vartheta') \rangle \sin 2\varphi' \\ -\langle F_{12}(\vartheta') \rangle \sin 2\varphi' & -\langle F_{22}(\vartheta') \rangle \sin 2\varphi' & \langle F_{33}(\vartheta') \rangle \cos 2\varphi' & \langle F_{34}(\vartheta') \rangle \cos 2\varphi' \\ 0 & 0 & -\langle F_{34}(\vartheta') \rangle & \langle F_{44}(\vartheta') \rangle \end{bmatrix}. \tag{4.47}$$

Inserting this formula and Eqs. (4.32) and (4.40) in Eq. (2.186) yields

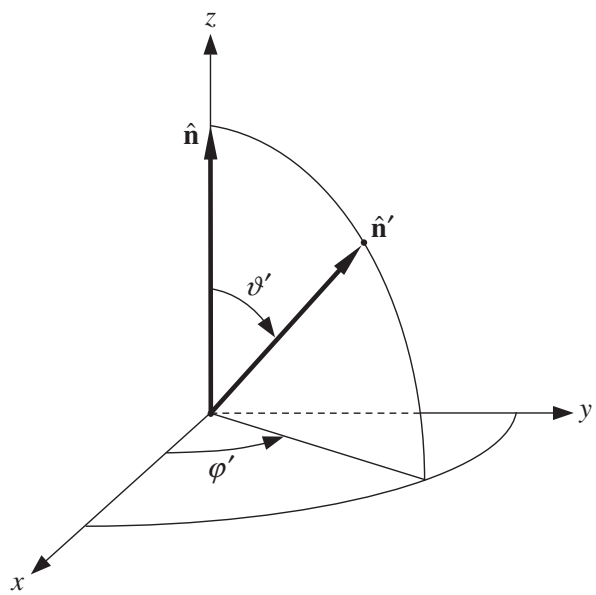

Figure 4.7. Illustration of the relationship between the phase and scattering matrices when the scattered light propagates along the positive z-axis.

$$\langle \mathbf{K}_{\mathrm{e}}(\hat{\mathbf{n}}, T, \omega)\rangle \equiv \langle \mathbf{K}_{\mathrm{e}}(T, \omega)\rangle = \langle C_{\mathrm{abs}}\rangle \mathbf{I}_{\mathrm{b}}(T, \omega), \tag{4.48}$$

where $\langle C_{\mathrm{abs}}\rangle$ may depend on frequency and $\mathbf{I}_{\mathrm{b}}(T, \omega)$ is the blackbody Stokes vector defined by Eq. (2.184). Thus, the radiation emitted by a small volume element comprising equal numbers of randomly oriented particles and their mirror-symmetric counterparts and/or randomly oriented particles having a plane of symmetry is not only isotropic but also unpolarized. The first (and the only non-zero) element of the average emission vector per particle is simply equal to the product of the average absorption cross section and the Planck function. Substituting Eq. (4.48) in Eq. (2.187), we see that the emission component of the average radiation force exerted on particles forming a macroscopically isotropic and mirror-symmetric medium is identically equal to zero:

$$\langle \mathbf{F}_{\mathrm{e}}(T)\rangle \equiv 0.$$

4.8 Spherically symmetric particles

The structure of the scattering matrix simplifies further for spherically symmetric particles, that is, for homogeneous or radially inhomogeneous spherical bodies composed of optically isotropic materials. The refractive index inside such particles is a function of only the distance from the particle center. Irrespective of their "orientation" relative to the laboratory reference frame, spherically symmetric particles are obviously mirror-symmetric with respect to the xz-plane. Directing the incident light

along the positive z-axis, restricting the scattering direction to the xz-plane with $x \geq 0$, and using this plane for reference, we find from Eqs. (4.2a) and (4.2c) that the amplitude scattering matrix is always diagonal ($S_{12} = S_{21} = 0$). Therefore, Eqs. (2.106), (2.111), (2.116), (2.121), and (4.7) yield

$$\mathbf{F}(\Theta) = \begin{bmatrix} F_{11}(\Theta) & F_{12}(\Theta) & 0 & 0 \\ F_{12}(\Theta) & F_{11}(\Theta) & 0 & 0 \\ 0 & 0 & F_{33}(\Theta) & F_{34}(\Theta) \\ 0 & 0 & -F_{34}(\Theta) & F_{33}(\Theta) \end{bmatrix}. \tag{4.49}$$

A scattering matrix of this type appears in the standard Lorenz–Mie theory of light scattering by homogeneous isotropic spheres; therefore, the above matrix will be referred to as the Lorenz–Mie scattering matrix. The results of the previous sections on forward and backward scattering imply that

$$F_{33}(0) = F_{11}(0) \quad \text{and} \quad F_{33}(\pi) = -F_{11}(\pi). \tag{4.50}$$

4.9 Effects of nonsphericity and orientation

The previous discussion of symmetries enables us to summarize the most fundamental effects of particle nonsphericity and orientation on single-scattering patterns. If particles are not spherically symmetric and do not form a macroscopically isotropic and mirror-symmetric medium, then, in general,

- the 4×4 extinction matrix does not degenerate to a direction- and polarization-independent scalar extinction cross section;
- the extinction, scattering, absorption, and radiation-pressure cross sections, the single-scattering albedo, and the asymmetry parameter depend on the direction and polarization state of the incident beam;
- all four elements of the emission vector are non-zero and orientation dependent;
- the direction of the radiation force does not coincide with the direction of incidence, and the emission component of the radiation force is non-zero;
- the scattering matrix $\mathbf{F}$ does not have the simple block-diagonal structure of Eq. (4.7): all 16 elements of the scattering matrix can be non-zero and depend on the incidence direction and the orientation of the scattering plane rather than only on the scattering angle;
- the phase matrix depends on the specific values of the azimuthal angles of the incidence and scattering directions rather than on their difference, it cannot be represented in the form of Eqs. (4.14) and (4.15), and it does not obey the symmetry relations (4.20) and (4.22).

Any of these effects can directly indicate the presence of oriented particles lacking spherical symmetry. For example, measurements of interstellar polarization are used in

astrophysics to detect preferentially oriented dust grains causing different values of extinction for different polarization components of the transmitted starlight (Martin 1978). Similarly, the depolarization of radiowave signals propagating through the Earth's atmosphere may indicate the presence of partially aligned nonspherical hydrometeors (Oguchi 1983).

If nonspherical particles are randomly oriented and form a macroscopically isotropic and mirror-symmetric scattering medium, then

- the extinction matrix reduces to the scalar extinction cross section, Eq. (4.32);
- all optical cross sections, the single-scattering albedo, and the asymmetry parameter become orientation and polarization independent;
- the emitted radiation becomes isotropic and unpolarized;
- the radiation force is directed along the incident beam, and the emission component of the radiation force vanishes;
- the phase matrix depends only on the difference between the azimuthal angles of the incidence and scattering directions rather than on their specific values, has the structure specified by Eqs. (4.14) and (4.15), and obeys the symmetry relations (4.20) and (4.22);
- the scattering matrix becomes block-diagonal (Eq. (4.7)), depends only on the scattering angle, and possesses almost the same structure as the Lorenz–Mie scattering matrix (4.49).

However, the remaining key point is that the Lorenz–Mie identities $F_{22}(\Theta) \equiv F_{11}(\Theta)$ and $F_{44}(\Theta) \equiv F_{33}(\Theta)$ do not hold, in general, for nonspherical particles. This difference makes measurements of the linear backscattering depolarization ratio $\delta_{\rm L} = [F_{11}(\pi) - F_{22}(\pi)]/[F_{11}(\pi) + F_{22}(\pi)]$ and the closely related circular backscattering depolarization ratio $\delta_{\rm C}$ the most reliable indicators of particle nonsphericity (Sections 10.2 and 10.11). Besides this qualitative distinction, which unequivocally distinguishes randomly oriented nonspherical particles from spheres, there can be significant quantitative differences in specific scattering patterns. They will be discussed in detail in the following chapters.

4.10 Normalized scattering and phase matrices

It is convenient and customary in many types of applications to use the so-called normalized scattering matrix

$$\widetilde{\mathbf{F}}(\Theta) = \frac{4\pi}{C_{\rm sca}}\mathbf{F}(\Theta) = \frac{4\pi}{\langle C_{\rm sca}\rangle}\langle \mathbf{F}(\Theta)\rangle = \begin{bmatrix} a_1(\Theta) & b_1(\Theta) & 0 & 0 \\ b_1(\Theta) & a_2(\Theta) & 0 & 0 \\ 0 & 0 & a_3(\Theta) & b_2(\Theta) \\ 0 & 0 & -b_2(\Theta) & a_4(\Theta) \end{bmatrix}, \tag{4.51}$$

the elements of which are dimensionless. Similarly, the normalized phase matrix can

be defined as

$$\widetilde{\mathbf{Z}}(\vartheta^{\rm sca}, \varphi^{\rm sca}; \vartheta^{\rm inc}, \varphi^{\rm inc}) = \frac{4\pi}{C_{\rm sca}} \mathbf{Z}(\vartheta^{\rm sca}, \varphi^{\rm sca}; \vartheta^{\rm inc}, \varphi^{\rm inc})$$
$$= \frac{4\pi}{\langle C_{\rm sca} \rangle} \langle \mathbf{Z}(\vartheta^{\rm sca}, \varphi^{\rm sca}; \vartheta^{\rm inc}, \varphi^{\rm inc}) \rangle. \tag{4.52}$$

The (1,1) element of the normalized scattering matrix, $a_1(\Theta)$, is traditionally called the phase function and, as follows from Eqs. (4.40) and (4.51), satisfies the normalization condition:

$$\frac{1}{2} \int_0^{\pi} \mathrm{d}\Theta \sin\Theta \, a_1(\Theta) = 1. \tag{4.53}$$

Remember that we have already used the term "phase function" to name the quantity p defined by Eq. (2.167). It can be easily seen from Eqs. (2.166), (2.167), (4.1), and (4.51) that the differential scattering cross section $\mathrm{d}C_{\rm sca}/\mathrm{d}\Omega$ reduces to $\langle F_{11} \rangle$, and so p reduces to a_1, when unpolarized incident light propagates along the positive z-axis and is scattered in the xz-plane with $x \geq 0$. Equations (4.41) and (4.51) yield

$$\langle \cos\Theta \rangle = \frac{1}{2} \int_0^{\pi} \mathrm{d}\Theta \sin\Theta \, a_1(\Theta) \cos\Theta. \tag{4.54}$$

The normalized scattering matrix possesses many properties of the regular scattering matrix, e.g.,

$$a_1 \geq 0, \tag{4.55}$$

$$|a_i| \leq a_1, \quad i = 2, 3, 4, \qquad |b_i| \leq a_1, \quad i = 1, 2, \tag{4.56}$$

$$(a_3 + a_4)^2 + 4b_2^2 \leq (a_1 + a_2)^2 - 4b_1^2, \tag{4.57}$$

$$|a_3 - a_4| \leq a_1 - a_2, \tag{4.58}$$

$$|a_2 - b_1| \leq a_1 - b_1, \tag{4.59}$$

$$|a_2 + b_1| \leq a_1 + b_1, \tag{4.60}$$

$$\widetilde{\mathbf{F}}(0) = \begin{bmatrix} a_1(0) & 0 & 0 & 0 \\ 0 & a_2(0) & 0 & 0 \\ 0 & 0 & a_2(0) & 0 \\ 0 & 0 & 0 & a_4(0) \end{bmatrix}, \tag{4.61}$$

$$\widetilde{\mathbf{F}}(\pi) = \begin{bmatrix} a_1(\pi) & 0 & 0 & 0 \\ 0 & a_2(\pi) & 0 & 0 \\ 0 & 0 & -a_2(\pi) & 0 \\ 0 & 0 & 0 & a_4(\pi) \end{bmatrix}, \tag{4.62}$$

$$a_4(\pi) = a_1(\pi) - 2a_2(\pi), \qquad a_2(\pi) \geq 0. \tag{4.63}$$

Also,

$$a_4(0) = 2a_2(0) - a_1(0), \qquad 0 \le a_2(0) \le a_1(0) \tag{4.64}$$

for rotationally symmetric particles and

$$\widetilde{\mathbf{F}}(\Theta) = \begin{bmatrix} a_1(\Theta) & b_1(\Theta) & 0 & 0 \\ b_1(\Theta) & a_1(\Theta) & 0 & 0 \\ 0 & 0 & a_3(\Theta) & b_2(\Theta) \\ 0 & 0 & -b_2(\Theta) & a_3(\Theta) \end{bmatrix}, \tag{4.65}$$

$$a_3(0) = a_1(0), \qquad a_3(\pi) = -a_1(\pi) \tag{4.66}$$

for spherically symmetric particles. Similarly, for $0 < \varphi^{\text{sca}} - \varphi^{\text{inc}} < \pi$ the normalized phase matrix is given by

$$\widetilde{\mathbf{Z}}(\vartheta^{\text{sca}}, \varphi^{\text{sca}}; \vartheta^{\text{inc}}, \varphi^{\text{inc}})$$

$$= \begin{bmatrix} a_1(\Theta) & C_1 b_1(\Theta) & S_1 b_1(\Theta) & 0 \\ C_2 b_1(\Theta) & C_1 C_2 a_2(\Theta) - S_1 S_2 a_3(\Theta) & S_1 C_2 a_2(\Theta) + C_1 S_2 a_3(\Theta) & S_2 b_2(\Theta) \\ -S_2 b_1(\Theta) & -C_1 S_2 a_2(\Theta) - S_1 C_2 a_3(\Theta) & -S_1 S_2 a_2(\Theta) + C_1 C_2 a_3(\Theta) & C_2 b_2(\Theta) \\ 0 & S_1 b_2(\Theta) & -C_1 b_2(\Theta) & a_4(\Theta) \end{bmatrix} \tag{4.67}$$

(cf. Eq. (4.14)) and has the same symmetry properties as the regular phase matrix:

$$\widetilde{\mathbf{Z}}(\vartheta^{\text{sca}}, \varphi^{\text{inc}}; \vartheta^{\text{inc}}, \varphi^{\text{sca}}) = \mathbf{\Delta}_{34} \widetilde{\mathbf{Z}}(\vartheta^{\text{sca}}, \varphi^{\text{sca}}; \vartheta^{\text{inc}}, \varphi^{\text{inc}}) \mathbf{\Delta}_{34}, \tag{4.68}$$

$$\widetilde{\mathbf{Z}}(\pi - \vartheta^{\text{sca}}, \varphi^{\text{sca}}; \pi - \vartheta^{\text{inc}}, \varphi^{\text{inc}}) = \mathbf{\Delta}_{34} \widetilde{\mathbf{Z}}(\vartheta^{\text{sca}}, \varphi^{\text{sca}}; \vartheta^{\text{inc}}, \varphi^{\text{inc}}) \mathbf{\Delta}_{34}, \tag{4.69}$$

$$\widetilde{\mathbf{Z}}(\pi - \vartheta^{\text{inc}}, \varphi^{\text{inc}} + \pi; \pi - \vartheta^{\text{sca}}, \varphi^{\text{sca}} + \pi) = \mathbf{\Delta}_3 [\widetilde{\mathbf{Z}}(\vartheta^{\text{sca}}, \varphi^{\text{sca}}; \vartheta^{\text{inc}}, \varphi^{\text{inc}})]^{\text{T}} \mathbf{\Delta}_3. \tag{4.70}$$

An important difference between the regular and normalized matrices is that the latter do not possess the property of additivity. Consider, for example, a small volume element containing N_1 particles of type 1 and N_2 particles of type 2. The total phase and scattering matrices of the volume element are obtained by adding the phase and scattering matrices of all particles,

$$\mathbf{Z} = N_1 \langle \mathbf{Z}_1 \rangle + N_2 \langle \mathbf{Z}_2 \rangle, \tag{4.71}$$

$$\mathbf{F} = N_1 \langle \mathbf{F}_1 \rangle + N_2 \langle \mathbf{F}_2 \rangle, \tag{4.72}$$

whereas the respective normalized matrices are given by more complicated relations,

$$\widetilde{\mathbf{Z}} = \frac{N_1 \langle C_{\text{sca}1} \rangle \widetilde{\mathbf{Z}}_1 + N_2 \langle C_{\text{sca}2} \rangle \widetilde{\mathbf{Z}}_2}{N_1 \langle C_{\text{sca}1} \rangle + N_2 \langle C_{\text{sca}2} \rangle}, \tag{4.73}$$

$$\widetilde{\mathbf{F}} = \frac{N_1 \langle C_{\text{sca}1} \rangle \widetilde{\mathbf{F}}_1 + N_2 \langle C_{\text{sca}2} \rangle \widetilde{\mathbf{F}}_2}{N_1 \langle C_{\text{sca}1} \rangle + N_2 \langle C_{\text{sca}2} \rangle} \tag{4.74}$$

(see Eqs. (4.51) and (4.52)).

4.11 Expansion in generalized spherical functions

A traditional way of specifying the elements of the normalized scattering matrix is to tabulate their numerical values at a representative grid of scattering angles (Deirmendjian 1969). However, a more mathematically appealing and efficient way is to expand the scattering matrix elements in so-called generalized spherical functions $P_{mn}^s(\cos\Theta)$ or, equivalently, in Wigner functions $d_{mn}^s(\Theta) = \mathrm{i}^{n-m} P_{mn}^s(\cos\Theta)$ (Siewert 1981; de Haan *et al.* 1987):

$$a_1(\Theta) = \sum_{s=0}^{s_{\max}} \alpha_1^s P_{00}^s(\cos\Theta) = \sum_{s=0}^{s_{\max}} \alpha_1^s d_{00}^s(\Theta), \tag{4.75}$$

$$a_2(\Theta) + a_3(\Theta) = \sum_{s=2}^{s_{\max}} (\alpha_2^s + \alpha_3^s) P_{22}^s(\cos\Theta) = \sum_{s=2}^{s_{\max}} (\alpha_2^s + \alpha_3^s) d_{22}^s(\Theta), \tag{4.76}$$

$$a_2(\Theta) - a_3(\Theta) = \sum_{s=2}^{s_{\max}} (\alpha_2^s - \alpha_3^s) P_{2,-2}^s(\cos\Theta) = \sum_{s=2}^{s_{\max}} (\alpha_2^s - \alpha_3^s) d_{2,-2}^s(\Theta), \tag{4.77}$$

$$a_4(\Theta) = \sum_{s=0}^{s_{\max}} \alpha_4^s P_{00}^s(\cos\Theta) = \sum_{s=0}^{s_{\max}} \alpha_4^s d_{00}^s(\Theta), \tag{4.78}$$

$$b_1(\Theta) = \sum_{s=2}^{s_{\max}} \beta_1^s P_{02}^s(\cos\Theta) = -\sum_{s=2}^{s_{\max}} \beta_1^s d_{02}^s(\Theta), \tag{4.79}$$

$$b_2(\Theta) = \sum_{s=2}^{s_{\max}} \beta_2^s P_{02}^s(\cos\Theta) = -\sum_{s=2}^{s_{\max}} \beta_2^s d_{02}^s(\Theta). \tag{4.80}$$

The number of non-zero terms in the expansions (4.75)–(4.80) is in principle infinite. In practice, however, the expansions are truncated at $s = s_{\max}$, $s_{\max}$ being chosen such that the corresponding finite sums differ from the respective scattering matrix elements on the entire interval $\Theta \in [0, \pi]$ of scattering angles within the desired numerical accuracy.

The properties of the generalized spherical functions and the Wigner *d*-functions are summarized in Appendix B. For given *m* and *n*, either type of function with $s \geq \max(|m|, |n|)$, when multiplied by $\sqrt{s + \frac{1}{2}}$, forms a complete orthonormal set of functions of $\cos\Theta \in [-1, +1]$ (see Eqs. (B.17) and (B.33)). Therefore, using the orthogonality relation (B.17), we obtain from Eqs. (4.75)–(4.80)

$$\alpha_1^s = (s + \tfrac{1}{2}) \int_0^\pi \mathrm{d}\Theta \sin\Theta \, a_1(\Theta) \, d_{00}^s(\Theta), \tag{4.81}$$

$$\alpha_2^s + \alpha_3^s = (s+\tfrac{1}{2}) \int_0^\pi \mathrm{d}\Theta \sin\Theta \, [a_2(\Theta) + a_3(\Theta)] \, d_{22}^s(\Theta), \tag{4.82}$$

$$\alpha_2^s - \alpha_3^s = (s+\tfrac{1}{2}) \int_0^\pi \mathrm{d}\Theta \sin\Theta \, [a_2(\Theta) - a_3(\Theta)] \, d_{2,-2}^s(\Theta), \tag{4.83}$$

$$\alpha_4^s = (s+\tfrac{1}{2}) \int_0^\pi \mathrm{d}\Theta \sin\Theta \, a_4(\Theta) \, d_{00}^s(\Theta), \tag{4.84}$$

$$\beta_1^s = -(s+\tfrac{1}{2}) \int_0^\pi \mathrm{d}\Theta \sin\Theta \, b_1(\Theta) \, d_{02}^s(\Theta), \tag{4.85}$$

$$\beta_2^s = -(s+\tfrac{1}{2}) \int_0^\pi \mathrm{d}\Theta \sin\Theta \, b_2(\Theta) \, d_{02}^s(\Theta) \tag{4.86}$$

(cf. Eq. (B.21)). These formulas suggest a simple, albeit not always the most elegant and efficient, way to compute the expansion coefficients by evaluating the integrals numerically using a suitable quadrature formula (de Rooij and van der Stap 1984). Of course, this procedure assumes the knowledge of the scattering matrix elements at the quadrature division points. The expansions (4.75)–(4.80) converge (in the sense of Eqs. (B.34)–(B.37) or Eqs. (B.18)–(B.21)) to the respective elements of the normalized scattering matrix if these elements are square integrable on the interval $\Theta \in [0, \pi]$. In view of the general inequality (4.56), it is sufficient to require that the phase function $a_1(\Theta)$ be square integrable to ensure such convergence.

Because the Wigner *d*-functions possess well-known and convenient mathematical properties and can be efficiently computed by using a simple and numerically stable recurrence relation, expansions (4.75)–(4.80) offer several practical advantages. First, we note that according to Eqs. (B.6)–(B.7),

$$d_{2,-2}^s(0) = d_{02}^s(0) = 0 \tag{4.87}$$

and

$$d_{22}^s(\pi) = d_{02}^s(\pi) = 0. \tag{4.88}$$

Therefore, Eqs. (4.76), (4.77), (4.79), and (4.80) reproduce identically the specific structure of the normalized scattering matrix for the exact forward and backward directions, Eqs. (4.61) and (4.62) (cf. Domke 1974). Second, when the expansion coefficients appearing in these expansions are known, then the elements of the normalized scattering matrix can be calculated easily for practically any number of scattering angles and with a minimal expenditure of computer time. Thus, instead of tabulating the elements of the scattering matrix for a large number of scattering angles (cf. Deirmendjian 1969) and resorting to interpolation in order to find the scattering matrix at intermediate points, one can provide a complete and accurate specification of the scattering matrix by tabulating a limited (and usually small) number of numerically significant expansion coefficients. This also explains why the expansion coefficients are especially convenient

in ensemble averaging: instead of computing ensemble-averaged scattering matrix elements, one can average a (much) smaller number of expansion coefficients.

An additional advantage of expanding the scattering matrix elements in generalized spherical functions is that the latter obey an addition theorem and thereby provide an elegant analytical way of calculating the coefficients in a Fourier decomposition of the normalized phase matrix (Kuščer and Ribarič 1959; Domke 1974; de Haan *et al.* 1987). This Fourier decomposition is then used to handle the azimuthal dependence of the solution of the vector radiative transfer equation efficiently. Another important advantage offered by expansions (4.75)–(4.80) is that the expansion coefficients for certain types of nonspherical particle can be calculated analytically without computing the scattering matrix itself (Section 5.5).

The expansion coefficients obey the general inequalities

$$|\alpha_j^s| \le 2s+1, \quad j=1,2,3,4, \tag{4.89}$$

$$|\beta_j^s| < (2s+1)\big/\sqrt{2}, \quad j=1,2. \tag{4.90}$$

These and other useful inequalities were derived by van der Mee and Hovenier (1990). Since, for each s, $d_{00}^s(\Theta)$ is a Legendre polynomial $P_s(\cos\Theta)$, Eq. (4.75) is also the well-known expansion of the phase function in Legendre polynomials (Chandrasekhar 1960; Sobolev 1975; van de Hulst 1980). Equation (B.12) gives $d_{00}^0(\Theta) \equiv 1$. Therefore, Eq. (4.81) and the normalization condition (4.53) yield the identity

$$\alpha_1^0 \equiv 1. \tag{4.91}$$

Similarly, the average asymmetry parameter, Eq. (4.54), can be expressed as

$$\langle \cos\Theta \rangle = \frac{\alpha_1^1}{3}. \tag{4.92}$$

4.12 Circular-polarization representation

Equations (4.75)–(4.80) become more compact and their origin becomes more transparent if one uses the circular-polarization representation of the Stokes vector (Kuščer and Ribarič 1959; Domke 1974; Hovenier and van der Mee 1983). We begin by defining the circular components of a transverse electromagnetic wave as

$$\begin{bmatrix} E_+ \\ E_- \end{bmatrix} = \mathbf{q} \begin{bmatrix} E_\vartheta \\ E_\varphi \end{bmatrix}, \tag{4.93}$$

where

$$\mathbf{q} = \frac{1}{\sqrt{2}} \begin{bmatrix} 1 & \mathrm{i} \\ 1 & -\mathrm{i} \end{bmatrix}. \tag{4.94}$$

Using Eqs. (2.30) and (4.94), we find that the corresponding circular-polarization amplitude scattering matrix $\mathbf{C}$ is expressed in terms of the regular amplitude scattering matrix as

$$\begin{aligned}\mathbf{C} &= \begin{bmatrix} C_{++} & C_{+-} \\ C_{-+} & C_{--} \end{bmatrix} \\ &= \mathbf{q}\mathbf{S}\mathbf{q}^{-1} \\ &= \frac{1}{2}\begin{bmatrix} S_{11} - \mathrm{i}S_{12} + \mathrm{i}S_{21} + S_{22} & S_{11} + \mathrm{i}S_{12} + \mathrm{i}S_{21} - S_{22} \\ S_{11} - \mathrm{i}S_{12} - \mathrm{i}S_{21} - S_{22} & S_{11} + \mathrm{i}S_{12} - \mathrm{i}S_{21} + S_{22} \end{bmatrix},\end{aligned} \tag{4.95}$$

where the arguments $(\hat{\mathbf{n}}^{\mathrm{sca}}, \hat{\mathbf{n}}^{\mathrm{inc}})$ are omitted for brevity and

$$\mathbf{q}^{-1} = \frac{1}{\sqrt{2}}\begin{bmatrix} 1 & 1 \\ -\mathrm{i} & \mathrm{i} \end{bmatrix}.$$

The usefulness of the circular electric vector components becomes clear from the simple formulas

$$I_2 = E_- E_+^*, \tag{4.96a}$$

$$I_0 = E_+ E_+^*, \tag{4.96b}$$

$$I_{-0} = E_- E_-^*, \tag{4.96c}$$

$$I_{-2} = E_+ E_-^*, \tag{4.96d}$$

which follow, after some algebra, from

$$\begin{bmatrix} E_\vartheta \\ E_\varphi \end{bmatrix} = \mathbf{q}^{-1}\begin{bmatrix} E_+ \\ E_- \end{bmatrix}$$

and Eqs. (1.54) and (1.60). It is easy to verify using the first equality of Eq. (4.95) and Eqs. (4.96) that the circular-polarization phase matrix is given by

$$\mathbf{Z}^{\mathrm{CP}} = \left\| Z_{pq}^{\mathrm{CP}} \right\| = \begin{bmatrix} C_{--}C_{++}^* & C_{-+}C_{++}^* & C_{--}C_{+-}^* & C_{-+}C_{+-}^* \\ C_{+-}C_{++}^* & C_{++}C_{++}^* & C_{+-}C_{+-}^* & C_{++}C_{+-}^* \\ C_{--}C_{-+}^* & C_{-+}C_{-+}^* & C_{--}C_{--}^* & C_{-+}C_{--}^* \\ C_{+-}C_{-+}^* & C_{++}C_{-+}^* & C_{+-}C_{--}^* & C_{++}C_{--}^* \end{bmatrix},$$

$$p, q = 2, 0, -0, -2. \tag{4.97}$$

Alternatively, it can be found from Eq. (2.123).

Consider now scattering by a macroscopically isotropic and mirror-symmetric medium. The normalized scattering and phase matrices in the circular-polarization representation are defined by analogy with the matrices $\widetilde{\mathbf{F}}$ and $\widetilde{\mathbf{Z}}$:

$$\widetilde{\mathbf{F}}^{\mathrm{CP}}(\Theta) = \frac{4\pi}{\langle C_{\mathrm{sca}} \rangle}\langle \mathbf{Z}^{\mathrm{CP}}(\vartheta^{\mathrm{sca}} = \Theta, \varphi^{\mathrm{sca}} = 0; \vartheta^{\mathrm{inc}} = 0, \varphi^{\mathrm{inc}} = 0)\rangle, \tag{4.98}$$

$$\widetilde{\mathbf{Z}}^{\mathrm{CP}}(\vartheta^{\mathrm{sca}}, \varphi^{\mathrm{sca}}; \vartheta^{\mathrm{inc}}, \varphi^{\mathrm{inc}}) = \frac{4\pi}{\langle C_{\mathrm{sca}} \rangle} \langle \mathbf{Z}^{\mathrm{CP}}(\vartheta^{\mathrm{sca}}, \varphi^{\mathrm{sca}}; \vartheta^{\mathrm{inc}}, \varphi^{\mathrm{inc}}) \rangle, \tag{4.99}$$

where $\langle \mathbf{Z}^{\mathrm{CP}}(\vartheta^{\mathrm{sca}}, \varphi^{\mathrm{sca}}; \vartheta^{\mathrm{inc}}, \varphi^{\mathrm{inc}}) \rangle$ is the average circular-polarization phase matrix per particle. From Eqs. (2.123), (4.51), (1.62), and (1.66) we have

$$\widetilde{\mathbf{F}}^{\mathrm{CP}} = \left\| \widetilde{F}_{pq}^{\mathrm{CP}} \right\| = \frac{1}{2} \begin{bmatrix} a_2 + a_3 & b_1 + \mathrm{i}b_2 & b_1 - \mathrm{i}b_2 & a_2 - a_3 \\ b_1 + \mathrm{i}b_2 & a_1 + a_4 & a_1 - a_4 & b_1 - \mathrm{i}b_2 \\ b_1 - \mathrm{i}b_2 & a_1 - a_4 & a_1 + a_4 & b_1 + \mathrm{i}b_2 \\ a_2 - a_3 & b_1 - \mathrm{i}b_2 & b_1 + \mathrm{i}b_2 & a_2 + a_3 \end{bmatrix},$$
$$p, q = 2, 0, -0, -2. \tag{4.100}$$

Obviously, this matrix has several symmetry properties:

$$\widetilde{F}_{pq}^{\mathrm{CP}}(\Theta) = \widetilde{F}_{qp}^{\mathrm{CP}}(\Theta) = \widetilde{F}_{-p,-q}^{\mathrm{CP}}(\Theta), \tag{4.101}$$

$$\widetilde{F}_{pp}^{\mathrm{CP}}(\Theta),\ \widetilde{F}_{p,-p}^{\mathrm{CP}}(\Theta) \text{ are real}, \tag{4.102}$$

$$\widetilde{F}_{20}^{\mathrm{CP}}(\Theta) = [\widetilde{F}_{2,-0}^{\mathrm{CP}}(\Theta)]^*. \tag{4.103}$$

An elegant and compact way to expand the elements $\widetilde{F}_{pq}^{\mathrm{CP}}$ is to use generalized spherical functions P_{pq}^s:

$$\widetilde{F}_{pq}^{\mathrm{CP}}(\Theta) = \sum_{s=\max(|p|,|q|)}^{s_{\max}} g_{pq}^s \, P_{pq}^s(\cos\Theta), \qquad p, q = 2, 0, -0, -2, \tag{4.104}$$

which indicates the rationale for the specific choice of values for the p, q indices for the circular-polarization phase matrix and the corresponding Stokes vector component subscripts (Eq. (4.96)). Another justification for this choice of expansion functions comes from the consideration of certain properties of the rotation group (Domke 1974). The expression for the expansion coefficients g_{pq}^s follows from Eqs. (4.104) and (B.37):

$$g_{pq}^s = \frac{2s+1}{2} \int_{-1}^{+1} \mathrm{d}(\cos\Theta)\, \widetilde{F}_{pq}^{\mathrm{CP}}(\Theta)\, P_{pq}^s(\cos\Theta), \qquad p, q = 2, 0, -0, -2. \tag{4.105}$$

Note that for $P_{pq}^s(\cos\Theta)$ no distinction is made between $p, q = 0$ and $p, q = -0$. For the values of p and q used here, all functions $P_{pq}^s(\cos\Theta)$ are real-valued (see Eq. (B.30)). Using Eqs. (4.101)–(4.103), (4.105), and (B.31), we derive the following symmetry relations:

$$g_{pq}^s = g_{qp}^s = g_{-p,-q}^s, \tag{4.106}$$

$$g_{pp}^s,\ g_{p,-p}^s \text{ are real}, \tag{4.107}$$

$$g_{20}^s = (g_{2,-0}^s)^*. \tag{4.108}$$

Finally, inserting Eq. (4.104) into Eq. (4.100) yields expansions (4.75)–(4.80) with expansion coefficients

$$\alpha_1^s = g_{00}^s + g_{0,-0}^s, \tag{4.109}$$

$$\alpha_2^s = g_{22}^s + g_{2,-2}^s, \tag{4.110}$$

$$\alpha_3^s = g_{22}^s - g_{2,-2}^s, \tag{4.111}$$

$$\alpha_4^s = g_{00}^s - g_{0,-0}^s, \tag{4.112}$$

$$\beta_1^s = 2\,\mathrm{Re}\, g_{02}^s, \tag{4.113}$$

$$\beta_2^s = 2\,\mathrm{Im}\, g_{02}^s. \tag{4.114}$$

By analogy with Eq. (4.14) and using Eqs. (1.101) and (4.100), we find for $0 < \varphi^{\mathrm{sca}} - \varphi^{\mathrm{inc}} < \pi$:

$$\begin{aligned}\widetilde{\mathbf{Z}}^{\mathrm{CP}}(\vartheta^{\mathrm{sca}}, \varphi^{\mathrm{sca}}; \vartheta^{\mathrm{inc}}, \varphi^{\mathrm{inc}}) &= \mathbf{L}^{\mathrm{CP}}(-\sigma_2)\widetilde{\mathbf{F}}^{\mathrm{CP}}(\Theta)\mathbf{L}^{\mathrm{CP}}(\pi - \sigma_1) \\ &= \frac{1}{2}\begin{bmatrix} (a_2 + a_3)\mathrm{e}^{-\mathrm{i}2(\sigma_1+\sigma_2)} & (b_1 + \mathrm{i}b_2)\mathrm{e}^{-\mathrm{i}2\sigma_2} & (b_1 - \mathrm{i}b_2)\mathrm{e}^{-\mathrm{i}2\sigma_2} & (a_2 - a_3)\mathrm{e}^{\mathrm{i}2(\sigma_1-\sigma_2)} \\ (b_1 + \mathrm{i}b_2)\mathrm{e}^{-\mathrm{i}2\sigma_1} & a_1 + a_4 & a_1 - a_4 & (b_1 - \mathrm{i}b_2)\mathrm{e}^{\mathrm{i}2\sigma_1} \\ (b_1 - \mathrm{i}b_2)\mathrm{e}^{-\mathrm{i}2\sigma_1} & a_1 - a_4 & a_1 + a_4 & (b_1 + \mathrm{i}b_2)\mathrm{e}^{\mathrm{i}2\sigma_1} \\ (a_2 - a_3)\mathrm{e}^{\mathrm{i}2(\sigma_2-\sigma_1)} & (b_1 - \mathrm{i}b_2)\mathrm{e}^{\mathrm{i}2\sigma_2} & (b_1 + \mathrm{i}b_2)\mathrm{e}^{\mathrm{i}2\sigma_2} & (a_2 + a_3)\mathrm{e}^{\mathrm{i}2(\sigma_1+\sigma_2)} \end{bmatrix},\end{aligned} \tag{4.115}$$

where we have omitted the argument Θ in the a's and b's. Applying Eq. (2.123) to Eqs. (4.68)–(4.70) we derive, after some algebra, the supplementary symmetry relations

$$\begin{aligned}\widetilde{\mathbf{Z}}^{\mathrm{CP}}(\vartheta^{\mathrm{sca}}, \varphi^{\mathrm{inc}}; \vartheta^{\mathrm{inc}}, \varphi^{\mathrm{sca}}) &= \mathbf{A}\boldsymbol{\Delta}_{34}\mathbf{A}^{-1}\widetilde{\mathbf{Z}}^{\mathrm{CP}}(\vartheta^{\mathrm{sca}}, \varphi^{\mathrm{sca}}; \vartheta^{\mathrm{inc}}, \varphi^{\mathrm{inc}})\mathbf{A}\boldsymbol{\Delta}_{34}\mathbf{A}^{-1} \\ &= \boldsymbol{\Delta}^{\mathrm{CP}}\widetilde{\mathbf{Z}}^{\mathrm{CP}}(\vartheta^{\mathrm{sca}}, \varphi^{\mathrm{sca}}; \vartheta^{\mathrm{inc}}, \varphi^{\mathrm{inc}})\boldsymbol{\Delta}^{\mathrm{CP}},\end{aligned} \tag{4.116}$$

$$\widetilde{\mathbf{Z}}^{\mathrm{CP}}(\pi - \vartheta^{\mathrm{sca}}, \varphi^{\mathrm{sca}}; \pi - \vartheta^{\mathrm{inc}}, \varphi^{\mathrm{inc}}) = \boldsymbol{\Delta}^{\mathrm{CP}}\widetilde{\mathbf{Z}}^{\mathrm{CP}}(\vartheta^{\mathrm{sca}}, \varphi^{\mathrm{sca}}; \vartheta^{\mathrm{inc}}, \varphi^{\mathrm{inc}})\boldsymbol{\Delta}^{\mathrm{CP}}, \tag{4.117}$$

$$\widetilde{\mathbf{Z}}^{\mathrm{CP}}(\pi - \vartheta^{\mathrm{inc}}, \varphi^{\mathrm{inc}} + \pi; \pi - \vartheta^{\mathrm{sca}}, \varphi^{\mathrm{sca}} + \pi) = [\widetilde{\mathbf{Z}}^{\mathrm{CP}}(\vartheta^{\mathrm{sca}}, \varphi^{\mathrm{sca}}; \vartheta^{\mathrm{inc}}, \varphi^{\mathrm{inc}})]^{\mathrm{T}}, \tag{4.118}$$

where

$$\boldsymbol{\Delta}^{\mathrm{CP}} = \begin{bmatrix} 0 & 0 & 0 & 1 \\ 0 & 0 & 1 & 0 \\ 0 & 1 & 0 & 0 \\ 1 & 0 & 0 & 0 \end{bmatrix}. \tag{4.119}$$

4.13 Radiative transfer equation

For macroscopically isotropic and mirror-symmetric media, the radiative transfer equation can be significantly simplified:

$$\frac{\mathrm{d}\mathbf{I}(\mathbf{r};\vartheta,\varphi;\omega)}{\mathrm{d}\tau(\mathbf{r},\omega)} = -\mathbf{I}(\mathbf{r};\vartheta,\varphi;\omega)$$
$$+\frac{\varpi(\mathbf{r},\omega)}{4\pi}\int_{-1}^{+1}\mathrm{d}(\cos\vartheta')\int_{0}^{2\pi}\mathrm{d}\varphi'\,\widetilde{\mathbf{Z}}(\mathbf{r};\vartheta,\vartheta',\varphi-\varphi';\omega)\mathbf{I}(\mathbf{r};\vartheta',\varphi';\omega)$$
$$+[1-\varpi(\mathbf{r},\omega)]\,\mathbf{I}_{\mathrm{b}}[T(\mathbf{r}),\omega], \tag{4.120}$$

where

$$\mathrm{d}\tau(\mathbf{r},\omega) = n_0(\mathbf{r})\langle C_{\mathrm{ext}}(\mathbf{r},\omega)\rangle\mathrm{d}s \tag{4.121}$$

is the optical pathlength element (cf. Eqs. (3.33), (4.32), (4.44), (4.45), (4.48), and (4.52)). By writing the normalized phase matrix in the form $\widetilde{\mathbf{Z}}(\mathbf{r};\vartheta,\vartheta',\varphi-\varphi';\omega)$, we explicitly indicate that it depends on the difference of the azimuthal angles of the scattering and incident directions rather than on their specific values (Section 4.3). This important property enables an efficient analytical treatment of the azimuthal dependence of the multiply scattered light, using a Fourier decomposition of the radiative transfer equation (Kuščer and Ribarič 1959; Domke 1974; de Haan *et al.* 1987). Numerical methods for solving Eq. (4.120) for the plane-parallel geometry are reviewed by Hansen and Travis (1974).

Equation (4.120) can be further simplified by neglecting polarization and so replacing the specific intensity vector by its first element (i.e., the radiance) and the normalized phase matrix by its (1, 1) element (i.e., the phase function):

$$\frac{\mathrm{d}I(\mathbf{r};\vartheta,\varphi;\omega)}{\mathrm{d}\tau(\mathbf{r},\omega)} = -I(\mathbf{r};\vartheta,\varphi;\omega)$$
$$+\frac{\varpi(\mathbf{r},\omega)}{4\pi}\int_{-1}^{+1}\mathrm{d}(\cos\vartheta')\int_{0}^{2\pi}\mathrm{d}\varphi' a_1(\mathbf{r},\Theta,\omega)I(\mathbf{r};\vartheta',\varphi';\omega)$$
$$+[1-\varpi(\mathbf{r},\omega)]\,I_{\mathrm{b}}[T(\mathbf{r}),\omega], \tag{4.122}$$

where

$$\cos\Theta = \cos\vartheta\cos\vartheta' + \sin\vartheta\sin\vartheta'\cos(\varphi-\varphi') \tag{4.123}$$

(see Eqs. (2.184), (4.17), and (4.67)). Although ignoring the vector nature of light and replacing the exact vector radiative transfer equation by its approximate scalar counterpart has no rigorous physical justification, this simplification is widely used when the medium is illuminated by unpolarized light and only the intensity of multiply scattered light needs to be computed. The scalar approximation gives poor accuracy when the size of the scattering particles is much smaller than the wavelength (Chandrasekhar 1960; Mishchenko *et al.* 1994), but provides acceptable results for particles comparable to and larger than the wavelength (Hansen 1971). Analytical and numerical solutions of the

scalar radiative transfer equation are discussed by Sobolev (1975), van de Hulst (1980), Lenoble (1985), Yanovitskij (1997), and Thomas and Stamnes (1999).

Part II

Calculation and Measurement of Scattering and Absorption Characteristics of Small Particles

The scattering, absorption, and emission characteristics introduced in Part I are intimately related to the physical and geometrical parameters of particles such as size, shape, relative refractive index, and orientation. Therefore, understanding natural optical phenomena and developing remote sensing and laboratory techniques for particle characterization require accurate quantitative knowledge of the electromagnetic scattering interaction as a function of the particle parameters.

Electromagnetic scattering properties of small particles can be either computed theoretically or measured experimentally, both approaches having their strengths, weaknesses, and limitations. Theoretical modeling does not involve expensive instrumentation, can be used to find any scattering characteristic, and often allows switching to another particle shape, size, refractive index, or orientation by changing a few lines in a computer code. However, applying exact methods to realistic polydispersions of irregular particles can be very costly, and sometimes not even possible, and often must be replaced by computations for simplified model shapes. Approximate techniques can be more flexible, but often have poorly characterized accuracy and range of applicability.

Laboratory and field measurements employing visible or infrared light can deal with real small particles, either natural or artificial. However, such measurements require complex and expensive hardware, are often incapable of providing simultaneously and accurately all scattering characteristics, and may be difficult to interpret because of lack of independent information on sample microphysics and composition. The microwave analog technique allows a much greater degree of independent sample characterization and enables true controlled laboratory measurements, but it involves even costlier equipment and cannot be applied readily to realistic distributions of particle sizes, shapes, and orientations. It is thus clear that only a creative combination of various theoretical and experimental approaches can lead to a significantly improved knowledge of light scattering by small particles.

All exact techniques for calculating electromagnetic scattering are based on solving the differential Maxwell equations or their integral counterparts in the time or frequency domain, either analytically or numerically. The search for an analytical solution has been equated, traditionally, to solving the vector wave equations for the time-harmonic electric fields outside and inside the scatterer (Eqs. (2.3) and (2.4)) using the separation of variables technique in one of the few coordinate systems in which this type of equation is separable (Morse and Feshbach 1953). The incident and internal fields are expanded in wave functions that are regular inside the scatterer, whereas the external scattered field is expanded in wave functions that behave as outgoing waves at infinity. These expansions are double series in general; a reduction to single series occurs only for spheres and infinite cylinders. Subject to the requirement of continuity of the tangential component of the electric and magnetic fields at the particle boundary (Eqs. (1.13) and (1.15)), the unknown coefficients in the internal-field and scattered-field expansions are determined from the known expansion coefficients of the incident field.

Unfortunately, the separation of variables technique generates a manageable solution only in a few simple cases. Lorenz in 1890 and, independently, Love (1899), Mie

(1908), and Debye (1909) derived the solution for an isotropic homogeneous sphere (see the historical remarks in Section 3.4 of Kerker 1969). We will refer to this solution as the Lorenz–Mie theory. This approach was extended to concentric core-mantle spheres (Aden and Kerker 1951), concentric multilayered spheres (Wait 1963), and radially inhomogeneous spheres (Wyatt 1962). Wait (1955) gave a full solution for electromagnetic scattering by a homogeneous infinite circular cylinder, whereas Kim and Yeh (1991) solved the general problem for an infinite elliptical cylinder. Finally, Oguchi (1973), Asano and Yamamoto (1975), and Onaka (1980) derived a general solution for homogeneous and core-mantle spheroids.

It is unlikely that this list of exact analytical results will be extended significantly in the future. Indeed, the separation of variables solution for spheroids, perhaps the simplest finite nonspherical particle, is already so complex that it behaves like a numerical solution in many respects and offers no definitive practical advantage over other available approaches. Some exact numerical approaches, in turn, often behave like analytical solutions since they involve the expansion of the incident and scattered fields in complete sets of eigenfunctions with well-known and convenient mathematical properties. As a consequence, the formerly rigid distinction between exact analytical and numerical solutions for nonspherical particles has become semantic rather than practical.

In Part II of this book we describe several theoretical and experimental techniques that have found extensive practical usage. We begin with a chapter on the T-matrix method because this is one of the most efficient, accurate, and widely employed exact techniques for simple and aggregated particles, includes the Lorenz–Mie theory as a particular case, and has remarkable analytical ties with the formalism outlined in Sections 4.10–4.12. In Chapters 6 and 7 we describe several alternative exact techniques and approximations and compare their relative performance and ranges of applicability. The closing chapter of Part II is devoted to experimental techniques employing visible, infrared, or microwave wavelengths.

Chapter 5

T-matrix method and Lorenz–Mie theory

The *T*-matrix method was initially introduced by Waterman (1965, 1971) as a technique for computing electromagnetic scattering by single, homogeneous, arbitrarily shaped particles based on the Huygens principle (this technique is otherwise known as the extended boundary condition method, the Schelkunoff equivalent current method, the Ewald–Oseen extinction theorem, and the null-field method). However, the concept, perceived at the time as auxiliary, of expanding the incident and scattered waves in appropriate vector spherical wave functions and relating these expansions by means of a transition (or *T*) matrix has proved to be extremely powerful by itself and has dramatically expanded the realm of the *T*-matrix approach. The latter now includes electromagnetic, acoustic, and elastodynamic wave scattering by single and aggregated scatterers, multiple scattering in discrete random media, and scattering by gratings and periodically rough surfaces (Varadan and Varadan 1980; Tsang *et al.* 1985). An attractive feature of the *T*-matrix approach is that it reduces exactly to the Lorenz–Mie theory when the scattering particle is a homogeneous or layered sphere composed of isotropic materials. The analyticity of the *T*-matrix formulation reveals close mathematical ties with the formalism of expanding normalized scattering matrices in generalized spherical functions (Sections 4.11 and 4.12) and has led to the development of efficient techniques for calculating orientation-averaged scattering characteristics.

At present, the *T*-matrix approach is one of the most powerful and widely used tools for rigorously computing electromagnetic scattering by single and compounded particles. In many applications it surpasses other frequently used techniques in terms of efficiency and size parameter range and is the only method that has been used in systematic surveys of nonspherical scattering based on calculations for thousands of particles in random orientation. Recent improvements have made this method applicable to particles much

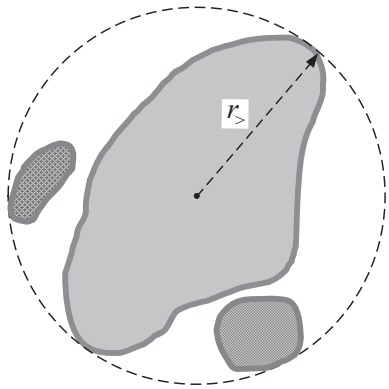

Figure 5.1. Cross section of an arbitrarily shaped, finite scattering object. $r_>$ is the radius of the smallest circumscribing sphere centered at the origin of the laboratory coordinate system.

larger than a wavelength and, therefore, suitable for checking the accuracy of the geometrical optics approximation and its modifications at lower frequencies (Section 7.4). Because of its high and readily controllable numerical accuracy, the *T*-matrix method is one of a very few sources of benchmark results for particles lacking spherical symmetry. Hence it appears natural to open Part II by a detailed survey of the *T*-matrix approach.

5.1 *T*-matrix ansatz

Consider scattering of a plane electromagnetic wave

$$\mathbf{E}^{\text{inc}}(\mathbf{r}) = \mathbf{E}_0^{\text{inc}} e^{ik_1 \hat{\mathbf{n}}^{\text{inc}} \cdot \mathbf{r}}, \qquad \mathbf{E}_0^{\text{inc}} \cdot \hat{\mathbf{n}}^{\text{inc}} = 0, \tag{5.1}$$

by an arbitrary finite scattering object in the form of a single particle or a fixed aggregate, as described in Chapter 2. We expand the incident and scattered fields in vector spherical wave functions as follows:

$$\mathbf{E}^{\text{inc}}(\mathbf{r}) = \sum_{n=1}^{\infty} \sum_{m=-n}^{n} [a_{mn} \text{Rg}\mathbf{M}_{mn}(k_1\mathbf{r}) + b_{mn} \text{Rg}\mathbf{N}_{mn}(k_1\mathbf{r})], \tag{5.2}$$

$$\mathbf{E}^{\text{sca}}(\mathbf{r}) = \sum_{n=1}^{\infty} \sum_{m=-n}^{n} [p_{mn} \mathbf{M}_{mn}(k_1\mathbf{r}) + q_{mn} \mathbf{N}_{mn}(k_1\mathbf{r})], \qquad r > r_>, \tag{5.3}$$

where k_1 is the wave number in the surrounding medium and $r_>$ is the radius of the smallest circumscribing sphere of the scatterer centered at the origin of the laboratory coordinate system (Fig. 5.1). The properties of the vector spherical wave functions are summarized in Appendix C. The functions $\text{Rg}\mathbf{M}_{mn}$ and $\text{Rg}\mathbf{N}_{mn}$ are regular (finite) at the origin, while the use of the outgoing functions $\mathbf{M}_{mn}$ and $\mathbf{N}_{mn}$ in Eq. (5.3) ensures that the scattered field satisfies the so-called radiation condition at infinity (i.e., the transverse component of the scattered electric field decays as $1/r$, whereas

the radial component decays faster than $1/r$ with $r \to \infty$; see Section 2.2 and Eqs. (C.30) and (C.31)). The requirement $r > r_>$ in Eq. (5.3) means that the scattered field is expanded in the functions $\mathbf{M}_{mn}$ and $\mathbf{N}_{mn}$ only outside the smallest circumscribing sphere of the scatterer (Fig. 5.1). The so-called Rayleigh hypothesis (e.g., Bates 1975; Paulick 1990) conjectures that the scattered field can be expanded in the outgoing wave functions not only in the outside region but also in the region between the particle surface and the smallest circumscribing sphere. Because the range of validity of this hypothesis is poorly known and is in fact questionable, the requirement $r > r_>$ in Eq. (5.3) is important in order to make sure that the Rayleigh hypothesis is not implicitly invoked (Lewin 1970).

The expansion coefficients of the plane incident wave are given by Eqs. (C.57) and (C.58):

$$a_{mn} = 4\pi(-1)^m \mathrm{i}^n d_n \mathbf{E}_0^{\mathrm{inc}} \cdot \mathbf{C}_{mn}^*(\vartheta^{\mathrm{inc}}) \exp(-\mathrm{i}m\varphi^{\mathrm{inc}}), \tag{5.4}$$

$$b_{mn} = 4\pi(-1)^m \mathrm{i}^{n-1} d_n \mathbf{E}_0^{\mathrm{inc}} \cdot \mathbf{B}_{mn}^*(\vartheta^{\mathrm{inc}}) \exp(-\mathrm{i}m\varphi^{\mathrm{inc}}). \tag{5.5}$$

Owing to the linearity of the Maxwell equations and constitutive relations (see Section 2.2), the relation between the scattered-field expansion coefficients p_{mn} and q_{mn} on the one hand and the incident field expansion coefficients a_{mn} and b_{mn} on the other hand must be linear and is given by the so-called transition matrix (or *T* matrix) $\mathbf{T}$ as follows (Waterman 1971; Tsang *et al.* 1985):

$$p_{mn} = \sum_{n'=1}^{\infty} \sum_{m'=-n'}^{n'} (T_{mnm'n'}^{11} a_{m'n'} + T_{mnm'n'}^{12} b_{m'n'}), \tag{5.6}$$

$$q_{mn} = \sum_{n'=1}^{\infty} \sum_{m'=-n'}^{n'} (T_{mnm'n'}^{21} a_{m'n'} + T_{mnm'n'}^{22} b_{m'n'}). \tag{5.7}$$

In compact matrix notation, Eqs. (5.6) and (5.7) can be rewritten as

$$\begin{bmatrix} \mathbf{p} \\ \mathbf{q} \end{bmatrix} = \mathbf{T} \begin{bmatrix} \mathbf{a} \\ \mathbf{b} \end{bmatrix} = \begin{bmatrix} \mathbf{T}^{11} & \mathbf{T}^{12} \\ \mathbf{T}^{21} & \mathbf{T}^{22} \end{bmatrix} \begin{bmatrix} \mathbf{a} \\ \mathbf{b} \end{bmatrix}, \tag{5.8}$$

which means that the column vector of the expansion coefficients of the scattered field is obtained by multiplying the *T* matrix and the column vector of the expansion coefficients of the incident field.

Equation (5.8) is the cornerstone of the *T*-matrix approach. Indeed, if the *T* matrix is known, then Eqs. (5.6), (5.7), (5.4), (5.5), and (5.3) give the scattered field and, thus, the scattering dyad defined by Eq. (2.26). Indeed, substituting the asymptotic formulas (C.30) and (C.31) in Eq. (5.3) yields Eq. (2.24) with

$$\mathbf{E}_1^{\mathrm{sca}}(\hat{\mathbf{n}}^{\mathrm{sca}}) = \frac{1}{k_1} \sum_{n=1}^{\infty} \sum_{m=-n}^{n} \mathrm{i}^{-n} \gamma_{mn} [-\mathrm{i}p_{mn} \mathbf{C}_{mn}(\vartheta^{\mathrm{sca}}, \varphi^{\mathrm{sca}}) + q_{mn} \mathbf{B}_{mn}(\vartheta^{\mathrm{sca}}, \varphi^{\mathrm{sca}})]. \tag{5.9}$$

Finally, using Eqs. (5.4)–(5.7), we easily derive

$$\ddot{A}(\hat{\mathbf{n}}^{\text{sca}}, \hat{\mathbf{n}}^{\text{inc}}) = \frac{4\pi}{k_1} \sum_{nmn'm'} \mathrm{i}^{n'-n-1}(-1)^{m+m'} d_n d_{n'} \exp[\mathrm{i}(m\varphi^{\text{sca}} - m'\varphi^{\text{inc}})]$$
$$\times \{[T^{11}_{mnm'n'}\mathbf{C}_{mn}(\vartheta^{\text{sca}}) + \mathrm{i}T^{21}_{mnm'n'}\mathbf{B}_{mn}(\vartheta^{\text{sca}})] \otimes \mathbf{C}^*_{m'n'}(\vartheta^{\text{inc}})$$
$$+ [-\mathrm{i}T^{12}_{mnm'n'}\mathbf{C}_{mn}(\vartheta^{\text{sca}}) + T^{22}_{mnm'n'}\mathbf{B}_{mn}(\vartheta^{\text{sca}})] \otimes \mathbf{B}^*_{m'n'}(\vartheta^{\text{inc}})\}. \tag{5.10}$$

Equations (2.31)–(2.34) and (5.10) then yield the amplitude matrix elements as follows:

$$S_{11}(\hat{\mathbf{n}}^{\text{sca}}, \hat{\mathbf{n}}^{\text{inc}}) = \frac{1}{k_1} \sum_{n=1}^{\infty} \sum_{n'=1}^{\infty} \sum_{m=-n}^{n} \sum_{m'=-n'}^{n'} \alpha_{mnm'n'} [T^{11}_{mnm'n'} \pi_{mn}(\vartheta^{\text{sca}}) \pi_{m'n'}(\vartheta^{\text{inc}})$$
$$+ T^{21}_{mnm'n'} \tau_{mn}(\vartheta^{\text{sca}}) \pi_{m'n'}(\vartheta^{\text{inc}}) + T^{12}_{mnm'n'} \pi_{mn}(\vartheta^{\text{sca}}) \tau_{m'n'}(\vartheta^{\text{inc}})$$
$$+ T^{22}_{mnm'n'} \tau_{mn}(\vartheta^{\text{sca}}) \tau_{m'n'}(\vartheta^{\text{inc}})] \exp[\mathrm{i}(m\varphi^{\text{sca}} - m'\varphi^{\text{inc}})], \tag{5.11}$$

$$S_{12}(\hat{\mathbf{n}}^{\text{sca}}, \hat{\mathbf{n}}^{\text{inc}}) = \frac{1}{\mathrm{i}k_1} \sum_{n=1}^{\infty} \sum_{n'=1}^{\infty} \sum_{m=-n}^{n} \sum_{m'=-n'}^{n'} \alpha_{mnm'n'} [T^{11}_{mnm'n'} \pi_{mn}(\vartheta^{\text{sca}}) \tau_{m'n'}(\vartheta^{\text{inc}})$$
$$+ T^{21}_{mnm'n'} \tau_{mn}(\vartheta^{\text{sca}}) \tau_{m'n'}(\vartheta^{\text{inc}}) + T^{12}_{mnm'n'} \pi_{mn}(\vartheta^{\text{sca}}) \pi_{m'n'}(\vartheta^{\text{inc}})$$
$$+ T^{22}_{mnm'n'} \tau_{mn}(\vartheta^{\text{sca}}) \pi_{m'n'}(\vartheta^{\text{inc}})] \exp[\mathrm{i}(m\varphi^{\text{sca}} - m'\varphi^{\text{inc}})], \tag{5.12}$$

$$S_{21}(\hat{\mathbf{n}}^{\text{sca}}, \hat{\mathbf{n}}^{\text{inc}}) = \frac{\mathrm{i}}{k_1} \sum_{n=1}^{\infty} \sum_{n'=1}^{\infty} \sum_{m=-n}^{n} \sum_{m'=-n'}^{n'} \alpha_{mnm'n'} [T^{11}_{mnm'n'} \tau_{mn}(\vartheta^{\text{sca}}) \pi_{m'n'}(\vartheta^{\text{inc}})$$
$$+ T^{21}_{mnm'n'} \pi_{mn}(\vartheta^{\text{sca}}) \pi_{m'n'}(\vartheta^{\text{inc}}) + T^{12}_{mnm'n'} \tau_{mn}(\vartheta^{\text{sca}}) \tau_{m'n'}(\vartheta^{\text{inc}})$$
$$+ T^{22}_{mnm'n'} \pi_{mn}(\vartheta^{\text{sca}}) \tau_{m'n'}(\vartheta^{\text{inc}})] \exp[\mathrm{i}(m\varphi^{\text{sca}} - m'\varphi^{\text{inc}})], \tag{5.13}$$

$$S_{22}(\hat{\mathbf{n}}^{\text{sca}}, \hat{\mathbf{n}}^{\text{inc}}) = \frac{1}{k_1} \sum_{n=1}^{\infty} \sum_{n'=1}^{\infty} \sum_{m=-n}^{n} \sum_{m'=-n'}^{n'} \alpha_{mnm'n'} [T^{11}_{mnm'n'} \tau_{mn}(\vartheta^{\text{sca}}) \tau_{m'n'}(\vartheta^{\text{inc}})$$
$$+ T^{21}_{mnm'n'} \pi_{mn}(\vartheta^{\text{sca}}) \tau_{m'n'}(\vartheta^{\text{inc}}) + T^{12}_{mnm'n'} \tau_{mn}(\vartheta^{\text{sca}}) \pi_{m'n'}(\vartheta^{\text{inc}})$$
$$+ T^{22}_{mnm'n'} \pi_{mn}(\vartheta^{\text{sca}}) \pi_{m'n'}(\vartheta^{\text{inc}})] \exp[\mathrm{i}(m\varphi^{\text{sca}} - m'\varphi^{\text{inc}})], \tag{5.14}$$

where

$$\alpha_{mnm'n'} = \mathrm{i}^{n'-n-1}(-1)^{m+m'} \left[\frac{(2n+1)(2n'+1)}{n(n+1)n'(n'+1)} \right]^{1/2}, \tag{5.15}$$

$$\pi_{mn}(\vartheta) = \frac{m d^n_{0m}(\vartheta)}{\sin\vartheta}, \qquad \pi_{-mn}(\vartheta) = (-1)^{m+1}\pi_{mn}(\vartheta), \tag{5.16}$$

$$\tau_{mn}(\vartheta) = \frac{\mathrm{d}d^n_{0m}(\vartheta)}{\mathrm{d}\vartheta}, \qquad \tau_{-mn}(\vartheta) = (-1)^m \tau_{mn}(\vartheta) \tag{5.17}$$

(see Eq. (B.5)). Knowledge of the amplitude matrix allows one to compute any of the scattering characteristics introduced in Chapter 2. Specifically, the Stokes phase and extinction matrices and the extinction cross section are given by Eqs. (2.106)–(2.121),

Eqs. (2.140)–(2.146), and Eq. (2.159), respectively. Alternatively, Eqs. (2.157), (5.9), (5.4) and (5.5) yield

$$C_{\text{ext}} = -\frac{1}{k_1^2|\mathbf{E}_0^{\text{inc}}|^2}\,\text{Re}\sum_{n=1}^{\infty}\sum_{m=-n}^{n}[a_{mn}(p_{mn})^* + b_{mn}(q_{mn})^*]. \tag{5.18a}$$

The formula for the scattering cross section follows from Eqs. (2.158) and (5.9) and the orthogonality and normalization conditions for the vector spherical harmonics, Eqs. (C.51) and (C.52):

$$\begin{aligned} C_{\text{sca}} &= \frac{1}{|\mathbf{E}_0^{\text{inc}}|^2}\int_0^{2\pi}\mathrm{d}\varphi^{\text{sca}}\int_0^{\pi}\mathrm{d}\vartheta^{\text{sca}}\sin\vartheta^{\text{sca}}|\mathbf{E}_1^{\text{sca}}(\vartheta^{\text{sca}},\varphi^{\text{sca}})|^2 \\ &= \frac{1}{k_1^2|\mathbf{E}_0^{\text{inc}}|^2}\sum_{n=1}^{\infty}\sum_{m=-n}^{n}[|p_{mn}|^2 + |q_{mn}|^2]. \end{aligned} \tag{5.18b}$$

A fundamental feature of the *T*-matrix approach is that the *T* matrix depends only on the physical and geometrical characteristics of the scattering particle (such as particle size relative to the wavelength, shape (morphology), relative refractive index, and orientation with respect to the laboratory reference frame; see subsection 5.8.2 below) and is completely independent of the propagation directions and polarization states of the incident and scattered fields. This means that the *T* matrix need be computed only once and then can be used in calculations for any direction of incidence and scattering and for any polarization state of the incident field.

5.2 General properties of the *T* matrix

The special functions appearing in the *T*-matrix formulation have been studied thoroughly and result in convenient mathematical properties and symmetries of the *T* matrix. In this and later sections we will demonstrate how the analyticity of the *T*-matrix approach can be exploited in order to enhance significantly the efficiency of computations for individual scatterers as well as for particle ensembles.

5.2.1 Rotation transformation rule

We begin by deriving the rotation transformation rule for the *T* matrix. Consider laboratory (L) and particle (P) coordinate systems having a common origin inside the scattering object. Let α, β, and γ be the Euler angles of rotation transforming the laboratory coordinate system into the particle coordinate system (cf. Section 2.4), and let (ϑ_L, φ_L) and (ϑ_P, φ_P) be the spherical angles of the same position vector $\mathbf{r}$ in the two coordinate systems, respectively. We now rewrite Eqs. (5.2) and (5.3) as follows:

$$\mathbf{E}^{\text{inc}}(\mathbf{r}) = \sum_{n=1}^{\infty}\sum_{m=-n}^{n}[a_{mn}(L)\text{Rg}\mathbf{M}_{mn}(k_1 r, \vartheta_L, \varphi_L) + b_{mn}(L)\text{Rg}\mathbf{N}_{mn}(k_1 r, \vartheta_L, \varphi_L)], \tag{5.19}$$

$$\mathbf{E}^{\text{sca}}(\mathbf{r}) = \sum_{n=1}^{\infty}\sum_{m=-n}^{n}[p_{mn}(L)\mathbf{M}_{mn}(k_1 r, \vartheta_L, \varphi_L) + q_{mn}(L)\mathbf{N}_{mn}(k_1 r, \vartheta_L, \varphi_L)], \qquad r > r_>, \tag{5.20}$$

$$\mathbf{E}^{\text{inc}}(\mathbf{r}) = \sum_{n=1}^{\infty}\sum_{m=-n}^{n}[a_{mn}(P)\text{Rg}\mathbf{M}_{mn}(k_1 r, \vartheta_P, \varphi_P) + b_{mn}(P)\text{Rg}\mathbf{N}_{mn}(k_1 r, \vartheta_P, \varphi_P)], \tag{5.21}$$

$$\mathbf{E}^{\text{sca}}(\mathbf{r}) = \sum_{n=1}^{\infty}\sum_{m=-n}^{n}[p_{mn}(P)\mathbf{M}_{mn}(k_1 r, \vartheta_P, \varphi_P) + q_{mn}(P)\mathbf{N}_{mn}(k_1 r, \vartheta_P, \varphi_P)], \qquad r > r_>. \tag{5.22}$$

According to Eqs. (C.64) and (C.65), we can use Wigner D-functions to write

$$\mathbf{M}_{mn}(k_1 r, \vartheta_P, \varphi_P) = \sum_{m'=-n}^{n}\mathbf{M}_{m'n}(k_1 r, \vartheta_L, \varphi_L)D^n_{m'm}(\alpha, \beta, \gamma), \tag{5.23}$$

$$\mathbf{M}_{mn}(k_1 r, \vartheta_L, \varphi_L) = \sum_{m'=-n}^{n}\mathbf{M}_{m'n}(k_1 r, \vartheta_P, \varphi_P)D^n_{m'm}(-\gamma, -\beta, -\alpha), \tag{5.24}$$

and similarly for Rg$\mathbf{M}$, $\mathbf{N}$, and Rg$\mathbf{N}$. Therefore, we immediately get

$$\begin{matrix} a_{mn}(P) \\ b_{mn}(P) \end{matrix} = \sum_{m'=-n}^{n}\begin{matrix} a_{m'n}(L) \\ b_{m'n}(L) \end{matrix} D^n_{mm'}(-\gamma, -\beta, -\alpha), \tag{5.25}$$

$$\begin{matrix} p_{mn}(L) \\ q_{mn}(L) \end{matrix} = \sum_{m'=-n}^{n}\begin{matrix} p_{m'n}(P) \\ q_{m'n}(P) \end{matrix} D^n_{mm'}(\alpha, \beta, \gamma). \tag{5.26}$$

Note that in Eqs. (5.25) and (5.26) we use a compact way of writing two formulas (for a_{mn} and b_{mn} and for p_{mn} and q_{mn}) as a single equation. Finally, from

$$\begin{bmatrix} \mathbf{p}(P) \\ \mathbf{q}(P) \end{bmatrix} = \begin{bmatrix} \mathbf{T}^{11}(P) & \mathbf{T}^{12}(P) \\ \mathbf{T}^{21}(P) & \mathbf{T}^{22}(P) \end{bmatrix}\begin{bmatrix} \mathbf{a}(P) \\ \mathbf{b}(P) \end{bmatrix}, \tag{5.27}$$

$$\begin{bmatrix} \mathbf{p}(L) \\ \mathbf{q}(L) \end{bmatrix} = \begin{bmatrix} \mathbf{T}^{11}(L; \alpha, \beta, \gamma) & \mathbf{T}^{12}(L; \alpha, \beta, \gamma) \\ \mathbf{T}^{21}(L; \alpha, \beta, \gamma) & \mathbf{T}^{22}(L; \alpha, \beta, \gamma) \end{bmatrix}\begin{bmatrix} \mathbf{a}(L) \\ \mathbf{b}(L) \end{bmatrix}, \tag{5.28}$$

and Eqs. (5.25) and (5.26), we derive (Tsang *et al.* 1985)

$$T^{kl}_{mnm'n'}(L; \alpha, \beta, \gamma) = \sum_{m_1=-n}^{n}\sum_{m_2=-n'}^{n'} D^n_{mm_1}(\alpha, \beta, \gamma)T^{kl}_{m_1 n m_2 n'}(P)\,D^{n'}_{m_2 m'}(-\gamma, -\beta, -\alpha),$$
$$k, l = 1, 2. \tag{5.29}$$

When $\alpha = \beta = \gamma = 0$, Eq. (5.29) must give

$$T^{kl}_{mnm'n'}(L; 0, 0, 0) \equiv T^{kl}_{mnm'n'}(P). \tag{5.30}$$

It is easy to verify that this identity indeed follows from Eqs. (B.38) and (B.6).

If we now assume that the matrix $\mathbf{T}(P)$ is already known and use the Euler angles of rotation α, β, and γ to specify the orientation of the particle with respect to the laboratory coordinate system, then Eq. (5.29) gives the T matrix in the laboratory co-

ordinate system. Therefore, Eqs. (5.11)–(5.14) and (5.29) are ideally suited for computing analytically orientation-averaged scattering characteristics using a single precalculated $\mathbf{T}(P)$ matrix (see Sections 5.3–5.6 below).

5.2.2 Symmetry relations

According to the reciprocity relation (2.64), we must have

$$\begin{aligned}&\mathbf{S}(\pi-\vartheta^{\text{inc}},\pi+\varphi^{\text{inc}};\pi-\vartheta^{\text{sca}},\pi+\varphi^{\text{sca}})\\&=\begin{bmatrix}S_{11}(\vartheta^{\text{sca}},\varphi^{\text{sca}};\vartheta^{\text{inc}},\varphi^{\text{inc}}) & -S_{21}(\vartheta^{\text{sca}},\varphi^{\text{sca}};\vartheta^{\text{inc}},\varphi^{\text{inc}})\\-S_{12}(\vartheta^{\text{sca}},\varphi^{\text{sca}};\vartheta^{\text{inc}},\varphi^{\text{inc}}) & S_{22}(\vartheta^{\text{sca}},\varphi^{\text{sca}};\vartheta^{\text{inc}},\varphi^{\text{inc}})\end{bmatrix}.\end{aligned}\tag{5.31}$$

Equations (5.16), (5.17), (B.7), and (B.25) give

$$\pi_{mn}(\pi-\vartheta)=(-1)^{n+1}\pi_{-mn}(\vartheta),\tag{5.32}$$

$$\tau_{mn}(\pi-\vartheta)=(-1)^{n+1}\tau_{-mn}(\vartheta).\tag{5.33}$$

Using Eqs. (5.11)–(5.15) and (5.32)–(5.33), it is straightforward to show that for Eq. (5.31) to be valid for any ϑ^{inc}, φ^{inc}, ϑ^{sca}, and φ^{sca}, the T matrix must obey the following general symmetry relation:

$$T^{lk}_{-m'n',-mn}=(-1)^{m+m'}T^{kl}_{mnm'n'},\quad k,l=1,2\tag{5.34}$$

(Waterman 1971).

An appropriate choice of the particle reference frame can often result in useful symmetries of the $\mathbf{T}(P)$ matrix. For example, the z-axis of the particle coordinate system for a rotationally symmetric body should be directed along the axis of rotation. Because any rotation about the symmetry axis gives the same particle, we must have

$$T^{kl}_{mnm'n'}(L;\alpha,0,0)\equiv T^{kl}_{mnm'n'}(L;0,0,0)=T^{kl}_{mnm'n'}(P),\tag{5.35}$$

which, in view of Eqs. (5.29), (B.38), and (B.6), gives

$$T^{kl}_{mnm'n'}(P)=\delta_{mm'}T^{kl}_{mnmn'}(P).\tag{5.36}$$

Thus, the T matrix becomes diagonal with respect to the azimuthal indices m and m'. If the axis of rotation is directed along the z-axis of the laboratory reference frame, then mirroring the particle with respect to the xz-plane gives the same particle; therefore, the amplitude matrix $\mathbf{S}(\vartheta^{\text{sca}},0;\vartheta^{\text{inc}},0)$ must be diagonal (see Eq. (4.2c)). We thus have from Eqs. (5.12), (5.13), (5.16), (5.17), (5.30), and (5.36)

$$T^{kl}_{-mn,-mn'}(P)=(-1)^{k+l}T^{kl}_{mnmn'}(P),\qquad T^{12}_{0n0n'}(P)\equiv 0,\qquad T^{21}_{0n0n'}(P)\equiv 0.\tag{5.37}$$

Furthermore, if the rotationally symmetric particle has a plane of symmetry perpendicular to the axis of rotation, then rotating the particle through an angle π around the y-axis of the laboratory reference frame gives the same particle, and we must have

$$T^{kl}_{mnm'n'}(L;0,\pi,0) \equiv T^{kl}_{mnm'n'}(L;0,0,0) = T^{kl}_{mnm'n'}(P). \tag{5.38}$$

Equations (5.29), (B.38), (B.6), (B.7), and (5.36)–(5.38) then imply that

$$T^{11}_{mnmn'}(P) = T^{22}_{mnmn'}(P) = 0 \quad \text{unless} \quad (-1)^{n+n'} = 1 \tag{5.39}$$

and

$$T^{12}_{mnmn'}(P) = T^{21}_{mnmn'}(P) = 0 \quad \text{unless} \quad (-1)^{n+n'} = -1. \tag{5.40}$$

Any rotation of a spherically symmetric particle renders the same particle, and we must have

$$T^{kl}_{mnm'n'}(L;\alpha,\beta,\gamma) \equiv T^{kl}_{mnm'n'}(L;0,0,0) = T^{kl}_{mnm'n'}(P). \tag{5.41}$$

Equations (5.29), (5.36), (5.37), and (B.47) then force us to conclude that the $\mathbf{T}(P)$ matrix for a spherically symmetric scatterer must be diagonal and independent of the azimuthal indices m and m':

$$T^{12}_{mnm'n'}(P) \equiv 0, \quad T^{21}_{mnm'n'}(P) \equiv 0, \tag{5.42}$$

$$T^{11}_{mnm'n'}(P) = -\delta_{mm'}\delta_{nn'}b_n, \tag{5.43}$$

$$T^{22}_{mnm'n'}(P) = -\delta_{mm'}\delta_{nn'}a_n. \tag{5.44}$$

We will see later that the quantities a_n and b_n coincide with expansion coefficients appearing in the Lorenz–Mie solution for homogeneous or radially inhomogeneous spheres. It is, therefore, natural to refer to these quantities as Lorenz–Mie coefficients.

The analytical symmetry relations for the T matrix can be used to test numerical codes as well as to simplify considerably many equations of the T-matrix method and develop efficient numerical procedures. Additional properties of the T matrix for particles with specific symmetries are discussed in Schulz *et al.* (1999a) and in Kahnert *et al.* (2001a).

5.2.3 Unitarity

We will now derive the unitarity property of the T matrix for nonabsorbing scatterers (i.e., with the imaginary part of the relative refractive index equal to zero) as a consequence of energy conservation. We begin by defining the so-called S matrix $\boldsymbol{S}$:

$$\boldsymbol{S} = \mathbf{E} + 2\mathbf{T} = \mathbf{E} + 2\begin{bmatrix} \mathbf{T}^{11} & \mathbf{T}^{12} \\ \mathbf{T}^{21} & \mathbf{T}^{22} \end{bmatrix}, \tag{5.45}$$

where $\mathbf{E}$ is a unit matrix. (Note that we use a sloping $\boldsymbol{S}$ to distinguish the S matrix from the amplitude matrix $\mathbf{S}$.) As follows from Eqs. (C.1) and (C.2), we can write

$$\begin{matrix} \mathrm{Rg}\mathbf{M}_{mn} \\ \mathrm{Rg}\mathbf{N}_{mn} \end{matrix}(k_1 r,\vartheta,\varphi) = \frac{1}{2}\begin{bmatrix} \mathbf{M}_{mn} \\ \mathbf{N}_{mn} \end{bmatrix}(k_1 r,\vartheta,\varphi) + \begin{matrix} \mathbf{M}^{(2)}_{mn} \\ \mathbf{N}^{(2)}_{mn} \end{matrix}(k_1 r,\vartheta,\varphi)\Bigg], \tag{5.46}$$

where the superscript (2) labels vector spherical wave functions given by Eqs. (C.14) and (C.15) but with $h_n^{(1)}(\mathrm{k}r)$ replaced by $h_n^{(2)}(\mathrm{k}r)$. The total electric field is the vector sum of the incident and scattered fields. From Eqs. (5.2), (5.3), (5.6), (5.7), (5.45), and (5.46), we obtain

$$\begin{aligned}\mathbf{E}(\mathbf{r}) = \tfrac{1}{2}\sum_{nmn'm'} \{&[S^{11}_{mnm'n'}a_{m'n'} + S^{12}_{mnm'n'}b_{m'n'}]\mathbf{M}_{mn}(k_1r,\vartheta,\varphi)\\ &+[S^{21}_{mnm'n'}a_{m'n'} + S^{22}_{mnm'n'}b_{m'n'}]\mathbf{N}_{mn}(k_1r,\vartheta,\varphi)\}\\ &+\tfrac{1}{2}\sum_{nm}[a_{mn}\mathbf{M}^{(2)}_{mn}(k_1r,\vartheta,\varphi) + b_{mn}\mathbf{N}^{(2)}_{mn}(k_1r,\vartheta,\varphi)].\end{aligned} \tag{5.47}$$

Since $h_n^{(2)}(k_1r) = [h_n^{(1)}(k_1r)]^*$, we have by analogy with Eqs. (C.30) and (C.31)

$$\mathbf{M}^{(2)}_{mn}(k_1r,\vartheta,\varphi) \underset{\substack{k_1r\to\infty\\ k_1r\gg n^2}}{=} \frac{\mathrm{i}^{n+1}\mathrm{e}^{-\mathrm{i}k_1r}}{k_1r}\gamma_{mn}\mathbf{C}_{mn}(\vartheta,\varphi), \tag{5.48}$$

$$\mathbf{N}^{(2)}_{mn}(k_1r,\vartheta,\varphi) \underset{\substack{k_1r\to\infty\\ k_1r\gg n^2}}{=} \frac{\mathrm{i}^{n}\mathrm{e}^{-\mathrm{i}k_1r}}{k_1r}\gamma_{mn}\mathbf{B}_{mn}(\vartheta,\varphi). \tag{5.49}$$

Using Eqs. (5.47)–(5.49) and (C.30), (C.31), we can represent the total field in the far-field zone as a superposition of outgoing and incoming transverse spherical waves:

$$\mathbf{E}(\mathbf{r}) \underset{k_1r\to\infty}{=} \frac{\mathrm{e}^{\mathrm{i}k_1r}}{r}\mathbf{E}_1(\vartheta,\varphi) + \frac{\mathrm{e}^{-\mathrm{i}k_1r}}{r}\mathbf{E}_2(\vartheta,\varphi), \tag{5.50}$$

where

$$\begin{aligned}\mathbf{E}_1(\vartheta,\varphi) = \frac{1}{2k_1}\sum_{nmn'm'}\gamma_{mn}\mathrm{i}^{-n-1}\{&[S^{11}_{mnm'n'}a_{m'n'} + S^{12}_{mnm'n'}b_{m'n'}]\mathbf{C}_{mn}(\vartheta,\varphi)\\ &+\mathrm{i}[S^{21}_{mnm'n'}a_{m'n'} + S^{22}_{mnm'n'}b_{m'n'}]\mathbf{B}_{mn}(\vartheta,\varphi)\},\end{aligned} \tag{5.51}$$

$$\mathbf{E}_2(\vartheta,\varphi) = \frac{1}{2k_1}\sum_{nm}\gamma_{mn}\mathrm{i}^{n+1}[a_{mn}\mathbf{C}_{mn}(\vartheta,\varphi) - \mathrm{i}b_{mn}\mathbf{B}_{mn}(\vartheta,\varphi)]. \tag{5.52}$$

Since the first relation of Eq. (2.1) and Eqs. (2.21), (2.40), and (2.49) give

$$\mathbf{H}(\mathbf{r}) \underset{k_1r\to\infty}{=} \sqrt{\frac{\varepsilon_1}{\mu_0}}\left\{\frac{\mathrm{e}^{\mathrm{i}k_1r}}{r}\hat{\mathbf{r}}\times\mathbf{E}_1(\vartheta,\varphi) - \frac{\mathrm{e}^{-\mathrm{i}k_1r}}{r}\hat{\mathbf{r}}\times\mathbf{E}_2(\vartheta,\varphi)\right\}, \tag{5.53}$$

the time-averaged Poynting vector is

$$\begin{aligned}\langle\mathbf{S}(\mathbf{r})\rangle &= \tfrac{1}{2}\mathrm{Re}[\mathbf{E}(\mathbf{r})\times\mathbf{H}^*(\mathbf{r})]\\ &\underset{k_1r\to\infty}{=} \hat{\mathbf{r}}\,\frac{1}{2r^2}\sqrt{\frac{\varepsilon_1}{\mu_0}}\,\{|\mathbf{E}_1(\vartheta,\varphi)|^2 - |\mathbf{E}_2(\vartheta,\varphi)|^2\}\end{aligned} \tag{5.54}$$

(cf. Eq. (1.40)).

If the scattering object is nonabsorbing, the integral of $\langle \mathbf{S}(\mathbf{r})\rangle \cdot \hat{\mathbf{r}}$ over a spherical surface at infinity must vanish:

$$\int_0^{2\pi} \mathrm{d}\varphi \int_0^{\pi} \mathrm{d}\vartheta \sin\vartheta \{|\mathbf{E}_1(\vartheta, \varphi)|^2 - |\mathbf{E}_2(\vartheta, \varphi)|^2\} = 0. \tag{5.55}$$

Recalling the orthogonality relations for vector spherical harmonics, Eqs. (C.51) and (C.52), we obtain

$$\begin{aligned}\int_0^{2\pi} \mathrm{d}\varphi \int_0^{\pi} \mathrm{d}\vartheta \sin\vartheta |\mathbf{E}_2(\vartheta, \varphi)|^2 &= \frac{1}{4k_1^2} \sum_{nm} \{|a_{mn}|^2 + |b_{mn}|^2\} \\ &= \frac{1}{4k_1^2} [\mathbf{a}^{*\mathrm{T}} \quad \mathbf{b}^{*\mathrm{T}}] \begin{bmatrix} \mathbf{a} \\ \mathbf{b} \end{bmatrix},\end{aligned} \tag{5.56}$$

where $[\mathbf{a}^{\mathrm{T}} \quad \mathbf{b}^{\mathrm{T}}]$ denotes the string of the expansion coefficients of the incident field. Similarly,

$$\begin{aligned}\int_0^{2\pi} \mathrm{d}\varphi \int_0^{\pi} \mathrm{d}\vartheta \sin\vartheta |\mathbf{E}_1(\vartheta, \varphi)|^2 &= \frac{1}{4k_1^2} \sum_{nm} \left\{ \left| \sum_{n'm'} [S^{11}_{mnm'n'} a_{m'n'} + S^{12}_{mnm'n'} b_{m'n'}] \right|^2 \right. \\ &\qquad \left. + \left| \sum_{n'm'} [S^{21}_{mnm'n'} a_{m'n'} + S^{22}_{mnm'n'} b_{m'n'}] \right|^2 \right\} \\ &= \frac{1}{4k_1^2} [\mathbf{a}^{*\mathrm{T}} \quad \mathbf{b}^{*\mathrm{T}}] \boldsymbol{S}^{*\mathrm{T}} \boldsymbol{S} \begin{bmatrix} \mathbf{a} \\ \mathbf{b} \end{bmatrix}.\end{aligned} \tag{5.57}$$

Since Eq. (5.55) must hold for any incident field, we finally derive the unitarity condition for nonabsorbing scatterers (Waterman 1971; Tsang *et al.* 1985),

$$\boldsymbol{S}^{*\mathrm{T}} \boldsymbol{S} = \mathbf{E}. \tag{5.58}$$

In terms of the T matrix, Eq. (5.58) becomes

$$\mathbf{T}^{*\mathrm{T}} \mathbf{T} = -\tfrac{1}{2}(\mathbf{T}^{*\mathrm{T}} + \mathbf{T}) \tag{5.59}$$

or

$$\sum_{j=1}^{2} \sum_{n_1=1}^{\infty} \sum_{m_1=-n_1}^{n_1} (T^{jk}_{m_1 n_1 mn})^* T^{jl}_{m_1 n_1 m'n'} = -\tfrac{1}{2}[(T^{lk}_{m'n'mn})^* + T^{kl}_{mnm'n'}]. \tag{5.60a}$$

Obviously, for absorbing particles (i.e., with a non-zero imaginary part of the relative refractive index) the integral in Eq. (5.55) must be negative, thereby leading to the inequality

$$\sum_{j=1}^{2} \sum_{n_1=1}^{\infty} \sum_{m_1=-n_1}^{n_1} (T^{jk}_{m_1 n_1 mn})^* T^{jl}_{m_1 n_1 m'n'} < -\tfrac{1}{2}[(T^{lk}_{m'n'mn})^* + T^{kl}_{mnm'n'}]. \tag{5.60b}$$

This condition is equivalent to the "contractivity" of the matrix $\boldsymbol{S}$ (cf. Eq. (5.45)), i.e.,

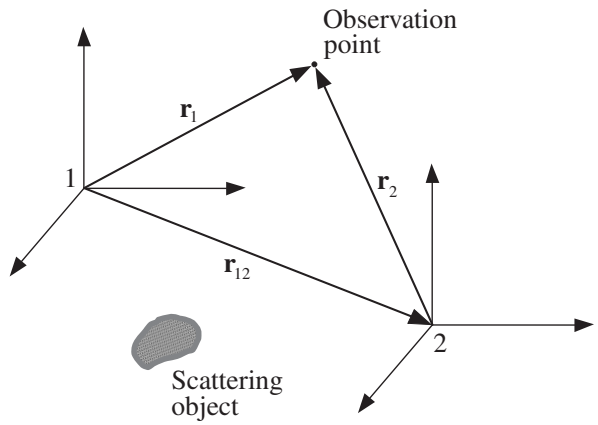

Figure 5.2. The vector $\mathbf{r}_{12}$ translates coordinate system 1 into coordinate system 2.

to the requirement that $\boldsymbol{S}$ map all nontrivial vectors into vectors with a smaller Euclidean norm. This in turn is equivalent to the requirement that $\mathbf{E}-\boldsymbol{S}^{*\mathrm{T}}\boldsymbol{S}$ must have only positive eigenvalues (see also Eq. (5.58)). Equations (5.58)–(5.60) are valid for any particle orientation with respect to the laboratory reference frame. Taking the trace of both sides of Eqs. (5.60a) and (5.60b) over the indices $\{k, l\}$ and $\{n, n'\}$, and making use of Eq. (5.36), we derive a consequence of the unitarity condition for a rotationally symmetric object provided that the z-axis of the particle reference frame is directed along the axis of rotation:

$$\sum_{k=1}^{2}\sum_{l=1}^{2}\sum_{n=\max(1,|m|)}^{\infty}\sum_{n'=\max(1,|m|)}^{\infty}|T_{mnmn'}^{kl}(P)|^2$$

$$\leq -\mathrm{Re}\sum_{n=\max(1,|m|)}^{\infty}[T_{mnmn}^{11}(P)+T_{mnmn}^{22}(P)], \qquad m=0,\pm1,\ldots, \qquad (5.61)$$

where the equality holds only for nonabsorbing scatterers (Wielaard *et al.* 1997).

5.2.4 Translation transformation rule

We saw in subsection 5.2.1 that the rotation transformation rule for vector spherical wave functions leads to a simple rotation transformation rule for the T matrix. Similarly, the translation addition theorem for vector spherical wave functions (Appendix C) can be used to derive a translation transformation rule for the T matrix (Mishchenko *et al.* 1996b).

Consider the same scattering problem in two coordinate systems that have identical spatial orientations but different origins (Fig. 5.2). Vectors $\mathbf{r}_1$ and $\mathbf{r}_2$ are position vectors of the same observation point in coordinate systems 1 and 2, respectively. The vector $\mathbf{r}_{12}$ connects the origin of coordinate system 1 with the origin of coordinate system 2, so that $\mathbf{r}_1=\mathbf{r}_{12}+\mathbf{r}_2$. The expansions of the incident field and the scattered field in the two coordinate systems are

$$\mathbf{E}^{\text{inc}}(\mathbf{r}_1) = \sum_{n=1}^{\infty}\sum_{m=-n}^{n}[a_{mn}^{(1)}\text{Rg}\mathbf{M}_{mn}(k_1\mathbf{r}_1) + b_{mn}^{(1)}\text{Rg}\mathbf{N}_{mn}(k_1\mathbf{r}_1)], \tag{5.62}$$

$$\mathbf{E}^{\text{sca}}(\mathbf{r}_1) = \sum_{n=1}^{\infty}\sum_{m=-n}^{n}[p_{mn}^{(1)}\mathbf{M}_{mn}(k_1\mathbf{r}_1) + q_{mn}^{(1)}\mathbf{N}_{mn}(k_1\mathbf{r}_1)], \qquad r_1 > r_>^{(1)}, \tag{5.63}$$

$$\mathbf{E}^{\text{inc}}(\mathbf{r}_2) = \sum_{n=1}^{\infty}\sum_{m=-n}^{n}[a_{mn}^{(2)}\text{Rg}\mathbf{M}_{mn}(k_1\mathbf{r}_2) + b_{mn}^{(2)}\text{Rg}\mathbf{N}_{mn}(k_1\mathbf{r}_2)], \tag{5.64}$$

$$\mathbf{E}^{\text{sca}}(\mathbf{r}_2) = \sum_{n=1}^{\infty}\sum_{m=-n}^{n}[p_{mn}^{(2)}\mathbf{M}_{mn}(k_1\mathbf{r}_2) + q_{mn}^{(2)}\mathbf{N}_{mn}(k_1\mathbf{r}_2)], \qquad r_2 > r_>^{(2)}, \tag{5.65}$$

where the superscripts (1) and (2) label quantities pertaining to coordinate systems 1 and 2, respectively. In Eqs. (5.63) and (5.65), $r_>^{(1)}$ and $r_>^{(2)}$ are the radii of the respective smallest circumscribing spheres of the scattering object centered at origins 1 and 2. According to the translation addition theorem (cf. Eqs. (C.66) and (C.67) of Appendix C),

$$\begin{aligned}\text{Rg}\begin{matrix}\mathbf{M}_{mn}\\ \mathbf{N}_{mn}\end{matrix}(k_1\mathbf{r}_2) = \sum_{\nu=1}^{\infty}\sum_{\mu=-\nu}^{\nu}\Bigg[&\text{Rg}\begin{matrix}A_{\mu\nu mn}\\ B_{\mu\nu mn}\end{matrix}(-k_1\mathbf{r}_{12})\text{Rg}\mathbf{M}_{\mu\nu}(k_1\mathbf{r}_1)\\ &+\text{Rg}\begin{matrix}B_{\mu\nu mn}\\ A_{\mu\nu mn}\end{matrix}(-k_1\mathbf{r}_{12})\text{Rg}\mathbf{N}_{\mu\nu}(k_1\mathbf{r}_1)\Bigg],\end{aligned} \tag{5.66}$$

$$\begin{aligned}\begin{matrix}\mathbf{M}_{mn}\\ \mathbf{N}_{mn}\end{matrix}(k_1\mathbf{r}_1) = \sum_{\nu=1}^{\infty}\sum_{\mu=-\nu}^{\nu}\Bigg[&\text{Rg}\begin{matrix}A_{\mu\nu mn}\\ B_{\mu\nu mn}\end{matrix}(k_1\mathbf{r}_{12})\mathbf{M}_{\mu\nu}(k_1\mathbf{r}_2)\\ &+\text{Rg}\begin{matrix}B_{\mu\nu mn}\\ A_{\mu\nu mn}\end{matrix}(k_1\mathbf{r}_{12})\mathbf{N}_{\mu\nu}(k_1\mathbf{r}_2)\Bigg], \qquad r_1 > r_{12}.\end{aligned} \tag{5.67}$$

The incident field and the scattered field at the observation point are, of course, independent of the choice of coordinate system. Therefore, the right-hand sides of Eqs. (5.62) and (5.64) and Eqs. (5.63) and (5.65) must be equal. Assuming for simplicity that both r_1 and r_2 in Eqs. (5.63) and (5.65) are greater than $\max(r_>^{(1)}, r_>^{(2)}, r_{12})$, we easily derive from the above equations

$$\begin{matrix}a_{\mu\nu}^{(1)}\\ b_{\mu\nu}^{(1)}\end{matrix} = \sum_{n=1}^{\infty}\sum_{m=-n}^{n}\left[\text{Rg}\begin{matrix}A_{\mu\nu mn}\\ B_{\mu\nu mn}\end{matrix}(-k_1\mathbf{r}_{12})\,a_{mn}^{(2)} + \text{Rg}\begin{matrix}B_{\mu\nu mn}\\ A_{\mu\nu mn}\end{matrix}(-k_1\mathbf{r}_{12})\,b_{mn}^{(2)}\right], \tag{5.68}$$

$$\begin{matrix}p_{\mu\nu}^{(2)}\\ q_{\mu\nu}^{(2)}\end{matrix} = \sum_{n=1}^{\infty}\sum_{m=-n}^{n}\left[\text{Rg}\begin{matrix}A_{\mu\nu mn}\\ B_{\mu\nu mn}\end{matrix}(k_1\mathbf{r}_{12})\,p_{mn}^{(1)} + \text{Rg}\begin{matrix}B_{\mu\nu mn}\\ A_{\mu\nu mn}\end{matrix}(k_1\mathbf{r}_{12})\,q_{mn}^{(1)}\right], \tag{5.69}$$

or

$$\begin{bmatrix}\mathbf{a}^{(1)}\\ \mathbf{b}^{(1)}\end{bmatrix} = \begin{bmatrix}\text{Rg}\mathbf{A}(-k_1\mathbf{r}_{12}) & \text{Rg}\mathbf{B}(-k_1\mathbf{r}_{12})\\ \text{Rg}\mathbf{B}(-k_1\mathbf{r}_{12}) & \text{Rg}\mathbf{A}(-k_1\mathbf{r}_{12})\end{bmatrix}\begin{bmatrix}\mathbf{a}^{(2)}\\ \mathbf{b}^{(2)}\end{bmatrix}, \tag{5.70}$$

$$\begin{bmatrix} \mathbf{p}^{(2)} \\ \mathbf{q}^{(2)} \end{bmatrix} = \begin{bmatrix} \mathrm{Rg}\mathbf{A}(k_1\mathbf{r}_{12}) & \mathrm{Rg}\mathbf{B}(k_1\mathbf{r}_{12}) \\ \mathrm{Rg}\mathbf{B}(k_1\mathbf{r}_{12}) & \mathrm{Rg}\mathbf{A}(k_1\mathbf{r}_{12}) \end{bmatrix} \begin{bmatrix} \mathbf{p}^{(1)} \\ \mathbf{q}^{(1)} \end{bmatrix}. \tag{5.71}$$

Since

$$\begin{bmatrix} \mathbf{p}^{(1)} \\ \mathbf{q}^{(1)} \end{bmatrix} = \begin{bmatrix} \mathbf{T}^{11}(1) & \mathbf{T}^{12}(1) \\ \mathbf{T}^{21}(1) & \mathbf{T}^{22}(1) \end{bmatrix} \begin{bmatrix} \mathbf{a}^{(1)} \\ \mathbf{b}^{(1)} \end{bmatrix}, \tag{5.72}$$

$$\begin{bmatrix} \mathbf{p}^{(2)} \\ \mathbf{q}^{(2)} \end{bmatrix} = \begin{bmatrix} \mathbf{T}^{11}(2) & \mathbf{T}^{12}(2) \\ \mathbf{T}^{21}(2) & \mathbf{T}^{22}(2) \end{bmatrix} \begin{bmatrix} \mathbf{a}^{(2)} \\ \mathbf{b}^{(2)} \end{bmatrix}, \tag{5.73}$$

we finally have

$$\begin{bmatrix} \mathbf{T}^{11}(2) & \mathbf{T}^{12}(2) \\ \mathbf{T}^{21}(2) & \mathbf{T}^{22}(2) \end{bmatrix} = \begin{bmatrix} \mathrm{Rg}\mathbf{A}(k_1\mathbf{r}_{12}) & \mathrm{Rg}\mathbf{B}(k_1\mathbf{r}_{12}) \\ \mathrm{Rg}\mathbf{B}(k_1\mathbf{r}_{12}) & \mathrm{Rg}\mathbf{A}(k_1\mathbf{r}_{12}) \end{bmatrix} \begin{bmatrix} \mathbf{T}^{11}(1) & \mathbf{T}^{12}(1) \\ \mathbf{T}^{21}(1) & \mathbf{T}^{22}(1) \end{bmatrix}$$
$$\times \begin{bmatrix} \mathrm{Rg}\mathbf{A}(-k_1\mathbf{r}_{12}) & \mathrm{Rg}\mathbf{B}(-k_1\mathbf{r}_{12}) \\ \mathrm{Rg}\mathbf{B}(-k_1\mathbf{r}_{12}) & \mathrm{Rg}\mathbf{A}(-k_1\mathbf{r}_{12}) \end{bmatrix}. \tag{5.74}$$

Note that unlike the asymptotic far-field translation transformation rule for the amplitude matrix (Eq. (2.191)), Eq. (5.74) is exact and does not involve the assumption of far-field scattering.

5.3 Extinction matrix for axially oriented particles

The rotation transformation rule for the T matrix can be used to develop efficient analytical procedures for averaging scattering characteristics over particle orientations. We begin by calculating the extinction matrix for nonspherical particles axially oriented by an external force (Mishchenko 1991b). As mentioned earlier, typical examples of axially oriented particles are interstellar dust grains oriented by cosmic magnetic fields (Martin 1978; Dolginov *et al*. 1995) and nonspherical hydrometeors in the earth atmosphere oriented by the aerodynamical force (Oguchi 1983; Liou 1992). The orientation distribution of interstellar dust grains is symmetric with respect to the direction of the local magnetic field, whereas the orientation distribution of hydrometeors is symmetric with respect to the vector of the particle velocity relative to the surrounding air mass.

By directing the z-axis of the laboratory reference frame along the axis of symmetry, we arrive at the orientation distribution function given by Eq. (3.28). Equations (2.140)–(2.146) and (5.11)–(5.14) show that in order to find the orientation-averaged extinction matrix, we must first calculate the orientation-averaged T matrix with respect to the laboratory reference frame. Assuming for simplicity that all particles have the same size and shape and taking into account that

$$\int_0^{2\pi} \mathrm{d}\alpha \exp[-\mathrm{i}(m-m')\alpha] = 2\pi\delta_{mm'}, \tag{5.75}$$

we have from Eqs. (3.28), (5.29), and (B.6)

$$\langle T^{kl}_{mnm'n'}(L)\rangle = \int_0^{2\pi} \mathrm{d}\alpha \int_0^{\pi} \mathrm{d}\beta \sin\beta \int_0^{2\pi} \mathrm{d}\gamma p_{\mathrm{o}}(\alpha, \beta, \gamma) T^{kl}_{mnm'n'}(L; \alpha, \beta, \gamma)$$

$$= \delta_{mm'} \sum_{m_1=-\min(n,n')}^{\min(n,n')} T^{kl}_{m_1nm_1n'}(P) \int_0^{\pi} \mathrm{d}\beta \sin\beta\, p_{\mathrm{o}}(\beta) d^{n}_{mm_1}(\beta) d^{n'}_{mm_1}(\beta), \qquad (5.76)$$

where $\mathbf{T}(P)$ is the T matrix in the particle reference frame. The Clebsch–Gordan expansion (B.50) and Eqs. (B.5) and (B.27) give

$$d^{n}_{mm_1}(\beta) d^{n'}_{mm_1}(\beta) = (-1)^{m+m_1} \sum_{n_1=|n-n'|}^{n+n'} C^{n_1 0}_{nm\, n'-m} P_n(\cos\beta) C^{n_1 0}_{nm_1\, n'-m_1}, \qquad (5.77)$$

where $C^{nm}_{n_1m_1\, n_2m_2}$ are Clebsch–Gordan coefficients (Appendix D). Thus

$$\langle T^{kl}_{mnm'n'}(L)\rangle = \delta_{mm'} T^{kl}_{mnn'}, \qquad k, l = 1, 2, \qquad (5.78)$$

where

$$T^{kl}_{mnn'} = \sum_{m_1=-\min(n,n')}^{\min(n,n')} \sum_{n_1=|n-n'|}^{n+n'} (-1)^{m+m_1} p_{n_1} C^{n_1 0}_{nm\, n'-m} C^{n_1 0}_{nm_1\, n'-m_1} T^{kl}_{m_1nm_1n'}(P) \qquad (5.79)$$

and

$$p_n = \int_0^{\pi} \mathrm{d}\beta \sin\beta\, P_n(\cos\beta) p_{\mathrm{o}}(\beta). \qquad (5.80)$$

In other words, the quantities p_n are coefficients in the expansion of the function $p_{\mathrm{o}}(\beta)$ in Legendre polynomials (cf. Eqs. (B.19) and (B.21)):

$$p_{\mathrm{o}}(\beta) = \sum_{n=0}^{\infty} \frac{2n+1}{2} p_n P_n(\cos\beta). \qquad (5.81)$$

Equations (5.78) and (5.79) provide a simple analytical expression of the orientation-averaged T matrix in terms of the T matrix computed in an arbitrarily chosen particle reference frame.

Substituting Eq. (5.78) in Eqs. (5.11)–(5.14) gives

$$\langle S_{11}(\hat{\mathbf{n}}, \hat{\mathbf{n}})\rangle = \frac{1}{k_1} \sum_{n=1}^{\infty} \sum_{n'=1}^{\infty} \sum_{m=-\min(n,n')}^{\min(n,n')} \mathrm{i}^{n'-n-1} \left[\frac{(2n+1)(2n'+1)}{n(n+1)n'(n'+1)}\right]^{1/2} [T^{11}_{mnn'} \pi_{mn}(\vartheta) \pi_{mn'}(\vartheta)$$

$$+ T^{21}_{mnn'} \tau_{mn}(\vartheta) \pi_{mn'}(\vartheta) + T^{12}_{mnn'} \pi_{mn}(\vartheta) \tau_{mn'}(\vartheta) + T^{22}_{mnn'} \tau_{mn}(\vartheta) \tau_{mn'}(\vartheta)], \qquad (5.82)$$

$$\langle S_{12}(\hat{\mathbf{n}}, \hat{\mathbf{n}})\rangle = \frac{1}{\mathrm{i}k_1} \sum_{n=1}^{\infty} \sum_{n'=1}^{\infty} \sum_{m=-\min(n,n')}^{\min(n,n')} \mathrm{i}^{n'-n-1} \left[\frac{(2n+1)(2n'+1)}{n(n+1)n'(n'+1)}\right]^{1/2} [T^{11}_{mnn'} \pi_{mn}(\vartheta) \tau_{mn'}(\vartheta)$$

$$+ T^{21}_{mnn'} \tau_{mn}(\vartheta) \tau_{mn'}(\vartheta) + T^{12}_{mnn'} \pi_{mn}(\vartheta) \pi_{mn'}(\vartheta) + T^{22}_{mnn'} \tau_{mn}(\vartheta) \pi_{mn'}(\vartheta)], \qquad (5.83)$$

$$\langle S_{21}(\hat{\mathbf{n}},\hat{\mathbf{n}})\rangle = \frac{\mathrm{i}}{k_1}\sum_{n=1}^{\infty}\sum_{n'=1}^{\infty}\sum_{m=-\min(n,n')}^{\min(n,n')} \mathrm{i}^{n'-n-1}\left[\frac{(2n+1)(2n'+1)}{n(n+1)n'(n'+1)}\right]^{1/2} [T^{11}_{mnn'}\tau_{mn}(\vartheta)\pi_{mn'}(\vartheta)$$
$$+T^{21}_{mnn'}\pi_{mn}(\vartheta)\pi_{mn'}(\vartheta)+T^{12}_{mnn'}\tau_{mn}(\vartheta)\tau_{mn'}(\vartheta)+T^{22}_{mnn'}\pi_{mn}(\vartheta)\tau_{mn'}(\vartheta)], \quad (5.84)$$

$$\langle S_{22}(\hat{\mathbf{n}},\hat{\mathbf{n}})\rangle = \frac{1}{k_1}\sum_{n=1}^{\infty}\sum_{n'=1}^{\infty}\sum_{m=-\min(n,n')}^{\min(n,n')} \mathrm{i}^{n'-n-1}\left[\frac{(2n+1)(2n'+1)}{n(n+1)n'(n'+1)}\right]^{1/2} [T^{11}_{mnn'}\tau_{mn}(\vartheta)\tau_{mn'}(\vartheta)$$
$$+T^{21}_{mnn'}\pi_{mn}(\vartheta)\tau_{mn'}(\vartheta)+T^{12}_{mnn'}\tau_{mn}(\vartheta)\pi_{mn'}(\vartheta)+T^{22}_{mnn'}\pi_{mn}(\vartheta)\pi_{mn'}(\vartheta)]. \quad (5.85)$$

The orientation-averaged Stokes extinction matrix per particle is obtained by substituting Eqs. (5.82)–(5.85) in Eqs. (2.140)–(2.146). Quite naturally, the axial symmetry of the particle orientation distribution makes the extinction matrix in the laboratory reference frame independent of the azimuthal angle of the incident beam.

The above equations become simpler and computationally more efficient for rotationally symmetric particles. Directing the z-axis of the particle reference frame along the axis of rotation yields symmetry relations (5.36) and (5.37). Taking into account the symmetry relation (D.7), we obtain from Eqs. (5.79), (5.82)–(5.85), (5.16), and (5.17)

$$T^{kl}_{mnn'} = (-1)^m \sum_{n_1=|n-n'|}^{n+n'} [1+(-1)^{n+n'+n_1+k+l}]p_{n_1}C^{n_1 0}_{nm\,n'-m}$$
$$\times \sum_{m_1=0}^{\min(n,n')} (-1)^{m_1}(1-\tfrac{1}{2}\delta_{m_1 0})C^{n_1 0}_{nm_1\,n'-m_1}T^{kl}_{m_1 n m_1 n'}(P), \quad (5.86)$$

$$T^{kl}_{-mnn'} = (-1)^{k+l}T^{kl}_{mnn'}, \quad (5.87)$$

$$\langle S_{11}(\hat{\mathbf{n}},\hat{\mathbf{n}})\rangle = \frac{1}{k_1}\sum_{n=1}^{\infty}\sum_{n'=1}^{\infty}\sum_{m=0}^{\min(n,n')} (2-\delta_{m0})\mathrm{i}^{n'-n-1}\left[\frac{(2n+1)(2n'+1)}{n(n+1)n'(n'+1)}\right]^{1/2}$$
$$\times[T^{11}_{mnn'}\pi_{mn}(\vartheta)\pi_{mn'}(\vartheta)+T^{21}_{mnn'}\tau_{mn}(\vartheta)\pi_{mn'}(\vartheta)$$
$$+T^{12}_{mnn'}\pi_{mn}(\vartheta)\tau_{mn'}(\vartheta)+T^{22}_{mnn'}\tau_{mn}(\vartheta)\tau_{mn'}(\vartheta)], \quad (5.88)$$

$$\langle S_{12}(\hat{\mathbf{n}},\hat{\mathbf{n}})\rangle = \langle S_{21}(\hat{\mathbf{n}},\hat{\mathbf{n}})\rangle = 0, \quad (5.89)$$

$$\langle S_{22}(\hat{\mathbf{n}},\hat{\mathbf{n}})\rangle = \frac{1}{k_1}\sum_{n=1}^{\infty}\sum_{n'=1}^{\infty}\sum_{m=0}^{\min(n,n')} (2-\delta_{m0})\mathrm{i}^{n'-n-1}\left[\frac{(2n+1)(2n'+1)}{n(n+1)n'(n'+1)}\right]^{1/2}$$
$$\times[T^{11}_{mnn'}\tau_{mn}(\vartheta)\tau_{mn'}(\vartheta)+T^{21}_{mnn'}\pi_{mn}(\vartheta)\tau_{mn'}(\vartheta)$$
$$+T^{12}_{mnn'}\tau_{mn}(\vartheta)\pi_{mn'}(\vartheta)+T^{22}_{mnn'}\pi_{mn}(\vartheta)\pi_{mn'}(\vartheta)]. \quad (5.90)$$

Finally, Eqs. (5.88)–(5.90) and (2.140)–(2.146) yield the average extinction matrix per particle:

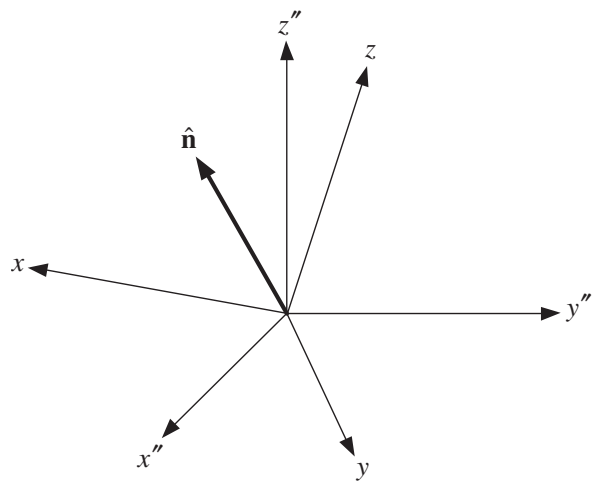

Figure 5.3. The laboratory reference frame $L\{x, y, z\}$ and the device reference frame $D\{x'', y'', z''\}$. The z-axis of the laboratory reference frame is directed along the axis of symmetry of the particle orientation distribution.

$$\langle \mathbf{K}(\vartheta)\rangle = \begin{bmatrix} \langle K_{11}(\vartheta)\rangle & \langle K_{12}(\vartheta)\rangle & 0 & 0 \\ \langle K_{12}(\vartheta)\rangle & \langle K_{11}(\vartheta)\rangle & 0 & 0 \\ 0 & 0 & \langle K_{11}(\vartheta)\rangle & \langle K_{34}(\vartheta)\rangle \\ 0 & 0 & -\langle K_{34}(\vartheta)\rangle & \langle K_{11}(\vartheta)\rangle \end{bmatrix}, \tag{5.91}$$

where

$$\langle K_{11}(\vartheta)\rangle = \frac{2\pi}{k_1}\mathrm{Im}[\langle S_{11}(\hat{\mathbf{n}}, \hat{\mathbf{n}})\rangle + \langle S_{22}(\hat{\mathbf{n}}, \hat{\mathbf{n}})\rangle], \tag{5.92}$$

$$\langle K_{12}(\vartheta)\rangle = \frac{2\pi}{k_1}\mathrm{Im}[\langle S_{11}(\hat{\mathbf{n}}, \hat{\mathbf{n}})\rangle - \langle S_{22}(\hat{\mathbf{n}}, \hat{\mathbf{n}})\rangle], \tag{5.93}$$

$$\langle K_{34}(\vartheta)\rangle = \frac{2\pi}{k_1}\mathrm{Re}[\langle S_{22}(\hat{\mathbf{n}}, \hat{\mathbf{n}})\rangle - \langle S_{11}(\hat{\mathbf{n}}, \hat{\mathbf{n}})\rangle]. \tag{5.94}$$

The reference frame associated with the measuring device (e.g., a telescope or an antenna) does not necessarily coincide with the laboratory reference frame having its z-axis directed along the axis of symmetry of the particle orientation distribution. Let $L\{x, y, z\}$ be the laboratory reference frame and $D\{x'', y'', z''\}$ the reference frame associated with the measuring device (see Fig. 5.3). Let η be the non-negative angle of rotation around $\hat{\mathbf{n}}$ that transforms the $\hat{\mathbf{n}}z$-plane into the $\hat{\mathbf{n}}z''$-plane. This angle is measured in the *clockwise* direction, when looking in the direction of $\hat{\mathbf{n}}$. Obviously, η is the angle between the meridional planes of the beam in the laboratory and device reference frames, respectively, and hence the angle between the unit vectors $\hat{\boldsymbol{\vartheta}}$ and $\hat{\boldsymbol{\vartheta}}''$ and the unit vectors $\hat{\boldsymbol{\varphi}}$ and $\hat{\boldsymbol{\varphi}}''$. We thus have for the average extinction matrix in the device reference frame:

$$\langle \mathbf{K}_{\mathrm{D}}(\hat{\mathbf{n}})\rangle = \mathbf{L}(\eta)\langle \mathbf{K}(\vartheta)\rangle \mathbf{L}(-\eta), \tag{5.95}$$

where the rotation matrix $\mathbf{L}$ is defined by Eq. (1.97).

The actual computer calculation of the orientationally averaged extinction matrix involves the following steps.

1. computation of the *T* matrix in the particle reference frame;
2. computation of the expansion coefficients p_n for a given orientation distribution function $p_o(\beta)$;
3. computation of the Clebsch–Gordan coefficients in Eq. (5.79) or Eq. (5.86);
4. computation of the orientation-averaged *T* matrix with respect to the laboratory reference frame via Eq. (5.79) for arbitrarily shaped particles or via Eq. (5.86) for rotationally symmetric particles;
5. computation of the angular functions $\pi_{mn}(\vartheta)$ and $\tau_{mn}(\vartheta)$;
6. computation of the orientation-averaged forward-scattering amplitude matrix via Eqs. (5.82)–(5.85) for arbitrarily shaped particles or via Eqs. (5.88)–(5.90) for rotationally symmetric particles;
7. computation of the orientation-averaged extinction matrix in the laboratory reference frame via Eq. (2.140)–(2.146) for arbitrarily shaped particles or via Eqs. (5.91)–(5.94) for rotationally symmetric particles;
8. computation of the orientation-averaged extinction matrix in the device reference frame via Eq. (5.95).

The computation of the *T* matrix for different types of particles will be discussed later in this chapter. Convenient and numerically stable and efficient recurrence formulas for computing the angular functions and the Clebsch–Gordan coefficients are given in Appendices B and D, respectively.

The analytical approach to computing orientation-averaged optical characteristics is a unique feature of the *T*-matrix method. It requires the *T* matrix to be computed only once, with respect to the particle reference frame, and then yields the average characteristics of a particle ensemble with respect to the laboratory reference frame by virtue of simple analytical formulas. It is not surprising, therefore, that the analytical method works much faster than the standard approach based on the numerical averaging of results computed for many discrete orientations of a nonspherical particle. Extensive timing tests have shown that the analytical averaging procedure (steps 2 through 8) is indeed very efficient and requires only a small fraction of the computer time spent on calculating the *T* matrix in the particle reference frame (step 1). This means that the *T*-matrix calculations of the extinction matrix for an axially symmetric distribution of particle orientations are nearly as fast as those for a single particle in a fixed orientation.

The analytical method for computing the orientation-averaged extinction matrix has been applied to interstellar dust grains (Mishchenko 1991b), nonspherical hydrometeors (Mishchenko 1992a), and bacterial cells and clusters of dielectric particles axially oriented by an external electrostatic field (Fucile *et al.* 1995; Khlebtsov *et al.* 1999).

5.4 Extinction cross section for randomly oriented particles

The orientation distribution function for randomly oriented particles is given by $p_{\rm o}(\beta) \equiv 1/2$ (cf. Eqs. (3.27) and (3.28)). Equations (5.76) and (B.17) then yield (Mishchenko 1990b)

$$\langle T^{kl}_{mnm'n'}(L)\rangle = \frac{\delta_{nn'}\delta_{mm'}}{2n+1}\sum_{m_1=-n}^{n} T^{kl}_{m_1nm_1n}(P), \qquad k, l = 1, 2. \tag{5.96}$$

Note that the averaged $T^{kl}(L)$ matrices are diagonal and that their elements are independent of the azimuthal indices m and m'.

Assume for simplicity that the scattering particles have a plane of symmetry. Then the extinction matrix for particles in random orientation is given by Eq. (4.32) with

$$\langle C_{\rm ext}\rangle = \frac{2\pi}{k_1}\,{\rm Im}[\langle S_{11}(\hat{\mathbf{n}}, \hat{\mathbf{n}})\rangle + \langle S_{22}(\hat{\mathbf{n}}, \hat{\mathbf{n}})\rangle]. \tag{5.97}$$

Using Eqs. (B.5), (B.6), and (B.25), it is straightforward to show that

$$\pi_{mn}(\vartheta) = \tfrac{1}{2}\sqrt{n(n+1)}[d^n_{1m}(\vartheta) + d^n_{-1m}(\vartheta)], \tag{5.98}$$

$$\tau_{mn}(\vartheta) = \tfrac{1}{2}\sqrt{n(n+1)}[d^n_{1m}(\vartheta) - d^n_{-1m}(\vartheta)]. \tag{5.99}$$

Therefore, the unitarity condition (B.47) yields

$$\sum_{m=-n}^{n}[\pi_{mn}(\vartheta)]^2 = \sum_{m=-n}^{n}[\tau_{mn}(\vartheta)]^2 = \tfrac{1}{2}n(n+1), \tag{5.100}$$

$$\sum_{m=-n}^{n}\pi_{mn}(\vartheta)\tau_{mn}(\vartheta) = 0. \tag{5.101}$$

Inserting Eqs. (5.96), (5.100), and (5.101) in Eqs. (5.11) and (5.14), we finally derive

$$\langle C_{\rm ext}\rangle = -\frac{2\pi}{k_1^2}\,{\rm Re}\sum_{n=1}^{\infty}\sum_{m=-n}^{n}[T^{11}_{mnmn}(P) + T^{22}_{mnmn}(P)] \tag{5.102}$$

(Mishchenko 1990b). This remarkably simple formula shows that the extinction cross section per particle averaged over the uniform orientation distribution is proportional to the real part of the sum of the diagonal elements of the T matrix computed in the particle reference frame.

The extinction cross section for randomly oriented particles must be invariant with respect to rotations of the coordinate system. Since the choice of the particle and laboratory reference frames is, in principle, arbitrary, we must have

$$\mathrm{Re}\sum_{n=1}^{\infty}\sum_{m=-n}^{n}[T_{mnmn}^{11}(L;\alpha,\beta,\gamma)+T_{mnmn}^{22}(L;\alpha,\beta,\gamma)]$$
$$=\mathrm{Re}\sum_{n=1}^{\infty}\sum_{m=-n}^{n}[T_{mnmn}^{11}(P)+T_{mnmn}^{22}(P)] \tag{5.103}$$

for any (α,β,γ). Indeed, Eqs. (5.29) and (B.41) yield the invariant

$$\sum_{m=-n}^{n}T_{mnmn}^{kl}(L;\alpha,\beta,\gamma)=\sum_{m=-n}^{n}T_{mnmn}^{kl}(P), \tag{5.104}$$

which leads to Eq. (5.103). The invariance of the extinction cross section with respect to translations of the coordinate system (Section 2.11) and Eq. (5.102) yield another invariant of the T matrix (see subsection 5.2.4):

$$\mathrm{Re}\sum_{nmk}T_{mnmn}^{kk}(2)=\mathrm{Re}\sum_{nmk}T_{mnmn}^{kk}(1). \tag{5.105}$$

If the scattering particles are rotationally symmetric and the z-axis of the particle reference frame is directed along the axis of rotation, then Eq. (5.37) applies, and we have

$$\langle T_{mnm'n'}^{kl}(L)\rangle=\frac{\delta_{nn'}\delta_{mm'}\delta_{kl}}{2n+1}\sum_{m_1=0}^{n}(2-\delta_{m_10})T_{m_1nm_1n}^{kl}(P),\qquad k,l=1,2, \tag{5.106}$$

$$\langle C_{\mathrm{ext}}\rangle=-\frac{2\pi}{k_1^2}\mathrm{Re}\sum_{n=1}^{\infty}\sum_{m=0}^{n}(2-\delta_{m0})[T_{mnmn}^{11}(P)+T_{mnmn}^{22}(P)]. \tag{5.107}$$

5.5 Scattering matrix for randomly oriented particles

Consider now the computation of the scattering matrix for randomly oriented particles. Following Section 4.2, we will assume that the incident wave propagates along the positive direction of the z-axis of the laboratory reference frame and that the xz-plane with $x\geq 0$ is the scattering plane. We will also assume that all particles are identical and have a plane of symmetry. Our ultimate task is to find the orientation-averaged scattering cross section per particle $\langle C_{\mathrm{sca}}\rangle$ and the elements of the normalized Stokes scattering matrix $\widetilde{\mathbf{F}}(\Theta)$. We will defer the computation of $\langle C_{\mathrm{sca}}\rangle$ to the following section and will focus now on computing the normalized scattering matrix given by Eq. (4.51), in which

$$\langle\mathbf{F}(\Theta)\rangle=\frac{1}{8\pi^2}\int_0^{2\pi}\mathrm{d}\alpha\int_0^{\pi}\mathrm{d}\beta\sin\beta\int_0^{2\pi}\mathrm{d}\gamma\,\mathbf{Z}(\vartheta^{\mathrm{sca}}=\Theta,\varphi^{\mathrm{sca}}=0;\vartheta^{\mathrm{inc}}=0,\varphi^{\mathrm{inc}}=0;\alpha,\beta,\gamma); \tag{5.108}$$

here the Euler angles of rotation α, β, and γ specify the particle orientation with respect to the laboratory reference frame (cf. Eq. (3.27)). The most straightforward

way to compute $\langle \mathbf{F}(\Theta)\rangle$ is to evaluate the integrals in Eq. (5.108) numerically by applying appropriate quadrature formulas and recomputing $\mathbf{Z}(\Theta, 0; 0, 0; \alpha, \beta, \gamma)$ for each new scattering angle and each new combination of the Euler angles (α, β, γ) (Wiscombe and Mugnai 1986; Barber and Hill 1990). However, we will demonstrate in Chapter 10 that $\mathbf{Z}(\Theta, 0; 0, 0; \alpha, \beta, \gamma)$ is a strongly oscillating function of (α, β, γ), thereby necessitating large numbers of quadrature division points in the numerical integrations. This makes the numerical averaging procedure very time-consuming, especially when results for many scattering angles are required.

We have seen in Section 4.11 that convenient representations of the elements of the normalized scattering matrix are expansions in the generalized spherical functions (4.75)–(4.80). The expansion coefficients appearing in these series are independent of the scattering angle and the polarization state of the incident and scattered beams and are functions of only the particle morphology, the size relative to the wavelength, and the relative refractive index (see subsection 5.8.2). Similarly, the particle T matrix is also a quantity independent of the incident and scattered waves and is fully determined by the particle geometry and composition. Therefore, one may expect a direct analytical relationship between the expansion coefficients and the T matrix that does not involve any angular or polarization variable. Mishchenko (1991a) showed that this relationship does exist and facilitates the development of an efficient analytical orientation-averaging procedure that avoids the time-consuming numerical integrations in Eq. (5.108).

Since many formulas become noticeably simpler in the circular-polarization representation, we begin by considering the normalized circular-polarization phase matrix defined by Eq. (4.98). By analogy with Eq. (5.108), the orientation-averaged circular-polarization phase matrix per particle $\langle \mathbf{Z}^{\mathrm{CP}}(\Theta, 0; 0, 0)\rangle$ is given by

$$\langle \mathbf{Z}^{\mathrm{CP}}(\Theta, 0; 0, 0)\rangle = \frac{1}{8\pi^2}\int_0^{2\pi} \mathrm{d}\alpha \int_0^{\pi} \mathrm{d}\beta \sin\beta \int_0^{2\pi} \mathrm{d}\gamma\, \mathbf{Z}^{\mathrm{CP}}(\Theta, 0; 0, 0; \alpha, \beta, \gamma) \tag{5.109}$$

and can be calculated using Eq. (4.97). It follows from Eqs. (5.98), (5.99), and (B.6) that

$$\pi_{mn}(0) = \delta_{m,\pm 1}\tfrac{1}{2}\sqrt{n(n+1)}, \tag{5.110}$$

$$\tau_{mn}(0) = m\delta_{m,\pm 1}\tfrac{1}{2}\sqrt{n(n+1)}. \tag{5.111}$$

Therefore, Eqs. (4.95), (5.11)–(5.14), (5.98), and (5.99) yield

$$\begin{aligned} C_{++}(\Theta, 0; 0, 0; \alpha, \beta, \gamma) = \sum_{n=1}^{\infty}\sum_{n'=1}^{\infty}\sum_{m=-n}^{n} t_{mnn'}\, d^{n}_{-1m}(\Theta)[T^{11}_{mn,-1n'}(L; \alpha, \beta, \gamma) \\ - T^{12}_{mn,-1n'}(L; \alpha, \beta, \gamma) - T^{21}_{mn,-1n'}(L; \alpha, \beta, \gamma) + T^{22}_{mn,-1n'}(L; \alpha, \beta, \gamma)], \end{aligned} \tag{5.112}$$

$$\begin{aligned} C_{+-}(\Theta, 0; 0, 0; \alpha, \beta, \gamma) = \sum_{n=1}^{\infty}\sum_{n'=1}^{\infty}\sum_{m=-n}^{n} t_{mnn'}\, d^{n}_{-1m}(\Theta)[T^{11}_{mn1n'}(L; \alpha, \beta, \gamma) \\ + T^{12}_{mn1n'}(L; \alpha, \beta, \gamma) - T^{21}_{mn1n'}(L; \alpha, \beta, \gamma) - T^{22}_{mn1n'}(L; \alpha, \beta, \gamma)], \end{aligned} \tag{5.113}$$

$$C_{-+}(\Theta, 0; 0, 0; \alpha, \beta, \gamma) = \sum_{n=1}^{\infty}\sum_{n'=1}^{\infty}\sum_{m=-n}^{n} t_{mnn'} d_{1m}^{n}(\Theta)[T_{mn,-1n'}^{11}(L; \alpha, \beta, \gamma)$$
$$-T_{mn,-1n'}^{12}(L; \alpha, \beta, \gamma) + T_{mn,-1n'}^{21}(L; \alpha, \beta, \gamma) - T_{mn,-1n'}^{22}(L; \alpha, \beta, \gamma)], \tag{5.114}$$

$$C_{--}(\Theta, 0; 0, 0; \alpha, \beta, \gamma) = \sum_{n=1}^{\infty}\sum_{n'=1}^{\infty}\sum_{m=-n}^{n} t_{mnn'} d_{1m}^{n}(\Theta)[T_{mn1n'}^{11}(L; \alpha, \beta, \gamma)$$
$$+T_{mn1n'}^{12}(L; \alpha, \beta, \gamma) + T_{mn1n'}^{21}(L; \alpha, \beta, \gamma) + T_{mn1n'}^{22}(L; \alpha, \beta, \gamma)], \tag{5.115}$$

where

$$t_{mnn'} = \frac{1}{2k_1} \mathrm{i}^{n'-n-1}(-1)^{m+1}\sqrt{(2n+1)(2n'+1)}. \tag{5.116}$$

From this point on, we will assume for simplicity that the scattering particles are rotationally symmetric, so that Eqs. (5.36) and (5.37) apply. We then use Eq. (5.29), (B.5), (B.50), (D.6), and (D.7) to derive

$$C_{++}(\Theta, 0; 0, 0; \alpha, \beta, \gamma) = \sum_{n=1}^{\infty}\sum_{m=-n}^{n}\sum_{n_1=|m-1|}^{\infty} f_{nn_1} d_{-1,-m}^{n}(\Theta) d_{1-m,0}^{n_1}(\beta)\exp[-\mathrm{i}\alpha(1-m)]B_{mnn_1}^{1}, \tag{5.117}$$

$$C_{+-}(\Theta, 0; 0, 0; \alpha, \beta, \gamma) = \sum_{n=1}^{\infty}\sum_{m=-n}^{n}\sum_{n_1=|m-1|}^{\infty} f_{nn_1} d_{-1m}^{n}(\Theta) d_{m-1,0}^{n_1}(\beta)\exp[-\mathrm{i}\alpha(m-1)]B_{mnn_1}^{2}, \tag{5.118}$$

$$C_{-+}(\Theta, 0; 0, 0; \alpha, \beta, \gamma) = \sum_{n=1}^{\infty}\sum_{m=-n}^{n}\sum_{n_1=|m-1|}^{\infty} f_{nn_1} d_{1,-m}^{n}(\Theta) d_{1-m,0}^{n_1}(\beta)\exp[-\mathrm{i}\alpha(1-m)]B_{mnn_1}^{2}, \tag{5.119}$$

$$C_{--}(\Theta, 0; 0, 0; \alpha, \beta, \gamma) = \sum_{n=1}^{\infty}\sum_{m=-n}^{n}\sum_{n_1=|m-1|}^{\infty} f_{nn_1} d_{1m}^{n}(\Theta) d_{m-1,0}^{n_1}(\beta)\exp[-\mathrm{i}\alpha(m-1)]B_{mnn_1}^{1}, \tag{5.120}$$

where

$$f_{nn_1} = \frac{1}{2\mathrm{i}k_1}(2n_1+1)\sqrt{2n+1}, \tag{5.121}$$

$$B_{mnn_1}^{j} = \sum_{n'=\max(1,|n-n_1|)}^{n+n_1} C_{nm\,n_1,1-m}^{n'1} A_{nn'n_1}^{j}, \qquad j = 1, 2, \tag{5.122}$$

$$A_{nn'n_1}^{j} = \frac{\mathrm{i}^{n'-n}}{\sqrt{2n'+1}} \sum_{m_1=-\min(n,n')}^{\min(n,n')} C_{nm_1\,n_1 0}^{n'm_1} T_{m_1nn'}^{j}, \qquad j = 1, 2, \tag{5.123}$$

$$T_{mnn'}^{1} = T_{mnmn'}^{11}(P) + T_{mnmn'}^{12}(P) + T_{mnmn'}^{21}(P) + T_{mnmn'}^{22}(P), \tag{5.124}$$

$$T_{mnn'}^{2} = T_{mnmn'}^{11}(P) + T_{mnmn'}^{12}(P) - T_{mnmn'}^{21}(P) - T_{mnmn'}^{22}(P). \tag{5.125}$$

Here, the $T_{mnmn'}^{kl}(P)$ are elements of the T matrix computed in the particle reference frame with the z-axis directed along the axis of particle symmetry and the

$C^{nm}_{n_1 m_1 n_2 m_2}$ are the Clebsch–Gordan coefficients (Appendix D). Finally, using Eqs. (4.97), (5.108), (4.98), (4.104), (B.17), and (B.30), we derive the following formulas that can be used in practical computer calculations:

$$g^s_{00} = \sum_{n=1}^{\infty} \sum_{i=\max(1,|n-s|)}^{n+s} h_{sni}\, C^{i1}_{n1\,s0} \sum_{m=-\min(n,i)}^{\min(n,i)} C^{im}_{nm\,s0}\, D^{00}_{mni}, \tag{5.126}$$

$$g^s_{0,-0} = \sum_{n=1}^{\infty} \sum_{i=\max(1,|n-s|)}^{n+s} h_{sni}\,(-1)^{n+i+s}\, C^{i1}_{n1\,s0} \sum_{m=-\min(n,i)}^{\min(n,i)} C^{im}_{nm\,s0}\, D^{0,-0}_{mni}, \tag{5.127}$$

$$g^s_{22} = \sum_{n=1}^{\infty} \sum_{i=\max(1,|n-s|)}^{n+s} h_{sni}\, C^{i1}_{n,-1\,s2} \sum_{m=m_{\min}}^{m_{\max}} C^{i,2-m}_{n,-m\,s2}\, D^{22}_{mni}, \tag{5.128}$$

$$g^s_{2,-2} = \sum_{n=1}^{\infty} \sum_{i=\max(1,|n-s|)}^{n+s} h_{sni}\,(-1)^{n+i+s}\, C^{i1}_{n,-1\,s2} \sum_{m=m_{\min}}^{m_{\max}} C^{i,2-m}_{n,-m\,s2}\, D^{2,-2}_{mni}, \tag{5.129}$$

$$g^s_{02} = -\sum_{n=1}^{\infty} \sum_{i=\max(1,|n-s|)}^{n+s} h_{sni}\, C^{i1}_{n1\,s0} \sum_{m=m_{\min}}^{m_{\max}} C^{i,2-m}_{n,-m\,s2}\, D^{02}_{mni}, \tag{5.130}$$

where

$$h_{sni} = \frac{(2s+1)\pi}{k_1^2 \langle C_{\text{sca}} \rangle} \sqrt{\frac{2n+1}{2i+1}}, \tag{5.131}$$

$$D^{00}_{mni} = \sum_{n_1=|m-1|}^{\infty} (2n_1+1)\, B^1_{mnn_1} (B^1_{min_1})^*, \tag{5.132}$$

$$D^{0,-0}_{mni} = \sum_{n_1=|m-1|}^{\infty} (2n_1+1)\, B^2_{mnn_1} (B^2_{min_1})^*, \tag{5.133}$$

$$D^{22}_{mni} = \sum_{n_1=|m-1|}^{\infty} (2n_1+1)\, B^1_{mnn_1} (B^1_{2-m,in_1})^*, \tag{5.134}$$

$$D^{2,-2}_{mni} = \sum_{n_1=|m-1|}^{\infty} (2n_1+1)\, B^2_{mnn_1} (B^2_{2-m,in_1})^*, \tag{5.135}$$

$$D^{02}_{mni} = \sum_{n_1=|m-1|}^{\infty} (2n_1+1)\, B^2_{mnn_1} (B^1_{2-m,in_1})^*, \tag{5.136}$$

$$m_{\min} = \max(-n, -i+2), \qquad m_{\max} = \min(n, i+2), \tag{5.137}$$

and $\langle C_{\text{sca}} \rangle$ is the orientation-averaged scattering cross section per particle.

Thus the computation of the expansion coefficients appearing in Eqs. (4.75)–(4.80) and the normalized Stokes scattering matrix involves the following steps:

1. computation of the T matrix of an axially symmetric scatterer in the particle reference frame, i.e., the matrix $\mathbf{T}(P)$;
2. computation of the orientation-averaged scattering cross section per particle

$\langle C_{\text{sca}} \rangle$ (Section 5.6);

3. computation of the quantities $T^{j}_{mnn'}$ via Eqs. (5.124) and (5.125);
4. computation of the quantities $A^{j}_{nn'n_1}$ via Eq. (5.123);
5. computation of the quantities $B^{j}_{mnn_1}$ via Eq. (5.122);
6. computation of the quantities D^{pq}_{mni} via Eqs. (5.132)–(5.136);
7. computation of the circular-polarization expansion coefficients g^{s}_{pq} via Eqs. (5.126)–(5.130);
8. computation of the Stokes-representation expansion coefficients via Eqs. (4.109)–(4.114);
9. computation of the elements of the normalized Stokes scattering matrix via Eqs. (4.75)–(4.80).

The most time-consuming part of any computations based on the *T*-matrix method is the evaluation of multiply nested summations. An important advantage of the analytical averaging procedure is that the maximal order of nested summations is only three, thereby making this procedure ideally suited to the development of an efficient computer code. Detailed timing tests have shown that the analytical averaging over orientations (steps 2–9) requires only a small fraction of the computer time needed to compute the $\mathbf{T}(P)$ matrix (Mishchenko 1991a, 1993; Mackowski and Mishchenko 1996; Wielaard *et al.* 1997). It comes as no surprise, therefore, that direct comparisons of the performance of the analytical and numerical methods indicate that the former is faster by a factor of several tens (Mishchenko 1991a; W. M. F. Wauben, personal communication). An equally rewarding feature of the analytical averaging procedure is the demonstration of the close connection between the *T*-matrix method and the concept of expanding the elements of the normalized scattering matrix in generalized spherical functions (or Wigner *d*-functions).

The analytical averaging method has been applied to a wide class of rotationally symmetric scatterers, such as spheroids, finite circular cylinders, osculating spheres, so-called Chebyshev particles, and linear chains of spheres (Sections 5.11 and 5.13). Mackowski and Mishchenko (1996) extended the method to asymmetric particles.

Khlebtsov (1992) and Fucile *et al.* (1993) developed theoretical formalisms that exploit the rotation transformation property of the *T* matrix, but are not based on expanding the normalized scattering matrix in generalized spherical functions and do not exploit the advantage of performing as much work analytically as possible. Borghese *et al.* (2001) considered several simple analytical orientation distribution functions other than the uniform orientation distribution. Paramonov (1995) straightforwardly extended the analytical orientation-averaging approach to arbitrary quadratically integrable orientation distribution functions. However, the resulting formulas involve highly nested summations, and their efficient numerical implementation may often be problematic. In such cases the standard averaging approach employing numerical integrations over Euler orientation angles in Eq. (3.19) and based on formulas of Section 2.4 may prove to be more efficient (cf. Battaglia *et al.* 2001).

5.6 Scattering cross section for randomly oriented particles

The scattering cross section per particle for randomly oriented particles with a plane of symmetry is given by Eq. (4.40), in which $\langle \mathbf{F}(\Theta) \rangle$ is given by Eq. (5.108). Rewriting Eq. (2.123) as

$$\mathbf{Z}(\hat{\mathbf{n}}^{\rm sca}, \hat{\mathbf{n}}^{\rm inc}) = \mathbf{A}^{-1}\mathbf{Z}^{\rm CP}(\hat{\mathbf{n}}^{\rm sca}, \hat{\mathbf{n}}^{\rm inc})\mathbf{A}, \tag{5.138}$$

we have

$$\begin{aligned} Z_{11}(\Theta, 0; 0, 0; \alpha, \beta, \gamma) = \tfrac{1}{2}[&Z_{00}^{\rm CP}(\Theta, 0; 0, 0; \alpha, \beta, \gamma) + Z_{0,-0}^{\rm CP}(\Theta, 0; 0, 0; \alpha, \beta, \gamma) \\ &+ Z_{-00}^{\rm CP}(\Theta, 0; 0, 0; \alpha, \beta, \gamma) + Z_{-0,-0}^{\rm CP}(\Theta, 0; 0, 0; \alpha, \beta, \gamma)]. \end{aligned} \tag{5.139}$$

Recall that Eqs. (5.112)–(5.115) are valid for arbitrary particles. Therefore, using Eqs. (4.97), (5.29), (B.17), and (B.47) and taking into account Eq. (5.75), we derive

$$\langle C_{\rm sca} \rangle = \frac{2\pi}{k_1^2} \sum_{n=1}^{\infty} \sum_{m=-n}^{n} \sum_{n'=1}^{\infty} \sum_{m'=-n'}^{n'} \sum_{k=1}^{2} \sum_{l=1}^{2} |T_{mnm'n'}^{kl}(P)|^2 \tag{5.140}$$

(Mishchenko 1991c). Thus the scattering cross section per particle averaged over the uniform orientation distribution is proportional to the sum of the squares of the absolute values of the T-matrix elements computed in the particle reference frame. This formula is as simple as Eq. (5.102) for the orientation-averaged extinction cross section. If the scattering particles are rotationally symmetric and the z-axis of the particle reference frame coincides with the axis of rotation, then Eqs. (5.36), (5.37), and (5.140) yield

$$\langle C_{\rm sca} \rangle = \frac{2\pi}{k_1^2} \sum_{n=1}^{\infty} \sum_{n'=1}^{\infty} \sum_{m=0}^{\min(n, n')} \sum_{k=1}^{2} \sum_{l=1}^{2} (2 - \delta_{m0})\, |T_{mnmn'}^{kl}(P)|^2. \tag{5.141}$$

After the average extinction and scattering cross sections per particle have been calculated, the average absorption cross section and the single-scattering albedo can be found from Eqs. (4.44) and (4.45).

Like the extinction cross section, the scattering cross section for randomly oriented particles must be invariant with respect to rotations of the coordinate system. Since the choice of the particle and laboratory reference frames is arbitrary, Eq. (5.140) implies that

$$\sum_{mm'} |T_{mnm'n'}^{kl}(L; \alpha, \beta, \gamma)|^2 = \sum_{mm'} |T_{mnm'n'}^{kl}(P)|^2 \tag{5.142}$$

for any (α, β, γ). This invariant indeed follows from Eqs. (5.29) and (B.41). The invariance of the scattering cross section with respect to translations of the coordinate system (Section 2.11) and Eq. (5.140) yield yet another invariant of the T matrix (cf. subsection 5.2.4):

$$\sum_{nmn'm'kl} |T^{kl}_{mnm'n'}(2)|^2 = \sum_{nmn'm'kl} |T^{kl}_{mnm'n'}(1)|^2. \tag{5.143}$$

The energy conservation law implies that $\langle C_{\text{sca}} \rangle \le \langle C_{\text{ext}} \rangle$, and we have from Eqs. (5.102) and (5.140)

$$\sum_{n=1}^{\infty}\sum_{m=-n}^{n}\sum_{n'=1}^{\infty}\sum_{m'=-n'}^{n'}\sum_{k=1}^{2}\sum_{l=1}^{2} |T^{kl}_{mnm'n'}(P)|^2 \le -\text{Re}\sum_{n=1}^{\infty}\sum_{m=-n}^{n}[T^{11}_{mnmn}(P)+T^{22}_{mnmn}(P)], \tag{5.144}$$

where the equality holds only for nonabsorbing particles. This formula can also be derived by taking the trace of both sides of Eqs. (5.60a) and (5.60b) over the indices $\{n, n'\}$, $\{m, m'\}$, and $\{k, l\}$.

5.7 Spherically symmetric scatterers (Lorenz–Mie theory)

All *T*-matrix equations become considerably simpler and reduce to the corresponding equations of the Lorenz–Mie theory when the scattering particle is spherically symmetric and Eqs. (5.42)–(5.44) apply. Specifically, Eqs. (5.11)–(5.14) become

$$S_{11}(\hat{\mathbf{n}}^{\text{sca}}, \hat{\mathbf{n}}^{\text{inc}}) = \frac{\text{i}}{k_1}\sum_{n=1}^{\infty}\sum_{m=-n}^{n}\frac{2n+1}{n(n+1)}\exp[\text{i}m(\varphi^{\text{sca}}-\varphi^{\text{inc}})]$$
$$\times[b_n\pi_{mn}(\vartheta^{\text{sca}})\pi_{mn}(\vartheta^{\text{inc}})+a_n\tau_{mn}(\vartheta^{\text{sca}})\tau_{mn}(\vartheta^{\text{inc}})], \tag{5.145}$$

$$S_{12}(\hat{\mathbf{n}}^{\text{sca}}, \hat{\mathbf{n}}^{\text{inc}}) = \frac{1}{k_1}\sum_{n=1}^{\infty}\sum_{m=-n}^{n}\frac{2n+1}{n(n+1)}\exp[\text{i}m(\varphi^{\text{sca}}-\varphi^{\text{inc}})]$$
$$\times[b_n\pi_{mn}(\vartheta^{\text{sca}})\tau_{mn}(\vartheta^{\text{inc}})+a_n\tau_{mn}(\vartheta^{\text{sca}})\pi_{mn}(\vartheta^{\text{inc}})], \tag{5.146}$$

$$S_{21}(\hat{\mathbf{n}}^{\text{sca}}, \hat{\mathbf{n}}^{\text{inc}}) = -\frac{1}{k_1}\sum_{n=1}^{\infty}\sum_{m=-n}^{n}\frac{2n+1}{n(n+1)}\exp[\text{i}m(\varphi^{\text{sca}}-\varphi^{\text{inc}})]$$
$$\times[b_n\tau_{mn}(\vartheta^{\text{sca}})\pi_{mn}(\vartheta^{\text{inc}})+a_n\pi_{mn}(\vartheta^{\text{sca}})\tau_{mn}(\vartheta^{\text{inc}})], \tag{5.147}$$

$$S_{22}(\hat{\mathbf{n}}^{\text{sca}}, \hat{\mathbf{n}}^{\text{inc}}) = \frac{\text{i}}{k_1}\sum_{n=1}^{\infty}\sum_{m=-n}^{n}\frac{2n+1}{n(n+1)}\exp[\text{i}m(\varphi^{\text{sca}}-\varphi^{\text{inc}})]$$
$$\times[b_n\tau_{mn}(\vartheta^{\text{sca}})\tau_{mn}(\vartheta^{\text{inc}})+a_n\pi_{mn}(\vartheta^{\text{sca}})\pi_{mn}(\vartheta^{\text{inc}})]. \tag{5.148}$$

Quite naturally, now the amplitude matrix depends only on the difference of the azimuthal angles of the incident and scattered waves rather than on their specific values. The amplitude matrix becomes especially simple when the incident wave propagates along the positive direction of the *z*-axis of the laboratory reference frame and $\varphi^{\text{sca}} = \varphi^{\text{inc}}$:

$$S_{11}(\vartheta^{\rm sca}, \varphi^{\rm inc}; 0, \varphi^{\rm inc}) = \frac{\rm i}{k_1}\sum_{n=1}^{\infty}\frac{2n+1}{\sqrt{n(n+1)}}[b_n\pi_{1n}(\vartheta^{\rm sca}) + a_n\tau_{1n}(\vartheta^{\rm sca})]$$

$$= \frac{\rm i}{k_1}\sum_{n=1}^{\infty}\frac{2n+1}{n(n+1)}[b_n\pi_n(\vartheta^{\rm sca}) + a_n\tau_n(\vartheta^{\rm sca})], \qquad (5.149)$$

$$S_{12}(\vartheta^{\rm sca}, \varphi^{\rm inc}; 0, \varphi^{\rm inc}) = S_{21}(\vartheta^{\rm sca}, \varphi^{\rm inc}; 0, \varphi^{\rm inc}) \equiv 0, \qquad (5.150)$$

$$S_{22}(\vartheta^{\rm sca}, \varphi^{\rm inc}; 0, \varphi^{\rm inc}) = \frac{\rm i}{k_1}\sum_{n=1}^{\infty}\frac{2n+1}{\sqrt{n(n+1)}}[b_n\tau_{1n}(\vartheta^{\rm sca}) + a_n\pi_{1n}(\vartheta^{\rm sca})]$$

$$= \frac{\rm i}{k_1}\sum_{n=1}^{\infty}\frac{2n+1}{n(n+1)}[b_n\tau_n(\vartheta^{\rm sca}) + a_n\pi_n(\vartheta^{\rm sca})] \qquad (5.151)$$

(cf. Eqs. (5.16)–(5.17) and (5.110)–(5.111)), where $\pi_n = \sqrt{n(n+1)}\,\pi_{1n}$ and $\tau_n = \sqrt{n(n+1)}\,\tau_{1n}$. If we take into account that the definition of associated Legendre functions adopted by Bohren and Huffman (1983) differs from ours by a factor $(-1)^m$ and use Eqs. (B.5) and (B.28), it becomes obvious that Eqs. (5.149)–(5.151) are equivalent to Eqs. (4.74) and (4.75) of Bohren and Huffman. In view of Eq. (5.150), we can easily show that the normalized Stokes scattering matrix for a spherically symmetric particle is given by Eq. (4.65) with

$$a_1(\Theta) \equiv a_2(\Theta) = \frac{2\pi}{C_{\rm sca}}\{|S_{11}(\Theta, 0; 0, 0)|^2 + |S_{22}(\Theta, 0; 0, 0)|^2\}, \qquad (5.152)$$

$$a_3(\Theta) \equiv a_4(\Theta) = \frac{4\pi}{C_{\rm sca}}{\rm Re}\{S_{11}(\Theta, 0; 0, 0)\,S_{22}^*(\Theta, 0; 0, 0)\}, \qquad (5.153)$$

$$b_1(\Theta) = \frac{2\pi}{C_{\rm sca}}\{|S_{11}(\Theta, 0; 0, 0)|^2 - |S_{22}(\Theta, 0; 0, 0)|^2\}, \qquad (5.154)$$

$$b_2(\Theta) = \frac{4\pi}{C_{\rm sca}}{\rm Im}\{S_{11}(\Theta, 0; 0, 0)\,S_{22}^*(\Theta, 0; 0, 0)\}. \qquad (5.155)$$

Equations (5.102) and (5.140) yield

$$C_{\rm ext} = \frac{2\pi}{k_1^2}{\rm Re}\sum_{n=1}^{\infty}(2n+1)(b_n + a_n), \qquad (5.156)$$

$$C_{\rm sca} = \frac{2\pi}{k_1^2}\sum_{n=1}^{\infty}(2n+1)\{|b_n|^2 + |a_n|^2\}. \qquad (5.157)$$

One way of calculating the coefficients in the expansions (4.75)–(4.80) is to evaluate numerically the integrals in Eqs. (4.81)–(4.86) after substituting Eqs. (5.152)–(5.155). One can also use closed-form analytical formulas that directly ex-

press the expansion coefficients in terms of the Lorenz–Mie coefficients a_n and b_n and so bypass the numerical angular integration. These formulas are a special case of the general formulation outlined in Section 5.5 and are derived as follows. We first write

$$C_{++}(\Theta, 0; 0, 0) = C_{--}(\Theta, 0; 0, 0) = \frac{\mathrm{i}}{2k_1}\sum_{n=1}^{\infty}(2n+1)(b_n + a_n)d_{11}^n(\Theta), \qquad (5.158)$$

$$C_{+-}(\Theta, 0; 0, 0) = C_{-+}(\Theta, 0; 0, 0) = \frac{\mathrm{i}}{2k_1}\sum_{n=1}^{\infty}(2n+1)(b_n - a_n)d_{-11}^n(\Theta) \qquad (5.159)$$

(cf. Eqs. (4.95), (5.98), (5.99), and (5.149)–(5.151)). We then substitute Eqs. (5.158) and (5.159) into Eq. (4.97) and expand the products of two *d*-functions in the Clebsch–Gordan series of Eq. (B.50). Finally, using Eqs. (4.98), (4.105), (B.5), (B.30), and (B.33) and switching from Clebsch–Gordan coefficients to 3*j* symbols (Appendix D), which are more symmetric, we obtain

$$g_{jj}^s = \frac{\pi(2s+1)}{k_1^2 C_{\mathrm{sca}}}\left\{2\,\mathrm{Re}\sum_{n=1}^{\infty}\sum_{m=M}^{s+n}\begin{pmatrix} s & m & n \\ j & -1 & 1-j \end{pmatrix}^2 (2n+1)(2m+1)(a_n^* + b_n^*)(a_m + b_m)\right.$$
$$\left. + \sum_{n=1}^{\infty}\begin{pmatrix} s & n & n \\ j & -1 & 1-j \end{pmatrix}^2 (2n+1)^2 |a_n + b_n|^2\right\}, \qquad j = 0, 2, \qquad (5.160)$$

$$g_{j,-j}^s = \frac{\pi(2s+1)}{k_1^2 C_{\mathrm{sca}}}\left\{2\,\mathrm{Re}\sum_{n=1}^{\infty}\sum_{m=M}^{s+n}\begin{pmatrix} s & m & n \\ j & -1 & 1-j \end{pmatrix}^2 (-1)^{s+m+n}\right.$$
$$\times(2n+1)(2m+1)(a_n^* - b_n^*)(a_m - b_m)$$
$$\left. + (-1)^s\sum_{n=1}^{\infty}\begin{pmatrix} s & n & n \\ j & -1 & 1-j \end{pmatrix}^2 (2n+1)^2 |a_n - b_n|^2\right\}, \quad j = 0, 2, \quad (5.161)$$

$$g_{02}^s = \frac{\pi(2s+1)}{k_1^2 C_{\mathrm{sca}}}\left\{\sum_{n=1}^{\infty}\sum_{m=M}^{s+n}\begin{pmatrix} s & m & n \\ 0 & -1 & 1 \end{pmatrix}\begin{pmatrix} s & m & n \\ 2 & -1 & -1 \end{pmatrix}(2n+1)(2m+1)\right.$$
$$\times[(a_m^* + b_m^*)(a_n - b_n) + (-1)^{s+m+n}(a_n^* + b_n^*)(a_m - b_m)]$$
$$\left. + \sum_{n=1}^{\infty}\begin{pmatrix} s & n & n \\ 0 & -1 & 1 \end{pmatrix}\begin{pmatrix} s & n & n \\ 2 & -1 & -1 \end{pmatrix}(2n+1)^2(a_n^* + b_n^*)(a_n - b_n)\right\}, \quad (5.162)$$

where $M = \max(s-n, n+1)$. These formulas were first derived by Domke (1975) and later corrected by Mishchenko (1990c). Finally, the Stokes-representation expansion coefficients are calculated using Eqs. (4.109)–(4.114). An alternative analytical method for computing the expansion coefficients was developed by Bugaenko (1976).

Taking into account that

$$\begin{pmatrix} 1 & m & n \\ 0 & -1 & 1 \end{pmatrix}$$

$$= (-1)^{n+1}[(n-1)(n+2) - m(m+1)]$$

$$\times \left[\frac{n(n+1)}{(n+m)(n+m+1)(n+m+2)m(m+1)(n-m+1)!(m-n+1)!} \right]^{1/2} \tag{5.163}$$

(cf. Eq. (45) in Section 8.5 of Varshalovich *et al*. (1988) and Eq. (D.8)) and using Eqs. (4.92) and (4.109), we derive, after somewhat tedious but simple algebra,

$$\langle \cos\Theta \rangle = \frac{4\pi}{k_1^2 C_{\text{sca}}} \text{Re} \sum_{n=1}^{\infty} \left[\frac{n(n+2)}{n+1} (a_n a_{n+1}^* + b_n b_{n+1}^*) + \frac{2n+1}{n(n+1)} a_n b_n^* \right] \tag{5.164}$$

(Debye 1909). The radiation force exerted on the spherical particle and the cross section for radiation pressure can be found from Eqs. (4.42), (4.43), (5.156), (5.157), and (5.164).

5.8 Extended boundary condition method

The attractive mathematical formalism outlined in the previous sections would serve little practical purpose if there were no efficient numerical techniques for computing the T matrix for various kinds of particles. Fortunately, several such techniques have been developed for both simple single-body particles and clusters composed of simple monomers. In this section we will discuss the computation of the T matrix for simple particles, while the following section will deal with clusters.

5.8.1 General formulation

The standard scheme for computing the T matrix for simple particles is based on the extended boundary condition method (EBCM) developed by Waterman (1965, 1971). Consider a finite scattering object in the form of a single homogeneous body occupying a region V_{INT} bounded by a closed surface S and imbedded in an infinite homogeneous, isotropic, nonmagnetic, and nonabsorbing medium (Fig. 5.4). The region V_{INT} is filled with an isotropic nonmagnetic material and is centered at the origin of the particle reference frame. The infinite region exterior to the particle is denoted by V_{EXT}. The electric fields in the regions V_{EXT} and V_{INT} satisfy Eqs. (2.3) and (2.4), respectively.

The vector Green's theorem for a regular surface S_1 bounding a volume V_1 is (Morse and Feshbach 1953)

$$\int_{V_1} \mathrm{d}V [\mathbf{a} \cdot (\nabla \times \nabla \times \mathbf{b}) - \mathbf{b} \cdot (\nabla \times \nabla \times \mathbf{a})] = \int_{S_1} \mathrm{d}S\, \hat{\mathbf{n}} \cdot [\mathbf{b} \times (\nabla \times \mathbf{a}) - \mathbf{a} \times (\nabla \times \mathbf{b})], \tag{5.165}$$

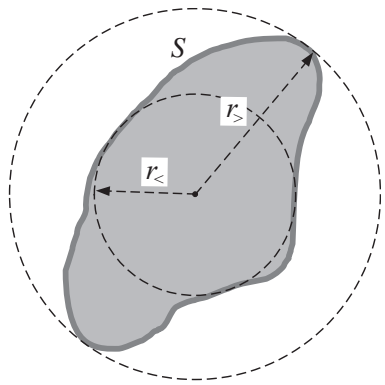

Figure 5.4. Cross section of an arbitrarily shaped, homogeneous scattering object bounded by a closed surface *S*. $r_>$ is the radius of the smallest circumscribing sphere centered at the origin of the particle coordinate system and $r_<$ is the radius of the largest concentric inscribed sphere.

where $\hat{\mathbf{n}}$ is the unit vector along the local outward normal to the surface. We apply Eq. (5.165) to the exterior region V_{EXT} and insert $\mathbf{a} = \mathbf{E}$ and $\mathbf{b} = \overleftrightarrow{G}(\mathbf{r}, \mathbf{r}') \cdot \mathbf{c}$, where $\overleftrightarrow{G}(\mathbf{r}, \mathbf{r}')$ is the free space dyadic Green's function, Eq. (2.13), and $\mathbf{c}$ is an arbitrary constant vector. The surface integral on the right-hand side of Eq. (5.165) is the sum of two integrals, an integral over the spherical surface S_∞ bounding the exterior region at infinity and an integral over the particle surface *S*. In view of Eqs. (2.3) and (2.8), Eq. (5.165) becomes

$$\left.\begin{array}{ll} \mathbf{E}(\mathbf{r}') \cdot \mathbf{c} & \text{if } \mathbf{r}' \in V_{\mathrm{EXT}} \\ 0 & \text{if } \mathbf{r}' \in V_{\mathrm{INT}} \end{array}\right\} = \left[-\int_{S_\infty} + \int_S \right] \mathrm{d}S\, \hat{\mathbf{n}} \cdot \Big([\nabla \times \mathbf{E}(\mathbf{r})] \times [\overleftrightarrow{G}(\mathbf{r}, \mathbf{r}') \cdot \mathbf{c}] + \mathbf{E}(\mathbf{r}) \times \{\nabla \times [\overleftrightarrow{G}(\mathbf{r}, \mathbf{r}') \cdot \mathbf{c}]\} \Big), \quad (5.166)$$

where $\hat{\mathbf{n}}$ is the local normal at either S_∞ or *S*; it is directed away from the particle. Since $\mathbf{c}$ is arbitrary, it can be cancelled out on both sides of Eq. (5.166). In view of Eqs. (2.20), (2.21), and (2.24), the contribution of the scattered field to the integral over S_∞ on the right-hand side of Eq. (5.166) vanishes. Therefore, the integral over S_∞ is independent of the presence of the particle and thus supplies the incident field at $\mathbf{r}'$. Hence we have for $\mathbf{r}' \in V_{\mathrm{EXT}}$

$$\mathbf{E}(\mathbf{r}') = \mathbf{E}^{\mathrm{inc}}(\mathbf{r}') + \mathbf{E}^{\mathrm{sca}}(\mathbf{r}'), \quad (5.167)$$

$$\mathbf{E}^{\mathrm{sca}}(\mathbf{r}') = \int_S \mathrm{d}S \{ \mathrm{i}\omega\mu_0 [\hat{\mathbf{n}} \times \mathbf{H}_+(\mathbf{r})] \cdot \overleftrightarrow{G}(\mathbf{r}, \mathbf{r}') + [\hat{\mathbf{n}} \times \mathbf{E}_+(\mathbf{r})] \cdot [\nabla \times \overleftrightarrow{G}(\mathbf{r}, \mathbf{r}')] \}, \quad (5.168)$$

where we have used Eq. (2.1) with $\mu_1 = \mu_0$ and the identities

$$\mathbf{a} \cdot (\mathbf{b} \times \mathbf{c}) = (\mathbf{a} \times \mathbf{b}) \cdot \mathbf{c}, \quad (5.169)$$

$$\mathbf{a} \cdot (\mathbf{b} \times \overleftrightarrow{C}) = (\mathbf{a} \times \mathbf{b}) \cdot \overleftrightarrow{C}. \quad (5.170)$$

The subscript plus in Eq. (5.168) indicates that the electric and magnetic fields inside the integral are those on the *exterior* side of the surface *S*. For $\mathbf{r}' \in V_{\mathrm{INT}}$,

$$\mathbf{E}^{\text{inc}}(\mathbf{r}') = -\int_S \mathrm{d}S\{\mathrm{i}\omega\mu_0[\hat{\mathbf{n}}\times\mathbf{H}_+(\mathbf{r})]\cdot\overleftrightarrow{G}(\mathbf{r},\mathbf{r}')+[\hat{\mathbf{n}}\times\mathbf{E}_+(\mathbf{r})]\cdot[\nabla\times\overleftrightarrow{G}(\mathbf{r},\mathbf{r}')]\}. \tag{5.171}$$

Equation (5.171) is called the extended boundary condition because it analytically extends $\mathbf{r}'$ to the interior region. The gist of the extended boundary condition method is that one finds the fields $\mathbf{E}_+(\mathbf{r})$ and $\mathbf{H}_+(\mathbf{r})$ on the exterior side of the particle surface using Eq. (5.171) and, assuming that the incident field is known, then calculates the scattered field using Eq. (5.168).

The free space dyadic Green's function can be expressed in terms of vector spherical wave functions according to Eq. (C.61). Let $r_>$ be the radius of the smallest circumscribing sphere of the scattering particle centered at the origin and $r_<$ be the radius of the largest concentric inscribed sphere (cf. Fig. 5.4). For all $r' < r_<$ and all r on S, we have $r' < r$. Therefore, substituting Eq. (C.61) in Eq. (5.171), we obtain

$$\mathbf{E}^{\text{inc}}(\mathbf{r}') = \sum_{n=1}^{\infty}\sum_{m=-n}^{n}[a_{mn}\mathrm{Rg}\mathbf{M}_{mn}(k_1\mathbf{r}')+b_{mn}\mathrm{Rg}\mathbf{N}_{mn}(k_1\mathbf{r}')], \qquad r' < r_<, \tag{5.172}$$

$$\begin{matrix} a_{mn} \\ b_{mn} \end{matrix} = k_1(-1)^m\int_S \mathrm{d}S\left\{\omega\mu_0[\hat{\mathbf{n}}\times\mathbf{H}_+(\mathbf{r})]\cdot\begin{matrix}\mathbf{M}_{-mn}(k_1r,\vartheta,\varphi)\\ \mathbf{N}_{-mn}(k_1r,\vartheta,\varphi)\end{matrix}\right.$$
$$\left.-\mathrm{i}k_1[\hat{\mathbf{n}}\times\mathbf{E}_+(\mathbf{r})]\cdot\begin{matrix}\mathbf{N}_{-mn}(k_1r,\vartheta,\varphi)\\ \mathbf{M}_{-mn}(k_1r,\vartheta,\varphi)\end{matrix}\right\}. \tag{5.173}$$

Similarly, for all $r' > r_>$ and all r on S, we have $r < r'$. Therefore, substituting Eq. (C.61) into Eq. (5.168) yields

$$\mathbf{E}^{\text{sca}}(\mathbf{r}') = \sum_{n=1}^{\infty}\sum_{m=-n}^{n}[p_{mn}\mathbf{M}_{mn}(k_1\mathbf{r}')+q_{mn}\mathbf{N}_{mn}(k_1\mathbf{r}')], \qquad r' > r_>, \tag{5.174}$$

$$\begin{matrix} p_{mn} \\ q_{mn} \end{matrix} = -k_1(-1)^m\int_S \mathrm{d}S\left\{\omega\mu_0[\hat{\mathbf{n}}\times\mathbf{H}_+(\mathbf{r})]\cdot\begin{matrix}\mathrm{Rg}\mathbf{M}_{-mn}(k_1r,\vartheta,\varphi)\\ \mathrm{Rg}\mathbf{N}_{-mn}(k_1r,\vartheta,\varphi)\end{matrix}\right.$$
$$\left.-\mathrm{i}k_1[\hat{\mathbf{n}}\times\mathbf{E}_+(\mathbf{r})]\cdot\begin{matrix}\mathrm{Rg}\mathbf{N}_{-mn}(k_1r,\vartheta,\varphi)\\ \mathrm{Rg}\mathbf{M}_{-mn}(k_1r,\vartheta,\varphi)\end{matrix}\right\}. \tag{5.175}$$

In order to compute the expansion coefficients of the scattered field via Eq. (5.175), we need first to find the electric and magnetic fields on the exterior side of the particle surface from Eq. (5.173). We will assume that the electric field everywhere inside the scattering object can be expanded in regular vector spherical wave functions of the *interior* wave equation:

$$\mathbf{E}(\mathbf{r}) = \sum_{n'=1}^{\infty}\sum_{m'=-n'}^{n'}[c_{m'n'}\mathrm{Rg}\mathbf{M}_{m'n'}(k_2\mathbf{r})+d_{m'n'}\mathrm{Rg}\mathbf{N}_{m'n'}(k_2\mathbf{r})], \qquad \mathbf{r}\in V_{\text{INT}}, \tag{5.176}$$

where k_2 is the wave number in the interior region. In view of Eq. (2.2) with $\mu_2(\mathbf{r})\equiv\mu_0$ and Eqs. (C.14) and (C.15), the matching magnetic field expansion is

$$\mathbf{H}(\mathbf{r}) = \frac{k_2}{\mathrm{i}\omega\mu_0}\sum_{n'=1}^{\infty}\sum_{m'=-n'}^{n'}[d_{m'n'}\mathrm{Rg}\mathbf{M}_{m'n'}(k_2\mathbf{r})+c_{m'n'}\mathrm{Rg}\mathbf{N}_{m'n'}(k_2\mathbf{r})], \qquad \mathbf{r}\in V_{\text{INT}}. \tag{5.177}$$

The boundary conditions require continuity of the tangential components of the electric and magnetic fields, i.e.,

$$\left.\begin{aligned}\hat{\mathbf{n}}\times\mathbf{E}_+(\mathbf{r})=\hat{\mathbf{n}}\times\mathbf{E}_-(\mathbf{r})\\ \hat{\mathbf{n}}\times\mathbf{H}_+(\mathbf{r})=\hat{\mathbf{n}}\times\mathbf{H}_-(\mathbf{r})\end{aligned}\right\},\qquad \mathbf{r}\in S, \tag{5.178}$$

where the subscript minus labels the fields on the *interior* side of the particle surface (cf. Eqs. (1.13) and (1.15)). Substituting Eqs. (5.176)–(5.178) into Eq. (5.173) and using Eq. (5.169), we have

$$\begin{bmatrix}\mathbf{a}\\ \mathbf{b}\end{bmatrix}=\mathbf{Q}\begin{bmatrix}\mathbf{c}\\ \mathbf{d}\end{bmatrix}=\begin{bmatrix}\mathbf{Q}^{11} & \mathbf{Q}^{12}\\ \mathbf{Q}^{21} & \mathbf{Q}^{22}\end{bmatrix}\begin{bmatrix}\mathbf{c}\\ \mathbf{d}\end{bmatrix}, \tag{5.179}$$

where

$$Q^{11}_{mnm'n'}=-\mathrm{i}k_1k_2J^{21}_{mnm'n'}-\mathrm{i}k_1^2J^{12}_{mnm'n'}, \tag{5.180}$$

$$Q^{12}_{mnm'n'}=-\mathrm{i}k_1k_2J^{11}_{mnm'n'}-\mathrm{i}k_1^2J^{22}_{mnm'n'}, \tag{5.181}$$

$$Q^{21}_{mnm'n'}=-\mathrm{i}k_1k_2J^{22}_{mnm'n'}-\mathrm{i}k_1^2J^{11}_{mnm'n'}, \tag{5.182}$$

$$Q^{22}_{mnm'n'}=-\mathrm{i}k_1k_2J^{12}_{mnm'n'}-\mathrm{i}k_1^2J^{21}_{mnm'n'}, \tag{5.183}$$

and

$$\begin{bmatrix}J^{11}_{mnm'n'}\\ J^{12}_{mnm'n'}\\ J^{21}_{mnm'n'}\\ J^{22}_{mnm'n'}\end{bmatrix}=(-1)^m\int_S \mathrm{d}S\,\hat{\mathbf{n}}\cdot\begin{bmatrix}\mathrm{Rg}\mathbf{M}_{m'n'}(k_2r,\vartheta,\varphi)\times\mathbf{M}_{-mn}(k_1r,\vartheta,\varphi)\\ \mathrm{Rg}\mathbf{M}_{m'n'}(k_2r,\vartheta,\varphi)\times\mathbf{N}_{-mn}(k_1r,\vartheta,\varphi)\\ \mathrm{Rg}\mathbf{N}_{m'n'}(k_2r,\vartheta,\varphi)\times\mathbf{M}_{-mn}(k_1r,\vartheta,\varphi)\\ \mathrm{Rg}\mathbf{N}_{m'n'}(k_2r,\vartheta,\varphi)\times\mathbf{N}_{-mn}(k_1r,\vartheta,\varphi)\end{bmatrix}. \tag{5.184}$$

Similarly, substituting Eqs. (5.176)–(5.178) into Eq. (5.175) yields

$$\begin{bmatrix}\mathbf{p}\\ \mathbf{q}\end{bmatrix}=-\mathrm{Rg}\mathbf{Q}\begin{bmatrix}\mathbf{c}\\ \mathbf{d}\end{bmatrix}=-\begin{bmatrix}\mathrm{Rg}\mathbf{Q}^{11} & \mathrm{Rg}\mathbf{Q}^{12}\\ \mathrm{Rg}\mathbf{Q}^{21} & \mathrm{Rg}\mathbf{Q}^{22}\end{bmatrix}\begin{bmatrix}\mathbf{c}\\ \mathbf{d}\end{bmatrix}, \tag{5.185}$$

where

$$\mathrm{Rg}Q^{11}_{mnm'n'}=-\mathrm{i}k_1k_2\mathrm{Rg}J^{21}_{mnm'n'}-\mathrm{i}k_1^2\,\mathrm{Rg}J^{12}_{mnm'n'}, \tag{5.186}$$

$$\mathrm{Rg}Q^{12}_{mnm'n'}=-\mathrm{i}k_1k_2\mathrm{Rg}J^{11}_{mnm'n'}-\mathrm{i}k_1^2\,\mathrm{Rg}J^{22}_{mnm'n'}, \tag{5.187}$$

$$\mathrm{Rg}Q^{21}_{mnm'n'}=-\mathrm{i}k_1k_2\mathrm{Rg}J^{22}_{mnm'n'}-\mathrm{i}k_1^2\,\mathrm{Rg}J^{11}_{mnm'n'}, \tag{5.188}$$

$$\mathrm{Rg}Q^{22}_{mnm'n'}=-\mathrm{i}k_1k_2\mathrm{Rg}J^{12}_{mnm'n'}-\mathrm{i}k_1^2\,\mathrm{Rg}J^{21}_{mnm'n'}, \tag{5.189}$$

and

$$\begin{bmatrix}\mathrm{Rg}J^{11}_{mnm'n'}\\ \mathrm{Rg}J^{12}_{mnm'n'}\\ \mathrm{Rg}J^{21}_{mnm'n'}\\ \mathrm{Rg}J^{22}_{mnm'n'}\end{bmatrix}=(-1)^m\int_S \mathrm{d}S\,\hat{\mathbf{n}}\cdot\begin{bmatrix}\mathrm{Rg}\mathbf{M}_{m'n'}(k_2r,\vartheta,\varphi)\times\mathrm{Rg}\mathbf{M}_{-mn}(k_1r,\vartheta,\varphi)\\ \mathrm{Rg}\mathbf{M}_{m'n'}(k_2r,\vartheta,\varphi)\times\mathrm{Rg}\mathbf{N}_{-mn}(k_1r,\vartheta,\varphi)\\ \mathrm{Rg}\mathbf{N}_{m'n'}(k_2r,\vartheta,\varphi)\times\mathrm{Rg}\mathbf{M}_{-mn}(k_1r,\vartheta,\varphi)\\ \mathrm{Rg}\mathbf{N}_{m'n'}(k_2r,\vartheta,\varphi)\times\mathrm{Rg}\mathbf{N}_{-mn}(k_1r,\vartheta,\varphi)\end{bmatrix}. \tag{5.190}$$

Comparing Eqs. (5.8), (5.179), and (5.185), we finally derive

$$\mathbf{T}(P) = -(\mathrm{Rg}\mathbf{Q})\,\mathbf{Q}^{-1}. \tag{5.191}$$

This formula expresses the elements of the T matrix in terms of integrals of vector products of vector spherical wave functions over the particle surface. The surface integrals in Eqs. (5.184) and (5.190) are usually calculated using appropriate coordinate systems and quadrature formulas. For example, in spherical coordinates the surface S is defined by the formula

$$\mathbf{r}(\vartheta, \varphi) = r(\vartheta, \varphi)\hat{\mathbf{r}}, \tag{5.192}$$

and we have (cf. Guggenheimer 1977)

$$\begin{aligned} \mathrm{d}S\,\hat{\mathbf{n}}(\mathbf{r}) &= \left[\frac{\partial \mathbf{r}}{\partial \vartheta} \times \frac{\partial \mathbf{r}}{\partial \varphi}\right] \mathrm{d}\vartheta\,\mathrm{d}\varphi \\ &= \left[r^2 \sin\vartheta\,\hat{\mathbf{r}} - r\sin\vartheta \frac{\partial r}{\partial \vartheta}\hat{\boldsymbol{\vartheta}} - r\frac{\partial r}{\partial \varphi}\hat{\boldsymbol{\varphi}}\right] \mathrm{d}\vartheta\,\mathrm{d}\varphi. \end{aligned} \tag{5.193}$$

Our derivation of the EBCM is similar to those given by Waterman (1971) and Tsang *et al.* (1985) and explicitly avoids invoking the Rayleigh hypothesis (cf. Section 5.1). Alternative derivations and formulations have been discussed by Barber and Yeh (1975), Ström (1975), Agarwal (1976), Bates and Wall (1977), Morita (1979), and Ström and Zheng (1987). The derivation given by Waterman (1979) made it especially clear that the EBCM is not based on the Rayleigh hypothesis and that the scattering objects need not be convex and close to spherical in order to ensure the validity of the method. It is interesting that in fact the EBCM can be derived from the Rayleigh hypothesis (Bates 1975; Chew 1995; Schmidt *et al.* 1998). This does not mean, however, that the EBCM is equivalent to the Rayleigh hypothesis or requires it to be valid (Lewin 1970). The equivalence of the two approaches would follow from a reciprocal derivation of the Rayleigh hypothesis from the EBCM, but it remains unclear whether such a derivation exists.

Peterson and Ström (1974) extended the EBCM to layered scatterers (see also Bringi and Seliga 1977; Wang and Barber 1979). Scattering by more general composite objects was considered by Ström and Zheng (1988) and Zheng and Ström (1989). Lakhtakia *et al.* (1985b) and Lakhtakia (1991) applied the EBCM to light scattering by chiral particles embedded in an achiral isotropic or chiral host medium.

The EBCM is a quite general technique and is applicable to arbitrarily shaped homogeneous and composite particles. However, relatively few attempts have been made to compute light scattering by bodies lacking rotational symmetry such as triaxial ellipsoids (Schneider and Peden 1988; Schneider *et al.* 1991), cubes (Laitinen and Lumme 1998; Wriedt and Comberg 1998; Wriedt and Doicu 1998a), finite hexagonal cylinders (Baran *et al.* 2001a,b; Havemann and Baran 2001), and general polyhedral cylinders of finite length (Kahnert 2001a). As we will show in subsection 5.8.3, Eqs. (5.180)–(5.184) and (5.186)–(5.190) become much simpler for bodies with

rotation symmetry and result in more efficient computer algorithms. Furthermore, we have seen in earlier sections of this chapter that the computation of scattering and absorption characteristics for rotationally symmetric particles in fixed, partial, and random orientations is also significantly less involved, owing to the symmetry relations (5.36) and (5.37). This explains why many EBCM codes have been specifically designed to deal with rotationally symmetric scatterers (e.g., Wiscombe and Mugnai 1986; Barber and Hill 1990; Mishchenko and Travis 1998; Quirantes 1999).

5.8.2 Scale invariance rule

Examination of Eqs. (5.180)–(5.184) and (5.186)–(5.191) leads to an important result, as follows. If we multiply all particle dimensions by a constant factor f (thereby not changing the particle shape) and multiply the wave numbers k_1 and k_2 for the exterior and interior regions, respectively, by the factor $1/f$ then the elements of the T matrix do not change. This "scale invariance" rule can be reformulated as follows. If the particle geometry is characterized by the shape and a typical dimension a (for example, the largest or the smallest particle dimension or the radius of a surface- or volume-equivalent sphere) then the elements of the T matrix do not depend on specific values of a, k_1, and k_2, but rather depend on the product of a and k_1, traditionally called the size parameter x, and the ratio of k_2 to k_1, which is simply the relative refractive index $m = k_2/k_1 = m_2/m_1$. (The size parameter can also be expressed, in terms of the wavelength of the incident wave in the exterior region $\lambda_1 = 2\pi/k_1$, as $x = 2\pi a/\lambda_1$.) Obviously, all scattering characteristics that involve only the elements of the T matrix also obey the scale invariance rule. Equations (5.11)–(5.14) show that the products of k_1 and the elements of the amplitude matrix are such characteristics. As a consequence, the scale invariance rule is also obeyed by: the products of k_1^2 and the elements of the phase and scattering matrices; the products of k_1^2 and the optical cross sections; the products of k_1^2 and the extinction matrix elements; the efficiency factors; the elements of the normalized scattering matrix; the coefficients in the expansions of the elements of the normalized scattering matrix in generalized spherical functions; the single-scattering albedo; and the asymmetry parameter. In general, the scale invariance rule applies to any dimensionless scattering characteristic. Although we have explicitly derived the scale invariance rule only for homogeneous particles, it can be shown to follow from Eqs. (2.18) and (2.27) for particles with arbitrary morphology (Mishchenko 2005).

The scale invariance rule can be very helpful in practice because it makes a single computation or measurement applicable to all couplets {size, wavelength} with the same ratio of size to wavelength, provided that the relative refractive index does not change. In particular, we will see in Section 8.2 that this rule underlies the basic idea of the microwave analog technique for laboratory measurements of electromagnetic scattering by small particles.

5.8.3 Rotationally symmetric particles

If the scattering particle is rotationally symmetric and the z-axis of the particle reference frame is directed along the axis of rotation then

$$\mathbf{r}(\vartheta, \varphi) = r(\vartheta)\hat{\mathbf{r}}, \tag{5.194}$$

$$\mathrm{d}S\hat{\mathbf{n}}(\mathbf{r}) = r^2 \sin\vartheta \left(\hat{\mathbf{r}} - \frac{r_\vartheta}{r} \hat{\boldsymbol{\vartheta}} \right) \mathrm{d}\vartheta \mathrm{d}\varphi, \tag{5.195}$$

where $r_\vartheta = \partial r / \partial \vartheta$. Therefore, the φ - integration in Eq. (5.184) gives simply $2\pi\delta_{mm'}$ (cf. Eq. (5.75)). Using Appendix C and Eqs. (5.16) and (5.17), we get

$$\begin{aligned} J^{11}_{mnm'n'} = &-\frac{\mathrm{i}}{2}\delta_{mm'}\left[\frac{(2n+1)(2n'+1)}{n(n+1)n'(n'+1)}\right]^{1/2} \\ &\times \int_{-1}^{+1} \mathrm{d}(\cos\vartheta) r^2 h_n^{(1)}(k_1 r) j_{n'}(k_2 r)[\pi_{mn}(\vartheta)\tau_{mn'}(\vartheta) + \tau_{mn}(\vartheta)\pi_{mn'}(\vartheta)], \end{aligned} \tag{5.196}$$

$$\begin{aligned} J^{12}_{mnm'n'} = &\frac{1}{2}\delta_{mm'}\left[\frac{(2n+1)(2n'+1)}{n(n+1)n'(n'+1)}\right]^{1/2} \\ &\times \int_{-1}^{+1} \mathrm{d}(\cos\vartheta) r^2 j_{n'}(k_2 r)\left\{\frac{1}{k_1 r}\frac{\mathrm{d}}{\mathrm{d}(k_1 r)}[k_1 r h_n^{(1)}(k_1 r)]\right. \\ &\left.\times[\pi_{mn}(\vartheta)\pi_{mn'}(\vartheta) + \tau_{mn}(\vartheta)\tau_{mn'}(\vartheta)] + \frac{r_\vartheta}{r} n(n+1)\frac{h_n^{(1)}(k_1 r)}{k_1 r} d^n_{0m}(\vartheta)\tau_{mn'}(\vartheta)\right\}, \end{aligned} \tag{5.197}$$

$$\begin{aligned} J^{21}_{mnm'n'} = &-\frac{1}{2}\delta_{mm'}\left[\frac{(2n+1)(2n'+1)}{n(n+1)n'(n'+1)}\right]^{1/2} \\ &\times \int_{-1}^{+1} \mathrm{d}(\cos\vartheta) r^2 h_n^{(1)}(k_1 r)\left\{\frac{1}{k_2 r}\frac{\mathrm{d}}{\mathrm{d}(k_2 r)}[k_2 r j_{n'}(k_2 r)]\right. \\ &\left.\times[\pi_{mn}(\vartheta)\pi_{mn'}(\vartheta) + \tau_{mn}(\vartheta)\tau_{mn'}(\vartheta)] + \frac{r_\vartheta}{r} n'(n'+1)\frac{j_{n'}(k_2 r)}{k_2 r}\tau_{mn}(\vartheta) d^{n'}_{0m}(\vartheta)\right\}, \end{aligned} \tag{5.198}$$

$$\begin{aligned} J^{22}_{mnm'n'} = &-\frac{\mathrm{i}}{2}\delta_{mm'}\left[\frac{(2n+1)(2n'+1)}{n(n+1)n'(n'+1)}\right]^{1/2} \\ &\times \int_{-1}^{+1} \mathrm{d}(\cos\vartheta) r^2 \left(\frac{1}{k_1 r}\frac{\mathrm{d}}{\mathrm{d}(k_1 r)}[k_1 r h_n^{(1)}(k_1 r)]\frac{1}{k_2 r}\frac{\mathrm{d}}{\mathrm{d}(k_2 r)}[k_2 r j_{n'}(k_2 r)]\right. \\ &\times[\pi_{mn}(\vartheta)\tau_{mn'}(\vartheta) + \tau_{mn}(\vartheta)\pi_{mn'}(\vartheta)] \\ &+ \frac{r_\vartheta}{r}\left\{ n(n+1)\frac{h_n^{(1)}(k_1 r)}{k_1 r}\frac{1}{k_2 r}\frac{\mathrm{d}}{\mathrm{d}(k_2 r)}[k_2 r j_{n'}(k_2 r)]\right. \\ &\left.\left. + \frac{1}{k_1 r}\frac{\mathrm{d}}{\mathrm{d}(k_1 r)}[k_1 r h_n^{(1)}(k_1 r)] n'(n'+1)\frac{j_{n'}(k_2 r)}{k_2 r}\right\}\pi_{mn}(\vartheta) d^{n'}_{0m}(\vartheta)\right). \end{aligned} \tag{5.199}$$

Corresponding formulas for $\mathrm{Rg}J^{kl}_{mnm'n'}$ are obtained from Eqs. (5.196)–(5.199) by replacing $h_n^{(1)}(k_1 r)$ with $j_n(k_1 r)$. Equations (5.196)–(5.199) are equivalent to Eqs. (39a)–(39d) on pp. 187 and 188 of Tsang *et al.* (1985), but we use Wigner *d*-functions instead of associated Legendre functions. As discussed in Appendix B, the computation of the Wigner *d*-functions using the recurrence relation of Eq. (B.22) is numerically stable and accurate, whereas the corresponding recurrence relation for the associated Legendre functions leads to computer overflows for large n and $|m|$.

Equations (5.179)–(5.191) and (5.196)–(5.199) show that the matrices $\mathbf{Q}$, $\mathrm{Rg}\mathbf{Q}$, and $\mathbf{T}(P)$ can be regrouped such that they become block-diagonal with each block corresponding to a different m. Since there is no coupling between the different m indices, each block is independent of all other blocks and can be computed separately. This results in significant savings of computer resources, especially for particles larger than the wavelength. An additional saving of computer time can be achieved by restricting the computer calculations to non-negative m and using the symmetry relation (5.37). Since $\pi_{0n}(\vartheta) \equiv 0$ (cf. Eq. (5.16)), Eqs. (5.196) and (5.199) yield

$$Q^{12}_{0n0n'} \equiv 0, \qquad Q^{21}_{0n0n'} \equiv 0, \tag{5.200}$$

$$\mathrm{Rg}Q^{12}_{0n0n'} \equiv 0, \qquad \mathrm{Rg}Q^{21}_{0n0n'} \equiv 0. \tag{5.201}$$

Therefore, $T^{12}_{0n0n'}(P) \equiv 0$ and $T^{21}_{0n0n'}(P) \equiv 0$, in agreement with Eq. (5.37).

The integrals in Eqs. (5.196)–(5.199) are usually evaluated by means of a Gauss quadrature applied to the interval $[-1, +1]$:

$$\int_{-1}^{+1} \mathrm{d}x\, f(x) \approx \sum_{p=1}^{N_\mathrm{G}} w_p f(x_p), \tag{5.202}$$

where x_p and w_p are quadrature division points and weights, respectively (e.g., Krylov 1962; Abramowitz and Stegun 1964). The quadrature must contain a large enough number N_G of division points to resolve the angular variation of the integrands, which may be very rapid for highly aspherical particles.

For particles with a plane of symmetry perpendicular to the axis of rotation, such as spheroids and circular cylinders,

$$r(\pi - \vartheta) = r(\vartheta), \tag{5.203}$$

$$r_\vartheta(\pi - \vartheta) = -r_\vartheta(\vartheta). \tag{5.204}$$

Therefore, the symmetry relations (cf. Eqs. (5.16), (5.17), (5.32), (5.33), and (B.7))

$$\pi_{mn}(\pi - \vartheta) = (-1)^{m+n} \pi_{mn}(\vartheta), \tag{5.205}$$

$$\tau_{mn}(\pi - \vartheta) = (-1)^{m+n+1} \tau_{mn}(\vartheta), \tag{5.206}$$

$$d^n_{0m}(\pi - \vartheta) = (-1)^{m+n} d^n_{0m}(\vartheta) \tag{5.207}$$

and Eqs. (5.196)–(5.199) yield

$$Q^{11}_{mnmn'} = Q^{22}_{mnmn'} = \mathrm{Rg}Q^{11}_{mnmn'} = \mathrm{Rg}Q^{22}_{mnmn'} = 0 \tag{5.208}$$

unless $n+n'$ is even and

$$Q^{12}_{mnmn'} = Q^{21}_{mnmn'} = \mathrm{Rg}Q^{12}_{mnmn'} = \mathrm{Rg}Q^{21}_{mnmn'} = 0 \tag{5.209}$$

unless $n+n'$ is odd, in full agreement with Eqs. (5.39) and (5.40). Equations (5.208) and (5.209) reduce the number of non-vanishing matrix elements by a factor of 2. Furthermore, the non-vanishing elements are computed twice as fast because one can restrict the summation in Eq. (5.202) to $1 \le p \le N_{\mathrm{G}}/2$ (assuming that N_{G} is even) and then double the result.

5.8.4 Convergence

Although expansions (5.2), (5.3) and (5.6), (5.7) and hence the T matrix are infinite, in general, in practical computer calculations they must be cut off to a finite size by truncating all expansions at an $n = n_{\max}$. This size depends on the required accuracy of computations and is found by increasing the size of the $\mathbf{Q}$ and Rg$\mathbf{Q}$ matrices in Eq. (5.191) until an accuracy criterion is satisfied. As an example, the dotted curve in Fig. 5.5(a) shows the quantity

$$\max\left\{\frac{\left|\langle C_{\mathrm{ext}}(n_{\max})\rangle - \langle C_{\mathrm{ext}}(n_{\max}-1)\rangle\right|}{\langle C_{\mathrm{ext}}(n_{\max})\rangle}, \frac{\left|\langle C_{\mathrm{sca}}(n_{\max})\rangle - \langle C_{\mathrm{sca}}(n_{\max}-1)\rangle\right|}{\langle C_{\mathrm{sca}}(n_{\max})\rangle}\right\} \tag{5.210}$$

versus $n_{\max}$ for randomly oriented oblate spheroids with an aspect ratio of 3, relative refractive index $m = 1.5 + \mathrm{i}0.02$, and surface-equivalent-sphere size parameter $x_{\mathrm{s}} = 2\pi r_{\mathrm{s}}/\lambda_1 = 15$, where r_{s} is the surface-equivalent-sphere radius and $\lambda_1 = 2\pi/k_1$ is the wavelength of the incident light in the surrounding medium. The results were obtained with a FORTRAN code employing double-precision (REAL*8 and COMPLEX*16) floating-point variables. The matrix $\mathbf{Q}$ was inverted using the standard Gaussian elimination scheme with partial pivoting (Forsythe *et al.* 1977). It is apparent that, for these particles, the EBCM provides a good convergence rate and excellent numerical accuracy.

It turns out, however, that numerical stability of the EBCM can become significantly worse in calculations for (partially) concave particles and particles with very large real and/or imaginary parts of the relative refractive index, large size parameters, and/or extreme geometries such as spheroids or cylinders with large aspect ratios. The broken curve in Fig. 5.5(a) exemplifies the unstable behavior of the double-precision EBCM calculations for a more challenging case of randomly oriented prolate spheroids with an aspect ratio of 4, relative refractive index $m = 1.5 + \mathrm{i}0.02$, and surface-equivalent-sphere size parameter $x_{\mathrm{s}} = 16$. The instability arises because different elements of the matrix $\mathbf{Q}$ can differ by many orders of magnitude, thereby making the numerical calculation of the inverse matrix $\mathbf{Q}^{-1}$ an ill-conditioned

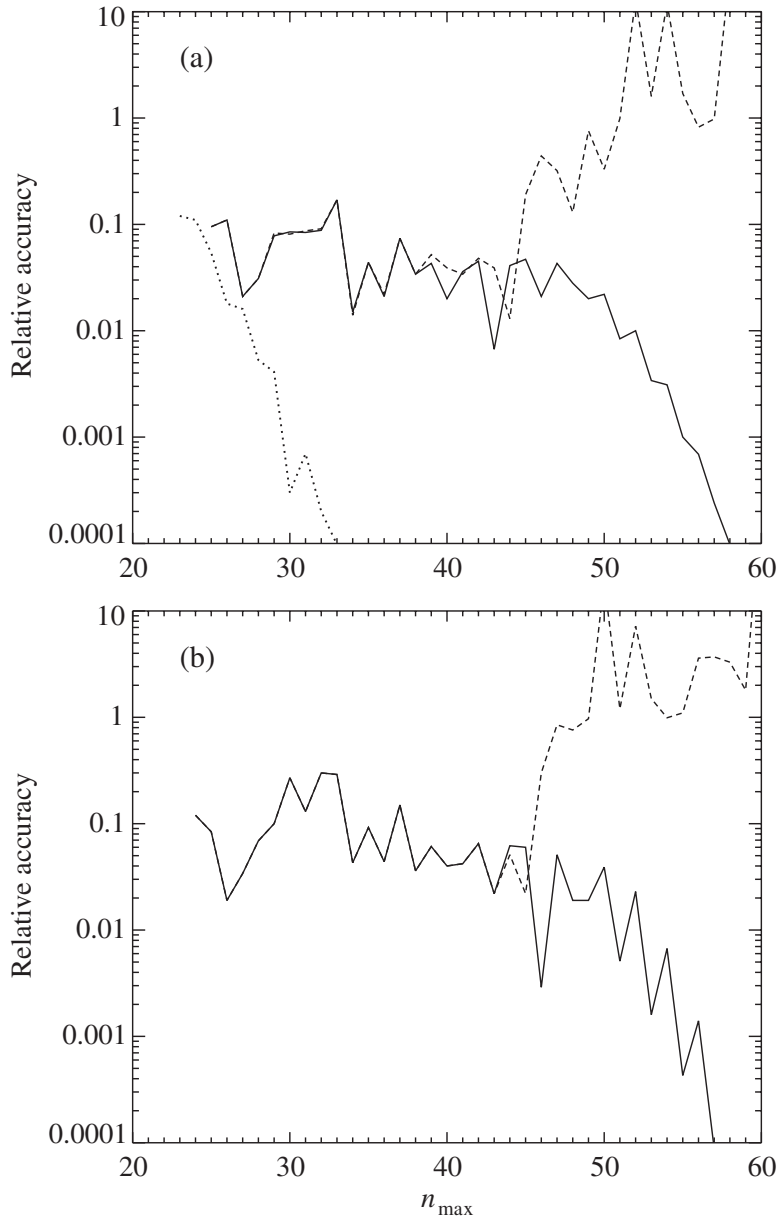

Figure 5.5. Convergence of different EBCM codes in computations for various kinds of particle (see text).

process strongly influenced by round-off errors. Because of this ill-conditioned nature, even small numerical errors in the computed elements of the $\mathbf{Q}$ matrix can result in large errors in the elements of the inverse matrix $\mathbf{Q}^{-1}$. The round-off errors become increasingly significant with increasing particle size parameter and/or aspect ratio and rapidly accumulate with increasing size of the $\mathbf{Q}$ matrix. As a result, the EBCM computations can become very slowly convergent or even divergent (Barber 1977; Varadan and Varadan 1980; Wiscombe and Mugnai 1986).

Efficient approaches for overcoming the numerical-instability problem in computing the T matrix for highly elongated particles are the so-called iterative EBCM (IEBCM) and a closely related multiple multipole EBCM (otherwise known as the null-field method with discrete sources) (Iskander *et al.* 1983, 1989b; Doicu and Wriedt 1997a,b; Wriedt and Doicu 1998a; Doicu 1999; Doicu *et al.* 2000). The main idea of the IEBCM is to represent the internal field by several sub-domain spherical function expansions centered on the major axis of an elongated scatterer. These sub-domain expansions are linked to each other by being explicitly matched in the appropriate overlapping zones. The IEBCM has been used to compute light scattering and absorption by highly elongated, absorbing and weakly absorbing dielectric scatterers with aspect ratios as large as 17. In some cases the use of the IEBCM instead of the regular EBCM has permitted stable computations at more than quadruple the former maximal convergent size parameter.

The disadvantage of the IEBCM is that its numerical stability is achieved at the expense of a considerable increase in computer code complexity and required computer time. Moreover, the IEBCM does not generate a single-expansion T matrix that could be used in the analytical orientation-averaging procedures. The latter problem was specifically addressed by Doicu and Wriedt (1999).

Mishchenko and Travis (1994a) showed that an efficient general approach to stabilizing the numerical process of inverting the $\mathbf{Q}$ matrix is to improve the accuracy with which this matrix is calculated and inverted. Specifically, they suggested calculating the elements of the $\mathbf{Q}$ matrix and performing the matrix inversion using extended-precision (REAL*16 and COMPLEX*32) instead of double-precision floating-point variables. As an example, the solid curve in Fig. 5.5(a) was computed using an extended-precision EBCM code and shows a good convergence rate and a quite acceptable accuracy for the same particles that could not be handled by the double-precision code (the broken curve). Extensive checks have demonstrated that using the extended-precision EBCM code more than doubles the maximal size parameter for which convergent results can be obtained. Timing tests performed on IBM RISC workstations have shown that the use of extended-precision arithmetic slows down computations by a factor of only 5–6. The key features of this approach are its simplicity and the fact that little additional programming effort and extra memory are required.

The numerical instability of the EBCM becomes especially noticeable for nonabsorbing or weakly absorbing particles. To ameliorate this problem, Waterman (1973) and Lakhtakia *et al.* (1984, 1985a) proposed to exploit the unitarity property of the T matrix for nonabsorbing scatterers, Eq. (5.59). Their technique is based on the so-called iterative orthogonalization of the T matrix and generates numerically stable results for elongated and flattened spheroids with large aspect ratios. The obvious disadvantage of this technique is that it applies only to particles with zero absorption. Wielaard *et al.* (1997) demonstrated that a superior approach is to invert the $\mathbf{Q}$ matrix using a special form of the so-called LU-factorization method. This approach is applicable to absorbing as well as nonabsorbing particles and increases the maximal

convergent size parameter for nonabsorbing and weakly absorbing scatterers several times. Figure 5.5(b) illustrates the performance of this technique in application to randomly oriented prolate spheroids with an aspect ratio of 4, relative refractive index $m = 1.5$, and surface-equivalent-sphere size parameter $x_s = 16$. The broken curve shows that the extended-precision EBCM code based on the Gaussian elimination scheme with partial pivoting fails to produce convergence, whereas the extended-precision code exploiting the special LU-factorization method generates very accurate results.

5.8.5 Lorenz–Mie coefficients

Consider finally the simplest case, a homogeneous spherical particle having a radius a. Using Eqs. (5.98), (5.99), and (B.17), it is easy to show that

$$\int_{-1}^{+1} \mathrm{d}(\cos\vartheta)[\pi_{mn}(\vartheta)\tau_{mn'}(\vartheta) + \tau_{mn}(\vartheta)\pi_{mn'}(\vartheta)] = 0 \tag{5.211}$$

and

$$\int_{-1}^{+1} \mathrm{d}(\cos\vartheta)[\pi_{mn}(\vartheta)\pi_{mn'}(\vartheta) + \tau_{mn}(\vartheta)\tau_{mn'}(\vartheta)] = \frac{2n(n+1)}{2n+1}\delta_{nn'}. \tag{5.212}$$

Taking also into account that $r_\vartheta(\vartheta) \equiv 0$ and defining the size parameter of the sphere as $x = k_1 a$, we derive from Eqs. (5.196)–(5.199)

$$J^{11}_{mnm'n'} \equiv 0, \quad J^{22}_{mnm'n'} \equiv 0, \quad \mathrm{Rg}J^{11}_{mnm'n'} \equiv 0, \quad \mathrm{Rg}J^{22}_{mnm'n'} \equiv 0, \tag{5.213}$$

$$J^{12}_{mnm'n'} = \delta_{mm'}\delta_{nn'}\frac{1}{k_1^2 m}\xi_n'(x)\psi_n(mx), \tag{5.214}$$

$$J^{21}_{mnm'n'} = -\delta_{mm'}\delta_{nn'}\frac{1}{k_1^2 m}\xi_n(x)\psi_n'(mx), \tag{5.215}$$

$$\mathrm{Rg}J^{12}_{mnm'n'} = \delta_{mm'}\delta_{nn'}\frac{1}{k_1^2 m}\psi_n'(x)\psi_n(mx), \tag{5.216}$$

$$\mathrm{Rg}J^{21}_{mnm'n'} = -\delta_{mm'}\delta_{nn'}\frac{1}{k_1^2 m}\psi_n(x)\psi_n'(mx), \tag{5.217}$$

where

$$\xi_n(z) = z h_n^{(1)}(z), \qquad \psi_n(z) = z j_n(z), \tag{5.218}$$

and $m = k_2/k_1$ is the relative refractive index. Equations (5.180)–(5.183), (5.186)–(5.189), and (5.191) finally yield Eqs. (5.42)–(5.44), where the Lorenz–Mie coefficients a_n and b_n are given by

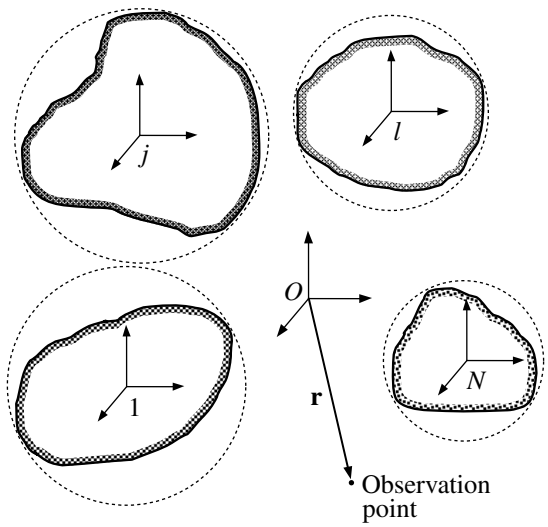

Figure 5.6. Local and common reference frames used to describe electromagnetic scattering by a cluster consisting of N arbitrarily shaped components.

$$a_n = \frac{m\psi_n(mx)\psi_n'(x) - \psi_n(x)\psi_n'(mx)}{m\psi_n(mx)\xi_n'(x) - \xi_n(x)\psi_n'(mx)}, \tag{5.219}$$

$$b_n = \frac{m\psi_n(x)\psi_n'(mx) - \psi_n(mx)\psi_n'(x)}{m\xi_n(x)\psi_n'(mx) - \psi_n(mx)\xi_n'(x)}. \tag{5.220}$$

Equations (5.219) and (5.220) are identical to Eqs. (4.56) and (4.57) of Bohren and Huffman (1983).

5.9 Aggregated and composite particles

Consider now the computation of the T matrix for a cluster consisting of N arbitrarily shaped and arbitrarily oriented components. We assume that the T matrices of all cluster components are known in their respective local coordinate systems with origins inside the components. We also assume that all these local coordinate systems have the same spatial orientation as the common reference frame of the cluster centered at O and that the smallest circumscribing spheres of the components centered at the origins of their respective local coordinate systems do not overlap (Fig. 5.6). The total electric field scattered by the cluster can be represented as a superposition of individual (partial) scattering contributions from each component:

$$\mathbf{E}^{\text{sca}}(\mathbf{r}) = \sum_{j=1}^{N} \mathbf{E}_j^{\text{sca}}(\mathbf{r}), \tag{5.221}$$

where $\mathbf{r}$ connects the origin of the common coordinate system and the observation point. Because of electromagnetic interactions between the components, the individual scattered fields are interdependent, and the total electric field exciting each component can be represented as a superposition of the external incident field $\mathbf{E}_0^{\text{inc}}(\mathbf{r})$ and

the sum of the partial fields scattered by all other components:

$$\mathbf{E}_j^{\text{inc}}(\mathbf{r}) = \mathbf{E}_0^{\text{inc}}(\mathbf{r}) + \sum_{\substack{l=1\\ l\neq j}}^{N} \mathbf{E}_l^{\text{sca}}(\mathbf{r}), \qquad j = 1, ..., N. \tag{5.222}$$

To make use of the information contained in the *j*th component *T* matrix, we must expand the fields incident on and scattered by this component in vector spherical wave functions centered at the origin of the component's local coordinate system:

$$\begin{aligned}\mathbf{E}_j^{\text{inc}}(\mathbf{r}) &= \sum_{nm} [a_{mn}^j \text{Rg}\mathbf{M}_{mn}(k_1\mathbf{r}_j) + b_{mn}^j \text{Rg}\mathbf{N}_{mn}(k_1\mathbf{r}_j)] \\ &= \sum_{nm} \left\{ \left(a_{mn}^{j0} + \sum_{l\neq j} a_{mn}^{jl} \right) \text{Rg}\mathbf{M}_{mn}(k_1\mathbf{r}_j) \right. \\ &\quad \left. + \left(b_{mn}^{j0} + \sum_{l\neq j} b_{mn}^{jl} \right) \text{Rg}\mathbf{N}_{mn}(k_1\mathbf{r}_j) \right\}, \qquad j = 1, ..., N, \end{aligned} \tag{5.223}$$

$$\mathbf{E}_j^{\text{sca}}(\mathbf{r}) = \sum_{nm} [p_{mn}^j \mathbf{M}_{mn}(k_1\mathbf{r}_j) + q_{mn}^j \mathbf{N}_{mn}(k_1\mathbf{r}_j)], \qquad r_j > r_{j>}, \qquad j = 1, ..., N, \tag{5.224}$$

where $\mathbf{r}_j$ connects the origin of the *j*th local coordinate system and the observation point, $r_{j>}$ is the radius of the smallest circumscribing sphere of the *j*th component, the coefficients a_{mn}^{j0} and b_{mn}^{j0} describe the external incident field, and the expansion coefficients a_{mn}^{jl} and b_{mn}^{jl} describe the contribution of the *l*th component to the field illuminating the *j*th component:

$$\mathbf{E}_0^{\text{inc}}(\mathbf{r}) = \sum_{nm} [a_{mn}^{j0} \text{Rg}\mathbf{M}_{mn}(k_1\mathbf{r}_j) + b_{mn}^{j0} \text{Rg}\mathbf{N}_{mn}(k_1\mathbf{r}_j)], \qquad j = 1, ..., N, \tag{5.225}$$

$$\mathbf{E}_l^{\text{sca}}(\mathbf{r}) = \sum_{nm} [a_{mn}^{jl} \text{Rg}\mathbf{M}_{mn}(k_1\mathbf{r}_j) + b_{mn}^{jl} \text{Rg}\mathbf{N}_{mn}(k_1\mathbf{r}_j)], \qquad j, l = 1, ..., N, \qquad l \neq j. \tag{5.226}$$

The expansion coefficients of the illuminating and scattered fields are related via the *j*th component *T* matrix $\mathbf{T}^j$:

$$\begin{bmatrix} \mathbf{p}^j \\ \mathbf{q}^j \end{bmatrix} = \mathbf{T}^j \left(\begin{bmatrix} \mathbf{a}^{j0} \\ \mathbf{b}^{j0} \end{bmatrix} + \sum_{l\neq j} \begin{bmatrix} \mathbf{a}^{jl} \\ \mathbf{b}^{jl} \end{bmatrix} \right), \qquad j = 1, ..., N. \tag{5.227}$$

The field scattered by the *l*th component can also be expanded in outgoing vector spherical wave functions centered at the origin of the *l*th local coordinate system:

$$\mathbf{E}_l^{\text{sca}}(\mathbf{r}) = \sum_{\nu\mu} [p_{\mu\nu}^l \mathbf{M}_{\mu\nu}(k_1\mathbf{r}_l) + q_{\mu\nu}^l \mathbf{N}_{\mu\nu}(k_1\mathbf{r}_l)], \qquad r_l > r_{l>}, \qquad l = 1, ..., N, \qquad l \neq j, \tag{5.228}$$

where $\mathbf{r}_l$ connects the origin of the lth coordinate system and the observation point. Using the translation addition theorem (C.68), the vector spherical wave functions appearing in Eq. (5.228) can be expanded in regular vector spherical wave functions centered at the origin of the jth reference frame:

$$\begin{matrix}\mathbf{M}_{\mu\nu}\\ \mathbf{N}_{\mu\nu}\end{matrix}(k_1\mathbf{r}_l)=\sum_{nm}\left[\begin{matrix}A_{mn\mu\nu}\\ B_{mn\mu\nu}\end{matrix}(k_1\mathbf{r}_{lj})\mathrm{Rg}\mathbf{M}_{mn}(k_1\mathbf{r}_j)+\begin{matrix}B_{mn\mu\nu}\\ A_{mn\mu\nu}\end{matrix}(k_1\mathbf{r}_{lj})\mathrm{Rg}\mathbf{N}_{\mu\nu}(k_1\mathbf{r}_j)\right],$$

$$r_j<r_{lj}, \qquad (5.229)$$

where the vector $\mathbf{r}_{lj}=\mathbf{r}_l-\mathbf{r}_j$ connects the origins of the lth and jth local coordinate systems and the translation coefficients $A_{mn\mu\nu}(k_1\mathbf{r}_{lj})$ and $B_{mn\mu\nu}(k_1\mathbf{r}_{lj})$ are given by Eqs. (C.69) and (C.70). Using Eqs. (5.226)–(5.229), we finally derive, in matrix notation,

$$\begin{bmatrix}\mathbf{p}^j\\ \mathbf{q}^j\end{bmatrix}=\mathbf{T}^j\left(\begin{bmatrix}\mathbf{a}^{j0}\\ \mathbf{b}^{j0}\end{bmatrix}+\sum_{l\neq j}\begin{bmatrix}\mathbf{A}(k_1\mathbf{r}_{lj}) & \mathbf{B}(k_1\mathbf{r}_{lj})\\ \mathbf{B}(k_1\mathbf{r}_{lj}) & \mathbf{A}(k_1\mathbf{r}_{lj})\end{bmatrix}\begin{bmatrix}\mathbf{p}^l\\ \mathbf{q}^l\end{bmatrix}\right), \qquad j=1,\ldots,N. \qquad (5.230)$$

Since the expansion coefficients of the external plane electromagnetic wave a_{mn}^{j0} and b_{mn}^{j0} and the translation coefficients $A_{mn\mu\nu}(k_1\mathbf{r}_{lj})$ and $B_{mn\mu\nu}(k_1\mathbf{r}_{lj})$ can be computed via closed form analytical formulas, Eq. (5.230) can be considered as a system of linear algebraic equations which can be solved numerically and yields the expansion coefficients of the individual scattered fields p_{mn}^j and q_{mn}^j for each of the cluster components. When these coefficients are known, Eqs. (5.224) and (5.221) give the total field scattered by the cluster.

Equation (5.230) forms the basis of the T-matrix superposition method for aggregates. It becomes especially simple for a cluster consisting of spherical components since in this case the individual component T matrices are diagonal, with standard Lorenz–Mie coefficients standing along their main diagonals (Eqs. (5.42)–(5.44)). The resulting equation becomes identical to that derived using the so-called multi-sphere superposition formulation or multi-sphere separation of variables technique (Bruning and Lo 1971a, b; Borghese *et al.* 1979; and especially Fuller and Mackowski 2000 and references therein). In this regard, the latter can be considered as a particular case of the superposition T-matrix method. Numerical solutions of Eq. (5.230) for clusters of spheres have been obtained using different techniques (direct matrix inversion, the method of successive orders of scattering, the conjugate gradients method, the method of iterations, the recursive method) and have been extensively reported in the literature (Hamid *et al.* 1991; Quinten and Kreibig 1993; Fuller, 1994, 1995a; Xu 1995; Jin and Huang 1996a; Videen *et al.* 1998a; Quinten 1999). Jin and Huang (1996b) and Huang and Jin (1998) applied the superposition T-matrix formalism to clusters of spheroids. Fikioris and Uzunoglu (1979), Borghese *et al.* (1992, 1994), Skaropoulos *et al.* (1994), Fuller (1995b), Mackowski and Jones (1995), and Auger *et al.* (2001) have extended the superposition approach to the case of internal aggregation by solving the problem of light scattering by spherical particles with eccentric spherical inclusions, whereas Videen *et al.* (1995) con-

sidered the more general case of a sphere with an irregular inclusion. Of course, particles with a single inclusion can also be treated using the standard EBCM for multilayered scatterers (Peterson and Ström 1974).

Inversion of Eq. (5.230) gives

$$\begin{bmatrix} \mathbf{p}^j \\ \mathbf{q}^j \end{bmatrix} = \sum_{l=1}^{N} \mathbf{T}^{jl} \begin{bmatrix} \mathbf{a}^{l0} \\ \mathbf{b}^{l0} \end{bmatrix}, \qquad j = 1, \ldots, N \tag{5.231}$$

(Mackowski 1994), where the matrix $\mathbf{T}^{jl}$ transforms the coefficients of the incident-field expansion centered at the *l*th origin into the *j*th-origin-centered expansion coefficients of the partial field scattered by the *j*th component. The calculation of the $\mathbf{T}^{jl}$ matrices entails the numerical inversion of a large matrix and can be a time-consuming process. However, these matrices are independent of the incident field and depend only on the cluster configuration and the shapes and orientations of the components. Therefore, they need be computed only once and then can be used in computations for any direction and polarization state of the incident field.

Furthermore, in the far-field region the scattered-field expansions from the individual components can be transformed into a single expansion centered at the origin O of the common reference frame (Fig. 5.6). This single origin can represent the average of the component particle positions but in general can be arbitrary. The first step is to expand the incident and total scattered fields in vector spherical wave functions centered at O, according to Eqs. (5.2) and (5.3). We again employ the translation addition theorem given by Eq. (C.66),

$$\mathrm{Rg}\begin{matrix}\mathbf{M}_{mn}\\ \mathbf{N}_{mn}\end{matrix}(k_1\mathbf{r}) = \sum_{\nu\mu}\left[\mathrm{Rg}\begin{matrix}A_{\mu\nu mn}\\ B_{\mu\nu mn}\end{matrix}(k_1\mathbf{r}_{Ol})\mathrm{Rg}\mathbf{M}_{\mu\nu}(k_1\mathbf{r}_l) + \mathrm{Rg}\begin{matrix}B_{\mu\nu mn}\\ A_{\mu\nu mn}\end{matrix}(k_1\mathbf{r}_{Ol})\mathrm{Rg}\mathbf{N}_{\mu\nu}(k_1\mathbf{r}_l)\right], \tag{5.232}$$

and by the reciprocal formula (C.67),

$$\begin{matrix}\mathbf{M}_{mn}\\ \mathbf{N}_{mn}\end{matrix}(k_1\mathbf{r}_j) = \sum_{\nu\mu}\left[\mathrm{Rg}\begin{matrix}A_{\mu\nu mn}\\ B_{\mu\nu mn}\end{matrix}(k_1\mathbf{r}_{jO})\mathbf{M}_{\mu\nu}(k_1\mathbf{r}) + \mathrm{Rg}\begin{matrix}B_{\mu\nu mn}\\ A_{\mu\nu mn}\end{matrix}(k_1\mathbf{r}_{jO})\mathbf{N}_{\mu\nu}(k_1\mathbf{r})\right], \qquad r > r_{jO}, \tag{5.233}$$

where $\mathbf{r}_{Ol} = \mathbf{r} - \mathbf{r}_l$ and $\mathbf{r}_{jO} = \mathbf{r}_j - \mathbf{r}$. We then easily derive

$$\begin{bmatrix} \mathbf{a}^{l0} \\ \mathbf{b}^{l0} \end{bmatrix} = \begin{bmatrix} \mathrm{Rg}\mathbf{A}(k_1\mathbf{r}_{Ol}) & \mathrm{Rg}\mathbf{B}(k_1\mathbf{r}_{Ol}) \\ \mathrm{Rg}\mathbf{B}(k_1\mathbf{r}_{Ol}) & \mathrm{Rg}\mathbf{A}(k_1\mathbf{r}_{Ol}) \end{bmatrix} \begin{bmatrix} \mathbf{a} \\ \mathbf{b} \end{bmatrix}, \qquad l = 1, \ldots, N, \tag{5.234}$$

$$\begin{bmatrix} \mathbf{p} \\ \mathbf{q} \end{bmatrix} = \sum_{j=1}^{N} \begin{bmatrix} \mathrm{Rg}\mathbf{A}(k_1\mathbf{r}_{jO}) & \mathrm{Rg}\mathbf{B}(k_1\mathbf{r}_{jO}) \\ \mathrm{Rg}\mathbf{B}(k_1\mathbf{r}_{jO}) & \mathrm{Rg}\mathbf{A}(k_1\mathbf{r}_{jO}) \end{bmatrix} \begin{bmatrix} \mathbf{p}^j \\ \mathbf{q}^j \end{bmatrix}. \tag{5.235}$$

Finally, using Eqs. (5.231), (5.234), and (5.235) we obtain Eq. (5.8), in which the cluster

T matrix is given by

$$\mathbf{T} = \sum_{j,l=1}^{N} \begin{bmatrix} \mathrm{Rg}\mathbf{A}(k_1\mathbf{r}_{jO}) & \mathrm{Rg}\mathbf{B}(k_1\mathbf{r}_{jO}) \\ \mathrm{Rg}\mathbf{B}(k_1\mathbf{r}_{jO}) & \mathrm{Rg}\mathbf{A}(k_1\mathbf{r}_{jO}) \end{bmatrix} \mathbf{T}^{jl} \begin{bmatrix} \mathrm{Rg}\mathbf{A}(k_1\mathbf{r}_{Ol}) & \mathrm{Rg}\mathbf{B}(k_1\mathbf{r}_{Ol}) \\ \mathrm{Rg}\mathbf{B}(k_1\mathbf{r}_{Ol}) & \mathrm{Rg}\mathbf{A}(k_1\mathbf{r}_{Ol}) \end{bmatrix} \tag{5.236}$$

(Peterson and Ström 1973; Mackowski 1994). This cluster T matrix can be used in Eqs. (5.11)–(5.14) to compute the amplitude matrix for a fixed cluster orientation and as input to the analytical procedures for averaging scattering characteristics over cluster orientations (Mishchenko and Mackowski 1994; Mackowski and Mishchenko 1996).

In agreement with Eqs. (5.36) and (5.37), the T matrix becomes much simpler when the cluster is a rotationally symmetric scatterer in the form of a linear chain of spheres and when the z-axis of the common reference frame is directed along the line connecting the centers of the component spheres (Mishchenko and Mackowski 1994). In general, one may need to combine Eq. (5.236) with the rotation transformation rule (5.29) in order to compute efficiently the T matrix for a cluster consisting of arbitrarily oriented and arbitrarily positioned nonspherical components (Jin and Huang 1996b).

Wang and Chew (1993) developed a recursive T-matrix algorithm, which computes the T matrix for a cluster consisting of n components by using the T matrix of the newly added nth component and the T matrix of the cluster consisting of the previous $n-1$ components. The apparent advantage of this technique is that it reduces computation of the T matrix for a cluster consisting of N components into a recursive sequence of $N-1$ two-component calculations. However, for reasons alluded to previously (Section 5.1), the smallest circumscribing sphere of each newly added component must always reside outside a sphere enclosing the cluster built at the previous recursion step. This constraint appears to limit the recursive algorithm to relatively simple and sparse clusters, for example, linear chains of spheres.

5.10 Lorenz–Mie code for homogeneous polydisperse spheres

The FORTRAN code for computing the scattering characteristics of an ensemble of polydisperse, homogeneous spherical particles is based on the Lorenz–Mie theory and is available on the World Wide Web at http://www.giss.nasa.gov/~crmim. This section discusses practical aspects of Lorenz–Mie calculations, describes the input and output parameters of the code, and provides an illustrative example.

5.10.1 Practical considerations

The numerical computation of the Lorenz–Mie coefficients a_n and b_n and the angular functions π_n and τ_n appearing in Eqs. (5.149) and (5.151) is considered in detail in many publications (e.g., Wiscombe 1980; Bohren and Huffman 1983; de Rooij and van der Stap 1984, and references therein) and will not be specifically discussed here.

In practical computer calculations, the infinite series of Eqs. (5.149) and (5.151) are truncated to a finite size $n_{\max}$ that depends on the size parameter $x = k_1 r$, where r is the particle radius. A simple empirical criterion for choosing $n_{\max}$ adopted in our code is

$$n_{\max}(x) = x + 4.05x^{1/3} + 8 \tag{5.237}$$

and is somewhat more conservative (i.e., it takes more terms than may be necessary) than that proposed by Wiscombe (1980).

The basic far-field optical characteristics of a homogeneous spherical particle are the extinction cross section C_{ext}, the scattering cross section C_{sca}, and the expansion coefficients α_p^s (p = 1, 2, 3, 4) and β_p^s (p = 1, 2) appearing in Eqs. (4.75)–(4.80). All these quantities can be directly expressed in terms of the Lorenz–Mie coefficients a_n and b_n (Section 5.7) and must be averaged over an appropriate normalized distribution of sphere radii $n(r)$ (Section 3.2) in order to obtain the scattering characteristics of a particle ensemble. All other cross sections, the single-scattering albedo, the efficiency factors, the asymmetry parameter, and the elements of the normalized scattering matrix for an arbitrary set of scattering angles are then found from Eqs. (4.43)–(4.46), (4.75)–(4.80), and (4.92). The Wigner d-functions entering Eqs. (4.75)–(4.80) are computed using the recurrence relation (B.22) and the initial conditions (B.23) and (B.24).

The computation of the ensemble-averaged extinction and scattering cross sections per particle is straightforward:

$$\langle C_{\text{ext}} \rangle = \int_{r_{\min}}^{r_{\max}} \mathrm{d}r\, n(r) C_{\text{ext}}(r) \approx \sum_{i=1}^{N_r} u_i n(r_i) C_{\text{ext}}(r_i), \tag{5.238}$$

$$\langle C_{\text{sca}} \rangle = \int_{r_{\min}}^{r_{\max}} \mathrm{d}r\, n(r) C_{\text{sca}}(r) \approx \sum_{i=1}^{N_r} u_i n(r_i) C_{\text{sca}}(r_i), \tag{5.239}$$

where r_i and u_i are the division points and weights, respectively, of a quadrature formula on the interval $[r_{\min}, r_{\max}]$. The ensemble-averaged expansion coefficients can be computed similarly using Eqs. (5.160)–(5.162) and (4.109)–(4.114). However, the necessity of keeping in computer memory large arrays containing the products of Lorenz–Mie coefficients with different indices appearing in Eqs. (5.160)–(5.162) imposes a limit on the maximum size parameter $x_{\max} = k_1 r_{\max}$ that can be handled by a given computer. Therefore, instead of using Eqs. (5.160)–(5.162), we compute the ensemble-averaged expansion coefficients by evaluating numerically the angular integrals in Eqs. (4.81)–(4.86) (de Rooij and van der Stap 1984). For example,

$$\begin{aligned} \alpha_1^s &= (s + \tfrac{1}{2}) \int_{-1}^{+1} \mathrm{d}(\cos\Theta) a_1(\Theta) d_{00}^s(\Theta) \\ &\approx (s + \tfrac{1}{2}) \sum_{j=1}^{N_\Theta} w_j a_1(\arccos\mu_j) d_{00}^s(\arccos\mu_j), \end{aligned} \tag{5.240}$$

where μ_j and w_j are the division points and weights of a Gaussian quadrature formula on the interval $[-1, +1]$,

$$a_1(\Theta) = \frac{1}{\langle C_{\text{sca}} \rangle} \int_{r_{\min}}^{r_{\max}} \mathrm{d}r\, n(r) C_{\text{sca}}(r) a_1(r; \Theta)$$
$$\approx \frac{1}{\langle C_{\text{sca}} \rangle} \sum_{i=1}^{N_r} u_i n(r_i) C_{\text{sca}}(r_i) a_1(r_i; \Theta) \tag{5.241}$$

is the ensemble-averaged (1,1)-element of the normalized Stokes scattering matrix (cf. Eq. (4.74)), and $a_1(r; \Theta)$ is given by Eq. (5.152). Other expansion coefficients are computed similarly. This numerical procedure involves computation of the elements of the normalized Stokes scattering matrix for N_Θ scattering angles and is slower than the analytical procedure based on Eqs. (5.160)–(5.162) and (4.109)–(4.114) by a factor of 2 (de Rooij and van der Stap 1984). However, the numerical procedure is applicable to significantly larger size parameters than the analytical method, assuming that the size of the computer memory is the same in both cases. Given the high speed of modern computers and hence the relatively low cost of the Lorenz–Mie computations, the advantages of the numerical approach seem to outweigh its disadvantages. de Rooij and van der Stap (1984) showed that a good *a priori* estimate for the number of quadrature division points in Eq. (5.240) is $N_\Theta = 2n_{\max}(x_{\max})$. It is more difficult to give an *a priori* estimate of the number N_r of quadrature division points in Eqs. (5.238), (5.239), and (5.241). In practice, this number should be increased in finite steps until all scattering characteristics of interest converge within a given accuracy.

It is often convenient to approximate natural size distributions using simple analytical distribution functions. The Lorenz–Mie code allows one to choose from the following set of six analytical size distributions:

- the modified gamma distribution

$$n(r) = \text{constant} \times r^{\alpha} \exp\left(-\frac{\alpha r^{\gamma}}{\gamma r_c^{\gamma}}\right); \tag{5.242}$$

- the log normal distribution

$$n(r) = \text{constant} \times r^{-1} \exp\left[-\frac{(\ln r - \ln r_g)^2}{2 \ln^2 \sigma_g}\right]; \tag{5.243}$$

- the power law distribution

$$n(r) = \begin{cases} \text{constant} \times r^{-3}, & r_1 \le r \le r_2, \\ 0, & \text{otherwise}; \end{cases} \tag{5.244}$$

- the gamma distribution

$$n(r) = \text{constant} \times r^{(1-3b)/b} \exp\left(-\frac{r}{ab}\right), \quad b \in (0, 0.5); \tag{5.245}$$

- the modified power law distribution

$$n(r) = \begin{cases} \text{constant}, & 0 \le r \le r_1, \\ \text{constant} \times (r/r_1)^{\alpha}, & r_1 \le r \le r_2, \\ 0, & r_2 < r; \end{cases} \tag{5.246}$$

- the modified bimodal log normal distribution

$$n(r) = \text{constant} \times r^{-4} \left\{ \exp\left[-\frac{(\ln r - \ln r_{g1})^2}{2 \ln^2 \sigma_{g1}} \right] + \gamma \exp\left[-\frac{(\ln r - \ln r_{g2})^2}{2 \ln^2 \sigma_{g2}} \right] \right\}. \tag{5.247}$$

The constant for each size distribution is chosen such that the size distribution satisfies the standard normalization of Eq. (3.26).

Implicitly, particle radii in the modified gamma, log normal, gamma, and modified bimodal log normal distributions extend to infinity. However, a finite $r_{\max}$ must be chosen in actual computer calculations. There are two different practical interpretations of a truncated size distribution. The first assumes that $r_{\max}$ is increased iteratively until the scattering and absorption characteristics of the size distribution converge within a prescribed numerical accuracy. In this case the converged truncated size distribution is numerically equivalent to the distribution with $r_{\max} = \infty$. In the second interpretation, the truncated distribution with a prescribed $r_{\max}$ is considered as a specific size distribution with scattering and absorption characteristics distinctly different from those for the distribution with $r_{\max} = \infty$. Similar considerations apply to the parameter $r_{\min}$, whose implicit value for the modified gamma, log normal, gamma, and modified bimodal log normal distributions is zero, but in practice can be any number smaller than $r_{\max}$. In this book, we adopt the first interpretation of a truncated size distribution, unless explicitly indicated otherwise. The actual numerical integration of scattering characteristics over a size distribution is achieved by subdividing the entire interval $[r_{\min}, r_{\max}]$ of particle radii into a number of equal subintervals and applying a Gaussian quadrature formula with a fixed number of division points to each subinterval.

We will see in later chapters that two important characteristics of a size distribution are the effective radius r_{eff} and effective variance v_{eff}, defined by

$$r_{\text{eff}} = \frac{1}{\langle G \rangle} \int_{r_{\min}}^{r_{\max}} \mathrm{d}r\, n(r) r \pi r^2, \tag{5.248}$$

$$v_{\text{eff}} = \frac{1}{\langle G \rangle r_{\text{eff}}^2} \int_{r_{\min}}^{r_{\max}} \mathrm{d}r\, n(r) (r - r_{\text{eff}})^2 \pi r^2, \tag{5.249}$$

where

$$\langle G \rangle = \int_{r_{\min}}^{r_{\max}} \mathrm{d}r\, n(r) \pi r^2 \tag{5.250}$$

is the average area of the geometric projection per particle (Hansen and Travis 1974).

r_{eff} is simply the projected-area-weighted mean radius, whereas the dimensionless effective variance provides a measure of the width of the size distribution. It is straightforward to show that for the gamma distribution with $r_{\min} = 0$ and $r_{\max} = \infty$, a and b coincide with r_{eff} and v_{eff}, respectively. For the other size distributions with specific values of $r_{\min}$ and $r_{\max}$ the effective radius and effective variance must be determined either analytically or numerically.

5.10.2 Input parameters of the Lorenz–Mie code

NDISTR, AA, BB, GAM:

The parameter NDISTR specifies the type of the particle size distribution. For the modified gamma distribution (5.242), $\text{NDISTR} = 1$, $\text{AA} = \alpha$, $\text{BB} = r_c$, and $\text{GAM} = \gamma$. For the log normal distribution (5.243), $\text{NDISTR} = 2$, $\text{AA} = r_g$, $\text{BB} = \ln^2\sigma_g$, and GAM is ignored. For the power law distribution (5.244), $\text{NDISTR} = 3$, $\text{AA} = r_{\text{eff}}$, $\text{BB} = v_{\text{eff}}$, and GAM is ignored. In this case the parameters R1 and R2 (see below) are calculated from Eqs. (5.244) and (5.248)–(5.250) for given r_{eff} and v_{eff}. For the gamma distribution (5.245), $\text{NDISTR} = 4$, $\text{AA} = a$, $\text{BB} = b$, and GAM is ignored. For the modified power law distribution (5.246), $\text{NDISTR} = 5$, $\text{BB} = \alpha$, and AA and GAM are ignored. Finally, for the modified bimodal log normal distribution (5.247), $\text{NDISTR} = 6$, $\text{AA1} = r_{g1}$, $\text{BB1} = \ln^2\sigma_{g1}$, $\text{AA2} = r_{g2}$, $\text{BB2} = \ln^2\sigma_{g2}$, and $\text{GAM} = \gamma$.

R1 and R2:

$\text{R1} = r_{\min}$ and $\text{R2} = r_{\max}$ are the minimal and maximal radii in the size distribution for NDISTR = 1–4 and 6. R1 and R2 are calculated automatically for the power law distribution $\text{NDISTR} = 3$ with given r_{eff} and v_{eff}, but they must be specified explicitly for other distributions. For the modified power law distribution NDISTR=5, $r_{\min} = 0$, $\text{R1} = r_1$, and $\text{R2} = r_2 = r_{\max}$.

LAM:

$\text{LAM} = \lambda_1$ is the wavelength of the incident light in the surrounding medium.

MRR and MRI:

$\text{MRR} = \text{Re}\, m$ and $\text{MRI} = \text{Im}\, m$ are the real and imaginary parts of the relative refractive index. MRI must be non-negative.

N, NP, and NK:

N is the number of equal integration subintervals on the interval [R1, R2]. NP is the number of equal integration subintervals on the interval [0, R1] for the modified power law distribution. NK is the number of Gaussian division points on each of the

integration subintervals. In other words, $N_r = \mathrm{N} * \mathrm{NK}$ for $\mathrm{NDISTR} = 1, 2, 3, 4, 6$ and $N_r = (\mathrm{N} + \mathrm{NP}) * \mathrm{NK}$ for $\mathrm{NDISTR} = 5$ in Eqs. (5.238), (5.239), and (5.241).

NPNA:
NPNA is the number of scattering angles at which the normalized scattering matrix is computed. This parameter appears in the PARAMETER statement in the subroutine MATR. The corresponding scattering angles are given by 180*(I–1)/(NPNA–1) (degrees), where I numbers the angles. This way of choosing scattering angles can be changed in the subroutine MATR by properly modifying the following lines,

```
N = NPNA
DN = 1D0/DFLOAT(N–1)
DA = DACOS(–1D0)*DN
DB = 180D0*DN
TB = –DB
TAA = –DA
DO 500 I1 = 1, N
    TAA = TAA+DA
    TB = TB+DB
```

and leaving the rest of the subroutine intact. This flexibility is provided by the fact that after the expansion coefficients α_p^s (p = 1, 2, 3, 4) and β_p^s (p = 1, 2) are computed by the subroutine SPHER, the scattering matrix can readily be computed for any set of scattering angles (cf. Section 4.11).

DDELT:
DDELT is the desired numerical accuracy of computation of the elements of the normalized scattering matrix.

5.10.3 Output information

R1 and R2:
For the power law size distribution $\mathrm{NDISTR} = 3$, $\mathrm{R1} = r_1$ and $\mathrm{R2} = r_2$ are the minimal and maximal radii, respectively, calculated for the input values of r_{eff} and v_{eff}.

REFF and VEFF:
$\mathrm{REFF} = r_{\mathrm{eff}}$ and $\mathrm{VEFF} = v_{\mathrm{eff}}$ are the effective radius and the effective variance of the size distribution, respectively.

CEXT and CSCA:
$\mathrm{CEXT} = \langle C_{\mathrm{ext}} \rangle$ and $\mathrm{CSCA} = \langle C_{\mathrm{sca}} \rangle$ are the ensemble-averaged extinction and scattering cross sections per particle, respectively.

< COS > and ALBEDO:
$<\mathrm{COS}> = \langle \cos\Theta \rangle$ and $\mathrm{ALBEDO} = \varpi$ are the ensemble-averaged asymmetry parameter and single-scattering albedo, respectively.

< G >:
$<\mathrm{G}> = \langle G \rangle$ is the average projected area per particle defined by Eq. (5.250).

< V >:
$<\mathrm{V}> = \langle V \rangle$ is the average volume per particle defined by

$$\langle V \rangle = \int_{r_{\min}}^{r_{\max}} \mathrm{d}r\, n(r) \tfrac{4}{3}\pi r^3. \tag{5.251}$$

< R >:
$<\mathrm{R}> = \langle r \rangle$ is the average radius defined by

$$\langle r \rangle = \int_{r_{\min}}^{r_{\max}} \mathrm{d}r\, n(r) r. \tag{5.252}$$

Rvw:
$\mathrm{Rvw} = r_{\mathrm{vw}}$ is the volume-weighted average radius defined by

$$r_{\mathrm{vw}} = \frac{1}{\langle V \rangle} \int_{r_{\min}}^{r_{\max}} \mathrm{d}r\, n(r) r \tfrac{4}{3}\pi r^3. \tag{5.253}$$

ALPHA1, …, BETA2:
$\mathrm{ALPHA1(S)} = \alpha_1^s$, $\mathrm{ALPHA2(S)} = \alpha_2^s$, $\mathrm{ALPHA3(S)} = \alpha_3^s$, $\mathrm{ALPHA4(S)} = \alpha_4^s$, $\mathrm{BETA1(S)} = \beta_1^s$, and $\mathrm{BETA2(S)} = \beta_2^s$ are the expansion coefficients appearing in Eqs. (4.75)–(4.80).

F11, F33, F12, and F34:
$\mathrm{F11} = a_1$, $\mathrm{F33} = a_3$, $\mathrm{F12} = b_1$, and $\mathrm{F34} = b_2$, are the elements of the normalized Lorenz–Mie scattering matrix of Eq. (4.65).

5.10.4 Additional comments and illustrative example

It is important to remember that all input parameters having the dimension of length (i.e., r_c, r_g, r_{eff}, a, r_1, r_2, r_{g1}, r_{g2}, λ_1) must be specified in the same units. If these parameters are specified, for example, in micrometers then output parameters having the dimension of length, area, and volume are given in micrometers, square micrometers, and cubical micrometers, respectively. For given size distribution parameters, the parameters N, NP, and/or NK should be increased until convergent results are obtained for the extinction and scattering cross sections and, especially, the

expansion coefficients and the elements of the normalized scattering matrix.

To calculate the scattering characteristics of a monodisperse particle having a radius r, one may use the following options:

```
AA = r
BB = 1D–1
NDISTR = 4
NK = 1
N = 1
R1 = AA*0.9999999 D0
R2 = AA*1.0000001 D0
```

The code has been extensively tested versus a program based on Eqs. (5.160)–(5.162) and (4.109)–(4.114) as well as versus the codes independently written by Hansen and Travis (1974) and de Rooij and van der Stap (1984). Excellent agreement has been found in all cases considered. In particular, we were able to reproduce the numbers in Tables 2–4 of de Rooij and van der Stap to within ± 1 in the last decimals given.

To illustrate the performance of the Lorenz–Mie code, Tables 5.1 and 5.2 list the expansion coefficients and the elements of the normalized scattering matrix for the power law distribution (5.244) with $r_{\text{eff}} = 0.6\,\mu\text{m}$ and $v_{\text{eff}} = 0.2$. The wavelength in the surrounding medium is $\lambda_1 = 0.63\,\mu\text{m}$ and the relative refractive index is $m = 1.53 + \text{i}0.008$. Other output parameters are as follows: $\langle C_{\text{ext}} \rangle = 1.92604\,\mu\text{m}^2$, $\langle C_{\text{sca}} \rangle = 1.78033\,\mu\text{m}^2$, $\varpi = 0.924351$, $\langle \cos\Theta \rangle = 0.703689$, $r_1 = 0.245830\,\mu\text{m}$, $r_2 = 1.19417\,\mu\text{m}$, $\langle G \rangle = 0.626712\,\mu\text{m}^2$, $\langle V \rangle = 0.501369\,\mu\text{m}^3$, $r_{\text{vw}} = 0.720000\,\mu\text{m}$, and $\langle r \rangle = 0.407726\,\mu\text{m}$. Table 5.1 demonstrates the typical behavior of the expansion coefficients with increasing s: on average, they first grow in absolute value and then decay to values below a reasonable numerical threshold. The larger the particles relative to the wavelength, the larger the maximal absolute value of the expansion coefficients and the slower their decay (cf. Fig. 5.7).

5.11 *T*-matrix code for polydisperse, randomly oriented, homogeneous, rotationally symmetric particles

The FORTRAN code for computing the far-field scattering and absorption characteristics of a polydisperse ensemble of randomly oriented, homogeneous, rotationally symmetric particles is based on the analytical orientation-averaging method described in Sections 5.4–5.6 and the extended boundary condition method described in Section 5.8; it is available on the World Wide Web at http://www.giss.nasa.gov/~crmim. This section discusses numerical and practical aspects of *T*-matrix and EBCM computations, lists the input and output parameters of the code, and describes several illustrative examples.

Table 5.1. Expansion coefficients for a power law size distribution of homogeneous spherical particles (see text)

s	α_1^s	α_2^s	α_3^s	α_4^s	β_1^s	β_2^s
0	1.00000	0.00000	0.00000	0.89795	0.00000	0.00000
1	2.11107	0.00000	0.00000	2.17321	0.00000	0.00000
2	2.80371	3.94496	3.70286	2.68232	– 0.11397	0.04016
3	2.75088	3.26632	3.32478	2.86830	– 0.04919	– 0.13012
4	2.78642	3.29211	3.08787	2.67642	– 0.11611	– 0.09967
5	2.51483	2.71962	2.76717	2.62148	0.02311	– 0.23388
6	2.37043	2.68850	2.53377	2.29258	– 0.08347	– 0.14514
7	2.12491	2.19572	2.22264	2.21115	0.03711	– 0.22087
8	1.94158	2.17567	2.05467	1.88603	– 0.07778	– 0.16015
9	1.72589	1.74352	1.76215	1.80127	0.02696	– 0.18509
10	1.54525	1.72822	1.62493	1.50006	– 0.07066	– 0.16683
11	1.33856	1.33822	1.35592	1.40884	0.01412	– 0.14733
12	1.18264	1.32442	1.23019	1.14003	– 0.06023	– 0.16558
13	0.98046	0.97712	0.99647	1.04645	0.00414	– 0.11420
14	0.85744	0.96367	0.87607	0.81429	– 0.04833	– 0.15555
15	0.66452	0.66350	0.68361	0.72364	– 0.00131	– 0.08708
16	0.57301	0.64891	0.56980	0.53010	– 0.03585	– 0.13776
17	0.39838	0.40032	0.41870	0.44708	– 0.00135	– 0.06506
18	0.33469	0.38531	0.31822	0.29493	– 0.02181	– 0.11245
19	0.19091	0.19427	0.20871	0.22691	0.00293	– 0.04528
20	0.15885	0.18833	0.13387	0.12268	– 0.00442	– 0.07658
21	0.06616	0.06753	0.07753	0.08893	0.00548	– 0.01461
22	0.06678	0.08074	0.04492	0.04153	– 0.00413	– 0.03682
23	0.02026	0.02103	0.02698	0.03304	– 0.00277	– 0.00397
24	0.02708	0.03337	0.01144	0.01048	– 0.00297	– 0.01952
25	0.00370	0.00393	0.00553	0.00797	0.00015	– 0.00132
26	0.00906	0.01105	0.00090	0.00065	0.00137	– 0.00486
27	– 0.00088	– 0.00088	– 0.00001	0.00051	– 0.00092	0.00187
28	0.00188	0.00215	– 0.00046	– 0.00040	– 0.00097	– 0.00118
29	0.00002	0.00003	0.00006	0.00005	0.00013	– 0.00006
30	0.00001	0.00002	0.00001	0.00001	0.00001	– 0.00001
31	0.00000	0.00000	0.00000	0.00000	0.00000	0.00000

Table 5.2. Elements of the normalized Stokes scattering matrix for a power law size distribution of homogeneous spherical particles (see text)

Θ (deg)	$a_1(\Theta)$	$a_3(\Theta)$	$b_1(\Theta)$	$b_2(\Theta)$
0	30.5485	30.5485	0.00000	0.00000
10	17.5868	17.5325	0.11636	0.74705
20	6.32160	6.19549	0.10722	0.51234
30	3.17426	3.07387	0.08634	0.28530
40	1.68979	1.59809	0.10664	0.12816
50	0.98175	0.89795	0.10301	0.04929
60	0.60514	0.52727	0.09051	– 0.00844
70	0.39723	0.32358	0.07470	– 0.02873
80	0.28182	0.21282	0.05192	– 0.03907
90	0.21054	0.14274	0.03917	– 0.04148
100	0.16867	0.10289	0.02996	– 0.03777
110	0.14492	0.07875	0.02723	– 0.03832
120	0.13501	0.06582	0.03002	– 0.04153
130	0.14110	0.06037	0.04039	– 0.05465
140	0.17064	0.05901	0.06230	– 0.07784
150	0.23806	0.05207	0.10700	– 0.11341
160	0.34927	0.00673	0.17620	– 0.12169
170	0.38436	– 0.27524	0.16140	0.10428
180	0.76915	– 0.76915	0.00000	0.00000

5.11.1 Computation of the *T* matrix for an individual particle

Equations (5.196)–(5.199) and the respective formulas for $\mathrm{Rg}J^{kl}_{mnm'n'}$ contain several angular and radial functions that must be computed numerically for argument values corresponding to the quadrature division points in Eq. (5.202). The functions $r(\vartheta)$ and $r_\vartheta(\vartheta)$ are computed analytically for a given particle shape. An accurate and numerically stable way of computing the Wigner *d*-functions $d^n_{0m}(\vartheta)$ and the functions $\pi_{mn}(\vartheta)$ and $\tau_{mn}(\vartheta)$ defined by Eqs. (5.16) and (5.17) is provided by the recurrence relations (B.22) and (B.26) supplemented by the initial values given by Eqs. (B.23) and (B.24). The symmetry relations (5.205)–(5.207) reduce the computational effort by a factor of 2.

The spherical Bessel functions of the first kind, $j_n(z)$ (where z is equal to $k_1 r$ or $k_2 r$ and is, in general, complex), satisfy the recurrence relation (Abramowitz and Stegun 1964):

$$j_{n+1}(z) = \frac{2n+1}{z} j_n(z) - j_{n-1}(z). \tag{5.254}$$

Since the upward recurrence relation for $j_n(z)$ is unstable, we define

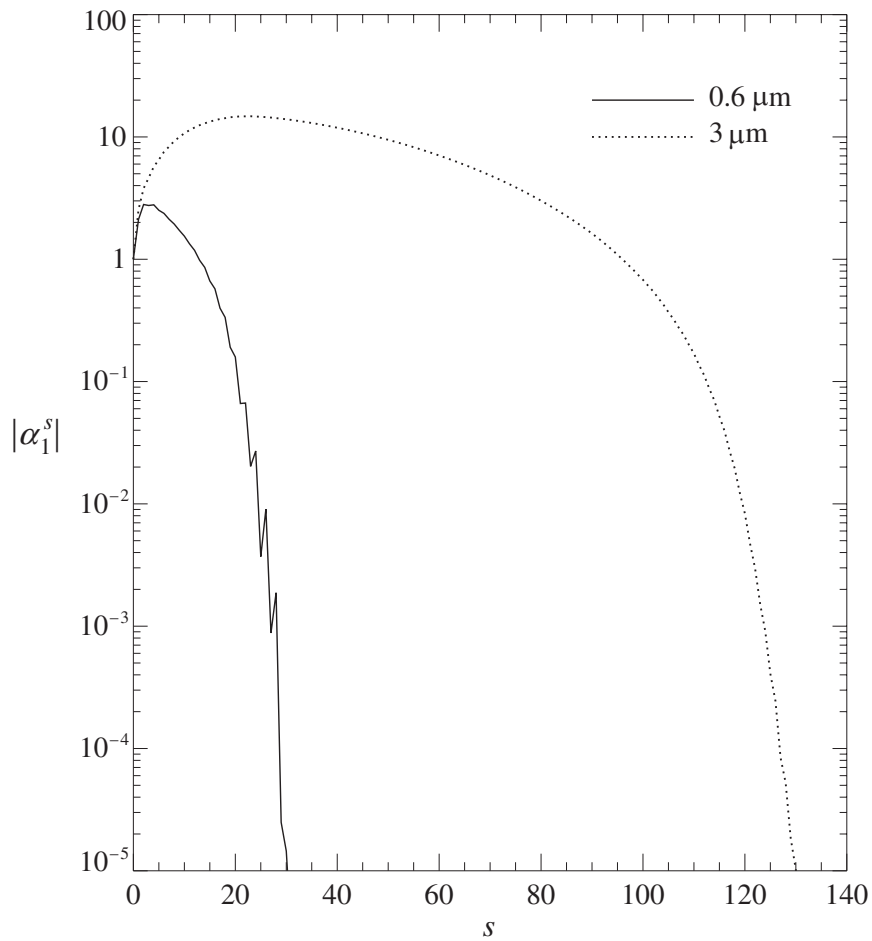

Figure 5.7. Absolute values of the coefficients α_1^s appearing in the Legendre expansion of the phase function for power law distributions of spherical particles with $r_{\text{eff}} = 0.6\,\mu\text{m}$ (solid line) and $3\,\mu\text{m}$ (dotted line), $v_{\text{eff}} = 0.2$, and $m = 1.53 + \text{i}0.008$. The wavelength in the surrounding medium is $\lambda_1 = 0.63\,\mu\text{m}$.

$$r_n(z) = \frac{j_n(z)}{j_{n-1}(z)}, \tag{5.255}$$

leading to the downward recurrence relation

$$r_n(z) = \left[\frac{2n+1}{z} - r_{n+1}(z)\right]^{-1}. \tag{5.256}$$

For $n \gg |z|$, we have

$$r_n(z) \underset{n \gg |z|}{\approx} \frac{z}{2n+1}. \tag{5.257}$$

If $n_{\max}$ is the largest n-value (cf. subsection 5.8.4), we start the downward recursion of Eq. (5.256) at $n = n_{\max} + n'$, where n' depends on the maximal particle dimension

relative to the wavelength (and, for $z = k_2 r$, the relative refractive index) and is chosen such that by the time n has been reduced to $n_{\max}$, the error in $r_{n_{\max}}(z)$ caused by using the approximate asymptotic formula (5.257) becomes negligibly small. We then compute $j_n(z)$, using the upward recursion

$$j_n(z) = r_n(z) j_{n-1}(z) \tag{5.258}$$

and starting at

$$j_0(z) = r_0(z) \frac{\cos z}{z}. \tag{5.259}$$

We also use the recurrence relation

$$\frac{1}{z}\frac{\mathrm{d}}{\mathrm{d}z}[z j_n(z)] = j_{n-1}(z) - \frac{n}{z} j_n(z), \tag{5.260}$$

which follows from Eq. (5.254) and the formula (Abramowitz and Stegun 1964)

$$(2n+1)\frac{\mathrm{d}}{\mathrm{d}z} j_n(z) = n j_{n-1}(z) - (n+1) j_{n+1}(z). \tag{5.261}$$

To compute the Hankel functions of the first kind, defined by Eq. (C.1), and their derivative we first find the spherical Bessel functions of the first kind, as described above, and then compute the spherical Bessel functions of the second kind using the numerically stable upward recurrence relation

$$y_{n+1}(z) = \frac{2n+1}{z} y_n(z) - y_{n-1}(z) \tag{5.262}$$

and the initial values

$$y_{-1}(z) = \frac{\sin z}{z}, \qquad y_0(z) = -\frac{\cos z}{z}, \tag{5.263}$$

where $z = k_1 r$ is real. Finally, we use the recurrence formula

$$\frac{1}{z}\frac{\mathrm{d}}{\mathrm{d}z}[z y_n(z)] = y_{n-1}(z) - \frac{n}{z} y_n(z), \tag{5.264}$$

derived in exactly the same way as Eq. (5.260).

As explained in subsection 5.8.3, the T matrix for rotationally symmetric particles calculated in the particle reference frame with the z-axis along the axis of rotation is block-diagonal, the different blocks $\mathbf{T}_m(P)$ corresponding to different m-values ($m = 0, 1, ..., n_{\max}$, where $n_{\max}$ is the converged n-value defined in subsection 5.8.4). Each block is computed separately by first calculating the respective $\mathbf{Q}_m$ and $\mathrm{Rg}\mathbf{Q}_m$ matrices from Eqs. (5.180)–(5.183) and (5.186)–(5.189) and then using

$$\mathbf{T}_m(P) = -(\mathrm{Rg}\mathbf{Q}_m)(\mathbf{Q}_m)^{-1}. \tag{5.265}$$

Using Eqs. (5.200) and (5.201) considerably shortens the computer time when $m = 0$. If the scatterer has a plane of symmetry perpendicular to the axis of rotation then us-

ing Eqs. (5.203)–(5.209) and restricting the integration in Eqs. (5.196)–(5.199) to $\cos\vartheta \in [-1, 0]$, with subsequent doubling of the result, further reduce the computational effort. The numerical stability and accuracy of the EBCM computations for particles with piecewise smooth surfaces, such as finite circular cylinders and osculating spheres, is improved by using special integration schemes that apply separate Gaussian quadratures to each smooth section (Barber and Hill 1990; Mishchenko *et al.* 1996a). The matrix inversion in Eq. (5.265) is performed using either standard Gaussian elimination with partial pivoting (Forsythe *et al.* 1977) or the special form of the LU-factorization method (Wielaard *et al.* 1997). As described in subsection 5.8.4, the latter provides much improved results for nonabsorbing or weakly absorbing particles. The matrices $(\mathbf{Q}_m)^{-1}$ and $\mathrm{Rg}\mathbf{Q}_m$ can be computed using either double-precision or extended-precision floating-point FORTRAN variables. As explained in subsection 5.8.4, the latter type of variable enables the code to handle significantly larger and/or more aspherical particles, albeit at the expense of increased computer time.

An important part of the code is the convergence procedure which checks whether the size of the T matrix and the number N_{G} of quadrature division points in Eq. (5.202) are sufficiently large that the scattering and absorption characteristics of interest are computed with the desired numerical accuracy (Mishchenko 1993). The procedure generates two $n_{\max}$-values: $n_{\max}$ and $\tilde{n}_{\max}$. The first, $n_{\max}$, is used to compute the matrices $\mathbf{Q}_m$, $\mathrm{Rg}\mathbf{Q}_m$, and $\mathbf{T}_m(P)$, whereas the second, $\tilde{n}_{\max}$, is used in the analytical orientation-averaging procedure described in Sections 5.4–5.6 and determines the maximal value of m. The fact that $\tilde{n}_{\max}$ is often significantly smaller than $n_{\max}$ means that a relatively large $n_{\max}$-value is required to accurately invert the $\mathbf{Q}_m$ matrices, whereas only a small number of leading T-matrix elements contribute to the orientation-averaged optical cross sections and scattering matrix elements. The code finds a reliable *a priori* estimate of both $n_{\max}$ and $\tilde{n}_{\max}$ using only the zeroth block, $\mathbf{T}_0(P)$, of the T matrix. $n_{\max}$ is increased in unit steps until the convergence criterion

$$\max\left\{\frac{|C_1(n_{\max}) - C_1(n_{\max}-1)|}{|C_1(n_{\max})|}, \frac{|C_2(n_{\max}) - C_2(n_{\max}-1)|}{|C_2(n_{\max})|}\right\} \le 0.1\Delta \tag{5.266}$$

is satisfied; here

$$C_1(n_{\max}) = -\frac{2\pi}{k_1^2}\mathrm{Re}\sum_{n=1}^{n_{\max}}(2n+1)[T_{0n0n}^{11}(P) + T_{0n0n}^{22}(P)], \tag{5.267}$$

$$C_2(n_{\max}) = \frac{2\pi}{k_1^2}\sum_{n=1}^{n_{\max}}(2n+1)\,\{|T_{0n0n}^{11}(P)|^2 + |T_{0n0n}^{22}(P)|^2\}, \tag{5.268}$$

and Δ is the required absolute accuracy of computing the expansion coefficients in Eqs. (4.75)–(4.80). The parameter $\tilde{n}_{\max}$ is then found as the smallest positive integer that ensures the inequality

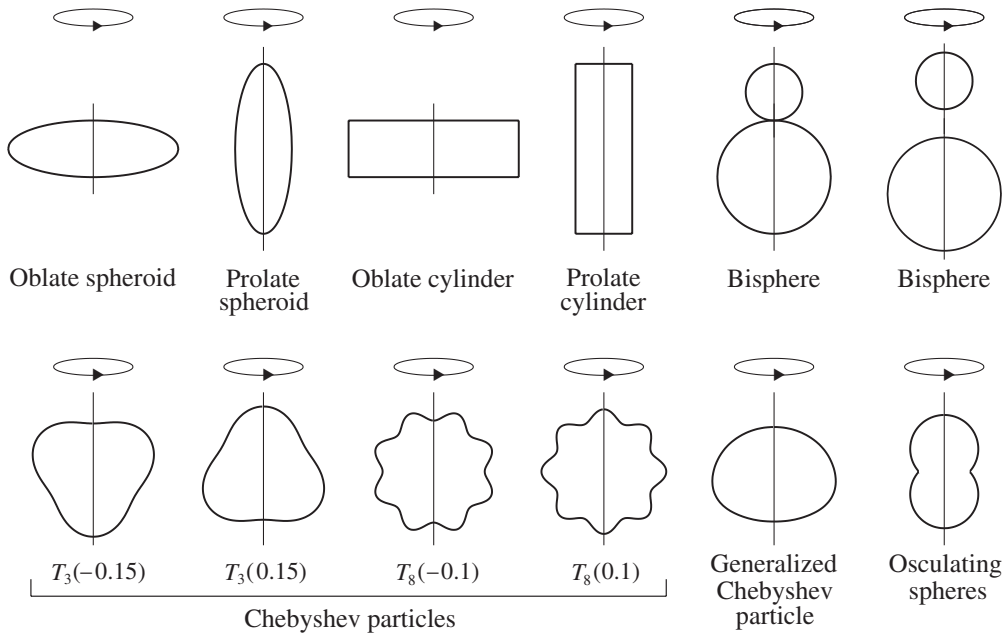

Figure 5.8. Typical rotationally symmetric shapes that can be handled by the *T*-matrix codes.

$$\max\left\{\frac{|C_1(\tilde{n}_{\max})-C_1(n_{\max})|}{|C_1(n_{\max})|},\frac{|C_2(\tilde{n}_{\max})-C_2(n_{\max})|}{|C_2(n_{\max})|}\right\}\le 0.1\Delta. \tag{5.269}$$

After $n_{\max}$ has been determined, N_{G} in Eq. (5.202) is increased until $C_1(n_{\max})$ and $C_2(n_{\max})$ converge within 0.1Δ. The initial N_{G}- value is chosen as a multiple of $n_{\max}$; the integer multiplicity factor NDGS is an important numerical parameter that must be optimized for each particle shape (see subsections 5.11.4 and 5.11.7).

5.11.2 Particle shapes and sizes

Although the *T*-matrix code can be easily tuned to handle essentially any rotationally symmetric shape, the current version of the code is directly applicable to spheroids, finite circular cylinders, and Chebyshev particles. Spheroids are formed by rotating an ellipse about its minor axis (oblate spheroid) or major axis (prolate spheroid) (Fig. 5.8). Their shape is described by the equation

$$r(\vartheta)=a\left(\sin^2\vartheta+\frac{a^2}{b^2}\cos^2\vartheta\right)^{-1/2}, \tag{5.270}$$

where b is the rotational (vertical) semi-axis and a is the horizontal semi-axis. The shape and size of a spheroid can be conveniently specified by the axis ratio a/b and the radius r_{s} of a sphere having the same surface area. The axis ratio is greater than 1 for oblate spheroids, smaller than 1 for prolate spheroids, and equal to 1 for spheres. Alternatively, one may use the axis ratio and the radius r_{v} of a sphere having the same volume.

Similarly, the shape and size of a finite circular cylinder (cf. Fig. 5.8) can be specified fully by the ratio of the diameter to the length, D/L, and the surface-equivalent-sphere radius r_s (or the volume-equivalent-sphere radius r_v). Note that D/L is smaller than 1 for prolate cylinders, equal to 1 for compact cylinders, and greater than 1 for oblate cylinders.

A Chebyshev particle is obtained by continuously deforming a sphere by means of a Chebyshev polynomial of degree n (Wiscombe and Mugnai 1986). Its shape is given by

$$r(\vartheta) = r_0[1+\xi T_n(\cos\vartheta)], \qquad |\xi|<1, \tag{5.271}$$

where r_0 is the radius of the unperturbed sphere, ξ is the deformation parameter, and $T_n(\cos\vartheta) = \cos n\vartheta$ is the Chebyshev polynomial of degree n (see Fig. 5.8, in which the different Chebyshev particles are indicated by the notation $T_n(\xi)$). All Chebyshev particles with $n \geq 2$ become partially concave as the absolute value of the deformation parameter increases and exhibit surface roughness in the form of waves running completely around the particle. Since the number of waves increases linearly with increasing n, the latter can be called the waviness parameter. The shape and size of a Chebyshev particle can be specified by the couplet $\{\xi, r_s\}$ (or by $\{\xi, r_v\}$).

5.11.3 Orientation and size averaging

After the T matrix for a specific shape and equivalent-sphere radius r has been computed, the orientation-averaged extinction, $\langle C_{\text{ext}}(r)\rangle$, and scattering, $\langle C_{\text{sca}}(r)\rangle$, cross sections per particle and the coefficients $\alpha_p^s(r)$ (p = 1, 2, 3, 4) and $\beta_p^s(r)$ (p = 1, 2) for identical particles in random orientation are calculated using Eqs. (5.107), (5.141), (5.126)–(5.130), and (4.109)–(4.114). Averaging over sizes is performed using straightforward numerical integration:

$$\langle C_{\text{ext}}\rangle = \int_{r_{\min}}^{r_{\max}} \mathrm{d}r\, n(r)\langle C_{\text{ext}}(r)\rangle \approx \sum_{i=1}^{N_r} u_i n(r_i)\langle C_{\text{ext}}(r_i)\rangle, \tag{5.272}$$

$$\langle C_{\text{sca}}\rangle = \int_{r_{\min}}^{r_{\max}} \mathrm{d}r\, n(r)\langle C_{\text{sca}}(r)\rangle \approx \sum_{i=1}^{N_r} u_i n(r_i)\langle C_{\text{sca}}(r_i)\rangle, \tag{5.273}$$

$$\begin{aligned}\alpha_p^s &= \frac{1}{\langle C_{\text{sca}}\rangle}\int_{r_{\min}}^{r_{\max}} \mathrm{d}r\, n(r)\langle C_{\text{sca}}(r)\rangle\alpha_p^s(r)\\ &\approx \frac{1}{\langle C_{\text{sca}}\rangle}\sum_{i=1}^{N_r} u_i n(r_i)\langle C_{\text{sca}}(r_i)\rangle\alpha_p^s(r_i), \qquad p=1,\ldots,4,\end{aligned} \tag{5.274}$$

$$\begin{aligned}\beta_p^s &= \frac{1}{\langle C_{\text{sca}}\rangle}\int_{r_{\min}}^{r_{\max}} \mathrm{d}r\, n(r)\langle C_{\text{sca}}(r)\rangle\beta_p^s(r)\\ &\approx \frac{1}{\langle C_{\text{sca}}\rangle}\sum_{i=1}^{N_r} u_i n(r_i)\langle C_{\text{sca}}(r_i)\rangle\beta_p^s(r_i), \qquad p=1,2,\end{aligned} \tag{5.275}$$

where $n(r)$ is an appropriate normalized distribution of equivalent-sphere radii. The use of analytical size distribution functions in actual computer calculations was discussed in subsection 5.10.1.

After the extinction and scattering cross sections and the expansion coefficients have been calculated, all other cross sections, the single-scattering albedo, the asymmetry parameter, and the elements of the normalized Stokes scattering matrix for an arbitrary set of scattering angles are found from Eqs. (4.43)–(4.45), (4.75)–(4.80), and (4.92). The Wigner *d*-functions appearing in expansions (4.75)–(4.80) are calculated using the recurrence relation (B.22) and initial values given by Eqs. (B.23) and (B.24).

5.11.4 Input parameters of the code

ICHOICE:
If ICHOICE = 1, then the code computes the inverse matrix $\mathbf{Q}^{-1}$ using the special LU-factorization scheme. If ICHOICE = 2, the inverse matrix is computed using the standard Gauss elimination procedure with partial pivoting. The execution time is roughly the same in both cases, but the LU-factorization procedure allows computations for significantly larger particles in the case of weak or no absorption (i.e., small or zero imaginary part of the relative refractive index).

RAT:
If RAT = 1, the size of the nonspherical particles is specified in terms of the equal-volume-sphere radius r_{v}. If RAT $\neq 1$, the size is specified in terms of the surface-equivalent-sphere radius r_{s}.

NDISTR, AXI, B, GAM, NPNAX, AXMAX:
The parameter NDISTR specifies the type of the particle size distribution. For the modified gamma distribution (5.242), NDISTR $=1$, AXI $=\alpha$, B $= r_c$, and GAM $=\gamma$. For the log normal distribution (5.243), NDISTR $= 2$, AXI $= r_g$, B $= \ln^2\sigma_g$, and GAM is ignored. For the power law distribution (5.244), NDISTR $= 3$, AXI $= r_{\mathrm{eff}}$, B $= v_{\mathrm{eff}}$, and GAM is ignored. In this case the parameters R1 and R2 (see below) are calculated from Eqs. (5.244) and (5.248)–(5.250) for given r_{eff} and v_{eff}. For the gamma distribution (5.245), NDISTR $= 4$, AXI $= a$, B $= b$, and GAM is ignored. Finally, for the modified power law distribution (5.246), NDISTR $= 5$, B $=\alpha$, and AXI and GAM are ignored. The code computes NPNAX size distributions of the same type and with the same values of B (and GAM for NDISTR = 1) in one run. The parameter AXI varies from AXMAX down to AXMAX/NPNAX in steps of AXMAX/NPNAX. If only one size distribution is needed, NPNAX is set to 1 and AXMAX is set equal to AXI of this size distribution.

R1 and R2:

$\mathrm{R1} = r_{\min}$ and $\mathrm{R2} = r_{\max}$ are the minimal and maximal radii of the size distribution for NDISTR = 1–4. R1 and R2 are calculated automatically for the power law distribution $\mathrm{NDISTR} = 3$ with given $\mathrm{AXI} = r_{\mathrm{eff}}$ and $\mathrm{B} = v_{\mathrm{eff}}$, but must be explicitly specified for other distributions after the statements

```
DO 600 IAX = 1, NPNAX
    AXI = AXMAX – DAX * DFLOAT(IAX – 1)
```

in the main program. For the modified power law distribution NDISTR = 5, $r_{\min} = 0$, $\mathrm{R1} = r_1$, and $\mathrm{R2} = r_2 = r_{\max}$.

NKMAX:

This parameter determines the number N_r of Gaussian quadrature points in Eqs. (5.272)–(5.275). NKMAX is an integer such that NKMAX + 2 is the number of quadrature points on the interval [R1, R2] (and on the interval [0, R1] for NDISTR = 5) for particles with AXI = AXMAX. For particles with AXI = AXMAX – AXMAX/NPNAX, AXMAX – 2*AXMAX/NPNAX, etc., the number of Gaussian division points decreases linearly.

LAM:

$\mathrm{LAM} = \lambda_1$ is the wavelength of the incident light in the surrounding medium.

MRR and MRI:

$\mathrm{MRR} = \mathrm{Re}\, m$ and $\mathrm{MRI} = \mathrm{Im}\, m$ are the real and imaginary parts of the relative refractive index, respectively. MRI must be non-negative.

EPS and NP:

These parameters specify the particle shape (cf. subsection 5.11.2). For spheroids, NP = –1, and EPS = a/b is the ratio of the horizontal to the rotational semi-axes. For circular cylinders, NP = –2 and EPS = D/L is the diameter-to-length ratio. For Chebyshev particles, NP, which must be positive, is the degree of the Chebyshev polynomial n in Eq. (5.271), while EPS = ξ is the deformation parameter.

DDELT:

This parameter enters the convergence criteria of Eqs. (5.266) and (5.269) and specifies the required numerical accuracy of the T-matrix calculations.

NPNA:

NPNA is the number of scattering angles at which the scattering matrix is computed. The corresponding scattering angles are given by 180*(I–1)/(NPNA–1) (in degrees), where I = 1, …, NPNA numbers the angles. This way of choosing scattering angles can be readily changed in the subroutine MATR (see subsection 5.10.2).

NDGS:
This integer parameter controls the initial value of the number N_G of Gaussian division points in the numerical evaluation of the integrals over the particle surface (cf. Eq. (5.202) and subsection 5.11.1)). For compact particles, the recommended value of NDGS is 2. For highly aspherical particles, larger values (NDGS = 3, 4, ...) may be necessary to obtain convergence (cf. subsection 5.11.7). Although the code checks the convergence over the number of Gaussian division points N_G (cf. subsection 5.11.1), it does not check the convergence over the initial value of N_G, which is equal to the product of n_{max} and NDGS. Therefore, too small a value of NDGS may cause false convergence in some cases, especially for highly elongated or flattened particles, and control comparisons of results obtained with different NDGS values are recommended.

5.11.5 Output information

R1 and R2:
For the power law size distribution (NDISTR = 3), $\mathrm{R1} = r_1$ and $\mathrm{R2} = r_2$ are the minimal and maximal radii, respectively, calculated for the input values of r_{eff} and v_{eff}.

REFF and VEFF:
$\mathrm{REFF} = r_{eff}$ and $\mathrm{VEFF} = v_{eff}$ are the effective radius and the effective variance of the size distribution, respectively.

CEXT and CSCA:
$\mathrm{CEXT} = \langle C_{ext} \rangle$ and $\mathrm{CSCA} = \langle C_{sca} \rangle$ are the orientation- and size-averaged extinction and scattering cross sections per particle, respectively.

< COS > and W:
$< \mathrm{COS} > = \langle \cos\Theta \rangle$ and $\mathrm{W} = \varpi$ are the orientation- and size-averaged asymmetry parameter and the single-scattering albedo, respectively.

ALPHA1, …, BETA2:
$\mathrm{ALPHA1(S)} = \alpha_1^s$, $\mathrm{ALPHA2(S)} = \alpha_2^s$, $\mathrm{ALPHA3(S)} = \alpha_3^s$, $\mathrm{ALPHA4(S)} = \alpha_4^s$, $\mathrm{BETA1(S)} = \beta_1^s$, and $\mathrm{BETA2(S)} = \beta_2^s$ are the coefficients appearing in the expansions (4.75)–(4.80).

F11, F22, F33, F44, F12, and F34:
$\mathrm{F11} = a_1$, $\mathrm{F22} = a_2$, $\mathrm{F33} = a_3$, $\mathrm{F44} = a_4$, $\mathrm{F12} = b_1$, and $\mathrm{F34} = b_2$ are the elements of the normalized Stokes scattering matrix (4.51).

5.11.6 Additional comments and recipes

The input parameters r_c, r_g, r_{eff}, a, r_1, r_2, and λ_1 must be specified in the same units of length. If these parameters are specified, for example, in micrometers then the extinction and scattering cross sections generated by the code are given in square micrometers.

The physical correctness of the numerical results is tested using inequalities derived by van der Mee and Hovenier (1990). Although the message that the test of van der Mee and Hovenier is satisfied does not guarantee the correctness of the results, the message that the test is not satisfied means that the results are likely to be wrong.

The required execution time rapidly increases with increasing values of the ratio radius/wavelength and/or with increasing particle asphericity. This should be taken into account in planning massive computations. The use of an optimizing compiler on IBM RISC workstations has been found to save about 70% of computer time compared with unoptimized code.

Execution can be automatically terminated if dimensions of certain arrays are not large enough. In all cases, a message appears explaining the cause of termination. The message "WARNING: NGAUSS = NPNG1" means that convergence over the parameter N_{G} cannot be obtained for the NPNG1 value specified in the PARAMETER statement. Often, however, this does not indicate a serious problem, especially for compact particles.

Larger and/or more aspherical particles may require larger values of the parameters NPN1, NPN4, and NPNG1. It is recommended that the relations NPN1 = NPN4 + 25 and NPNG1 = (NDGS+1)*NPN1 be maintained. Note that the memory requirement increases as the third power of NPN4. If the memory of a computer is too small to accommodate the code in its current setting then the parameters NPN1, NPN4, and NPNG1 should be reduced. However, this will decrease the maximal particle size parameter that can be handled by the code.

In some cases any increase of NPN1 will not make the T-matrix computations convergent. This means that the particle is too extreme in terms of size parameter and/or aspect ratio for a given value of the relative refractive index. The main program contains several PRINT statements which are currently commented out. If uncommented, these statements will produce the ratios that enter the convergence criteria of Eqs. (5.266) and (5.269) and can be used to determine whether the T-matrix computations for given particle parameters will converge at all.

The recommended value of the parameter DDELT is 0.001 (Mishchenko 1993) because larger values can generate false convergence. The message "WARNING: W IS GREATER THAN 1" means that the single-scattering albedo exceeds the maximal possible value, unity. If W is greater than 1 by significantly more than DDELT, this message can be an indication of numerical instability caused by extreme values of particle parameters.

Some of the common blocks are used to save memory rather than to transfer data. Therefore, if a compiler generates a warning message that the lengths of a common block are different in different subroutines, this is not a manifestation of a programming error.

In computations for spheres, one should use EPS = 1.000001 instead of EPS = 1 because the use of EPS = 1 can cause overflows in some rare cases. To calculate scattering by a monodisperse particle in random orientation, one may use the options

```
NPNAX = 1
AXMAX = r
B = 1D–1
NKMAX = –1
NDISTR = 4
⋮
DO 600 IAX = 1, NPNAX
    AXI = AXMAX – DAX*DFLOAT(IAX–1)
    R1 = 0.9999999*AXI
    R2 = 1.0000001*AXI
    ⋮
```

where r is the equivalent-sphere radius.

When there is no definite preference for a specific size distribution, we recommend using the power law or the modified power law size distribution rather than the gamma, modified gamma, or log normal distributions, because this can render convergent solutions for larger r_{eff} and v_{eff} values (Mishchenko and Travis 1994c). If results for many different size distributions are required and the relative refractive index is fixed, then an alternative approach can be more efficient than running this code many times. Specifically, scattering results should be computed for monodisperse particles with sizes ranging from essentially zero to some maximal value with a small step size. The results should be stored on disk and then can be used along with spline interpolation to compute the scattering characteristics of particles with intermediate sizes and to evaluate numerically the integrals in Eqs. (5.272)–(5.275). Scattering patterns for monodisperse nonspherical particles in random orientation are smoother than those for monodisperse spheres (e.g., Mishchenko and Travis 1994b and Section 10.1), and spline interpolation usually produces satisfactory results. In this way, averaging over any new size distribution can be a matter of a few seconds of computer time.

Table 5.3. Maximal convergent size parameters x_s and x_a and the respective NDGS values in extended-precision EBCM calculations for monodisperse oblate spheroids with relative refractive index 1.311 and axis ratios a/b varying from $3/2$ to 20

a/b	x_s	x_a	NDGS
20	12	17	30
10	17	24	15
5	27	37	5
3	42	54	4
2	92	111	3
3/2	>160	>180	2

5.11.7 Illustrative examples

As for all exact techniques for calculating electromagnetic scattering by nonspherical particles, the performance of the *T*-matrix code depends on the numerical options used and particle characteristics such as shape, size parameter, and relative refractive index. Table 5.3 shows the values of the maximum convergent surface-equivalent-sphere size parameter $x_s = 2\pi r_s/\lambda_1$ for monodisperse oblate spheroids with relative refractive index 1.311 and axis ratios a/b varying from 3/2 to 20. The results are obtained for DDELT = 0.001 using the extended-precision version of the *T*-matrix code and the LU-factorization matrix inversion scheme. Note that the maximal size parameter $x_a = 2\pi a/\lambda_1$ measured along the major semi-axis a can be significantly larger than the maximal surface-equivalent-sphere size parameter, especially for highly flattened spheroids. Table 5.3 also shows the respective values of the parameter NDGS, which controls the initial number of Gauss points in Eq. (5.202). Table 5.4 is analogous to Table 5.3, but is computed for prolate spheroids and shows the major-axis size parameter $x_b = 2\pi b/\lambda_1$ rather than x_a. It is clear that the maximal convergent size parameters strongly depend on the spheroid axis ratio and significantly increase as the particles become less aspherical. Tables 5.3 and 5.4 also demonstrate that converged computations for highly flattened and elongated spheroids may require large values of the parameter NDGS. Table 5.5 shows that the maximal convergent size parameters also depend on the particle relative refractive index and can significantly decrease with increasing m_R and/or m_I. Table 5.6 demonstrates the advantage of using extended-precision instead of double-precision computer arithmetic and using the special LU-factorization-based matrix inversion procedure in place of the traditional Gauss elimination scheme with partial pivoting. Finally, comparison of Tables 5.6 and 5.7 shows that although cylinders are particles with sharp rectangular edges, they can be handled by the *T*-matrix code almost as efficiently as smooth spheroids with a similar aspect ratio.

Table 5.4. Maximal convergent size parameters x_s and x_b and the respective NDGS values in extended-precision EBCM calculations for monodisperse prolate spheroids with relative refractive index 1.311 and axis ratios a/b varying from $2/3$ to $1/20$

a/b	x_s	x_b	NDGS
1/20	3	15	30
1/10	7	25	25
1/5	14	35	10
1/3	30	57	5
1/2	73	112	2
2/3	> 150	> 194	2

Table 5.5. Maximal convergent size parameters x_s and x_a and the respective NDGS values in extended-precision EBCM calculations for monodisperse oblate spheroids with axis ratio $a/b = 3$ and varying relative refractive index

Refractive index	x_s	x_a	NDGS
1.311	42	54	4
1.53 + i0.008	38	48	4
1.78 + i0.005	32	41	4
2 + i0.6	25	32	4

Table 5.6. Maximal convergent size parameter x_s versus axis ratio a/b in different types of EBCM computations for monodisperse oblate spheroids with relative refractive index 1.311

a/b	Extended precision LU-factorization	Double precision LU-factorization	Double precision Gauss elimination
20	12	4	4
10	17	7	5
5	27	12	7
3	42	19	10
2	92	38	14
3/2	> 160	97	24

Extensive comparisons of EBCM results with results generated by the separation of variables method for spheroids have shown that (i) the internal convergence of EBCM computations with increasing $n_{\max}$ is a reliable indication of their absolute convergence, and (ii) the EBCM is capable of producing very accurate numbers suit-

Table 5.7. Maximal convergent size parameter x_s versus diameter-to-length ratio D/L in different types of EBCM computations for monodisperse oblate cylinders with relative refractive index 1.311

D/L	Extended precision LU-factorization	Double precision LU-factorization	Double precision Gauss elimination
20	7	1.5	0.8
10	13	3	0.9
5	24	10	1.2
3	43	17	5
2	70	30	12
1	>180	93	21

able for use as benchmarks in testing the performance of other theoretical as well as experimental techniques (Kuik *et al.* 1992; Hovenier *et al.* 1996). Benchmark numbers for randomly oriented spheroids, circular cylinders, and Chebyshev particles have been published by Mishchenko (1991a), Kuik *et al.* (1992), Mishchenko *et al.* (1996a), and Wielaard *et al.* (1997). They cover the range of equivalent-sphere size parameters from a few units up to 60 and are given with up to nine correct decimals.

To supplement the existing set of benchmark results, we list in Table 5.8 the expansion coefficients α_p^s ($p = 1, 2, 3, 4$) and β_p^s ($p = 1, 2$) and in Table 5.9 the elements of the normalized Stokes scattering matrix for a polydispersion of randomly oriented oblate spheroids with an aspect ratio of 1.8 and a relative refractive index of $1.53 + \mathrm{i}0.008$. The size distribution is given by Eq. (5.244); r_1 and r_2 correspond to the effective surface-equivalent-sphere radius $r_{\mathrm{eff}} = 0.6\,\mu\mathrm{m}$ and the effective variance $v_{\mathrm{eff}} = 0.2$. The wavelength of the incident light in the surrounding medium is $\lambda_1 = 0.63\,\mu\mathrm{m}$. The integrals in Eqs. (5.272)–(5.275) were evaluated using 500 Gauss quadrature points. Other output parameters are as follows:

$$\langle C_{\mathrm{ext}} \rangle = 1.87101\,\mu\mathrm{m}^2, \qquad \langle C_{\mathrm{sca}} \rangle = 1.73760\,\mu\mathrm{m}^2,$$
$$\varpi = 0.928698, \qquad \langle \cos\Theta \rangle = 0.702091,$$
$$r_1 = 0.245830\,\mu\mathrm{m}, \qquad r_2 = 1.194170\,\mu\mathrm{m}.$$

The entire calculation took five minutes on an IBM RISC model 397 workstation. All output numbers are expected to be accurate to within ± 1 in the last decimals given.

5.12 *T*-matrix code for a homogeneous, rotationally symmetric particle in an arbitrary orientation

The FORTRAN *T*-matrix code for computing the amplitude and phase matrices for a homogeneous rotationally symmetric particle in an arbitrary orientation is available

Table 5.8. Expansion coefficients for a power law size distribution of homogeneous, randomly oriented oblate spheroids (see text)

s	α_1^s	α_2^s	α_3^s	α_4^s	β_1^s	β_2^s
0	1.00000	0.00000	0.00000	0.89928	0.00000	0.00000
1	2.10627	0.00000	0.00000	2.14323	0.00000	0.00000
2	2.79060	3.87999	3.71405	2.77094	– 0.05078	0.11537
3	3.00175	3.43981	3.37319	2.99128	– 0.09531	– 0.16185
4	2.83538	3.40580	3.34945	2.82333	– 0.04264	– 0.10973
5	2.60924	2.83160	2.81673	2.63846	– 0.02124	– 0.12877
6	2.39351	2.67150	2.60857	2.38094	– 0.04844	– 0.15852
7	2.12900	2.26075	2.23342	2.13666	– 0.00214	– 0.15971
8	1.89793	2.05330	2.02056	1.90065	– 0.02984	– 0.13873
9	1.67405	1.75096	1.72982	1.68165	– 0.01212	– 0.14309
10	1.47871	1.57690	1.54673	1.47595	– 0.02144	– 0.13788
11	1.27239	1.32218	1.31043	1.28250	– 0.01149	– 0.11999
12	1.10939	1.17407	1.14826	1.10498	– 0.01821	– 0.12428
13	0.92807	0.96196	0.95375	0.93662	– 0.01070	– 0.10080
14	0.79349	0.83674	0.81484	0.78766	– 0.01320	– 0.10570
15	0.64122	0.66391	0.65900	0.64845	– 0.00874	– 0.07936
16	0.53774	0.56598	0.54728	0.53055	– 0.00853	– 0.08365
17	0.41897	0.43337	0.43096	0.42479	– 0.00687	– 0.05712
18	0.34603	0.36382	0.34899	0.33914	– 0.00630	– 0.06120
19	0.25939	0.26825	0.26772	0.26439	– 0.00693	– 0.03890
20	0.21083	0.22196	0.21000	0.20432	– 0.00589	– 0.04365
21	0.14967	0.15492	0.15512	0.15334	– 0.00643	– 0.02593
22	0.11751	0.12443	0.11526	0.11193	– 0.00501	– 0.02989
23	0.07529	0.07824	0.07872	0.07778	– 0.00506	– 0.01639
24	0.05545	0.05944	0.05252	0.05057	– 0.00289	– 0.01953
25	0.02894	0.03041	0.03051	0.02993	– 0.00154	– 0.00847
26	0.01933	0.02088	0.01713	0.01637	– 0.00062	– 0.00899
27	0.00773	0.00822	0.00802	0.00776	0.00028	– 0.00288
28	0.00451	0.00492	0.00380	0.00359	0.00015	– 0.00236
29	0.00144	0.00154	0.00138	0.00130	0.00024	– 0.00066
30	0.00069	0.00074	0.00049	0.00046	0.00008	– 0.00035
31	0.00017	0.00018	0.00014	0.00013	0.00004	– 0.00009
32	0.00010	0.00011	0.00003	0.00003	0.00003	– 0.00004
33	0.00001	0.00001	0.00001	0.00001	0.00000	0.00000
34	0.00000	0.00000	0.00000	0.00000	0.00000	0.00000

Table 5.9. Elements of the normalized Stokes scattering matrix for a power law size distribution of homogeneous, randomly oriented oblate spheroids (see text)

Θ (deg)	$a_1(\Theta)$	$a_2(\Theta)$	$a_3(\Theta)$	$a_4(\Theta)$	$b_1(\Theta)$	$b_2(\Theta)$
0	30.8948	30.8569	30.8569	30.8190	0.0000	0.0000
10	17.7021	17.6717	17.6513	17.6282	0.0837	0.5816
20	6.7304	6.7047	6.6468	6.6343	0.0846	0.4295
30	3.1470	3.1251	3.0620	3.0572	0.0839	0.2200
40	1.5974	1.5778	1.5155	1.5151	0.0859	0.1116
50	0.8639	0.8454	0.7853	0.7872	0.0786	0.0365
60	0.5079	0.4895	0.4320	0.4353	0.0670	– 0.0069
70	0.3337	0.3146	0.2566	0.2614	0.0529	– 0.0356
80	0.2529	0.2319	0.1686	0.1755	0.0382	– 0.0585
90	0.2244	0.1997	0.1242	0.1338	0.0244	– 0.0833
100	0.2255	0.1947	0.1037	0.1166	0.0085	– 0.1089
110	0.2344	0.1963	0.0941	0.1106	– 0.0111	– 0.1256
120	0.2318	0.1870	0.0862	0.1063	– 0.0267	– 0.1192
130	0.2137	0.1647	0.0724	0.0956	– 0.0271	– 0.0927
140	0.1924	0.1415	0.0499	0.0753	– 0.0107	– 0.0665
150	0.1780	0.1281	0.0210	0.0464	0.0120	– 0.0512
160	0.1652	0.1222	– 0.0109	0.0103	0.0295	– 0.0306
170	0.1610	0.0994	– 0.0658	– 0.0187	0.0161	0.0319
180	0.2876	0.1526	– 0.1526	– 0.0176	0.0000	0.0000

on the World Wide Web at http://www.giss.nasa.gov/~crmim. Many relevant aspects of T-matrix computations were discussed in the preceding section. Therefore, below we mostly focus on issues specific to particles in a fixed orientation, list the input and output parameters of the code, and provide several benchmark results.

The general scheme for computing the single-particle T-matrix in the particle reference frame having its z-axis along the axis of particle symmetry was described in subsection 5.11.1. The only difference is that now the parameter $\tilde{n}_{\max}$ is ignored, so that the maximal value of m is equal to $n_{\max}$ and the entire T-matrix is used in amplitude and phase matrix computations.

The current version of the T-matrix code is directly applicable to spheroids, finite circular cylinders, Chebyshev particles, and so-called generalized Chebyshev particles (Fig. 5.8). The latter are described by the expansion

$$r(\vartheta) = r_0 \left[1 + \sum_{n=0}^{N} c_n T_n(\cos\vartheta) \right] \tag{5.276}$$

and are often used to model the shape of distorted falling raindrops (Chuang and Beard 1990). The size of either type of particle is specified by the surface-equivalent-sphere radius r_s or the volume-equivalent-sphere radius r_v.

The orientation of a scattering particle with respect to the laboratory reference

frame is specified by the Euler angles of rotation (α, β, γ) that describe the transformation of the laboratory reference frame into the particle reference frame (cf. Section 2.4). Since the particle is assumed to be rotationally symmetric, the amplitude scattering matrix with respect to the laboratory reference frame is given by Eq. (2.72) with $\gamma = 0$. The formulas for computing the amplitude scattering matrix with respect to the particle reference frame follow from Eqs. (5.11)–(5.17) and (5.36)–(5.37):

$$\begin{aligned} S_{11}^{P}(\hat{\mathbf{n}}^{\mathrm{sca}}, \hat{\mathbf{n}}^{\mathrm{inc}}) = {} & \frac{1}{k_1} \sum_{n=1}^{n_{\max}} \sum_{n'=1}^{n_{\max}} \sum_{m=0}^{\min(n,\, n')} (2-\delta_{m0}) \\ & \times \mathrm{i}^{n'-n-1} \left[\frac{(2n+1)(2n'+1)}{n(n+1)n'(n'+1)} \right]^{1/2} \cos[m(\varphi_P^{\mathrm{sca}} - \varphi_P^{\mathrm{inc}})] \\ & \times [T_{mnmn'}^{11}(P)\, \pi_{mn}(\vartheta_P^{\mathrm{sca}})\, \pi_{mn'}(\vartheta_P^{\mathrm{inc}}) + T_{mnmn'}^{21}(P)\, \tau_{mn}(\vartheta_P^{\mathrm{sca}})\, \pi_{mn'}(\vartheta_P^{\mathrm{inc}}) \\ & + T_{mnmn'}^{12}(P)\, \pi_{mn}(\vartheta_P^{\mathrm{sca}})\, \tau_{mn'}(\vartheta_P^{\mathrm{inc}}) + T_{mnmn'}^{22}(P)\, \tau_{mn}(\vartheta_P^{\mathrm{sca}})\, \tau_{mn'}(\vartheta_P^{\mathrm{inc}})], \end{aligned} \tag{5.277}$$

$$\begin{aligned} S_{12}^{P}(\hat{\mathbf{n}}^{\mathrm{sca}}, \hat{\mathbf{n}}^{\mathrm{inc}}) = {} & \frac{2}{k_1} \sum_{n=1}^{n_{\max}} \sum_{n'=1}^{n_{\max}} \sum_{m=1}^{\min(n,\, n')} \mathrm{i}^{n'-n-1} \left[\frac{(2n+1)(2n'+1)}{n(n+1)n'(n'+1)} \right]^{1/2} \sin[m(\varphi_P^{\mathrm{sca}} - \varphi_P^{\mathrm{inc}})] \\ & \times [T_{mnmn'}^{11}(P)\, \pi_{mn}(\vartheta_P^{\mathrm{sca}})\, \tau_{mn'}(\vartheta_P^{\mathrm{inc}}) + T_{mnmn'}^{21}(P)\, \tau_{mn}(\vartheta_P^{\mathrm{sca}})\, \tau_{mn'}(\vartheta_P^{\mathrm{inc}}) \\ & + T_{mnmn'}^{12}(P)\, \pi_{mn}(\vartheta_P^{\mathrm{sca}})\, \pi_{mn'}(\vartheta_P^{\mathrm{inc}}) + T_{mnmn'}^{22}(P)\, \tau_{mn}(\vartheta_P^{\mathrm{sca}})\, \pi_{mn'}(\vartheta_P^{\mathrm{inc}})], \end{aligned} \tag{5.278}$$

$$\begin{aligned} S_{21}^{P}(\hat{\mathbf{n}}^{\mathrm{sca}}, \hat{\mathbf{n}}^{\mathrm{inc}}) = {} & -\frac{2}{k_1} \sum_{n=1}^{n_{\max}} \sum_{n'=1}^{n_{\max}} \sum_{m=1}^{\min(n,\, n')} \mathrm{i}^{n'-n-1} \left[\frac{(2n+1)(2n'+1)}{n(n+1)n'(n'+1)} \right]^{1/2} \sin[m(\varphi_P^{\mathrm{sca}} - \varphi_P^{\mathrm{inc}})] \\ & \times [T_{mnmn'}^{11}(P)\, \tau_{mn}(\vartheta_P^{\mathrm{sca}})\, \pi_{mn'}(\vartheta_P^{\mathrm{inc}}) + T_{mnmn'}^{21}(P)\, \pi_{mn}(\vartheta_P^{\mathrm{sca}})\, \pi_{mn'}(\vartheta_P^{\mathrm{inc}}) \\ & + T_{mnmn'}^{12}(P)\, \tau_{mn}(\vartheta_P^{\mathrm{sca}})\, \tau_{mn'}(\vartheta_P^{\mathrm{inc}}) + T_{mnmn'}^{22}(P)\, \pi_{mn}(\vartheta_P^{\mathrm{sca}})\, \tau_{mn'}(\vartheta_P^{\mathrm{inc}})], \end{aligned} \tag{5.279}$$

$$\begin{aligned} S_{22}^{P}(\hat{\mathbf{n}}^{\mathrm{sca}}, \hat{\mathbf{n}}^{\mathrm{inc}}) = {} & \frac{1}{k_1} \sum_{n=1}^{n_{\max}} \sum_{n'=1}^{n_{\max}} \sum_{m=0}^{\min(n,\, n')} (2-\delta_{m0}) \\ & \times \mathrm{i}^{n'-n-1} \left[\frac{(2n+1)(2n'+1)}{n(n+1)n'(n'+1)} \right]^{1/2} \cos[m(\varphi_P^{\mathrm{sca}} - \varphi_P^{\mathrm{inc}})] \\ & \times [T_{mnmn'}^{11}(P)\, \tau_{mn}(\vartheta_P^{\mathrm{sca}})\, \tau_{mn'}(\vartheta_P^{\mathrm{inc}}) + T_{mnmn'}^{21}(P)\, \pi_{mn}(\vartheta_P^{\mathrm{sca}})\, \tau_{mn'}(\vartheta_P^{\mathrm{inc}}) \\ & + T_{mnmn'}^{12}(P)\, \tau_{mn}(\vartheta_P^{\mathrm{sca}})\, \pi_{mn'}(\vartheta_P^{\mathrm{inc}}) + T_{mnmn'}^{22}(P)\, \pi_{mn}(\vartheta_P^{\mathrm{sca}})\, \pi_{mn'}(\vartheta_P^{\mathrm{inc}})]. \end{aligned} \tag{5.280}$$

The angular functions $\pi_{mn}(\vartheta)$ and $\tau_{mn}(\vartheta)$ defined by Eqs. (5.16) and (5.17) are found from recurrence relations (B.22) and (B.26) and initial conditions (B.23) and (B.24). After the amplitude matrix with respect to the laboratory reference frame has been computed, the phase matrix is calculated using Eqs. (2.106)–(2.121).

The *T*-matrix code has the following *input* parameters.

ICHOICE:
If ICHOICE = 1 then the code computes the inverse matrix $\mathbf{Q}^{-1}$ using the special LU-factorization scheme. If ICHOICE = 2, the inverse matrix is computed using the standard Gauss elimination procedure with partial pivoting.

RAT:
If RAT = 1 then the size of the nonspherical particle is specified in terms of the volume-equivalent-sphere radius r_{v}. If RAT $\neq$ 1 then the size is specified in terms of the surface-equivalent-sphere radius r_{s}.

AXI:
AXI is the equivalent-sphere radius r_{v} or r_{s}.

LAM:
LAM $= \lambda_1$ is the wavelength of the incident light in the surrounding medium. LAM must be specified in the same units of length as AXI.

MRR and MRI:
MRR $= \mathrm{Re}\, m$ and MRI $= \mathrm{Im}\, m$ are the real and imaginary parts of the relative refractive index, respectively. MRI must be non-negative.

EPS and NP:
These parameters specify the shape of the particle. For a spheroid, NP = –1 and EPS = a/b is the ratio of the horizontal to the rotational semi-axis. For a circular cylinder, NP = –2 and EPS = D/L is the diameter-to-length ratio. For a Chebyshev particle, NP must be positive and is the degree of the Chebyshev polynomial n in Eq. (5.271), while EPS = ξ is the deformation parameter. For a generalized Chebyshev particle, NP = –3 and the expansion coefficients entering Eq. (5.276) are specified in the subroutine DROP.

DDELT:
This parameter enters the convergence criterion (5.266) and specifies the required numerical accuracy of the *T*-matrix calculations.

NDGS:
This integer parameter controls the initial value of the number N_{G} of Gaussian division points in the numerical evaluation of integrals over the particle surface (cf. subsection 5.11.4).

ALPHA and BETA:
ALPHA $= \alpha$ and BETA $= \beta$ are the Euler angles (in degrees) specifying the orientation of the axially symmetric particle with respect to the laboratory reference frame.

THET0, PHI0, THET, and PHI:
The angles THET0 = ϑ_L^{inc}, PHI0 = φ_L^{inc}, THET = ϑ_L^{sca}, and PHI = φ_L^{sca} (in degrees) specify the incidence and scattering directions with respect to the laboratory reference frame (cf. Section 2.4).

The parameters ALPHA, BETA, THET0, PHI0, THET, and PHI are specified at the end of the main program before the line

```
CALL AMPL (NMAX, ...)
```

The part of the main program following the line

```
C COMPUTATION OF THE AMPLITUDE AND PHASE MATRICES
```

can be repeated any number of times for different directions of illumination and scattering and different particle orientations because by this time the $\mathbf{T}(P)$ matrix for the given scattering particle has already been computed.

As the *output*, the code generates the four complex-valued elements of the amplitude scattering matrix $\mathbf{S}^L(\vartheta_L^{\text{sca}}, \varphi_L^{\text{sca}}; \vartheta_L^{\text{inc}}, \varphi_L^{\text{inc}}; \alpha, \beta, \gamma = 0)$ and the 16 real-valued elements of the Stokes phase matrix $\mathbf{Z}^L(\vartheta_L^{\text{sca}}, \varphi_L^{\text{sca}}; \vartheta_L^{\text{inc}}, \varphi_L^{\text{inc}}; \alpha, \beta, \gamma = 0)$ with respect to the laboratory reference frame. If AXI and LAM are specified, e.g., in micrometers, then the dimensions of the elements of the amplitude and phase matrices are micrometers and square micrometers, respectively.

To demonstrate the performance of the code, we applied it to the following four particle models:

- prolate spheroid with $a/b = 1/2$;
- prolate circular cylinder with a diameter-to-length ratio $1/2$;
- Chebyshev particle, Eq. (5.271), with $n = 4$ and $\xi = 0.1$;
- generalized Chebyshev particle with shape given by Eq. (5.276) with $N = 10$, $c_0 = -0.0481$, $c_1 = 0.0359$, $c_2 = -0.1263$, $c_3 = 0.0244$, $c_4 = 0.0091$, $c_5 = -0.0099$, $c_6 = 0.0015$, $c_7 = 0.0025$, $c_8 = -0.0016$, $c_9 = -0.0002$, and $c_{10} = 0.0010$ (cf. Fig. 5.8).

The surface-equivalent-sphere radius for the first three particles and the volume-equivalent-sphere radius for the fourth particle is 10 μm. All particles have the same relative refractive index, 1.5 + i0.02, and the same orientation with respect to the laboratory reference frame, given by $\alpha = 145°$ and $\beta = 52°$. The directions of the incident and scattered beams relative to the laboratory reference frame are given by the angles $\vartheta_L^{\text{inc}} = 56°$, $\varphi_L^{\text{inc}} = 114°$, $\vartheta_L^{\text{sca}} = 65°$, and $\varphi_L^{\text{sca}} = 128°$. The wavelength of the incident light in the surrounding medium is 6.283185 μm. The respective amplitude scattering matrices (with elements given in micrometers) are as follows:

$$\begin{bmatrix} -5.0941 + \mathrm{i}24.402 & -1.9425 + \mathrm{i}1.9971 \\ -1.1521 - \mathrm{i}3.0978 & -6.9323 + \mathrm{i}24.748 \end{bmatrix}, \tag{5.281}$$

$$\begin{bmatrix} -1.727+\mathrm{i}19.706 & -0.562+\mathrm{i}0.247 \\ -2.013-\mathrm{i}2.398 & -3.088+\mathrm{i}20.401 \end{bmatrix}, \tag{5.282}$$

$$\begin{bmatrix} 4.5123+\mathrm{i}18.092 & -1.6350+\mathrm{i}3.5274 \\ -3.0970-\mathrm{i}0.9215 & 3.2658+\mathrm{i}18.617 \end{bmatrix}, \tag{5.283}$$

$$\begin{bmatrix} 11.307+\mathrm{i}9.6184 & -2.6519+\mathrm{i}2.3589 \\ -4.9044-\mathrm{i}0.6241 & 9.9947+\mathrm{i}11.295 \end{bmatrix}. \tag{5.284}$$

These numbers are expected to be accurate to within ± 2 in the last decimals given.

In order to provide an additional test of the accuracy of the computer code for particles in a fixed orientation, the authors have used it to calculate the elements of the normalized Stokes scattering matrix for a uniform orientation distribution by first numerically evaluating the angular integrals in Eq. (5.108) and then using Eq. (4.51). These results were then compared with those rendered by the code based on the analytical averaging method for randomly oriented particles (Section 5.11). Since the latter code completely avoids the evaluation of the amplitude scattering matrix for specific particle orientations and illumination and scattering directions, it provides an excellent independent check. The perfect agreement that was found (to five and more significant digits) suggests that both codes provide high numerical accuracy and can be used in practical applications and as sources of benchmark results for testing alternative numerical techniques.

5.13 Superposition *T*-matrix code for randomly oriented two-sphere clusters

The World Wide Web site http://www.giss.nasa.gov/~crmim provides access to a superposition *T*-matrix code for computing the far-field scattering characteristics of a monodisperse two-sphere cluster (bisphere) in random orientation, as described in Section 5.9. The component spheres can be identical or different in terms of their size and relative refractive index and can be touching or separated. The *T* matrices of the component spheres are diagonal, the diagonal elements being the respective Lorenz–Mie coefficients (Eqs. (5.42)–(5.44)). The cluster *T* matrix is expanded about the geometrical center of the cluster (i.e., the center of the smallest sphere that encloses the cluster) and is diagonalized by means of directing the *z*-axis of the particle coordinate system along the line connecting the component sphere centers. The $\mathbf{T}_m$ blocks are computed sequentially for $m = 0, 1, ..., n_{\max}(1)$, where $n_{\max}(1)$ is the maximal order of numerically significant Lorenz–Mie coefficients for the larger sphere. $n_{\max}(1)$ and $n_{\max}(2)$ for the larger and the smaller sphere, respectively, are computed as (cf. Eq. (5.237))

$$n_{\max}(i) = x_i + 4.05x_i^{1/3} + \mathrm{NODR1}, \qquad i = 1, 2, \tag{5.285}$$

where x_i is the size parameter of sphere *i* and NODR1 is an input integer parameter (see below). The code does not check convergence over the parameter $n_{\max}$ specifying the size of the cluster *T* matrix (subsection 5.8.4) but rather uses an *a priori* estimate computed from

$$n_{\max} = x_{12} + 4.05x_{12}^{1/3} + \text{NODRT1}, \tag{5.286}$$

where $x_{12} = 2\pi r_{12}/\lambda_1$, r_{12} is the distance between the centers of the component spheres, and NODRT1 is another input integer parameter.

The code has the following *input* parameters.

LAM:
$\text{LAM} = \lambda_1$ is the wavelength of the incident light in the surrounding medium.

R, N, and K:
$\text{R(I)} = r_i$, $\text{N(I)} = \text{Re}\, m_i$, and $\text{K(I)} = \text{Im}\, m_i$ are the radius and the real and imaginary parts of the relative refractive index, respectively, for sphere *i* (*i* = 1, 2). K must be non-negative. If the spheres are of unequal size, the larger sphere must be number 1 and the smaller must be number 2.

R12:
$\text{R12} = r_{12}$ is the distance between component sphere centers. In general, R12 ≥ R(1) + R(2). Touching spheres have R12 = R(1) + R(2).

NODR1 and NODRT1:
NODR1 and NODRT1 are integers entering Eqs. (5.285) and (5.286). Usually NODR1 = 2 and NODRT1 = 2 provide acceptable accuracy. However, we recommend occasional checks of convergence of the solution over these parameters.

NPNA:
NPNA is the number of scattering angles at which the scattering matrix is computed. The corresponding scattering angles are given by 180*(I–1)/(NPNA–1) (in degrees), where I = 1, …, NPNA numbers the angles. This way of choosing scattering angles can be readily changed in the subroutine MATR (see subsection 5.10.2).

The code provides the following *output* information.

CEXT and CSCA:
$\text{CEXT} = \langle C_{\text{ext}} \rangle$ and $\text{CSCA} = \langle C_{\text{sca}} \rangle$ are the orientation-averaged extinction and scattering cross sections, respectively.

< COS > and W:
$< \text{COS} > = \langle \cos\Theta \rangle$ and $\text{W} = \varpi$ are the orientation-averaged asymmetry parameter and single-scattering albedo, respectively.

ALPHA1, …, BETA2:
$\mathrm{ALPHA1(S)} = \alpha_1^s$, $\mathrm{ALPHA2(S)} = \alpha_2^s$, $\mathrm{ALPHA3(S)} = \alpha_3^s$, $\mathrm{ALPHA4(S)} = \alpha_4^s$, $\mathrm{BETA1(S)} = \beta_1^s$, and $\mathrm{BETA2(S)} = \beta_2^s$ are the coefficients appearing in expansions (4.75)–(4.80).

F11, F22, F33, F44, F12, and F34:
$\mathrm{F11} = a_1$, $\mathrm{F22} = a_2$, $\mathrm{F33} = a_3$, $\mathrm{F44} = a_4$, $\mathrm{F12} = b_1$, and $\mathrm{F34} = b_2$ are the elements of the normalized Stokes scattering matrix (4.51).

The input parameters LAM, R(1), R(2), and R12 must be specified in the same units of length. If they are specified, for example, in micrometers then the extinction and scattering cross sections generated by the code are given in square micrometers. The general physical correctness of the numerical results is tested using inequalities derived by van der Mee and Hovenier (1990). The correctness and expected accuracy of the code is also demonstrated by the following additional tests (Mishchenko and Mackowski 1996).

(1) *T*-matrix computations for a bisphere with components of different size converge to the regular Lorenz–Mie solution for the bigger component as the size of the smaller component approaches zero.

(2) *T*-matrix computations for a bisphere with increasing distance between identical components converges to the Lorenz–Mie solution for independent spheres. The only exception is the direction of exact forward scattering, where the interference of light singly scattered by the bisphere components is constructive for any bisphere orientation and nearly doubles the height of the forward-scattering phase function peak as compared to that of a single sphere (Mishchenko *et al.* 1995).

(3) The computation of the *T* matrix for a bisphere in the particle coordinate system with the *z*-axis connecting the component sphere centers requires specification of the size parameters of the upper and lower components. If the size parameters are different then one has a choice of assigning the larger size parameter to the upper or to the lower sphere. However, the scattering results for randomly oriented bispheres must be independent of the choice, and, indeed, the code produces the same results whatever the choice is. Similarly, bisphere components can have different relative refractive indices, and, as expected, the code produces results that do not depend on assigning a particular relative refractive index to the upper or to the lower component.

(4) For nonabsorbing particles (i.e., particles for which the imaginary part of the relative refractive index is equal to zero) the scattering and extinction cross sections must be equal. The code reproduces this equality with very high accuracy.

(5) The accuracy of computing the bisphere *T* matrix was tested by using the numerical data for a fixed bisphere orientation reported by Flatau *et al.* (1993), who computed the scattered field without computing the *T* matrix. Agreement of up to four significant digits was found.

(6) Analytical *T*-matrix computations of the phase function and the degree of linear

polarization for randomly oriented bispheres with touching and separated components show agreement of up to three significant digits with the calculations of Tishkovets (1994), who employed the standard orientation-averaging method based on numerical angle integrations.

These tests indicate that the superposition *T*-matrix code is capable of producing very accurate numerical results. Mishchenko and Mackowski (1996) used the code to tabulate benchmark results for the following two models:

- monodisperse, randomly oriented bispheres, with touching identical components having size parameter 10;
- monodisperse, randomly oriented bispheres, with identical separated components having the size parameter 5. The distance between the sphere centers is twice their diameter.

The relative refractive index for both models is 1.5 + i0.005.

Further reading

Bohren (1974) and He and Cao (1998) developed analytical solutions for electromagnetic scattering by optically active (chiral) and bi-isotropic spheres, respectively. The computation of the Lorenz–Mie coefficients for concentric core–mantle spheres was considered by Kerker (1969), Toon and Ackerman (1981), Fuller (1993), and Kaiser and Schweiger (1993). Mikulski and Murphy (1963), Wait (1963), Bhandari (1985), and Mackowski *et al.* (1990) developed (recursive) algorithms for concentric multilayered spheres, whereas Wyatt (1962) and Perelman (1996) studied the problem of scattering by inhomogeneous spheres with a radially symmetric distribution of the refractive index. The scattering and absorption of light by a sphere imbedded in an absorbing host medium have been discussed by Chýlek (1977), Bohren and Gilra (1979), Bruscaglioni *et al.* (1993), Quinten and Rostalski (1996), Lebedev *et al.* (1999), Fu and Sun (2001), and Sudiarta and Chýlek (2001). Gouesbet *et al.* (1991) developed a so-called generalized Lorenz–Mie theory describing the scattering of an arbitrarily shaped incident beam by an arbitrarily located homogeneous spherical particle. The special case of a focused Gaussian beam has been considered, among others, by Gouesbet *et al.* (1988), Barton *et al.* (1989), and Lock (1995).

An interesting method for computing the *T* matrix for spheroids was developed by Schulz *et al.* (1998a). They first derived the *T* matrix in spheroidal coordinates using the separation of variables method and then converted it into the regular *T* matrix in spherical coordinates. Mishchenko and Videen (1999) reported the results of EBCM computations of electromagnetic scattering by randomly oriented osculating spheres. Kahnert *et al.* (2001a, b) have developed an efficient EBCM algorithm for computing the scattering and absorption properties of finite polyhedral cylinders.

Tsang *et al.* (1992), Zurk *et al.* (1995, 1996), and Siqueira and Sarabandi (2000) used the superposition *T*-matrix method to compute the extinction rate, effective permittivity, and scattering properties of media composed of densely packed, randomly positioned spheres. A modified version of the superposition *T*-matrix approach has been applied to

the problem of electromagnetic scattering by a particle or a cluster of particles located above or below (with respect to the incident wave) a plane interface separating two homogeneous half-spaces with different refractive indices. We refer the reader to the pioneering paper by Kristensson (1980) and recent publications by Videen (1996), Wriedt and Doicu (1998b), Denti *et al.* (1999a, b), Doicu *et al.* (1999), and Moreno and González (2000), where further literature citations can be found. Mackowski (2001) developed an approximate method to compute the *T* matrix for large-scale clusters of spheres by combining the superposition *T*-matrix method and an effective medium theory (see also Botet *et al.* 1997). He showed that this approximation can provide accurate predictions of the scattering and absorption properties of clusters containing a large number of uniformly packed spheres using only a fraction of the computer time required for the exact solution. Hamid (1996) and Saija *et al.* (2001) simulated electromagnetic scattering by spheroids and hexagonal cylinders by applying the superposition *T*-matrix method to clusters of appropriately arranged small spheres.

Appendix B of Bohren and Huffman (1983) contains a FORTRAN code for computing the Lorenz–Mie coefficients for a concentric core–mantle sphere and discusses its range of applicability. Additional codes for multilayered spheres are listed in Flatau (2000) and Wriedt (2000). The World Wide Web site ftp://ftp.eng.auburn.edu/pub/dmckwski/scatcodes/index.html provides access to two multi-sphere superposition *T*-matrix codes. The code SCSMFO is designed to calculate the Stokes scattering matrix and optical cross sections for a large-scale sphere cluster in a fixed orientation relative to the incident plane wave. On-line documentation provides the formulation and description of the code and a sample data input file. The code SCSMTM calculates the *T* matrix of a sphere cluster and the orientation-averaged scattering matrix and optical cross sections, as described by Mackowski and Mishchenko (1996). The on-line directories created and maintained by Wriedt (2000) and Flatau (2000) provide links to several Lorenz–Mie codes for homogeneous and concentrically layered spheres, single-particle EBCM codes, and superposition *T*-matrix codes for aggregated spheres and spheres with asymmetrically located spherical inclusions.

Numerous practical applications of the *T*-matrix method have been reviewed by Mishchenko *et al.* (1996b, 2000d). Further applications to biophysics, geophysics, astrophysics, and particle characterization can be found in the monographs by Lopatin and Sid'ko (1988) and Borghese *et al*. (2003) and papers by Quirantes and Delgado (1995), Borrmann *et al.* (1996, 2000), Doicu *et al.* (1997, 1998), Astafieva and Babenko (1999), Aydin and Walsh (1999), Bantges *et al.* (1999), Czekala *et al.* (1999, 2001), Ding and Xu (1999), Francis *et al.* (1999), Kouzoubov *et al.* (1999), Krotkov *et al.* (1999), Liu *et al.* (1999), Petrova (1999), Porstendorfer *et al.* (1999), Prodi *et al.* (1999), Ruppin (1999), Stubenrauch *et al.* (1999), Tsias *et al.* (1999), Vermeulen (1999), Volten *et al.* (1999), Wirth *et al.* (1999), Carey *et al.* (2000), Gledhill and McCall (2000), Hogan *et al.* (2000), Petrova *et al.* (2000), Reichardt *et al.* (2000a), Shvalov *et al.* (2000), Voshchinnikov *et al.* (2000), Zrnić *et al.* (2000), Alpers *et al.* (2001), Keenan *et al.* (2001), Kerola and Larson (2001), Prigent *et al.* (2001), and Vargas and Niklasson (2001). Nieminen *et al.* (2001) used the *T*-matrix method to compute laser trapping forces on a glass spheroid immersed in water.

A comprehensive list of peer-reviewed *T*-matrix publications was compiled by Mishchenko *et al*. (2004b) and is available at http://www.giss.nasa.gov/~crmim/publications.

Chapter 6

Miscellaneous exact techniques

All needs of a practitioner interested in light scattering by spherical particles are served well by the Lorenz–Mie theory, whereas those interested in exact calculations for nonspherical objects must resort to one of the more general and complex solutions. Although exact techniques for computing electromagnetic scattering by nonspherical particles may seem to be innumerable, some of them have been re-derived several times under different names, and most of them belong to one of two broad categories. Differential equation methods compute the scattered field by solving the Maxwell or the vector wave equations, subject to appropriate boundary conditions, in the time domain (Eqs. (1.1)–(1.4)) or in the frequency domain (Eqs. (1.17)–(1.20)). Integral equation methods are based on the volume or surface integral counterparts of the Maxwell equations; the boundary conditions are included in the solution automatically. A third category of methods includes hybrid techniques and methods that can be derived using different approaches.

This chapter briefly reviews several widely used exact theoretical approaches. Because of space limitations, the discussion here is much more concise than that in the previous chapter on the T-matrix method and Lorenz–Mie theory. More detailed information on specific numerical techniques can be found in the literature cited. In most cases we mention a recent review or a monograph providing further references. A general updated source of information on electromagnetic scattering techniques for nonspherical particles is the recent book edited by Mishchenko *et al.* (2000a).

Most theoretical methods yield the scattered electric field for a single particle in a fixed orientation, whereas practical applications often require the knowledge of size-, shape-, and orientation-averaged quantities such as the optical cross sections and phase and scattering matrix elements. Therefore, we will specifically indicate how ensemble averaging affects the performance of a technique. Since conventional ver-

sions of many techniques are applicable only to homogeneous, isotropic, optically inactive particles, we will mention explicitly possible extensions to inhomogeneous, anisotropic, and/or chiral scatterers. We will not discuss specifically theoretical techniques for such peculiar two-dimensional scatterers as infinite cylinders because our interest is in three-dimensional scattering by finite objects.

In what follows, scattering particles will be often characterized by: (i) the size parameter $x = 2\pi a/\lambda_1$, where a is a characteristic particle size (e.g., the semi-major dimension or the radius of a surface- or volume-equivalent sphere) and λ_1 is the wavelength of the incident light in the surrounding medium; (ii) the aspect ratio ε, which is the ratio of the maximum to minimum particle dimensions; and (iii) the index of refraction m relative to the surrounding medium. The efficiency of a numerical technique will be described usually in terms of its computational complexity, i.e., the dependence of the number of computer operations on the particle size parameter. It should be realized, however, that although the computational complexity of two different techniques can be proportional to the same power of the size parameter, the respective proportionality factors can be quite different, thereby making one technique much slower than the other.

6.1 Separation of variables method for spheroids

The separation of variables method (SVM) for single, homogeneous, isotropic spheroids was pioneered by Oguchi (1973), Asano and Yamamoto (1975), and Sinha and MacPhie (1977). With this method, the electromagnetic scattering problem is solved for a prolate or an oblate spheroid in the respective spheroidal coordinate system by expanding the incident, internal, and scattered fields in vector spheroidal wave functions (Flammer 1957). The expansion coefficients of the incident field are computed analytically, whereas the unknown expansion coefficients of the internal and scattered fields are determined through the requirement of continuity of the tangential electric and magnetic field components on the spheroid boundary (Eqs. (1.13) and (1.15)). Because the vector spheroidal wave functions are not orthogonal on the spheroidal surface, this procedure results in an infinite set of linear algebraic equations for the unknown expansion coefficients, which must be truncated and solved numerically. Farafonov (1983) (see also Voshchinnikov and Farafonov 1993) developed a version of the SVM in which one finds separately the axisymmetric part of the solution (i.e., the part independent of the azimuthal angle) and the non-axisymmetric part of the solution and uses a modified set of expansion functions.

For spheroids significantly larger than a wavelength and/or for large relative refractive indices, the system of linear equations becomes large and ill-conditioned. Furthermore, the computation of the vector spheroidal wave functions is a difficult mathematical and numerical problem, especially for absorbing particles (i.e., those with non-zero imaginary part of the relative refractive index). These factors have

limited the applicability of the SVM to equivalent-sphere size parameters less than about 40. Another obvious limitation of the technique is that it is applicable only to spheroidal scatterers. The main advantage of the SVM is that it can produce very accurate results. Furthermore, the version of the SVM developed by Farafonov provides numerically stable results for spheroids with extreme aspect ratios. The computational complexity of the SVM is $O(x^3) - O(x^4)$.

Various improvements of the SVM have been discussed by Asano (1979), Kurtz and Salib (1993), Do-Nhat and MacPhie (1997), Li *et al.* (1998a, 2001), Eide *et al.* (1999), and Qingan *et al.* (1999). The SVM has been extended to core–mantle spheroids by Onaka (1980), Cooray and Ciric (1992), Sebak and Sinha (1992), and Farafonov *et al.* (1996) (see also Gurwich *et al.* 2000), and to optically active spheroids by Cooray and Ciric (1993). Schulz *et al.* (1998a) developed an analytical technique for computing electromagnetic scattering by an ensemble of randomly oriented spheroids. They first used the Asano and Yamamoto version of the SVM to compute the T matrix in the spheroidal coordinate system, then converted it into a T matrix in the spherical coordinate system, and finally used the orientation-averaging approach described in Chapter 5. SVM computations for homogeneous and core–mantle spheroids have been reported by Asano (1979, 1983), Rogers and Martin (1979), Asano and Sato (1980), Schaefer (1980), de Haan (1987), Stammes (1989), Voshchinnikov and Farafonov (1994), Kim and Martin (1995), Somsikov (1996), Voshchinnikov (1996), Il'in and Voshchinnikov (1998), Li *et al.* (1998b), Schulz *et al.* (1998b, 1999b), Ciric and Cooray (1999), Eide *et al.* (2000), Kang *et al.* (2000), and Voshchinnikov *et al.* (2000). Available SVM computer codes are listed in Flatau (2000) and Wriedt (2000). An extensive review of the SVM is provided by Ciric and Cooray (2000).

6.2 Finite-element method

The finite-element method (FEM) is a differential equation technique that computes the scattered time-harmonic electric field by solving numerically the vector Helmholtz equation subject to the standard boundary conditions (Morgan and Mei 1979; Silvester and Ferrari 1996). The particle is imbedded in a finite computational domain that is discretized into many small-volume cells called elements, with about 10 to 20 elements per wavelength. The electric field values are specified at the nodes of these elements and are initially unknown. Through the requirement of the boundary conditions, the differential equation is converted into a matrix equation for the unknown node electric field values. This equation is solved using, e.g., standard Gaussian elimination (GE) or one of the preconditioned iterative methods such as the conjugate gradient method (CGM). Because of the local nature of the differential equation, electric fields at the nodes are directly related only to their neighbors, thereby making the resultant matrix equation sparse and banded, which significantly reduces

the numerical effort. The computational complexity of the FEM with sparse GE is $O(x^7)$, whereas that of the FEM with the CGM is only $O(x^4)$. The disadvantage of the FEM with the CGM is that computations must be repeated for each new direction of incidence, but the number of requisite incidence directions may be reduced by exploiting symmetries of the scattering problem and the reciprocity relation.

Although scattering in the far-field zone is an unbounded-space problem, the FEM must be implemented always in a finite computational domain in order to limit the number of unknowns to a manageable size. As a consequence, approximate absorbing boundary conditions must be imposed at the outer boundary of the computational domain in order to suppress wave reflections back into the domain and permit the numerical analogs of the outward-propagating waves to exit the domain almost as it were infinite (Mittra and Ramahi 1990). Another approach (e.g., Volakis *et al.* 1998; Sheng *et al.* 1998) is to couple the FEM with a surface integral equation in order to satisfy accurately the radiation condition at infinity (i.e., to ensure the $1/r$ decay of the transverse component and a faster than $1/r$ decay of the radial component of the scattered electric field in the far-field zone; see Section 2.2). The drawback of the latter technique is that it can destroy the sparsity of the finite-element matrix.

Another way of enforcing the radiation condition is the so-called unimoment method (Mei 1974; Morgan and Mei 1979; Morgan 1980). This modification of the FEM uses a spherical computational domain and an expansion of the scattered field outside the computational domain in outgoing spherical wave functions with unknown coefficients. The total external field is the sum of this unknown expansion and the known expansion of the incident field. The unknown expansion coefficients are found by applying the FEM scheme inside the computational domain and matching the FEM nodal fields and the spherical wave function expansions at the boundary of the computational domain. The scattered field in the far-field zone is calculated by evaluating the spherical wave function expansion and automatically satisfies the radiation condition. Since the unimoment method always uses a spherical computational domain, the volume of the domain can become much larger than the volume of the scatterer for objects with high aspect ratios, thereby making this technique inefficient.

The important advantages of the FEM are that it can be applied to arbitrarily shaped and inhomogeneous particles, is simple in concept and implementation, and avoids the singular-kernel problem typical of integral equation methods (see Section 6.5). However, FEM computations are spread over the entire computational domain rather than confined to the scatterer itself as in the integral equation methods. This tends to make FEM calculations rather time consuming and limits the maximum size parameter to values less than about 10. Features such as the finite spatial discretization and approximate absorbing boundary condition make the FEM unsuitable for applications in which achieving a very high and controllable numerical accuracy is important. Further information about the FEM and the closely related finite-difference method (FDM) can be found in Morgan (1990), Silvester and Ferrari

(1996), and Volakis *et al.* (1998). Several FEM computer codes are listed in Wriedt (2000).

6.3 Finite-difference time-domain method

Unlike the FEM, the finite-difference time-domain method (FDTDM) calculates electromagnetic scattering in the time domain by solving Maxwell's time-dependent curl equations (1.2) and (1.4) directly (Yee 1966). The space and time derivatives of the electric and magnetic fields are approximated using a finite-difference scheme with space and time discretizations selected to constrain computational errors and ensure numerical stability of the algorithm. Hence, time is approximated by a sequence of discrete steps, and a marching-in-time procedure is used to track the evolution of the fields from their initial values at some initial time. As in the FEM, the scattering object is imbedded in a finite computational domain, and absorbing boundary conditions are employed to model scattering in unbounded space (e.g., Berenger 1996; Grote and Keller 1998; Yang and Liou 1998b; Sun *et al.* 1999). The fields are specified at spatial grid points with discretization density similar to that needed for the FEM. Values at the grid points for the previous and current time steps are used to calculate the values at the next time step, thereby making the system of equations to update the fields fully explicit. As a consequence, there is no need to solve a large system of linear equations, and the memory-size requirement is proportional to the total number of grid points. The common practice of modeling scattering objects with curved boundaries using rectangular grid cells causes a so-called staircasing effect and increases numerical errors. This effect becomes especially pronounced for particles with large relative refractive indices and must be reduced using special techniques (Yang and Liou 1996a; Sun and Fu 2000). The operation count grows approximately as the fourth power of the particle size parameter. Since the FDTDM computes the near field in the time domain, a special near-zone to far-zone transformation must be invoked in order to compute the scattered far field in the frequency domain (Taflove 1995; Yang and Liou 1996a; Martin 1998).

The FDTDM has become rather popular recently, owing to its conceptual simplicity, flexibility, and ease of implementation. Since the method tracks the time-varying field throughout a volume of space, FDTDM results are well suited for animation using modern computer graphics so that the user is provided with a visual demonstration of the temporal and spatial behavior of the electromagnetic field. The FDTDM shares the advantages of the FEM with the CGM as well as its limitations in terms of accuracy, computational complexity, size parameter range, and the need to repeat all computations with changing direction of illumination. Applications of the FDTDM to far-field scattering computations have been described by Tang and Aydin (1995), Aydin and Tang (1997a, b), Yang *et al.* (1997, 2000b), Liou *et al.* (1998, 2000), Videen *et al.* (1998b), Aydin and Walsh (1999), Drezek *et al.* (1999), and Fu

et al. (1999). Additional information on the FDTDM can be found in the monographs by Kunz and Luebbers (1993) and Taflove (1995, 1998) and in the recent review by Yang and Liou (2000). Available FDTDM computer codes are listed by Wriedt (2000).

6.4 Point-matching method

The point-matching method (PMM) is a differential equation technique based on expanding the incident and internal fields in vector spherical wave functions that are regular at the origin and expanding the scattered field outside the scatterer in outgoing vector spherical wave functions. The expansion coefficients of the incident field are known (Eqs. (5.4) and (5.5)), whereas the expansion coefficients of the internal and scattered fields are found by truncating the expansions to a finite size and matching the fields at the surface of the scatterer via application of the boundary conditions. In the simple PMM, the fields are matched at as many points on the surface as there exist unknown expansion coefficients (Oguchi 1973).

The general idea of the PMM is so simple and attractive that the method continues to be reinvented (e.g., Sarkar and Halas 1997). However, it often produces poorly converging and unstable results. It is possible that such behavior may be attributed to the fact that it relies on the Rayleigh hypothesis (RH; see Section 5.1), whereas the validity of this hypothesis is questionable. For example, the results of Doicu *et al.* (1999), Ngo *et al.* (1997), and Mishchenko and Videen (1999) seem to imply that the RH may in fact be wrong.

The use of vector spherical wave functions to represent the incident, internal, and scattered fields makes the PMM similar to the T-matrix method. Moreover, it appears that the RH can be used to derive the extended boundary condition method (EBCM); see Chew (1995). Since the EBCM is exact, this derivation has been interpreted sometimes as evidence of the validity of the RH and of the equivalence of the RH and the EBCM (Burrows 1969; Schmidt *et al.* 1998). However, the fact that the EBCM can be derived from the RH means only that the RH is a sufficient condition of validity of the EBCM but not a necessary condition. The equivalence of the RH and the EBCM and hence the validity of the RH would follow only from reciprocal derivation of the RH from the EBCM, but this has not been accomplished so far. Therefore, one should not exclude the possibility that the RH may be violated despite the fact that the EBCM is exact (Millar 1969; Lewin 1970).

A modification of the PMM called the boundary-matching method was developed by Barton and Alexander (1991). Instead of imposing the boundary conditions at a finite number of distributed points, the boundary condition equations are expanded in spherical harmonics and matched for each angular mode. This results in a set of simultaneous algebraic equations from which the expansion coefficients can be determined. Since the method shows poor convergence for spheroids with aspect ratios

larger than 1.4, Barton and Alexander concluded that it is best suited to the analysis of near-spherical particles.

The convergence problem of the simple PMM appears to be partly ameliorated in the generalized PMM (GPMM) by the creation of an overdetermined system of equations for the unknown expansion coefficients. This is accomplished by matching the fields in the least squares sense at a number of surface points significantly greater than the number of unknowns (Morrison and Cross 1974; Oguchi and Hosoya 1974; Al-Rizzo and Tranquilla 1995a, b). The performance of the GPMM has been further improved by employing multiple spherical expansions to describe the fields both inside and outside the scattering object (Joo and Iskander 1990; Al-Rizzo and Tranquilla 1995c). This multiple-expansion GPMM (ME-GPMM) does not rely on the RH; it is also known as the generalized multipole technique, the discrete sources method, and the Yasuura method (Hafner 1990; Ludwig 1991; Eremin and Orlov 1998; Wriedt 1999). It is claimed that the ME-GPMM for rotationally symmetric scatterers is numerically stable, sufficiently accurate, and applicable to large size parameters (Al-Rizzo and Tranquilla 1995c). Piller and Martin (1998a) extended the ME-GPMM to anisotropic scatterers.

6.5 Integral equation methods

The interaction of a plane electromagnetic wave with an object of volume V_{INT} is described fully by the volume integral equation (2.16). The calculation of the scattered field using Eq. (2.16) would be straightforward except that the internal electric field is unknown. Therefore, this equation must first be solved for the internal field. The integral in Eq. (2.16) is usually approximated by discretizing the interior region into N small cubic cells of a volume ΔV with about 10 to 30 cells per wavelength and assuming that the electric field and the refractive index within each cell are constant:

$$\mathbf{E}(\mathbf{r}_i) = \mathbf{E}^{\mathrm{inc}}(\mathbf{r}_i) + k_1^2 \Delta V \sum_{j=1}^{N} \overleftrightarrow{G}(\mathbf{r}_i, \mathbf{r}_j) \cdot \mathbf{E}(\mathbf{r}_j)[m^2(\mathbf{r}_j) - 1], \quad i = 1, ..., N, \tag{6.1}$$

where $\mathbf{r}_i \in V_{\mathrm{INT}}$ is the central point of the ith cell. Physically this procedure is equivalent to representing the internal field at each point of the interior region V_{INT} as a sum of the incident field and the field induced by sources at all interior points, including the self point. Equations (6.1) form a system of N linear algebraic equations for the N unknown internal fields $\mathbf{E}(\mathbf{r}_i)$ and must be solved numerically. Since the internal fields interact with each other throughout the object, the resultant matrix is full. Once the internal fields are found, the total external field is determined from

$$\mathbf{E}(\mathbf{r}) = \mathbf{E}^{\mathrm{inc}}(\mathbf{r}) + k_1^2 \Delta V \sum_{j=1}^{N} \overleftrightarrow{G}(\mathbf{r}, \mathbf{r}_j) \cdot \mathbf{E}(\mathbf{r}_j)[m^2(\mathbf{r}_j) - 1], \quad \mathbf{r} \in V_{\mathrm{EXT}}. \tag{6.2}$$

Finally, the scattered field is computed by subtracting the incident field from the total external field. This version of the volume integral equation method (VIEM) is known as the method of moments (MOM). Since the free space dyadic Green's function given by Eqs. (2.13) and (2.15) becomes singular as $|\mathbf{r}-\mathbf{r}'|\to 0$, special techniques must be used to handle the self-interaction term $(j=i)$ in the sum on the right-hand side of Eq. (6.1) (Lakhtakia and Mulholland 1993).

Several modifications of the MOM have been developed under different names: the digitized Green's function algorithm (Goedecke and O'Brien 1988), the volume integral equation formulation (Iskander *et al.* 1989a; Hage *et al.* 1991; Lumme and Rahola 1998), and the variational volume integral equation method (Peltoniemi 1996). The main difference among these techniques is the way in which they treat the self-interaction term.

The straightforward approach to solving the MOM matrix equation using the standard GE entails a computational complexity of $O(N^3)\propto O(x^9)$ and is not practical for size parameters exceeding unity. The conjugate or bi-conjugate gradient method together with the fast Fourier transform (CGM-FFT or BCGM-FFT) (Gan and Chew 1995; Peterson *et al.* 1998, Chapter 4) has the computational complexity $O(N^{1+\alpha}\log N)\propto O(x^{3+3\alpha}\log x)$, where N^{α} with $0<\alpha<1$ is the total number of iterations required to achieve a specific accuracy; this method can be applied to significantly larger size parameters. Furthermore, the CGM-FFT (BCGM-FFT) and related techniques can significantly reduce computer memory requirements. The standard drawback of using the CGM (BCGM) and other preconditioned iterative techniques is that computations must be fully repeated for each new illumination direction.

Another version of the VIEM is the so-called discrete dipole approximation (DDA), otherwise known as the coupled dipole method. Whereas the MOM deals with the *actual* electric fields in the central points of the cells constituting the scattering object (Eq. (6.1)), the DDA exploits the concept of *exciting* field. It is based on partitioning a particle into a number N of elementary polarizable units called dipoles. The electromagnetic response of the dipoles to the local electric field is assumed to be known. The field exciting a dipole is a superposition of the external field and the fields scattered by all other dipoles. This allows one to write a system of N linear equations for N fields exciting the N dipoles. An important way in which the DDA matrix equation differs from the MOM matrix equation is that the former does not contain the troublesome self-interaction term. The numerical solution of the DDA matrix equation is then used to compute the N partial fields scattered by the dipoles and thereby the total scattered field. Although the original derivation of the DDA by Purcell and Pennypacker (1973) was heuristic, Lakhtakia and Mulholland (1993) showed that the DDA can in fact be derived from the volume integral equation and is closely related to the MOM.

Since the pioneering paper by Purcell and Pennypacker (1973), the DDA has been improved by modifying the treatment of the dipole polarizability (Draine 1988;

Dungey and Bohren 1991; Draine and Goodman 1993; Lumme and Rahola 1994; Okamoto 1995), including magnetic dipole and dielectric quadrupole terms in addition to the electric dipole term (Mulholland *et al.* 1994; Lemaire 1997), applying the CGM-FFT and other preconditioned iterative methods to solve the DDA matrix equation with a $O(x^{3+3\alpha}\log x)$ computational complexity (Goodman *et al.* 1991; Flatau 1997), and employing concepts of the sampling theory (Piller and Martin 1998b). Varadan *et al.* (1989), Lakhtakia (1992), and Piller (1999) extended the DDA to anisotropic, bi-anisotropic, and high-permittivity materials, respectively. Ku (1993) compared the numerical performance of the MOM (Iskander *et al.* 1989a) and the DDA (Dungey and Bohren 1991). Chiappetta (1980) and Singham and Bohren (1987, 1988) developed a scattering-order formulation of the DDA. Hoekstra *et al.* (1998) investigated the performance of a DDA implementation on a parallel supercomputer. McClain and Ghoul (1986), Singham *et al.* (1986), and Khlebtsov (2001) have developed analytical DDA procedures for computing the scattering of light by randomly oriented particles based on re-expanding Cartesian tensor products in terms of spherical tensor products and exploiting analytical properties of Wigner *D*-functions (Appendix B). Unfortunately, this approach involves a time-consuming matrix inversion (computational complexity $O(x^9)$) and is applicable only to particles smaller than a wavelength. Draine and Weingartner (1996) and Kimura and Mann (1998) used the DDA to compute the radiation force and torque on nonspherical particles and fluffy aggregates. Hoekstra *et al.* (2000) extended their work by deriving DDA formulas for computing the radiation force experienced by each dipole.

The major advantages of the MOM and DDA are that they automatically satisfy the radiation condition at infinity (Eq. (2.24)), are confined to the scatterer itself, thereby resulting in fewer unknowns than the differential equation methods, and can be applied to inhomogeneous, anisotropic, and/or optically active scatterers (e.g., Su 1989; Rojas 1992). However, the numerical accuracy of the methods is relatively low, especially for the scattering matrix elements, and improves slowly with increasing N, whereas the computer time grows rapidly with increasing size parameter (Singham 1989; Draine and Flatau 1994; Evans and Stephens 1995; Okamoto *et al.* 1995). A major source of numerical errors is the approximate representation of smooth particle surfaces by discrete cubical dipoles (Lemke *et al.* 1998). Another disadvantage of the above techniques is the need to repeat the entire calculation for each new direction of incidence (for the MOM and DDA with the CGM-FFT). These factors have made MOM and DDA computations time consuming, especially for particle size, shape, and/or orientation distributions, and have limited the particle size parameter to relatively small values.

The attractiveness and simplicity of the physical idea of the DDA and the public availability of the well-documented DDA code by Draine and Flatau (1997) have resulted in widespread applications of this technique during the last decade. Further information on the MOM and DDA and their applications can be found in Miller *et al.* (1991), Wang (1991), Draine and Flatau (1994), Lumme *et al.* (1997), Lemke and

Quante (1999), Murayama *et al.* (1999), and Draine (2000).

Equation (2.16) is a Fredholm-type integral equation with a singular kernel at $\mathbf{r}' = \mathbf{r}$. Holt *et al.* (1978) removed the singularity by applying the Fourier transform to the internal field and converting the volume integral into an integral in wave number coordinate space. Discretization of the latter results in a matrix equation that is solved numerically and gives the scattered field.

The scattered field obtained with this Fredholm integral equation method (FIEM) satisfies a variational principle and is claimed to be numerically stable and convergent to the exact result, even for particles with large aspect ratios, albeit the size parameter in actual computations for highly aspherical scatterers has been relatively small so far. Numerical implementation of the technique becomes much simpler for homogeneous, rotationally symmetric bodies.

The major limitation of the FIEM is that the matrix elements must be evaluated analytically, thereby requiring different programs for each type of scatterer. As a consequence, FIEM computations have been limited to only a few model shapes such as spheroids, triaxial ellipsoids, and finite circular cylinders (Evans and Holt 1977; Holt *et al.* 1978; Holt and Shepherd 1979; Shepherd and Holt 1983; Matsumura and Seki 1991, 1996). The majority of reported FIEM results pertain to size parameters smaller than 5 and tend to be rather time consuming (Holt 1982). Larger particles (volume-equivalent-sphere size parameters up to 36.7) were considered by Stamatakos *et al.* (1997). However, the relative refractive index was restricted to 1.04, and a comparison of FIEM results for a sphere with exact Lorenz–Mie computations showed poor agreement at scattering angles exceeding $25°$.

An important advantage of the FIEM is that a significant part of the calculation, the integrals, depends only on the particle size parameter and shape. Therefore, changing the relative refractive index and/or the direction and polarization state of the incident wave does not require a complete new calculation. A similar saving of computer time is achieved in performing convergence checks. Papadakis *et al.* (1990) and Karonis *et al.* (1999) extended the FIEM to anisotropic and chiral dielectric ellipsoids, while Stamatakos and Uzunoglu (1997) applied the FIEM to scattering by a linear chain of triaxial dielectric ellipsoids.

Electromagnetic scattering by homogeneous or layered dielectric bodies can be computed using a surface integral counterpart of Eq. (2.16) (Poggio and Miller 1973; Umashankar *et al.* 1986; Medgyesi-Mitschang *et al.* 1994; Swatek and Ciric 2000a, b). Although surface integral equation methods (SIEMs) cannot be applied to highly inhomogeneous scatterers, their important advantage is that the dimensionality of the problem is reduced by one, and the number of unknowns N is proportional to x^2 rather than to x^3, as in the VIEM, thereby resulting in a computational complexity of $O(x^6)$ for SIEMs with the GE and $O(x^{4+2\alpha})$ for SIEMs with the CGM.

6.6 Superposition method for compounded spheres and spheroids

The separation of variables solution for a single sphere (the Lorenz–Mie theory) can be extended to clusters of spheres by using the translation addition theorem for vector spherical wave functions (Bruning and Lo 1971a, b; Borghese *et al.* 1979; Hamid *et al.* 1990; Fuller 1991; Mackowski 1991). The total field scattered by a multi-sphere cluster can be represented as a superposition of individual fields scattered from each sphere. These individual fields are interdependent because of electromagnetic interactions between the component spheres. The external electric field illuminating the cluster and the individual fields scattered by the component spheres are expanded in vector spherical wave functions with origins at the individual sphere centers. To exploit the orthogonality of the vector spherical wave functions in the sphere boundary conditions, one uses the translation addition theorem with a vector spherical wave function centered at one sphere origin then re-expanded about another sphere origin (Appendix C). This procedure ultimately results in a matrix equation for the scattered-field expansion coefficients of each sphere. Numerical solution of this equation for the specific direction and polarization state of the incident wave gives the individual scattered fields and thereby the total scattered field.

Alternatively, inversion of the cluster matrix equation gives sphere-centered transition matrices that transform the expansion coefficients of the incident wave into the expansion coefficients of the individual scattered fields. The advantage of this approach is that the individual-sphere transition matrices are independent of the direction and polarization state of the incident field. In the far-field region, the individual scattered-field expansions can be transformed into a single expansion centered at a common origin inside the cluster. This procedure gives a matrix that transforms the incident-wave expansion coefficients into the common-origin expansion coefficients of the total scattered field. This matrix is completely equivalent to the cluster T matrix (Borghese *et al.* 1984; Mackowski 1994) and can be used in the analytical averaging of scattering characteristics over cluster orientations, as described in Section 5.9 (Fucile *et al.* 1993, 1995; Mishchenko and Mackowski 1994; Mackowski and Mishchenko 1996). Therefore, the superposition method can also be considered as a particular case of the general T-matrix method for aggregated scatterers (Section 5.9) in which the latter is applied to a cluster of spheres (Peterson and Ström 1973; Mishchenko *et al.* 1996b).

The superposition method has been extended to aggregates of concentrically layered spheres (Hamid *et al.* 1992), to spheres with one or more eccentrically positioned spherical inclusions (Fikioris and Uzunoglu 1979; Borghese *et al.* 1992, 1994; Fuller 1995b; Mackowski and Jones 1995), and to pairs of osculating spheres (Videen *et al.* 1996). Cooray and Ciric (1991) developed a superposition method for a cluster of dielectric spheroids in an arbitrary configuration by combining the SVM solution for individual spheroids with the use of appropriate rotational–translational addition theo-

rems for vector spheroidal wave functions (Cooray and Ciric 1989; see also Nag and Sinha 1995).

The computational complexity of the superposition method strongly depends on the number of components and their size parameters and configuration. Obtaining converged results for a larger number of components usually necessitates smaller values for the component size parameters, and vice versa. The superposition method is especially efficient for linear configurations of spheres, owing to the axial symmetry of such a configuration. Because of the analyticity of its mathematical formulation, this method is capable of producing very accurate results. Fuller and Mackowski (2000) gave a detailed review of the superposition method for compounded spheres, while Ciric and Cooray (2000) reviewed the superposition method for systems of spheroids.

6.7 Comparison of methods, benchmark results, and computer codes

The very existence and use of several exact techniques for computing electromagnetic scattering by nonspherical particles testifies that there is no single universal method that provides the best results in all cases. Depending on the application in hand, one particular technique may prove to be the most appropriate in terms of efficiency, accuracy, and applicability to specific particle parameters. Moreover, it is often difficult to formulate and implement simple and objective criteria for comparing the performance of different numerical techniques in a wide range of applications. Ideally, one should use the same type of computer and consider the same scattering problems using codes written by authors with comparable levels of programming skills. Even in this idealistic situation, however, the specific characteristics of the computer used can favorably enhance the performance of one technique and degrade the efficiency of another. For example, one technique may become especially efficient when implemented on a parallel computer, whereas the performance of another technique may benefit from the availability and efficient organization of double or extended precision computations. Furthermore, direct comparisons of different techniques can face serious organizational problems (e.g., Hovenier *et al.* 1996) and have always been restricted to a few techniques and a few scattering problems (Flatau *et al.* 1993; Cooper *et al.* 1996; Wriedt and Comberg 1998; Comberg and Wriedt 1999; Kimura 2001; Schuh and Wriedt 2001; Baran *et al.* 2001b). Thus, it may be that the actual decision in favor of a specific technique has often been based on indirect semi-quantitative evidence scattered over many publications (e.g., Oguchi 1981; Holt 1982) and/or on the availability of a well-documented public-domain computer code.

The paper by Hovenier *et al.* (1996) is a good example of a concerted effort to compare the accuracy and computer-time requirements of three exact techniques: the SVM for spheroids (Voshchinnikov and Farafonov 1993), the *T*-matrix method

(Mishchenko *et al.* 1996b), and the DDA (Lumme and Rahola 1994). Computations were performed for four rotationally symmetric objects: a prolate and an oblate spheroid each with aspect ratio 2, a circular cylinder with length-to-diameter ratio 2, and a bisphere with equal touching components. All particles had the same relative refractive index $m = 1.5 + \mathrm{i}0.01$ and the same volume-equivalent-sphere size parameter $x_{\mathrm{v}} = 5$. The orientation of the rotation axis of each particle with respect to the laboratory reference frame was specified by the Euler angles $\alpha = 0°$, $\beta = 50°$, and $\gamma = 0°$ (Section 2.4). The particles were illuminated by a plane electromagnetic wave incident in the direction of the positive *z*-axis of the laboratory coordinate system, the scattering directions were confined to the *xz*-halfplane with $x \geq 0$, and the comparison quantity was the phase matrix $\mathbf{Z}(\vartheta^{\mathrm{sca}}, \varphi^{\mathrm{sca}} = 0; \vartheta^{\mathrm{inc}} = 0, \varphi^{\mathrm{inc}} = 0)$ (multiplied by k_1^2, where k_1 is the wave number in the surrounding medium) as a function of the zenith angle of the scattered light $\vartheta^{\mathrm{sca}} \in [0°, 180°]$. Scattering by the prolate and oblate spheroids was computed using all three techniques, whereas that by the cylinder and the bisphere was calculated using only the *T*-matrix method and the DDA. The numbers of dipoles *N* in the DDA representation of the scattering objects were 8320, 8664, 6656, and 8448 for the prolate spheroid, the oblate spheroid, the cylinder, and the bisphere, respectively. For the DDA computations, the final results were averages over four discrete orientations of the dipole arrays about the axis of rotational symmetry; this approach was used to reduce the errors incurred in modeling the smooth rotationally symmetric particles by groups of discrete dipoles.

The comparison showed that the results of the SVM and *T*-matrix computations for the spheroids converged to within nine significant figures. Since these two techniques are completely independent, the excellent agreement is an indication of their superb absolute accuracy. The computer time and memory requirements for these two techniques were also comparable, whereas the DDA computations were more time consuming and less accurate. Figure 6.1 (adapted from Hovenier *et al.* 1996) compares the results of *T*-matrix calculations (solid curves) and DDA calculations (diamonds) of the ratio $-Z_{21}/Z_{11}\,(\%)$ for the four scattering models considered. It is evident that the DDA results deviate noticeably from the *T*-matrix curves, although the general trends and features are reproduced with accuracy perhaps good enough for many practical applications.

The evidence accumulated in the published literature suggests that, besides the Lorenz–Mie theory, the only methods capable of providing very accurate results (to five and more correct significant figures) for particles comparable to and larger than a wavelength are the SVM, the *T*-matrix method, and the superposition method. Each of these techniques incorporates an internal convergence test that provides a good measure of the absolute accuracy (Kuik *et al.* 1992; Hovenier *et al.* 1996). Benchmark results for monodisperse and polydisperse spheroids, finite circular cylinders, Chebyshev particles, and two-sphere clusters in fixed and random orientations have been reported by Mishchenko (1991a, 2000), Kuik *et al.* (1992), Hovenier *et al.* (1996), Mishchenko and Mackowski (1996), Mishchenko *et al.* (1996a), Wielaard *et al.*

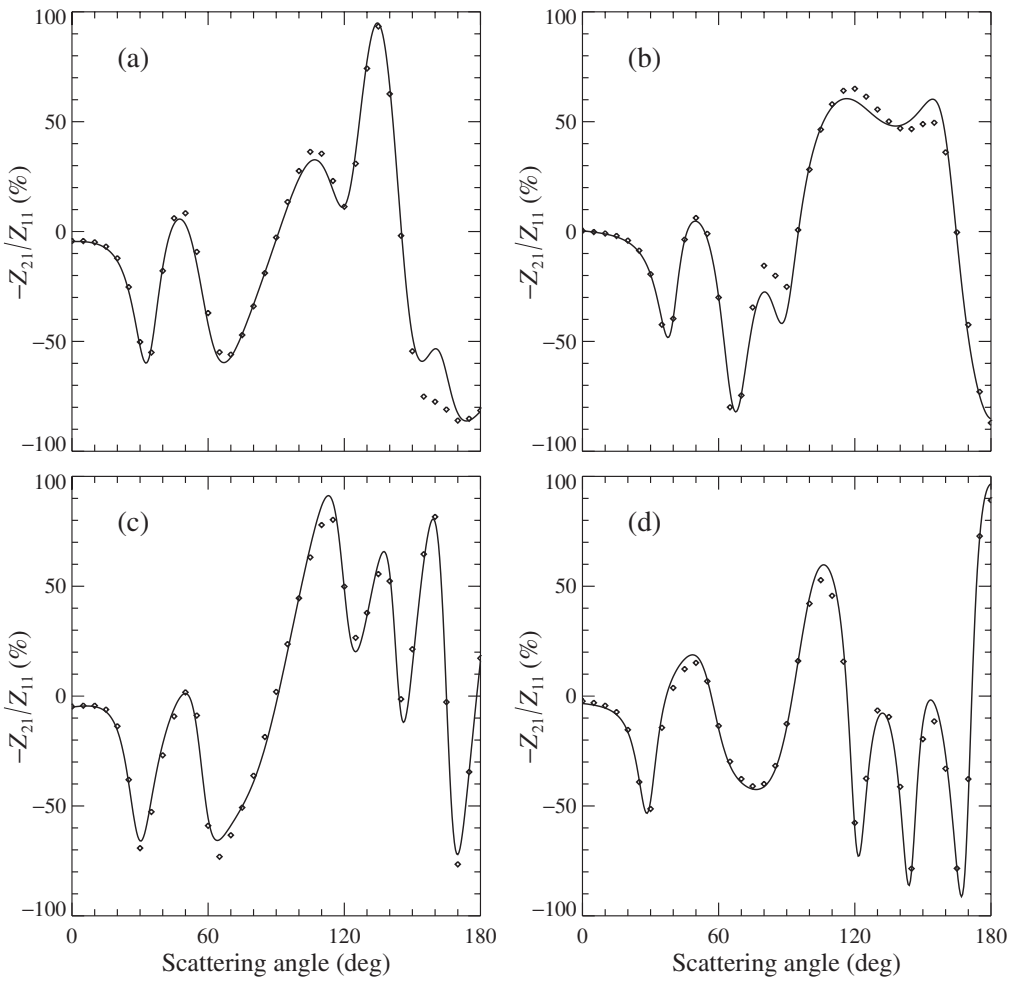

Figure 6.1. The ratio $-Z_{21}/Z_{11}$ as a function of the zenith angle of the scattering direction for (a) a prolate spheroid, (b) an oblate spheroid, (c) a finite circular cylinder, and (d) a bisphere, as specified in the text. The solid curves and the diamonds depict the results of *T*-matrix and DDA computations, respectively.

(1997), and Voshchinnikov *et al.* (2000). Additional benchmark cases were considered in subsection 5.11.7 and Section 5.12. These data cover a wide range of equivalent-sphere size parameters from a few units to 60 (Wielaard *et al.* 1997) and are given correct up to nine significant figures. Since these numbers are accurate to a few units in the last digit, they provide an important tool for testing the accuracy of other exact and approximate theoretical approaches.

The SVM, the *T*-matrix method, the superposition method, the GPMM, and the ME-GPMM are the only techniques that have been used extensively in computations for particles significantly larger than a wavelength. The first three techniques appear to be the most efficient methods for computing electromagnetic scattering by homogeneous and composite objects of revolution (i.e., having rotational symmetry). The availability of the analytical orientation-averaging procedure makes the *T*-matrix

method the fastest technique for randomly oriented symmetric particles (e.g., rotationally symmetric particles, ellipsoids, and polyhedral cylinders) with moderate aspect ratios and also for randomly oriented clusters of spheres. Scattering by particles with larger aspect ratios can be computed with the improved version of the SVM for spheroids developed by Farafonov (1983), the iterative EBCM (cf. subsection 5.8.4), and the ME-GPMM. SIEMs (e.g., Zuffada and Crisp 1997) and the FIEM can also be applied to homogeneous, rotationally symmetric particles with large aspect ratios, although they appear to be slower and less accurate than the other techniques.

Computations for anisotropic objects and homogeneous and inhomogeneous asymmetric particles often may have to rely on more flexible techniques such as the FEM, FDM, FDTDM, MOM, and DDA. All these techniques are simple in concept and computer implementation and appear to have comparable performance characteristics (e.g., Wriedt and Comberg 1998), although often their simplicity and flexibility are accompanied by a loss in efficiency and accuracy and by stronger practical limitations on the maximal particle size parameter. Further effort is obviously required in order to develop improved exact approaches that are both efficient, flexible, and applicable to a wide range of size parameters.

A number of software implementations of the techniques described in this chapter are currently available, and many of them are in the public domain. Extensive lists of available computer codes have been compiled by Flatau (2000) and Wriedt (2000).

Further reading

Farafonov *et al.* (1999) developed a surface integral equation technique for homogeneous rotationally symmetric objects that closely resembles the EBCM but employs a different set of functions to expand the incident, scattered, and internal fields.

Rother and Schmidt (1996) and Rother (1998) developed a differential equation technique called the discretized Mie formalism (DMF), which solves the vector Helmholtz equation for homogeneous scatterers using a method of lines. The main advantage of this method is its analytic incorporation of the radiation condition at infinity. Like many other exact techniques, the DMF becomes much more efficient when the scattering object is rotationally symmetric.

Kattawar *et al.* (1987) found the solution of Eq. (2.16) by first solving a simpler equation for a resolvent kernel matrix. An attractive feature of their approach is that the resolvent kernel matrix is computed only once for the entire range of relative refractive indices.

Vechinski *et al.* (1994) developed a time-domain SIEM to compute the scattering from arbitrarily shaped homogeneous dielectric bodies. The advantage of their technique over the FDTDM is that the radiation condition at infinity is satisfied automatically and the memory requirement is reduced (see also Pocock *et al.* 1998).

Further information on exact scattering methods can be found in the review by Kahnert (2003), in the collection of selected papers edited by Kerker (1988), and in special journal issues edited by Shafai (1991), Barber *et al.* (1994), Hovenier (1996), Lumme (1998), Mishchenko *et al.* (1999a), and Videen *et al.* (2001).

Chapter 7

Approximations

The practical importance of approximate theories of electromagnetic scattering and absorption by small particles diminishes as various exact techniques mature and become applicable to a wider range of problems and as computers become ever more powerful. This is of course especially true of spherical particles, for which the Lorenz–Mie theory can be used to generate accurate numerical results for essentially any size parameter and relative refractive index. Nonetheless, approximate theories still remain a valuable source of physical insight into the processes of scattering and absorption of electromagnetic radiation. Furthermore, it is likely that at least one approximation, the geometrical optics approach, will never become obsolete because its accuracy can only improve as the particle size parameter grows whereas all exact theoretical techniques for nonspherical particles cease to be practical whenever the size parameter exceeds a certain threshold value.

7.1 Rayleigh approximation

Rayleigh (1897) derived an approximation for scattering in the small-particle limit by assuming that the incident field inside and near the particle behaves almost as an electrostatic field and the internal field is homogeneous. Hence the conditions of validity of the Rayleigh approximation (RA) are $x \ll 1$ and $|mx| \ll 1$, where $x = 2\pi a/\lambda_1$, a is the semi-major particle dimension, λ_1 is the wavelength of the incident light in the surrounding medium, and m is the relative refractive index. A detailed account of the RA was given by Kleinman and Senior (1986). A completely analytical solution exists for only a few simple shapes, including triaxial ellipsoids. For general shapes, one must solve numerically a simple integral equation for the polari-

zability tensor. Bohren and Huffman (1983, Chapter 5) gave analytical formulas for the optical cross sections and the scattering matrix elements of randomly oriented spheroids. Note that direct use of the optical theorem (Section 2.8) in the framework of the RA yields only the absorption component of the extinction cross section and must be supplemented by the computation of the scattering cross section via Eq. (2.160).

Kerker *et al.* (1978) and Ku and Felske (1984) compared approximate and exact Lorenz–Mie results for the scattering matrix and the extinction and scattering efficiency factors of small homogeneous spheres and concluded that the range of validity of the RA in terms of the maximal size parameter varied with relative refractive index and scattering angle. Mishchenko (1990b, 1991b) and Voshchinnikov and Farafonov (2000) used the exact T-matrix and the separation of variables methods to analyze the range of validity of RA computations of the extinction matrix and extinction, scattering, and absorption efficiencies for homogeneous spheres and perfectly and partially aligned as well as randomly oriented spheroids.

Farafonov (2000) derived the formulas of the RA for multilayered ellipsoids. Muinonen (1996, 2000) and Battaglia *et al.* (1999) applied the RA to so-called Gaussian random spheres. Jones (1979) extended the RA to clusters of small spheres (see also Mackowski 1995, and references therein).

Stevenson (1953) generalized the RA by expanding the internal and scattered electric fields in powers of the size parameter x. The first term, which is $O(x^2)$, gives the RA whereas the second term, $O(x^4)$, gives the so-called Rayleigh–Gans–Stevenson approximation. This approach was extended to inhomogeneous objects by von Ross (1971) and applied to various scattering problems by Stevenson (1968) and Khlebtsov (1979).

Another way of deriving the formulas of the Rayleigh or higher-order approximations is to analyze an exact solution in the limit $x \to 0$. For example, one can use the expansions

$$j_n(z) = \frac{z^n}{1\times 3\times 5\times\cdots\times(2n+1)}\left\{1 - \frac{\frac{1}{2}z^2}{1!(2n+3)} + \frac{(\frac{1}{2}z^2)^2}{2!(2n+3)(2n+5)} - \cdots\right\}, \tag{7.1}$$

$$y_n(z) = -\frac{1\times 3\times 5\times\cdots\times(2n-1)}{z^{n+1}}\left\{1 - \frac{\frac{1}{2}z^2}{1!(1-2n)} + \frac{(\frac{1}{2}z^2)^2}{2!(1-2n)(3-2n)} - \cdots\right\}, \quad n = 0, 1, 2, \ldots \tag{7.2}$$

for the spherical Bessel functions of the first and second kind (Abramowitz and Stegun 1964, p. 437) along with Eq. (C.1) and Lorenz–Mie formulas of Section 5.7 and subsection 5.8.5 to derive the following classical equations of the RA for small homogeneous spheres:

$$Q_{\text{sca}} \underset{x\to 0}{=} \frac{8}{3}x^4\left|\frac{m^2-1}{m^2+2}\right|^2, \tag{7.3}$$

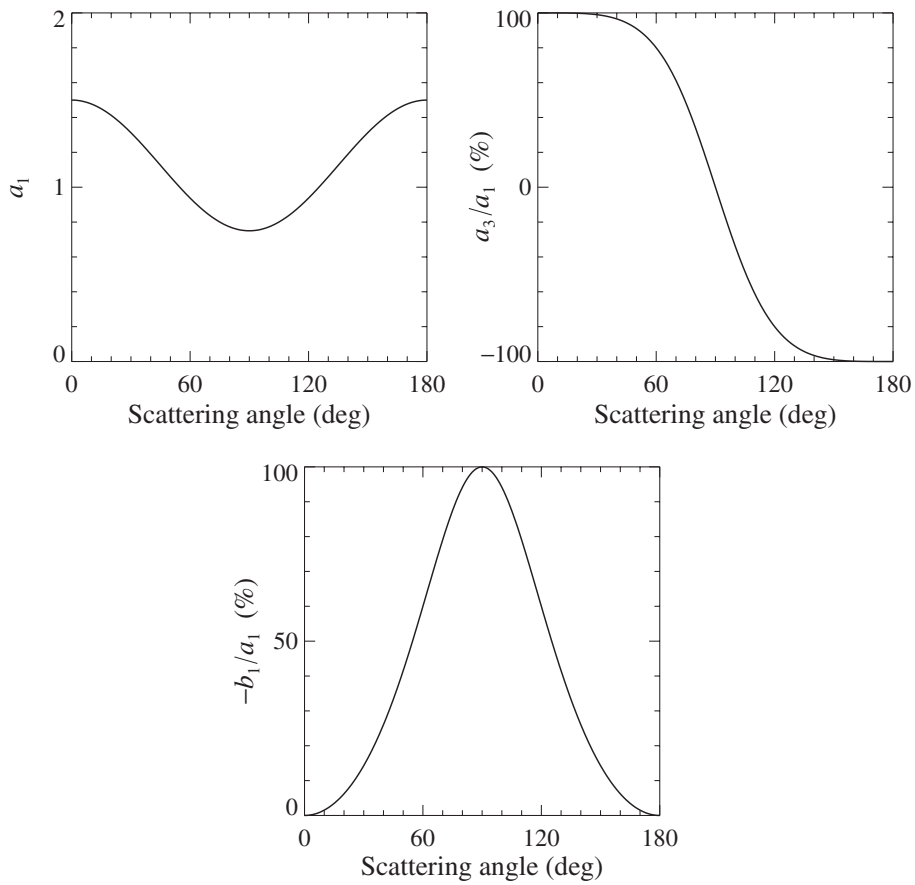

Figure 7.1. The phase function $a_1(\Theta)$ and the ratios $a_3(\Theta)/a_1(\Theta)$ and $-b_1(\Theta)/a_1(\Theta)$ versus scattering angle Θ for a homogeneous sphere in the Rayleigh limit.

$$Q_{\text{abs}} \underset{x\to 0}{=} 4x\,\text{Im}\left(\frac{m^2-1}{m^2+2}\right), \tag{7.4}$$

$$\tilde{\mathbf{F}}(\Theta) \underset{x\to 0}{=} \frac{3}{4}\begin{bmatrix} 1+\cos^2\Theta & -\sin^2\Theta & 0 & 0 \\ -\sin^2\Theta & 1+\cos^2\Theta & 0 & 0 \\ 0 & 0 & 2\cos\Theta & 0 \\ 0 & 0 & 0 & 2\cos\Theta \end{bmatrix}, \tag{7.5}$$

where $x = 2\pi r/\lambda_1$ is the size parameter and r is the sphere radius (Bohren and Huffman 1983). Figure 7.1 visualizes the elements of the normalized Stokes scattering matrix of Eq. (7.5), whereas Table 7.1 lists the respective expansion coefficients (de Rooij 1985). The scattering efficiency factor in the Rayleigh approximation is inversely proportional to the fourth power of the wavelength, the absorption efficiency factor is inversely proportional to the wavelength, and the absorption cross section $C_{\text{abs}} = \pi r^2 Q_{\text{abs}}$ is proportional to the particle volume $V = \frac{4}{3}\pi r^3$:

Table 7.1. Expansion coefficients for the normalized Stokes scattering matrix of a homogeneous sphere in the Rayleigh limit

s	α_1^s	α_2^s	α_3^s	α_4^s	β_1^s	β_2^s
0	1	0	0	0	0	0
1	0	0	0	$3/2$	0	0
2	$1/2$	3	0	0	$\sqrt{3/2}$	0

$$Q_{\text{sca}} \underset{x\to 0}{\propto} \frac{1}{\lambda_1^4}, \qquad Q_{\text{abs}} \underset{x\to 0}{\propto} \frac{1}{\lambda_1}, \qquad C_{\text{abs}} \underset{x\to 0}{\propto} V. \tag{7.6}$$

Equations (7.3) and (7.4) indicate that for small particles with at least moderate absorption, extinction is dominated by absorption. The rapid increase in the scattering cross section with decreasing wavelength causes air molecules to scatter more blue than red light and transmit more red than blue light. This behavior explains the blue color of the clear sky and the familiar reddening of the sunset. The Rayleigh phase function (the upper left panel in Fig. 7.1) is nearly isotropic and is symmetric with respect to the scattering angle $\Theta = 90°$, thereby yielding an asymmetry parameter equal to zero:

$$\langle \cos\Theta \rangle \underset{x\to 0}{=} 0. \tag{7.7}$$

The degree of linear polarization of scattered light for unpolarized incident light, $P_Q(\Theta) = -Q^{\text{sca}}(\Theta)/I^{\text{sca}}(\Theta) = -b_1(\Theta)/a_1(\Theta)$ (the panel at the lower level in Fig. 7.1), is always positive, has the classical bell-like shape, and reaches 100% at the scattering angle $\Theta = 90°$.

In a similar fashion, the extended boundary condition method can be used to derive closed-form analytical formulas of the RA for very small spheroids (Tsang *et al.* 1985, pp. 192–3).

7.2 Rayleigh–Gans approximation

The conditions of validity of the Rayleigh–Gans approximation (RGA) (otherwise known as the Rayleigh–Debye or Born approximation; e.g., Ishimaru 1997, Section 2.6) are $x|m-1| \ll 1$ and $|m-1| \ll 1$. In other words, the particles are assumed to be not too large (although they may be larger than in the case of Rayleigh scattering) and optically "soft". The fundamental assumption of the RGA is that each volume element of the scattering object is excited only by the incident field. The scattered field is then computed from Eq. (2.22) after substituting $\mathbf{E}(\mathbf{r}') = \mathbf{E}^{\text{inc}}(\mathbf{r}')$. This simplifying assumption leads to significant analytical progress in many specific cases. Also, like many other asymptotic approximations, the RGA may often be useful outside its formally defined range of validity (e.g., Barber and Wang 1978). Acquista (1976) generalized the RGA by applying the method of successive iterations (Shifrin 1968) to

Eq. (2.16). This approach was applied to spheroids and finite circular cylinders and is valid for $x|m-1| \lesssim 1$ (Haracz *et al.* 1984, 1985, 1986). Khlebtsov (1984) derived an exact integral equation of Lippman–Schwinger type by taking the Fourier transform of Eq. (2.16). Successive iterations of this equation give the RGA, the Acquista result, and higher-order approximations. This approach was extended to anisotropic scatterers and applied to suspensions of aligned particles by Khlebtsov and Melnikov (1991) and Khlebtsov *et al.* (1991). Muinonen (1996, 2000) applied the RGA to particles with Gaussian random surfaces.

7.3 Anomalous diffraction approximation

The anomalous diffraction approximation (ADA) was introduced by van de Hulst (1957, Chapter 11) as a means of computing the extinction cross section for large, optically soft spheres with $x \gg 1$ and $|m-1| \ll 1$. Since the second condition means that rays are weakly deviated as they cross the particle boundary and there is negligible reflection, the ADA implies that extinction is caused by (i) absorption of light passing through the particle and (ii) interference of the light passing through the particle and the light passing around the particle. This simplification allows a general representation of the extinction and absorption cross sections as simple integrals over the particle projection on the plane perpendicular to the incident beam. The integrals can be evaluated numerically or, in some special cases, analytically. The ADA has been applied to prismatic columns (Chýlek and Klett 1991a, b), hexagonal ice crystals (Chýlek and Videen 1994; Sun and Fu 1999), spheroids (Evans and Fournier 1994; Baran *et al.* 1998), cubes (Masłowska *et al.* 1994), ellipsoids (Streekstra *et al.* 1994), and finite circular cylinders (Liu *et al.* 1998). Comparisons of the ADA and the exact T-matrix results (Liu *et al.* 1998) suggest that the ADA estimate of extinction is more accurate for randomly oriented nonspherical particles than for spheres, and that the ADA errors in absorption decrease with increasing imaginary part of the relative refractive index. Meeten (1982) and Khlebtsov (1993) extended the ADA to scattering by anisotropic particles and fractal clusters, respectively. The ADA and the closely related Wentzel–Kramers–Brillouin and eikonal approximations belong to the family of high-energy approximations (e.g., Perrin and Lamy 1986; Bourrely *et al.* 1989; Klett and Sutherland 1992; Sharma and Somerford 1999; Shepelevich *et al.* 1999).

7.4 Geometrical optics approximation

The geometrical optics approximation (GOA) (otherwise known as the ray-tracing or ray optics approximation) is a universal approximate method for computing light scattering by arbitrarily shaped and arbitrarily oriented particles with sizes much larger than the incident wavelength. The GOA is based on the assumption that the

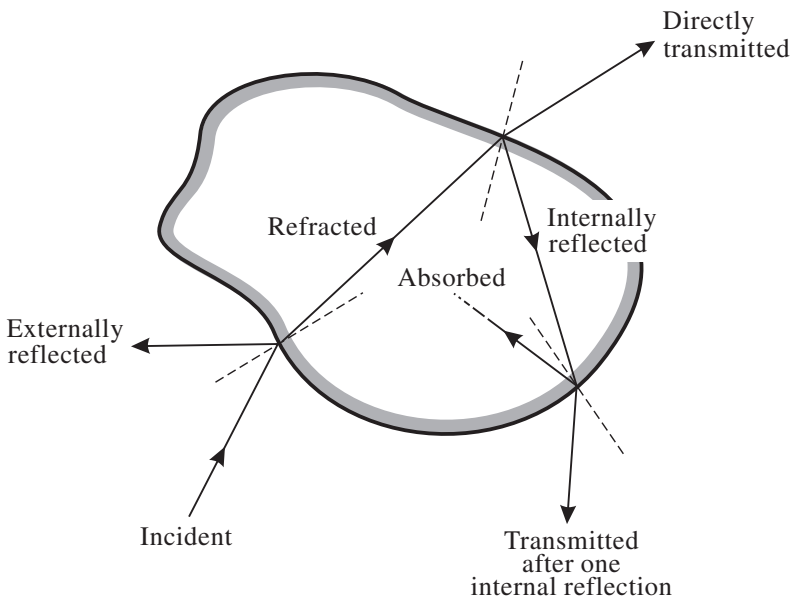

Figure 7.2. Ray-tracing diagram for scattering at a single particle.

incident plane wave can be represented as a collection of parallel rays which pursue independent paths and that it is possible to distinguish between rays striking different local regions on the particle's surface. Numerical results are obtained by tracing the histories of a large number of uniformly spaced rays striking the particle. Each incident ray is partially refracted into the particle and partially reflected (Fig. 7.2). The Stokes parameters of the refracted and reflected parts of the ray and the direction of the refracted part are determined using Fresnel's formula and Snell's law, respectively (Jackson 1998, Section 7.3). The refracted ray may emerge after another refraction, possibly following one or more internal reflections, and it may be attenuated by absorption inside the particle. Each internal ray is traced until its intensity decreases below a prescribed cut-off value. Varying the polarization state of the incident rays, sampling all escaping rays into predefined narrow angular bins, and adding incoherently the respective Stokes parameters yields a quantitative representation of the particle scattering properties in terms of the ray-tracing phase matrix $\mathbf{Z}^{\mathrm{RT}}$. Because all rays impinging on the particle surface are either scattered or absorbed irrespective of their polarization state, the ray-tracing extinction matrix is always diagonal and is given by

$$\mathbf{K}^{\mathrm{RT}} = C_{\mathrm{ext}}^{\mathrm{RT}} \mathbf{\Delta}, \tag{7.8}$$

where $\mathbf{\Delta}$ is the 4×4 unit matrix. The ray-tracing extinction cross section $C_{\mathrm{ext}}^{\mathrm{RT}}$ does not depend on the polarization state of the incident light and is equal to the geometrical area G of the particle projection on the plane perpendicular to the incidence direction:

$$C_{\mathrm{ext}}^{\mathrm{RT}} = G. \tag{7.9}$$

Since the presence of the particle modifies the incident plane wave front by eliminating a part that has the shape and size of the geometrical projection of the particle, the ray-tracing scattering pattern must be supplemented by the computation of Fraunhofer diffraction of the incident wave on the particle projection. The diffraction component of the phase matrix $\mathbf{Z}^{\mathrm{D}}$ is confined to a narrow angular cone centered at the exact forward-scattering direction and is usually computed in the Kirchhoff approximation (Jackson 1998), thereby contributing only to the diagonal elements of the total phase matrix (Muinonen 2000). The diffraction component $\mathbf{K}^{\mathrm{D}}$ of the total geometrical optics extinction matrix $\mathbf{K}^{\mathrm{GO}}$ is simply the product of G and the 4×4 unit matrix and is equal to the ray-tracing component $\mathbf{K}^{\mathrm{RT}}$. We thus have

$$\mathbf{Z}^{\mathrm{GO}} = \mathbf{Z}^{\mathrm{RT}} + \mathbf{Z}^{\mathrm{D}} = \mathbf{Z}^{\mathrm{RT}} + Z_{11}^{\mathrm{D}}\mathbf{\Delta}, \tag{7.10}$$

$$\mathbf{K}^{\mathrm{GO}} = \mathbf{K}^{\mathrm{RT}} + \mathbf{K}^{\mathrm{D}} = C_{\mathrm{ext}}^{\mathrm{GO}}\mathbf{\Delta}, \tag{7.11}$$

where

$$C_{\mathrm{ext}}^{\mathrm{GO}} = C_{\mathrm{ext}}^{\mathrm{RT}} + C_{\mathrm{ext}}^{\mathrm{D}} = 2G. \tag{7.12}$$

The geometrical optics scattering cross section is the sum of the ray-tracing and diffraction components:

$$C_{\mathrm{sca}}^{\mathrm{GO}} = C_{\mathrm{sca}}^{\mathrm{RT}} + C_{\mathrm{sca}}^{\mathrm{D}}. \tag{7.13}$$

Since the diffracted energy is not absorbed, the diffraction scattering cross section is equal to the diffraction extinction cross section:

$$C_{\mathrm{sca}}^{\mathrm{D}} = C_{\mathrm{ext}}^{\mathrm{D}} = G. \tag{7.14}$$

The ray-tracing scattering cross section $C_{\mathrm{sca}}^{\mathrm{RT}}$ is found from $\mathbf{Z}^{\mathrm{RT}}$ and Eq. (2.160). Energy conservation requires that it be always smaller than or equal to the ray-tracing extinction cross section:

$$C_{\mathrm{sca}}^{\mathrm{RT}} \le C_{\mathrm{ext}}^{\mathrm{RT}} = G. \tag{7.15}$$

GOA computations are particularly straightforward for spheres because the ray paths always remain in a plane (Liou and Hansen 1971), thereby simplifying the ray-tracing part of the computation, while the diffraction component of the phase matrix is given by a closed-form analytical formula (cf. Bohren and Huffman 1983, p. 110)

$$\mathbf{Z}^{\mathrm{D}}(\hat{\mathbf{n}}^{\mathrm{sca}}, \hat{\mathbf{n}}^{\mathrm{inc}}) \underset{x\to\infty}{=} \frac{Gx^2}{16\pi}\left[\frac{2J_1(x\sin\Theta)}{x\sin\Theta}\right]^2 (1+\cos\Theta)^2\mathbf{\Delta}, \tag{7.16}$$

where x is the size parameter of the sphere, $\Theta = \arccos(\hat{\mathbf{n}}^{\mathrm{sca}}\cdot\hat{\mathbf{n}}^{\mathrm{inc}})$ is the scattering angle, and $J_1(z)$ is the Bessel function of order unity. Figure 7.3 shows the quantity $[2J_1(x\sin\Theta)/(x\sin\Theta)]^2$ as a function of $x\sin\Theta$. It is seen that for $x \gg 1$ essentially all the diffracted light is confined within an angular cone of half-width $\Theta \cong 7/x$. The respective ray-tracing asymmetry parameter is equal to unity to high precision:

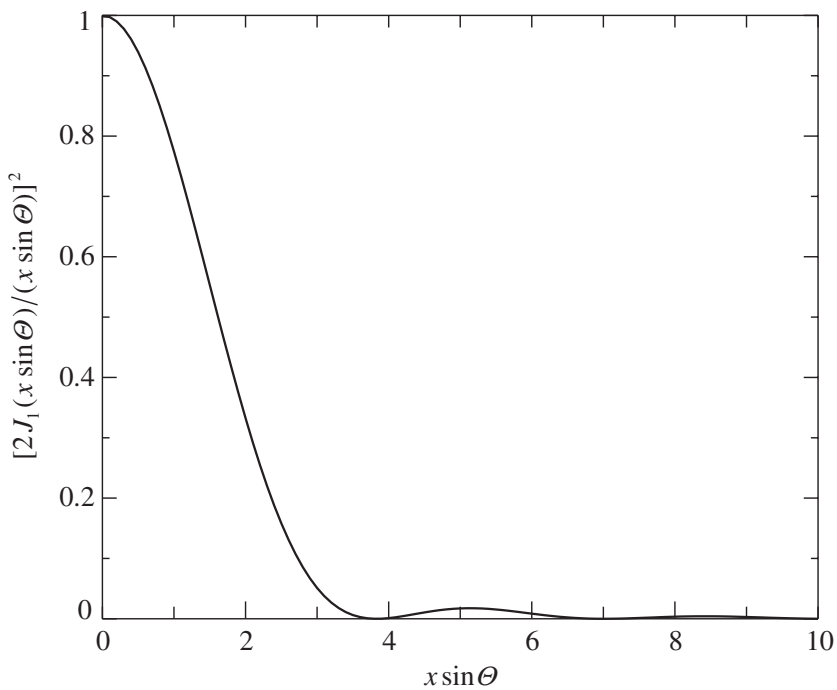

Figure 7.3. Angular distribution of the diffracted intensity.

$$\langle\cos\Theta\rangle^{\mathrm{RT}} \underset{x\to\infty}{\to} 1. \tag{7.17}$$

For nonspherical particles, ray tracing is usually performed using a Monte Carlo approach, whereas the diffraction is often approximated by Eq. (7.16) evaluated for an equal-projected-area sphere (more accurate approaches have been discussed by Takano and Asano (1983), Muinonen (1989), Petrushin (1994), and Yang and Liou (1998a)). Wendling *et al.* (1979), Cai and Liou (1982), Volkovitsky *et al.* (1984), Takano and Jayaweera (1985), Rockwitz (1989), Takano and Liou (1989a), Masuda and Takashima (1992), and Xu *et al.* (1997) applied the GOA to hexagonal columns and plates in random and horizontal orientations, whereas Yang and Cai (1991), Macke and Mishchenko (1996), and Kokhanovsky and Nakajima (1998) computed scattering by randomly oriented spheroids and finite circular cylinders. Light scattering by various polyhedral shapes has been studied by Liou *et al.* (1983), Muinonen *et al.* (1989), Macke (1993), Iaquinta *et al.* (1995), Takano and Liou (1995), Liu *et al.* (1996), Macke *et al.* (1996b), and Yang and Liou (1998a). The GOA has been applied also to distorted raindrops (Macke and Großklaus 1998; Nousiainen and Muinonen 1999; Nousiainen 2000) and large randomly shaped (stochastic) particles (Peltoniemi *et al.* 1989; Macke *et al.* 1996b; Muinonen *et al.* 1996; Hess *et al.* 1998; Yang and Liou, 1998a; Han *et al.* 1999; Grundy *et al.* 2000; Muinonen 2000).

Macke *et al.* (1996a), Mishchenko and Macke (1997), C.-Labonnote *et al.* (2000), Macke (2000), and Hillier and Buratti (2001) have used the GOA to compute scattering and absorption properties of large particles containing multiple randomly posi-

tioned small inclusions with an index of refraction different from that of the host. The ray-tracing procedure assumes that each inclusion scatters light independently of all other inclusions, thereby implying that the mean distance between the inclusions is greater than a few times their radii (Section 3.3). The inclusions are usually assumed to be spherical, and their single-scattering and absorption properties are computed using the Lorenz–Mie theory. However, nonspherical inclusions can also be accommodated. After an incident ray is refracted into the host particle, it is allowed to travel a straight random path length that depends on the number density of the inclusions and their average extinction cross section. If the ray has not reached the boundary of the host particle, its propagation direction is then changed in accordance with the average inclusion phase function and its energy is multiplied by the average inclusion single-scattering albedo. This process is continued until the ray reaches the host boundary, where it is partially refracted out of the host and partially internally reflected. The entire procedure is repeated for the internally reflected component. The history of the internal ray is traced until its energy falls below a specific threshold. This technique is in essence a Monte Carlo solution of the radiative transfer equation for the interior of the host particle subject to the Fresnel boundary conditions on the host particle surface (Section 3.4).

A collection of GOA codes applicable to a wide variety of problems has been developed by Andreas Macke and is publicly available at http://www.ifm-geomar.de/index.php?id=981&L=1.

The main advantage of the GOA is that it can be applied to essentially any shape. However, this technique is approximate by definition, and its range of applicability in terms of the smallest allowable size parameter must be checked by comparing the GOA results with exact numerical solutions of the Maxwell equations. As an example, Figs. 7.4 and 7.5 depict the results of GOA and Lorenz–Mie computations of the phase function $a_1(\Theta)$ and the ratio $-b_1(\Theta)/a_1(\Theta)$ versus scattering angle Θ for nonabsorbing homogeneous spheres with relative refractive indices m = 1.33 and m = 1.53 and size parameters x = 40, 160, and 600. The computations were performed using the ray-tracing code described by Macke and Mishchenko (1996) and the Lorenz–Mie code described in Section 5.10. In order to smooth out interference and resonance effects (Section 9.1), the Lorenz–Mie results have been averaged over a narrow size distribution given by Eq. (5.245) with b = 0.07, so that x represents the effective size parameter $2\pi r_{\text{eff}}/\lambda_1$, where r_{eff} is given by Eq. (5.248). The ray-tracing and diffraction components of the GOA phase functions have been averaged over 1°-wide angular bins. It is clear that the GOA phase-function results for spheres become reasonably accurate only at size parameters exceeding several hundred. Furthermore, the GOA completely fails to reproduce the strong enhancement of intensity in the backscattering direction $(\Theta \cong 180°)$ observed for m = 1.33 and usually associated with so-called surface waves (cf. Section 9.4). Obtaining good accuracy in GOA computations of the ratio $-b_1(\Theta)/a_1(\Theta)$ requires even larger size parameters (Fig. 7.5).

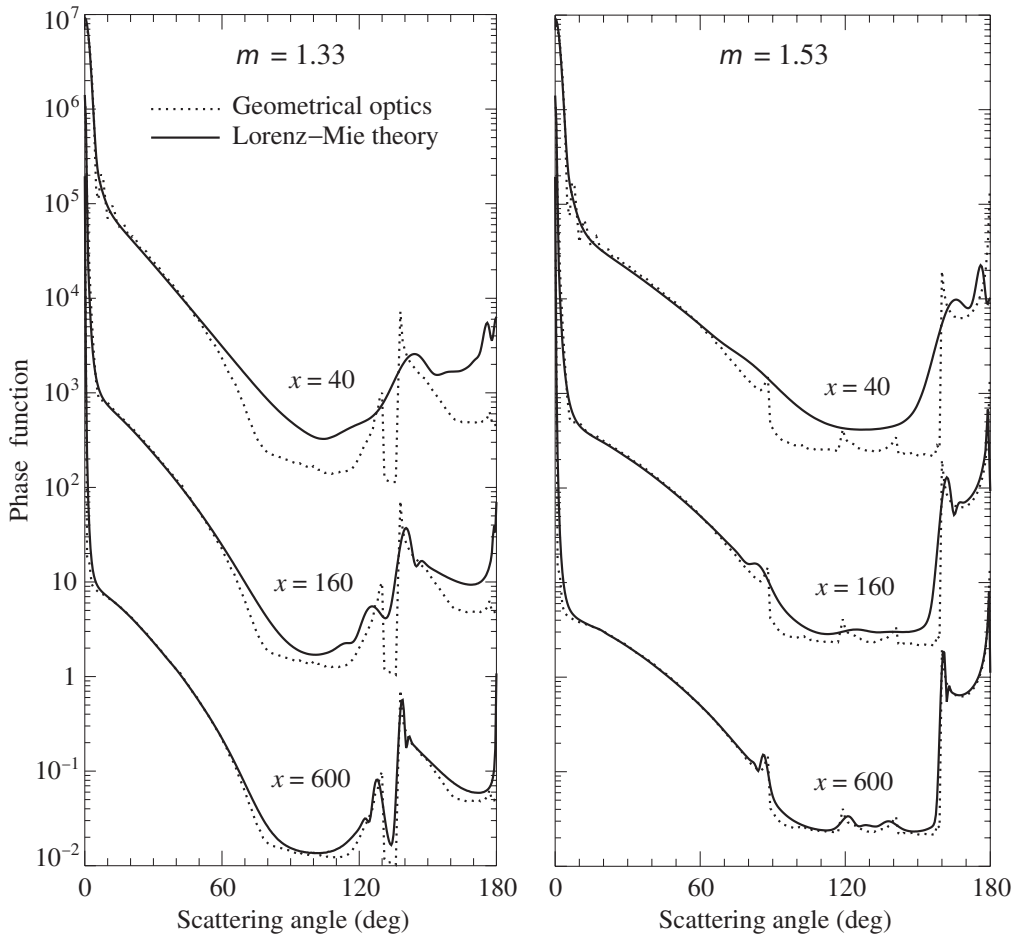

Figure 7.4. Phase function $a_1(\Theta)$ versus scattering angle Θ computed with the GOA and the Lorenz–Mie theory for homogeneous spheres with relative refractive indices $m = 1.33$ and $m = 1.53$ and size parameters $x = 40$, 160, and 600. The vertical axis scale applies to the curves with $x = 600$, the other curves being successively displaced upward by a factor of 100. (After Hansen and Travis 1974.)

Shown in Fig. 7.6 are results of GOA and *T*-matrix computations of the phase function for monodisperse, randomly oriented circular cylinders with a diameter-to-length ratio of unity, relative refractive index $m = 1.311$, and surface-equivalent-sphere size parameters x_s varying from 40 to 180; Fig. 7.7 depicts all elements of the normalized Stokes scattering matrix for $x_s = 180$. The small-amplitude ripple in the *T*-matrix curves is caused by interference effects characteristic of monodisperse particles. Averaging over cylinder orientations makes this ripple much weaker than for monodisperse surface-equivalent spheres and can be eliminated entirely by averaging over a narrow size distribution. Contrasting Figs. 7.4 and 7.5 with Figs. 7.6 and 7.7 seems to suggest that GOA results for nonspherical particles may be somewhat more accurate for a given size parameter than those for surface-equivalent spheres (Macke *et al.* 1995; Mishchenko and Macke 1999). However, it is clear that although the

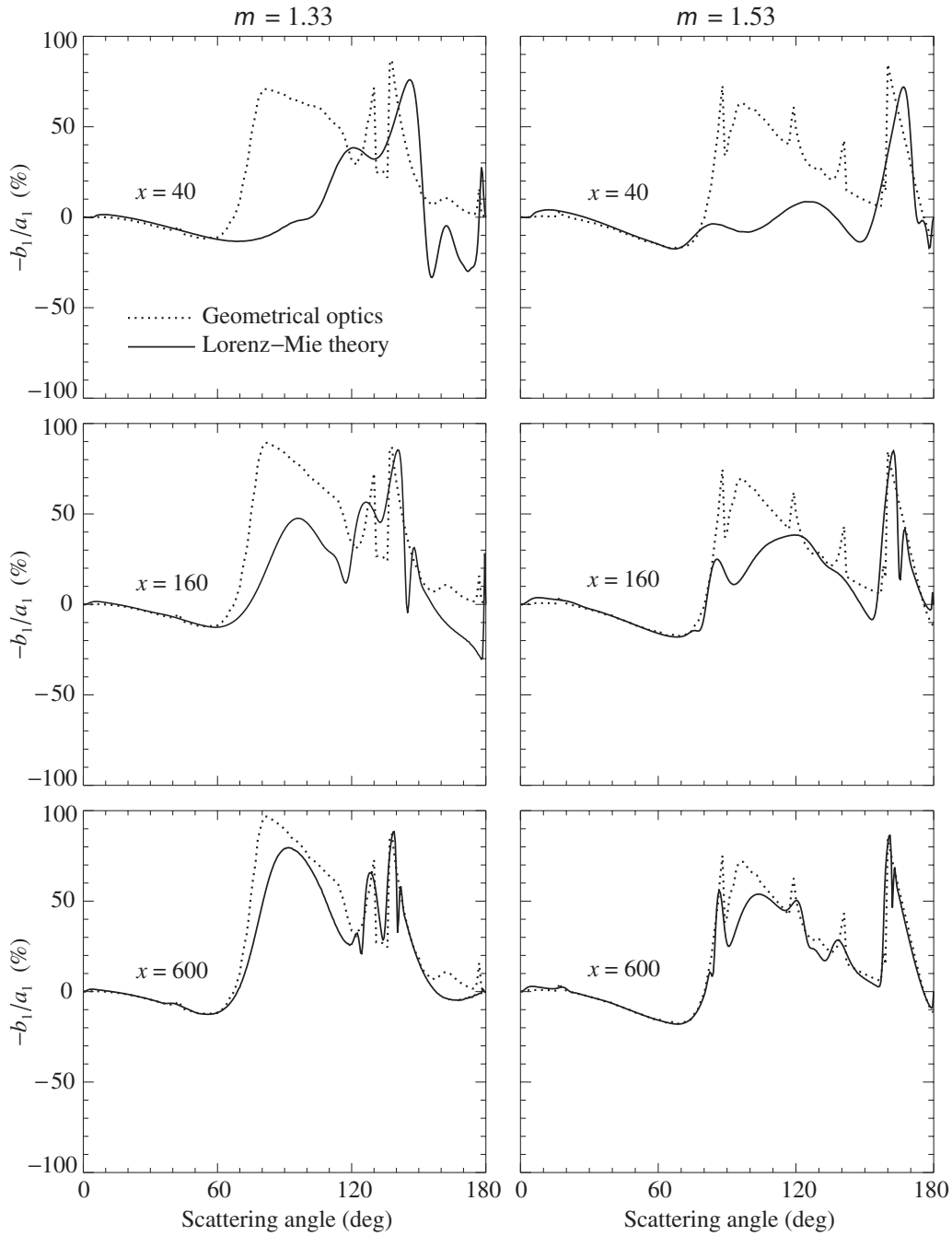

Figure 7.5. The ratio $-b_1(\Theta)/a_1(\Theta)$ versus scattering angle Θ computed with the GOA and the Lorenz–Mie theory for homogeneous spheres with relative refractive indices $m = 1.33$ and $m = 1.53$ and size parameters $x = 40$, 160, and 600. (After Hansen and Travis 1974.)

main geometrical optics features can be qualitatively reproduced by particles with size parameters less than 100, obtaining good quantitative accuracy in GOA computations of the scattering matrix for nonspherical particles still requires size parameters exceeding a few hundred.

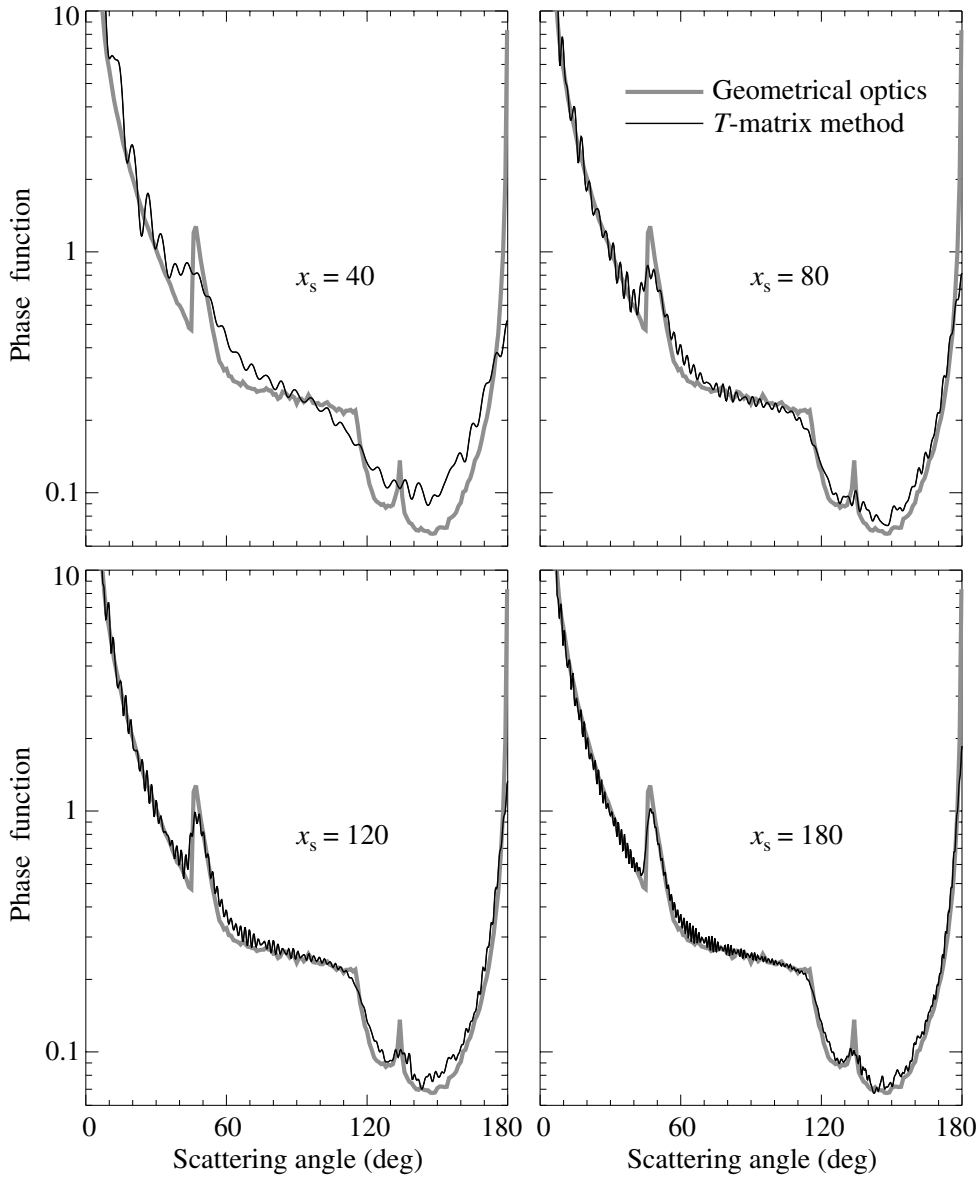

Figure 7.6. GOA and *T*-matrix phase functions for monodisperse, randomly oriented circular cylinders with surface-equivalent-sphere size parameters x_s = 40, 80, 120, and 180.

GOA computations for absorbing particles (i.e., with a non-zero imaginary part of the relative refractive index) are more complicated because in this case the refracted waves are inhomogeneous, so that the surface of constant amplitude does not coincide with the surface of constant phase. Formally, Snell's law can still be used, but it must be modified as described by Stratton (1941, Section 9.8) (see also Ulaby *et al.* 1981, Section 2-8). The consequences of this modification were discussed by Yang and Liou (1995) and Zhang and Xu (1995) and may often be neglected. The effect of absorption on the accuracy of ray-tracing computations has been analyzed further by Yang *et al.* (2001a).

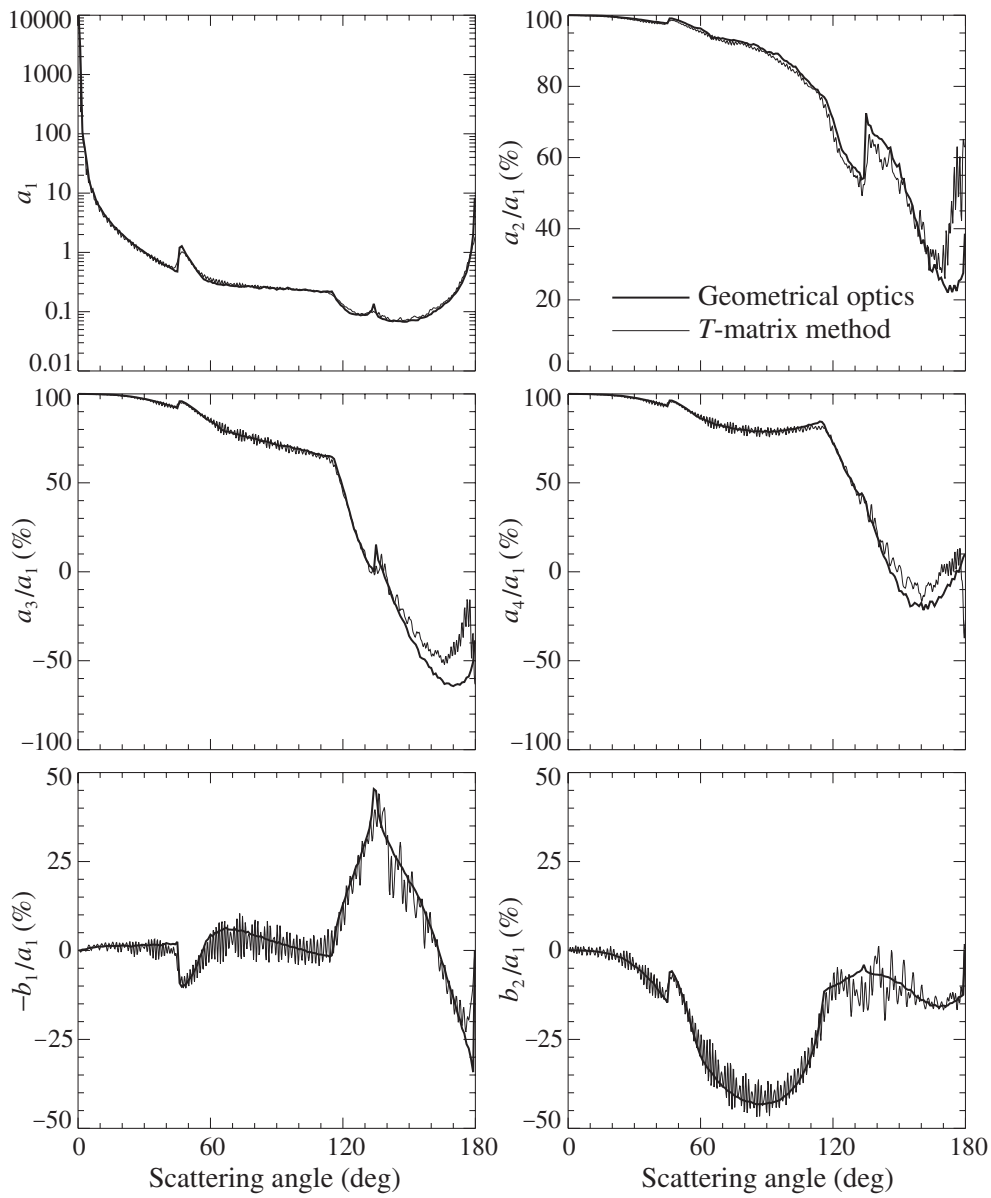

Figure 7.7. Elements of the normalized Stokes scattering matrix for monodisperse, randomly oriented circular cylinders with a surface-equivalent-sphere size parameter $x_s = 180$.

The failure to reproduce the backscattering enhancement of intensity caused by surface waves in spherical particles is not the only inherent deficiency of the GOA. For example, the GOA predicts that for crystals with parallel plane facets the ray-tracing component of the phase function should have a delta-function peak in the exact forward-scattering direction because the direction of the incident rays is not changed after they undergo two refractions through parallel plane interfaces, as demonstrated in Fig. 7.8. This effect is called the delta-function transmission (Liou 1992). It is clear, however, that the GOA predicts the infinitesimally narrow trans-

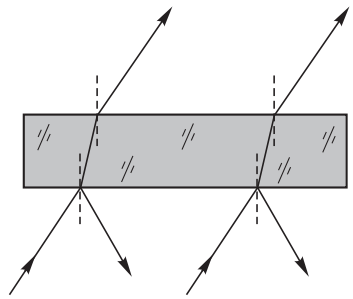

Figure 7.8. The direction of incident rays is not changed after they are refracted twice by parallel plane facets.

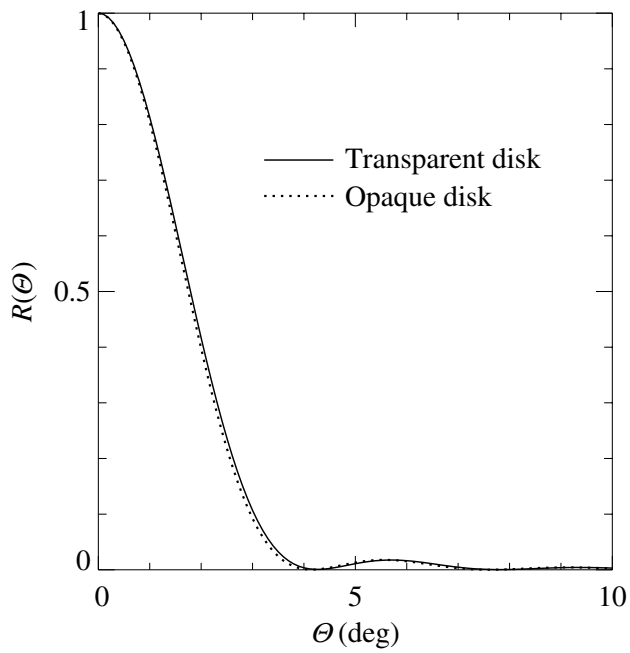

Figure 7.9. The angular profile of the ratio R defined by Eq. (7.18) for transparent and opaque circular disks.

mission peak only because it ignores physical optics effects. Figure 7.9 shows the results of exact T-matrix computations of the ratio

$$R(\Theta) = \frac{Z_{11}(\vartheta^{\text{sca}} = \Theta, \varphi^{\text{sca}} = 0; \vartheta^{\text{inc}} = 0, \varphi^{\text{inc}} = 0)}{Z_{11}(\vartheta^{\text{sca}} = 0, \varphi^{\text{sca}} = 0; \vartheta^{\text{inc}} = 0, \varphi^{\text{inc}} = 0)} \tag{7.18}$$

for two circular disks with diameter-to-length ratio 3 and size parameter $\pi D/\lambda_1 = 50$, where D is the diameter of each disk and λ_1 is the wavelength of the incident light in the surrounding medium. The first disk has a relative refractive index of 1.31 and is transparent (nonabsorbing), whereas the second disk has a relative refractive index of 1.31 + i0.1 and is rather opaque. Both disks are illuminated by unpolarized light inci-

dent along their axis of rotation, and $R(\Theta)$ is the ratio of the intensity of light scattered at an angle Θ to the intensity of light scattered in the exact forward direction. If the GOA prediction of the delta-function transmission were correct then the curve for the opaque disk would have only the diffraction component whereas that for the transparent disk would be a superposition of the diffraction pattern and a much narrower delta-function transmission component. However, the rigorous T-matrix computations show that although the $Z_{11}(0, 0; 0, 0)$ value for the transparent disk is almost three times greater than that for the opaque disk, the angular profiles of the ratio $R(\Theta)$ for both disks is essentially the same. This result unequivocally indicates that the delta-function transmission contribution is not a true delta function but rather has the same angular profile as the Fraunhofer diffraction peak (Mishchenko and Macke 1998).

The explanation of this result is that a wave front emerging from any finite flat crystal facet (e.g., from the top facet of the particle shown in Fig. 7.8) should spread and produce an angular intensity distribution in the far-field zone similar to the Fraunhofer diffraction pattern (Volkovitsky *et al.* 1984; Muinonen *et al.* 1989). This applies not only to the transmitted light but also to the externally reflected light. For example, the plane wave front emerging from the bottom facet of the particle shown in Fig. 7.8 also spreads and produces a Fraunhofer-like angular distribution of the specularly reflected intensity, albeit twice as narrow as the diffracted intensity distribution (Mishchenko *et al.* 1997b). Both effects can have significant ramifications for laboratory and remote sensing techniques exploiting exact forward-scattering, backscattering, and specular directions (e.g., Platt 1978; Chepfer *et al.* 1999; Reichardt *et al.* 2000b).

Since the standard ray-tracing procedure does not take into account phase relations between different rays, the GOA ignores the effect of coherent backscattering (Section 3.4). It may, therefore, underestimate the contribution of rays propagating inside the particle along the same paths but in opposite directions and exiting the particle in the direction opposite to the incidence direction. This underestimation may be especially significant for particles with multiple internal inclusions, and one should correct for it by explicitly tracing not only the energies (or, more generally, the Stokes parameters) of the rays but also their phases and by taking into account interference effects (e.g., Göbel *et al.* 1998). Although coherent backscattering does not change the optical cross sections of the composite particle and is unlikely to modify noticeably its asymmetry parameter, it may increase substantially the backscattering phase function and, therefore, affect the results of laboratory and remote sensing studies using backscattered light (e.g., the results of lidar measurements).

To improve the performance of the geometrical optics approximation, Ravey and Mazeron (1982, 1983) developed the so-called physical optics or Kirchhoff approximation. This approach is based on Eq. (5.168) supplemented by the far-field asymptotic of Eq. (2.20). Equation (5.168) expresses the scattered field in terms of the electric and magnetic fields on the exterior side of the particle surface. The latter are

computed approximately using Fresnel's formulas and the standard ray-tracing procedure. The main difference from the conventional GOA scheme is the coherent adding of fields rather than the incoherent adding of Stokes parameters of the scattered rays; this allows the Kirchhoff approximation to preserve the phase information and reproduce physical optics effects completely ignored by the GOA scheme. The physical optics approach was used, with some variations, by Muinonen (1989), Yang and Liou (1995, 1996b), Mazeron and Muller (1996), and Yang *et al.* (2000a) and was found to be rather time consuming. Since this technique is still an approximation, its accuracy as a function of size parameter should be extensively tested versus exact solutions, especially when the full scattering matrix is computed.

7.5 Perturbation theories

The idea of the perturbation theory (PT) approach is to define the surface of an irregular particle in spherical coordinates by $r(\vartheta, \varphi) = r_0[1 + \xi f(\vartheta, \varphi)]$, where r_0 is the radius of the "unperturbed" sphere, ξ is a "smallness parameter", and $f(\vartheta, \varphi)$ obeys the condition $|f(\vartheta, \varphi)| < 1$. The fields inside and outside the particle are expanded in vector spherical wave functions and the expansion coefficients, which are determined through the requirement of the standard boundary conditions, are expressed as power series in ξ (Oguchi 1960; Yeh 1964; Erma 1969). Similar approaches were developed by Ogura and Takahashi (1990) and Martin (1993). Note that the application of the boundary conditions explicitly relies on the (unproven) validity of the Rayleigh hypothesis (see Section 6.4).

Schiffer (1989, 1990) combined the PT with an analytical orientation-averaging procedure to compute the scattering properties of randomly oriented particles. He also reported many numerical results obtained with the second-order PT and compared them with exact *T*-matrix computations by Mugnai and Wiscombe (1980) and Wiscombe and Mugnai (1988) for Chebyshev particles. The second-order PT showed good accuracy only for $2\pi r_0/\lambda_1 < 7$ and only if the surface deviations from the unperturbed sphere were much smaller than the wavelength. Similar conclusions were reached by Kiehl *et al.* (1980) on the basis of first-order PT computations. Battaglia *et al.* (1999), Muinonen (2000), and Nousiainen *et al.* (2001) have applied the second-order PT to Gaussian random particles.

Lacoste *et al.* (1998) and Lacoste and van Tiggelen (1999) considered light scattering by a Faraday-active dielectric sphere imbedded in an isotropic medium with no magneto-optical properties and subject to a homogeneous external magnetic field. They computed the amplitude and Stokes scattering matrices by using a perturbation approach and keeping only terms proportional to the first order of the magnetic field.

7.6 Other approximations

If the thickness of a particle in one of its dimensions is much smaller than a wavelength, it is often possible to approximate the integral equations describing the scattering process. This approach was applied to thin finite cylinders by Uzunoglu *et al.* (1978), to thin cylinders and disks by Schiffer and Thielheim (1979) and Fung (1994, Section 11.2), to thin disks by Weil and Chu (1980), and to thin-walled cylinders by Senior and Weil (1977).

Equation (2.16) can be used to compute the scattered field provided that the internal field is known. Le Vine *et al.* (1985) calculated the electromagnetic scattering from a homogeneous dielectric disk with a radius much larger than its thickness by approximating the internal field by the field that would exist inside an infinite homogeneous slab of the same thickness, orientation, and relative refractive index. Similarly, Karam and Fung (1988) and Seker and Schneider (1988) computed the scattering from long circular cylinders by approximating the internal field using the exact solution for an infinitely long cylinder with the same radius, orientation, and relative refractive index. A surface-field analog of this approximation was developed by Lin and Sarabandi (1995) and was extended to finite hexagonal cylinders by Rother *et al.* (1999) by virtue of computing the surface field for an infinite hexagonal cylinder using the discretized Mie formalism (Rother 1998). Because this approach ignores the contributions from the cylinder's top and bottom, it cannot reproduce such scattering features as the $46°$ halo for circular and hexagonal ice cylinders attributed to the minimal angle of deviation by $90°$ prisms and the strong backscattering enhancement caused by double internal reflections from perpendicular facets (see Fig. 7.6 and Section 10.6).

A similar approach was applied by Kuzmin and Babenko (1981) to the problem of scattering by spherical particles composed of a weakly anisotropic material. They computed the scattered field via Eq. (2.16) by approximating the internal field by that of an "equivalent" isotropic sphere.

Pollack and Cuzzi (1980) developed a semi-empirical theory based on the results of microwave analog measurements by Zerull (1976). They approximated the scattering properties of nonspherical particles with $x < x_0$ using the Lorenz–Mie results for volume-equivalent spheres, where x_0 is a tunable parameter typically close to 5. The absorption cross section for larger nonspherical particles was still computed using the Lorenz–Mie theory, while the phase function was represented as a sum of the Fraunhofer diffraction, the rays reflected from a sphere, and transmitted rays that were fitted to mimic Zerull's measurements by the use of another tunable parameter. Coletti (1984) proposed another semi-empirical theory based on his own optical measurements and similar in some respects to that of Pollack and Cuzzi.

Drossart (1990) proposed a model for calculating the scattering properties of irregular, randomly oriented particles based on modified Lorenz–Mie formulas for volume-equivalent spheres. The underlying assumption of the model is that the ampli-

tude scattering matrix for nonspherical particles can still be described by the Lorenz–Mie equations (5.149)–(5.151), but each summand on the right-hand side of Eqs. (5.149) and (5.151) experiences an independent random phase shift modeled by factors $\exp(\mathrm{i}\alpha_n)$ and $\exp(\mathrm{i}\beta_n)$ for S_{11} and S_{22}, respectively. An obvious deficiency of this approximation is that Eq. (5.150) is still applied despite the assumption of particle nonsphericity. As a consequence, the model preserves the Lorenz–Mie structure of the Stokes scattering matrix (Eq. (4.49)) and predicts linear and circular depolarization ratios identically equal to zero irrespective of the particle shape. Furthermore, the model does not provide a recipe for choosing the random phase factors based on particle microphysical characteristics.

Latimer (1975) developed several hybrid approximations for spheroids using the Lorenz–Mie theory and assigning an effective sphere radius and relative refractive index depending on the spheroid orientation and axis ratio. Latimer and Barber (1978) examined the accuracy of this approach by comparing its results with those obtained using the exact T-matrix method. Grenfell and Warren (1999) approximated the scattering and absorption properties of a long ice cylinder in random orientation using a collection of independent spheres having the same total volume and total surface area as the cylinder.

Further reading

Useful discussions of approximate theories can be found in the books by van de Hulst (1957), Kerker (1969), Bohren and Huffman (1983), Volkovitsky *et al.* (1984), Lopatin and Sid'ko (1988), and Kokhanovsky (1999) as well as in the recent review by Jones (1999). In Markel *et al.* (2000) approximate approaches are used to compute the scattering and absorption properties of smoke clusters.

The physical foundation of the geometrical optics concept of rays is explained in Chapter III of Born and Wolf (1999) and in a book by Kravtsov and Orlov (1990). Associated concepts of caustics and catastrophes are discussed by Marston (1992) and Kravtsov and Orlov (1999). A collection of selected papers on the geometrical theory of diffraction and wave fields near caustics relevant to scattering problems was edited by Marston (1994).

Chapter 8

Measurement techniques

Despite the availability of advanced theoretical techniques, laboratory and *in situ* experiments remain a useful (and sometimes the only) source of information about light scattering by many types of natural and artificial particles. Existing techniques for measuring the electromagnetic scattering characteristics of small particles traditionally fall into two categories:

- the measurement of visible and infrared light scattering by particles with sizes ranging from several hundredths of a micron to several hundred microns;
- the measurement of microwave scattering by millimeter- and centimeter-sized objects.

Measurements in the visible and infrared benefit from the availability of sensitive detectors (photomultipliers and avalanche semiconductor photodiodes), intense sources of radiation (lasers), and high-quality optical elements. They involve relatively cheap and portable instrumentation and in some cases can be performed in the field nearly as well as in the laboratory. By contrast, microwave scattering experiments require more cumbersome and expensive instrumentation and large (and often stationary) measurement facilities but typically provide better control and knowledge of the scatterer's geometrical and physical characteristics.

8.1 Measurements in the visible and infrared

We have mentioned already, in Section 2.6, that many detectors of electromagnetic energy (especially in the visible and infrared spectral regions) are polarization-insensitive, so that the detector response is determined only by the first Stokes pa-

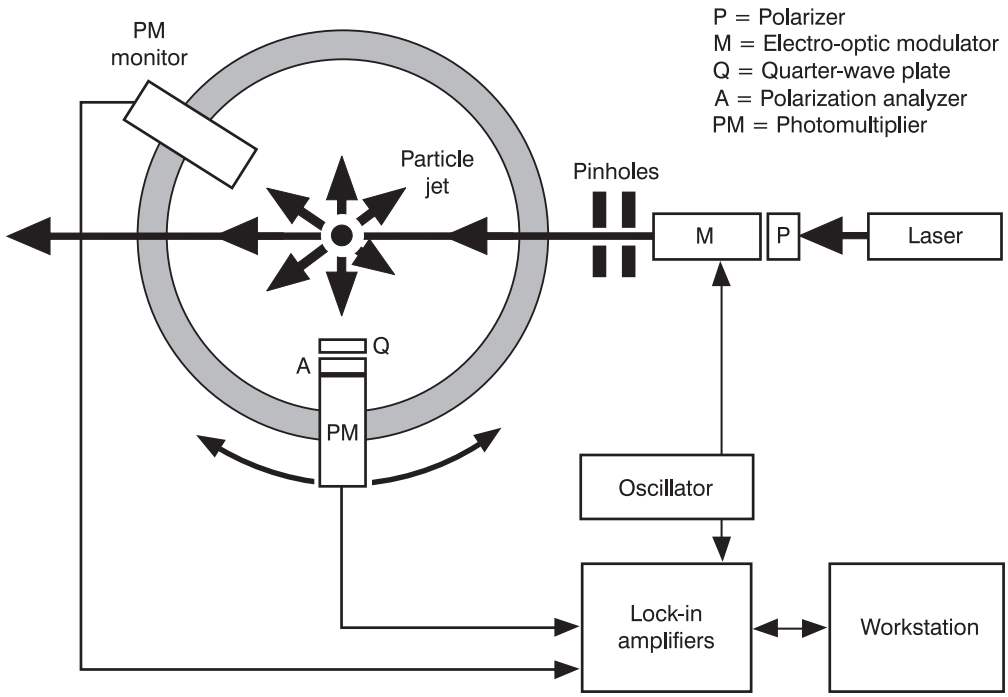

Figure 8.1. Schematic view of an experimental scattering setup using visible or infrared light. (After Hovenier 2000.)

rameter of the beam impinging on the detector. Therefore, in order to measure all elements of the scattering matrix for a particle or a collection of particles, one has to insert into the beam various optical elements that can vary the polarization state of the light, before and after scattering, in a controllable way. In Fig. 8.1, the beam generated by a light source (usually a laser) passes a linear polarizer and a polarization modulator and then illuminates particles contained in a jet stream or a scattering chamber. Light scattered by the particles at an angle Θ passes a quarter-wave plate (optionally) and a polarization analyzer before its intensity is measured by a detector. The Stokes vector of the beam reaching the detector, $\mathbf{I}'$, is given by

$$\mathbf{I}' \propto \mathbf{AQF}(\Theta)\mathbf{MPI} = \mathbf{AQ}N\langle\mathbf{F}(\Theta)\rangle\mathbf{MPI}, \tag{8.1}$$

where $\mathbf{I}$ is the Stokes vector of the beam leaving the light source, $\mathbf{A}$, $\mathbf{Q}$, $\mathbf{M}$, and $\mathbf{P}$ are 4×4 Mueller transformation matrices of the analyzer, quarter-wave plate, modulator, and polarizer, respectively, $\mathbf{F}(\Theta)$ is the total scattering matrix of the particles contributing to the scattered beam, N is the number of the particles, and $\langle\mathbf{F}(\Theta)\rangle$ is the ensemble-averaged scattering matrix per particle. It is implied that the scattering plane serves as the reference frame for defining the Stokes parameters. The Mueller matrices of the polarizer, modulator, quarter-wave plate, and analyzer depend on their orientation with respect to the scattering plane and can be varied precisely. Since the

detector measures only the first element of the Stokes vector $\mathbf{I}'$, several measurements with different orientations of the optical components with respect to the scattering plane are required for full determination of the scattering matrix. In the case of randomly oriented particles with a plane of symmetry and/or in the case of particles and their mirror counterparts in equal numbers and in random orientation, the six independent scattering matrix elements (Eq. (4.7)) can be determined using four different orientation combinations (Kuik *et al.* 1991). This procedure is repeated at different scattering angles in order to determine the angular profile of the scattering matrix.

The accuracy of an experimental setup can be tested by performing measurements for particles with known scattering characteristics such as spherical water droplets (e.g., Muñoz *et al.* 2000a). One can also check the block-diagonal structure of the scattering matrix, Eq. (4.7), which should exist when particles form a macroscopically isotropic and mirror-symmetric medium. Additional tests are provided by the general relationships for the scattering matrix elements (Hovenier and van der Mee 2000).

Early measurements of the scattering matrix used a simple subtraction method that relied on pairs of intensities measured separately with different combinations of polarizing elements; the results were subtracted in order to obtain scattering matrix elements (Pritchard and Elliott 1960; Beardsley 1968; Rozenberg *et al.* 1970). This technique has low accuracy because of the need to determine small differences between two large signals. The measurements of the two large signals are separated in time and this requires one to assume that the sensitivity of the detector and also the scattering sample (e.g., the number N of scattering particles) do not change with time, which is often not the case.

Hunt and Huffman (1973) developed the technique of high-frequency sinusoidal time modulation of the polarization of the light before it is scattered (Fig. 8.1), combined with intensity normalization. Followed by lock-in detection, this technique improves the measurement accuracy by enabling direct measurements of the scattering matrix elements normalized by the (1, 1) element of the matrix and yields the capability to determine several elements from only one detected signal. Advanced experimental setups based on this technique have been described by Bickel *et al.* (1976), Thompson (1978), Thompson *et al.* (1980), Anderson (1992), Kuik (1992), Hovenier (2000), and Kaplan *et al.* (2000).

A major advantage of measurements at visible and infrared wavelengths is that they can deal with real particle ensembles. However, they often suffer from the lack of accurate independent characterization of the particle size and shape distribution and relative refractive index, thereby making comparisons of experimental and theoretical results difficult. The number of particles N contributing to the scattered beam is also seldom known, which precludes the absolute measurement of the (1, 1) element of the ensemble-averaged scattering matrix per particle $\langle \mathbf{F}(\Theta) \rangle$ (measurements of elements other than the (1, 1) element are usually reported in the form of N-independent ratios of the elements to the (1, 1) element). Another drawback is that the arrangement of the source of light and the detector usually precludes measurements at scattering angles close to 0° and 180° (although it is possible to add a

backscattering measurement capability using a beam splitter). For example, the setup described by Hovenier (2000) has the range of scattering angles $[5°, 175°]$. This makes problematic absolute measurement of the phase function by means of satisfying the normalization condition of Eq. (4.53). As a consequence, experimental phase functions are often normalized to the value at a fixed scattering angle. An alternative way of presenting experimentally determined phase functions is to assume that the phase-function value at the smallest scattering angle available is the same as for volume- or surface-equivalent spheres. This approach may or may not be accurate, depending on the (often unknown) validity of the underlying assumption.

The error in determining the scattering cross section per particle by integrating the scattered intensities over all scattering angles also relies on a knowledge of N and depends on how much of the forward- and back-scattered energy is not detected (Anderson *et al.* 1996; Heintzenberg and Charlson 1996; Rosen *et al.* 1997). As discussed in Section 7.4, the phase function of particles larger than the wavelength of the incident light has a strong and narrow diffraction peak that may contain more than 50% of the total scattered energy (Figs. 7.3 and 7.4 and Eqs. (7.13)–7.15)). This factor alone can cause errors exceeding 50% in the measured scattering cross section.

The extinction cross section is often determined by measuring the attenuation of the directly transmitted beam. Specifically, the extinction cross section is proportional to the difference in the readings of detector 1 in Fig. 2.3 corresponding to the situations without and with the particle(s) interposed between the source of light and the detector (Sections 2.8 and 3.1). This measurement unavoidably suffers from the problem that a detector with a finite angular aperture picks up some of the light *scattered* by the particle(s) in the forward direction. Depending on the average particle size and thus the magnitude and angular width of the diffraction component of the phase function (Fig. 7.3), the extinction can be underestimated by as much as a factor of 2. Indeed, we saw in Section 7.4 that, for particles larger than the wavelength, the scattering cross section due to the diffraction peak is equal to the area of the particle's projection on the plane perpendicular to the incidence direction, Eq. (7.14), and, thus, is equal to one-half of the extinction cross section, Eq. (7.12). If the detector picks all the energy contained in the narrow diffraction cone, then the energy removed by the particle from the incident beam and thus the extinction cross section will be underestimated by 50%. Therefore, if a detector is to measure accurately the full extinction by particles with size parameters $x \gg 1$ then its acceptance angle must be much smaller than $7/x$, say less than $1/(2x)$ (see Fig. 7.3). Correction for the diffraction contamination is possible if the average particle projection is known and is large, but this is not always the case. With significant potential errors in the extinction and scattering cross sections, little may be said about the difference between the former and the latter, i.e., the absorption cross section, or about the ratio of the latter to the former, i.e., the single-scattering albedo, Eqs. (2.161) and (2.162).

Ashkin and Dziedzic (1980) obtained direct backscatter measurements by using the optical levitation technique, which involved the suspension of particles by light

pressure from the source laser beam alone. An instrument specifically designed for remote sensing measurements at the exact backscattering direction is a lidar, built of a pointing laser emitting a powerful beam and a receiving telescope–detector combination affixed to the laser (Sassen 2000). The laser beam is usually polarized either linearly $(P = 1,\ V = 0)$ or circularly $(P = 1,\ V = \pm I)$. The laser light scattered by aerosol and cloud particles is collected by the telescope, and its intensity and polarization characteristics are precisely measured. Since lidars measure backscattering from particles located at large distances (hundreds and thousands of meters) from the instrument, the scattering angle can be made arbitrarily close to 180°. Important quantities measured by a polarization lidar are the so-called linear and circular depolarization ratios. Because both ratios must vanish for spherically symmetric scatterers, the detection of non-zero ratios may directly indicate the presence of nonspherical particles (see Sections 10.2 and 10.11).

Early scattering experiments used unpolarized incident light and were limited to measurements of the scattered intensity and the degree of linear polarization (Hodkinson 1963; Napper and Ottewill 1963). The first measurements of other elements of the scattering matrix were performed using the simple subtraction method. The development of the polarization modulation technique resulted in a number of accurate measurements of the complete scattering matrix. The results of extensive measurements using visible and infrared light were reviewed by Hoekstra and Sloot (2000), Mishchenko *et al.* (2000c), and Quinby-Hunt *et al.* (2000). Among more recent results, we note measurements of the scattering matrix for iron oxide ellipsoids and latex sphere suspensions (Kaplan *et al.* 1999, 2000), rutile particles in water (Volten *et al.* 1999), olivine and Allende meteorite particles (Muñoz *et al.* 2000a), ice crystals (Bacon and Swanson 2000), various mineral aerosols (Volten 2001; Volten *et al.* 2001), and fly ash and clay particles (Muñoz *et al.* 2000b, 2001). Worms *et al.* (2000) measured the degree of linear polarization for various scattering samples under microgravity conditions. Card and Jones (1999a,b) investigated the potential of measuring polarized light scattering for characterization of irregular particles. Tavker and Kumar (2000) performed laboratory measurements of the linear depolarization ratio for artificial crystallized H_2O/H_2SO_4 acid clouds. Gerber *et al.* (2000) and Garrett *et al.* (2001) used a so-called cloud integrating nephelometer to measure the asymmetry parameter for water droplet and ice crystal clouds. Wurm *et al.* (2000) measured the intensity and polarization of light scattered by laboratory-generated dust aggregates consisting of micrometer-sized components. Barkey and Liou (2001) reported measurements of the phase function of laboratory-generated water microdroplets and ice crystals using a portable lightweight nephelometer specifically designed for deployment on a balloon-borne platform in cirrus cloud conditions.

To demonstrate the particle-characterization potential of measurements using visible light, we show in Fig. 8.2 laboratory results for the phase function $a_1(\Theta)$ and the ratio $b_1(\Theta)/a_1(\Theta)$ at two wavelengths (442 and 633 nm) measured for an artificial cloud of spherical water droplets with a refractive index m = 1.33 relative to that of

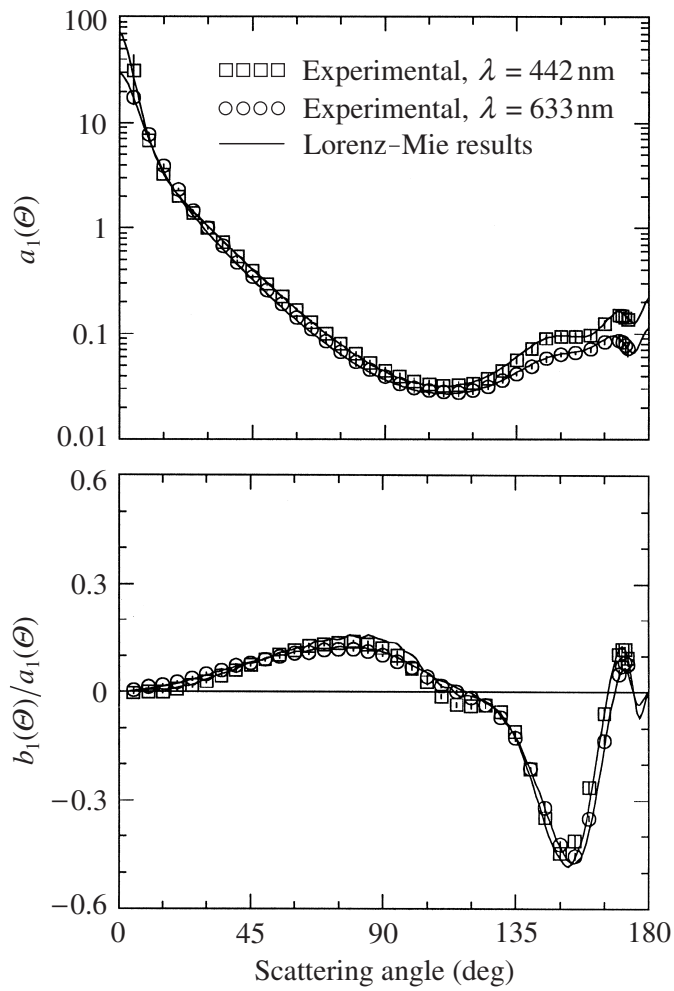

Figure 8.2. The phase function $a_1(\Theta)$ and the ratio $b_1(\Theta)/a_1(\Theta)$ measured by Muñoz *et al.* (2000a) for an artificial cloud of spherical water droplets at two wavelengths. The solid curves show the results of Lorenz–Mie computations for a log normal size distribution of water spheres, with effective radius and effective variance chosen such that they minimize the differences between the measured and calculated scattering matrix elements as functions of scattering angle.

air. The experimental phase functions are normalized to unity at $\Theta = 30°$. Measurement errors (shown by vertical error bars) are negligibly small at most scattering angles. The laboratory results are compared with the results of Lorenz–Mie calculations for a log normal size distribution, Eq. (5.243), the parameters r_g and σ_g being chosen such that the effective radius and effective variance of the distribution, Eqs. (5.248) and (5.249), are $r_{\text{eff}} = 1.1\,\mu\text{m}$ and $v_{\text{eff}} = 0.3$, respectively. These values were found to minimize the differences between the measured and calculated scattering matrix elements as functions of scattering angle. Clearly, the quantitative agreement between the measurements and the calculations is good over the entire scattering an-

gle range. The remaining differences may be due to the fact that the actual size distribution deviated somewhat from the assumed log normal distribution.

Knowledge of the scattering matrix provides a complete characterization of the angular distribution and polarization state of the scattered light for spherically symmetric or randomly oriented particles. However, averaging over orientations reduces the potential information content of the scattered light by smoothing out specific features generated by a nonspherical particle having a fixed orientation relative to the incidence and scattering directions. Therefore, several attempts have been made recently to measure the intensity of the scattered light for single nonspherical particles in a fixed orientation as a function of both the zenith and the azimuth angle and to assess the particle characterization potential of such measurements (Hirst *et al.* 1994, 2001; Hirst and Kaye 1996; Kaye *et al.* 1996, 1997; Holler *et al.* 1998, 1999, 2000; Sachweh *et al.* 1999; Borovoi *et al.* 2000; Secker *et al.* 2000; Videen *et al.* 2000a). Plate 8.1 shows four examples of two-dimensional angular scattering measurements for the case of laser light incident along the positive direction of the x-axis (cf. Fig. 1.2). The measurements show a distinctive irregular patchy structure, with the patch density per solid angle increasing with cluster diameter. Although the amount of information contained in such two-dimensional angular scattering patterns may often be overwhelming and may be difficult to interpret definitively, this technique appears to be a promising particle characterization tool and should be pursued further. An obvious improvement would be measurement of the polarization state as well as the intensity of the scattered light.

8.2 Microwave measurements

Measurements of scattering properties of millimeter- and centimeter-sized objects at microwave frequencies are important for such applications as the remote sensing of precipitation and communication technology (Oguchi 1983; Aydin 2000; Haferman 2000). In addition, the scale invariance rule (subsection 5.8.2) states that particle size in the theoretical formulation of electromagnetic scattering is only encountered as a ratio to the wavelength as long as one deals with dimensionless scattering and absorption characteristics. Therefore, the strategy of the microwave analog technique is to manufacture a centimeter-sized scattering object with the desired shape and relative refractive index, study the scattering of a microwave beam by this object, and finally extrapolate the results to other wavelengths (e.g., visible or infrared) by keeping the ratio of size to wavelength fixed (Greenberg *et al.* 1961; Lind *et al.* 1965).

In a modern microwave scattering setup, radiation from a transmitting conical horn antenna passes through a collimating lens and a polarizer (see Fig. 8.3). The lens produces a nearly flat wave front, which is scattered by an analog particle model target. The scattered wave passes through another polarizer and lens and is measured by a receiving horn antenna. The receiver end of the setup can be positioned at any

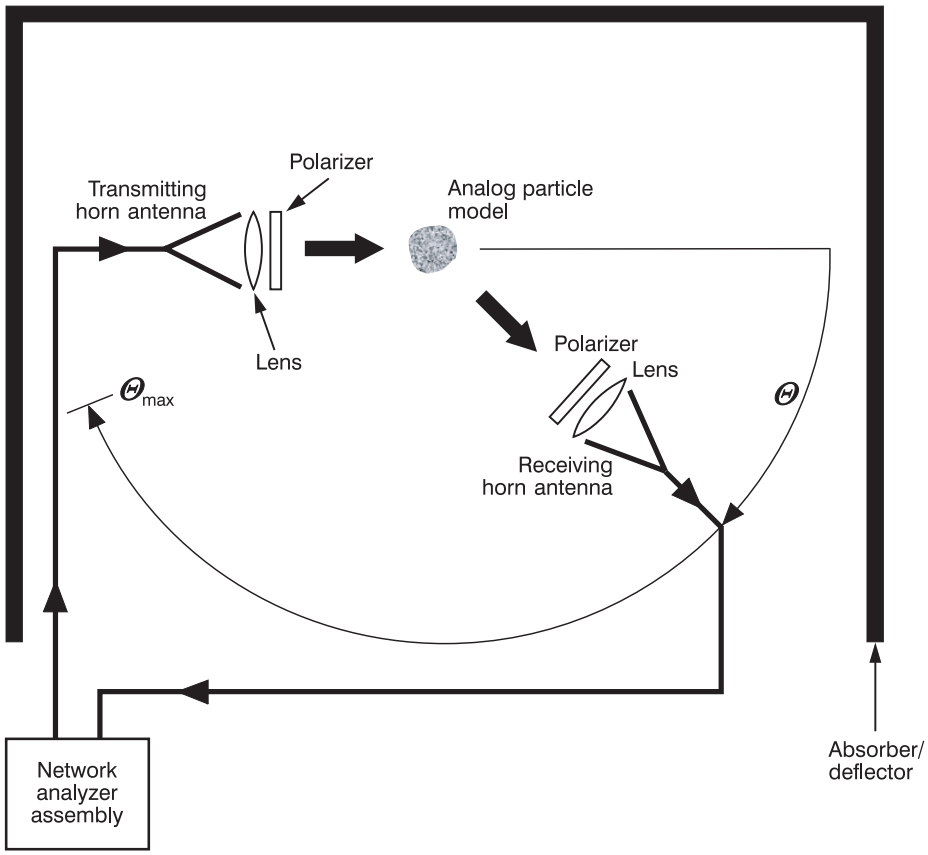

Figure 8.3. Layout of an advanced microwave analog facility. (After Gustafson 2000.)

scattering angle from $0°$ to $\Theta_{max} \cong 170°$, thereby providing measurements of the angular distribution of the scattered radiation. By precisely varying the orientations of the two polarizers, one can measure all elements of the scattering matrix. Detailed discussions of various experimental aspects of the microwave analog technique have been provided by Gustafson (1996, 2000).

Microwave measurements allow coverage of a wide range of scattering angles, including the exact forward direction, and a much greater degree of control over the target size, shape, and orientation than optical or infrared measurements. Using special techniques, even the extinction cross section (or, more generally, the extinction matrix) can be measured. Measurements at angles close to the backscattering direction are usually problematic because the transmitting and receiving antennas would overlap. It is possible, however, to add a backscattering measurement capability ($\Theta = 180°$) by using the transmitting antenna as a receiver. Because the size of the scattering object is typically of the order of centimeters for microwave analog measurements, high-precision target manufacturing is easy and can involve computer-controlled milling or stereo lithography. Therefore, the results of controlled laboratory measurements at microwave frequencies can be compared with theory easily. A

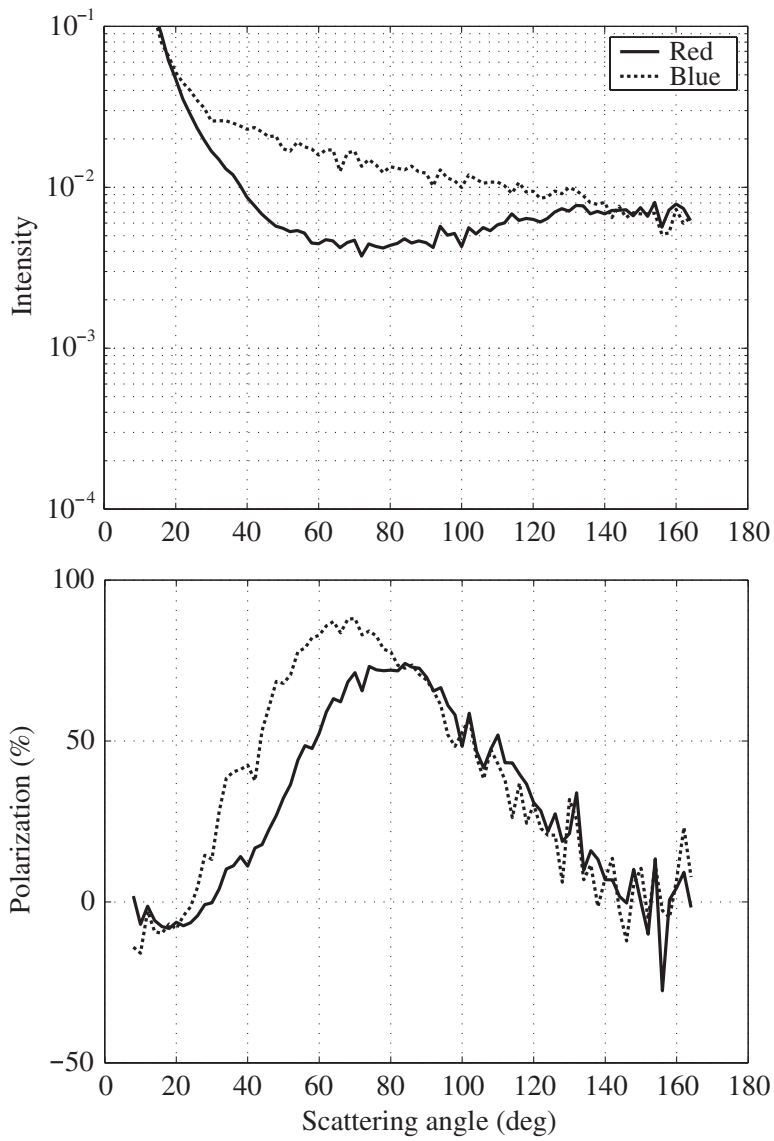

Figure 8.4. Microwave analog measurements of the scattered intensity (in arbitrary units) and the degree of linear polarization for a thin acrylic plate in random orientation (from Waldemarsson and Gustafson 2000). The diameter of the plate is 50.8 mm, the thickness is 1.52 mm, and the relative refractive index is 1.62 + i0.003. The broken and solid curves correspond to the wavelength intervals 2.7–3.0 mm and 3.5–4.0 mm, respectively.

disadvantage of microwave measurements is that they can be performed only for one particle size, shape, and orientation at a time, thereby making ensemble averaging a time-consuming procedure.

Although the microwave analog technique was introduced several decades ago, the complexity and the high cost of the equipment involved have limited the number of operating experimental facilities to only a few. Publications reporting and analyz-

ing the results of microwave analog measurements have been reviewed by Gustafson (2000) and Mishchenko *et al.* (2000c). Recent results include a laboratory comparison of the backscattering ability of raindrops and ice particles (Qingan *et al.* 1998), a systematic experimental study of the angular and wavelength dependence of the intensity and polarization of light scattered by aggregated particles (Gustafson and Kolokolova 1999), laboratory measurements of the polarimetric radar signatures of spherical and spheroidal water droplets at 30GHz (Tazaki *et al.* 2000), and the use of microwave analog measurements for heterogeneous objects in testing the validity of various effective-medium theories (Kolokolova and Gustafson 2001).

Figure 8.4 gives an example of microwave analog measurements. The scattered intensity and the degree of linear polarization $P_Q = -b_1(\Theta)/a_1(\Theta)$ are shown for unpolarized light incident on a thin acrylic plate in random orientation (Waldemarsson and Gustafson 2000). The diameter of the plate is 50.8 mm, the thickness is 1.52 mm, and the relative refractive index is 1.62 + i0.003. The total number of orientations used to simulate the uniform orientation distribution was 1620 and the tilt angle between the normal to the plane facets of the plate and the spin axis was varied in 10° steps. Measurement results were averaged over the wavelength intervals 2.7–3.0 mm and 3.5–4.0 mm. The experiment was designed to model the scattering of unpolarized visible light by randomly oriented silicate flakes with diameter 8 μm and thickness 0.25 μm in the wavelength intervals 0.44–0.49 μm ("blue") and 0.57–0.65 μm ("red"). The fine structure in the curves is mostly due to the limited number of orientations used in the ensemble averaging. The implications of these laboratory results will be discussed in Section 10.4.

Radars form a special class of instruments providing active polarization measurements for remote targets at microwave and radiowave frequencies. Monostatic radars use the same antenna to transmit and receive electromagnetic waves and are limited to measurements at the exact backscattering direction ($\Theta = 180°$). Bistatic lidars use one or more additional receiving antennas, which provide supplementary information for other scattering angles. Remote sensing applications of the radar technique have been reviewed by Aydin (2000) and Bringi and Chandrasekar (2001).

Part III

Scattering and Absorption Properties of Small Particles and Illustrative Applications

There are two classes of problems involving electromagnetic scattering by small particles: the direct problem and the inverse problem. Thus far, we have dealt primarily with the direct problem of calculating or measuring the scattering by a known, well-defined system. The so-called inverse problem is to characterize a system of interest using scattering data collected from laboratory measurements or remote sensing observations.

Given the unlimited diversity of particle types in nature and in the laboratory, one may expect a significant variability in the optical properties of particles encountered in different applications. Therefore, solving the inverse problem may often be facilitated by previous knowledge of how the various absorption and scattering properties of small particles may depend on the particle size parameter, morphology, relative refractive index, and orientation. This knowledge may be the cumulative result of analyzing many specific cases supplemented by careful interpolation or extrapolation to the range of particle characteristics not specifically covered by existing theoretical or experimental results.

The purpose of the following two chapters is to discuss the current understanding of the optical properties of small particles. Although we have not attempted an exhaustive summary of all published results, we hope that these chapters will provide useful information to those interested in a preliminary qualitative or semi-quantitative analysis of a specific problem as well as to those evaluating the feasibility of a more precise quantitative solution and considering various solution approaches. We also discuss a few selected applications which demonstrate the great potential of electromagnetic scattering as a noninvasive particle characterization and remote sensing tool.

Chapter 9

Scattering and absorption properties of spherical particles

The decisive advantages of the Lorenz–Mie theory compared to any other theoretical technique are its unparalleled numerical accuracy, high computational efficiency, and applicability to essentially any size parameter and relative refractive index. These attributes permit a comprehensive study of electromagnetic scattering by at least one class of small particles, viz., isotropic and homogeneous spheres. Although a substantial fraction of the particles encountered in natural and laboratory conditions are nonspherical, the Lorenz–Mie theory provides a first-order description of many optical effects that are common to all small particles and may not be intuitively obvious. Furthermore, there are many practical situations in which the scattering particles in question are almost, if not precisely, spherical so that the Lorenz–Mie theory can be expected to apply directly. Hence our approach is to begin by a detailed analysis of the scattering and absorption properties of spherical particles and continue, in the following chapter, with a discussion of the effects caused by particle nonsphericity. All numerical data discussed in this chapter have been computed using the Lorenz–Mie code described in Section 5.10 and the ray-tracing code described by Macke and Mishchenko (1996).

9.1 Monodisperse spheres

Two properties of the extinction efficiency factor Q_{ext} make it often a more convenient quantity to display than the extinction cross section. First, $Q_{\text{ext}} = C_{\text{ext}}/(\pi r^2)$ is a function of the dimensionless size parameter $x = 2\pi r/\lambda_1$ (subsection 5.8.2), whereas the extinction cross section C_{ext} itself depends on both the particle radius, r, and the wavelength in the surrounding medium, λ_1. Second, Eq. (7.12) shows that, in the

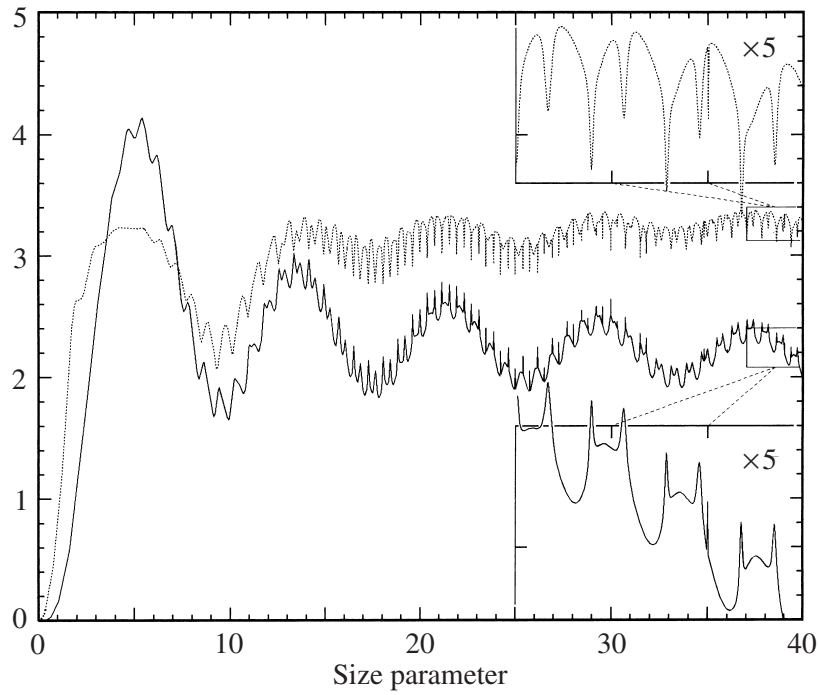

Figure 9.1. Extinction efficiency factor Q_{ext} (solid curve) and asymmetry parameter $\langle\cos\Theta\rangle$ multiplied by a factor of 4 (dotted curve) versus size parameter x for monodisperse spherical particles with a relative refractive index $m = 1.4$.

large-particle limit, C_{ext} is proportional to the second power of r and hence may span many orders of magnitude, depending on the range of particle radii displayed, whereas the asymptotic value of Q_{ext} is 2 and its maximum value is often not much greater than the asymptotic value.

The solid curve in Fig. 9.1 shows the extinction efficiency factor Q_{ext} as a function of size parameter for monodisperse spherical particles with a relative refractive index $m = 1.4$, and the dotted curve depicts the asymmetry parameter $\langle\cos\Theta\rangle$. Since the imaginary part of the relative refractive index is here set at zero, the scattering efficiency factor is equal to the extinction efficiency factor, the absorption efficiency factor is equal to zero, and the single-scattering albedo is equal to unity. In agreement with Eqs. (7.3), (7.7), and (7.12), both Q_{ext} and $\langle\cos\Theta\rangle$ rapidly vanish as x approaches zero, and Q_{ext} tends to its asymptotic value 2 as $x \to \infty$. In the intermediate (so-called resonance) region of size-parameter values, the extinction efficiency factor can exceed the geometrical optics value, 2, especially as the real part of the relative refractive index is increasing (cf. Fig. 9.2).

Both curves in Fig. 9.1 are characterized by a succession of major low-frequency maxima and minima with superimposed high-frequency ripples composed of sharp, irregularly spaced extrema, some of which are super-narrow spike-like features. The major maxima and minima are called the "interference structure" since, as traditionally explained, they are the result of interference of the light diffracted and

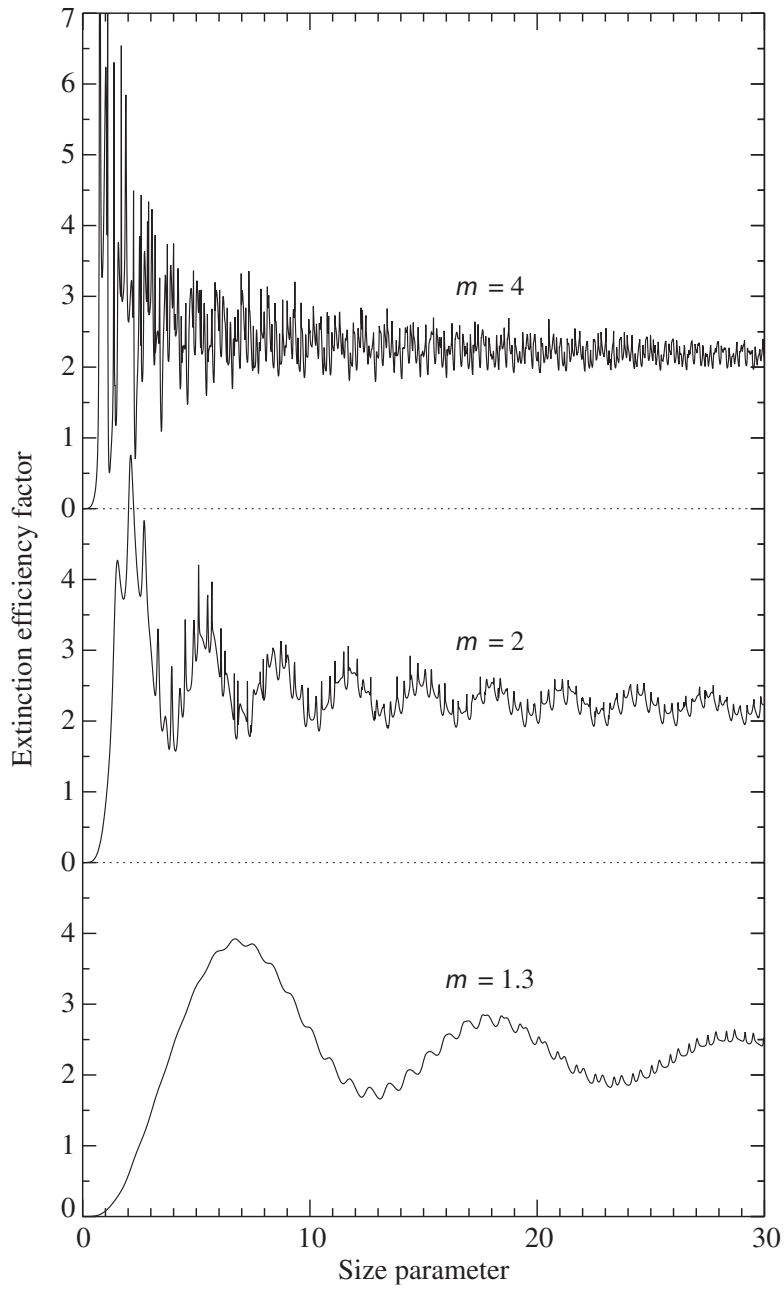

Figure 9.2. Extinction efficiency factor Q_{ext} versus size parameter x for monodisperse spherical particles with relative refractive indices m = 1.3, 2, and 4.

transmitted by the particle (van de Hulst 1957; Chýlek and Zhan 1989; Lock and Yang 1991). A light ray passing through the center of a sphere acquires a phase shift $\rho = 2x(m_{\text{R}} - 1)$, where m_{R} is the real part of the relative refractive index. Therefore, constructive and destructive interference and, thus, maxima and minima in the extinction efficiency curve, occur successively at intervals $\approx 2\pi$ in ρ (see Fig. 9.3, which shows Q_{ext} as a function of ρ for monodisperse spheres with various real

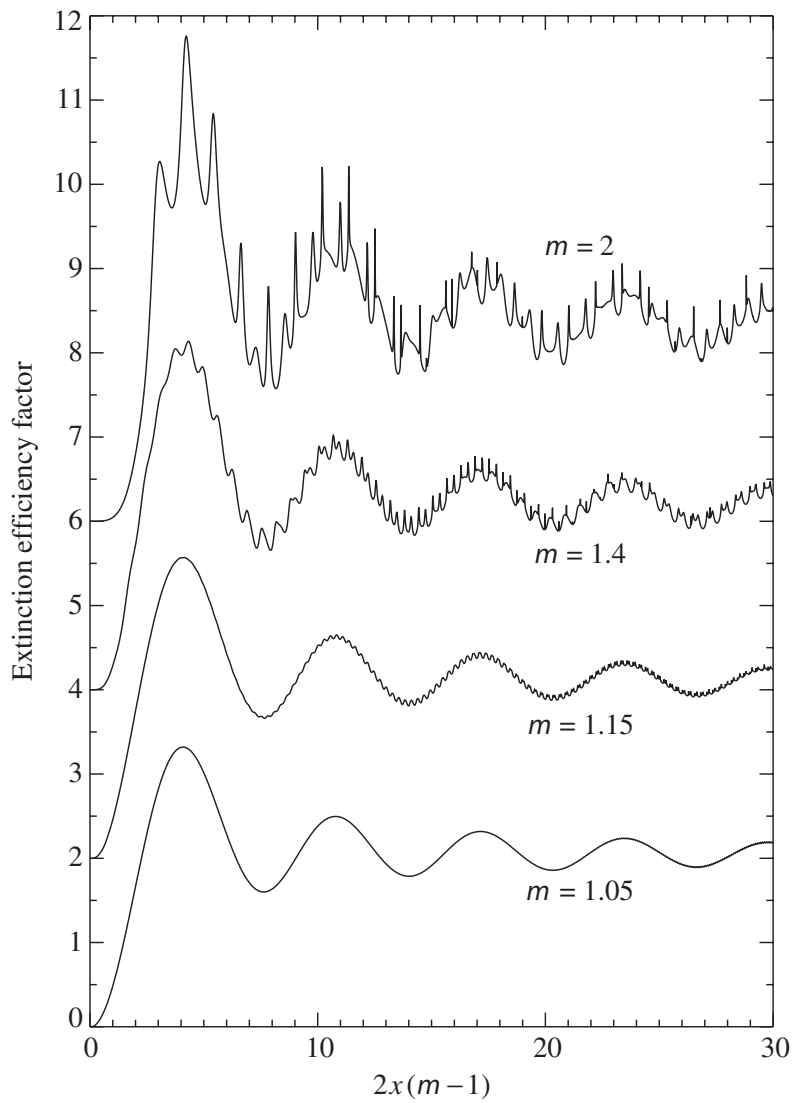

Figure 9.3. Extinction efficiency factor versus phase shift for monodisperse spherical particles with relative refractive indices m = 1.05, 1.15, 1.4, and 2. The vertical scale applies to the curve for m = 1.05, the other curves being successively displaced upward by 2.

relative refractive indices). With $m_R \to \infty$, the central transmitted rays are increasingly attenuated by the external reflection, and the interference structure becomes less pronounced (cf. Fig. 9.2) and ultimately disappears (Chýlek and Zhan 1989).

Unlike the interference structure, the ripple is caused by the resonance behavior of the Lorenz–Mie coefficients a_n and b_n (see, e.g., the review by Hill and Benner (1988) and references therein). The resonances in lower-order coefficients are relatively broad and often overlap. As n increases, the resonance features become narrower, and starting with $n \sim 20$ (for m = 1.4) each feature in the ripple structure can be identified with an individual resonance in the corresponding partial coefficient a_n or b_n. As the size parameter approaches a resonant value, the denominator of a Lo-

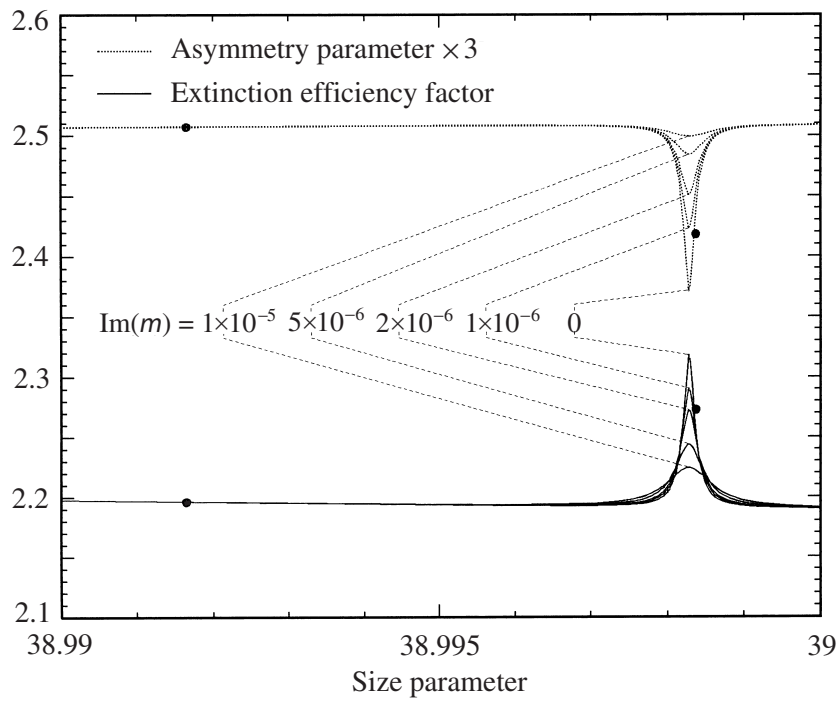

Figure 9.4. Profile of the resonance centered at $x \approx 38.9983$ for $m_R = 1.4$ and five values of m_I. The dots show the sampling resolution used in Fig. 9.1.

renz–Mie coefficient a_n or b_n approaches a local minimum, thereby causing a local extremum (maximum or minimum) in the curve for a specific scattering characteristic. Accordingly, the numbers of spike-like extrema in the two curves in Fig. 9.1 are identical, and a sharp local maximum in the extinction curve always corresponds to a sharp local minimum in the asymmetry parameter curve. Some of the resonance features can be extremely narrow. This is demonstrated in Fig. 9.4, which shows the angular profile of the resonance centered at $x \approx 38.9983$. The dots indicate the sampling resolution used in Fig. 9.1, illustrating that it is just coincidence that the resonance depicted in Fig. 9.4 is resolved in Fig. 9.1.

Figure 9.5 demonstrates that the resonance features shown in Fig. 9.4 are not simply an isolated peak in Q_{ext} and an isolated hollow in $\langle \cos\Theta \rangle$. Instead, Fig. 9.4 depicts merely a cross section (corresponding to m = 1.4) of a long crest and a co-located long canyon appearing in the surface plots of Q_{ext} and $\langle \cos\Theta \rangle$, respectively, as functions of size parameter and real relative refractive index. It is interesting that the middle of the crest and the middle of the canyon in Fig. 9.5 follow the curves mx = constant. This means that, for a given resonance, increasing the relative refractive index shifts the location of the maximum in Q_{ext} (and the minimum in $\langle \cos\Theta \rangle$) towards smaller size parameters.

It is straightforward to show (Chýlek 1973; Probert-Jones 1984) that the Lorenz–Mie coefficients given by Eqs. (5.219) and (5.220) can be expressed as

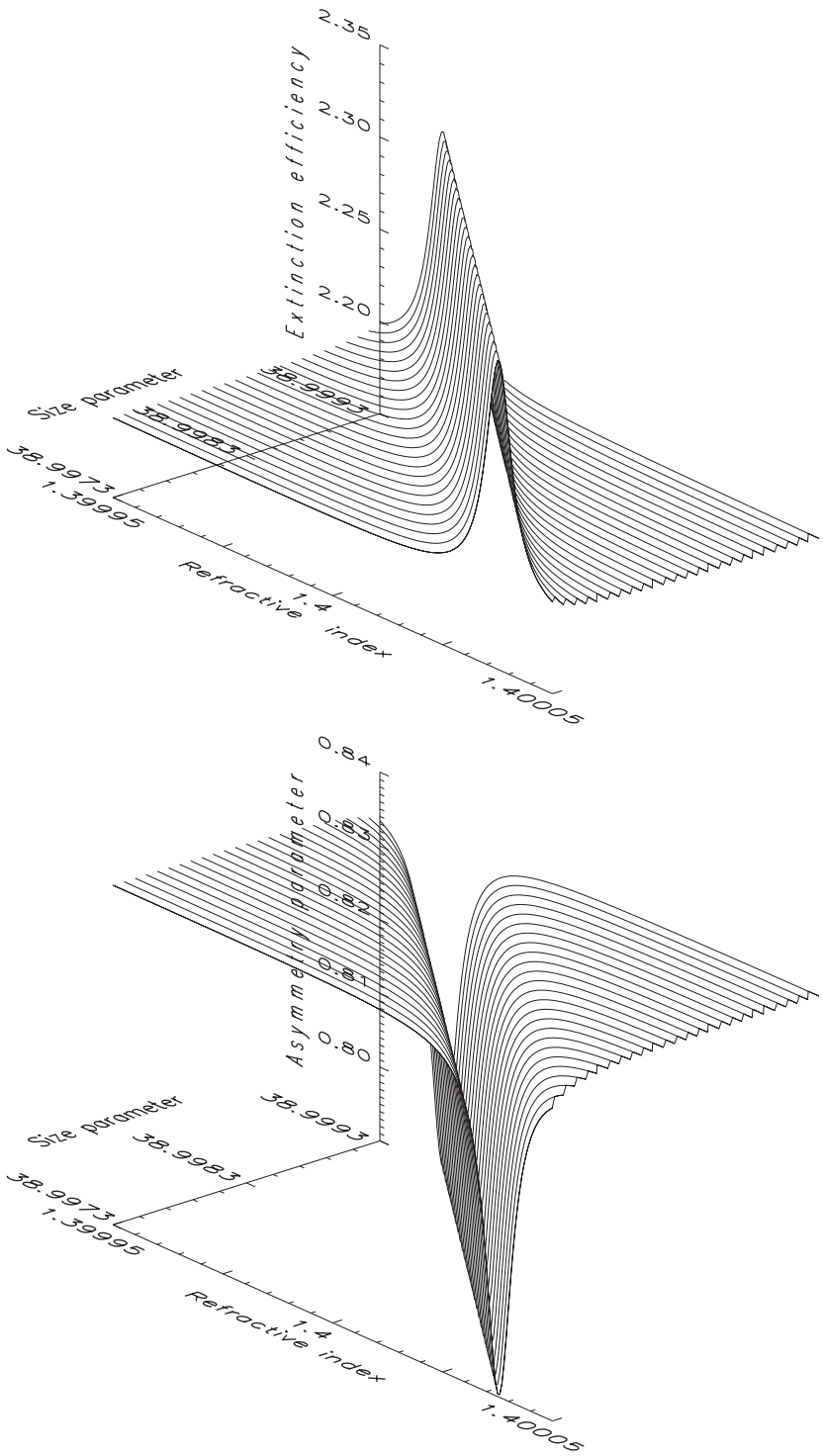

Figure 9.5. High-resolution surface plots of the extinction efficiency factor and asymmetry parameter versus size parameter and relative refractive index for monodisperse nonabsorbing spherical particles.

$$a_n(x, m) = \frac{p_n(x, m)}{p_n(x, m) + \mathrm{i}q_n(x, m)}$$

$$= \frac{[p_n(x,m)]^2}{[p_n(x,m)]^2 + [q_n(x,m)]^2} - \mathrm{i}\frac{p_n(x, m)q_n(x, m)}{[p_n(x, m)]^2 + [q_n(x, m)]^2}, \tag{9.1}$$

$$b_n(x, m) = \frac{r_n(x, m)}{r_n(x, m) + \mathrm{i}s_n(x, m)}$$

$$= \frac{[r_n(x, m)]^2}{[r_n(x, m)]^2 + [s_n(x, m)]^2} - \mathrm{i}\frac{r_n(x, m)\, s_n(x, m)}{[r_n(x, m)]^2 + [s_n(x, m)]^2}, \tag{9.2}$$

where

$$p_n(x, m) = m\psi_n(mx)\psi_n'(x) - \psi_n(x)\psi_n'(mx), \tag{9.3}$$

$$q_n(x, m) = -m\psi_n(mx)\chi_n'(x) + \chi_n(x)\psi_n'(mx), \tag{9.4}$$

$$r_n(x, m) = m\psi_n(x)\psi_n'(mx) - \psi_n(mx)\psi_n'(x), \tag{9.5}$$

$$s_n(x, m) = -m\chi_n(x)\psi_n'(mx) + \psi_n(mx)\chi_n'(x), \tag{9.6}$$

and $\chi_n(x) = -xy_n(x)$ (cf. Eqs. (5.218) and (C.1)). The convenience of writing $a_n(x, m)$ and $b_n(x, m)$ in this form is that the functions $p_n(x, m)$, $q_n(x, m)$, $r_n(x, m)$, and $s_n(x, m)$ are real if the relative refractive index is real. The denominators of Eqs. (9.1) and (9.2) can vanish completely only for complex size parameters, whereas for real size parameters they always remain finite. Therefore, what happens at a resonance is that either $q_n(x, m)$ or $s_n(x, m)$ vanish. For this specific set of x-, m-, and n-values, the real part of $a_n(x, m)$ or $b_n(x, m)$ reaches its maximum possible value, unity, and the imaginary part vanishes (Chýlek 1976). Accordingly, quantities like $\mathrm{Re}\, a_n(x, m)$ and $|a_n(x, m)|$ or $\mathrm{Re}\, b_n(x, m)$ and $|b_n(x, m)|$ exhibit a local maximum, thereby causing spikes in the two-dimensional extinction and scattering curves corresponding to fixed m or x (cf. Eqs. (5.156) and (5.157)). Thus Eqs. (9.4) and (9.6) give the following mathematical condition for a resonance:

$$-m\psi_n(mx)\chi_n'(x) + \chi_n(x)\psi_n'(mx) = 0 \tag{9.7a}$$

or

$$-m\chi_n(x)\psi_n'(mx) + \psi_n(mx)\chi_n'(x) = 0. \tag{9.7b}$$

Note that for given n and m, these equations have infinitely many solutions at discrete values of x.

Another way to look at resonances is to consider the complex size-parameter plane (though still with the restriction of a real relative refractive index) and write $a_n(x, m)$ or $b_n(x, m)$ as a simple pole, e.g.,

$$a_n(x, m) = \frac{\alpha}{x - z}, \tag{9.8}$$

where z is the position of the pole and α is the residue (Conwell *et al.* 1984; Hunter *et al.* 1988). The resonant size parameter is then given by the real part of z.

A physical interpretation of resonances is that of a situation where rays propagate around the inside surface of a spherical particle, confined by an almost total internal reflection (Hill and Benner 1988): the rays approach the internal surface at an angle beyond the critical angle and are totally reflected each time. After propagating around the sphere, the rays return to their respective entrance points exactly in phase and then follow the same path all over again without being attenuated by destructive interference. Therefore, it takes longer for the electromagnetic energy of the rays to leak out of the sphere, and very large energy densities can be accumulated inside the particle near its surface. Since the accumulated energy is removed from the incident beam, the result of the resonance process is an increased extinction efficiency of the particle. It can be shown that the longer the internal path of the rays, the narrower the resonance (e.g., Roll and Schweiger 2000).

For a fixed m and each index n, there is a sequence of resonance x-values for either $a_n(x, m)$ or $b_n(x, m)$. Hence it is convenient to label each local extremum with the type of mode causing the resonance (a or b), the subscript n, and a superscript l indicating the sequential order of x (Chýlek 1976; Chýlek *et al.* 1978). This labeling convention is illustrated in the upper panel of Fig. 9.6, which shows the resonance extinction features for a water droplet within the interval $x \in [50, 51]$. The main traits of the resonance features are that their width decreases as n increases for a given l and their width increases as l increases for a given n. For n greater than about 50, the $l = 1$ resonance can become extremely narrow, as demonstrated in the lower panel of Fig. 9.6.

Figure 9.4 shows the behavior of the super-narrow resonance centered at $x \approx 38.9983$ (for $m = 1.4$) with increasing imaginary part of the relative refractive index m_{I}. It is seen that raising m_{I} from 0 to a very small value of 10^{-5} almost completely destroys this spike-like feature while causing no change whatsoever in the background Q_{ext} and $\langle \cos\Theta \rangle$ values. It takes significantly greater m_{I}-values to eliminate the broader resonances and still greater values (of order 0.1) to eliminate the interference structure (Figure 9.7). This is not surprising. Indeed, the diffracted rays are unaffected by absorption, whereas attenuation of the transmitted rays gives weaker interference in the near-forward direction and a decrease in amplitude of the interference structure. The transmitted rays are attenuated as they pass through the center of the sphere and thus travel inside the particle a distance equal to one sphere diameter. The super-narrow resonances correspond to much longer internal ray paths (several sphere circumferences) and are much more stronly affected by internal absorption. Therefore, measurements within super-narrow resonances can be far more sensitive to weak absorption than measurements in the "continuum" or within broader ripple features.

It appears that manifestations of the ripple structure can be even more spectacular in the elements of the scattering matrix than in the optical cross sections and the

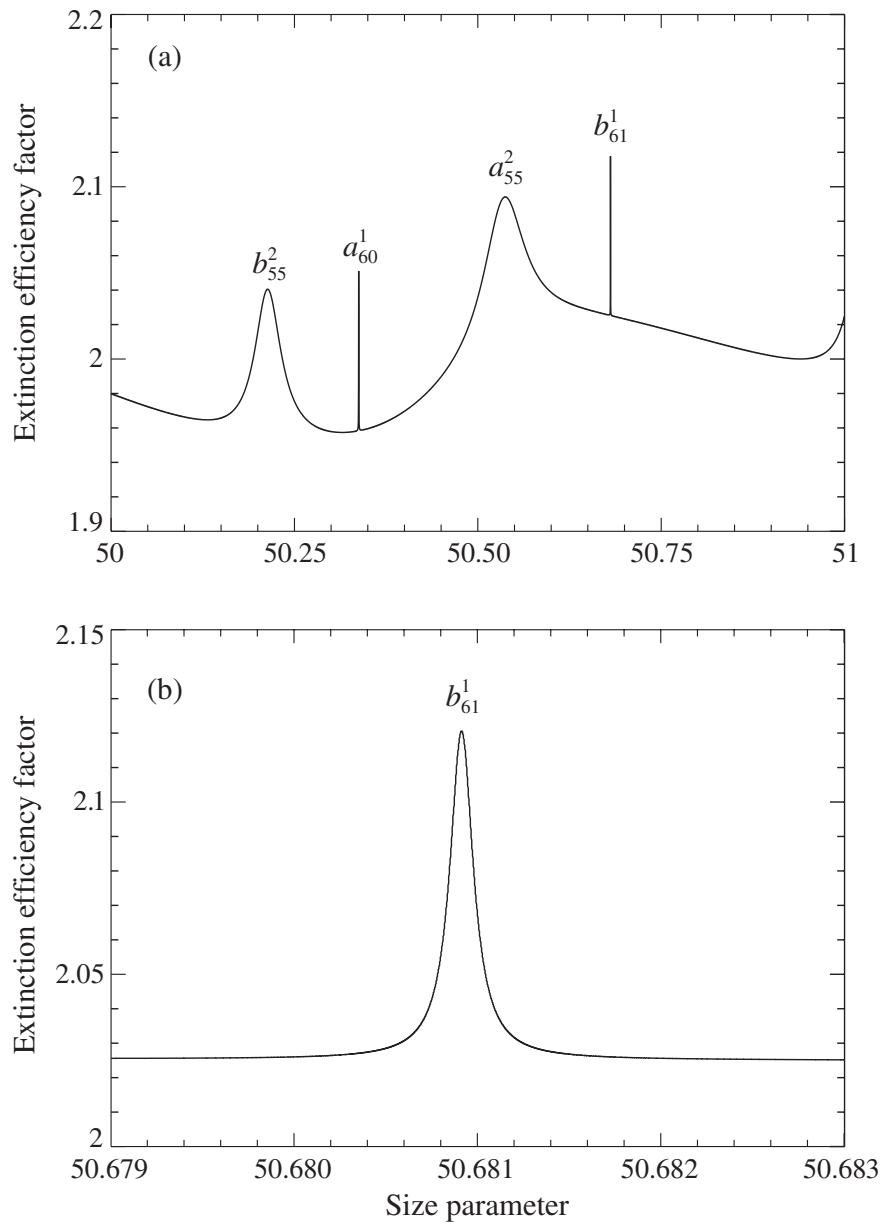

Figure 9.6. (a) Ripple structure of extinction by a water droplet $(m = 1.33 + \mathrm{i} \times 10^{-8})$ on the interval [50, 51] of size parameters. (b) High-resolution profile of the resonance b_{61}^1.

asymmetry parameter (Mishchenko and Lacis 2000). Since the normalized Stokes scattering matrix (4.65) for a fixed relative refractive index depends on two variables, viz., the size parameter x and the scattering angle Θ, it is convenient to visualize the elements of this matrix using two-dimensional color images plotted with fine angular and size-parameter sampling resolutions.

Plate 9.1 shows the degree of linear polarization of scattered light for an unpolarized incident beam, $P_Q = -Q^{\mathrm{sca}}/I^{\mathrm{sca}} = -b_1/a_1$ (%), as a function of Θ and x for monodisperse spheres with a relative refractive index m = 1.4. This image was

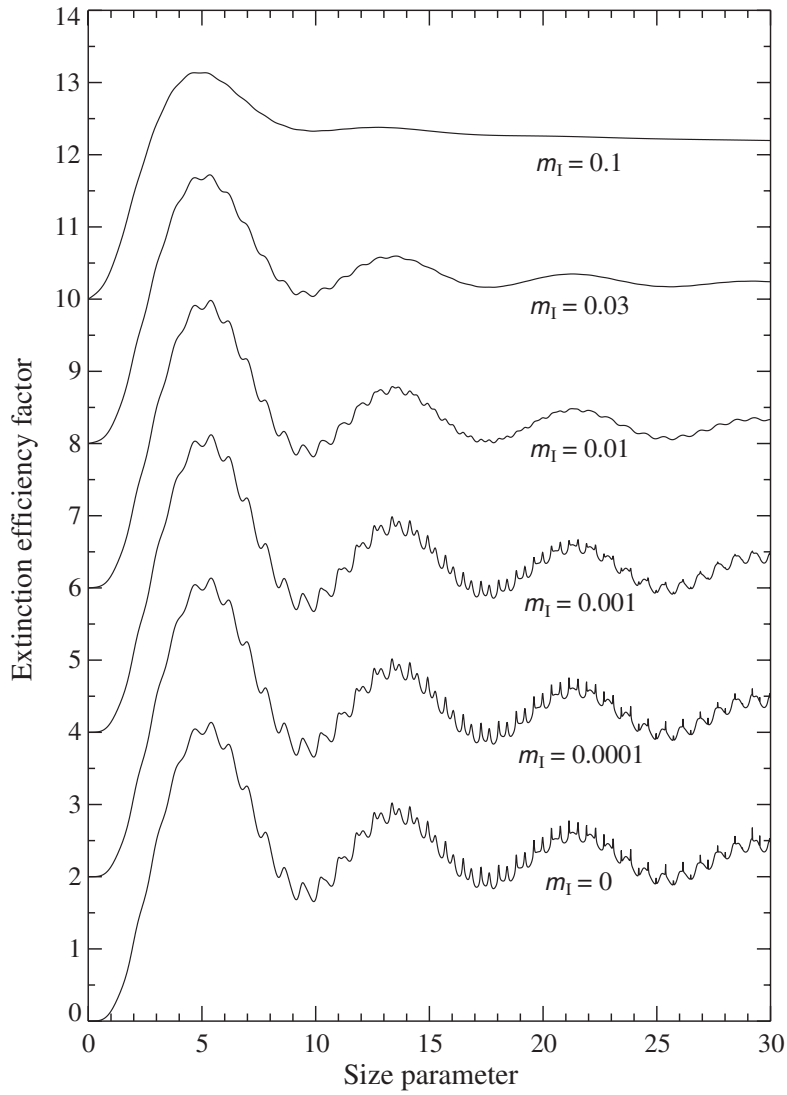

Figure 9.7. The set of curves (bottom to top) shows the effect of increasing absorption on the interference and ripple structure of the extinction efficiency factor for monodisperse spherical particles with real part of the relative refractive index $m_R = 1.4$. The vertical axis scale applies to the curve with $m_I = 0$, the other curves being successively displaced upward by 2.

created using sampling resolutions $\Delta\Theta = 1/3°$ and $\Delta x = 0.05$. With the exception of the region of Rayleigh scattering ($x \lesssim 2$; cf. the lowest panel of Fig. 7.1), the entire polarization image is a field of sharp, alternating maxima and minima. The frequencies of the maxima and minima over both Θ and x increase with increasing size parameter. This very complex "butterfly" structure, which appears both to be chaotic and to reveal a slightly perceptible order, was first discovered by Hansen and Travis (1974) and results from interference and resonance effects for particles of a single size. In their paper published 30 years ago, Hansen and Travis could use only white and black and, therefore, blackened the regions of positive polarization and left the

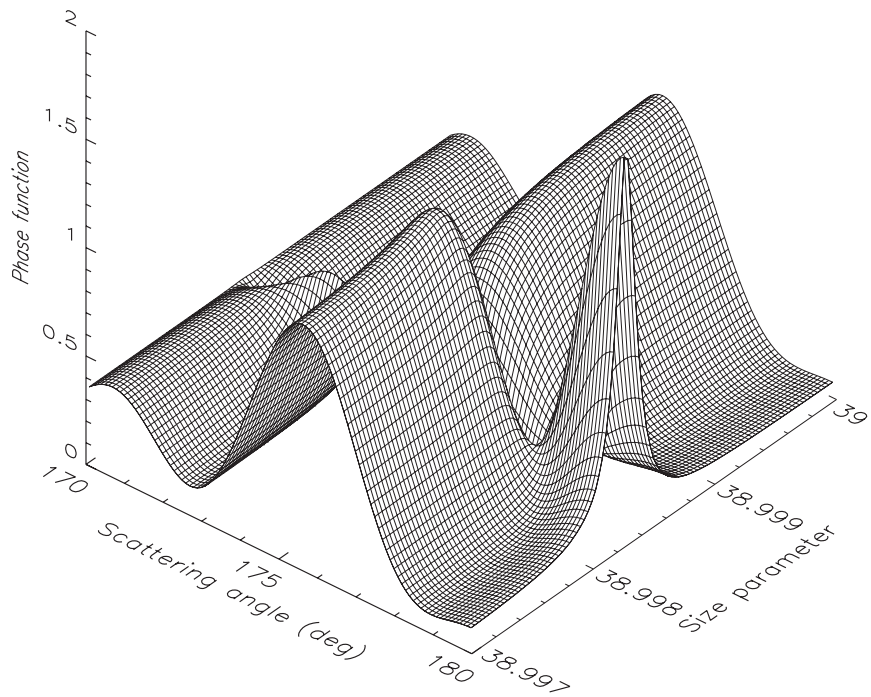

Figure 9.8. High-resolution surface plot of the phase function within the super-narrow resonance centered at $x \approx 38.9983$ for monodisperse spherical particles with $m = 1.4$.

regions of negative polarization white. The use of the continuous color bar shown in Plate 9.1 allowed us to build a complete image of the butterfly structure with a detailed gradation of the magnitude of polarization as well as its sign.

Plate 9.2 provides a zoomed image of a small part of the field covered by Plate 9.1 and reveals with much greater detail the enormous complexity of the scattering pattern. Now the sampling resolution ($\Delta\Theta = 0.1°$ and $\Delta x = 0.007$) is fine enough to exhibit several horizontal "dislocations" or "anomalous strips", which are first indicators of super-narrow resonances. One of these is centered at $x \approx 38.9983$ and is shown with even greater sampling resolution ($\Delta\Theta = 0.05°$ and $\Delta x = 0.00001$) in the top middle panel of Plate 9.3. The top left and top right panels of this plate depict the ratios a_3/a_1 and b_2/a_1 and demonstrate an immense degree of variability within the resonance, including drastic changes of sign and strong dependence on scattering angle. The latter is not surprising, since the corresponding resonance Lorenz–Mie coefficient contributes differently to the different expansion coefficients appearing in Eqs. (4.75)–(4.80) (see also Eqs. (4.109)–(4.114) and (5.160)–(5.162)). In consequence, its effect on the scattering matrix elements is different at different scattering angles. This conclusion is corroborated by Fig. 9.8, which shows a very strong angle-dependent change in the phase function a_1 within the resonance, including a sharp peak at the backscattering direction.

The middle three panels of Plate 9.3 are analogous to the top three panels, but

show the degree of linear polarization computed for three increasing values of the imaginary part of the relative refractive index. Although most polarization features within the resonance gradually weaken and ultimately disappear, the super-narrow minimum located at $\Theta \approx 177°$ and $x \approx 38.99828$ for $m_{\mathrm{I}} = 0$ (the top middle panel of Plate 9.3) becomes much more pronounced and shifts toward larger Θ and x before it finally disappears at $m_{\mathrm{I}} = 10^{-4}$. This behavior is quite different from that observed for Q_{ext} and $\langle \cos\Theta \rangle$ (Fig. 9.4).

The bottom three panels of Plate 9.3 show the degree of linear polarization versus Θ and m_{R} for $x = 38.9983$ and $m_{\mathrm{I}} = 0$. Interestingly, these panels are hardly distinguishable from the top three panels. This suggests again that, at least for nonabsorbing particles, the behavior of super-narrow resonances is determined by the product of the relative refractive index and size parameter rather than by each of these quantities separately. This also means that precise measurements of super-narrow resonances can be used not only for particle sizing but also for an accurate determination of the relative refractive index, provided that the particle size is already known.

A question that is naturally raised is whether the super-sharp resonances are physically "real", or are artifacts of a too-literal application of the theoretical macroscopic concept of "sphere" to microscopic objects. However, high-quality laboratory data, e.g., measurements of the intensity of light scattered by a gradually evaporating glycerol micro-droplet (Chýlek *et al.* 1992), provide an impressive experimental demonstration of the actual occurrence of this phenomenon and its practical usefulness as an optical particle-characterization tool (Section 9.7). As follows from the previous discussion, high-precision measurements within super-narrow resonances should be particularly useful for accurate particle sizing, determining the real part of the relative refractive index, and detecting minute deviations of the imaginary part of the relative refractive index from zero.

The extreme sharpness of some resonances may also help explain some of the minor, but nevertheless perplexing, differences that sometimes appear in intercomparisons of the Lorenz–Mie results for polydisperse spheres obtained by different groups (e.g., Boucher *et al.* 1998). In view of the fact that the Lorenz–Mie theory is exact, one would expect that, for given values of particle size and relative refractive index, precise agreement must be found for the resultant Lorenz–Mie parameters to many significant figures. Thus, the first step in such intercomparisons should be to verify that the Lorenz–Mie codes produce identical results for the same monodisperse size parameter and relative refractive index. Since the polydisperse scattering characteristics involve integration over a size distribution of particles (Section 3.2) with a number of integration points large enough to provide the desired numerical accuracy (Section 5.10), it is clear from the results in Figs. 9.1 and 9.4 that convergence may not be uniformly monotonic as the number of integration points is increased. Indeed, if an integration mesh point hits a sharp resonance, there may be an apparent local discontinuity that is greater than 5% compared to the background value. Hence for

precise Lorenz–Mie scattering characteristics, an exceedingly high resolution in size parameter space may be needed to resolve the resonance features fully.

9.2 Effects of averaging over sizes

Most natural and artificial ensembles of spherical particles do not exhibit the spike-like resonances described in the previous section because even a narrow polydispersion washes out features that strongly depend on particle size. Figure 9.9 illustrates the effect of increasing width of the size distribution on the extinction efficiency factor for the gamma size distribution, Eq. (5.245), of spherical particles with a relative refractive index m = 1.4. The figure shows $Q_{\text{ext}} = \langle C_{\text{sca}} \rangle / \langle G \rangle$ versus effective size parameter $x_{\text{eff}} = k_1 r_{\text{eff}}$ for five increasing values of the effective variance v_{eff}, where k_1 is the wave number in the surrounding medium and $\langle C_{\text{sca}} \rangle$ and $\langle G \rangle$ are the ensemble-averaged scattering and geometrical cross sections per particle, respectively. The effective radius r_{eff} and the effective variance v_{eff} are defined by Eqs. (5.248) and (5.249) and, for the gamma distribution with $r_{\min} = 0$ and $r_{\max} = \infty$, coincide with the parameters a and b of Eq. (5.245), respectively. (The computational meaning of the upper limit $r_{\max} = \infty$ was discussed in subsection 5.10.1.) Figure 9.10 demonstrates the broadening of the size distribution with increasing v_{eff} while the effective radius is kept constant. Note that the size distribution with $v_{\text{eff}} = 0$ corresponds to monodisperse particles with radius $r = r_{\text{eff}}$, the effective variance values in the range [0.05, 0.1] are characteristic of sulfuric acid particles forming the clouds on Venus (Hansen and Hovenier 1974), and the value $v_{\text{eff}} = 0.2$ is typical of water cloud particles in the Earth's atmosphere (Mazin and Khrgian 1989).

As was the case with increasing absorption, increasing the width of the size distribution first extinguishes the ripple and then eliminates the interference structure in Q_{ext}. It is in fact remarkable that as narrow a dispersion of sizes as that corresponding to $v_{\text{eff}} = 0.01$ completely washes out the ripple structure. The first major maximum of the interference structure persists to larger values of v_{eff}, but eventually fades away too. For distributions with $v_{\text{eff}} \gtrsim 0.2$, the only surviving features are the reddening at small size parameters discussed in Section 7.1 and the asymptotic geometrical optics trend $Q_{\text{ext}} \to 2$ as $x \to \infty$ discussed in Section 7.4.

The presence of the first maximum of the interference structure for relatively narrow size distributions creates the possibility of an infrequent phenomenon for which aerosol particles of just the right size have a lower extinction efficiency factor in the blue than that at the larger wavelengths in the red. Thus, in contrast to the familiar reddening of the setting sun owing to enhanced Rayleigh scattering, a sufficiently narrow size distribution of aerosol particles in the atmosphere, with an average size such that $4 \lesssim 2x(m_{\text{R}} - 1) \lesssim 7$ for visible wavelengths (cf. Fig. 9.3), can produce a blue cast to the sun or moon and is perhaps responsible for the implied rarity associated with the phrase, "once in a blue moon" (cf. Bohren and Huffman 1983, Chapter 4;

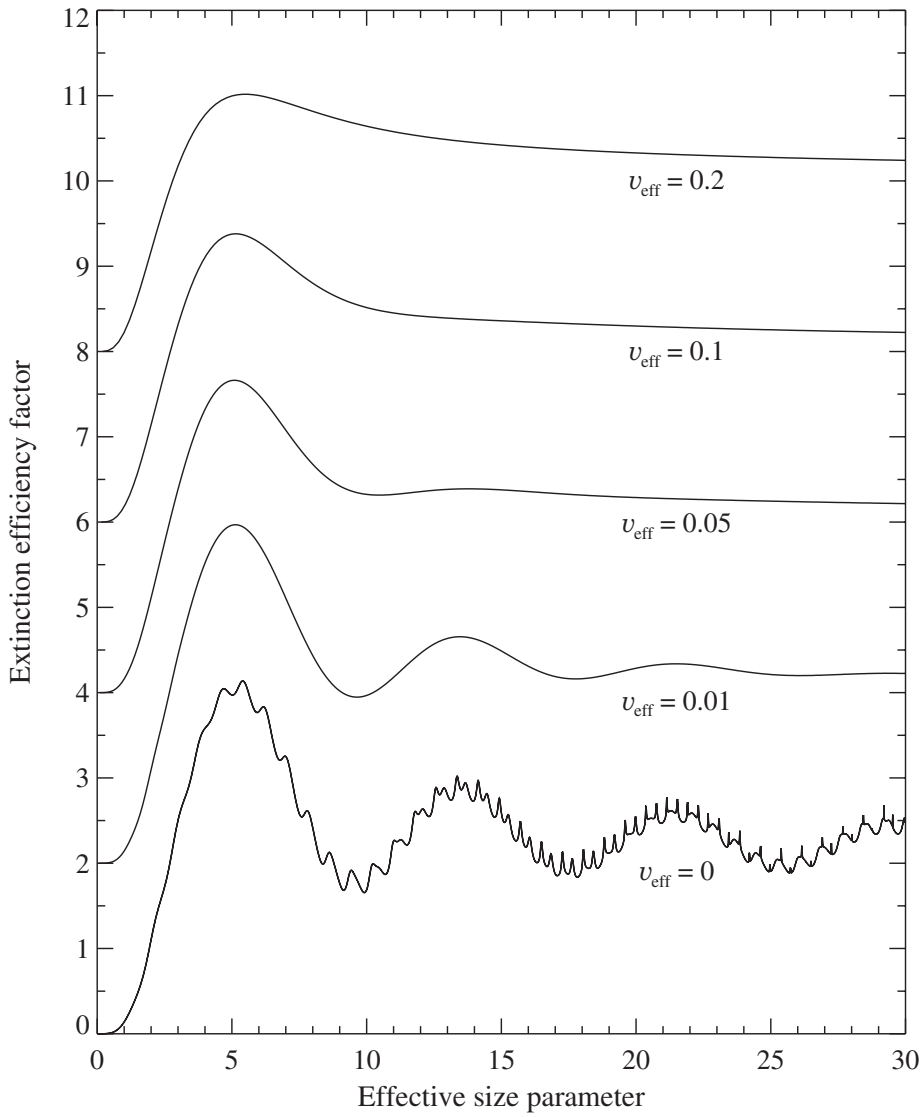

Figure 9.9. The effect of increasing width of the size distribution on the interference and ripple structure in Q_{ext} for nonabsorbing spherical particles with relative refractive index 1.4. The vertical axis scale applies to the curve with $v_{\text{eff}} = 0$, the other curves being successively displaced upward by 2.

Lynch and Livingston 1995).

Plate 9.4 shows the evolution of the linear polarization pattern with increasing width of the size distribution. The case $v_{\text{eff}} = 0.01$ demonstrates that even a very narrow size distribution is sufficient to extinguish most of the interference and resonance effects. With increasing v_{eff}, the maxima are smoothed out, the minima are filled in, and the polarization becomes more neutral. Additional effects of increasing v_{eff} are the depression to smaller size parameters of the region of maximal polarization corresponding to Rayleigh scattering and the erosion of the bridge of positive polarization connecting the Rayleigh region and the area of positive polarization at

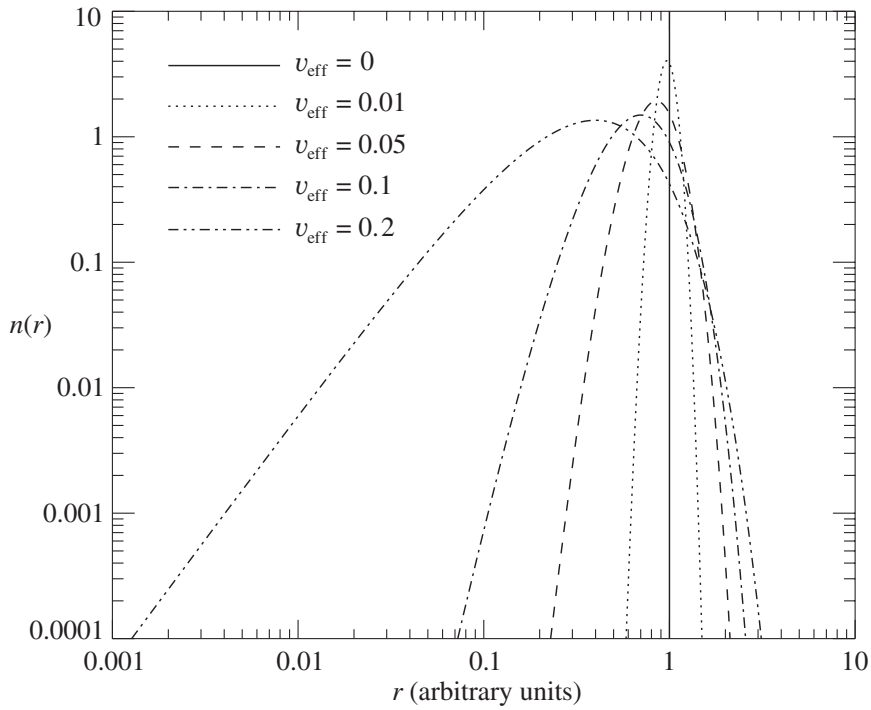

Figure 9.10. Gamma size distribution $n(r)$, Eq. (5.245), with $r_{\min} = 0$, $r_{\max} = \infty$, $r_{\rm eff} = 1$ (in arbitrary units of length), and $v_{\rm eff} = 0$, 0.01, 0.05, 0.1, and 0.2. The size distribution is normalized according to Eq. (3.26).

scattering angles around 160°. The island of positive polarization at $x_{\rm eff} \sim 10$ and $\Theta \sim 25°$ for $v_{\rm eff} = 0.01$ is an anomalous diffraction feature produced by the interference of diffracted light and light reflected and refracted by the particles in the near-forward direction (Hansen and Travis 1974). The magnitude of this feature strongly depends on the width of the size distribution: the feature significantly weakens as $v_{\rm eff}$ increases from 0.01 to 0.07 and has completely disappeared for $v_{\rm eff} = 0.2$. All these effects of broadening the size distribution are easy to understand qualitatively in terms of taking weighted averages along vertical lines of increasing length in the polarization diagram for monodisperse particles.

9.3 Optical cross sections, single-scattering albedo, and asymmetry parameter

In the rest of this chapter we will analyze the scattering and absorption properties of polydisperse spherical particles. Most of the illustrative examples will be based on computations for the gamma distribution of particle radii with $r_{\min} = 0$, $r_{\max} = \infty$, and a fixed effective variance $v_{\rm eff} = 0.15$. The latter is a value characteristic of a size distribution that is neither particularly narrow nor broad.

Figure 9.11 presents surface plots of the extinction efficiency factor versus effec-

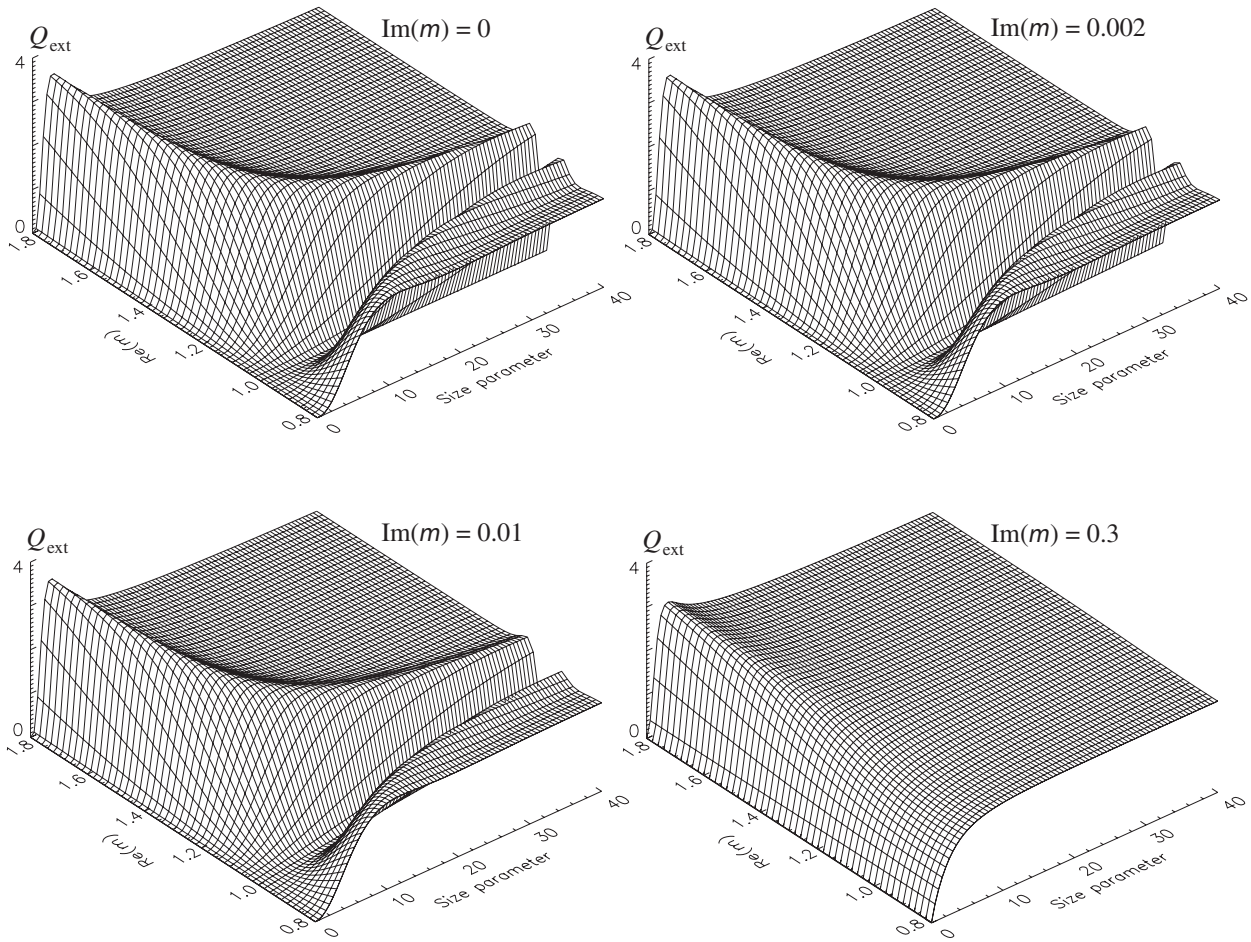

Figure 9.11. Extinction efficiency factor versus effective size parameter and real part of the relative refractive index for a gamma size distribution of spherical particles with $v_{\text{eff}} = 0.15$. The imaginary part of the relative refractive index varies from 0 to 0.3.

tive size parameter and real part of the relative refractive index, for four values of the imaginary part ranging from 0 to 0.3. Figures 9.12–9.16 are analogous to Fig. 9.11 and present visualizations of the scattering and absorption efficiency factors, the single-scattering albedo, the asymmetry parameter, and the radiation-pressure efficiency factor. The 51 refractive index gridlines are drawn at 0.02 intervals and correspond to relative refractive indices m = 0.8, 0.82, … 1.78, and 1.8. The 81 size parameter gridlines are drawn at 0.5 intervals and correspond to size parameters x_{eff} = 0, 0.5, 1, …, 39.5, and 40.

The upper left panel of Fig. 9.11 shows that the first interference maximum in Q_{ext} indeed follows the curves $x_{\text{eff}}|m_{\text{R}} - 1| = \text{constant}$, as discussed in Section 9.1. For m = 1, both Q_{ext} and Q_{sca} vanish because there is no scattering and absorption when the particle refractive index matches that of the nonabsorbing surrounding medium. This does not mean, however, that dimensionless quantities such as the single-scattering albedo, the asymmetry parameter, and the phase function must also disap-

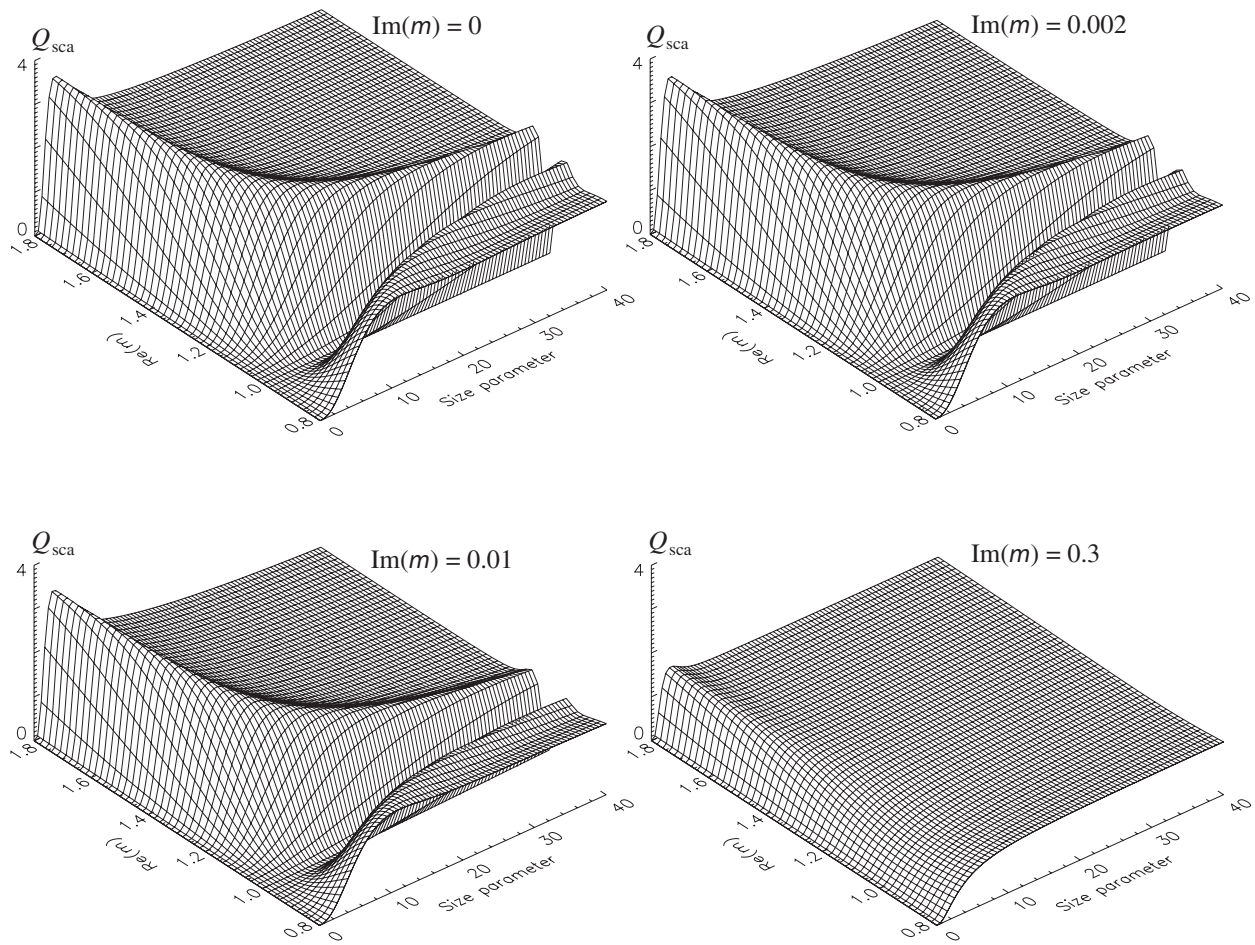

Figure 9.12. As in Fig. 9.11, but for the scattering efficiency factor.

pear as $m \to 1$. All of these are ratios of vanishing quantities and remain finite in the mathematical sense as the particle refractive index approaches that of the surrounding medium. The extinction and scattering efficiency factors tend to zero as $x_{\text{eff}} \to 0$. In the limit $x_{\text{eff}} \to \infty$, the extinction efficiency factor approaches the geometrical optics value 2. As m_{I} increases from 0 to 0.3, the first interference maximum in both Q_{ext} and Q_{sca} weakens and almost disappears, except for m_{R} close to 1.8. With the exception of m_{R} close to unity, the scattering efficiency factor in Fig. 9.12 decreases with increasing m_{I}. With either $m_{\text{I}} \to \infty$ or $m_{\text{R}} \to \infty$, Q_{sca} for very large particles asymptotically approaches the value for a perfect reflector, i.e., $Q_{\text{sca}} \to 2$.

The absorption efficiency factor is zero for $m_{\text{I}} = 0$ but rapidly grows with increasing imaginary part of the relative refractive index (Fig. 9.13). It can even exceed unity in the resonance region of the size parameters, which means that a particle can absorb significantly more power than the value obtained by multiplying the incident intensity by the area of its geometrical cross section. This phenomenon shows that

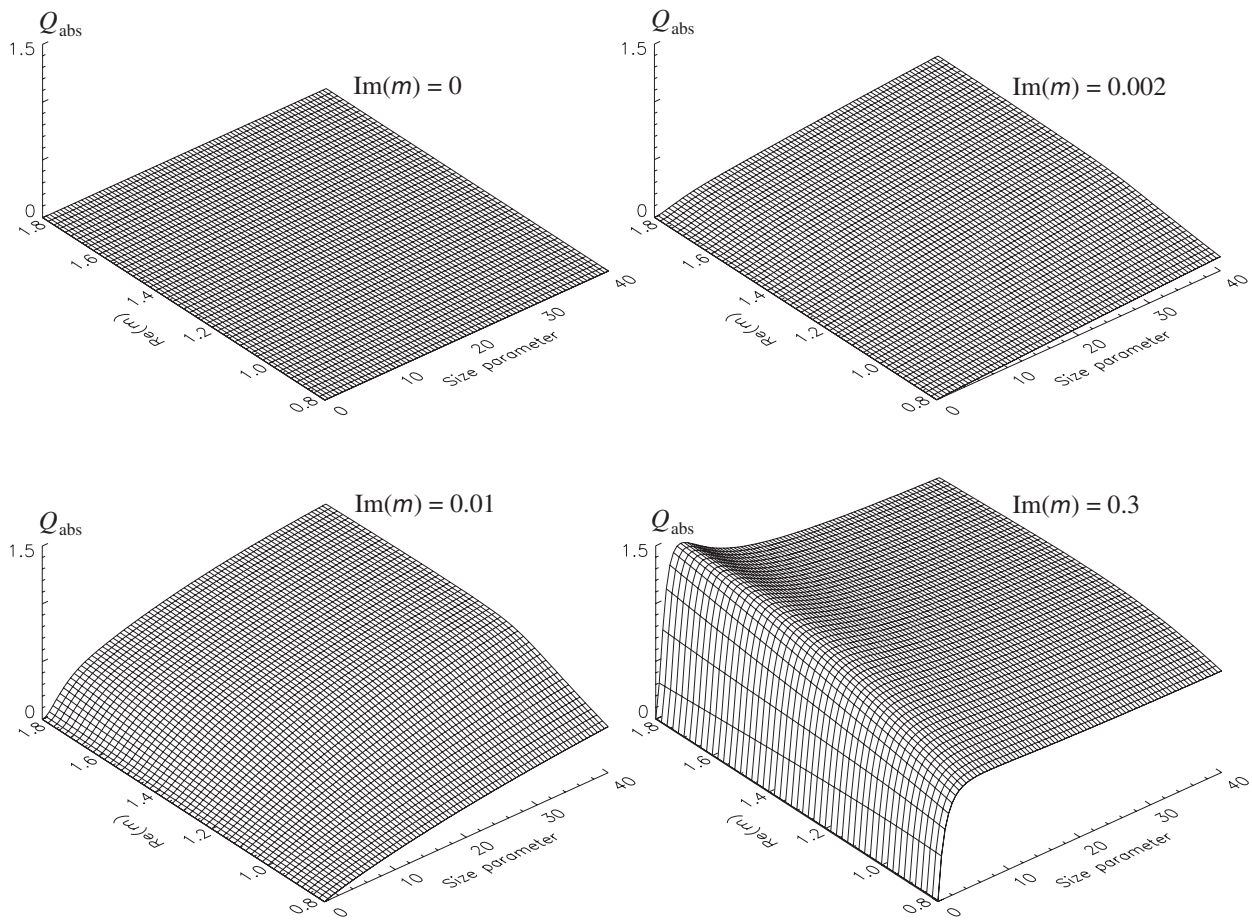

Figure 9.13. As in Fig. 9.11, but for the absorption efficiency factor.

spherical particles can perturb the electromagnetic field far beyond their physical confines and illustrates once again the limited applicability of the geometrical optics approximation, which predicts that the absorption efficiency factor cannot exceed unity. As $m_I \to \infty$, the particles become perfect reflectors, and Q_{abs} vanishes.

The single-scattering albedo is identically equal to unity for nonabsorbing particles but almost vanishes for $m_R \approx 1$ and small m_I, because essentially all the light extracted by the particles from the incident beam is absorbed rather than scattered (the upper right and lower left panels of Fig. 9.14). As m_I deviates from zero, the single-scattering albedo vanishes in the Rayleigh region, in accordance with Eqs. (7.3) and (7.4), decreases for all m_R and x_{eff}, and develops a feature resembling the first interference maximum in Q_{ext} and Q_{sca}. With the exception of m_R-values close to unity coupled with small or zero m_I, the single-scattering albedo depends only weakly on the real part of the relative refractive index. In the limit $m_I \to \infty$, the single-scattering albedo reaches the asymptotic value unity for perfectly reflecting spheres. For particles much larger than the wavelength, ϖ cannot be smaller than 0.5. Indeed, this value can only be reached when the ray-tracing scattering cross section in Eq.

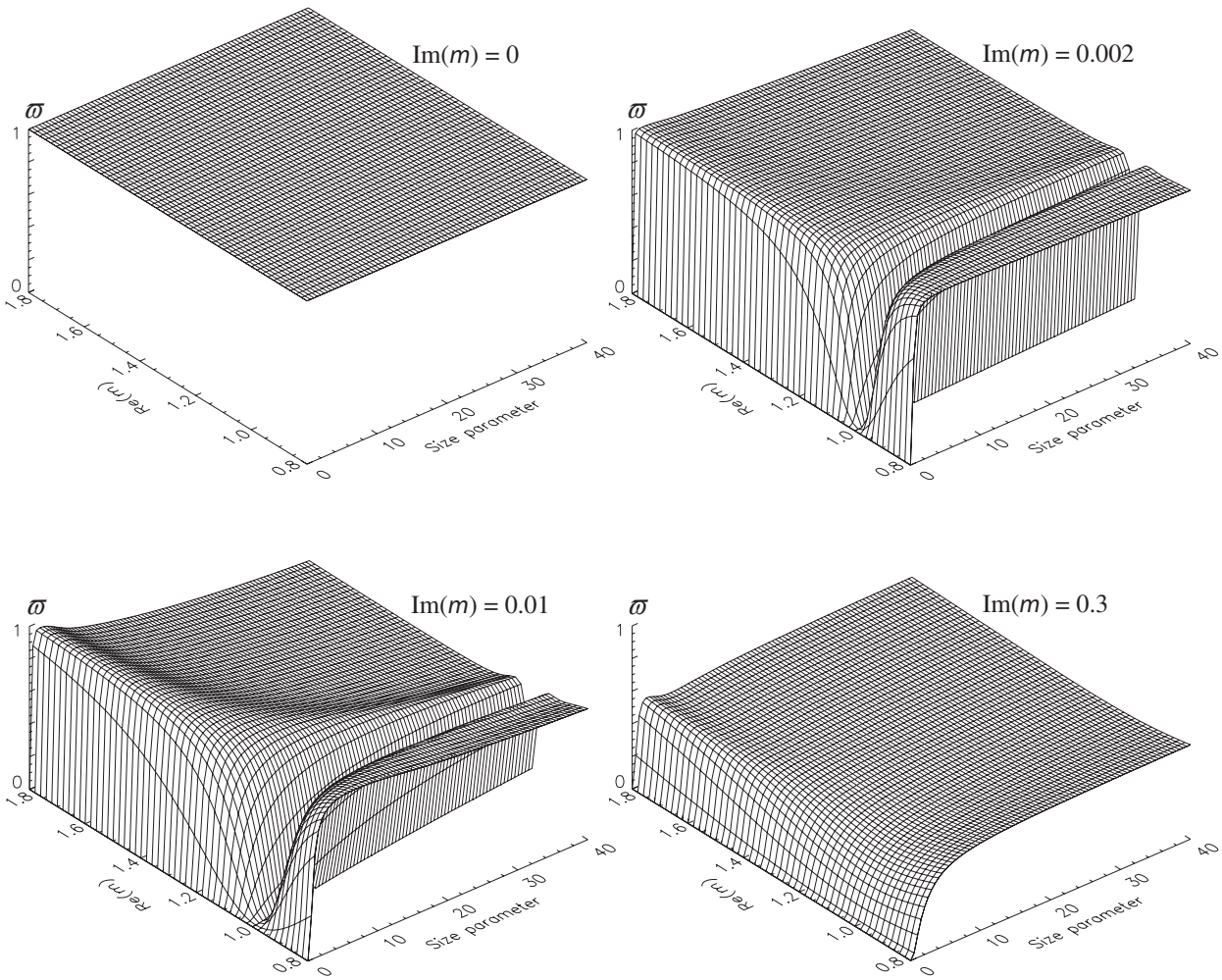

Figure 9.14. As in Fig. 9.11, but for the single-scattering albedo.

(7.13) vanishes, which implies that all light striking the particle is refracted into the particle and is internally absorbed.

The asymmetry parameter, $\langle \cos\Theta \rangle$, is zero for very small particles, in agreement with the prediction of the Rayleigh approximation, but then rapidly grows as x_{eff} increases from 0 to about 2 (Fig. 9.15). Then it remains positive, thereby indicating forward-scattering particles, and shows little dependence on the particle size parameter. For particles with $m \approx 1$, $\langle \cos\Theta \rangle$ becomes independent of m and depends on the size parameter according to the Rayleigh–Gans approximation (Irvine 1963). In particular, for very large nonabsorbing particles with $m \approx 1$, $\langle \cos\Theta \rangle$ can reach values approaching unity because the diffraction lobe becomes extremely narrow, there are no reflected rays, and the incident rays striking the particle pass through it essentially undeviated. The asymmetry parameter becomes almost independent of m_{R} for strongly absorbing particles (lower right panel of Fig. 9.15) because the scattered light

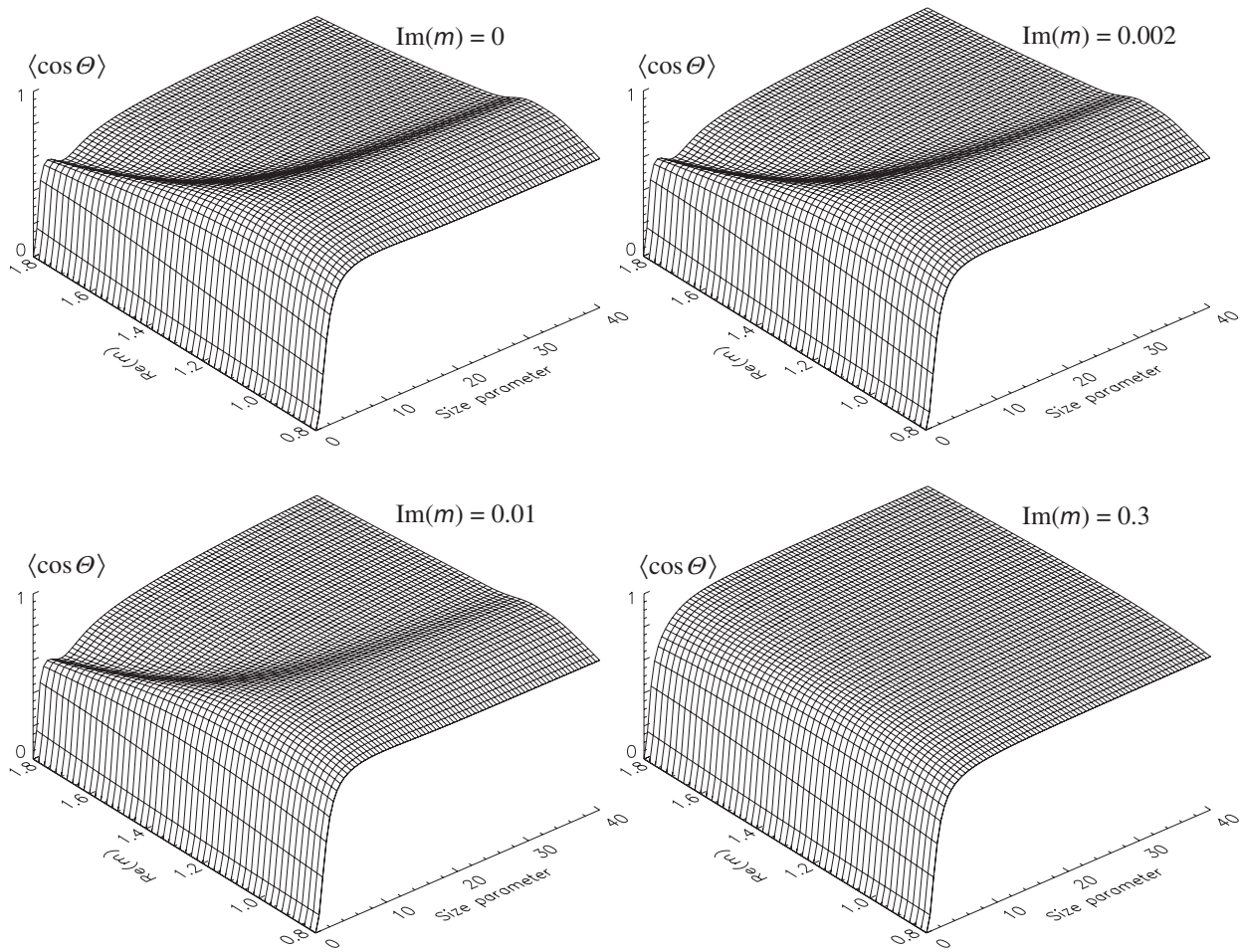

Figure 9.15. As in Fig. 9.11, but for the asymmetry parameter.

is dominated by the diffracted and externally reflected components. As $m_R \to \infty$ or $m_I \to \infty$, the asymmetry parameter for very large particles tends to 1/2 because half the scattered radiation is diffracted in the forward direction and half is externally reflected. The reflected rays are isotropically distributed (van de Hulst 1957) and make no contribution to $\langle \cos\Theta \rangle$, whereas $\langle \cos\Theta \rangle$ for the diffracted light is unity, Eq. (7.17), thereby yielding total asymmetry parameter equal to 1/2. In the limit $x \to 0$ and $m_R \to \infty$ or $m_I \to \infty$, $\langle \cos\Theta \rangle \to -0.4$ (van de Hulst 1957, Section 10.61).

In a similar way to the extinction and scattering efficiency factors, the radiation-pressure efficiency factor Q_{pr} vanishes for very small particles and particles with $m \approx 1$. Q_{pr} in Fig. 9.16 always increases with m_I and, for nonabsorbing and mildly absorbing spheres, always increases as m_R increases from 1 to 1.8. However, the dependence on the real part of the relative refractive index weakens as m_I reaches the value 0.3. In the limit $m_I \to \infty$ or $m_R \to \infty$, the radiation pressure efficiency factor for very large particles approaches that of a perfect reflector, i.e., $Q_{pr} \to 1$.

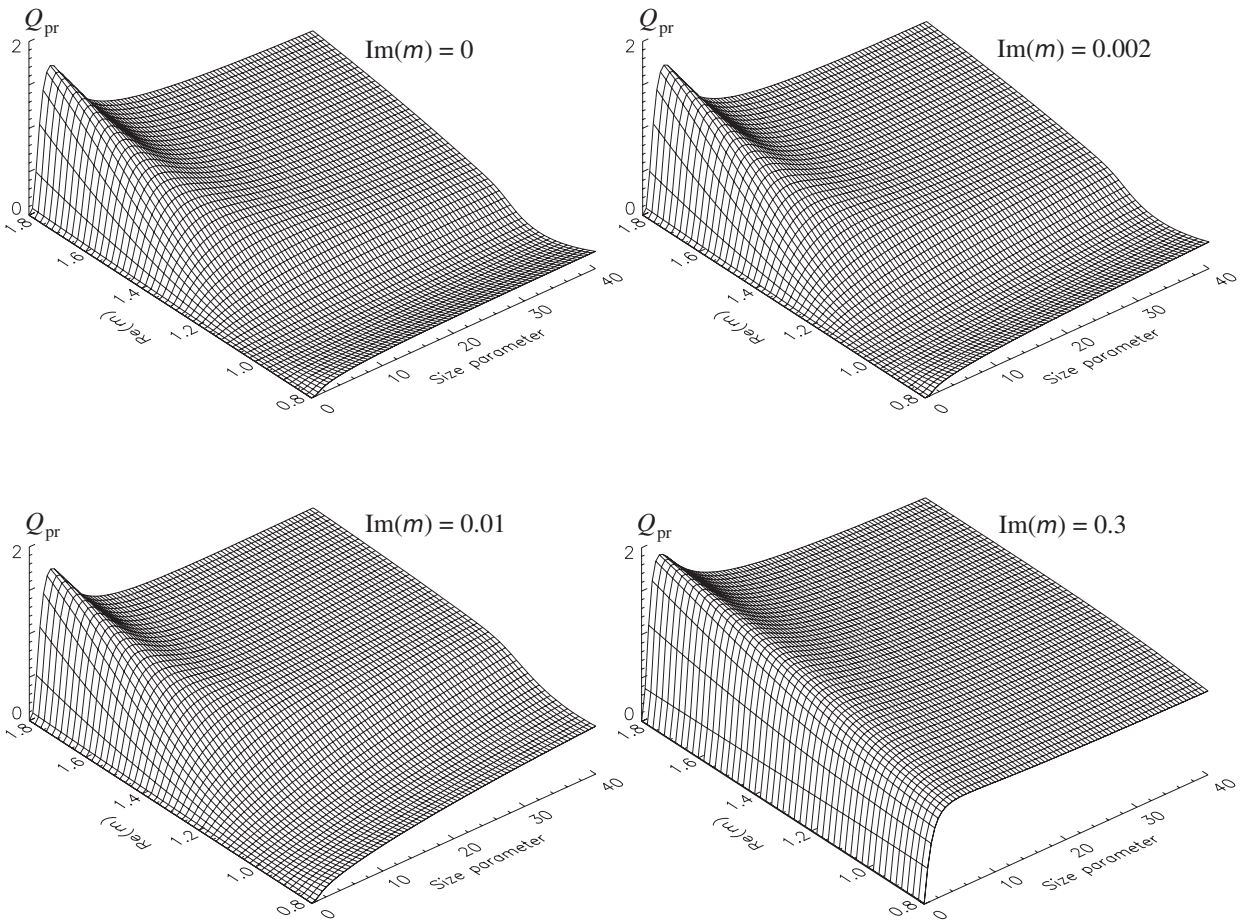

Figure 9.16. As in Fig. 9.11, but for the radiation-pressure efficiency factor.

9.4 Phase function $a_1(\Theta)$

Many phase function features for particles larger than the incident wavelength (Fig. 7.4) can be explained through the concepts of geometrical optics, using the terminology introduced in Fig. 9.17. Specifically, the concentration of light near $\Theta = 0°$ is caused by diffraction (i = 0 in Fig. 9.17). The external reflection (i = 1) does not generate any distinctive feature, whereas the twice refracted rays (i = 2) cause a broad enhancement of the phase function in the forward-scattering hemisphere.

The features in Fig. 7.4 at $\Theta \approx 137°$ and 130° for m = 1.33 (160° and 88° for m = 1.53) are the primary and secondary rainbows generated by i = 3 and i = 4 rays, respectively. To explain the origin of the rainbows, one needs to express the scattering angle Θ of the emerging ray as a function of the local angle of incidence $\alpha \in [0°, 90°]$ (Fig. 9.17) for i = 3, 4, … . This is always possible because the entire ray path remains in the plane containing the incident ray and the center of the sphere. When the derivative $\mathrm{d}\Theta_i(\alpha)/\mathrm{d}\alpha$ vanishes, the scattering angle becomes nearly constant for a range of incidence angles, thereby causing an increased concentration of

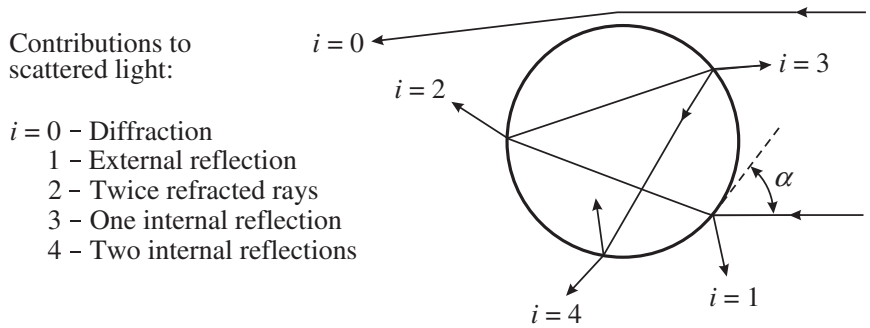

Figure 9.17. Geometrical optics representation of scattering by a large sphere with $m_R > 1$. (After Hansen and Travis 1974.)

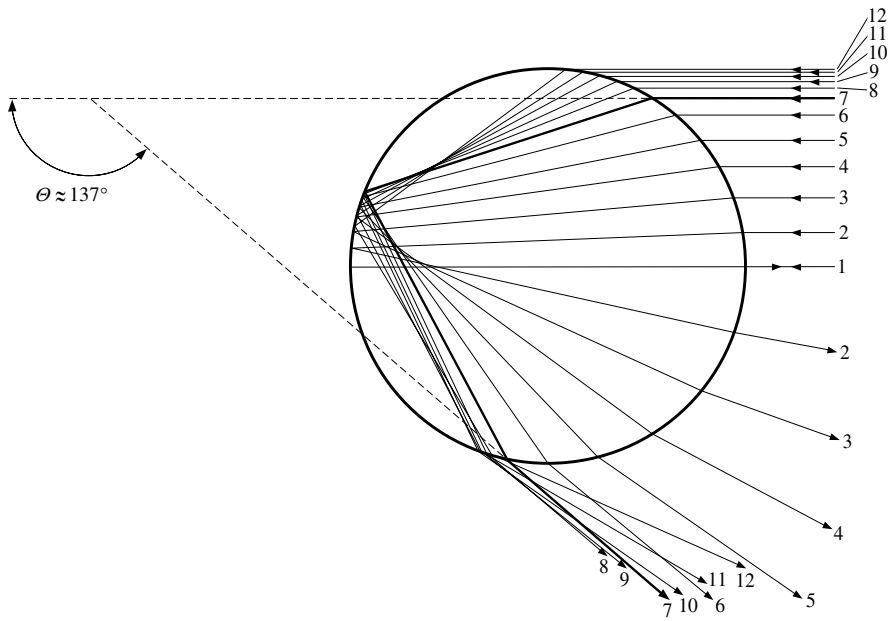

Figure 9.18. Ray-tracing diagram explaining the origin of the primary rainbow for a large spherical particle with $m = 1.33$ (after Greenler 1980). The diagram shows that incident rays corresponding to a finite range of incidence angles α emerge at almost the same scattering angle, thereby creating a localized enhancement of intensity. The respective scattering angle $\Theta \approx 137°$ is the angle of minimum deviation for $i = 3$.

emerging rays. The respective scattering angle is called the rainbow angle. The condition $\mathrm{d}\Theta_i(\alpha)/\mathrm{d}\alpha = 0$ implies that the rainbow angles correspond to *extrema* of the functions $\Theta_i(\alpha)$. Whether the extremum is a *minimum* or a *maximum* depends on i. The primary rainbow angle $137°$ for $m = 1.33$ ($160°$ for $m = 1.53$) corresponds to a minimum in $\Theta_3(\alpha)$ (ray 7 in Fig. 9.18), whereas the angle $130°$ for $m = 1.33$ ($88°$ for $m = 1.53$) corresponds to a maximum of $\Theta_4(\alpha)$. As a consequence, there is a low-intensity zone (about $7°$ wide for $m = 1.33$ and $72°$ wide for $m = 1.53$) between the primary and secondary rainbows (the so-called Alexander's dark band), where the phase function is mostly determined by the externally reflected rays ($i = 1$). Note,

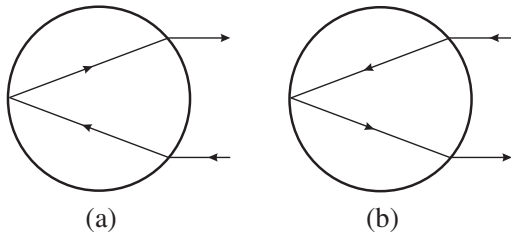

Figure 9.19. Rays contributing to the glory for real relative refractive indices m in the range $2^{1/2} < m < 2$.

however, that both rainbow angles correspond to rays that experience the least *cumulative* deviation from the initial incidence direction and hence are angles of *minimum deviation*. The slight change of the rainbow angle with wavelength caused by dispersion (change of the relative refractive index with wavelength) gives rise to the spectacular colorful rainbows often observed during showers illuminated by the sun at an altitude lower than about $40°$ (Lynch and Livingston 1995).

The maxima in Fig. 7.4 at $\Theta = 119°$ and $141°$ for m = 1.53 are the i = 6 and 7 rainbows, respectively. A minor feature on the large-scattering-angle side of the primary rainbow results from the interference of two i = 3 rays corresponding to different local incidence angles but emerging at the same scattering angle. This feature is called the first supernumerary bow and is not reproduced by the standard geometrical optics.

The enhancement of intensity in the backscattering direction $(\Theta \approx 180°)$ is called the "glory" and can be seen from an airplane as a series of colored rings around the shadow cast by the airplane on a cloud top (Lynch and Livingston 1995). Obvious but relatively weak contributors to the glory are the central rays $(\alpha = 90°)$ externally (i = 1) and internally (i = 3, 5, …) reflected in the backscattering direction. Snell's law predicts that for real relative refractive indices in the range $2^{1/2} \le m \le 2$, a noncentral incident ray $(0° < \alpha < 90°$ in Fig. 9.17) may emerge at $\Theta = 180°$ after just one internal reflection (i = 3, Fig. 9.19). Furthermore, the ray shown in Fig. 9.19(a) always interferes constructively with the conjugate ray propagating along the same path but in the opposite direction, Fig. 9.19(b), thereby potentially doubling the i = 3 contribution to the backscattered intensity. This contribution may partially account for the intense glory in the phase function for m = 1.53 and $x_{\text{eff}} = 600$ in Fig. 7.4.

However, this mechanism does not explain the equally pronounced glory generated by water droplets with $m = 1.33$ $(< 2^{1/2})$ and $x_{\text{eff}} = 600$. Therefore, it is often claimed that a major contributor to the glory is that of the edge rays $(\alpha \approx 0°)$, which set up so-called surface waves on the sphere. The latter are not included in the geometrical optics formulation and are discussed by van de Hulst (1957), Nussenzveig (1992), and Grandy (2000).

Figures 9.20–9.22 illustrate the behavior of the phase function for nonabsorbing polydisperse spheres in the Rayleigh and resonance regions of the effective size

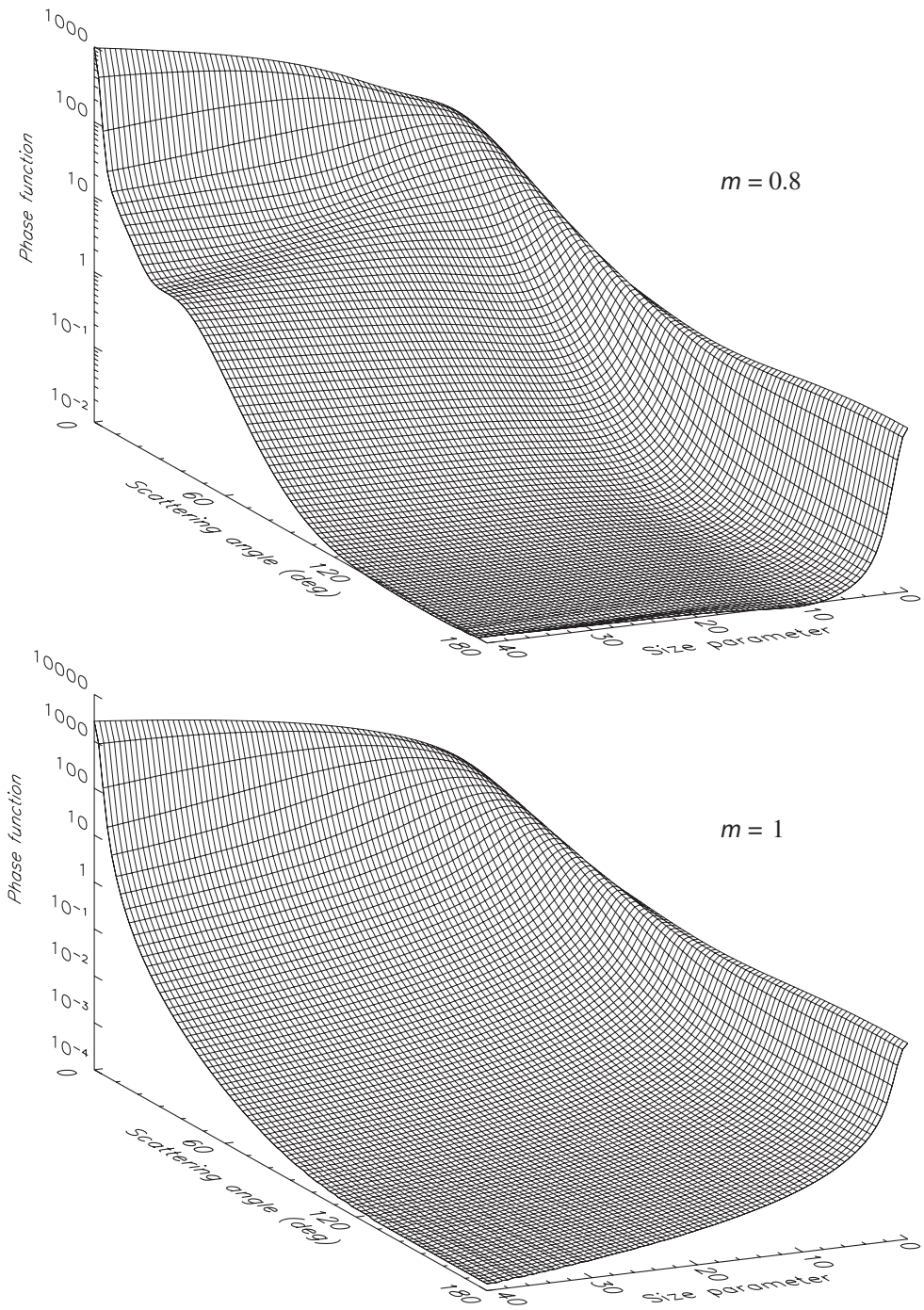

Figure 9.20. Phase function versus effective size parameter and scattering angle for a gamma size distribution of spherical particles with $v_{\text{eff}} = 0.15$ and two values of the relative refractive index, $m = 0.8$ and 1.

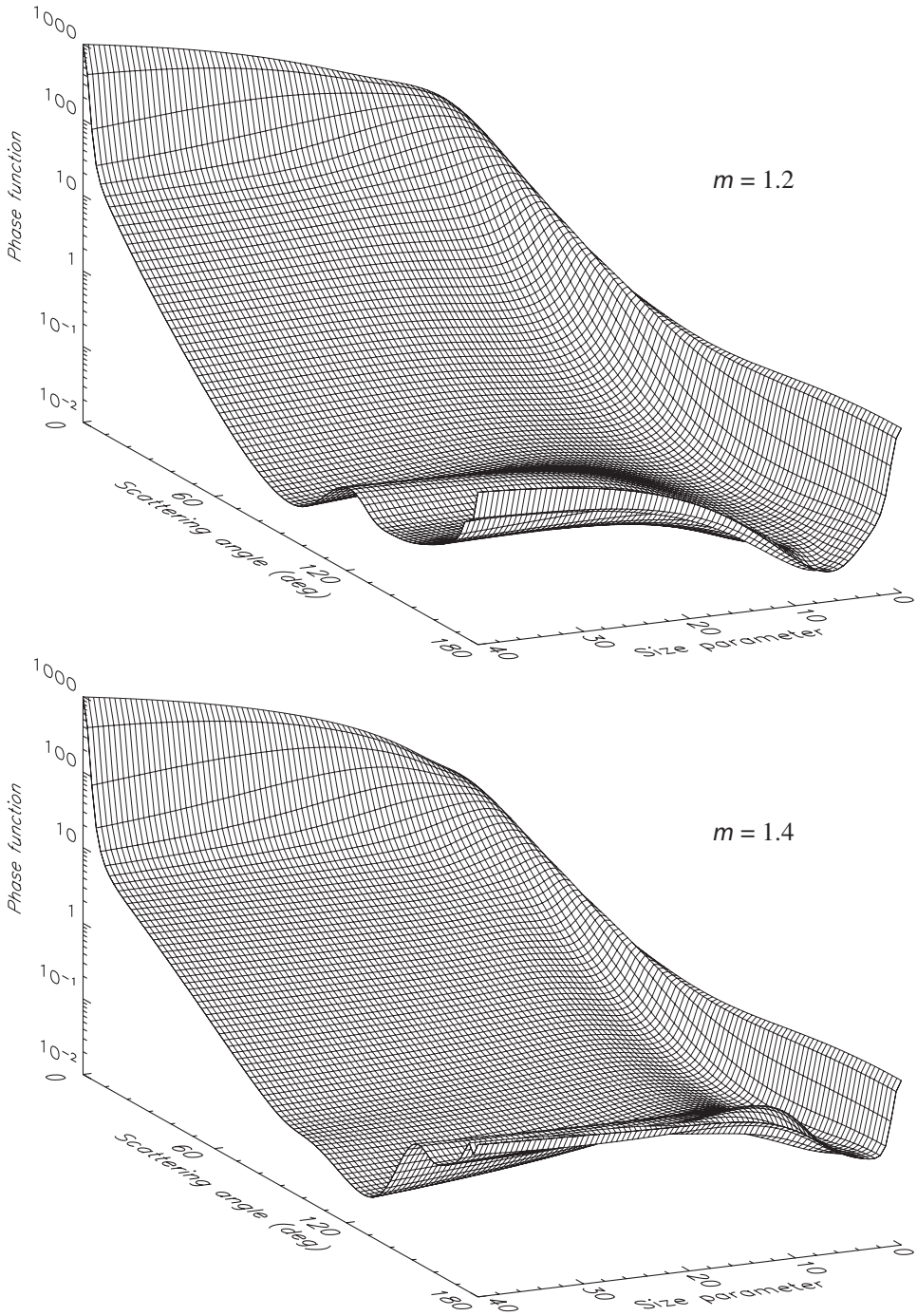

Figure 9.21. As in Fig. 9.20, but for $m = 1.2$ and 1.4.

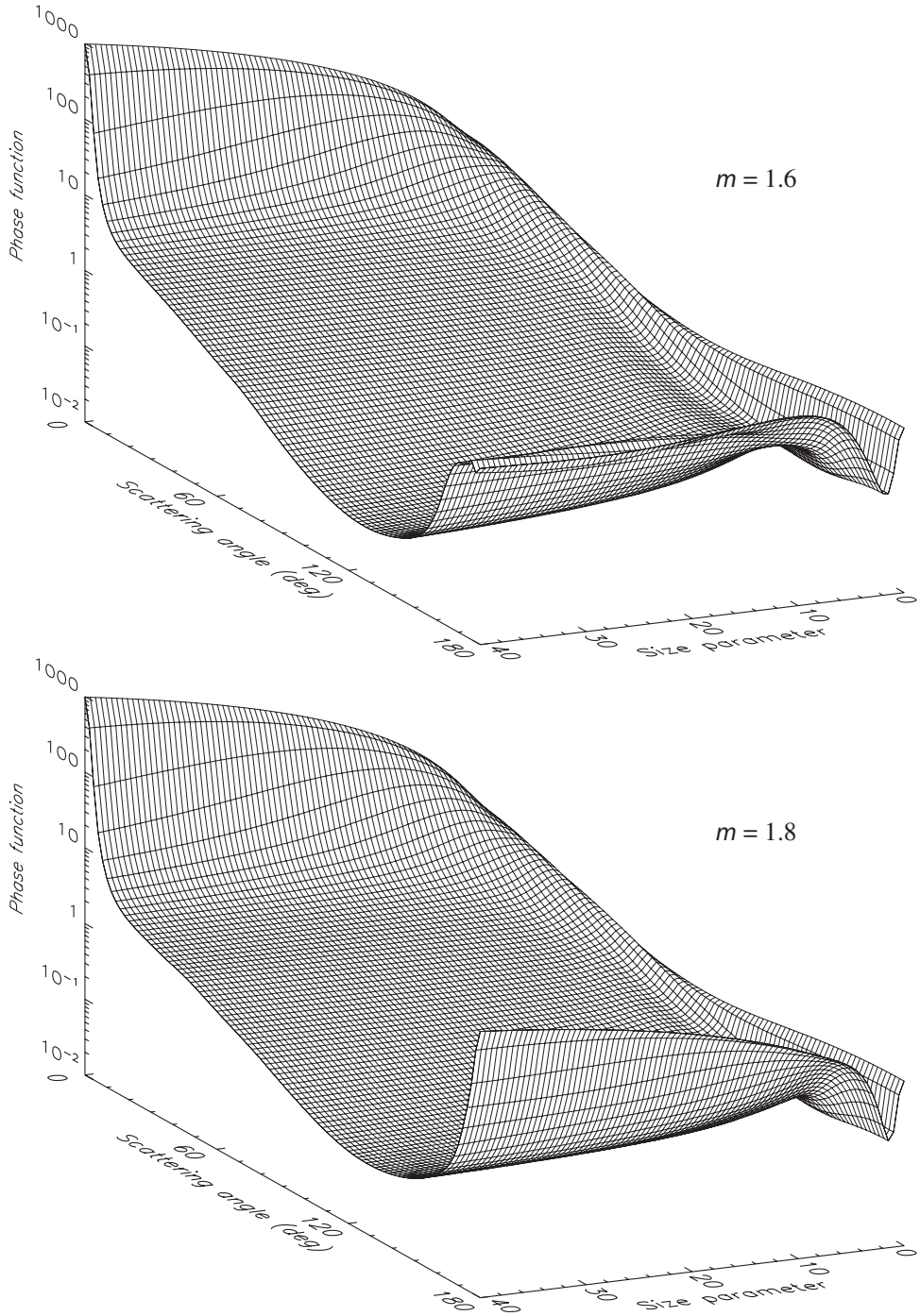

Figure 9.22. As in Fig. 9.20, but for $m = 1.6$ and 1.8.

parameter. The 91 scattering angle gridlines are drawn at $2°$ intervals and correspond to scattering angles $\Theta = 0°, 2°, ..., 178°,$ and $180°$. The 81 size-parameter gridlines are drawn at 0.5 intervals and correspond to effective size parameters x_{eff} = 0, 0.5, 1, …, 39.5, and 40.

In the Rayleigh limit $x_{\text{eff}} \to 0$, the phase functions are nearly isotropic and are given by

$$a_1(\Theta) \underset{x_{\text{eff}} \to 0}{=} \tfrac{3}{4}(1+\cos^2\Theta) \tag{9.9}$$

(see Eq. (7.5)). As the effective size parameter increases, the phase functions become anisotropic, owing to increased forward scattering and decreased backscattering. The phase functions exhibit the strongest variability with size parameter in the range $0 < x_{\text{eff}} \lesssim 20$. As x_{eff} approaches 40, the phase functions for m = 1.2, 1.4, 1.6, and 1.8 begin to develop typical geometrical optics features such as the strong diffraction peak, the primary rainbow, and the glory. As m increases, the scattering angle of the primary rainbow increases (cf. Liou and Hansen 1971; Liou 1980) and the glory becomes more pronounced. The primary rainbow angle for m = 1.8 is so large $(\Theta = 176°)$ that the rainbow essentially merges with the intense glory. The rainbow and the glory are absent in the Rayleigh–Gans phase function (the lower panel of Fig. 9.20) because particles with $m \approx 1$ do not refract and reflect the incident light. For the same reason the forward-scattering peak for $m \approx 1$ is noticeably stronger than that for the other relative refractive indices (note that in the lower panel of Fig. 9.20 the scale goes up to 10 000). The phase function in the Rayleigh–Gans limit $m \to 1$ becomes independent of m and depends only on the size parameter (Kerker 1969). Large particles with m = 0.8 do not generate rainbows, but instead exhibit an interesting horizontal "shelf" at side-scattering angles followed by a sharp decrease of intensity at larger scattering angles. The origin of this feature for real m smaller than but close to 1 is explained in Fig. 9.23. Rays with local incidence angles $\alpha > \arccos m$ are twice refracted in the forward or near-forward directions, whereas rays with $\alpha < \arccos m$ are totally externally reflected. The scattering angle of the externally reflected rays decreases with decreasing α. Therefore, $\Theta = 2\arccos m$ is the critical scattering angle, beyond which the scattered intensity is expected to fall rapidly. This explanation is corroborated by Fig. 9.24, which shows the results of geometrical optics and Lorenz–Mie computations of the phase function for a gamma distribution of spherical particles with m = 0.8, $x_{\text{eff}} = 600$, and $v_{\text{eff}} = 0.07$. As expected, a sharp precipice in the phase functions occurs at $\Theta \approx 2\arccos(0.8) = 73.74°$.

Figure 9.25 demonstrates the effect of increasing absorption on the phase functions for $m_{\text{R}} = 1.4$. Comparison with the lower panel of Fig. 9.21 shows that although increasing m_{I} does not change the phase function for very small (Rayleigh) particles, the phase functions for larger particles become significantly smoother. The suppression of refracted rays $(i \geq 2)$ weakens and ultimately extinguishes the rainbow and the glory. The scattering by large particles with $m_{\text{I}} = 0.3$ is dominated by diffraction and externally reflected rays, so that the phase function consists essentially of a strong

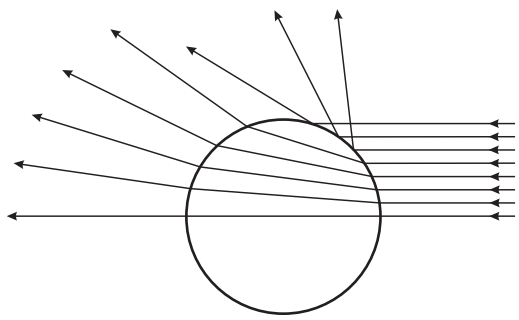

Figure 9.23. Ray-tracing diagram for a spherical particle with a real relative refractive index that is less than but close to unity.

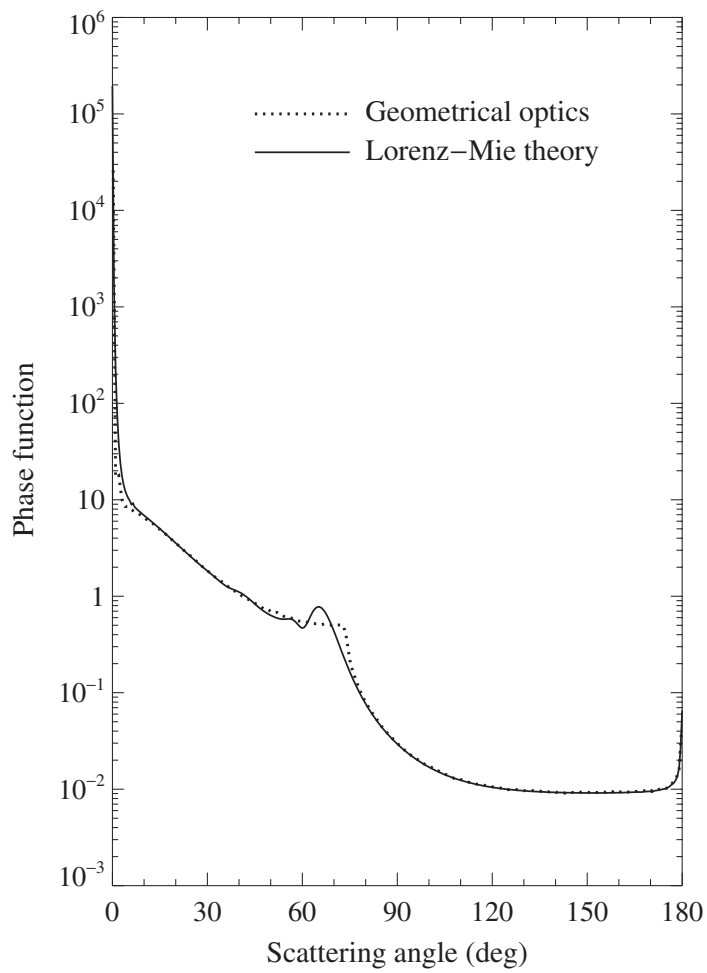

Figure 9.24. Geometrical optics and Lorenz–Mie phase functions for a gamma distribution of spherical particles with $m = 0.8$, $x_{\text{eff}} = 600$, and $v_{\text{eff}} = 0.07$.

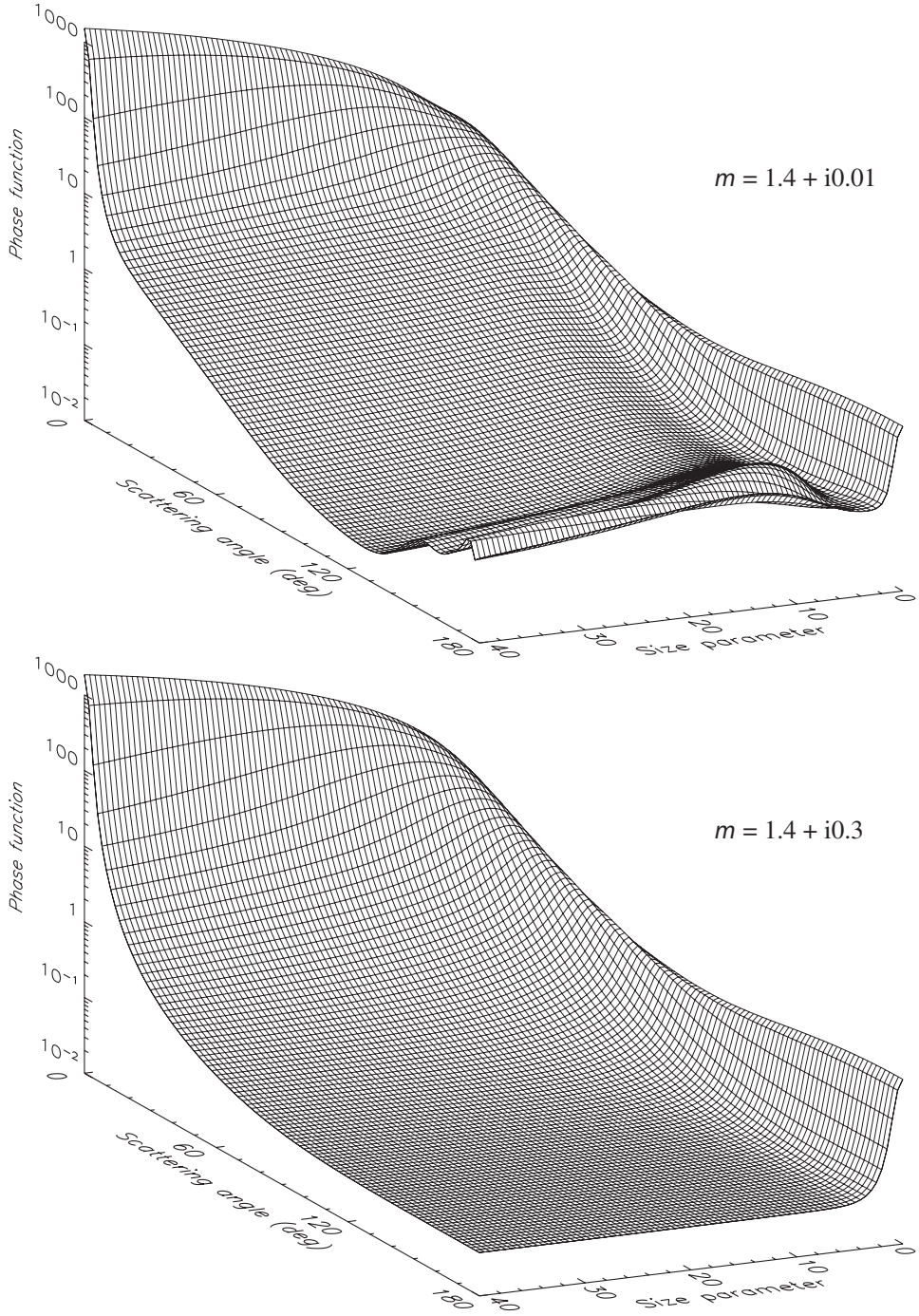

Figure 9.25. As in Fig. 9.20, but for $m = 1.4 + i0.01$ and $1.4 + i0.3$.

diffraction peak in the forward direction and nearly isotropic scattering in the backward hemisphere. As a consequence, the angular profile of the phase function becomes remarkably similar to that for $m = 1$ (lower panel of Fig. 9.20), although the virtually zero contribution of the reflected rays in the case $m = 1$ makes the background phase function value in the backward hemisphere significantly lower.

9.5 Backscattering

Figure 9.26 shows that the phase-function value at $\Theta = 180°$ can vary by orders of magnitude with changing size parameter and/or real and imaginary parts of the relative refractive index. This variability makes difficult the analysis of backscattering intensity measurements and explains the large amount of attention paid by those interpreting radar and lidar observations to quantities like the average backscattering cross section per particle,

$$\langle C_{\mathrm{b}} \rangle = \left\langle \frac{\mathrm{d}C_{\mathrm{sca}}}{\mathrm{d}\Omega} \right\rangle_{\Theta=180°} = \frac{\langle C_{\mathrm{sca}} \rangle a_1(180°)}{4\pi}, \tag{9.10}$$

the average radar backscattering cross section per particle,

$$\langle \sigma_{\mathrm{b}} \rangle = 4\pi \langle C_{\mathrm{b}} \rangle \tag{9.11}$$

the extinction-to-backscatter ratio,

$$R_{\mathrm{eb}} = \frac{\langle C_{\mathrm{ext}} \rangle}{\langle \sigma_{\mathrm{b}} \rangle} = \frac{1}{\varpi a_1(180°)}, \tag{9.12}$$

and the backscatter-to-extinction ratio

$$R_{\mathrm{be}} = \frac{\langle \sigma_{\mathrm{b}} \rangle}{\langle C_{\mathrm{ext}} \rangle} = \varpi a_1(180°) \tag{9.13}$$

(e.g., Battan 1973; Reagan *et al.* 1989; Stephens 1994). The behavior of these backscattering characteristics is illustrated in Figs. 9.27 and 9.28, which show the backscattering efficiency factor

$$Q_{\mathrm{b}} = \frac{\langle C_{\mathrm{b}} \rangle}{\langle G \rangle} \tag{9.14}$$

and the backscatter-to-extinction ratio as a function of effective size parameter for a range of the real and imaginary parts of the relative refractive index. Note that Q_{b} vanishes in the limit $m \to 1$, because particles with the refractive index equal to that of the surrounding medium do not scatter light, whereas the dimensionless backscattering phase function and backscatter-to-extinction ratio remain finite.

A common feature of $a_1(180°)$, Q_{b}, and R_{be} is that the larger the imaginary part of the relative refractive index, the faster they reach their respective geometrical

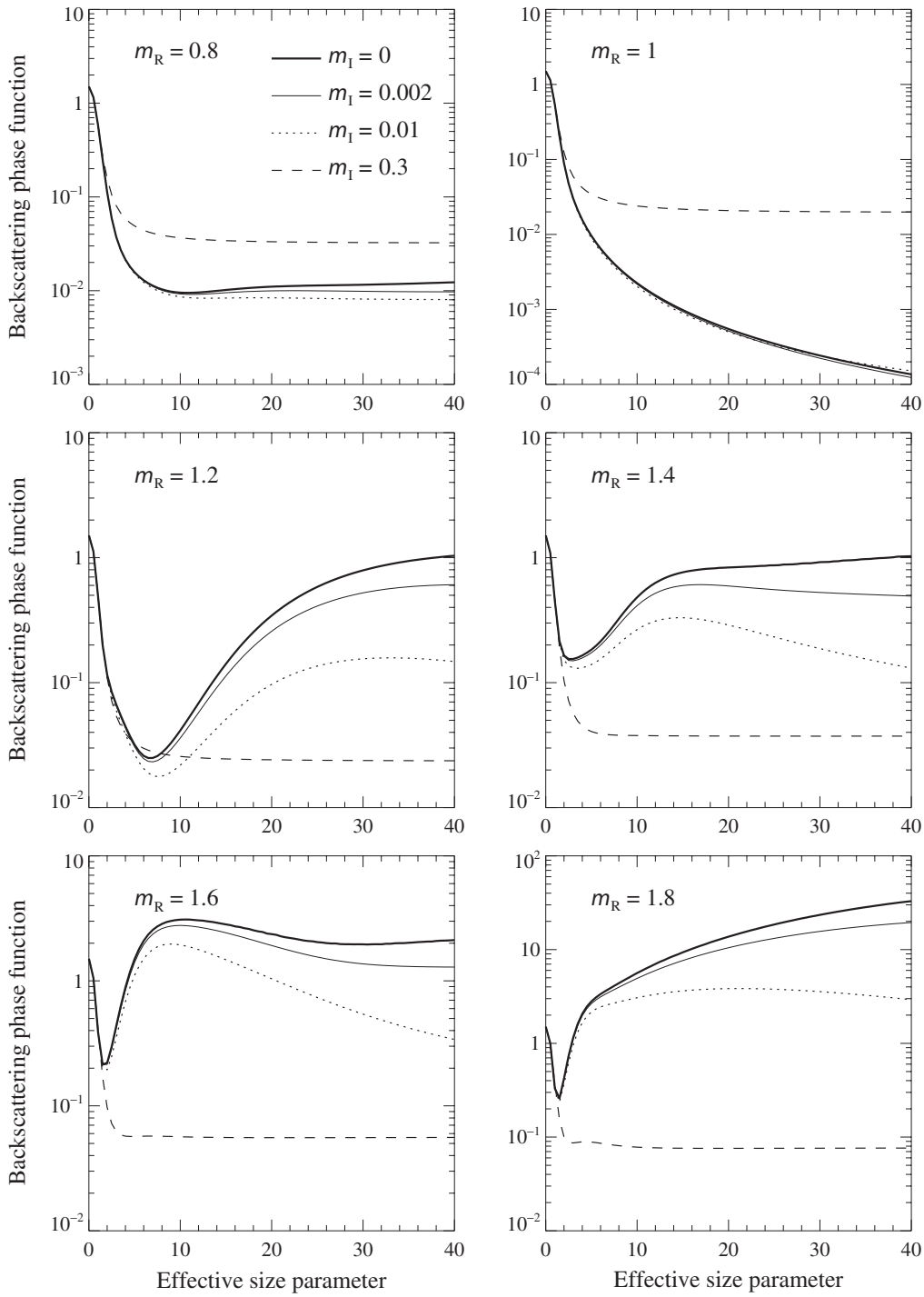

Figure 9.26. Backscattering phase function $a_1(180°)$ versus effective size parameter for a gamma distribution of spherical particles with $v_{eff} = 0.15$, $m_R = 0.8$, 1, 1.2, 1.4, 1.6, and 1.8, and $m_I = 0$, 0.002, 0.01, and 0.3.

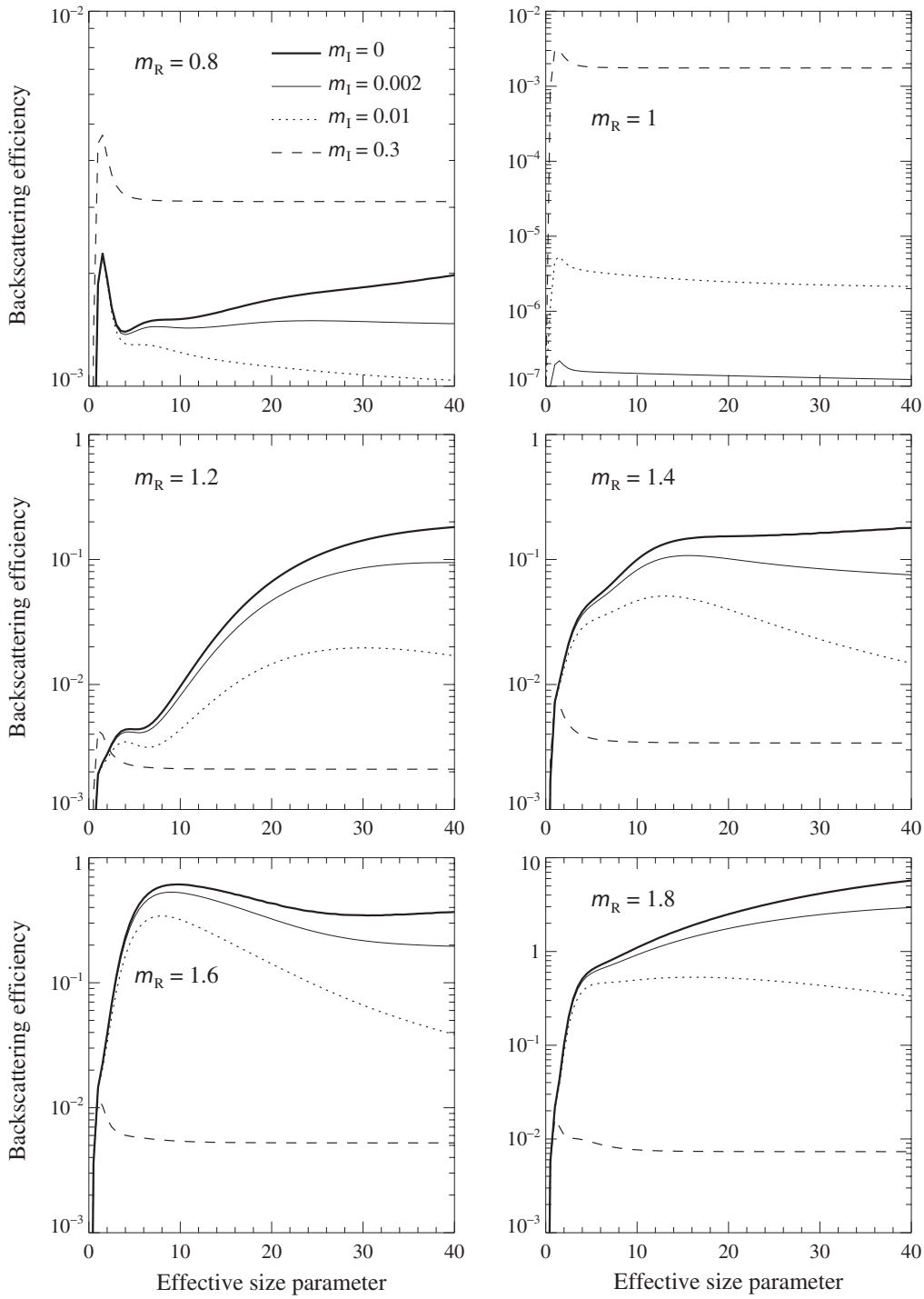

Figure 9.27. As in Fig. 9.26, but for the backscattering efficiency factor.

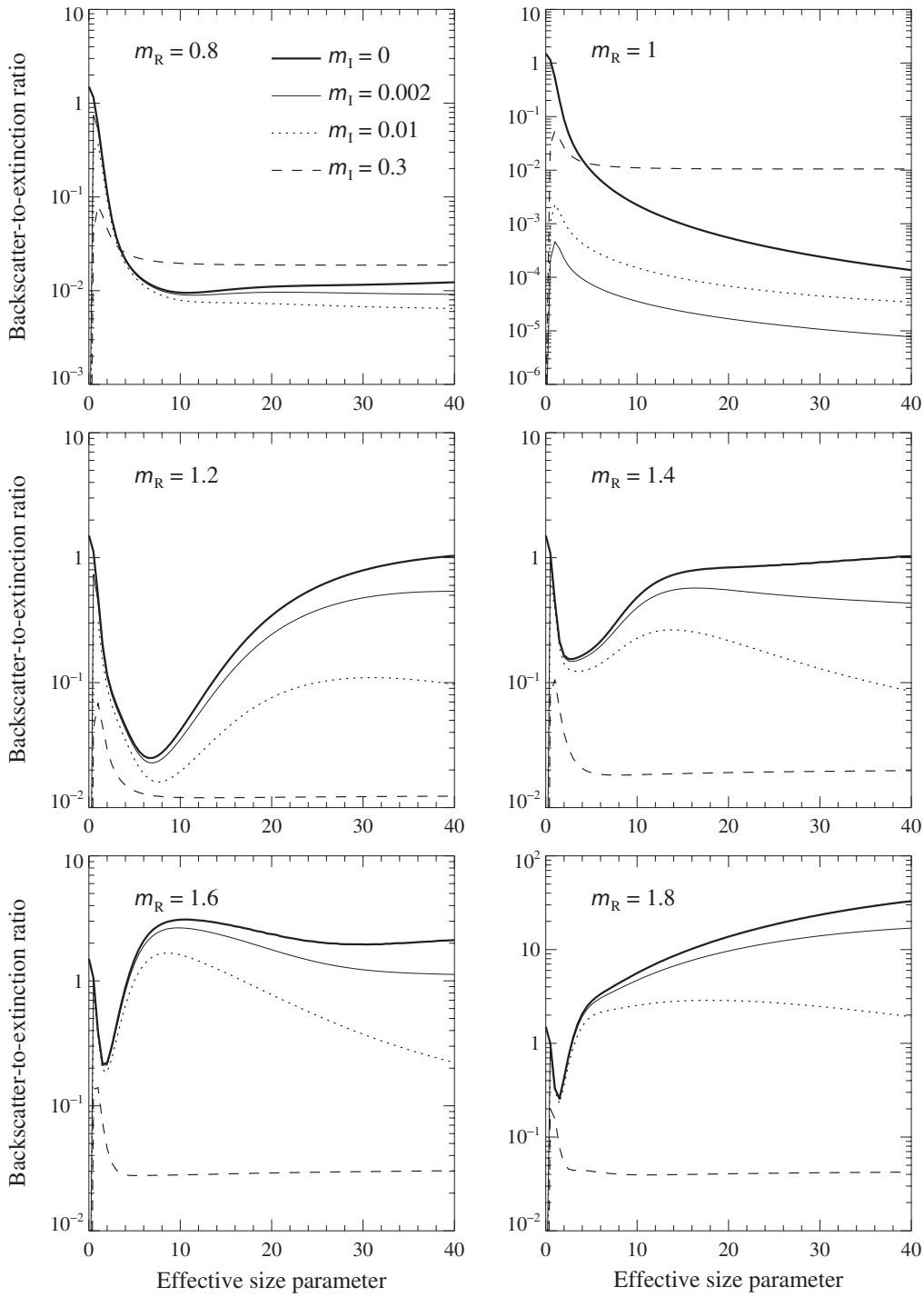

Figure 9.28. As in Fig. 9.26, but for the backscatter-to-extinction ratio.

optics limits with increasing x_{eff}. An additional property of these backscattering characteristics is that they almost always decrease with increasing m_{I} for $m_{\text{R}} = 1.2$, 1.4, 1.6, and 1.8. For $m_{\text{R}} = 0.8$, they first decrease as m_{I} grows from 0 to 0.01 but then significantly increase as m_{I} reaches the value 0.3 (except the backscatter-to-extinction ratio for $x_{\text{eff}} \lesssim 4$). The backscattering phase function and the backscatter-to-extinction ratio for $m_{\text{R}} \neq 1$ have a local minimum at small effective size parameters, which is especially deep for $m = 1.2$. The minimum becomes less pronounced and eventually vanishes with increasing absorption.

9.6 Other elements of the scattering matrix

Plates 9.5 and 9.6 parallel Figs. 9.20–9.22 and 9.25 and show the ratios $a_3(\Theta)/a_1(\Theta)$, $-b_1(\Theta)/a_1(\Theta)$, and $b_2(\Theta)/a_1(\Theta)$ (in %) versus scattering angle Θ and effective size parameter. The use of 21 discrete colors in these contour plots (with 20 contours at ±5%, ±15%, …, ±85%, and ±95%) allows the reader to quantify the diagrams using white as the reference. The ratio $-b_1(\Theta)/a_1(\Theta)$ is the degree of linear polarization P_Q for the scattering of unpolarized incident light provided that the Stokes parameters are defined with respect to the scattering plane. Furthermore, according to Eqs. (1.112) and (4.14) the quantity $|b_1(\Theta)|/a_1(\Theta)$ gives the degree of linear polarization P_{L} in the general case of the scattering of unpolarized incident light. The significance of this and the other two element ratios of the normalized Stokes scattering matrix in cases involving polarized incident light and arbitrary incidence and scattering directions follows from Eq. (4.14).

In agreement with Eqs. (4.61), (4.62), and (4.66), the ratios $-b_1(\Theta)/a_1(\Theta)$ and $b_2(\Theta)/a_1(\Theta)$ vanish at $\Theta = 0°$ and 180°, whereas $a_3(0°)/a_1(0°) = 1$ and $a_3(180°)/a_1(180°) = -1$.

In the limit $x_{\text{eff}} \to 0$ Rayleigh scattering occurs. In accordance with Eq. (7.5), there is strong positive polarization with the maximal 100% value at scattering angle 90°, whereas the ratio $b_2(\Theta)/a_1(\Theta)$ vanishes completely. The Rayleigh scattering region is similar for all relative refractive indices but is compressed to smaller size parameters for the larger values of m. The ratio $a_3(\Theta)/a_1(\Theta)$ is antisymmetric with respect to scattering angle 90°: $a_3(180° - \Theta)/a_1(180° - \Theta) = -a_3(\Theta)/a_1(\Theta)$.

In the limit $m \to 1$, all three ratios become independent of size parameter and the ratio $b_2(\Theta)/a_1(\Theta)$ vanishes. This is consistent with the well-known result of the Rayleigh–Gans approximation, that the normalized Stokes scattering matrix is given by

$$\tilde{\mathbf{F}}_{\text{RG}}(\Theta, x_{\text{eff}}) = \psi(\Theta, x_{\text{eff}}) \begin{bmatrix} 1+\cos^2\Theta & -\sin^2\Theta & 0 & 0 \\ -\sin^2\Theta & 1+\cos^2\Theta & 0 & 0 \\ 0 & 0 & 2\cos\Theta & 0 \\ 0 & 0 & 0 & 2\cos\Theta \end{bmatrix} \tag{9.15}$$

(Kerker 1969). The degree of linear polarization and the ratio $a_3(\Theta)/a_1(\Theta)$ are the same as for Rayleigh scattering.

In what follows we will normally omit the argument Θ of the scattering matrix elements. The ratio a_3/a_1 is almost always positive in the forward hemisphere, where it is weakly dependent on relative refractive index and size parameter. However, it shows a considerable degree of variability with m and x_{eff} in the backward hemisphere. The pattern of the ratio b_2/a_1 for most relative refractive indices and size parameters consists of narrow regions of positive or neutral values at small and large scattering angles separated by a wide region of negative values at side-scattering angles. Of the three ratios, the degree of linear polarization $-b_1/a_1$ exhibits the largest degree of variability with relative refractive index and/or size parameter. This explains the remarkable potential of polarimetry as a particle characterization and remote sensing tool (Section 9.7).

With increasing x_{eff}, the scattering matrix starts to develop typical geometrical optics features. At small scattering angles the linear polarization is small because of the predominance of unpolarized diffracted light (for unpolarized incident light). Most of the light scattered in the near-forward direction is due to twice-refracted rays (i = 2) and is negatively polarized, as follows from Fresnel's equations. Externally reflected rays (i = 1) are positively polarized at all scattering angles. As m increases, the intensity of these rays increases too, especially for grazing values of the local incidence angle α (Fig. 9.17), and becomes sufficient to cause a long peninsula of positive polarization values at scattering angles between $10°$ and $30°$ for m = 1.8. The steep ridge of positive polarization in the two right-hand columns of Plate 9.5 for m = 1.2, 1.4, 1.6, and 1.8 is the primary rainbow. The weaker positive feature at $\Theta \sim 165°$ for m = 1.2 and $\Theta \sim 110°$ for m = 1.4 is the secondary rainbow. Although the secondary rainbow can be reliably identified in the polarization maps, it is barely seen in the respective phase function plots even for $x_{\text{eff}} = 40$ (cf. Fig. 9.21). For m = 1.2 the primary and secondary rainbow regions merge with the region of Rayleigh scattering, whereas for m = 1.4, 1.6, and 1.8 these regions are separated by areas of neutral or negative polarization.

The two columns on the right of Plate 9.6 illustrate the effect of increasing the imaginary part of the relative refractive index on the ratios a_3/a_1, $-b_1/a_1$, and b_2/a_1 for $m_{\text{R}} = 1.4$. The corresponding panels in Plate 9.5 and on the left of Plate 9.6 provide a comparison for $m_{\text{I}} = 0$. For small effective size parameters the effect of increasing m_{I} from 0 to 0.01 is relatively weak. For large particles the absorption of refracted rays $(i \geq 2)$ results in a dominance of diffracted light and externally reflected rays. The latter are positively polarized and, for m = 1.4 + i0.3, yield a polarization pattern similar to that of Rayleigh and Rayleigh–Gans scattering (compare the rightmost middle panel of Plate 9.6 with the rightmost top panel of Plate 9.5). The only significant difference is that the maximum of polarization occurs at the scattering angle $\Theta' = 180° - 2\arctan m_{\text{R}} = 71.08°$ rather than at 90°; here $\arctan m_{\text{R}}$ is the Brewster angle. The bridge of positive a_3/a_1 values at $\Theta \sim 165°$ fades out with

increasing m_{I} and eventually disappears. As a result, the pattern of the ratio a_3/a_1 for m = 1.4 + i0.3 also closely resembles that of Rayleigh and Rayleigh–Gans scattering (compare the rightmost top panel of Plate 9.6 with the top panel of the second column of Plate 9.5), except that the scattering angle of zero values is now Θ' rather than 90°. The ratio b_2/a_1 for large particles decreases with increasing imaginary part of the relative refractive index and almost vanishes for $m_{\mathrm{I}} = 0.3$.

9.7 Optical characterization of spherical particles

As we have mentioned previously, the potentially strong dependence of the scattering properties of spherical particles on their size parameter and relative refractive index makes measurements of electromagnetic scattering a powerful noninvasive means of particle characterization. In fact, there are so many applications of optical particle characterization in laboratory and remote sensing research that simply listing them would take an inordinate amount of space. Therefore, we will describe only a few selected examples, directing the reader for more details and further references to the books by Kerker (1969), Bayvel and Jones (1981), Gouesbet and Gréhan (1988), Stephens (1994), and Xu (2000), the feature journal issue edited by Hirleman and Bohren (1991), and the recent review by Jones (1999).

The lower curve in Fig. 9.29 depicts measurements of the intensity of the light scattered by a slowly evaporating glycerol droplet at a scattering angle of approximately 90°. The droplet was illuminated by a linearly polarized laser beam at a wavelength $\lambda_1 = 0.5145\,\mu\mathrm{m}$, the same beam being used to levitate the particle. The upper curve shows the results of Lorenz–Mie computations for a spherical droplet with a radius ranging from 4.38 to 4.67 μm and a relative refractive index of 1.4746 corresponding to that of glycerol at the visible wavelength. Comparison of the two curves demonstrates that by identifying the locations of the resonance features in the experimental data the diameters of spherical droplets can be determined with extreme precision. Chýlek *et al.* (1983) developed a technique for determining the relative refractive index as well as the size of an optically levitated spherical particle illuminated by a tunable dye laser. The technique is based on analyzing both the wavelengths of the resonance peaks and the line profiles in the curve of the backscattered intensity as a function of laser wavelength. More recent developments have been described by Huckaby *et al.* (1994), Ray and Nandakumar (1995), and Tu and Ray (2001).

We already discussed in Section 8.1 the use of measurements of the Stokes scattering matrix for sizing polydisperse water droplets (cf. Fig. 8.2). Figure 9.30 illustrates another application of this technique. The solid curves depict ratios of the elements of the normalized Stokes scattering matrix measured by Bottiger *et al.* (1980) in the scattering-angle range $12° \le \Theta \le 165°$ for a spherical latex particle. As the source of light, Bottiger *et al.* used a He–Cd laser operating at a wavelength 441.6

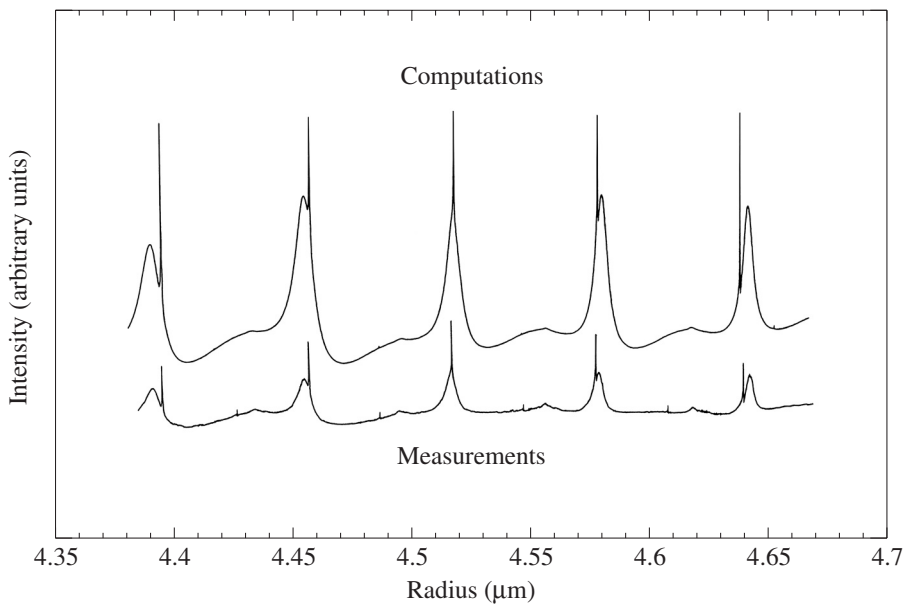

Figure 9.29. Measurements and computations of the intensity (in arbitrary units) scattered by a glycerol droplet at a scattering angle of approximately $90°$ versus droplet radius (after Chýlek *et al.* 1992).

nm. The electrostatic levitation technique allowed them to select a single particle and trap it in a very small volume. Bottiger *et al.* did not measure the size of the particle and only indicated that the average diameter of latex microspheres used in their experiments was 1091 nm with standard deviation 8 nm. The results of monodisperse Lorenz–Mie computations for the diameter 1091 nm and relative refractive index of latex in air 1.588 showed no resemblance to the Bottiger *et al.* data (Mishchenko and Mackowski 1996). However, a very good agreement was found for the diameter 1122 nm, as demonstrated in Fig. 9.30 by the dotted curves. Although Bottiger *et al.* did not specify the magnitude of their experimental errors, the latter can perhaps be inferred by comparing the experimental curves for the ratios a_3/a_1 and a_4/a_1, which must be the same for homogeneous spherical particles. Despite some residual differences between the experimental data and the results of theoretical computations, the numbers of major maxima and minima in the solid curves and their locations are reproduced almost perfectly. The dotted curves in the left- and right-hand panels of Fig. 9.31 were computed for diameters 1108 and 1136 nm, respectively, and deviate significantly from the experimental curves. This demonstrates that the accuracy of sizing the latex particle using measurements of the Stokes scattering matrix is better than ±14 nm or 1.2%.

The final example illustrates the use of polarimetry for remotely retrieving cloud-particle microphysics and represents what is perhaps the most spectacular achievement of planetary remote sensing. Figures 9.32 and 9.33 show the results of ground-based measurements of the linear polarization of sunlight reflected by Venus as a

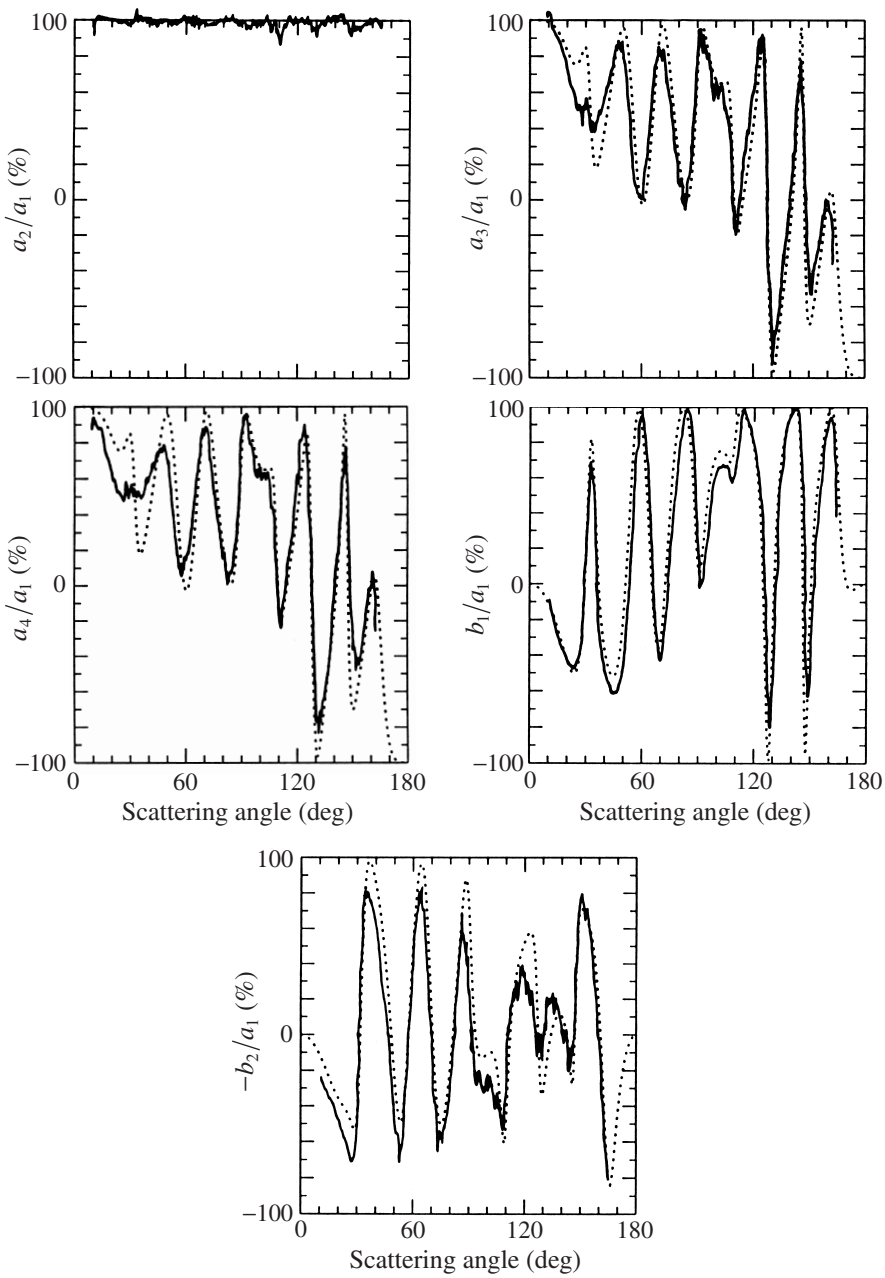

Figure 9.30. Ratios of the elements of the normalized Stokes scattering matrix for a single latex sphere. The solid curves depict the laboratory data by Bottiger *et al.* (1980), whereas the dotted curves show the results of Lorenz–Mie computations for the sphere diameter 1122 nm.

function of scattering angle at wavelengths 0.55 and 0.99 μm, respectively. The curves depict the results of theoretical calculations based on a simple model of the Venus atmosphere in the form of a homogeneous, optically semi-infinite, locally plane-parallel cloud layer uniformly covering the entire planet (Hansen and Hovenier 1974). The cloud particles were assumed to be spherical, and their single-scattering

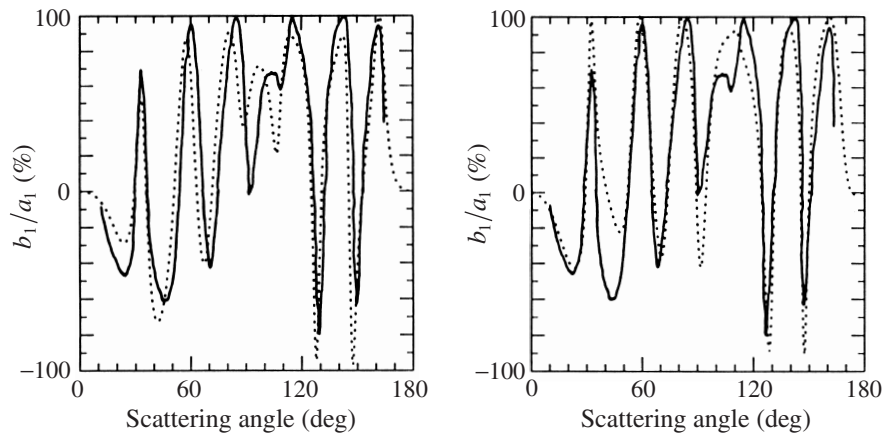

Figure 9.31. As in Fig. 9.30, but for diameters 1108 nm (left panel) and 1136 nm (right panel).

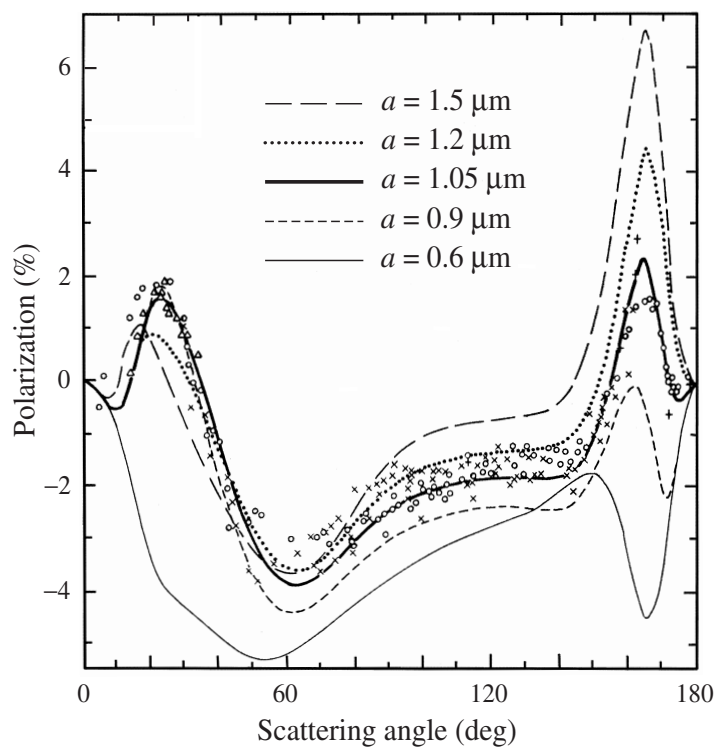

Figure 9.32. Observations of the polarization of sunlight reflected by Venus in the visual wavelength region (symbols) and theoretical computations at 0.55 μm wavelength (curves). The theoretical results are based on a model of nonabsorbing spherical particles with fixed relative refractive index (m = 1.44) and fixed effective variance of the size distribution ($v_{\text{eff}} = 0.07$) (curves). The different curves show the influence of the effective radius $a \equiv r_{\text{eff}}$ on the polarization. (After Hansen and Hovenier 1974.)

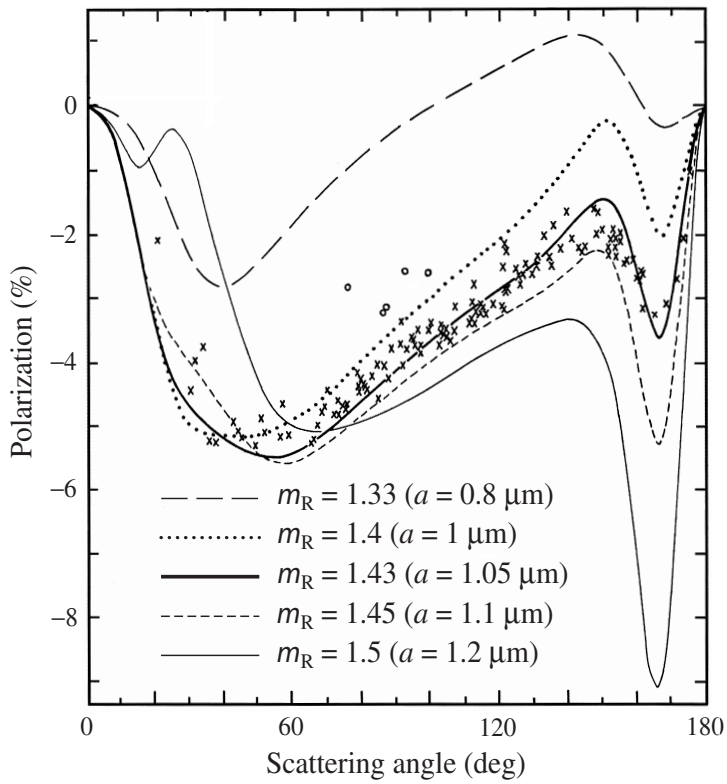

Figure 9.33. Observations (symbols) and theoretical computations (curves) of the polarization of the sunlight reflected by Venus at 0.99 μm wavelength. The different theoretical curves are for various relative refractive indices, the effective radius being selected in each case to yield the closest agreement with the observations. The effective variance of the cloud-particle size distribution is fixed at 0.07. (After Hansen and Hovenier 1974.)

properties were modeled using the Lorenz–Mie theory. The computations of multiple scattering of light in the atmosphere were based on the so-called adding/doubling procedure for the numerical solution of the vector radiative transfer equation (Hovenier 1971; Hansen and Travis 1974). Hansen and Hovenier used the simple gamma distribution (5.245) to represent analytically the distribution of cloud particles over sizes and found the parameters a $(= r_{\text{eff}})$ and b $(= v_{\text{eff}})$ of this distribution, as well as the relative refractive index, by minimizing the differences between the observational data and the results of model computations. From the comparisons between the computed and observed quantities, Hansen and Hovenier deduced the following.

- The observations can indeed be reproduced quantitatively using a model of nonabsorbing spherical particles. The observational data at visible wavelengths contain a clear signature of the spherical particle shape, such as the primary rainbow at $\Theta \sim 160°$ and the anomalous diffraction feature at $\Theta \sim 25°$ (cf. Fig. 9.32 and the lower left panel of Plate 9.4). This interpretation is confirmed by the spectral variation of the observed polarization.

- The effective radius of the cloud particles is 1.05 ± 0.10 μm.
- The particle size distribution is narrow, with an effective variance $v_{\text{eff}} = 0.07 \pm 0.02$.
- The cloud-particle refractive index has a normal dispersion, decreasing from 1.46 ± 0.015 at a wavelength $0.365\,\mu\text{m}$ to 1.43 ± 0.015 at a wavelength 0.99 μm.

Based on the spectral dependence of the refractive index, Hansen and Hovenier concluded that the cloud particles consist of a concentrated (76% by weight) aqueous solution of sulfuric acid $(H_2SO_4 - H_2O)$. This remarkable result has been confirmed by subsequent *in situ* measurements and observations from Venus-orbiting satellites (e.g., Sato *et al.* 1996 and references therein).

Further reading

Scattering phenomena associated with homogeneous spherical particles are extensively discussed in van de Hulst (1957), Nussenzveig (1992), Lynch and Livingston (1995), and Grandy (2000). An overview of scattering and absorption properties of layered and radially inhomogeneous spherically symmetric particles can be found in the books by Kerker (1969), Prishivalko *et al.* (1984), and Babenko *et al*. (2003).

The use of laboratory measurements of scattering matrix elements for sizing spherical particles is described by Maltsev *et al.* (1997) and Kaplan *et al.* (2000). The book edited by Gehrels (1974) contains many applications of polarimetry to particle characterization in astrophysics and planetary remote sensing. The use of polarimetry in remote sensing of the terrestrial atmosphere is described by Brogniez *et al.* (1992), Buriez *et al.* (1997), Mishchenko and Travis (1997), Deuzé *et al.* (2000), Masuda *et al.* (2000), Sano and Mukai (2000), and Chowdhary *et al.* (2001). Dubovik and King (2000) and Lacis *et al.* (2000) discussed the retrieval of microphysical properties of spherical aerosols using multi-wavelength measurements of extinction and sky radiances. The characterization of water-cloud droplets and spherical aerosol particles using radiance measurements from space is reviewed by Nakajima and King (1990), King *et al.* (1999), and Rossow and Schiffer (1999).

Chapter 10

Scattering and absorption properties of nonspherical particles

The convenient availability and simplicity of the Lorenz–Mie theory has resulted in a widespread practice of treating nonspherical particles (especially those in random orientation) as if they were spheres to which Lorenz–Mie results are applicable. However, the assumption of sphericity is rarely made after first having studied the effects of nonsphericity and concluded that they are negligible but, rather, is usually based upon a perceived lack of practical alternatives. In fact, overwhelming evidence suggests that the scattering properties of nonspherical particles, including those in random orientation, can significantly differ from those of volume- or surface-equivalent spheres. Hence, the goal of this chapter is to provide a brief summary of recent research efforts aimed at a significantly better understanding of the effects of particle shape and morphology on electromagnetic scattering.

10.1 Interference and resonance structure of scattering patterns for nonspherical particles in a fixed orientation; the effects of orientation and size averaging

We have seen in Section 9.1 that scattering patterns for monodisperse spheres are heavily burdened with various interference and resonance features. The interference and resonance structure for monodisperse nonspherical particles in a fixed orientation is even more intricate because it acquires new complex, orientation-specific features. This is demonstrated in Figs. 10.1–10.3, which show the results of T-matrix computations of the intensity scattered by three types of particle in various orientations (all "orientations" of a

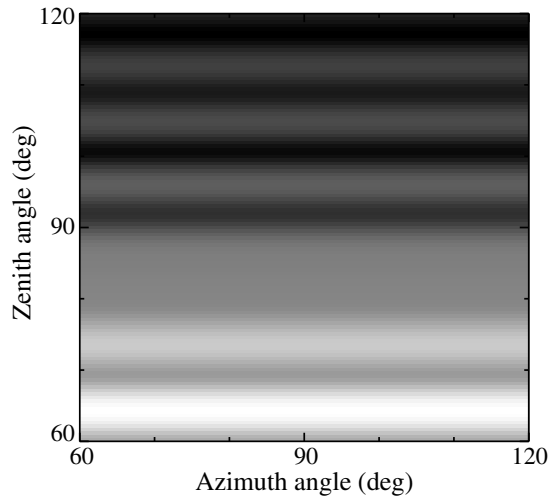

Figure 10.1. Scattered intensity (in arbitrary units) versus ϑ^{sca} and φ^{sca} for a spherical particle illuminated by an unpolarized beam of light incident along the z-axis of the laboratory reference frame (cf. Fig. 1.2). The size parameter of the sphere is 20 and the relative refractive index is 1.53 + i0.008.

spherical particle yield, of course, the same scattering pattern). The sphere (Fig. 10.1) and also the spheroid and cylinder with rotation axes oriented along the z-axis of the laboratory coordinate system (the upper left panels of Figs. 10.2 and 10.3, respectively) show no azimuthal dependence of the scattered intensity, because the scattering geometry is axially symmetric and the incident light is unpolarized. However, the other panels of Figs. 10.2 and 10.3 demonstrate patchy patterns similar to those shown in Plate 8.1. The number of patches and the complexity of the scattering patterns rapidly mount with growing size parameter (Figs. 10.4 and 10.5), making it increasingly difficult to establish a definitive relationship between the physical and geometrical particle characteristics on the one hand and the structure of the scattering pattern on the other.

Panels (a)–(c) of Plate 10.1 represent another way of looking at the effects of nonsphericity and orientation on scattering patterns. They depict the degree of linear polarization of the scattered light, for unpolarized incident light, versus the zenith angle of the scattering direction and the surface-equivalent-sphere size parameter for monodisperse spheres (a) and for monodisperse, surface-equivalent oblate spheroids with two orientations of the rotation axis relative to the laboratory reference frame (b), (c). The polarization patterns for the spheres and the spheroids in the two fixed orientations are dramatically different. In particular, the lack of axial symmetry for the light-scattering geometry in panel (c) results in non-zero polarization values at $\vartheta^{\text{sca}} = 0°$ and 180°.

Plate 10.1(d) shows that the polarization pattern computed for monodisperse spheroids in random orientation is much smoother and less complex than those for spheroids in fixed orientations. This smoothing effect of averaging over orientations is reinforced by averaging over sizes, which totally removes the residual interference

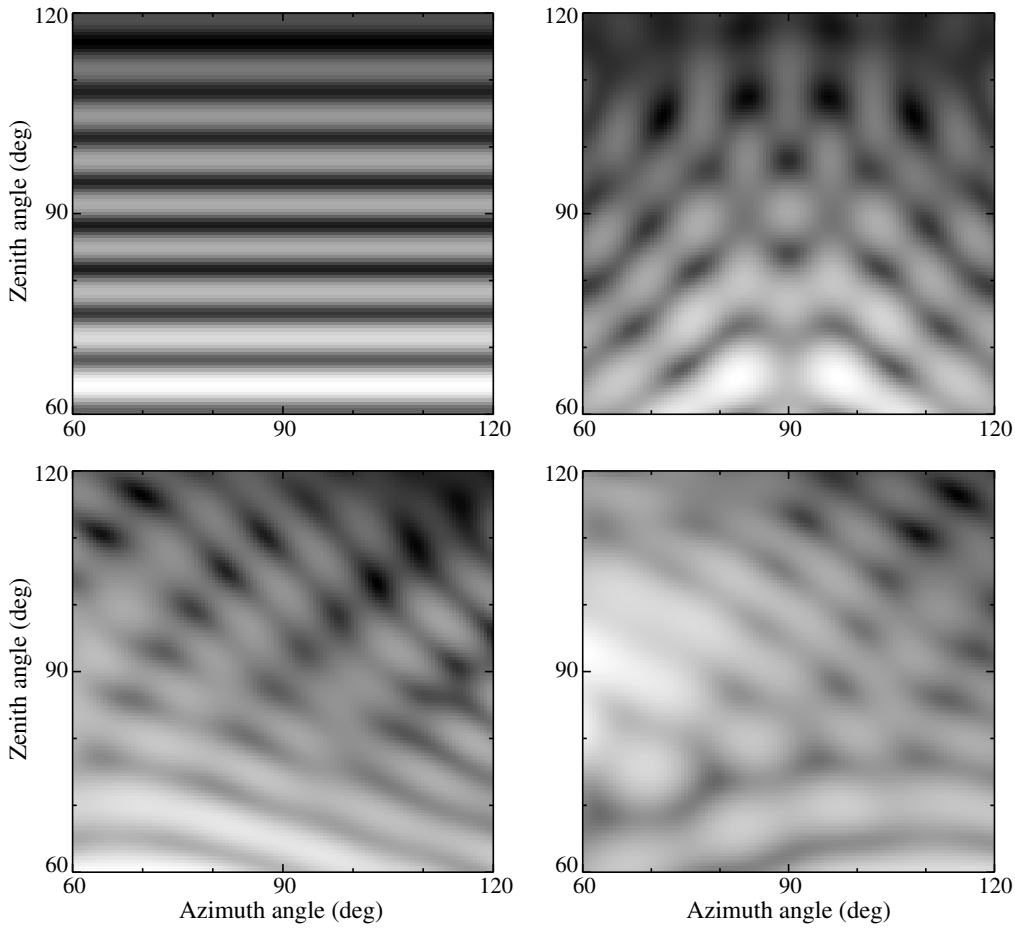

Figure 10.2. Scattered intensity (in arbitrary units) versus ϑ^{sca} and φ^{sca} for a prolate spheroid with an axis ratio $a/b = 1/2$ illuminated by an unpolarized beam of light incident along the z-axis of the laboratory reference frame. The surface-equivalent-sphere size parameter of the spheroid is 20 and the relative refractive index is 1.53 + i0.008. The orientation of the spheroid rotation axis relative to the laboratory coordinate system is specified by the Euler angles $\alpha = 0°$, $\beta = 0°$ (upper left panel), $\alpha = 0°$, $\beta = 90°$ (upper right panel), $\alpha = 0°$, $\beta = 45°$ (lower left panel), and $\alpha = 45°$, $\beta = 45°$ (lower right panel).

and resonance structure still evident in Plate 10.1(d). This is demonstrated by Plate 10.2(d), which shows the T-matrix results for a modified power law distribution of surface-equivalent-sphere radii, given by Eq. (5.246) with $\alpha = -3$ and $v_{\text{eff}} = 0.1$.

The most obvious reason for performing computations and measurements of light scattering by polydisperse rather than monodisperse particles is the desire to represent more closely natural particle ensembles, in which particles are most often distributed over a range of sizes and orientations. The second reason is the presence of the complicated and highly variable interference and resonance structure, which makes it highly problematic to compare computation and/or measurement results for monodisperse particles in a fixed orientation in order to derive useful conclusions about the

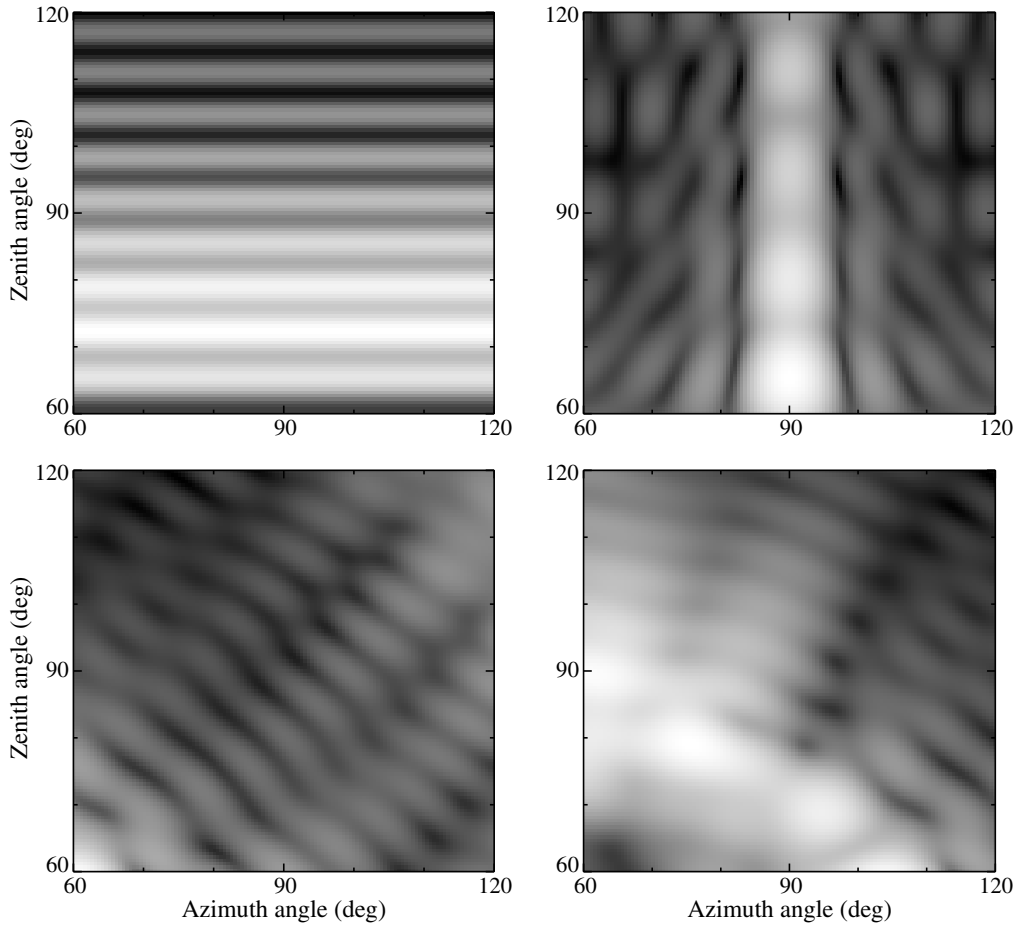

Figure 10.3. As in Fig.10.2, but for a prolate cylinder with a diameter-to-length ratio $1/2$.

specific effects of particle shape on electromagnetic scattering. Averaging over sizes for spheres and averaging over orientations and sizes for nonspherical particles largely removes the interference and resonance structure and enables meaningful comparisons of the scattering properties of different types of particle. Therefore, in the following sections we will mostly analyze polydisperse ensembles of randomly oriented nonspherical particles.

10.2 Randomly oriented, polydisperse spheroids with moderate aspect ratios

There are two reasons to begin our survey by considering spheroidal particles. First, the shape of a spheroid has the advantage of being described by only one shape pa-

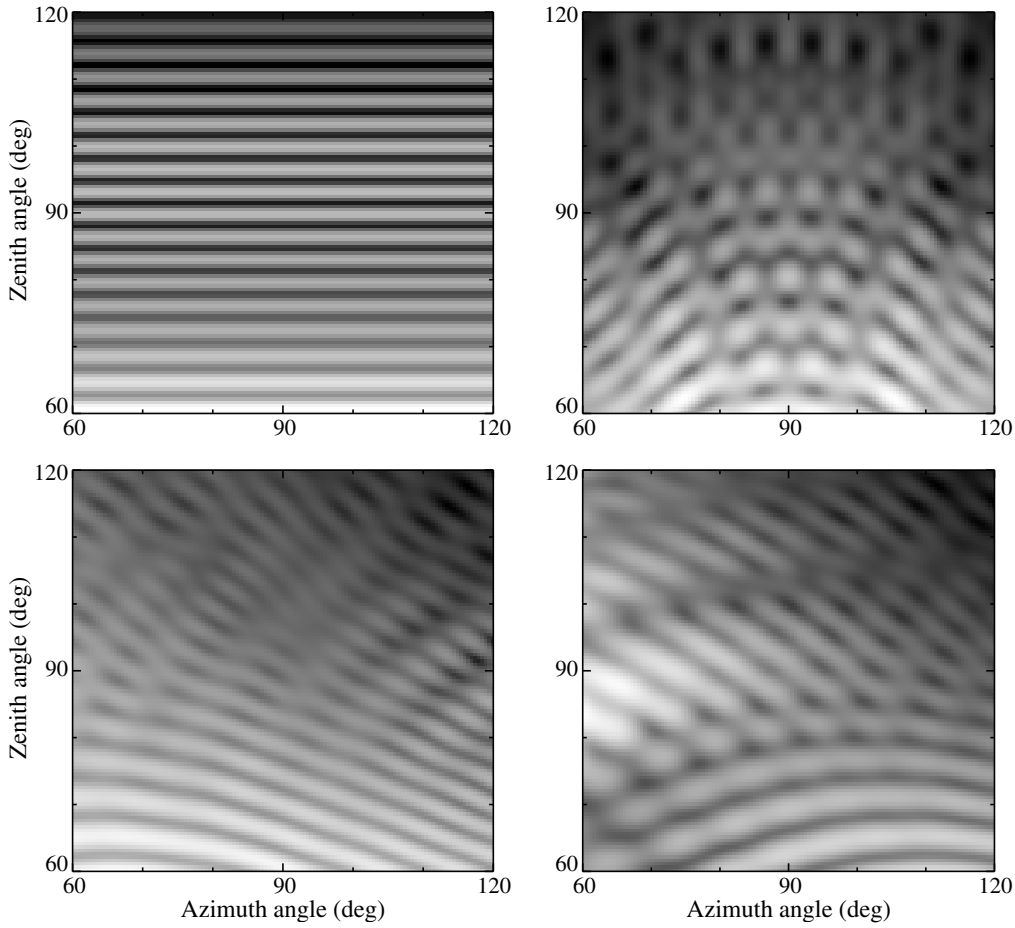

Figure 10.4. As in Fig.10.2, but for spheroid surface-equivalent-sphere size parameter 40.

rameter, specifically, the axis ratio a/b. By varying this single parameter, one can model a continuous sequence of shapes varying from perfect spheres $(a/b=1)$ and nearly spherical particles $(a/b \sim 1)$ to needles $(a/b \ll 1)$ and plates $(a/b \gg 1)$. Second, spheroids are rotationally symmetric scatterers and, therefore, are especially suitable for efficient T-matrix computations (cf. subsection 5.8.3).

The T-matrix code described in Section 5.11 provides the option of using several types of size distribution function, given by Eqs. (5.242)–(5.246). As discussed in subsection 5.10.1, the maximum equivalent-sphere radius $r_{\max}$ for the modified gamma, log normal, and gamma size distributions must be increased until the scattering results converge within a prescribed numerical accuracy. This requirement may often necessitate a rather large value of the maximum radius, which can result in quite time-consuming T-matrix computations or even failure if the maximum radius is so large relative to the wavelength that the T-matrix code does not converge (cf. subsection 5.11.7). However, Hansen and Travis (1974) and Mishchenko and Travis

Table 10.1. Efficiency factors, single-scattering albedo, and asymmetry parameter for log normal, gamma, and modified power law size distributions of randomly oriented oblate spheroids with an axis ratio $a/b = 1.6$[a]

Size distribution	Q_{ext}	Q_{sca}	Q_{abs}	ϖ	$\langle \cos \Theta \rangle$
Log normal	2.35	1.90	0.445	0.810	0.747
Gamma	2.35	1.90	0.445	0.811	0.746
Modified power law	2.37	1.93	0.442	0.813	0.747

[a]All three distributions of surface-equivalent-sphere radii have the same effective radius, $r_{eff} = 1.5\,\mu m$, and effective variance, $v_{eff} = 0.1$. The power exponent of the modified power law size distribution is $\alpha = -3$. The relative refractive index is 1.53 + i0.008, and the wavelength of light in the surrounding medium is 0.6283 μm.

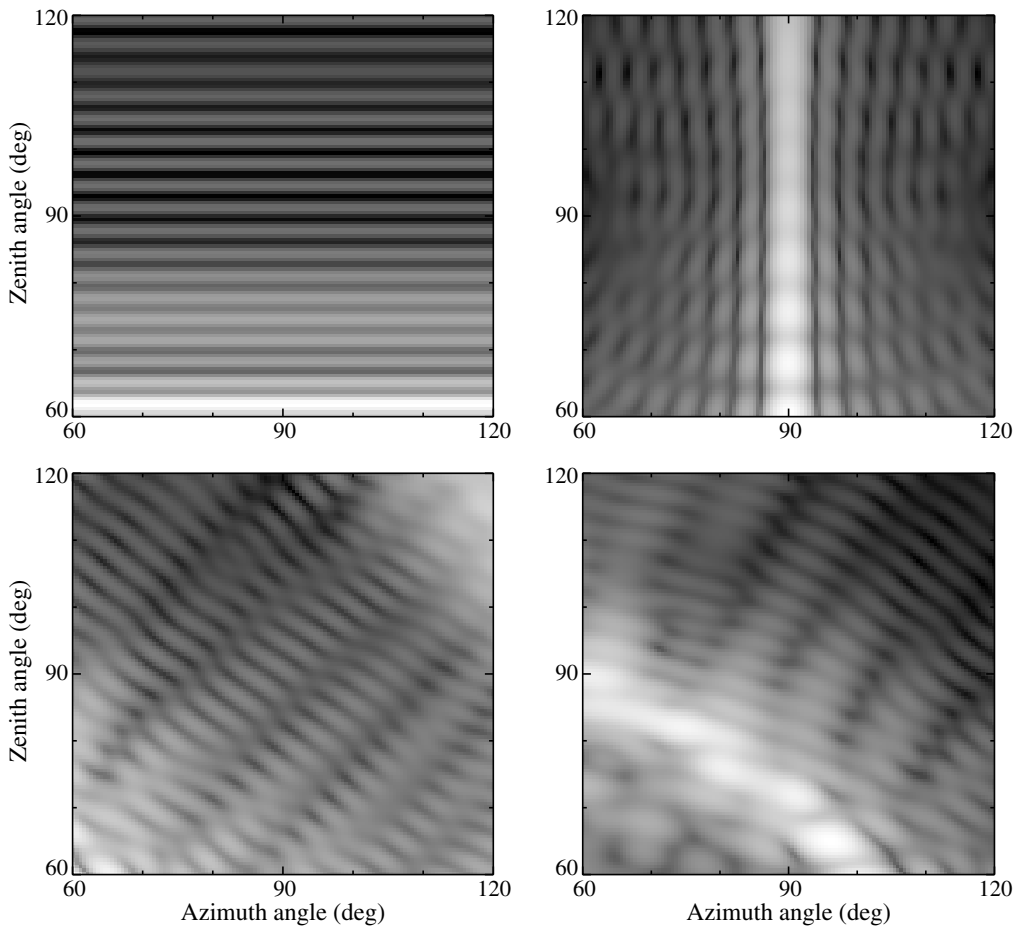

Figure 10.5. As in Fig. 10.3, but for cylinder surface-equivalent-sphere size parameter 40.

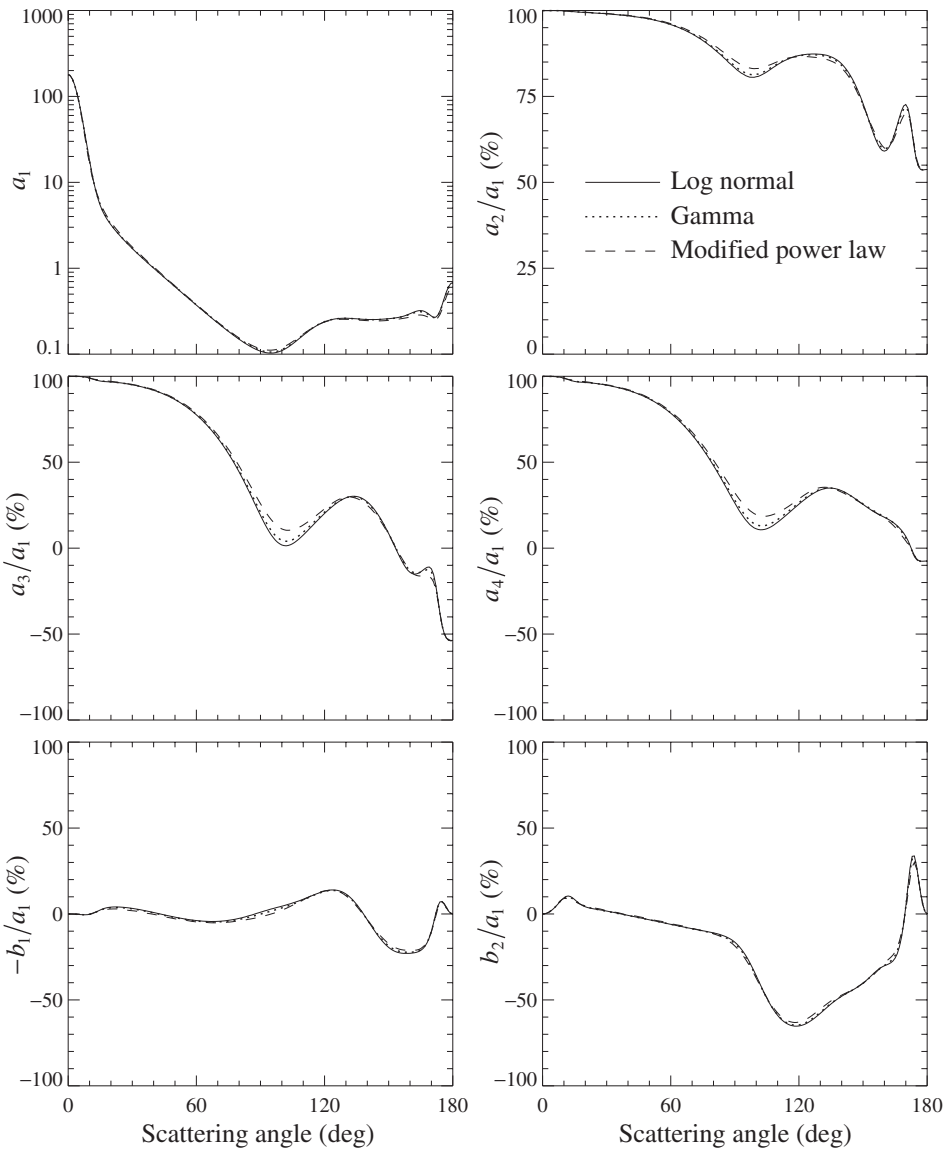

Figure 10.6. Elements of the normalized Stokes scattering matrix for log normal, gamma, and modified power law size distributions of randomly oriented oblate spheroids with an axis ratio $a/b = 1.6$. All three distributions of the surface-equivalent-sphere radii have the same effective radius $r_{\text{eff}} = 1.5\,\mu\text{m}$ and effective variance $v_{\text{eff}} = 0.1$. The power exponent of the modified power law size distribution is $\alpha = -3$. The relative refractive index is 1.53 + i0.008, and the wavelength of light in the surrounding medium is $0.6283\,\mu\text{m}$.

(1994c) showed that, in practice, many plausible size distributions of spherical and nonspherical particles can be adequately represented by just two parameters, viz., the effective radius and the effective variance, defined by Eqs. (5.248) and (5.249), respectively. This means that different size distributions that have the same values of r_{eff} and v_{eff} can be expected to have similar *dimensionless* scattering and absorption characteristics, as illustrated by Table 10.1 and Fig. 10.6. In this regard, the power

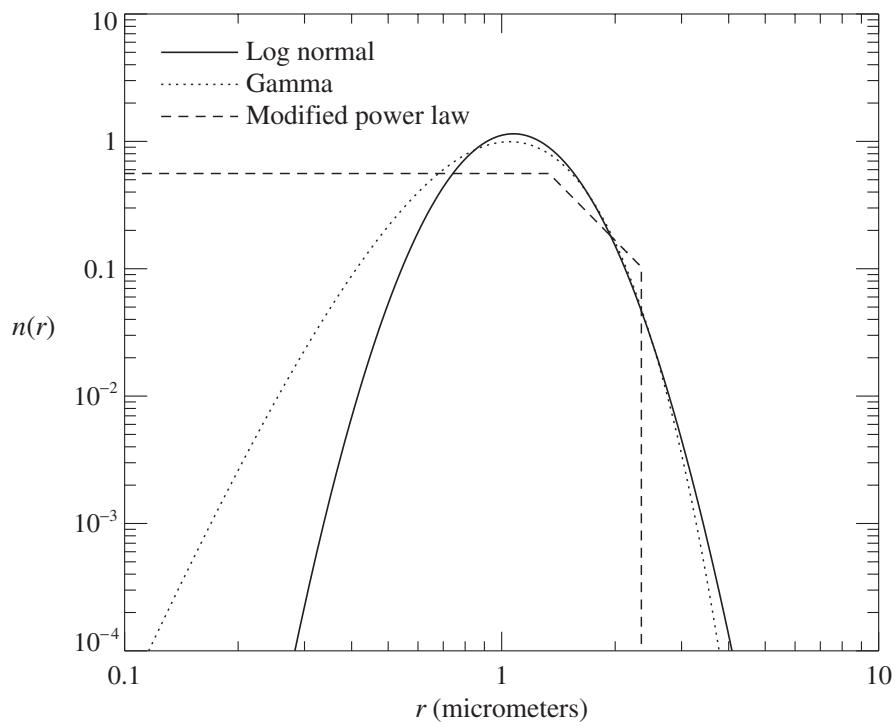

Figure 10.7. Log normal, gamma, and modified power law size distributions with $r_{\text{eff}} = 1.5\,\mu\text{m}$ and $v_{\text{eff}} = 0.1$. The power exponent of the modified power law size distribution is $\alpha = -3$.

and modified power law size distributions given by Eqs. (5.244) and (5.246) have the important practical advantage that their respective maximal radii $r_{\max} = r_2$ are finite by definition and can be significantly smaller than the corresponding convergent radii of the modified gamma, log normal, and gamma distributions with the same r_{eff} and v_{eff} (Fig. 10.7). Furthermore, the absence of a sharp cut-off at $r = r_1$ makes the scattering patterns generated by the modified power law distribution significantly smoother than those produced by the standard power law distribution. Hence, the majority of numerical results discussed in this and the following section have been computed using the modified power law size distribution. We used a fixed power exponent value of $\alpha = -3$ and determined the formal parameters of the size distribution, r_1 and r_2, from the system of equations (5.248), (5.249) for given values of the effective radius and effective variance. It is straightforward to show that for fixed α and v_{eff}, $r_1 = p_1 r_{\text{eff}}$ and $r_2 = p_2 r_{\text{eff}}$, where p_1 and p_2 are constant proportionality factors. The numerical values of these factors for a selection of v_{eff}-values are listed in Table 10.2.

Figures 10.8–10.11 show the phase function versus the scattering angle and the effective size parameter $x_{\text{eff}} = k_1 r_{\text{eff}}$ for polydisperse spheres and polydisperse, randomly oriented, surface-equivalent spheroids with $m = 1.53 + i0.008$, while the right-hand two columns of Plate 10.2 depict the ratio ρ of the phase function for spheroids

Table 10.2. Factors p_1 and p_2, for the modified power law distribution defined by Eq. (5.246) with $\alpha = -3$, as functions of v_{eff}

v_{eff}	p_1	p_2
0.1	0.89031	1.56538
0.2	0.61383	1.94912
0.4	0.37433	2.52160
1	0.11958	3.91046

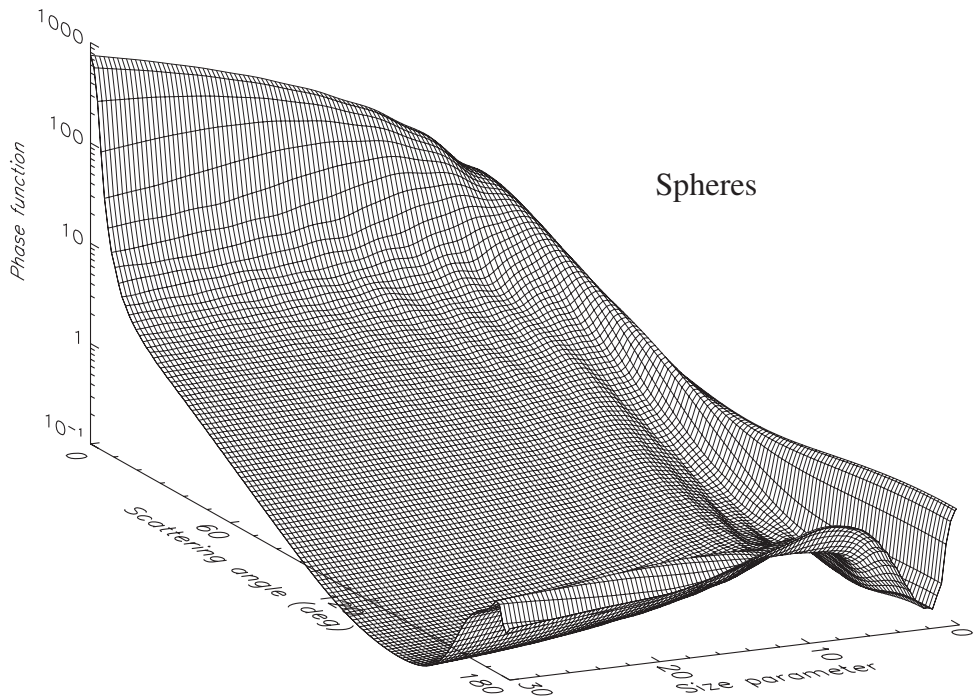

Figure 10.8. Phase function $a_1(\Theta)$ versus scattering angle and effective size parameter for the modified power law distribution of spheres with $\alpha = -3$ and $v_{\text{eff}} = 0.1$. The relative refractive index is 1.53 + i0.008.

to that for spheres. Note that the relative refractive index 1.53 + i0.008 is typical of dust-like and mineral terrestrial aerosols at visible wavelengths (d'Almeida *et al.* 1991). The 121 scattering angle gridlines in Figs. 10.8–10.11 are drawn at 1.5° intervals and correspond to scattering angles $\Theta = 0°, 1.5°, ..., 178.5°$, and 180°, while the 101 size parameter gridlines are drawn at 0.3 intervals and correspond to size parameters x_{eff} = 0, 0.3, …, 29.7, and 30. The residual small-amplitude ripple in Fig. 10.8 is caused by the cut-off at $r = r_2$ in Eq. (5.246) and is almost completely eliminated by averaging over spheroid orientations (Figs. 10.9–10.11).

It can be seen clearly that, excluding the region of Rayleigh scattering, five distinct ρ-value regions exist. In order of increasing scattering angle for both prolate and oblate spheroids they are:

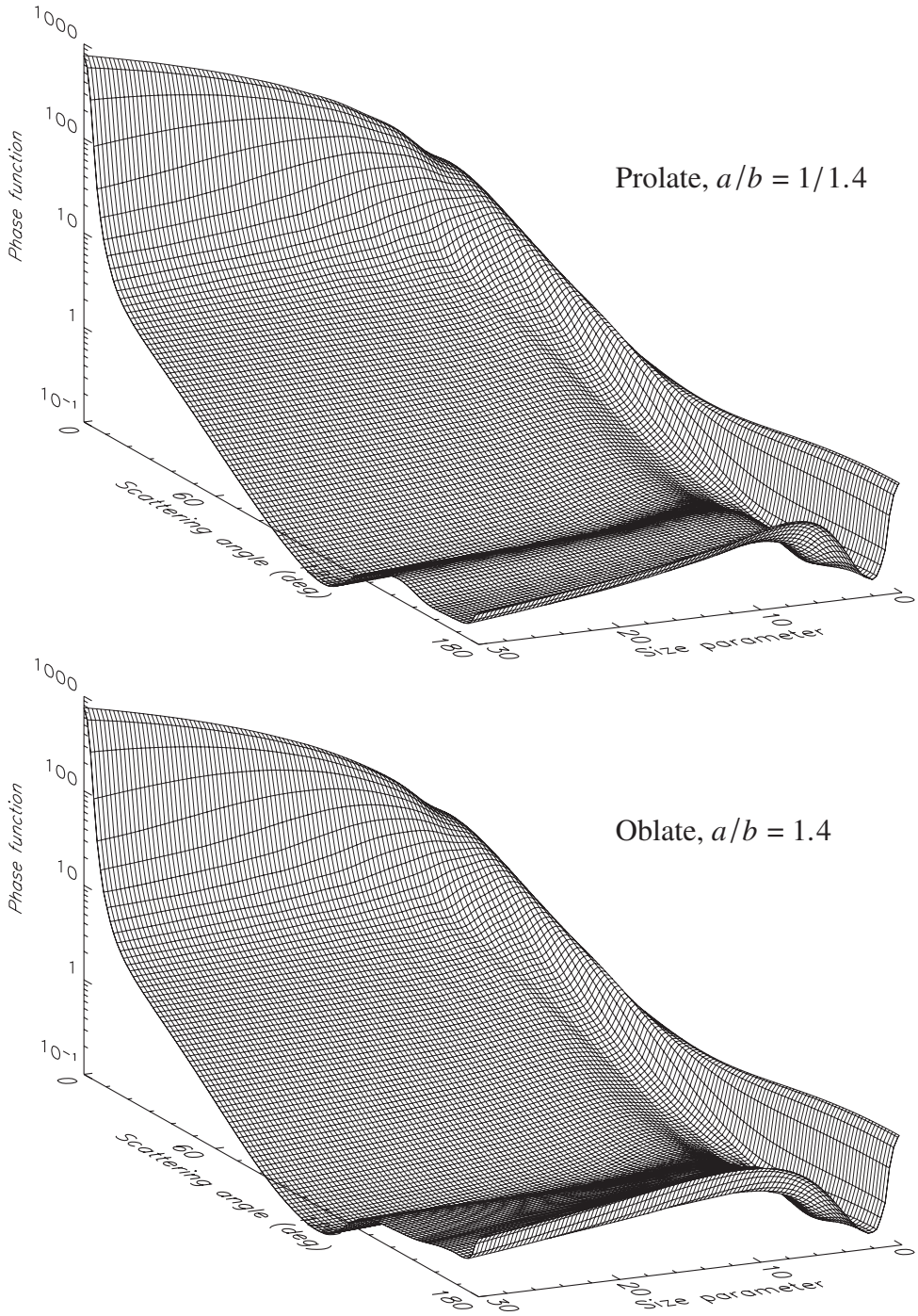

Figure 10.9. As in Fig. 10.8, but for surface-equivalent, randomly oriented prolate and oblate spheroids with aspect ratio 1.4.

(1) nonsphere ≈ sphere, i.e., $\rho \approx 1$; (2) nonsphere > sphere, i.e., $\rho > 1$;

(3) nonsphere < sphere, i.e., $\rho < 1$; (4) nonsphere ≫ sphere, i.e., $\rho \gg 1$; (10.1)

(5) nonsphere ≪ sphere i.e., $\rho \ll 1$.

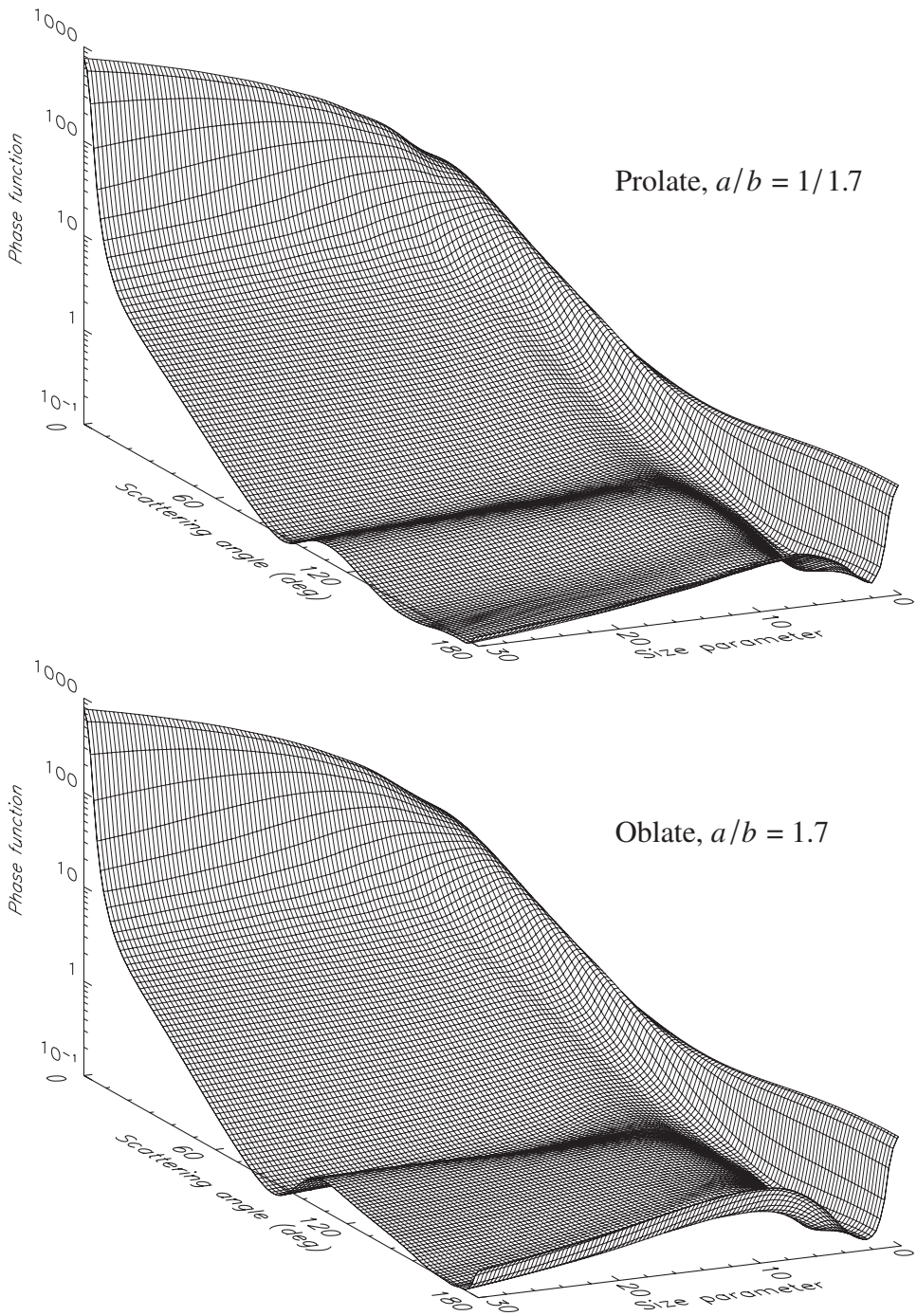

Figure 10.10. As in Fig. 10.8, but for surface-equivalent, randomly oriented prolate and oblate spheroids with aspect ratio 1.7.

The first of these regions is the region of nearly direct forward scattering. It is the region least sensitive to particle nonsphericity, because of the dominance of the diffraction contribution to the phase function; the latter is determined by the average area of the particle geometrical cross section (Section 7.4), which is the same for

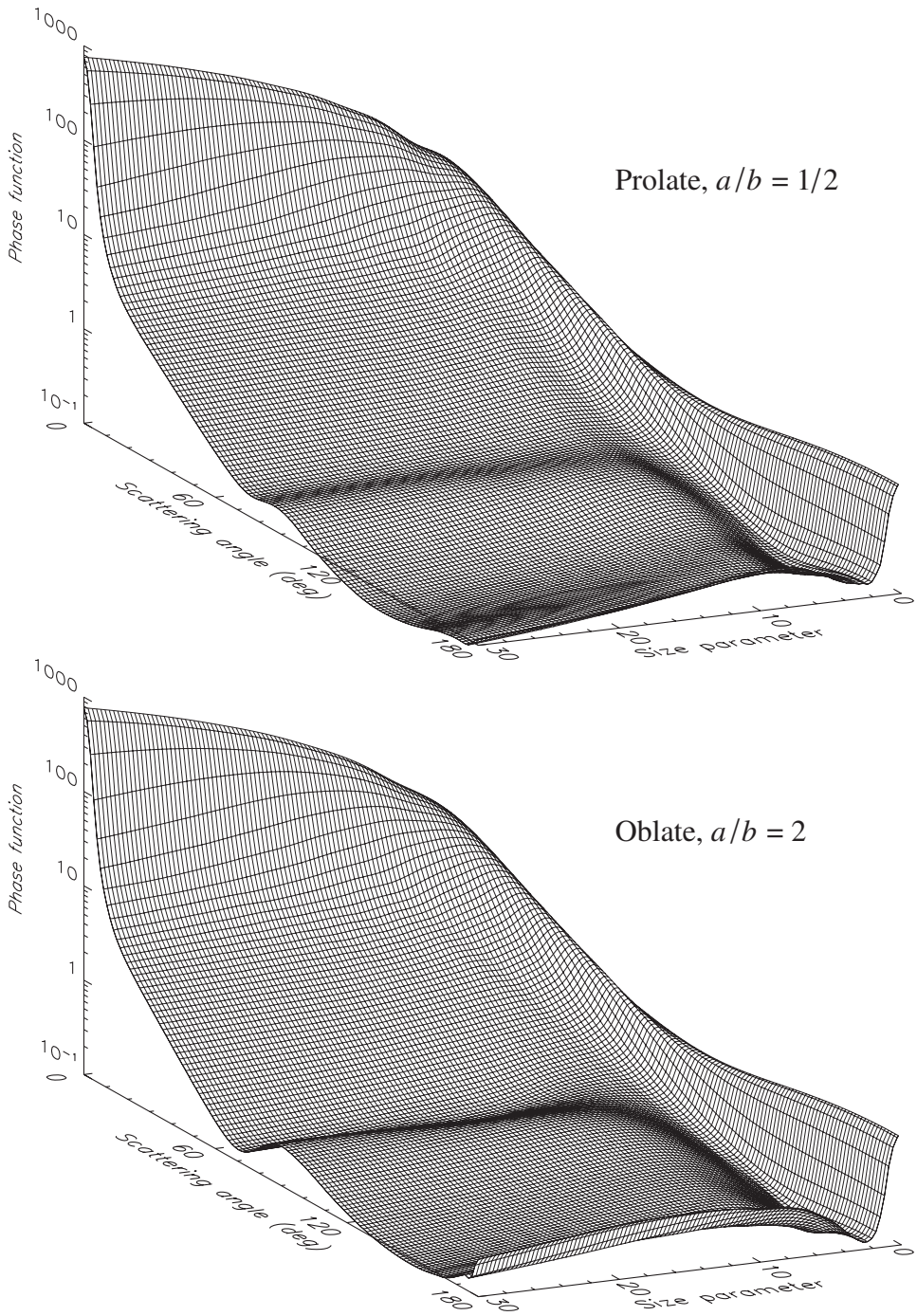

Figure 10.11. As in Fig. 10.8, but for surface-equivalent, randomly oriented prolate and oblate spheroids with aspect ratio 2.

surface-equivalent convex particles such as spheres and spheroids (Vouk 1948). The second region, $\rho > 1$, extends from about $5°$ to $30°$ and becomes more pronounced with increasing spheroid aspect ratio ε (i.e., the ratio of the larger to the smaller spheroid axes). Depending on aspect ratio, region 3, $\rho < 1$, extends from about $30° -$

$35°$ to $80°-110°$ and becomes narrower with increasing ε. In this region nonspherical–spherical differences are greater for oblate than for prolate spheroids with the same value of ε; the differences increase with increasing ε.

Region 4 extends from about $80°-110°$ to $150°-160°$ and is wider for particles with larger aspect ratios. In this region ρ can well exceed 4, indicating strongly enhanced side scattering as opposed to the deep and wide side-scattering minimum that is found for spherical particles (cf. Figs. 10.8–10.11). Both the left-hand boundary of this region and the position of maximum ρ-values shift towards smaller scattering angles with increasing ε. Interestingly, for prolate spheroids the maximum ρ-values are greater for the moderate aspect ratio 1.4 than for the larger aspect ratios 1.7 and 2.

In region 5, ρ can fall to values below 0.25, which means that another major effect of nonsphericity is to suppress the strong rainbow and glory features seen in calculations for surface-equivalent spheres (cf. Fig. 10.8). However, the backscattering enhancement traditionally associated with the glory survives as a rise of the backscattered intensity at $180°$ relative to that at $170°$. Furthermore, as evident from Figs. 10.8 and 10.9, oblate spheroids with aspect ratio 1.4 can have even greater phase-function values at $\Theta = 180°$ than surface-equivalent spheres, thereby producing ρ-values exceeding unity and causing an exception to the region-5 criterion $\rho \ll 1$. The top two panels of Fig. 10.12 also show that for most size parameters oblate spheroids have larger backscattering phase function values than prolate spheroids with the same aspect ratio and that the ratio of the nonspherical to spherical phase functions at $\Theta = 180°$ has a distinct minimum at effective-size-parameter values 6–9. Also worth noting is that, for prolate spheroids, region 5 becomes more pronounced with increasing ε whereas for oblate spheroids ρ can be smaller for ε = 1.7 than for ε = 2, at larger effective-size-parameter values.

A comparison of the polydisperse polarization diagrams for randomly oriented spheroids and for spheres (cf. the two columns on the left of Plate 10.2 and the top middle panel of Plate 10.6) reveals that, at scattering angles larger than $60°$, the degree of linear polarization for unpolarized incident light, $-b_1/a_1$, is strongly ε-dependent, the spherical–nonspherical differences becoming more pronounced with increasing ε; this indicates that the Lorenz–Mie theory is an inappropriate approximation for nonspherical particles in that region. However, at scattering angles less than $60°$ the linear polarization is weakly dependent on particle shape, thereby suggesting that polarization measurements at near-forward-scattering angles coupled with Lorenz–Mie computations are potentially useful for sizing nonspherical particles. In general, the polarization generated by spheroids is more neutral than that for spheres and shows less variability with size parameter and scattering angle. It is interesting, however, that the Rayleigh region extends to larger size parameters with increasing aspect ratio. The most prominent polarization feature for spheroids is the bridge of positive polarization near $120°$, which extends from the region of Rayleigh scattering and separates two regions of negative or neutral polarization at small and large scattering angles. This bridge is absent for spherical particles and near-spherical

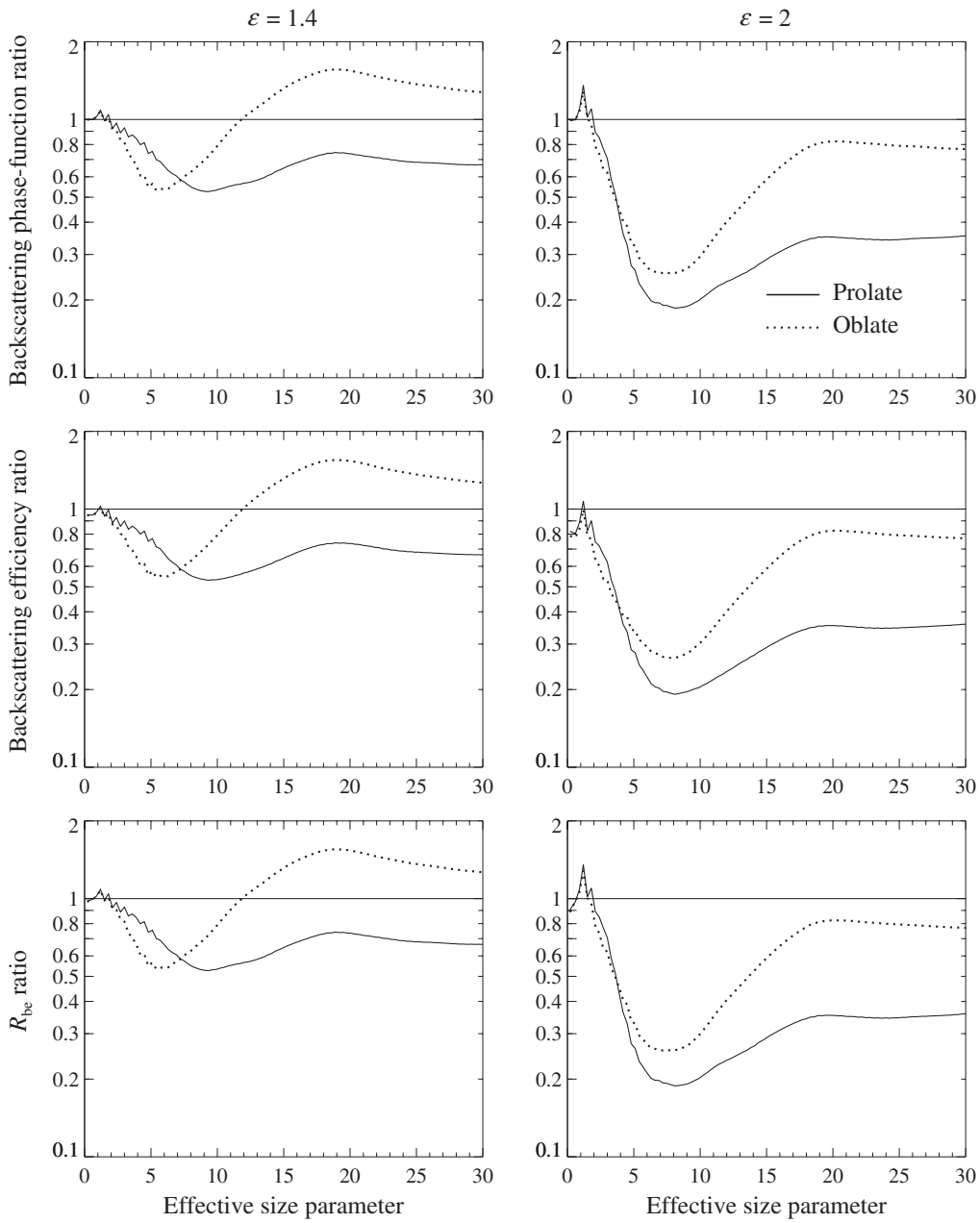

Figure 10.12. Top two panels: ratio of the phase function at $\Theta = 180°$ for randomly oriented polydisperse spheroids with aspect ratios of 1.4 and 2 to that for surface-equivalent spheres, versus effective size parameter. Middle two panels: as in the top panels, but for the ratio of the respective backscattering efficiency factors. Bottom two panels: as in the top panels, but for the ratio of the respective R_{be}-values. Curves are shown for prolate and for oblate spheroids.

spheroids, but develops fully for spheroids with ε - values greater than 1.6–1.7, being somewhat more pronounced for oblate than for prolate spheroids with the same ε (Mishchenko and Travis 1994b).

Whereas for spherical particles $a_2(\Theta)/a_1(\Theta) \equiv 1$, the two left-hand columns of

Plate 10.3 demonstrate that for spheroids this ratio can significantly deviate from unity, especially at side- and backscattering angles. The angular dependence of a_2/a_1 is quite different for prolate and oblate spheroids with the same ε-value, thereby making this ratio well suited for discriminating between elongated and flattened particles. For prolate spheroids, a_2/a_1 has a pronounced minimum centered at $120° - 145°$ which shifts towards smaller scattering angles as ε increases. Another minimum occurs at backscattering angles and, surprisingly, is deeper for the less aspherical spheroids, with ε = 1.4, than for the spheroids with ε = 1.7 and 2. Oblate spheroids exhibit a shallow minimum at around $150° - 170°$, which becomes more pronounced for particles with ε = 2, and another minimum at exactly the backscattering direction, $\Theta = 180°$, which exhibits a complicated dependence on ε. Also, oblate spheroids with ε = 1.4 show a shallow minimum at about $100° - 110°$, which disappears with increasing ε. For both prolate and oblate spheroids, the ratio a_2/a_1 at scattering angles less than $70°$ and in the region of Rayleigh scattering is close to unity and is essentially insensitive to particle size and shape.

For spherical particles the ratio $a_3(\Theta)/a_1(\Theta)$ is identically equal to the ratio $a_4(\Theta)/a_1(\Theta)$; these are shown in the top middle and right-hand panels of Plate 10.5. For spheroids, these two ratios can substantially differ from each other, the ratio a_4/a_1 being larger than a_3/a_1 for most effective size parameters and scattering angles (cf. the two right-hand columns of Plate 10.3 and the two left-hand columns of Plate 10.4). For spheres, the ratio a_3/a_1, and thus a_4/a_1 also, has two negative regions at side- and backscattering angles, separated by a narrow positive branch. With increasing ε, the side-scattering negative region shifts towards smaller scattering angles, weakens in magnitude, and ultimately disappears, while the backscattering negative region becomes wider, especially for prolate spheroids. The backscattering region of negative a_3/a_1 values is wider and deeper than that for a_4/a_1. Unlike the ratio a_3/a_1, the ratio a_4/a_1 can become positive at backscattering angles. Both a_3/a_1 and a_4/a_1 are rather strongly size- and ε-dependent and thus can be sensitive indicators of particle size and shape. In particular, the regions of negative a_3/a_1 and a_4/a_1 are wider and deeper for prolate than for oblate spheroids with the same ε-value. The size-parameter dependence of the ratio a_4/a_1 at backscattering angles is also rather different for prolate and oblate spheroids with the same ε-value.

The right-hand top panel of Plate 10.6 and the two right-hand columns of Plate 10.4 show that the general pattern of the sign of the ratio $b_2(\Theta)/a_1(\Theta)$ is the same for spheres and spheroids, with a broad side-scattering region of negative values separating two positive branches at small and large scattering angles. The forward-scattering region is especially aspect-ratio independent, which renders possible the use of the Lorenz–Mie theory at small scattering angles for sizing nonspherical particles. However, large variations in magnitude of the ratio b_2/a_1 with particle shape at side- and backscattering angles make it sensitive to particle nonsphericity and appreciably different for prolate and oblate spheroids of the same aspect ratio. In particular, with increasing ε the region of smallest b_2/a_1 values becomes more shallow and shifts

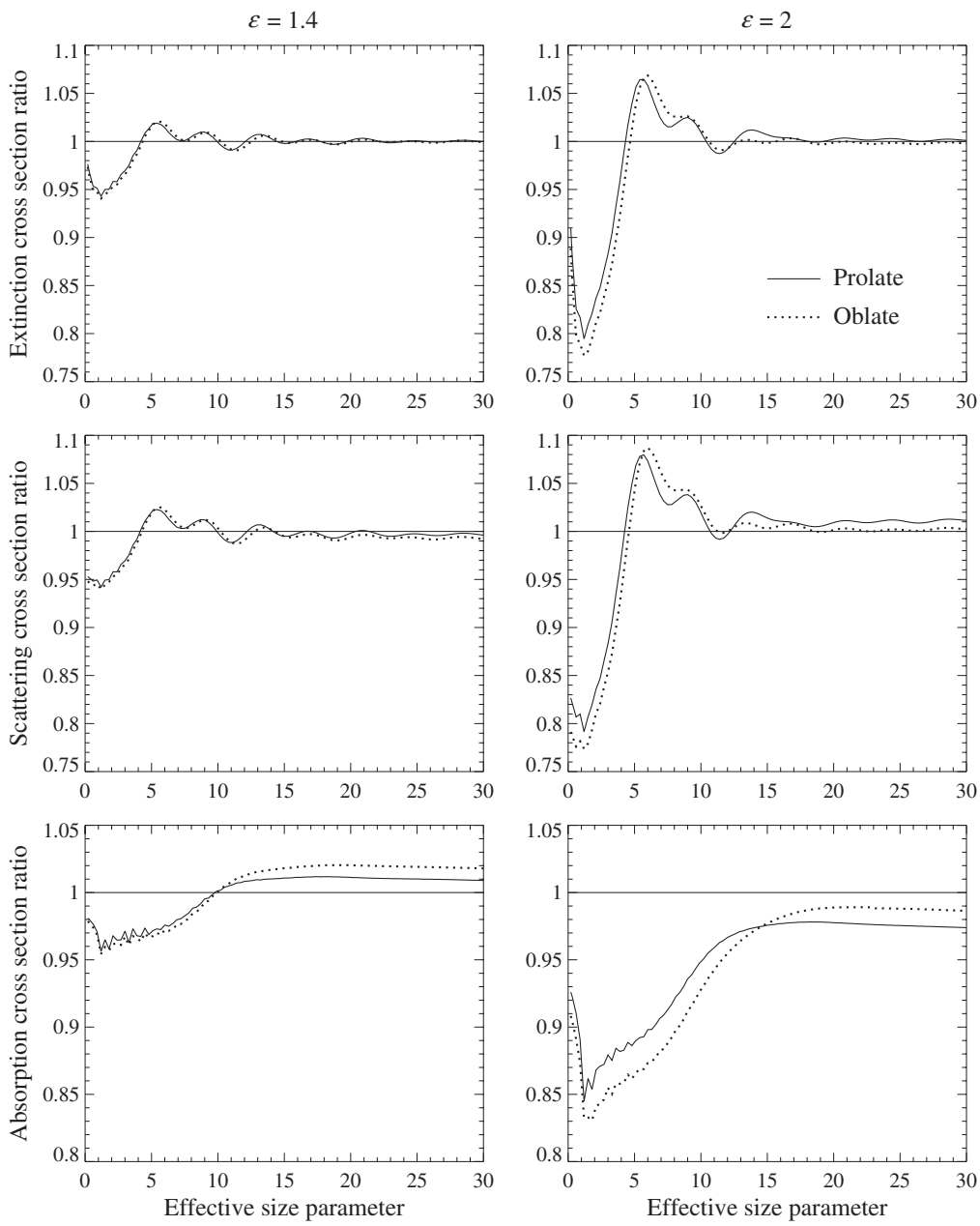

Figure 10.13. Top two panels: ratio of the extinction cross section for randomly oriented polydisperse spheroids with aspect ratios of 1.4 and 2 to that for surface-equivalent spheres, versus effective size parameter. Middle two panels: as in the top panels, but for the ratio of the respective scattering cross sections. Bottom two panels: as in the top panels, but for the ratio of the respective absorption cross sections. Curves are shown for prolate and for oblate spheroids.

towards smaller scattering angles, while the backscattering positive branch becomes less developed. The region of negative values is more shallow and the backscattering positive branch is much weaker for prolate than for oblate spheroids. In general, the differences between prolate spheroids and spheres are larger than those between ob-

late spheroids and spheres.

Unlike the elements of the scattering matrix, the integral photometric characteristics (the extinction, scattering, and absorption cross sections, the single-scattering albedo, and the asymmetry parameter) are much less dependent on particle shape, as Figs. 10.13 and 10.14 demonstrate. In most cases the nonspherical–spherical differences tend to decrease with increasing effective size parameter. For the optical cross sections and the single-scattering albedo, the differences are maximal at effective size parameters smaller than 5. The asymptotic geometrical optics limit, unity, for the extinction cross section ratio (cf. Section 7.4) is reached at relatively small size parameters of about 15. The nonspherical–spherical differences are especially small for the single-scattering albedo at size parameters exceeding unity. The curves for prolate and oblate spheroids with the same aspect ratio are very close to one another except for the asymmetry parameter, in which case the differences between the curves for prolate and oblate spheroids can be much larger than the differences between those for prolate spheroids and for spheres.

As discussed in Section 9.5, important backscattering characteristics widely used in radar and lidar applications are the backscattering efficiency factor Q_{b}, defined by Eqs. (9.10) and (9.14), and the backscatter-to-extinction ratio R_{be}, defined by Eq. (9.13). The four lower diagrams of Fig. 10.12 depict the ratios of these backscattering characteristics for randomly oriented polydisperse prolate and oblate spheroids to those for surface-equivalent spheres. Not surprisingly, these ratios differ from the backscattering-phase-function ratio (see the top two diagrams of Fig. 10.12) only at small size parameters, where the ratio of the scattering cross sections and the ratio of the single-scattering albedos for nonspherical and surface-equivalent spherical particles deviate noticeably from unity. It is seen that nonspherical–spherical differences in the backscattering efficiency factor and the backscatter-to-extinction ratio are quite significant, thus suggesting that shape effects should be explicitly taken into account in analyzing backscattering measurements for nonspherical particles. In general, spheroids are weaker backscatterers than surface-equivalent spheres, especially at size parameters from about 5 to 15. However, as we noted above, the curves for oblate spheroids with aspect ratio 1.4 illustrate that suppressed scattering at $\Theta = 180°$ is not a universal optical characteristic of nonspherical particles.

Two quantities that are traditionally considered unequivocal indicators of particle nonsphericity are the linear and circular backscattering depolarization ratios, δ_{L} and δ_{C}, defined as

$$\delta_{\mathrm{L}} = \frac{a_1(180°) - a_2(180°)}{a_1(180°) + a_2(180°)} \geq 0, \tag{10.2}$$

$$\delta_{\mathrm{C}} = \frac{a_1(180°) + a_4(180°)}{a_1(180°) - a_4(180°)} \geq 0 \tag{10.3}$$

(see Eqs. (4.55) and (4.56)). For macroscopically isotropic and mirror-symmetric media these ratios are not independent, because Eq. (4.63) yields

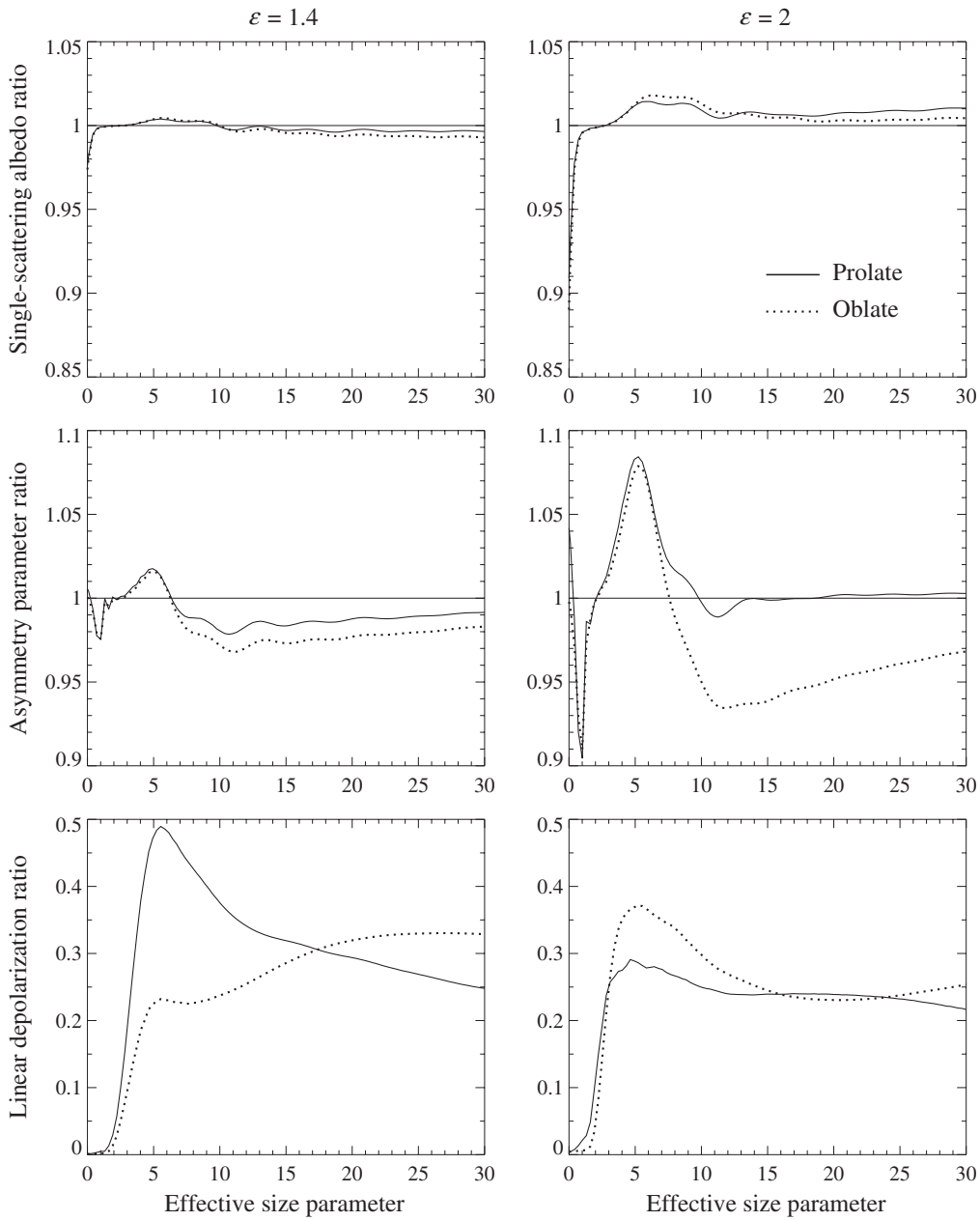

Figure 10.14. Top two panels: ratio of the single-scattering albedo for randomly oriented polydisperse spheroids with aspect ratios of 1.4 and 2 to that for surface-equivalent spheres, versus effective size parameter. Middle two panels: as in the top panels, but for the ratio of the respective asymmetry parameters. Bottom two panels: linear backscattering depolarization ratio for randomly oriented polydisperse spheroids with aspect ratios of 1.4 and 2 versus effective size parameter. Curves are shown for prolate and for oblate spheroids.

$$\delta_{\mathrm{C}} = \frac{2\delta_{\mathrm{L}}}{1-\delta_{\mathrm{L}}} \tag{10.4}$$

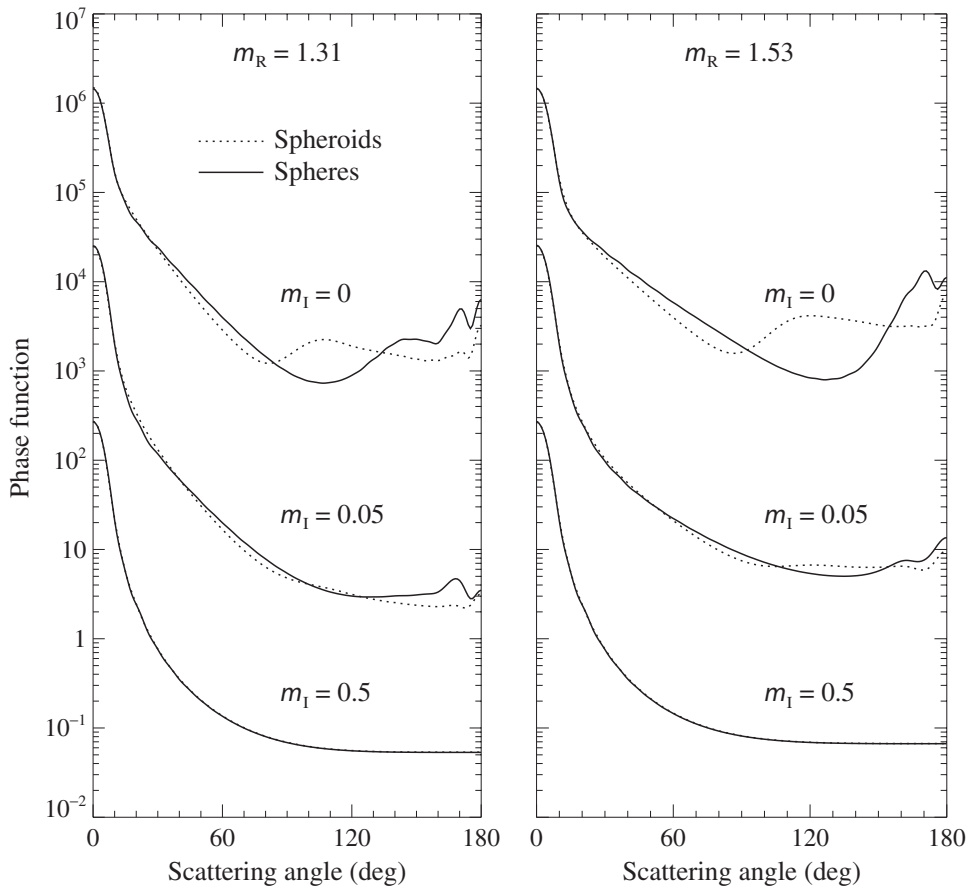

Figure 10.15. Phase function a_1 versus scattering angle Θ for polydisperse, randomly oriented oblate spheroids with an axis ratio 1.7 and for surface-equivalent spheres. The results are shown for two values of the real part of the relative refractive index ($m_R = 1.31$ and 1.53) and three values of the imaginary part ($m_I = 0$, 0.05, and 0.5). The size distribution is given by Eq. (5.246) with $\alpha = -3$ and $v_{eff} = 0.1$. The effective size parameter is $x_{eff} = 15$. The vertical axis scale applies to the curves with $m_I = 0.5$, the other curves being successively displaced upward by a factor of 100.

(Mishchenko and Hovenier 1995). For spheres, both ratios vanish since $a_2(180°) = a_1(180°)$ and $a_4(180°) = -a_1(180°)$ (see Eqs. (4.65) and (4.66)). For nonspherical particles these equalities do not generally hold, thus causing non-zero backscattering depolarization ratios. The bottom two diagrams in Fig. 10.14 show the linear depolarization ratio computed for randomly oriented polydisperse spheroids. It is seen that for both prolate and oblate spheroids δ_L can deviate substantially from zero, thus illustrating its use as an indicator of nonsphericity. However, the depolarization ratios cannot be considered an unambiguous measure of the degree of the departure of the particle shape from that of a sphere. Indeed, for prolate spheroids with $\varepsilon = 1.4$ the maximal δ_L-value is significantly larger than that for $\varepsilon = 2$. We will see later that even larger δ_L-values can be produced by spheroids with aspect ratios as small as 1.05.

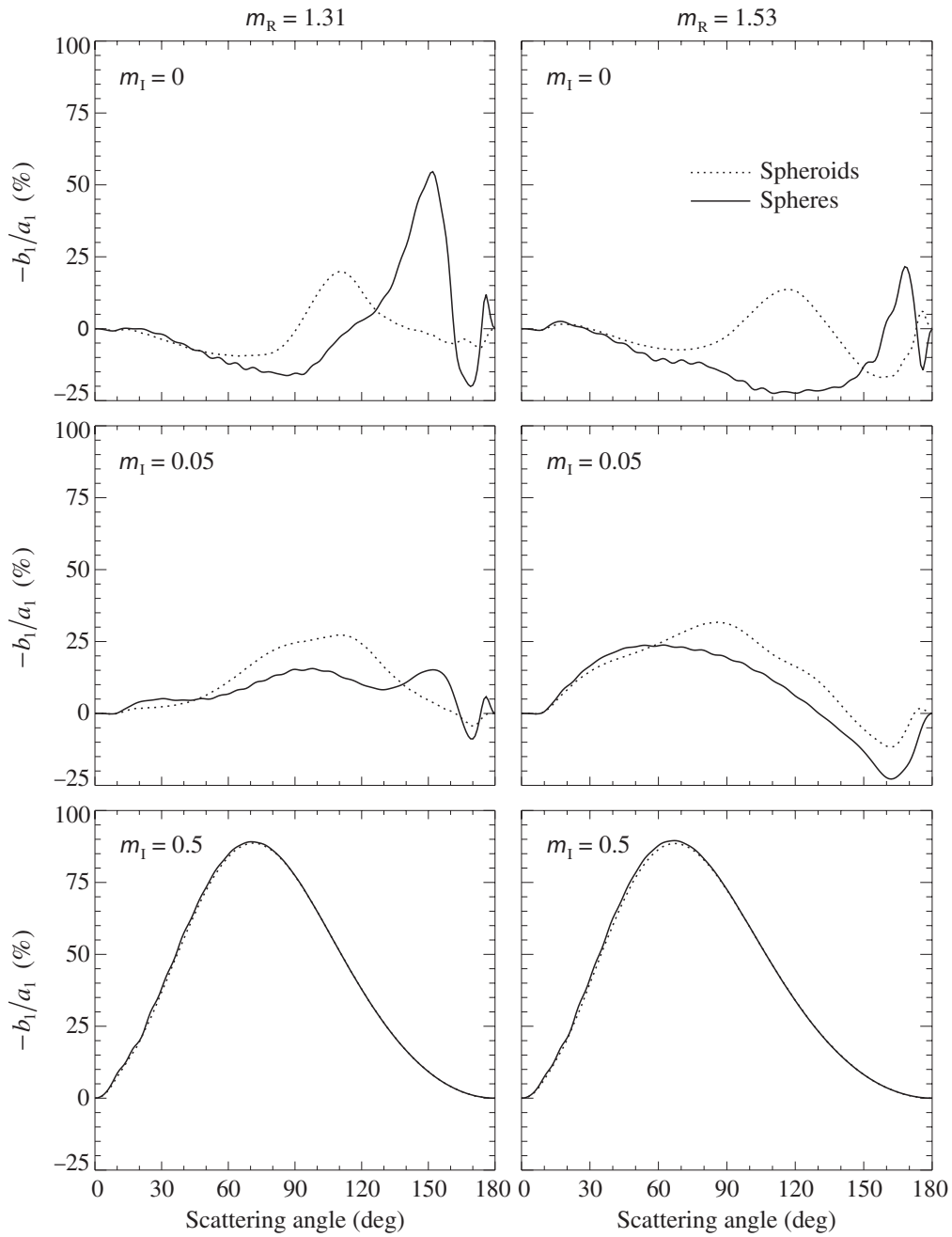

Figure 10.16. As in Fig. 10.15, but for the ratio $-b_1/a_1$.

Figures 10.15 and 10.16 show that with increasing imaginary part of the relative refractive index, nonspherical–spherical differences weaken and ultimately disappear (Mishchenko and Travis 1994b; Mishchenko *et al.* 1997a). For these particle distributions with effective size parameter of $x_{\text{eff}} = 15$, the scattering patterns with $m_I = 0.5$ are dominated by diffraction and external reflections and are essentially the same for spheres and surface-equivalent randomly oriented spheroids. This example

illustrates the general theorem formulated by van de Hulst (1957, Section 8.42): the scattering pattern caused by external reflection from very large convex particles with random orientation is identical to that caused by external reflection from a very large sphere composed of the same material.

10.3 Randomly oriented, polydisperse circular cylinders with moderate aspect ratios

Another class of rotationally symmetric nonspherical particles that can be efficiently studied using the *T*-matrix method are finite circular cylinders. Unlike spheroids, the surface of finite cylinders is not completely smooth but, rather, is characterized by sharp, rectangular edges. These edges make cylinders less regular nonspherical particles than spheroids and might well be expected to have an effect on the scattering and absorption characteristics (Kuik *et al.* 1994; Mishchenko *et al.* 1996a).

For spheroids, nonspherical–spherical differences in all scattering and absorption characteristics vanish as the axis ratio becomes unity, since spheroids with axis ratio unity are spherical particles. Circular cylinders with diameter-to-length ratio unity are, however, already nonspherical particles with a shape deviating significantly from that of a sphere (the ratio of the largest to the smallest cylinder dimension equals $2^{1/2} \approx 1.414$). Accordingly, Figs. 10.17–10.21 show that nonspherical–spherical differences in the extinction, scattering, and absorption cross sections, the single-scattering albedo, and the asymmetry parameter between cylinders with $D/L = 1$ and spheres are already significant. Furthermore, the differences in C_{ext}, C_{sca}, and $\langle \cos\Theta \rangle$ do not necessarily increase with increasing cylinder aspect ratio. In fact, at effective size parameters larger than approximately 7, nonspherical–spherical differences in the extinction and scattering cross sections and in the asymmetry parameter are smaller for prolate cylinders with $D/L = 1/2$ than for more compact cylinders with $D/L = 1,\ 1/1.4$, and 1.4. However, nonspherical–spherical differences in the absorption cross section and single-scattering albedo do increase with increasing aspect ratio. The absorption cross section systematically decreases with increasing ε, as is the case for spheroids, whereas ϖ and $\langle \cos\Theta \rangle$ increase with increasing ε at effective size parameters larger than 3. The maximum nonspherical–spherical differences in the integral photometric characteristics for cylinders occur at effective size parameters smaller than about 5, which resembles the case for spheroids (cf. Section 10.2). Similarly, at effective size parameters larger than about 10 the differences in the integral photometric characteristics become relatively small. However, the magnitude of the nonspherical–spherical differences for cylinders can be noticeably larger than that for axis-ratio-equivalent spheroids.

The backscattered fraction for isotropically incident radiation, $\overline{\beta}$, is defined as

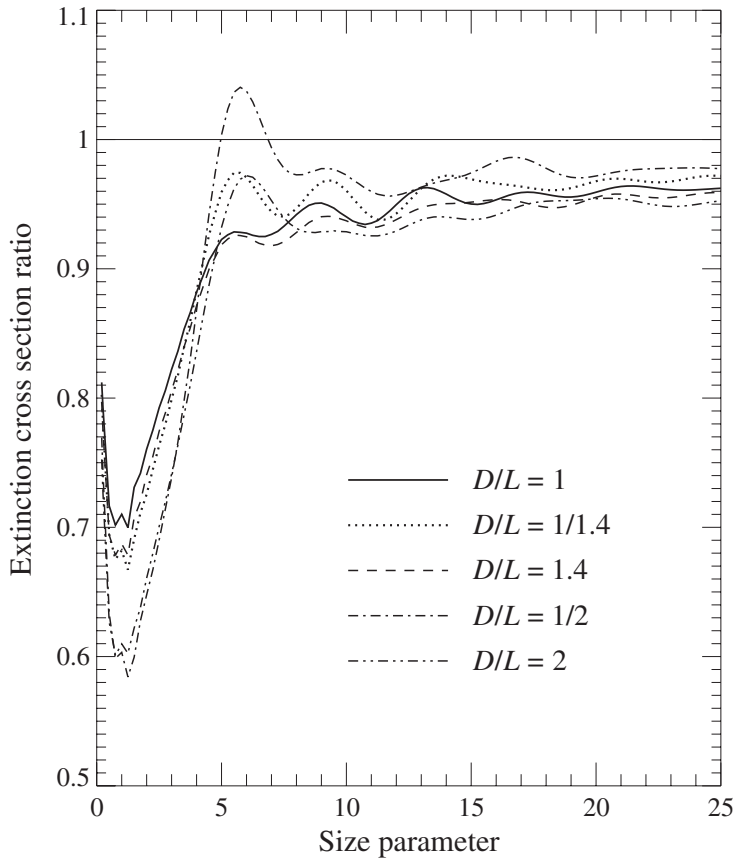

Figure 10.17. Ratio of the extinction cross section for randomly oriented, polydisperse cylinders to that for surface-equivalent spheres, versus effective size parameter; $D/L = 1,\ 1/1.4,\ 1.4,\ 1/2,$ and 2. The distribution of surface-equivalent-sphere radii is given by Eq. (5.246) with $\alpha = -3$ and $v_{\text{eff}} = 0.1$. The relative refractive index is 1.53 + i0.008.

$$\overline{\beta} = \frac{1}{2\pi} \int_0^{\pi} \mathrm{d}\Theta\, a_1(\Theta)\, \Theta \sin\Theta \tag{10.5}$$

(Coakley and Chýlek 1975; Wiscombe and Grams 1976). This quantity enters the two-stream approximation to the scalar radiative transfer equation for plane-parallel media and is sometimes used to estimate experimentally the asymmetry parameter of the phase function (Marshall *et al.* 1995). Figure 10.22 shows the ratio $\overline{\beta}(\text{cylinders})/\overline{\beta}(\text{spheres})$ as a function of x_{eff} and reveals that nonspherical–spherical differences in the backscattered fraction are relatively small. Interestingly, the asymmetry parameter and the backscattered fraction ratios depicted in Figs. 10.21 and 10.22 are approximately mirror images of one another with respect to the horizontal line at the level unity, so that for each size parameter, the larger the asymmetry parameter ratio the smaller the backscattered fraction ratio. This relationship was first found by Mugnai and Wiscombe (1986) in their *T*-matrix computations for randomly oriented Chebyshev particles and then by Mishchenko *et al.* (1997a) in computations

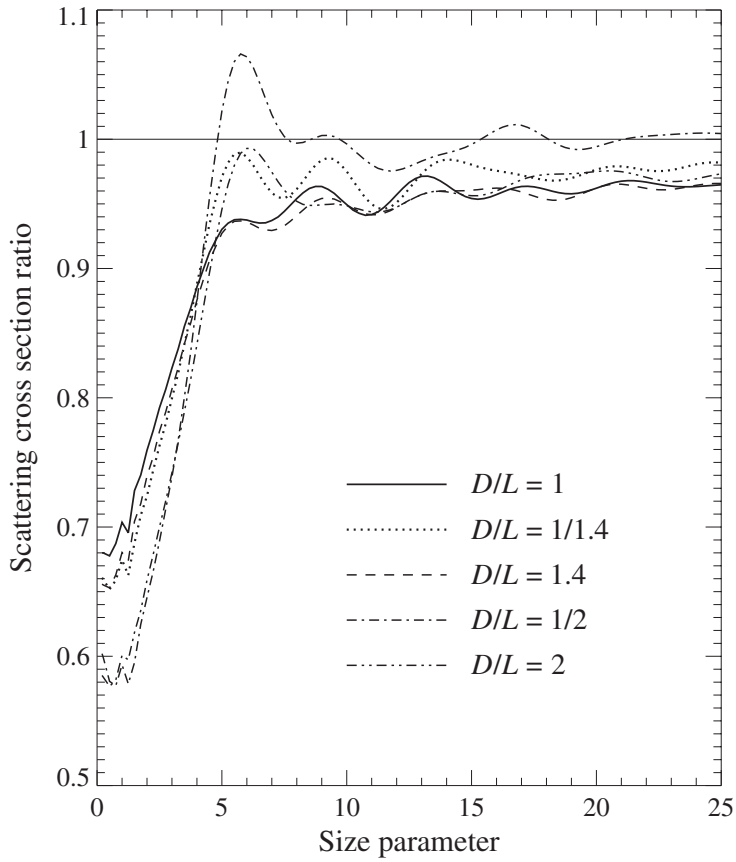

Figure 10.18. As in Fig. 10.17, but for the scattering cross section ratio.

for polydisperse, randomly oriented spheroids.

Plate 10.5 (left-hand column, three lower diagrams) shows that the pattern of the ratio ρ of the phase function for polydisperse, randomly oriented cylinders to that for surface-equivalent spheres, as a function of effective size parameter and scattering angle, strikingly resembles that for spheroids and spheres and shows, for size parameters $\gtrsim 5$, the same five distinct ρ - regions in order of increasing scattering angle (see Eq. (10.1)). The only significant difference between the ρ - patterns for spheroids and cylinders is the noticeably weak dependence of the ρ - pattern for cylinders on the aspect ratio. This means that for cylinders the boundaries of the five regions remain essentially fixed as the diameter-to-length ratio varies; for spheroids, however, the boundaries move substantially with axis ratio.

Region 1, where $\rho \approx 1$, is the region of exact or nearly exact forward scattering, dominated by diffraction. Region 2, where $\rho > 1$, is the region of near-forward scattering and becomes more pronounced with increasing asphericity for both prolate and oblate cylinders, thus resembling the case for spheroids. The third region, where $\rho < 1$, extends from about $20°$ to about $70°$ and is more pronounced for oblate than for prolate cylinders, again in agreement with computations for prolate versus oblate spheroids. Region 4 is the region of side scattering and extends from about $75°$ to

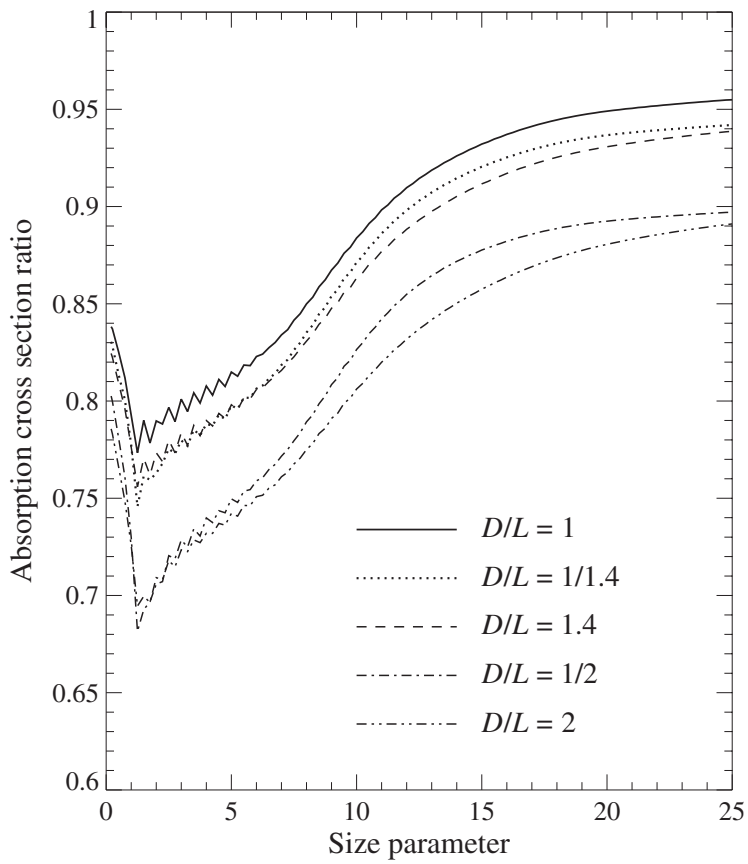

Figure 10.19. As in Fig. 10.17, but for the absorption cross section ratio.

about 155°. Here ρ can exceed 2.5. Although this value is smaller than that for surface-equivalent spheroids, for which ρ can exceed 4, it nonetheless indicates a strongly enhanced side-scattering, as opposed to the wide and deep side-scattering minimum in the phase function for spherical particles (cf. Fig. 10.23). Finally, region 5 is the region of near-backward scattering, where ρ - values as small as 0.3 demonstrate again how nonsphericity can suppress the glory and rainbow features prominent in the phase function for spherical particles. Computations indicate, however, that cylinders with effective size parameters larger than 16 can have larger phase function values at exactly the backscattering direction than surface-equivalent spheres. This is illustrated well in Fig. 10.24, which shows the ratio of the phase function at $\Theta = 180°$ for cylinders to that for surface-equivalent spheres. The only exception among these cases is that of oblate cylinders with a diameter-to-length ratio 2. Since this enhanced scattering at $\Theta = 180°$ for cylinders occurs at relatively larger size parameters, it might be explained using geometrical optics considerations, specifically, in terms of double internal reflections from mutually perpendicular facets (see Section 10.6). We should recall, however, that oblate spheroids with aspect ratios less than about 1.4 and effective size parameters larger than about 12 can also produce greater backscattering phase-function values than surface-equivalent spheres (cf. Plate 10.2(h)).

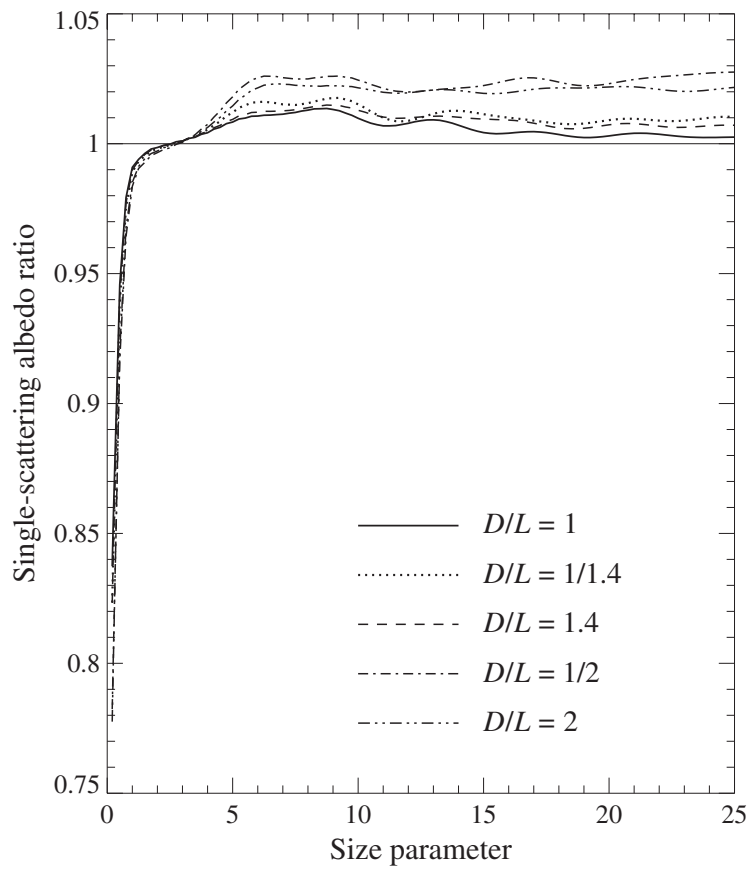

Figure 10.20. As in Fig. 10.17, but for the single-scattering albedo ratio.

Figure 10.25 demonstrates that the backscatter-to-extinction ratio is also strongly shape dependent, so that the ratio $R_{\mathrm{be}}(\text{cylinders})/R_{\mathrm{be}}(\text{spheres})$ can be either much larger or much smaller than unity. Again, these results as well as those for spheroids strongly suggest that the effect of particle shape should be taken into account explicitly in analyzing radar and lidar measurements for nonspherical particles. As was pointed out in Chapter 8, laboratory measurements of light scattering at exactly the backscattering direction can be rather difficult, thereby enhancing the value of rigorous theoretical computations of nonspherical–spherical differences.

For spheroids with $\varepsilon = 1$, i.e., for spheres, the ratio a_2/a_1 is identically equal to unity. Cylinders with $D/L = 1$ are already nonspherical particles and show a significant deviation of a_2/a_1 from unity (Plate 10.6, left-hand column). For the cylinders with $D/L = 1/2, 1/1.4, 1,$ 1.4, and 2 the patterns of the ratio a_2/a_1 as a function of effective size parameter and scattering angle are qualitatively similar, showing side- and back-scattering minima separated by a vertical bridge of larger values centered at around 170°. However, the depths of the minima depend on D/L. The side-scattering minimum is deeper for compact $(D/L = 1)$ and prolate $(D/L < 1)$ cylinders, whereas the depth of the back-scattering minimum increases with increasing aspect ratio. The ratio a_2/a_1 for spheroids also shows a distinct backscattering

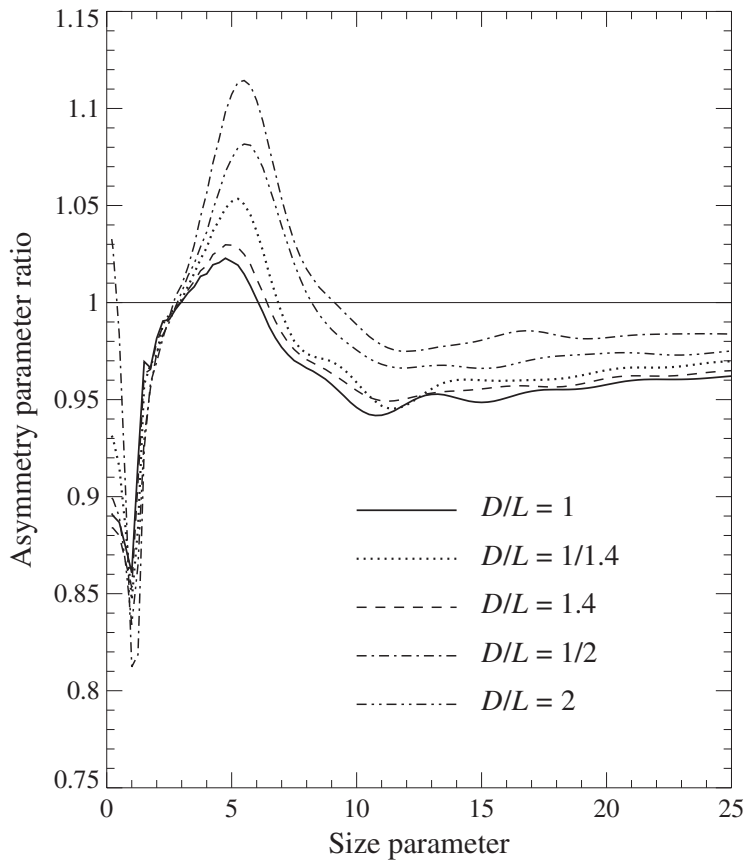

Figure 10.21. As in Fig. 10.17, but for the asymmetry parameter ratio.

minimum. However, unlike the case for cylinders, this minimum becomes significantly deeper as the ε-value for prolate spheroids decreases from 2 to 1.4. As for spheroids, the ratio a_2/a_1 for cylinders is nearly shape independent and close to unity at scattering angles smaller than $90°$ and/or at effective size parameters smaller than 2. In general, cylinders show less variability of this ratio with shape than surface-equivalent spheroids.

Plate 10.5 shows that the narrow positive branch separating the side- and backscattering negative regions in the ratios a_3/a_1 and a_4/a_1 for spheres is already absent for the least aspherical cylinders, with $D/L = 1$, and that the shape dependence of both ratios for cylinders is rather weak. As for the case of spheroids, the region of negative a_3/a_1 values is wider and deeper than that for a_4/a_1. For most scattering angles and size parameters a_4/a_1 is larger than a_3/a_1. Also, unlike the ratio a_3/a_1, the ratio a_4/a_1 can be positive at backscattering angles. However, the shape dependence of the backscattering region of positive a_4/a_1 values may represent a noticeable difference between cylinders and spheroids. Specifically, for cylinders this region becomes more pronounced with increasing ε, whereas for prolate spheroids it can become significantly weaker.

As discussed in the preceding section, the most remarkable feature of the linear

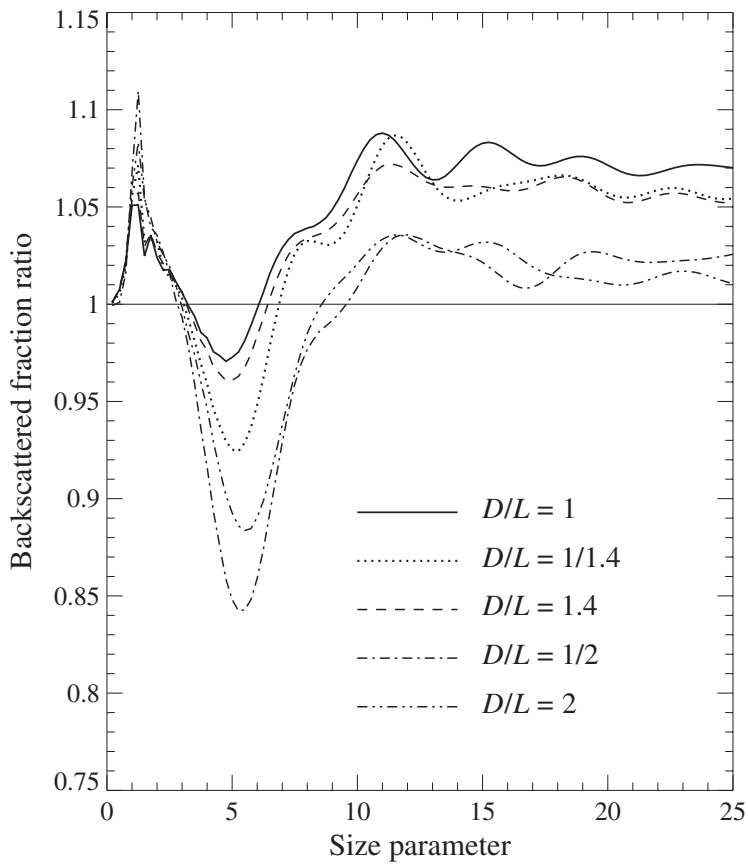

Figure 10.22. As in Fig. 10.17, but for the backscattered fraction ratio.

polarization for polydisperse, randomly oriented spheroids is a bridge of positive polarization at scattering angles near 120° extending upwards from the region of Rayleigh scattering. This bridge was observed by Perry *et al.* (1978) in laboratory measurements of light scattering by narrow size distributions of nearly cubical NaCl particles with mean size parameters ranging from 3.1 to 19.9. Positive polarization at side-scattering angles was also found in laboratory measurements by Sassen and Liou (1979) for platelike ice crystals and in measurements by Kuik (1992) for irregular quartz grains (see also Section 10.7). Plate 10.6 (middle column) shows that randomly oriented polydisperse cylinders do not produce as pronounced a bridge of positive polarization as that found for spheroids. Instead, prolate and oblate cylinders with $D/L = 1/2$ and 2 produce what can be called a bridge of neutral polarization at about the same scattering angles, whereas the axis-ratio-equivalent spheroids produce a bridge of weak but distinctly positive polarization (Plates 10.2(e), (f)). As for spheroids, one of the effects of increasing aspect ratio for cylinders is to make the overall polarization pattern more neutral and featureless. Another common effect of increasing asphericity is to extend the region of Rayleigh polarization to larger size parameters (Section 10.4).

As we have seen previously, the general pattern of the sign of the ratio b_2/a_1 is

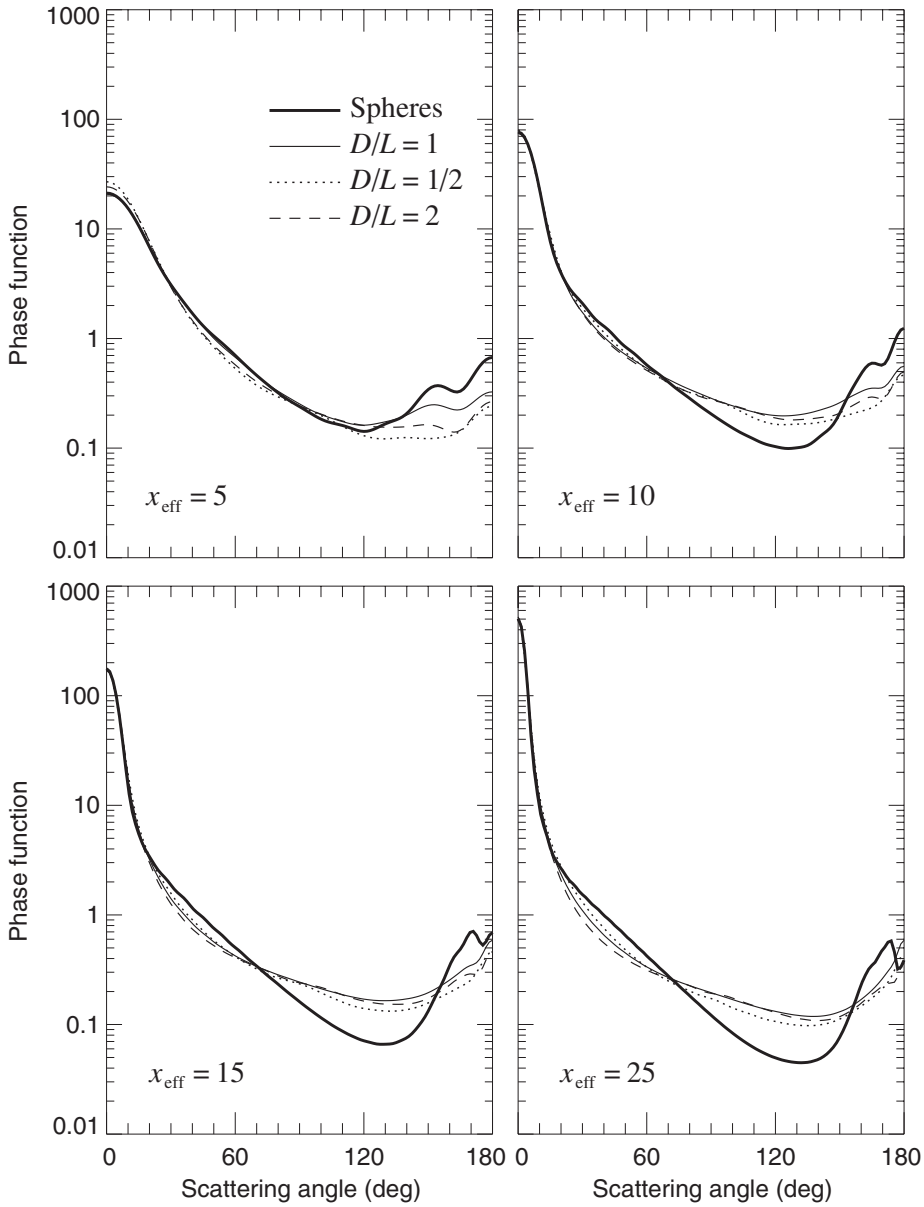

Figure 10.23. Phase function versus scattering angle for polydisperse, randomly oriented cylinders and surface-equivalent spheres with effective size parameters x_{eff} = 5, 10, 15, and 25.

the same for spheres and spheroids, with a broad side-scattering region of negative values separating two positive branches at small and large scattering angles. Plate 10.6 (right-hand column) suggests that this general pattern is also typical of polydisperse, randomly oriented cylinders. However, cylinders show less variability of the ratio b_2/a_1 with particle shape than spheroids. The forward-scattering region seems to be especially shape independent, thus rendering possible the use of the Lorenz–Mie theory at small scattering angles for sizing nonspherical particles. This conclusion is

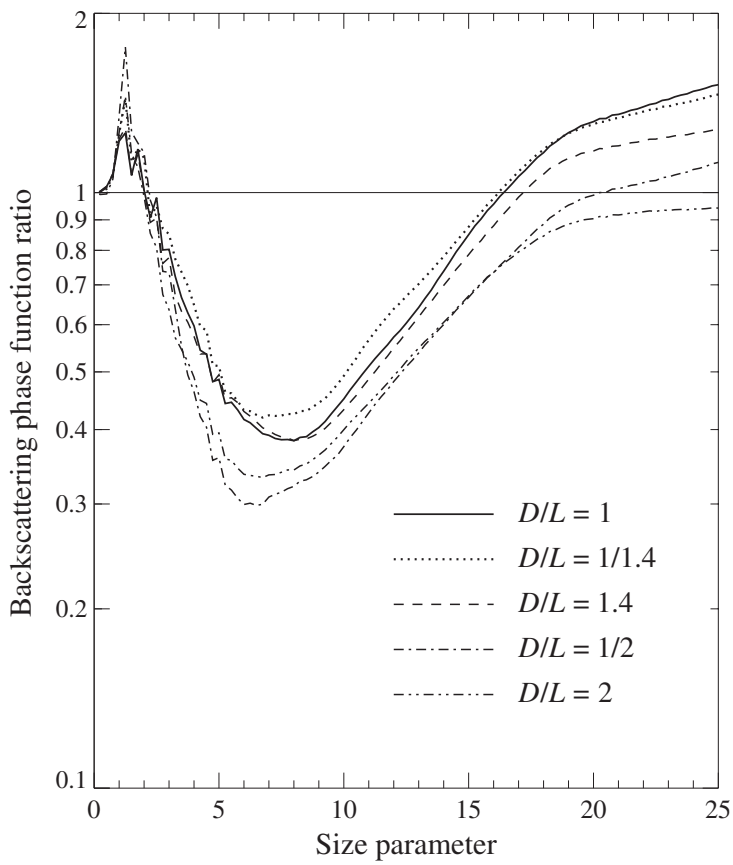

Figure 10.24. As in Fig. 10.17, but for the ratio of the phase function values at $\Theta = 180°$.

in full agreement with the above-mentioned laboratory measurements by Perry *et al.* (1978) for wavelength-sized salt particles.

Figures 10.26 and 10.27 show linear and circular backscattering depolarization ratios computed for randomly oriented polydisperse cylinders. As was the case for spheroids, both ratios for cylinders deviate substantially from zero, thus illustrating their usefulness as indicators of nonsphericity. Similarly, large and even maximal depolarization values can be reached at size parameters smaller than 6, i.e., for particles with equivalent-sphere radii smaller than the wavelength of the incident light.

10.4 Randomly oriented spheroids and circular cylinders with extreme aspect ratios

It turns out that wavelength-sized spheroids and cylinders with extreme aspect ratios may have scattering properties dramatically different from those of moderately aspherical particles. We begin by discussing the results of *T*-matrix calculations for the following five particle shapes: spheres, prolate spheroids with axis ratios $a/b = 1/2$

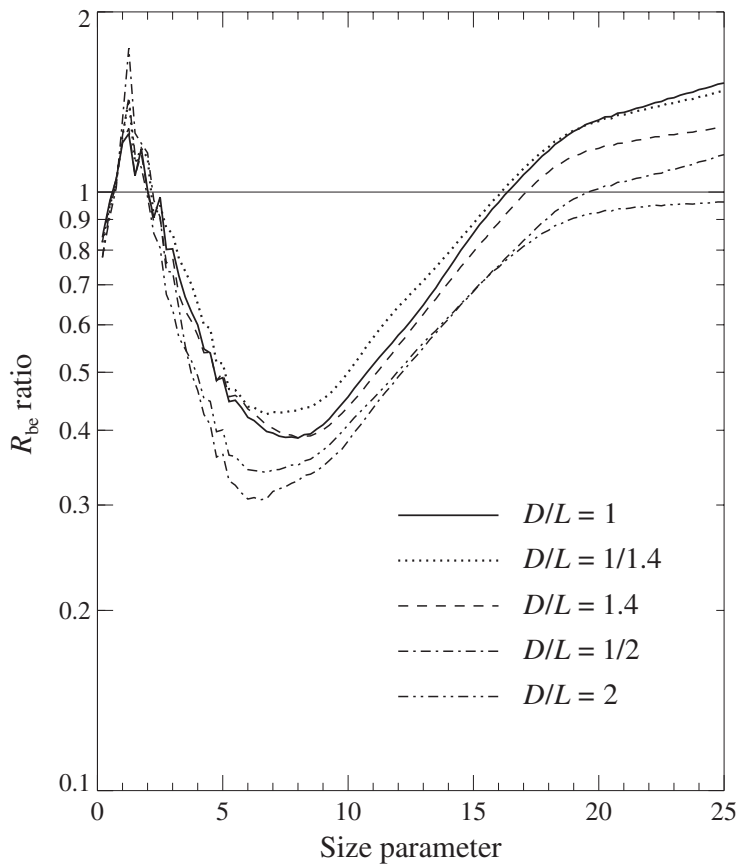

Figure 10.25. As in Fig. 10.17, but for the ratio of the respective R_{be} values.

and $1/20$, and oblate spheroids with $a/b = 2$ and 20 (Zakharova and Mishchenko 2000). The size of a spheroid is specified in terms of the surface-equivalent-sphere radius r_s. To suppress the interference structure in light-scattering patterns for spheres and randomly oriented spheroids with $a/b = 1/2$ and 2, the computation results are averaged over a narrow gamma distribution of equivalent-sphere radii, given by Eq. (5.245) with an effective variance of $v_{\text{eff}} = 0.05$. Size averaging is unnecessary for needlelike and platelike spheroids with $a/b = 1/20$ and 20, respectively, since their scattering patterns are sufficiently smoothed out by orientation averaging. Table 10.3 lists the surface-equivalent-sphere size parameters $x_s = 2\pi r_s/\lambda_1$ for monodisperse spheroids with $a/b = 1/20$ and 20 and the effective surface-equivalent-sphere size parameters $x_{s,\text{eff}} = 2\pi r_{s,\text{eff}}/\lambda_1$ for spheres and polydisperse spheroids with $a/b = 1/2$ and 2 used in the computations. The maximum values of x_s for spheroids with $a/b = 1/20$ and 20 were limited by the growing numerical instability of the T-matrix computations (subsections 5.8.4 and 5.11.7). For comparison, Table 10.3 also lists the corresponding values of the volume-equivalent-sphere size parameters $x_v = 2\pi r_v/\lambda_1$ and $x_{v,\text{eff}} = 2\pi r_{v,\text{eff}}/\lambda_1$, as well as the respective size parameters along the horizontal and vertical spheroid axes $x_a = 2\pi a/\lambda_1$, $x_{a,\text{eff}} = 2\pi a_{\text{eff}}/\lambda_1$,

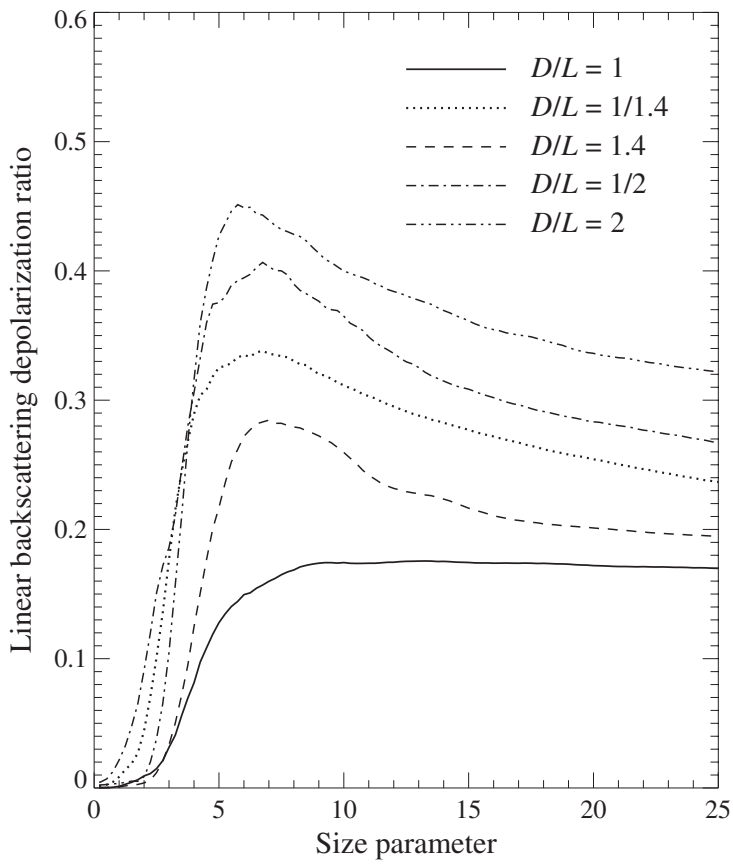

Figure 10.26. Linear backscattering depolarization ratio versus effective size parameter for randomly oriented polydisperse cylinders.

$x_b = 2\pi b/\lambda_1$, and $x_{b,\text{eff}} = 2\pi b_{\text{eff}}/\lambda_1$. The relative refractive index is fixed at 1.311, which is a value typical of water ice in air at visible wavelengths (Warren 1984).

Figure 10.28 shows the extinction efficiency factor $Q_{\text{ext}} = \langle C_{\text{ext}} \rangle / \langle G \rangle$, the asymmetry parameter $\langle \cos\Theta \rangle$, and the efficiency factor for radiation pressure $Q_{\text{pr}} = Q_{\text{ext}}[1 - \langle \cos\Theta \rangle]$, where $\langle C_{\text{ext}} \rangle$ is the ensemble-averaged scattering cross section per particle and $\langle G \rangle$ is the average area of the particle geometric projection. Because the imaginary part of the relative refractive index is set to be zero, the scattering efficiency factor is equal to Q_{ext}, the absorption efficiency factor is equal to zero, and the single-scattering albedo is equal to unity. Figures 10.29 and 10.30 depict the elements of the normalized Stokes scattering matrix versus scattering angle.

Figures 10.29 and 10.30 show that needlelike and platelike particles with moderate equivalent-sphere size parameters possess unique scattering properties. While their phase functions are similar to those of surface-equivalent spheres and compact spheroids and have a pronounced forward-scattering lobe, all other elements of the scattering matrix closely resemble those of particles much smaller than the wavelength (Rayleigh scatterers). In particular, all linear polarization curves $(-b_1/a_1)$ for

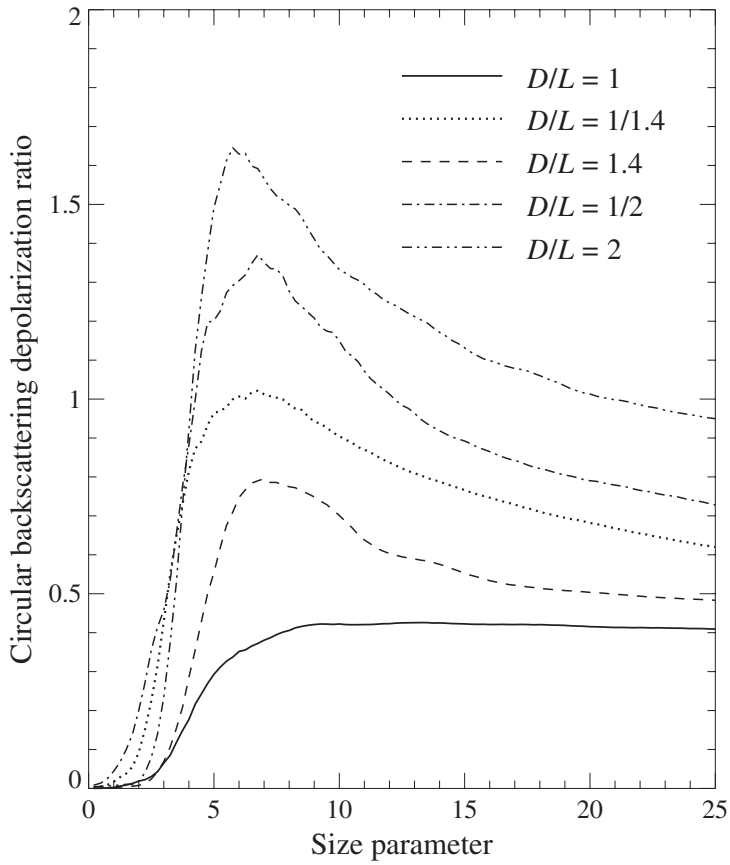

Figure 10.27. As in Fig. 10.26, but for the circular backscattering depolarization ratio.

the spheroids with axis ratios $1/20$ (first row) and 20 (fifth row) have a characteristic bell-like shape, with a maximum reaching nearly 100% at scattering angles close to $90°$; a_2/a_1 is very close to unity; and the elements a_3 and a_4 are nearly equal to each other. The fact that $a_2(\pi) \approx a_1(\pi)$ and $a_4(\pi) \approx -a_1(\pi)$ yields linear and circular depolarization ratios (as defined by Eqs. (10.2) and (10.3)) close to zero, whereas wavelength-sized spheroids with axis ratios $1/2$ and 2 give rise to significant backscattering depolarization. This demonstrates once again that the magnitude of the depolarization ratios is not a universal indicator of the degree of particle asphericity. The extinction and radiation-pressure efficiency factors for highly aspherical spheroids are significantly smaller than those for spheres and compact spheroids having the same average projected area, whereas the values of the asymmetry parameter are rather similar. This is yet another indication that the particular scattering properties of platelike and needlelike spheroids with moderate size parameters can resemble either those of Rayleigh particles or those of surface-equivalent spheres.

The linear polarization curves for spheres show that the regime of Rayleigh scattering breaks down at size parameters close to unity. According to Table 10.3, the

Table 10.3. Surface-equivalent-sphere size parameters x_s (or $x_{s,eff}$), volume-equivalent-sphere size parameters x_v (or $x_{v,eff}$), and size parameters x_a (or $x_{a,eff}$) along the horizontal spheroid axes and x_b (or $x_{b,eff}$) along the vertical spheroid axes, as used in the *T*-matrix computations

$a/b = 1/20$	x_s	x_v	x_a	x_b
	1	0.6845	0.2522	5.0432
	2	1.3690	0.5043	10.087
	3.5	2.3957	0.8826	17.651
$a/b = 1/2$	$x_{s,eff}$	$x_{v,eff}$	$x_{a,eff}$	$x_{b,eff}$
	1	0.9637	0.7649	1.5298
	2	1.9274	1.5298	3.0596
	3.5	3.3730	2.6771	5.3543
	12	11.565	9.1788	18.358
$a/b = 2$	$x_{s,eff}$	$x_{v,eff}$	$x_{a,eff}$	$x_{b,eff}$
	1	0.9554	1.2038	0.6019
	2	1.9109	2.4076	1.2038
	3.5	3.3441	4.2132	2.1066
	12	11.465	14.445	7.2227
$a/b = 20$	x_s	x_v	x_a	x_b
	1	0.5186	1.4077	0.0704
	2	1.0372	2.8155	0.1408
	3.5	1.8151	4.9271	0.2464
	12	6.2233	16.893	0.8446

size parameter along the shorter axis of the spheroids with axis ratios $1/20$ and 20 is smaller than unity even for the largest x_s-values considered. Therefore, these *T*-matrix results may be indicating that the asymmetry parameter and the phase function are mostly determined by the value of the size parameter of the sphere having the same projected area, whereas all other elements of the scattering matrix and the optical cross sections are more sensitive to the value of the size parameter along the smallest particle dimension. It is interesting to note in this regard that West (1991) found similar features in light scattering by low-density aggregates of spheres with outer diameters comparable to the wavelength and monomer sizes much smaller than the wavelength. He concluded that the forward-scattering lobe of the phase function was diagnostic of the mean projected area of the entire cluster, whereas the angular dependence of the linear polarization depended largely on the monomer radius.

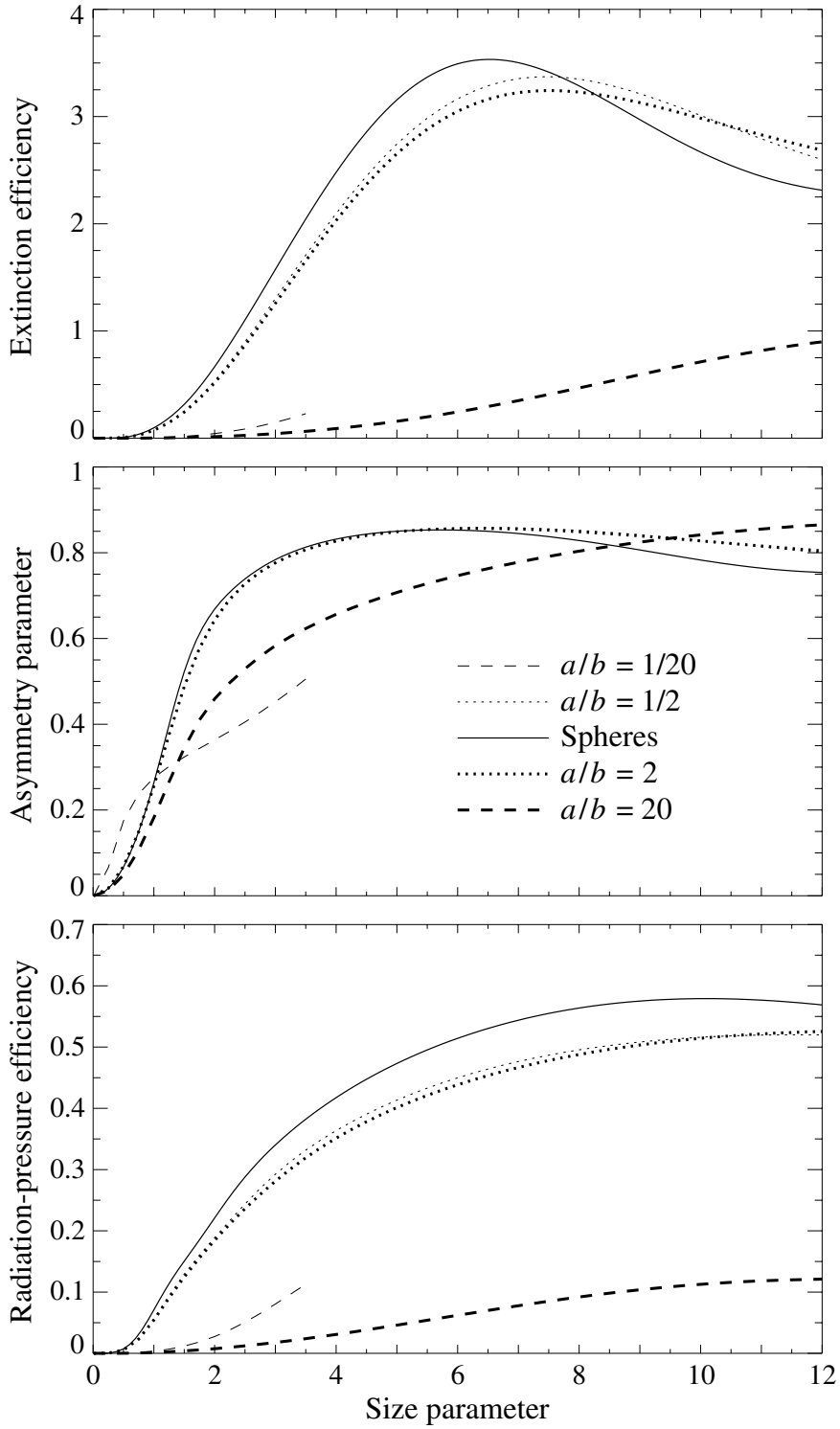

Figure 10.28. Extinction efficiency factor, asymmetry parameter, and radiation-pressure efficiency factor versus surface-equivalent-sphere size parameter for spheres and randomly oriented spheroids with various axis ratios a/b. Note that the asymmetry parameter curves for spheroids with $a/b = 1/2$ and 2 almost coincide.

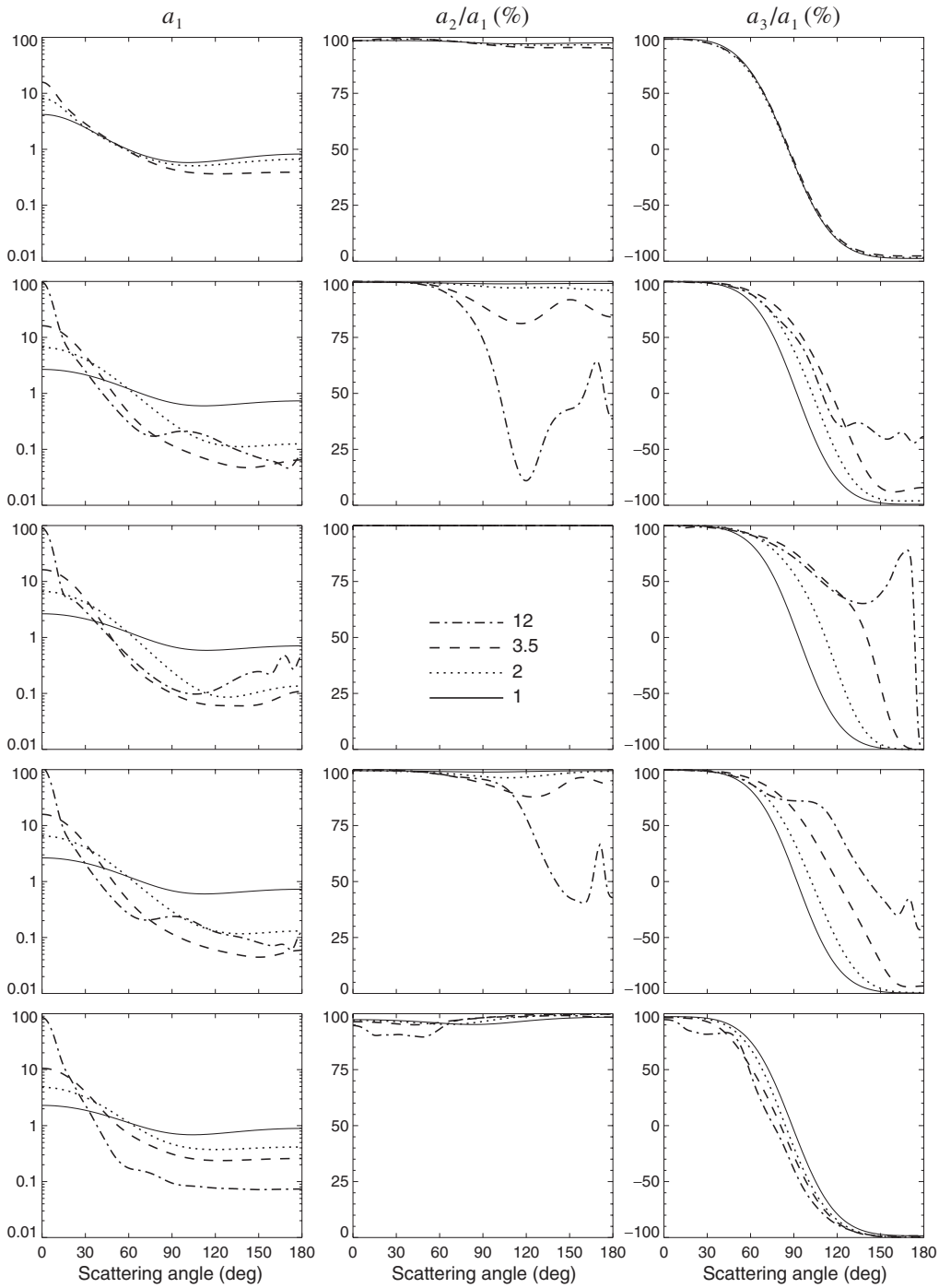

Figure 10.29. The phase function a_1 and the ratios a_2/a_1 and a_3/a_1 versus scattering angle Θ for spheres and surface-equivalent, randomly oriented spheroids with size parameters ranging from 1 to 12 (see legend) and axis ratios $1/20$ (first row), $1/2$ (second row), 1 (third row), 2 (fourth row), and 20 (fifth row). Note that for spheres $a_2/a_1 \equiv 100\%$.

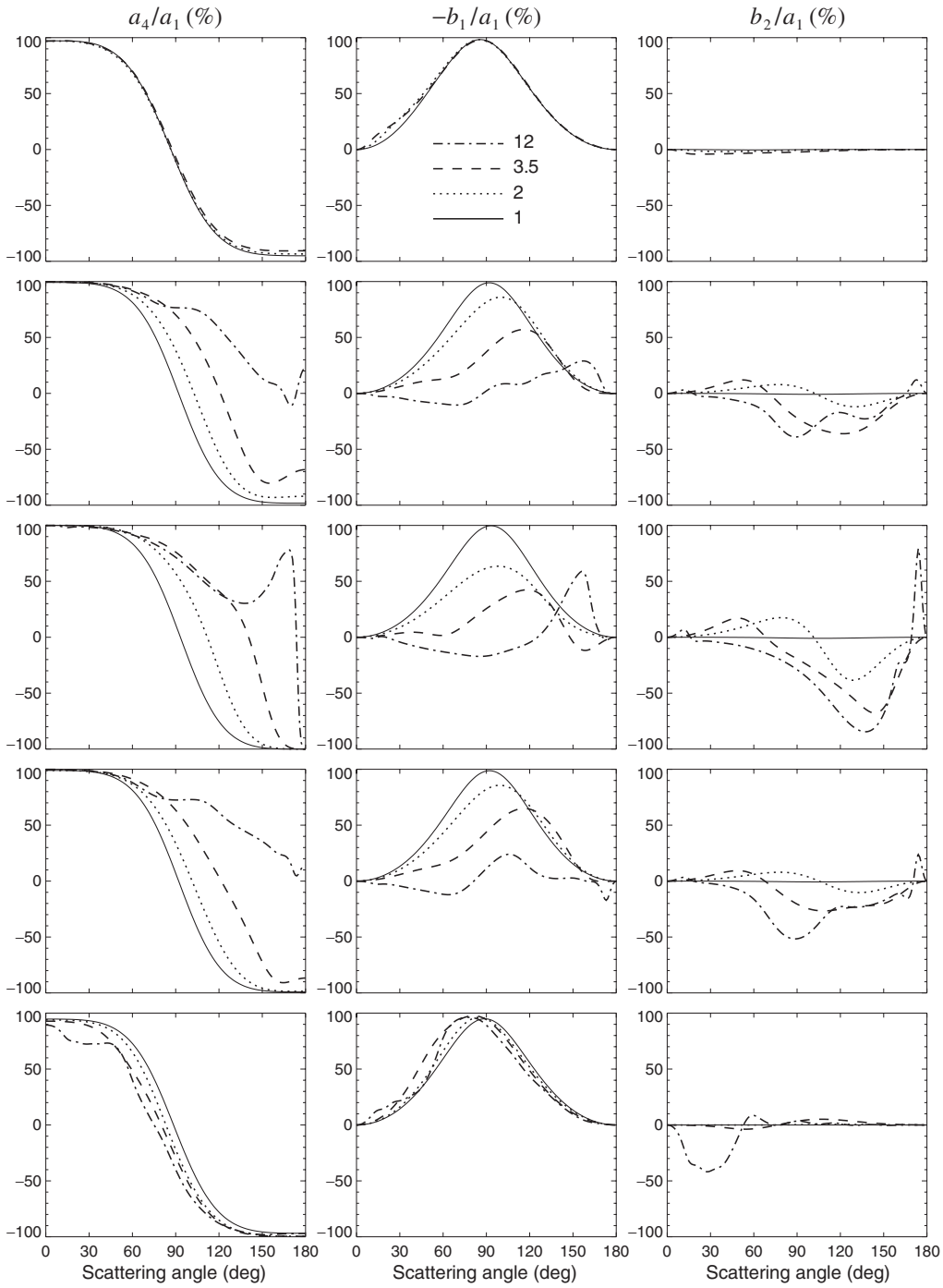

Figure 10.30. The ratios a_4/a_1, $-b_1/a_1$, and b_2/a_1 versus scattering angle Θ for spheres and surface-equivalent, randomly oriented spheroids with size parameters ranging from 1 to 12 (see legend) and axis ratios $1/20$ (first row), $1/2$ (second row), 1 (third row), 2 (fourth row), and 20 (fifth row).

Since spheroids are particles with smooth surfaces, it is instructive to verify whether sharp-edged wavelength-sized cylinders with extreme aspect ratios possess similar scattering properties. The computation of light scattering by prolate ice cylinders with very large length-to-diameter ratios L/D turns out to be problematic even with the extended-precision *T*-matrix code, because of poor convergence. However, Zakharova and Mishchenko (2001) managed to perform computations for randomly oriented oblate ice cylinders with surface-equivalent-sphere size parameters up to 12 and diameter-to-length ratios D/L as large as 20. The results of their computations for cylinders with $D/L = 1$ and 20 and surface-equivalent spheres are summarized in Figs. 10.31–10.33. As in previous computations, the interference structure is suppressed by averaging the results for spheres and cylinders with $D/L = 1$ over a narrow gamma distribution of surface-equivalent-sphere radii with effective variance $v_{\text{eff}} = 0.05$. The curves for monodisperse cylinders with $D/L = 20$ are sufficiently smooth already and do not require averaging over sizes. Accordingly, the size of the cylinders with $D/L = 20$ is specified in Figs. 10.31–10.33 in terms of the monodisperse surface-equivalent-sphere size parameter x_{s}, whereas the size of polydisperse spheres and cylinders with $D/L = 1$ is specified in terms of the effective surface-equivalent-sphere size parameter $x_{\text{s,eff}}$. The relative refractive index is fixed at 1.311.

Examination of Figs. 10.31–10.33 shows that, despite their sharp-edged shapes, wavelength-sized circular ice disks with extreme aspect ratios possess the same scattering properties as smooth platelike spheroids. Specifically, their phase functions are similar to those of surface-equivalent spheres and nonspherical particles (spheroids and cylinders) with moderate aspect ratios and have a forward-scattering lobe whose magnitude rapidly increases with size parameter. In contrast, all other elements of the scattering matrix closely resemble those of the Rayleigh scattering matrix as long as the size parameter along the smallest cylinder dimension is less than unity. Specifically, all curves of linear polarization $(-b_1/a_1)$ for plates with $D/L = 20$ have the renowned bell-like shape with a maximum approaching 100% at side-scattering angles. Unlike the case for the compact particles, the scattering angle of maximal positive polarization decreases rather than increases with increasing size parameter. The ratio a_2/a_1 is close to unity, the elements a_3 and a_4 are almost the same and do not vary significantly with size parameter, and the ratio b_2/a_1 is close to zero at most scattering angles. This behavior differs substantially from that exhibited by surface-equivalent spheres and compact nonspherical particles.

These *T*-matrix results are in excellent agreement with the results of recent laboratory measurements of electromagnetic scattering by randomly oriented plates with very large diameter-to-thickness ratios and thicknesses smaller than the wavelength (Waldemarsson and Gustafson 2000). Indeed, these microwave analog data (Fig. 8.4) also show phase functions characteristic of compact wavelength-sized particles and polarization curves typical of Rayleigh scattering. In particular, the observed maximal polarization values approach 100% and occur at scattering angles less than 90°.

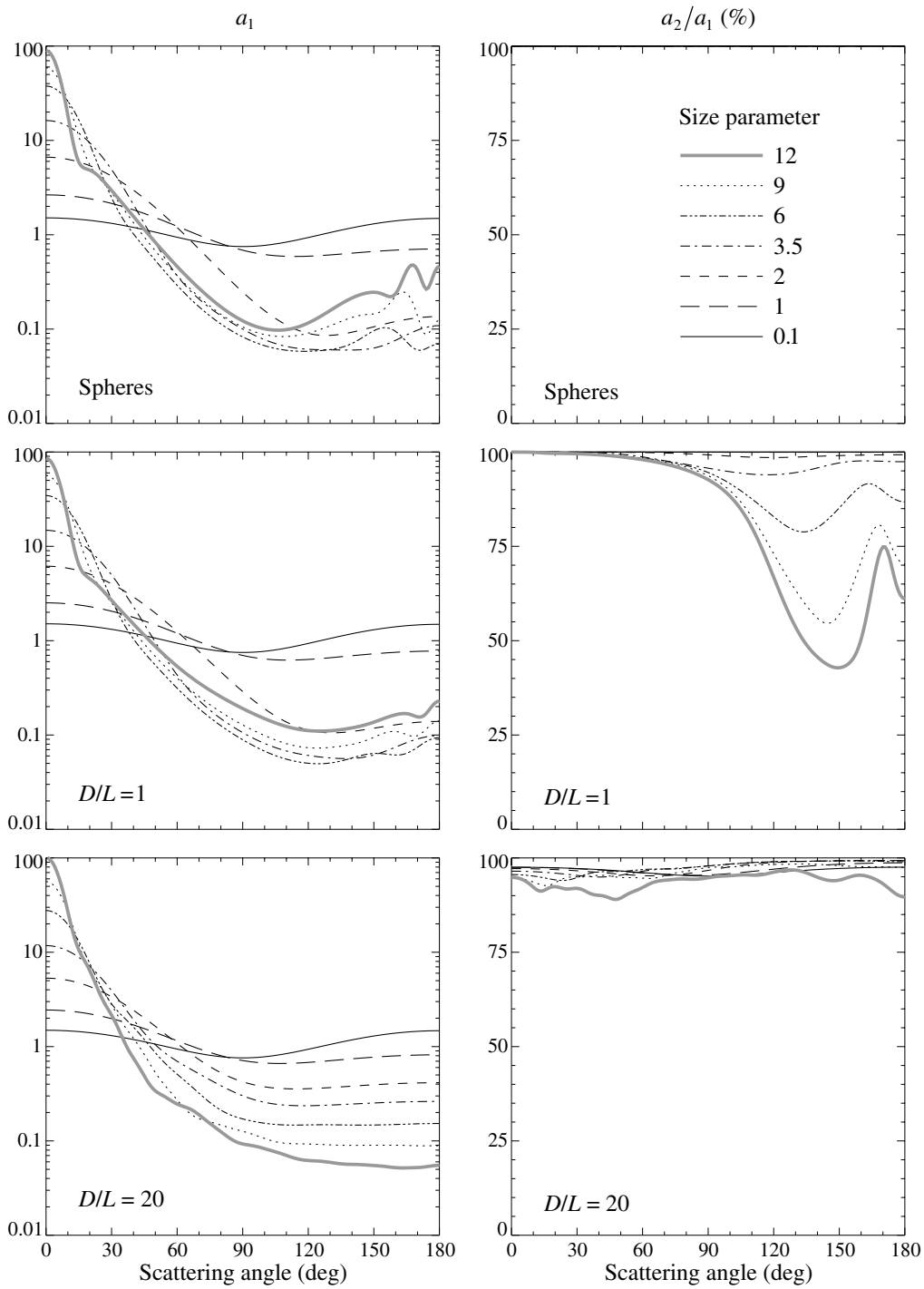

Figure 10.31. The phase function a_1 and the ratio a_2/a_1 versus scattering angle Θ for spheres with size parameters ranging from 0.1 to 12 (see legend) and surface-equivalent, randomly oriented circular cylinders with $D/L = 1$ and 20. Note that for spheres $a_2/a_1 = 100\%$ for all values of Θ.

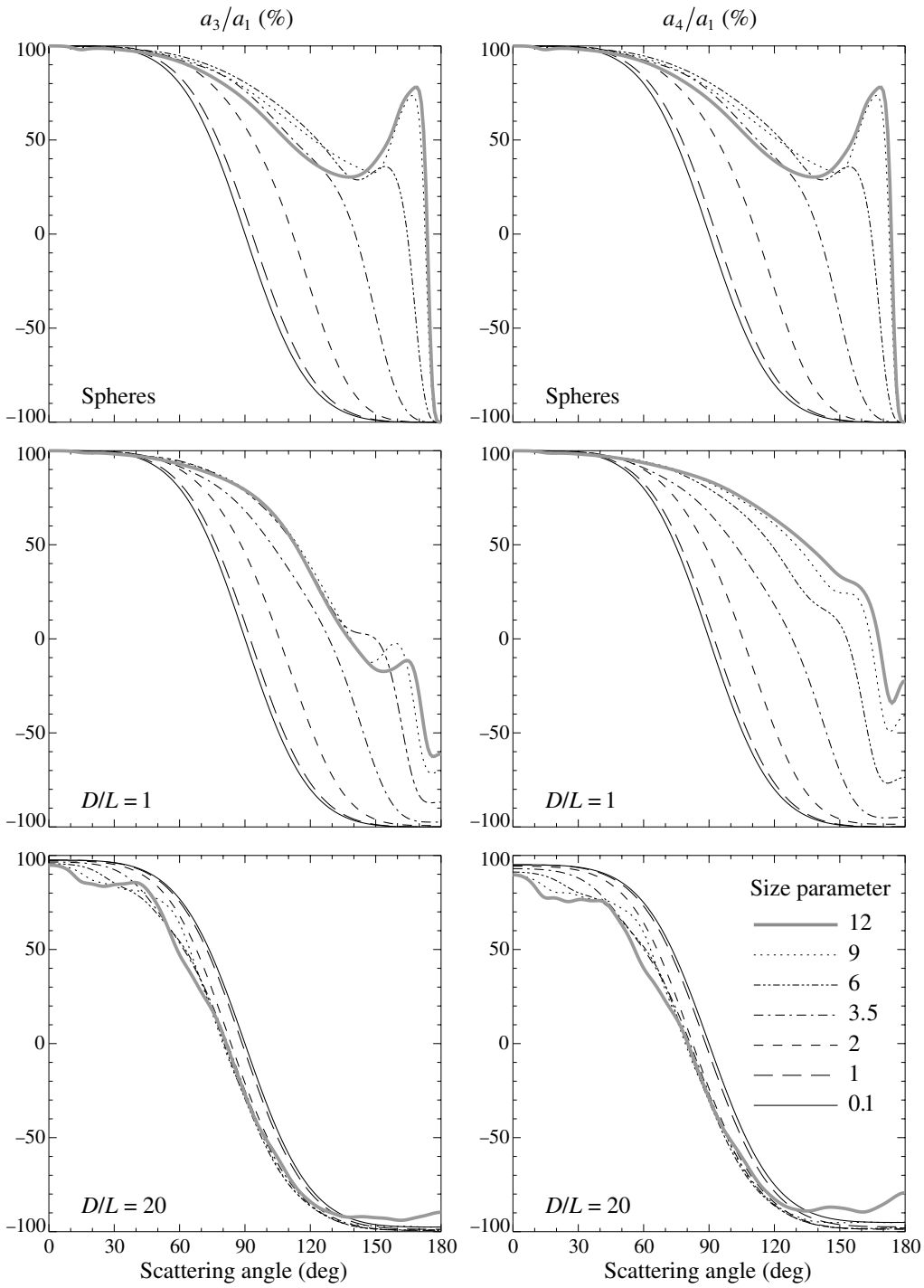

Figure 10.32. The ratios a_3/a_1 and a_4/a_1 versus scattering angle Θ for spheres with size parameters ranging from 0.1 to 12 (see legend) and surface-equivalent, randomly oriented circular cylinders with $D/L = 1$ and 20.

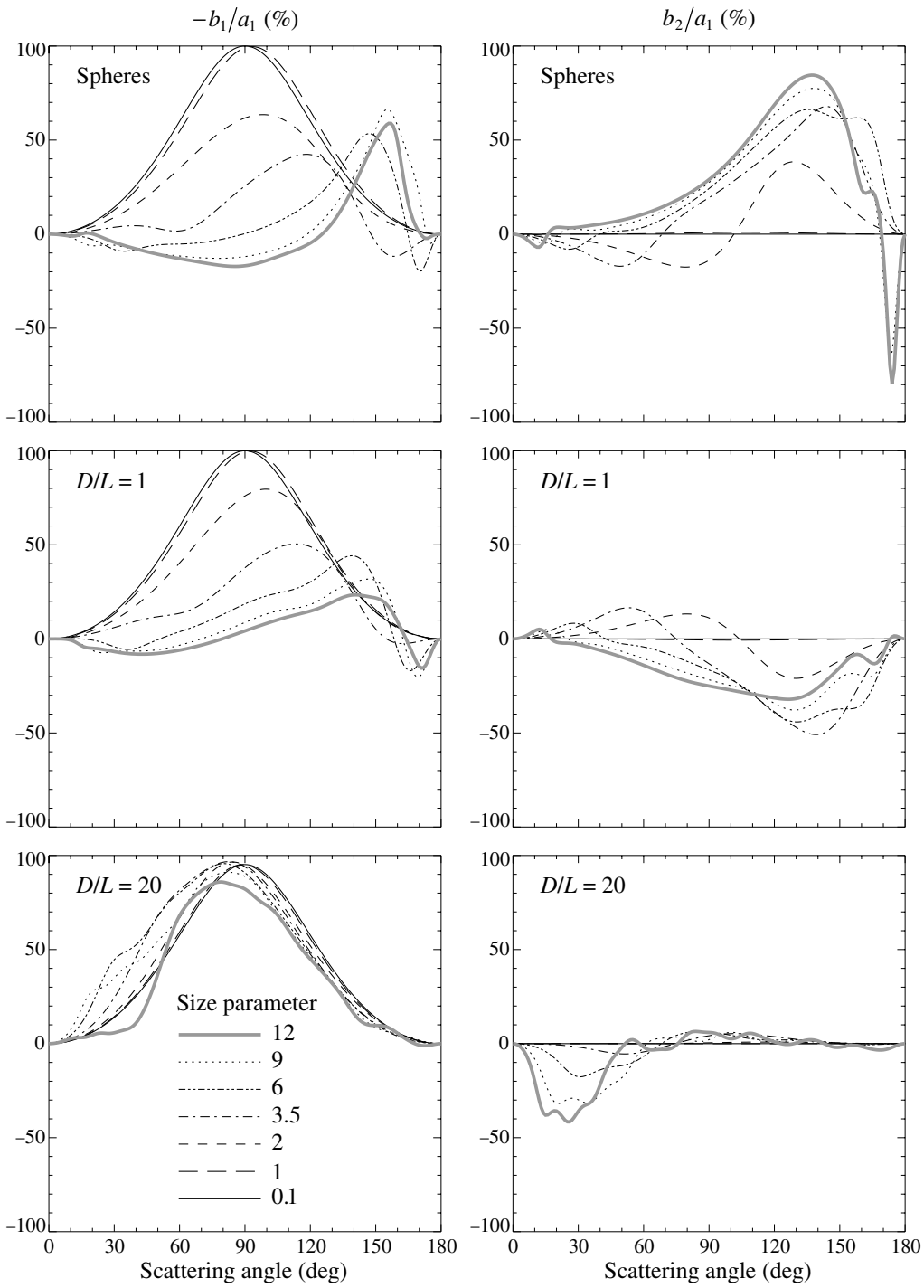

Figure 10.33. The ratios $-b_1/a_1$ and b_2/a_1 versus scattering angle Θ for spheres with size parameters ranging from 0.1 to 12 (see legend) and surface-equivalent, randomly oriented circular cylinders with $D/L = 1$ and 20.

As discussed by Zakharova and Mishchenko (2000), the unusual scattering properties of wavelength-sized nonspherical particles with extreme aspect ratios should be given adequate consideration in analyses of laboratory and remote sensing measurements of light scattering. For example, small measured values of depolarization should not be identified automatically with Rayleigh scattering or a spherical particle shape. Similarly, measurements of Rayleigh-like polarization (e.g. Tozer and Beeson 1974; Witt *et al.* 1976; Tomasko *et al.* 1978; West and Smith 1991) should not be attributed necessarily to particles much smaller than a wavelength.

The simplicity of the normalized Stokes scattering matrix for needlelike and platelike particles with moderate size parameters allows for a convenient analytical parameterization similar to those developed by West *et al.* (1983) and Braak *et al.* (2001). Such parameterizations can be useful in first-order analyses of remote sensing observations when the plausible range of particle microphysical characteristics is unknown and is difficult to guess. Also, the *T*-matrix results discussed in this section provide a benchmark for checking the accuracy of approximate formulations of light scattering by wavelength-sized particles with one dimension much smaller than the wavelength (Weil and Chu 1976, 1980; Uzunoglu *et al.* 1978; Schiffer and Thielheim 1979).

10.5 Chebyshev particles

An interesting study of electromagnetic scattering by rotationally symmetric Chebyshev particles (see subsection 5.11.2 and Fig. 5.8) was performed by Wiscombe and Mugnai (see Mugnai and Wiscombe 1980, 1986, 1989; Wiscombe and Mugnai 1986, 1988). They compared the radiometric scattering and absorption characteristics of randomly oriented Chebyshev particles having various deformation and waviness parameters and those of volume-equivalent spheres. The relative refractive index was fixed at 1.5 + i0.02. The results of Wiscombe and Mugnai largely parallel those described in Sections 10.2 and 10.3. Minor differences in the conclusions reached may be the consequence of comparing the optical properties of volume-equivalent rather than surface-equivalent spherical and nonspherical particles. Perhaps the most interesting geometrical property of Chebyshev particles is that they become partially concave as the absolute value of the deformation parameter exceeds a certain threshold range, whereas spheroids and circular cylinders are always convex bodies. In this regard the conclusion of Wiscombe and Mugnai that concavity almost always enhances the nonspherical–spherical differences appears to be especially important and deserves further study. Mishchenko and Travis (1994b) computed linear polarization patterns for randomly oriented, polydisperse Chebyshev particles with $n = 4$, $\xi = \pm 0.1$, and m = 1.5 + i0.02 and concluded that they were distinctly different from those computed for volume-equivalent spheroids with a comparable degree of asphericity.

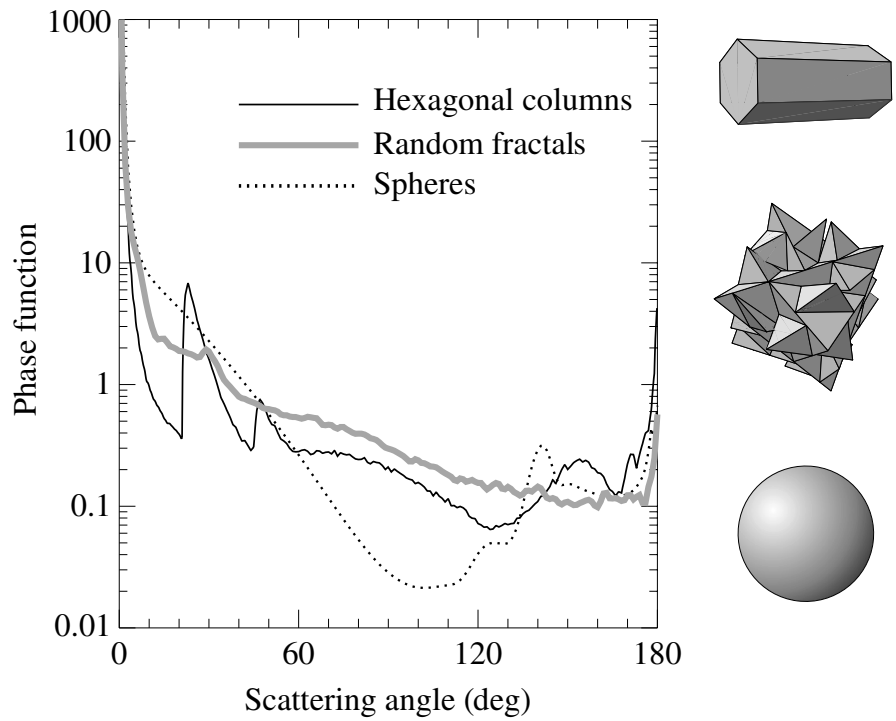

Figure 10.34. Phase function versus scattering angle for polydisperse randomly oriented hexagonal ice columns with length-to-diameter ratio 2, polydisperse random-fractal ice particles in random orientation, and polydisperse spherical water droplets at a wavelength $\lambda_1 = 0.63\,\mu\text{m}$.

10.6 Regular polyhedral particles

By definition, polyhedral particles are bounded by surfaces composed of plane facets. Typical examples of regular polyhedrons are tetrahedrons, cubes, and hexagonal cylinders. The scattering and absorption properties of such particles have been computed mostly using the geometrical optics approximation, hence assuming (explicitly or implicitly) that the wavelength of the incident light is much smaller than the size of the smallest facet on the particle surface. As an example, the heavy solid curve in Fig. 10.34 shows the phase function computed for large, randomly oriented hexagonal ice columns at a visible wavelength. Each hexagonal cylinder comprises three different types of prism: a $60°$ prism formed by alternate side faces, a $90°$ prism formed by side and end faces, and a $120°$ prism formed by adjacent side faces (see Fig. 10.35). The $120°$ prism plays only a minor role in light scattering by ice crystals because total internal reflections prevent any ray entering the first face from being refracted through the second. The most pronounced phase-function features for hexagonal ice crystals are the primary and secondary halos centered at $\Theta \approx 22°$ and $\Theta \approx 46°$ and the strong and narrow backscattering peak. The primary and secondary halos are generated by the same mechanism as the rainbows discussed in Section 9.4 and correspond to minimum angles of deviation for the $60°$ and $90°$ prisms, respec-

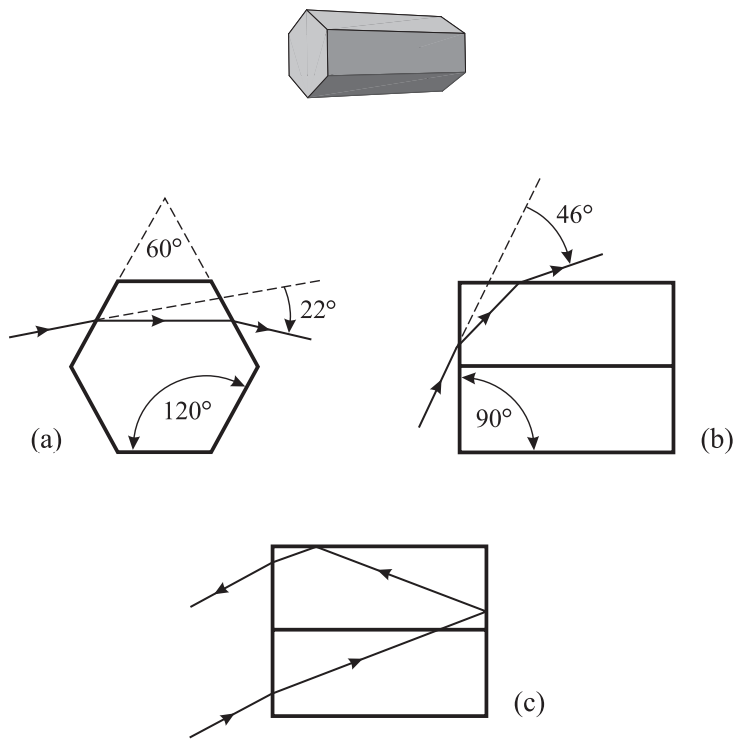

Figure 10.35. (a), (b) Refraction by a hexagonal ice crystal showing the rays associated with the 22° and 46° degree halos. (c) Double internal reflections causing the backscattering intensity peak.

tively, whereas the backscattering peak is caused by rays twice internally reflected by mutually perpendicular faces (see Figs. 10.35 and 10.36). This explains why large, randomly oriented, circular ice cylinders generate the secondary halo and the backscattering peak, but not the primary halo (see the top left-hand panel in Fig. 7.7). The same is true of large, randomly oriented cubes and parallelepipeds (Liou *et al.* 1983).

The geometrical optics approximation allows one to compute the scattering functions for polyhedral particles with extremely complicated shapes (see, e.g., Macke 1993; Iaquinta *et al.* 1995; Takano and Liou 1995; and especially Yang and Liou 1998a) and explains qualitatively many optical phenomena observed for ice crystal clouds (Lynch and Livingston 1995). However, the uncertain numerical accuracy and range of applicability of this approximation are always a concern and often make desirable, if not mandatory, the use of an exact theoretical technique. Figure 10.37 illustrates the application of the finite-difference time-domain method to phase-function computations for randomly oriented, monodisperse polyhedral particles (Yang *et al.* 2000b). Such computations are also possible with the extended boundary condition method (e.g., Laitinen and Lumme 1998; Wriedt and Comberg 1998) and volume integral equation methods (Section 6.5) but they are still limited in terms of the size parameter range and the ability to handle polydisperse ensembles of randomly oriented particles. Further theoretical efforts are obviously required in order to char-

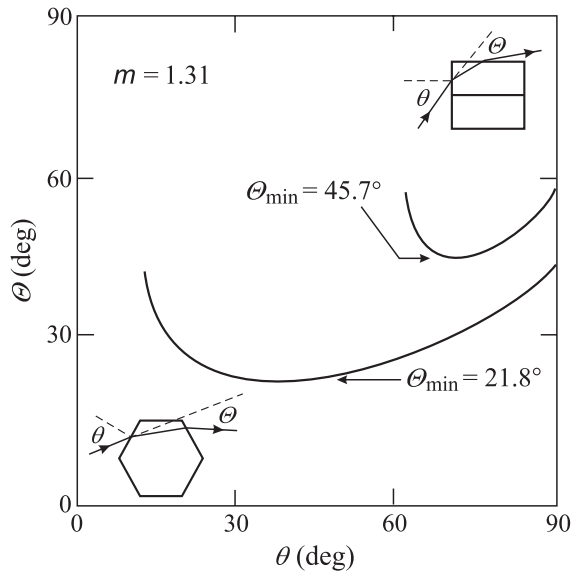

Figure 10.36. Deviation (scattering) angle versus incidence angle for $m = 1.31$. The angle of minimum deviation Θ_{min} is about 22° for the 60° prism and 46° for the 90° prism. The angle of deviation is at a minimum when the light passes symmetrically through the prism and is greater at all other angles of incidence. (After Lynch and Livingston 1995.)

acterize and quantify the specific effects of polyhedral shapes on the scattering and absorption properties of wavelength-sized particles.

10.7 Irregular particles

Many particles encountered in natural and artificial environments have irregular and highly variable shapes. As an example, Fig. 10.38 demonstrates that the shapes of natural cirrus cloud particles can significantly deviate from those of pristine hexagonal columns and plates. In fact, the study by Korolev *et al.* (1999, 2000) indicated that the majority of atmospheric ice particles can be highly irregular, which may explain why, when cirrus clouds are observed, halos and other optical displays characteristic of regular polyhedral ice crystals are seen rather infrequently (e.g., Sassen *et al.* 1994; Francis 1995; Gayet *et al.* 1998; Francis *et al.* 1998; Lawson *et al.* 1998).

The scattering of light by randomly (i.e., stochastically) shaped particles with size parameters less than about 5 has been analyzed using volume integral equation methods and the second-order perturbation approximation (e.g., Lumme and Rahola 1998; Lumme 2000; Muinonen 2000; Chamaillard and Lafon 2001; Nousiainen *et al.* 2001). Nevertheless, the majority of computations for irregular particles have been based on the geometrical optics approximation. For example, Macke *et al.* (1996b) (see also Hess *et al.* 1998) modeled scattering by an ensemble of imperfect hexagonal ice

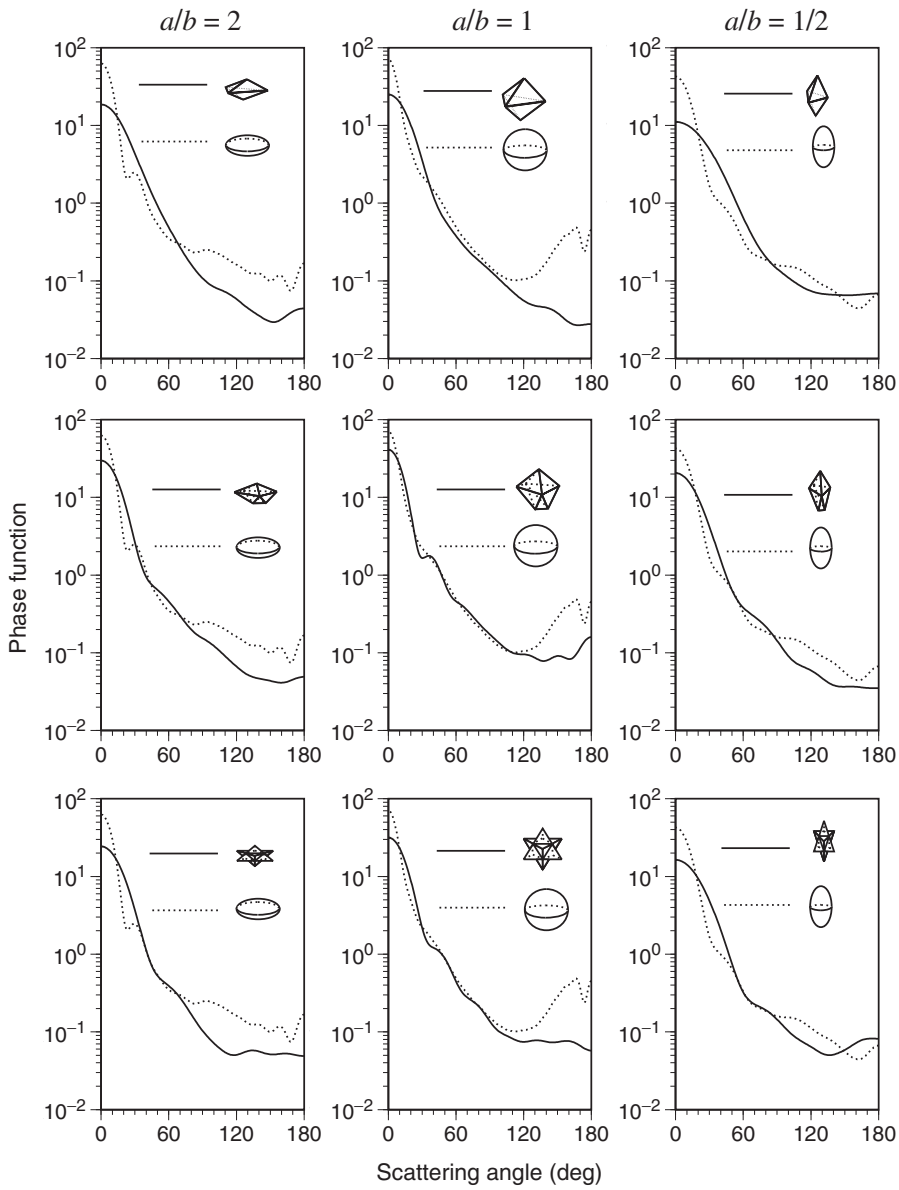

Figure 10.37. Phase functions for monodisperse, randomly oriented, regular polyhedral particles and for spheroids; the relative refractive index is $1.38 + i3.9\times10^{-9}$. In the top row, the polyhedra have six faces, in the middle row, ten faces. All particles have the same size parameter, 10, along the semi-major particle dimension. (From Yang *et al.* 2000b.)

crystals by introducing a statistical local distortion of the crystal faces. Specifically, for each reflection–refraction event, the local normal to the crystal surface was tilted randomly about its original direction. The zenith and azimuth tilt angles were chosen randomly from the intervals $[0, \theta^{\max}]$ and $[0, 2\pi]$, respectively, and the degree of crystal distortion was defined by the parameter $t = \theta^{\max}/90°$. Figure 10.39 shows the ray-tracing component of the phase function (i.e., excluding diffraction) and also the linear polarization for large, randomly oriented, prolate ice crystals with an average

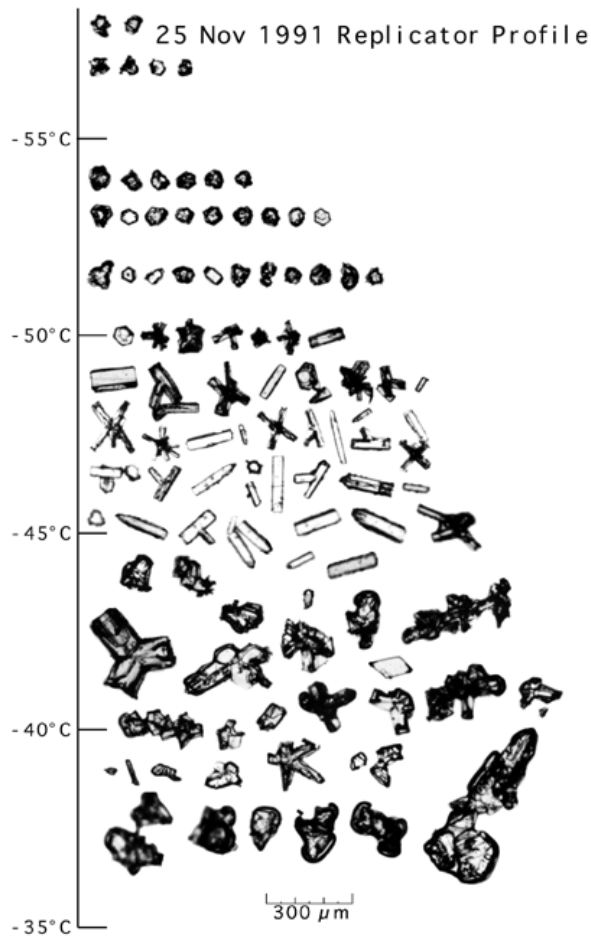

Figure 10.38. Balloon-borne ice crystal replicator data collected on 25 November 1991 near Coffeyville, Kansas. The approximate temperature at the replicator height is indicated along the ordinate. (From Heymsfield and Iaquinta 2000.)

length-to-diameter ratio of 6.2 and three increasing values of the distortion parameter t. Since the relative refractive index is real, the ray-tracing computations do not depend on the particle size relative to the wavelength. While the $t = 0.01$ case shows almost the same phase function and polarization features as those for perfect hexagonal columns (cf. Fig. 10.34), a further increase in the distortion parameter results in progressively smoother phase-function and linear polarization curves. In particular, the primary and secondary halos and the strong backscattering phase-function peak essentially disappear for t-values exceeding 0.1. The side scattering is only slightly affected by increasing crystal distortion because it primarily results from external reflections that are not sensitive to the shape of randomly oriented convex particles. The locations of the neutral polarization points also do not change significantly with increasing t.

Yang and Liou (1998a) employed a similar geometrical optics approach by assuming that surfaces of real ice crystals are rough and consist of a large number of

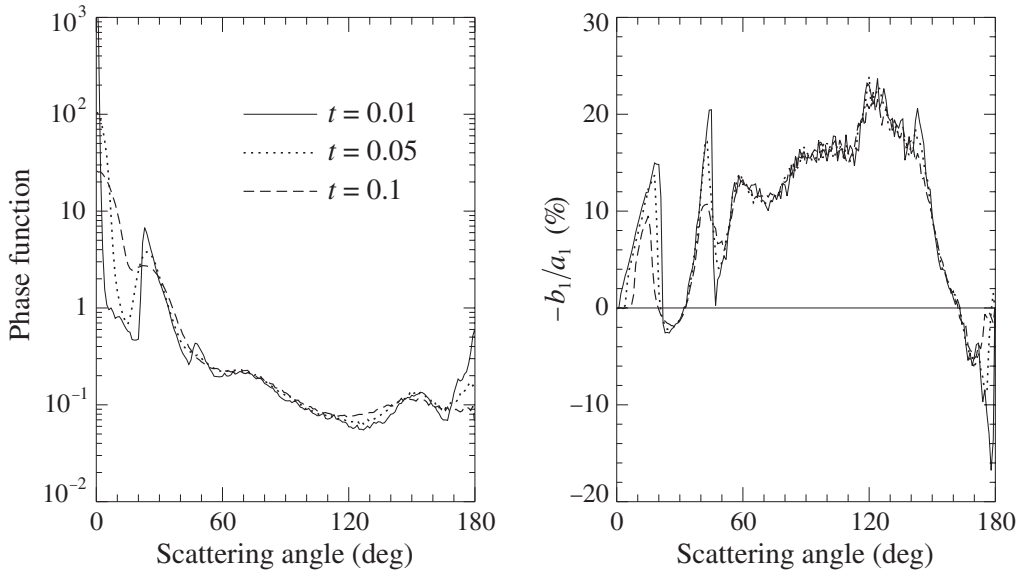

Figure 10.39. The ray-tracing phase function and ratio $-b_1/a_1$ versus scattering angle for randomly oriented hexagonal ice columns with $L/D = 6.2$ and distortion parameters $t = 0.01$, 0.05, and 0.1. The relative refractive index is $m = 1.311$.

microscopic facets that are locally planar and randomly tilted from their orientations corresponding to the case of a smooth surface. The distribution of slopes was assumed to be isotropic and Gaussian with a mean-square surface slope $\sigma^2/2$. Figure 10.40 shows the computation results for randomly oriented clusters composed of non-overlapping hexagonal ice columns. It is evident that increasing surface roughness strongly affects the scattering properties of ice particles. For the case of smooth crystal surfaces $(\sigma = 0)$, the pronounced peaks at $\Theta = 22°, 46°$, and $180°$ as well as the intensity maximum at $\Theta \approx 154°$ are features typical of single hexagonal ice crystals in random orientation (cf. Fig. 10.34). Increasing σ smoothes these features out so that the phase function for $\sigma = 0.1$ consists of a strong diffraction peak and a relatively featureless and flat background. Among the other elements of the scattering matrix, the effect of increasing roughness on the ratio $-b_1/a_1$ appears to be the most significant and makes the scattered polarization largely neutral.

In order to model light scattering by highly irregular polyhedral ice particles, Macke *et al.* (1996b) used a random shape generator based on three-dimensional Koch fractals. The construction of a random Koch fractal is demonstrated in Fig. 10.41. The initial particle (zeroth-generation fractal) is a regular tetrahedron. The first- and second-generation regular Koch fractals are shown in the left-hand column and are obtained via the standard process of self-replication. Progressively disordered versions of these particles are achieved by introducing increasing random displacements of the particle vertices, as shown in the right-hand column. The degree of distortion is defined by the maximum displacement length divided by the length of the crystal segments (as a percentage). Figure 10.42 shows the evolution of the ray-

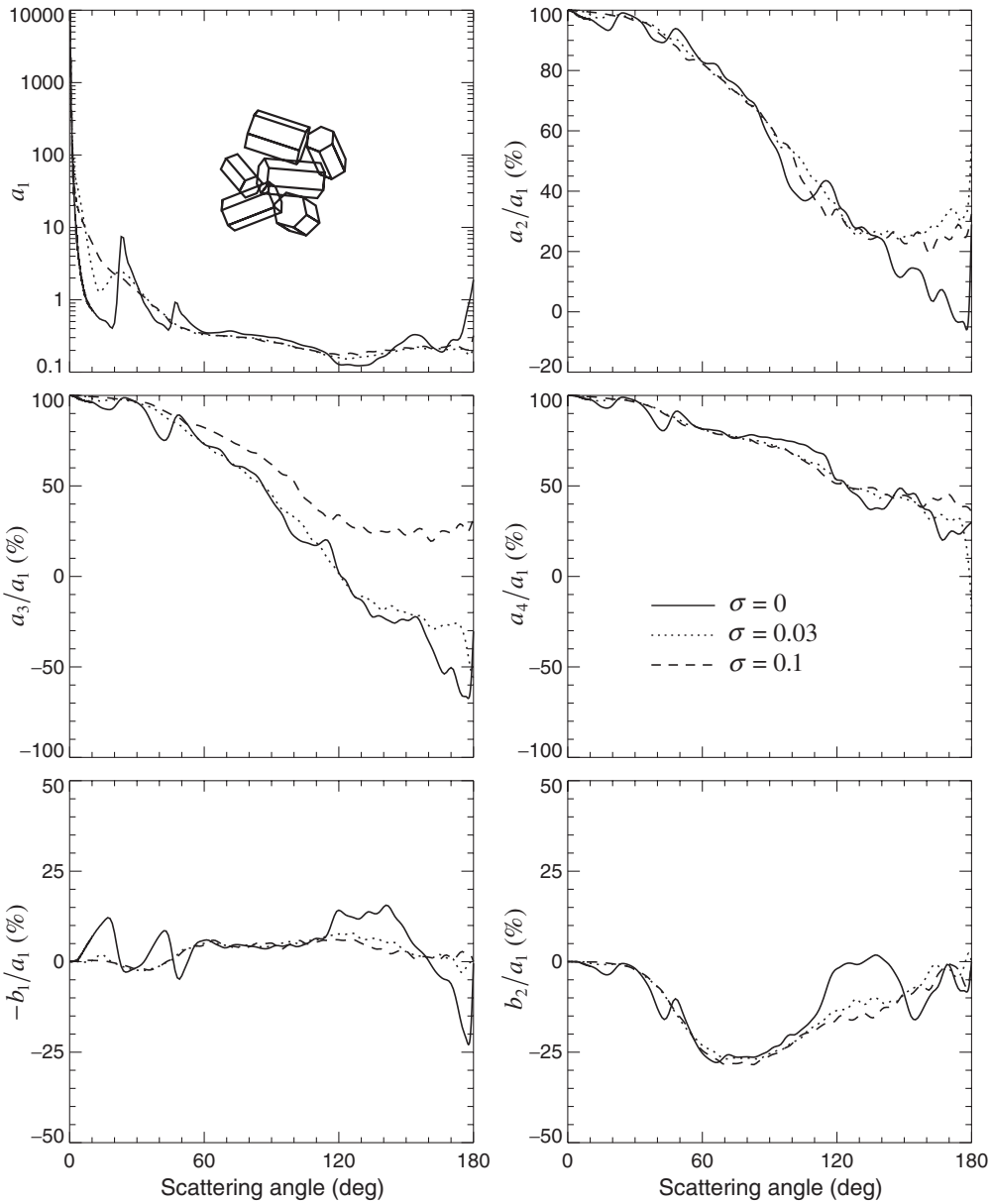

Figure 10.40. Elements of the normalized Stokes scattering matrix versus scattering angle for randomly oriented ice aggregates with smooth $(\sigma = 0)$, moderately rough $(\sigma = 0.03)$, and deeply rough $(\sigma = 0.1)$ surfaces. The maximum dimension of the aggregates is $200\,\mu\text{m}$, the relative refractive index is 1.311, and the wavelength of light in the surrounding medium is $0.55\,\mu\text{m}$. (After Yang and Liou 1998a.)

tracing component of the phase function for large, randomly oriented, second-generation ice fractals with increasing distortion. The decrease in direct forward scattering occurs at the expense of an increase in the scattering into adjacent forward-scattering directions. Eventually the phase function becomes almost featureless and approaches a slope at side- and backscattering angles that stays almost constant with a

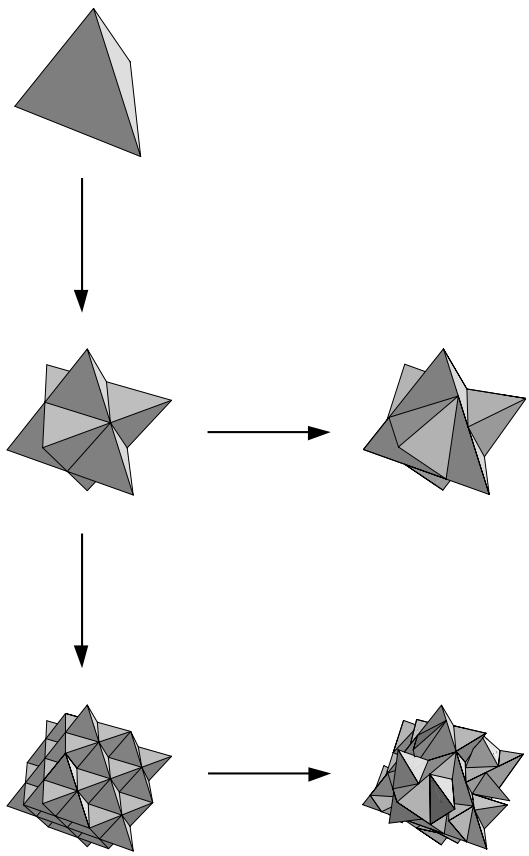

Figure 10.41. Deterministic (left-hand column) and randomized (right-hand column) triadic Koch fractals. Three generations are shown, the zeroth (top) to the second (bottom). (After Macke *et al*. 1996b).

further increase in distortion. This may imply that above a certain level of disorder, the phase function becomes essentially invariant against the particular realization of a random particle shape.

Figure 10.34 contrasts the phase functions computed for randomly oriented hexagonal ice crystals, random second-generation ice fractals with an 18% distortion, and spherical water droplets. The quantitative differences between these phase functions are so large that using an incorrect particle model in retrieval algorithms can seriously affect the results of cloud remote sensing (e.g., Mishchenko *et al.* 1996c; Yang *et al.* 2001b). The corresponding asymmetry parameter differences are relatively smaller: $\langle \cos\Theta \rangle = 0.816$ for the hexagonal ice columns, 0.752 for the random ice fractals, and 0.862 for the water droplets. However, the effect of particle shape on the albedo of

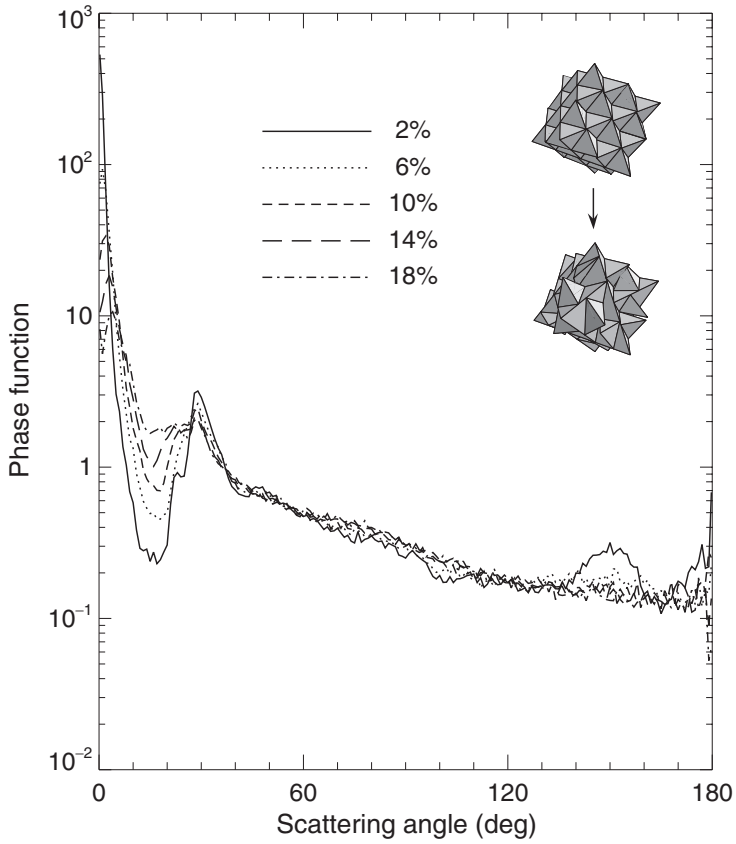

Figure 10.42. Ray-tracing phase function versus scattering angle for randomly oriented second-generation Koch fractals with increasing distortion. The relative refractive index is m = 1.311. (After Macke *et al*. 1996b.)

optically thick clouds and the associated radiative forcing of climate can be very strong (e.g., Stephens *et al.* 1990; Mishchenko *et al.* 1996c; Liou *et al.* 2000).

An interesting approach to modeling nearly spherical particles with random rough surfaces was introduced by Muinonen *et al.* (1996). The size and shape of their so-called Gaussian random spheres are specified by the mean and the covariance function of the radius vector. The covariance function is derived from the covariance function of the logarithmic radius, which is expanded in Legendre polynomials. The expansion coefficients are non-negative and provide the spectral weights of the corresponding spherical harmonic components in the Gaussian sphere. The zeroth-degree term controls the overall particle size. The first-degree term is mainly a translation: it moves the particle surface relative to the origin, but the shape itself does not change much. The second-order term produces a deformation with an elongated shape, while higher-degree terms create increasingly complex deformations with larger numbers of protuberances and hollows per solid angle. Increasing the variance of the radius enhances the protuberances and hollows radially. The scattering of light by Gaussian random spheres in the geometrical optics limit has been studied by Muinonen *et al.*

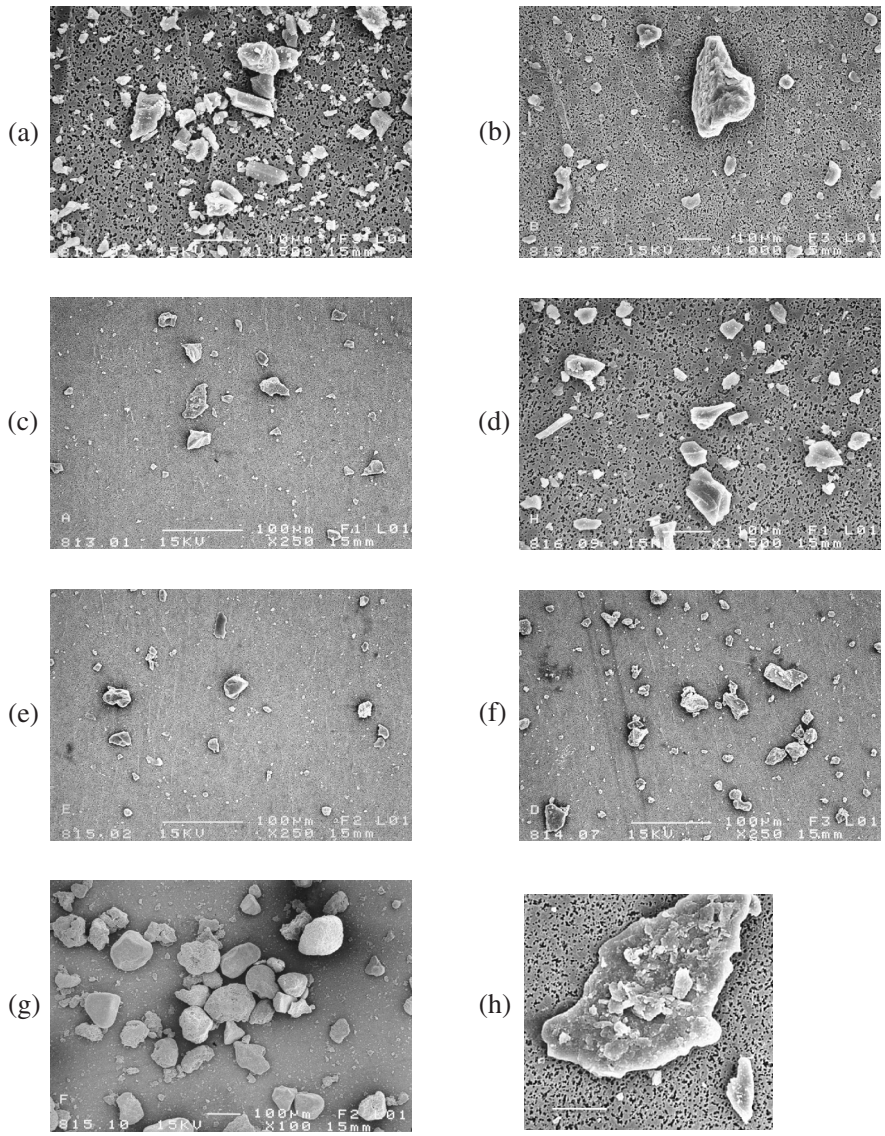

Figure 10.43. Scanning electron microscope images of seven aerosol samples: (a) feldspar, (b) red clay, (c) quartz, (d) Pinatubo volcanic ash, (e) loess, (f) Lokon volcanic ash, and (g) Sahara sand. Panel (h) demonstrates the irregularity of a single quartz particle. The length of the white bars corresponds to $10\,\mu m$ in panels (a), (b), (d), and (h) and to $100\,\mu m$ in the remaining panels. (From Volten *et al.* 2001.)

(1996) and Nousiainen and Muinonen (1999) (see also the review by Muinonen 2000).

Despite the recent progress in theoretical modeling, laboratory and *in situ* measurements remain a major source of information about light scattering by irregular particles. Besides the widely acclaimed study by Perry *et al.* (1978), a unique body of experimental data has been collected using the advanced laboratory setup developed at the Free University in Amsterdam (Kuik *et al.* 1991; Kuik 1992; Volten *et al.* 1998,

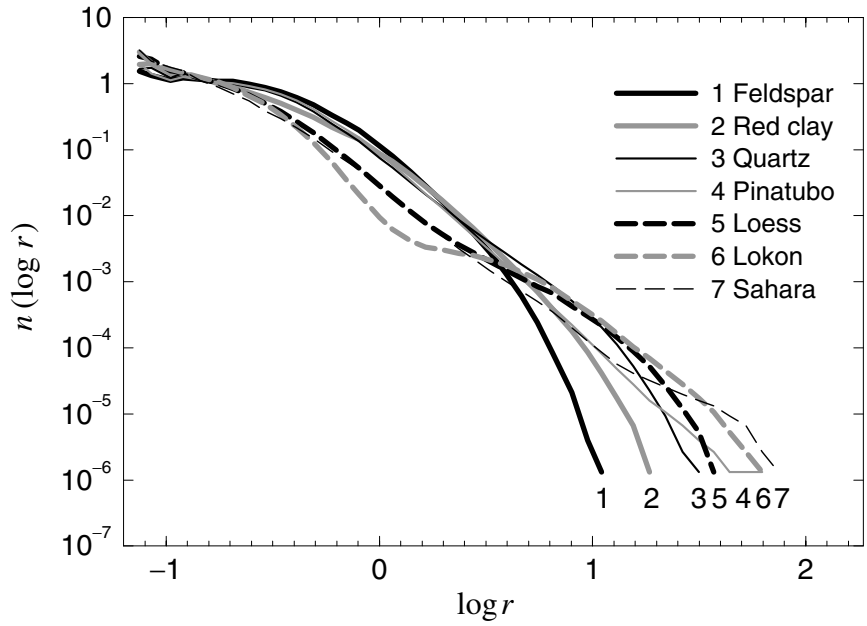

Figure 10.44. Measured normalized size distributions $n(\log r) = rn(r)\ln 10$ of the projected-area-equivalent-sphere radius r for the seven aerosol samples shown in Fig. 10.43. (From Volten *et al.* 2001.)

1999, 2001; Vermeulen 1999; Hovenier 2000; Muñoz *et al.* 2000a, b, 2001; Volten 2001). For example, Fig. 10.43 shows microphotographs of seven mineral aerosol samples studied by Volten *et al.* (2001), while Fig. 10.44 depicts the respective normalized distributions of projected-area-equivalent-sphere radii (in micrometers). It is evident that all particles studied have irregular and strongly variable compact shapes. Table 10.4 provides a brief characterization of the samples including the corresponding effective radii and approximate ranges of the real part of the relative refractive index based on the literature values for the main constituent minerals. The results of measurements at the wavelengths 632.8 and 441.6 nm are shown in Figs. 10.45–10.51. The phase functions are normalized to unity at $\Theta = 30°$. Other elements of the normalized Stokes scattering matrix are shown relative to the corresponding phase function. The measurements were taken at $5°$ intervals for Θ in the range from $5°$ to $170°$ and at $1°$ intervals for Θ from $170°$ to $173°$. Scattering matrix elements other than those shown in these figures were found to be zero within the error bars, which was a good indication that the particles formed a macroscopically isotropic and mirror-symmetric scattering medium.

The phase functions for all samples studied are smooth functions of the scattering angle and exhibit a steep forward peak and essentially no structure at side- and back-scattering angles. Most of the phase-function curves are remarkably shallow at side-scattering angles (cf. Perry *et al.* 1978; Nakajima *et al.* 1989; Muñoz *et al.* 2000a) and do not show the deep side-scattering minimum typical of spherical particles, caused

Table 10.4. Characteristics of seven mineral particle samples studied by Volten *et al.* (2001)

Sample	Composition	r_{eff} (μm)	m_{R}	Color
Feldspar	K-feldspar, plagioclase, quartz	1.0	1.5–1.6	light pink
Red clay	biotite, illite, quartz	1.5	1.5–1.7	red brown
Quartz	quartz	2.3	1.54	white
Pinatubo volcanic ash	glass, plagioclase, amphibole, magnetite	3.0	1.5–1.7 2.1	light gray
Loess	K-feldspar, illite, quartz, calcite, chlorite, albite	3.9	1.5–1.7	yellow brown
Lokon volcanic ash	silica glass, plagioclase, magnetite	7.1	1.5–1.6 2.1	dark brown
Sahara sand	quartz, clay minerals, calcium carbonate	8.2	1.5–1.7	yellow brown

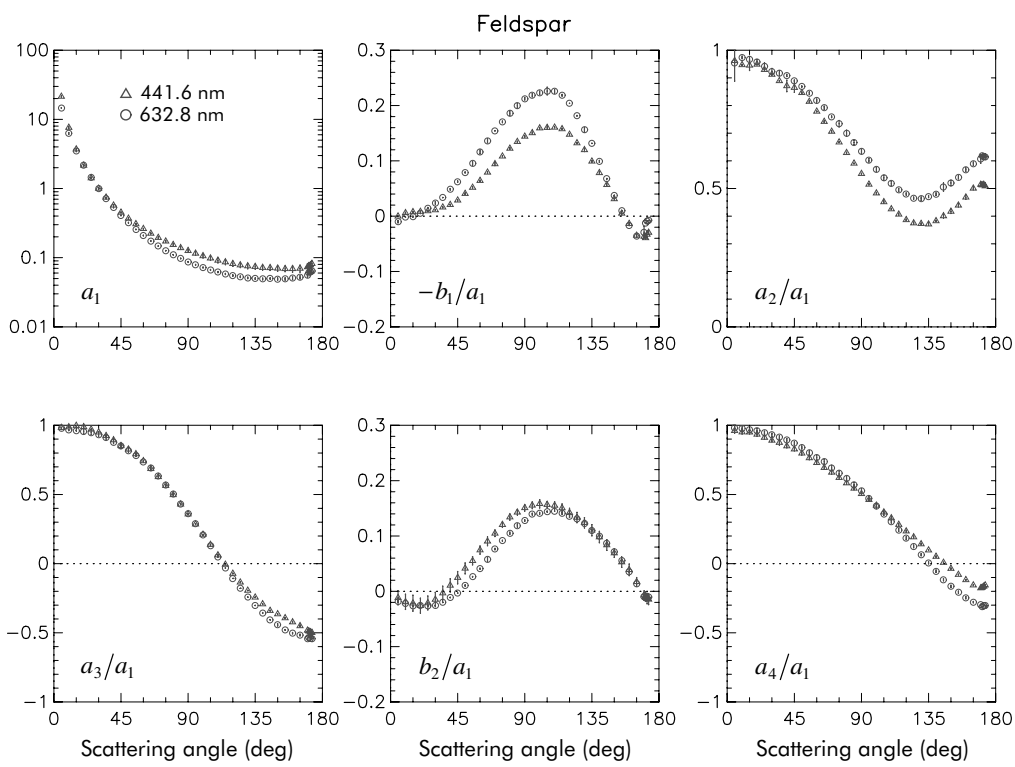

Figure 10.45. The phase function a_1 and the scattering matrix element ratios $-b_1/a_1$, a_2/a_1, a_3/a_1, b_2/a_1, and a_4/a_1 versus scattering angle Θ for feldspar. The circles and triangles denote measurements at wavelengths 632.8 and 441.6 nm, respectively, together with their error bars. The phase functions are normalized to unity at $\Theta = 30°$. The sign of the ratio b_2/a_1 is opposite to that adopted elsewhere in this book. (From Volten *et al*. 2001.)

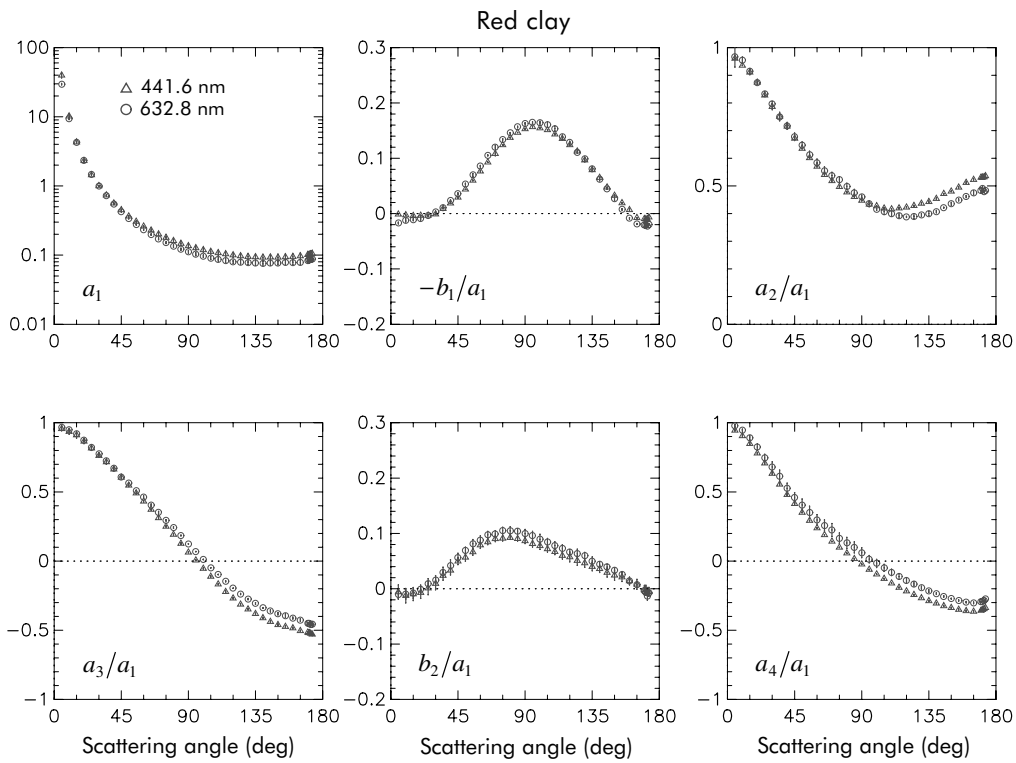

Figure 10.46. As in Fig. 10.45, but for red clay (from Volten *et al*. 2001).

by the Alexander's dark band lying between the primary and secondary rainbows (cf. Fig. 7.4 and Section 9.4). Some of the phase-function curves seem to show the beginning of a backscattering enhancement, but the lack of measurements for $\Theta > 173°$ makes this observation inconclusive. The curves for the ratio $-b_1/a_1$ are also similar for all samples and display a broad positive maximum at side-scattering angles and a weak and narrow negative branch at backscattering angles. The curves for the ratio a_2/a_1 are remarkably similar as well and deviate significantly from unity at side- and backscattering angles: they descend from almost unity at small scattering angles to a minimum at scattering angles close to $120° - 130°$ and then increase again as Θ approaches 180°. The depth of the minimum appears to be size dependent and increases as the effective radius grows from $1.0\,\mu\text{m}$ for feldspar to $8.2\,\mu\text{m}$ for Sahara sand. The curves for the ratios a_3/a_1 and a_4/a_1 are largely featureless and deviate significantly from –1 at backscattering angles. The ratio a_4/a_1 is always larger than the ratio a_3/a_1 in the backward hemisphere. Volten *et al.* (2001) use the time factor $\exp(\mathrm{i}\omega t)$ rather than $\exp(-\mathrm{i}\omega t)$ to define the Stokes parameters, which causes a sign change in the numerical values of the ratio b_2/a_1 (cf. Mishchenko *et al.* 2000b). Therefore, in terms of the time-factor convention adopted in this book, the results of Volten *et al.* show that this ratio typically has weak positive branches at small and large scattering angles separated by a wide range of negative values. Most of these observations are in qualitative agreement with the conclusions derived from the *T*-

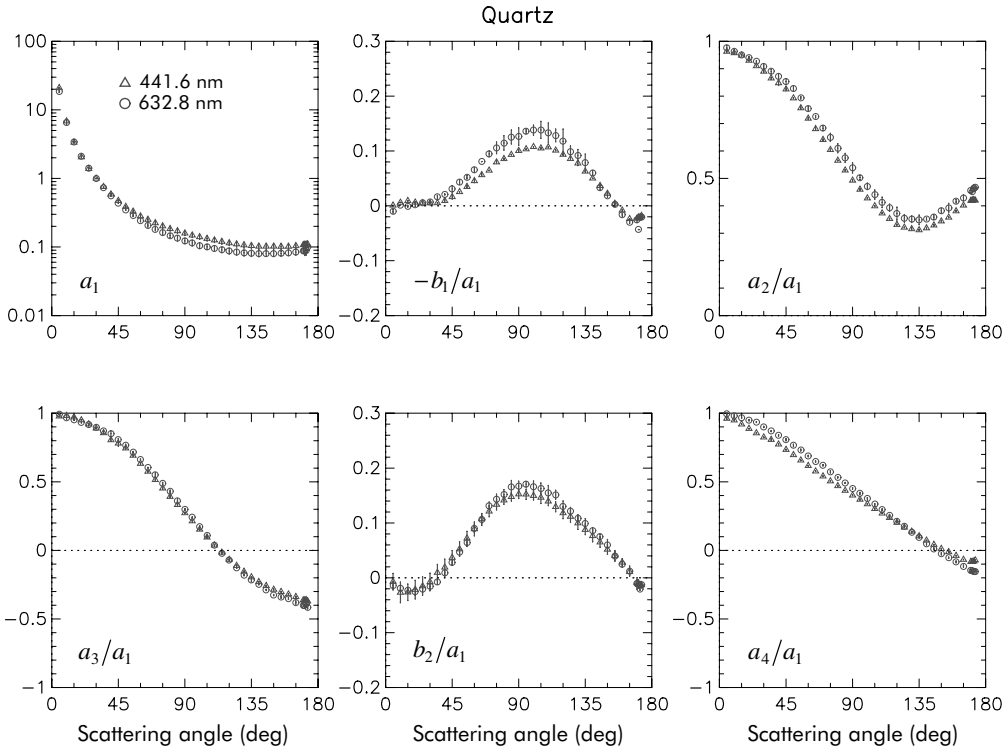

Figure 10.47. As in Fig. 10.45, but for quartz (from Volten *et al*. 2001).

matrix results for moderately aspherical polydisperse spheroids and cylinders as discussed in Sections 10.2 and 10.3.

The similarity of the laboratory results for the different mineral-particle samples prompted Volten *et al.* (2001) to construct an average scattering matrix for use in qualitative or semi-quantitative analyses of remote sensing observations or laboratory and *in situ* measurements, especially in those cases when the specific microphysical characteristics of mineral particles are not known *a priori*. The average phase function was calculated by averaging the 14 phase functions measured at both wavelengths. Since no scattering cross sections were available, the experimental phase functions were averaged by giving them equal weights. Therefore, the normalization to unity at $\Theta = 30°$ also holds for the average phase function. Each measured element ratio was multiplied by the normalized phase function measured for the particular sample and wavelength, thereby yielding elements instead of element ratios. Finally, each element was averaged over the respective 14 measurements and divided by the average phase function. The resulting average phase function and element ratios are depicted in Fig. 10.52. For comparison, this figure also shows the bands of sample variability, defined as the areas between the highest and lowest measured values in Figs. 10.45–10.51 not taking into account the error bars for the individual measurements. The laboratory data displayed in Figs. (10.45)–(10.52) were presented by Volten (2001) in tabular form and will undoubtedly prove very useful in future

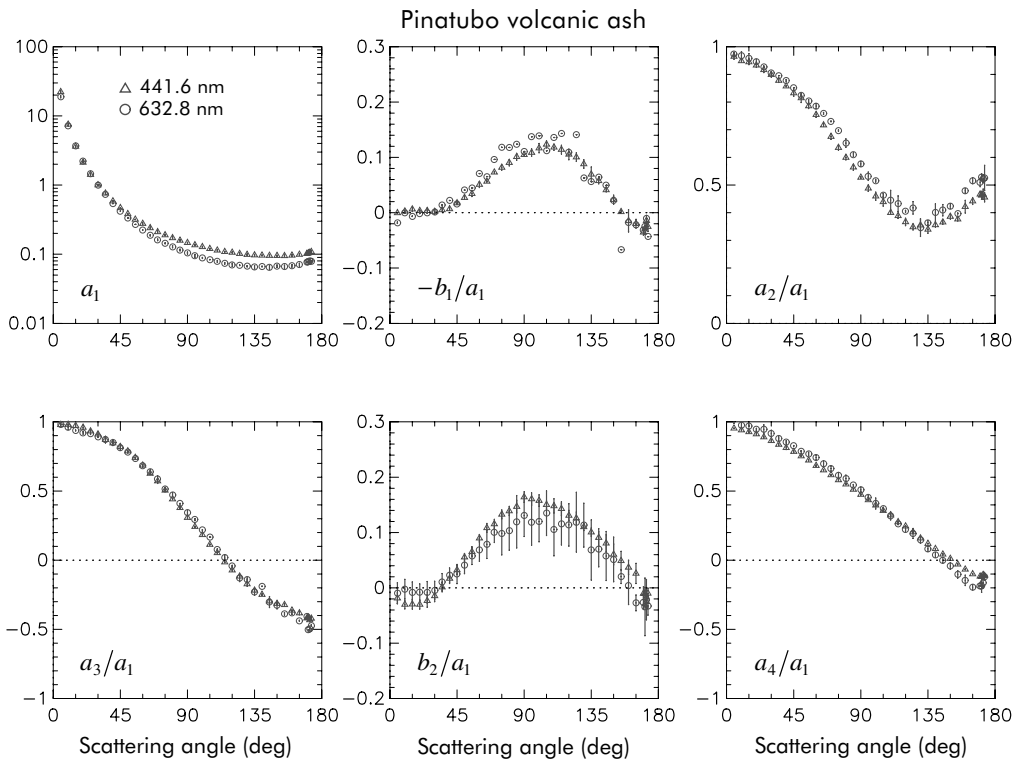

Figure 10.48. As in Fig. 10.45, but for Pinatubo volcanic ash (from Volten *et al*. 2001).

analyses of light scattering by irregular particles. For example, the laboratory data for green clay particles with an effective radius of 1.55 μm (Muñoz *et al.* 2000b) generally agree with the overall trends exhibited by the average scattering matrix elements and fall within the bands of sample variability (Fig 10.53). This comparison suggests that the average model derived by Volten *et al.* (2001) may indeed be representative of ensembles of irregular, compact mineral particles with sizes comparable to and larger than a wavelength.

10.8 Statistical approach

Since theoretical computations for irregular particles with sizes comparable to the wavelength remain problematic, several attempts have been made to model the scattering and absorption properties of irregular particles using simple, regular shapes. These attempts are based on the realization that in addition to size and orientation averaging, as discussed in Section 10.1, averaging over shapes may also prove to be necessary in many cases. More often than not, natural and artificial particle samples exhibit a great variety of shapes, thereby making questionable the ability of a single nonspherical shape to represent scattering properties of a shape mixture. We have

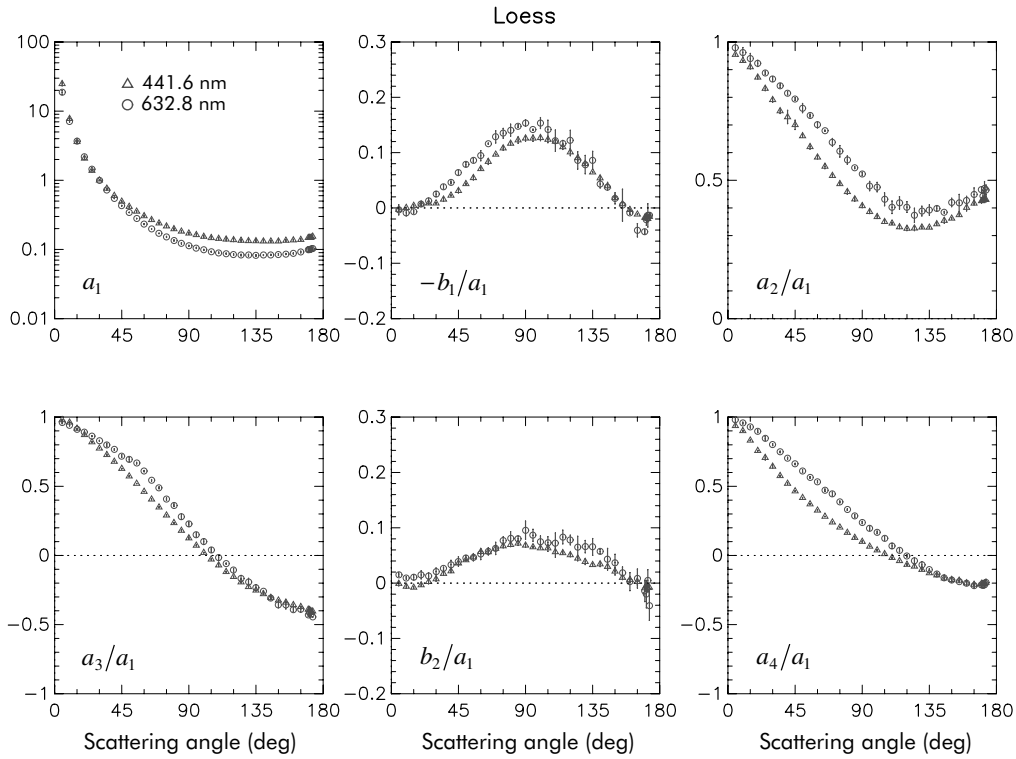

Figure 10.49. As in Fig. 10.45, but for loess (from Volten *et al*. 2001).

seen, indeed, that even after size and orientation averaging, essentially any deterministic particle shape produces a unique, shape-specific scattering pattern, whereas experimental measurements for real nonspherical particles usually show smooth, featureless patterns. As an example, Plate 10.7(a) depicts the phase function for a monodisperse sphere with radius 1.163 μm and surface-equivalent, monodisperse, randomly oriented prolate spheroids with aspect ratios ε increasing from 1.2 to 2.4. The wavelength of the light in the surrounding medium is 0.443 μm, and the relative refractive index is 1.53 + i0.008. Whereas the monodisperse curves form a tangle of lines with no clear message, averaging over sizes, as shown in Plate 10.7(b), makes the phase functions much smoother and reveals a systematic change with increasing aspect ratio that renders each phase-function curve unique and dissimilar to all other curves. However, this uniqueness is suppressed and ultimately removed by averaging over an increasingly wide aspect-ratio distribution of prolate spheroids, centered on $\varepsilon = 1.8$, Plate 10.7(c), and by a subsequent mixing of prolate and oblate spheroids, Plate 10.7(d). The resulting phase function (the red curve in Plate 10.7(d)) is very smooth and featureless and, in fact, almost perfectly coincides with the phase function experimentally measured by Jaggard *et al.* (1981) for micrometer-sized, irregularly shaped soil particles (cf. Fig. 10.54). Both phase functions show the typical en-

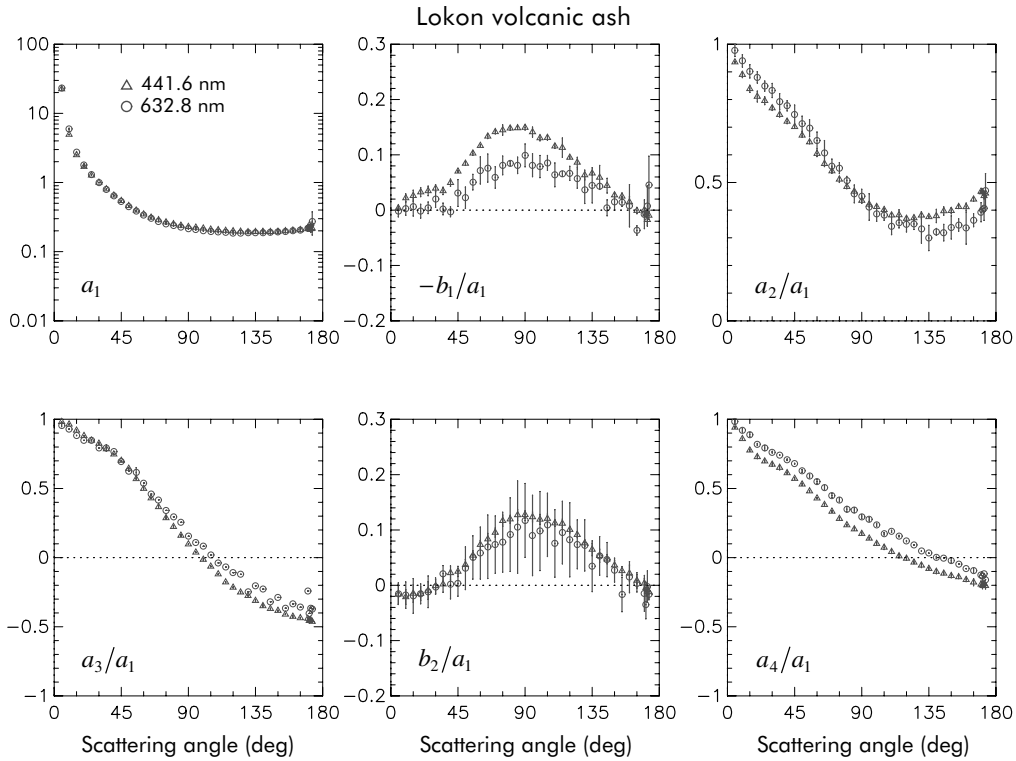

Figure 10.50. As in Fig. 10.45, but for Locon volcanic ash (from Volten *et al*. 2001).

hancement of side scattering and suppression of backscattering relative to the phase function for surface-equivalent spheres.

This example may have two important implications. First, it may indicate that the often observed smooth scattering-angle dependence of the elements of the scattering matrix for samples of natural and artificial nonspherical particles is largely caused by the diversity of particle shapes in the samples. Second, it may suggest that at least some scattering properties of ensembles of irregular particles can be adequately modeled using a polydisperse shape mixture of simple particles such as spheroids. The assumptions that particles chosen for the purposes of ensemble averaging need not be in one-to-one correspondence with the ensemble of irregular particles of interest and that they may have relatively simple shapes are central to the so-called statistical approach (Shifrin and Mikulinsky 1987; Mugnai and Wiscombe 1989; Bohren and Singham 1991). The need for this kind of approach stems from the fact that it is often impossible to specify exactly the shapes and sizes of all particles forming a natural or artificial sample. Even if it were possible, the low efficiency of the exact numerical techniques applicable to arbitrarily shaped particles would entail a prohibitively expensive computational effort. However, the availability of techniques like the *T*-matrix method, which is very fast for randomly oriented, rotationally symmetric particles and is applicable to large size parameters, makes the statistical approach feasible. Applications of this approach by Bohren and

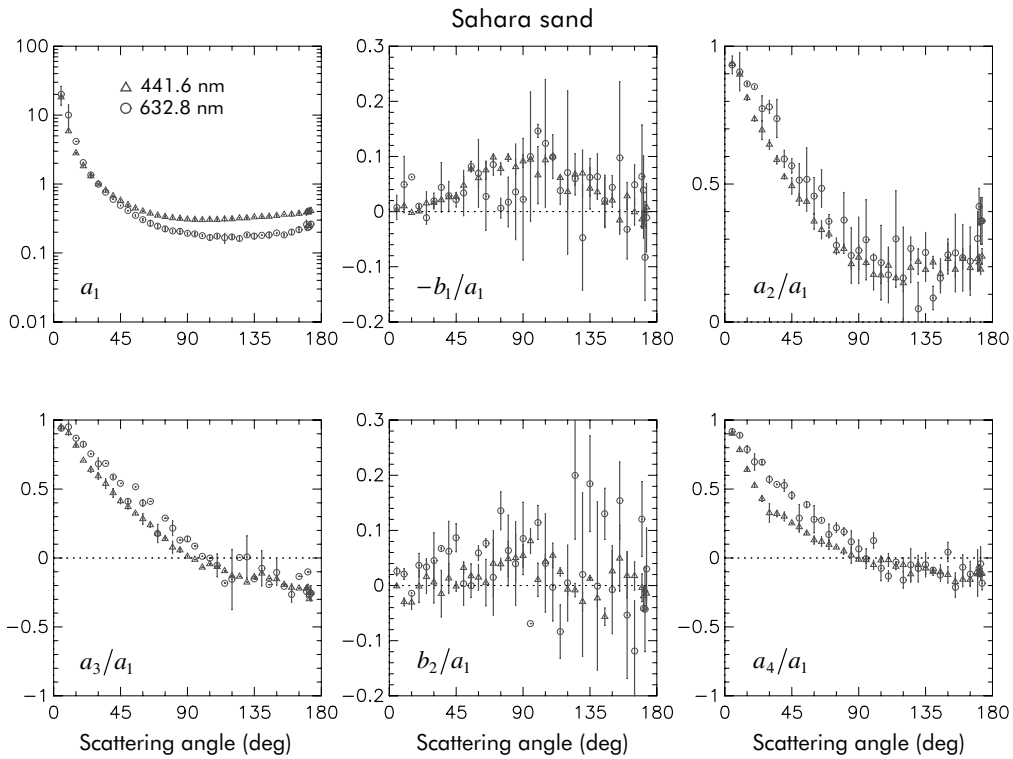

Figure 10.51. As in Fig. 10.45, but for Sahara sand (from Volten *et al*. 2001).

Huffman (1983, Chapter 12), Nevitt and Bohren (1984), Hill *et al.* (1984), Mishchenko *et al.* (1997a), and Goncharenko *et al.* (1999) suggest that it may indeed be a valuable practical tool in many cases.

10.9 Clusters of spheres

The scattering and absorption properties of simple two-sphere clusters (bispheres) have been extensively studied by Mishchenko *et al.* (1995) using the superposition *T*-matrix method. Panels (b) and (c) of Plate 10.8 depict the degree of linear polarization for scattering of unpolarized incident light, i.e., the ratio

$$-\frac{Z_{21}(\vartheta^{\rm sca}, \varphi^{\rm sca}=0; \vartheta^{\rm inc}=0, \varphi^{\rm inc}=0)}{Z_{11}(\vartheta^{\rm sca}, \varphi^{\rm sca}=0; \vartheta^{\rm inc}=0, \varphi^{\rm inc}=0)},$$

as a function of the zenith angle of the scattering direction and the monodisperse constituent-sphere size parameter for two orientations of the bisphere axis with respect to the laboratory reference frame. The bispheres have identical touching components, and the bisphere axis is defined as the line connecting the constituent-sphere centers. These plots show that the bisphere polarization is strongly dependent on the particle

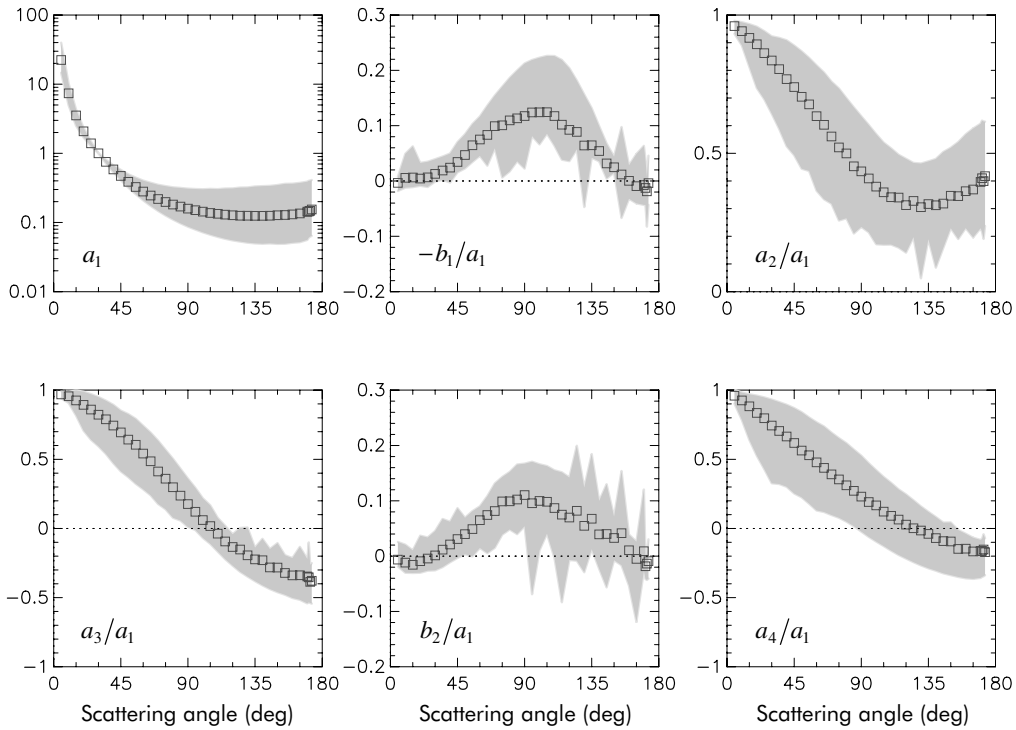

Figure 10.52. The squares show the average phase function a_1 (normalized to unity at $\Theta = 30°$) and the scattering matrix element ratios $-b_1/a_1$, a_2/a_1, a_3/a_1, b_2/a_1, and a_4/a_1 versus scattering angle Θ. The gray bands indicate the domains spanned by the measurements for individual particle samples. The sign of the ratio b_2/a_1 is opposite to that adopted elsewhere in this book. (From Volten *et al*. 2001.)

orientation and reveals a much more complicated structure than the single-sphere polarization pattern shown in Plate 10.8(a). In particular, the lack of axial symmetry for the scattering geometry in Plate 10.8(c) makes the linear polarization non-zero at $\vartheta^{\text{sca}} = 0°$ and, more noticeably, at $\vartheta^{\text{sca}} = 180°$. Also, the number of local maxima and minima has increased sharply. This means that in addition to the single-sphere resonant structure the bispheres exhibit a significant contribution due to the cooperative scattering of light from the two constituent spheres.

Plate 10.8(d) shows the calculation results for monodisperse bispheres in random orientation. Somewhat unexpectedly, we see a polarization pattern that is strikingly similar to that of single monodisperse spheres, Plate 10.8(a). The only obvious difference is that the amplitudes of the local maxima and minima are reduced, although their locations and numbers are exactly the same. This means that averaging over bisphere orientations largely cancels the cooperative scattering contribution and slightly blurs the single-sphere resonant structure. This result is well illustrated by Fig. 10.55, which shows the elements of the normalized Stokes scattering matrix for a randomly oriented two-sphere cluster with identical touching components, together with those for a single sphere with size parameter equal to that of the cluster compo-

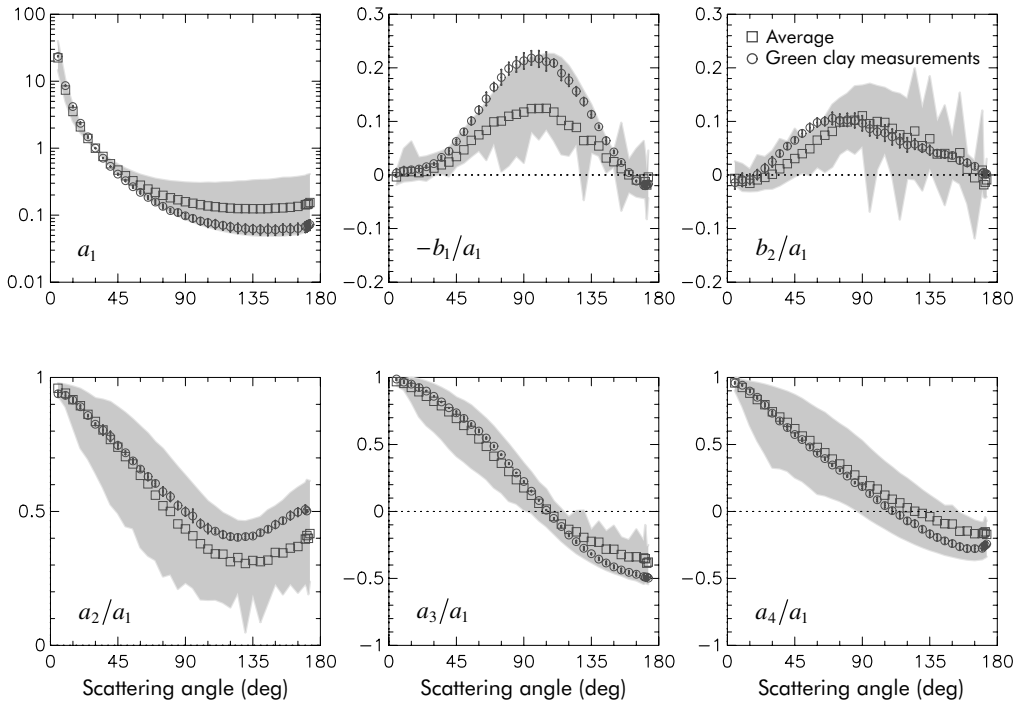

Figure 10.53. The circles depict the measured phase function a_1 and scattering matrix element ratios $-b_1/a_1$, b_2/a_1, a_2/a_1, a_3/a_1, and a_4/a_1 versus scattering angle for green clay particles at a wavelength 633 nm (from Muñoz *et al.* 2000b). The squares and the gray bands indicate the average scattering matrix and the domains spanned by the measurements for seven mineral particle samples (Volten *et al.* 2001).

nents for comparison. It is obvious that the dominant feature in the cluster scattering is the single scattering from the component spheres, albeit diminished by orientation averaging. The only distinct manifestations of the fact that the bisphere is a nonspherical particle are the departure of the ratio a_2/a_1 from unity and the detectable lack of equality of the elements a_3 and a_4. These two effects are especially noticeable at backscattering angles and are further illustrated in Fig. 10.56, which shows the linear and circular depolarization ratios for randomly oriented bispheres with touching components as a function of the component-sphere size parameter. Both depolarization ratios vanish in the limit of zero size parameter, but become appreciable for $x \gtrsim 1$ and reach especially large values at size parameters from about 15 to 20.

Figures 10.57 and 10.58 show ratios of bisphere and single-sphere quantities: the optical cross sections, the single-scattering albedo, and the asymmetry parameter. The bispheres are randomly oriented and the size of the single sphere is equal to the size of each bisphere component. Interestingly, all these ratios are nearly constant at size parameters exceeding 15. The ratio of the extinction cross sections (the solid curve in Fig. 10.57) shows both high-frequency ripple and low-frequency oscillations. However, the amplitude of the oscillations is small, and the entire curve for size parameters exceeding

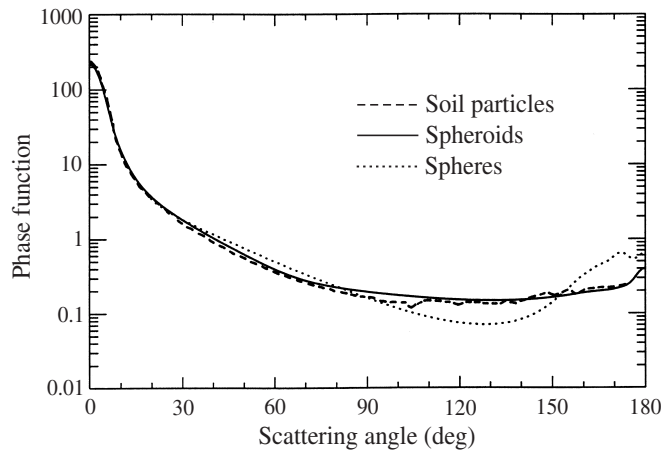

Figure 10.54. Phase functions measured by Jaggard *et al.* (1981) for natural wavelength-sized soil particles and computed for a broad shape distribution of polydisperse, randomly oriented spheroids and surface-equivalent spheres.

6 is close to 1.8–1.85. The ratio of the orientation-averaged geometrical cross section of a bisphere to the geometrical cross section of a sphere with size equal to that of each bisphere component is 1.849. Therefore, in the geometrical optics limit the ratio of the bisphere and single-sphere extinction cross sections must be equal to this value, 1.849. It can be seen that the extinction ratio curve shows a distinct trend toward this limit with increasing size parameter. However, it is interesting that the extinction ratio is close to the geometrical optics limit for size parameters as small as 7.

Despite a small-amplitude high-frequency ripple, the ratio of the absorption cross sections (the broken-and-dotted curve in Fig. 10.57) is close to 2 for the entire range of size parameters shown, thus indicating that the absorption cross section is roughly proportional to the particle volume. However, if the imaginary part of the relative refractive index is non-zero then in the limit of infinite size parameter all light refracted into the particle is absorbed and does not escape. Therefore we should expect that the ratio of the absorption cross sections should decrease with increasing size parameter and approach the geometrical cross section ratio of 1.849, as seen indeed in Fig. 10.57. The scattering cross section ratio (the dotted curve in Fig. 10.57) closely follows the extinction cross section ratio except at size parameters smaller than unity, where extinction is dominated by absorption.

The single-scattering albedo ratio (the dotted curve in Fig. 10.58) is especially size-parameter independent for size parameters greater than unity and varies within a very narrow range, 1 ± 0.02. The asymmetry parameter ratio (the solid curve in Fig. 10.58) is also close to unity. However, all these ratios, except for the absorption cross section ratio, rise substantially as the size parameter becomes smaller than 2, which demonstrates the increasing influence of cooperative scattering effects for smaller particles.

As we have seen previously, one of the main effects of averaging scattering

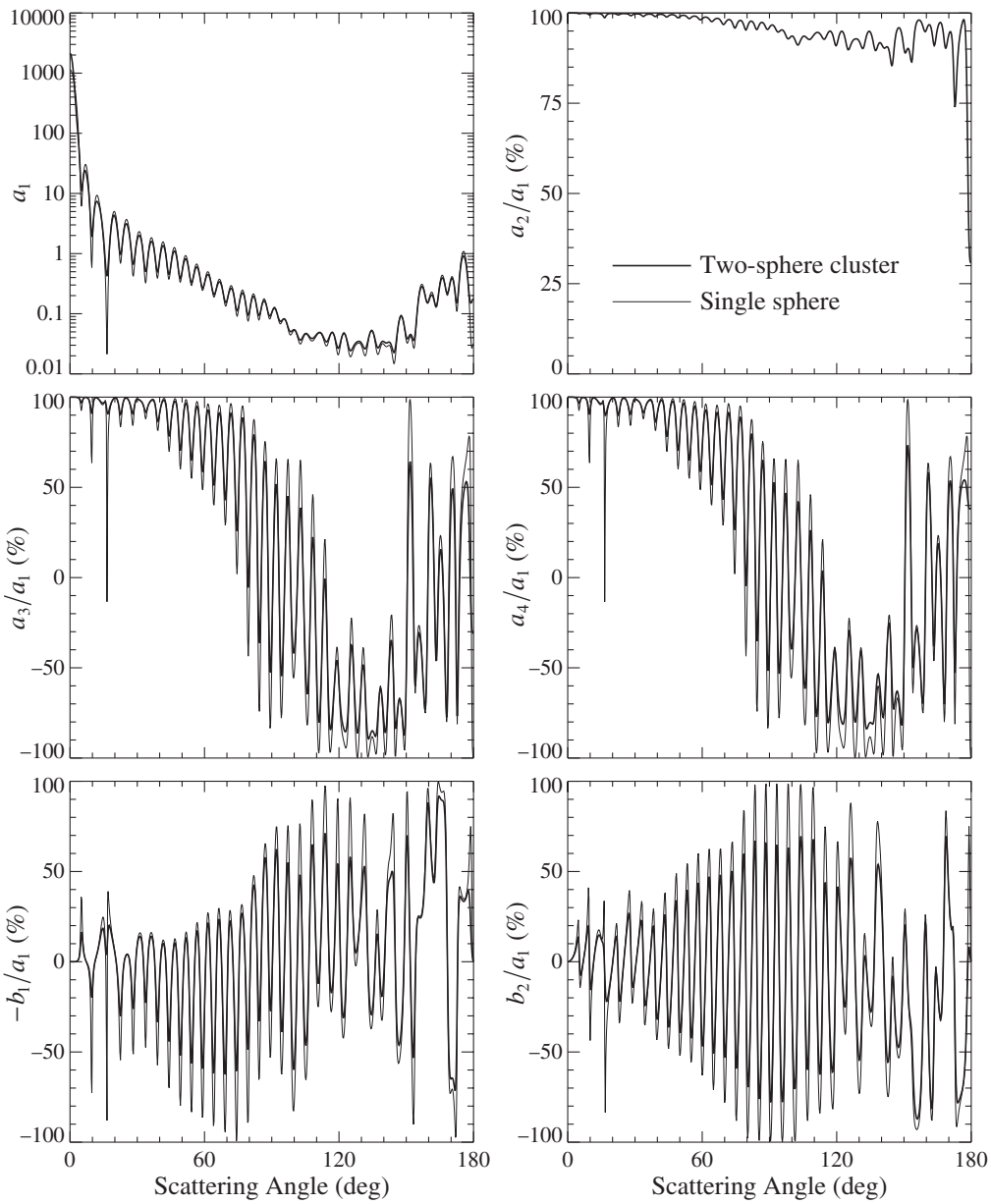

Figure 10.55. Scattering matrix elements for a randomly oriented two-sphere cluster with touching components and a single sphere. The component spheres and the single sphere have the same size parameter 40 and the same relative refractive index 1.5 + i0.005.

characteristics over a size distribution is to wash out the resonance structure typical of monodisperse particles. This effect facilitates comparisons of light-scattering properties of particles with different shapes and is illustrated in Fig. 10.59, which shows the elements of the normalized Stokes scattering matrix for power law size distributions of spheres and of randomly oriented bispheres. This figure demonstrates again that the angular dependence of the elements of the scattering matrix for bispheres is similar to that for single spheres with effective size parameter equal to the effective

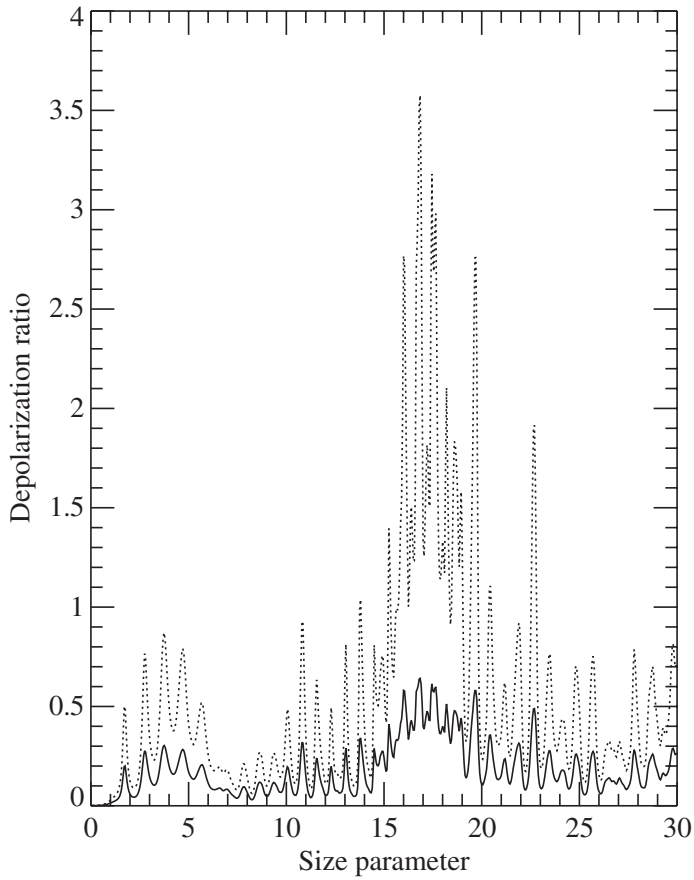

Figure 10.56. Linear (solid curve) and circular (dotted curve) backscattering depolarization ratios versus constituent-sphere size parameter for randomly oriented monodisperse bispheres with equal touching components and a relative refractive index 1.5 + i0.005.

bisphere monomer size parameter. The ratios $-b_1/a_1$ and b_2/a_1 for the bispheres and the single spheres are especially similar. The phase functions a_1 are also close to one another except at scattering angles smaller than 10°, where the bisphere intensity is nearly twice that for single spheres because of the constructive interference of light singly scattered by bisphere components in the exact forward direction (Mishchenko 1996a). Again, the only unequivocal indications of particle nonsphericity for bispheres are the differences between the ratios a_3/a_1 and a_4/a_1 and the departure of the ratio a_2/a_1 from unity. For comparison, Fig. 10.59 also depicts the scattering matrix elements for polydisperse, randomly oriented prolate spheroids with aspect ratio 2 and effective volume-equivalent-sphere size parameter 10. It is seen that, unlike the case for the spheres and the bispheres, the spheroid phase function exhibits enhanced side scattering and suppressed backscattering, while the degree of linear polarization is positive at scattering angles around 120°. The differences between the ratios a_2/a_1, a_3/a_1, a_4/a_1, and b_2/a_1 for the spheres and the spheroids are also greater than those for the spheres and the bispheres.

Figures 10.60 and 10.61 depict the scattering matrix elements for two distinctly

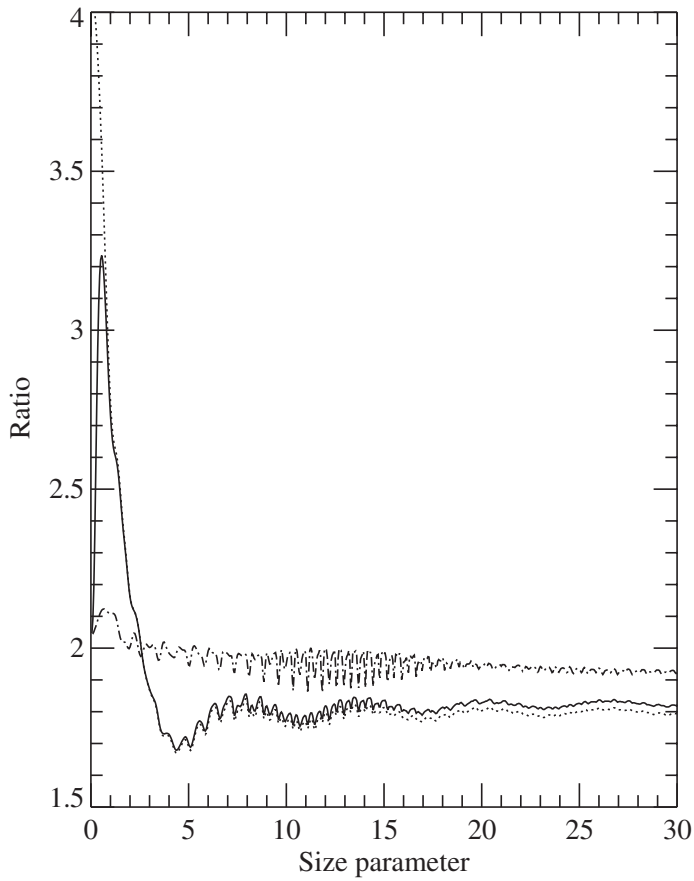

Figure 10.57. Ratios of extinction (solid curve), scattering (dotted curve), and absorption (broken-and-dotted curve) cross sections for monodisperse randomly oriented bispheres with equal touching components and for monodisperse single spheres, versus single-sphere size parameter. For bispheres, the horizontal axis shows the values of the constituent-sphere size parameter. The relative refractive index is 1.5 + i0.005.

different types of sphere cluster, each with N_s identical wavelength-sized components, for $N_s = 1, 2, 3, 4,$ or 5. In Fig. 10.60 the cluster is a straight chain whereas in Fig. 10.61 the spheres are packed into a tetrahedral lattice. These two types of clusters represent extrema in the packing density of touching spheres. A quick inspection of the figures reveals that the configuration of the component spheres can have a significant effect on the cluster scattering properties. Aside from the increase in the forward-scattering value of the phase function caused by the constructive interference of the light singly scattered by the cluster components in the exact forward direction, the matrix elements for the straight chain (Fig. 10.60) attain a form that is nearly independent of N_s for $N_s \geq 2$. As for bispheres, clustering results in a damping of the oscillations in the matrix elements compared with those for a single sphere, yet the locations of the maxima and minima for the chain are essentially the same as those for the single-sphere case. The obvious exception is the ratio a_2/a_1, which is identically unity for the sphere. However, the matrix elements for the densely packed cluster

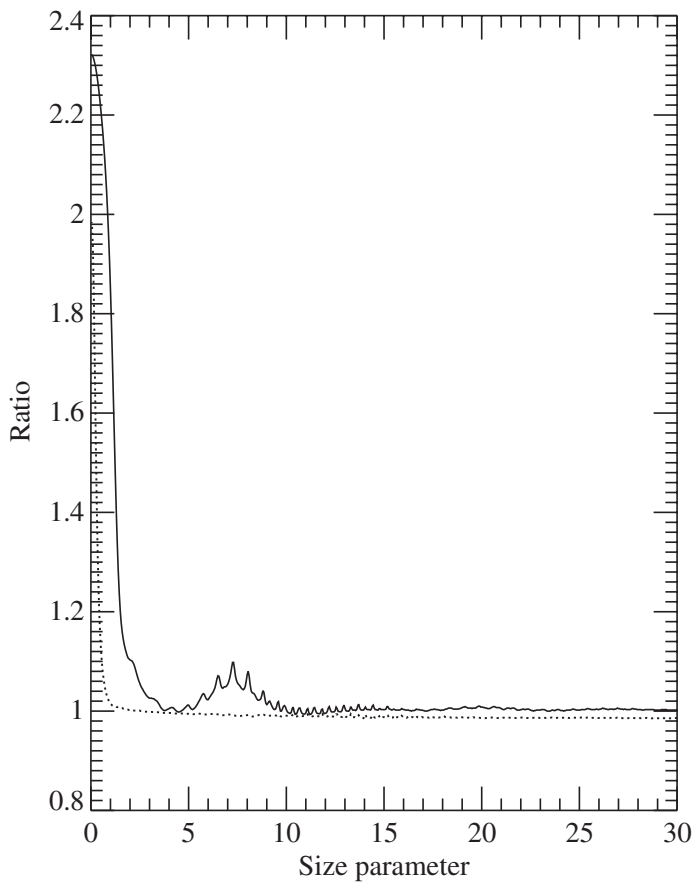

Figure 10.58. As in Fig. 10.57, but for the ratios of the single-scattering albedos (dotted curve) and of the asymmetry parameters (solid curve).

change significantly with increasing N_s and appear to approach a saturation level in which all oscillations eventually vanish. The effect of packing density is especially noticeable in the backward-direction values of the ratios a_2/a_1, a_3/a_1, and a_4/a_1 and, thus, in increased linear and circular depolarization ratios.

To explain the differences in the scattering patterns for these two types of cluster configuration, we first note that the two major effects of aggregation on scattering are interference of the fields scattered by the cluster components in the far-field zone and multiple internal scattering among the components. When the size parameters of the spheres are of order unity or greater (as is the case for Figs. 10.60 and 10.61), averaging over a uniform orientation distribution acts to zero out the effect of interference in all directions but the exact forward direction. The differences between the single-sphere and orientation-averaged cluster scattering patterns are therefore caused mostly by multiple scattering. Multiple scattering for the linear chain configuration occurs primarily between neighboring spheres, and because of this the scattering matrix elements for $N_s \geq 3$ do not differ much from those of the bisphere – except for the phase function at $\Theta = 0°$. However, the packed-cluster configuration offers a

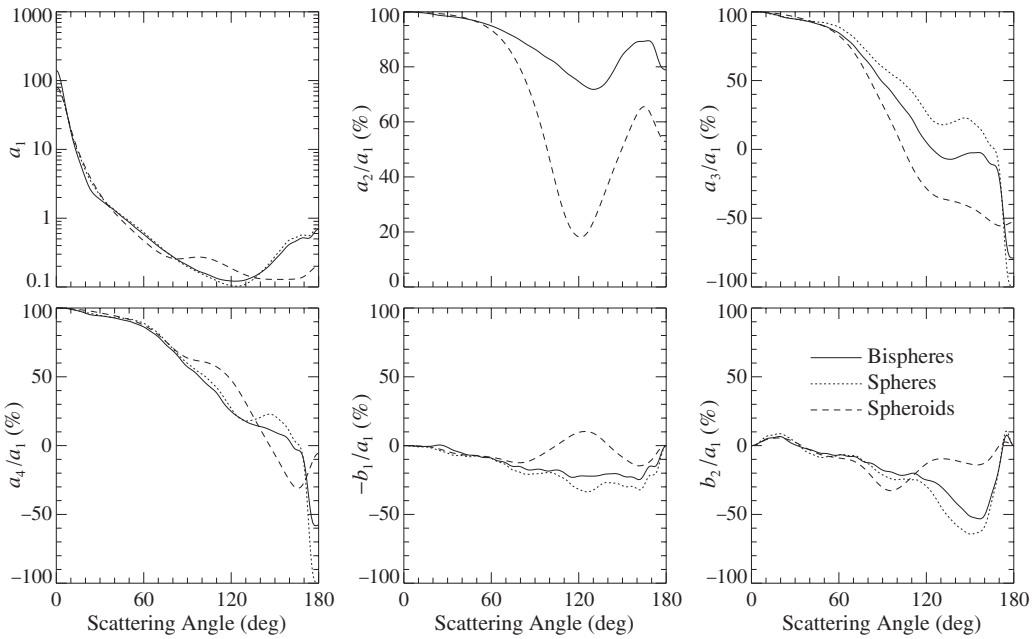

Figure 10.59. Elements of the normalized Stokes scattering matrix for polydisperse randomly oriented bispheres with equal touching components and effective constituent-sphere size parameter $x_{\text{eff}} = 10$ and for polydisperse single spheres with the same effective size parameter. For comparison, the figure also shows the results for polydisperse, randomly oriented prolate spheroids with aspect ratio 2 and effective volume-equivalent-sphere size parameter 10. The relative refractive index is 1.5 + i0.005 and the size distribution is given by Eq. (5.244) with an effective variance $v_{\text{eff}} = 0.2$.

much greater opportunity for multiple scattering among all the spheres forming the cluster and results in stronger differences between the single-sphere and random-orientation-cluster elements of the scattering matrix.

Based on the results for linear chains of spheres, we may expect that scattering patterns for low-density aggregates of wavelength-sized particles look similar to those for bispheres. This is indeed demonstrated by the laboratory data measured by Muñoz *et al.* (2000b, 2001) for a sample of fly ash aerosols (fluffy aggregates composed of nearly spherical inorganic particles; see Fig. 10.62). Figure 10.63 shows that the normalized scattering matrix for this sample is distinctly different from the average scattering matrix for compact irregular particles derived by Volten *et al.* (2001) (see Section 10.7). Moreover, the experimental results depicted in Fig. 10.63 appear to be remarkably similar to the results of theoretical computations displayed in Fig. 10.59. In particular, the phase function of fly ash particles has the deep side-scattering minimum typical of single spheres and bispheres, the ratios a_3/a_1 and a_4/a_1 tend to values close to –1 as the scattering angle approaches 180°, and the ratio a_2/a_1 is closer to unity than that for compact nonspherical particles. Also, the ratios $-b_1/a_1$ and b_2/a_1 for fly ash and compact irregular particles are qualitatively similar to those computed for polydisperse bispheres and spheroids, respectively.

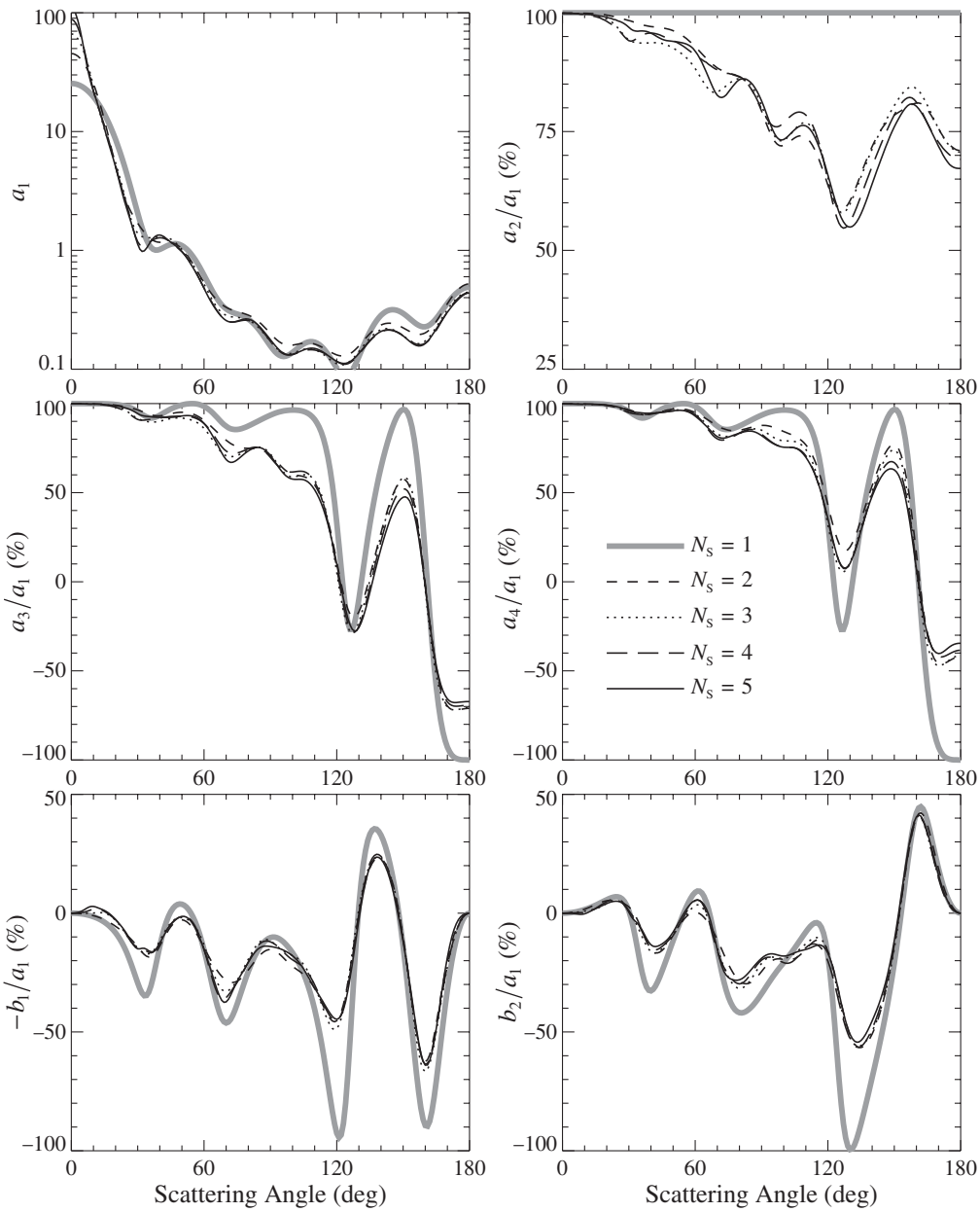

Figure 10.60. Orientation-averaged scattering matrix elements for linear chains of N_s equal spheres. The component-sphere size parameter is 5 and the relative refractive index is 1.5 + i0.005. (After Mackowski and Mishchenko 1996.)

Since clusters of small monomers are abundant in various natural and artificial environments, cluster optics is an important and active area of research. Detailed information and further references can be found in the reviews by Fuller and Mackowski (2000) and Sorensen (2001) and the book edited by Markel and George (2001).

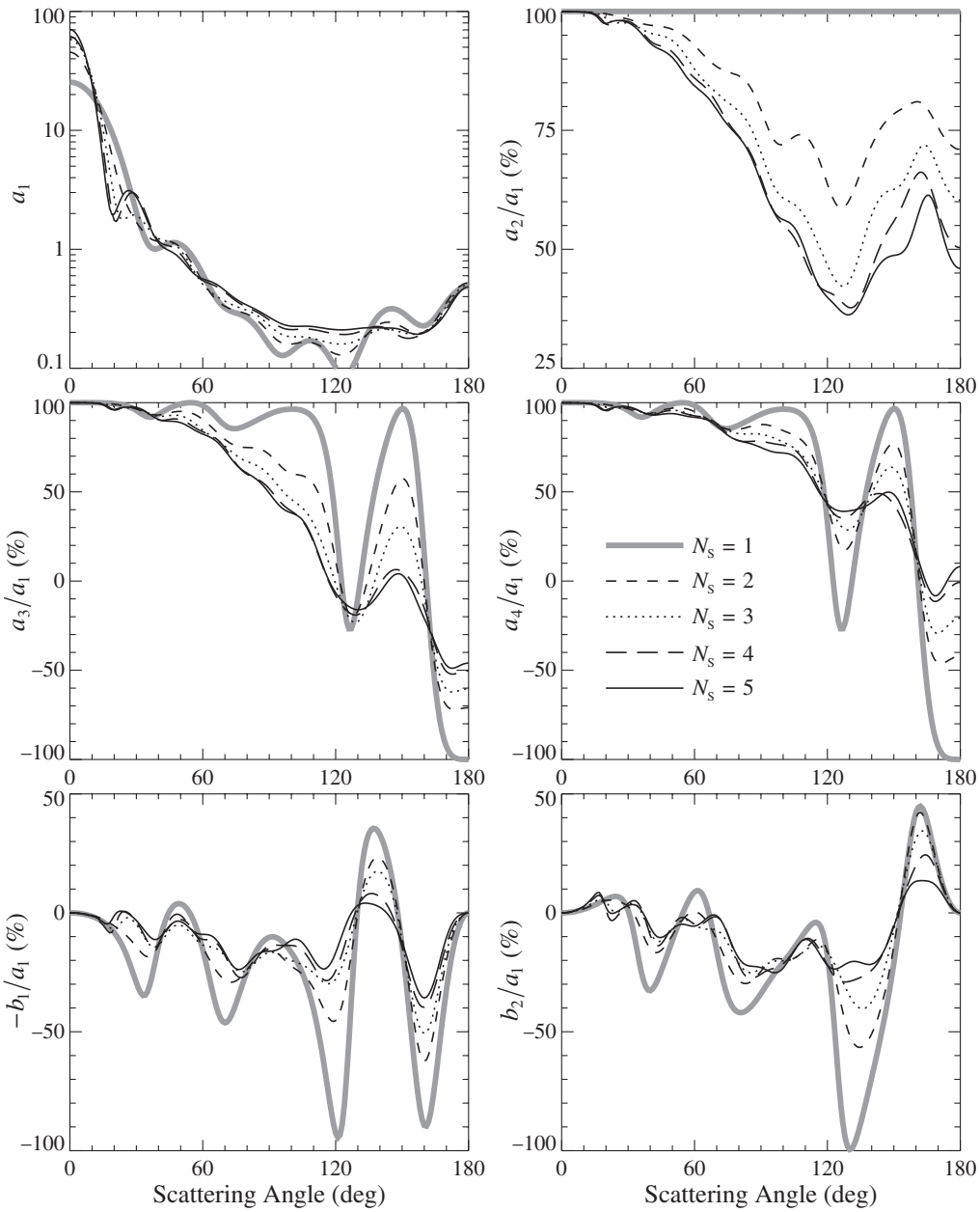

Figure 10.61. As in Fig. 10.60, but for packed clusters of N_s equal spheres. (After Mackowski and Mishchenko 1996.)

10.10 Particles with multiple inclusions

Another interesting class of scatterers are particles with multiple randomly positioned inclusions. Typical examples are water droplets and sulfate aerosols in the terrestrial atmosphere that contain various insoluble impurities (Chýlek *et al.* 1995, 1996), ice particles with internally trapped air bubbles and mineral and soot inclusions (Macke

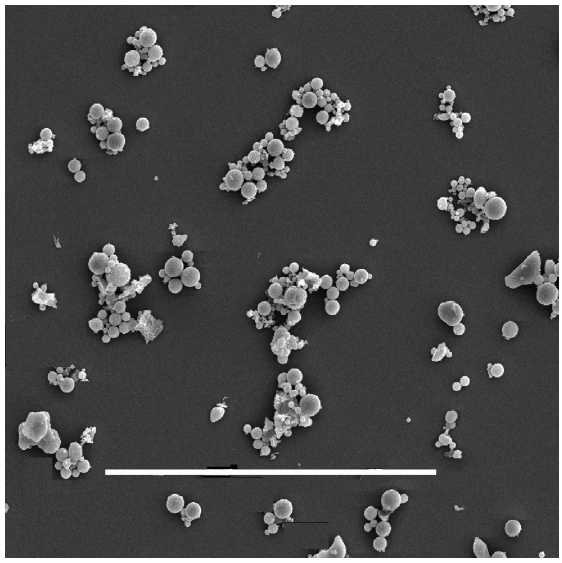

Figure 10.62. Scanning electron microscope photograph of inorganic fly ash particles produced by the combustion of powdered coal in electric powerplants. The length of the white bar corresponds to 100 μm. (From Muñoz *et al.* 2000b.)

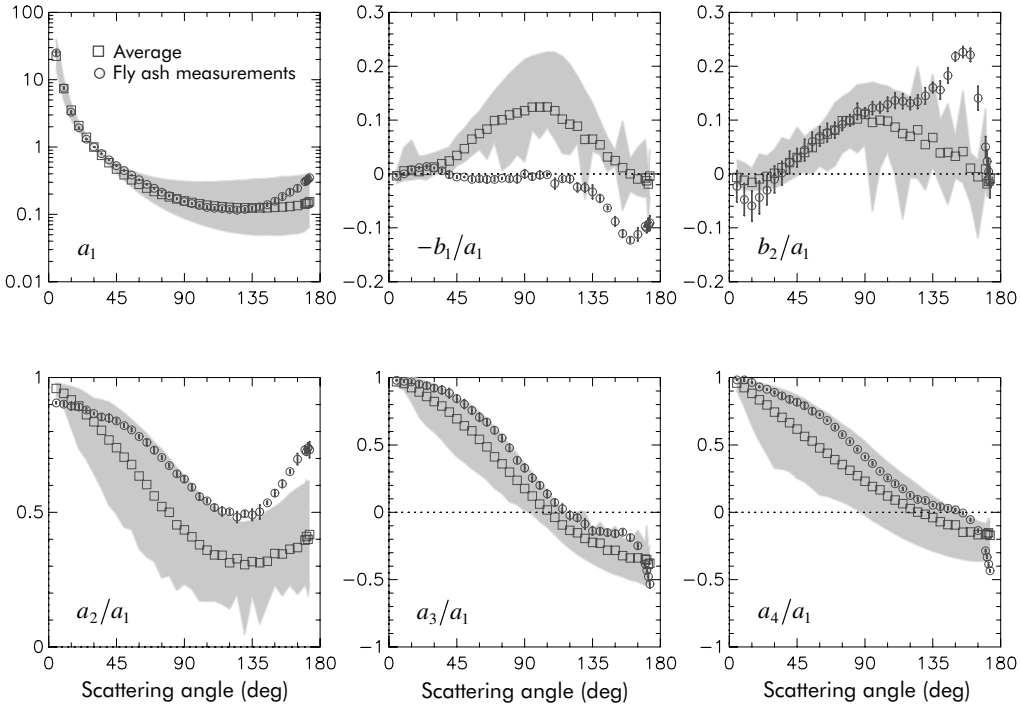

Figure 10.63. The circles depict the measurements by Muñoz *et al.* (2000b) for fly ash particles at a wavelength 633 nm. The squares show the average scattering matrix derived by Volten *et al.* (2001) using measurements for seven samples of compact mineral particles, while the gray bands indicate the domains of sample variability. The sign of the ratio b_2/a_1 is opposite to that adopted elsewhere in this book.

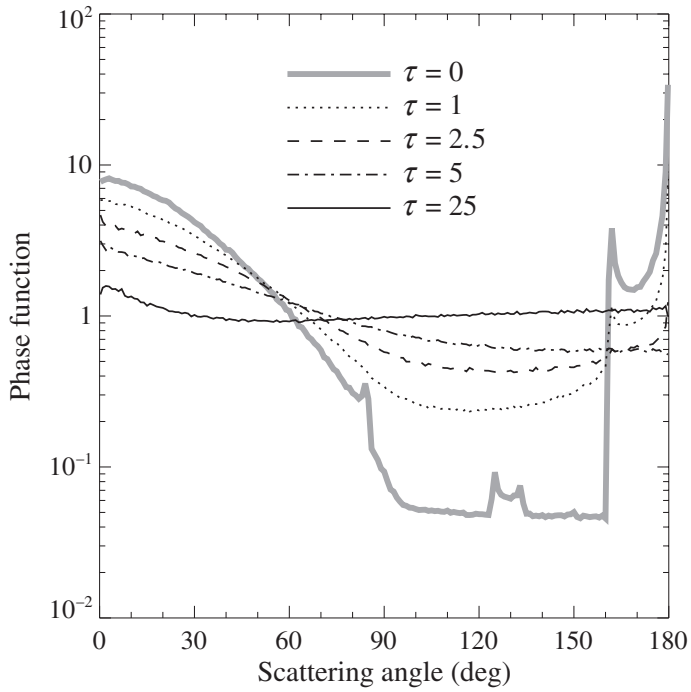

Figure 10.64. The ray-tracing part of the phase function versus scattering angle for a 50-μm-diameter spherical particle containing type-1 inclusions. The optical thickness of the inclusions increases from $\tau = 0$ (no inclusions) to $\tau = 25$ (after Mishchenko and Macke 1997).

et al. 1996a; C.-Labonnote *et al.* 2001), and inhomogeneous composites of mineral particles.

Light scattering by wavelength-sized spheres with a few inclusions can be computed using the superposition *T*-matrix method (cf. Section 5.9). When the host particle is much larger than the wavelength of the incident light, the only feasible approach is the Monte Carlo ray-tracing procedure described in Section 7.4. Figures 10.64 and 10.65 show the ray-tracing part of the phase function for a large spherical host particle with two types of small inclusions. The host has diameter $D = 50\,\mu\text{m}$ and refractive index relative to vacuum 1.55. The latter is a value typical of the real part of the refractive index of silicate materials. The inclusions are modeled as a gamma distribution, Eq (5.245), of spherical particles, with effective radius $0.5\,\mu\text{m}$ and effective variance 0.1. The refractive indices of the inclusions relative to vacuum are 1 (type 1, shown in Fig. 10.64) and 2 (type 2, Fig. 10.65). Type-1 inclusions represent small voids inside the host particle, whereas type-2 inclusions correspond to highly refractive impurities. The vacuum wavelength of the light is fixed at $0.55\,\mu\text{m}$. The overall scattering and absorption effect of the inclusions depends on their "optical thickness" $\tau = n_0 D \langle C_{\text{ext}} \rangle$, where n_0 is the inclusion number density and $\langle C_{\text{ext}} \rangle$ the average extinction cross section per inclusion. For reference, the total numbers of type-1 and type-2 inclusions inside the 50-μm-diameter spherical host corresponding to $\tau = 25$ are 29 469 and 18 967, respectively.

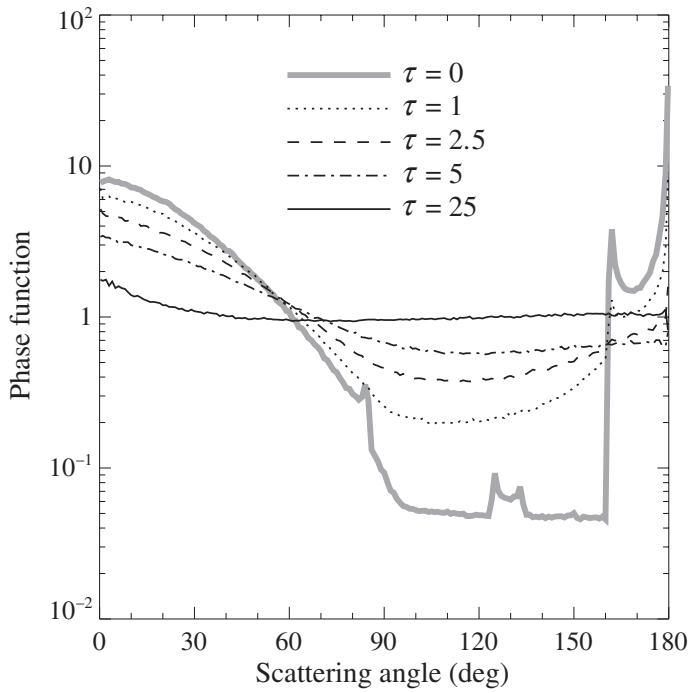

Figure 10.65. As in Fig. 10.64, but for type-2 inclusions (after Mishchenko and Macke 1997).

Figures 10.64 and 10.65 show that the ray-tracing phase function for a clear host (i.e., one having no inclusions) exhibits the pronounced geometrical optics features that are typical of large spherical particles and are discussed in detail in Section 9.4. With increasing τ, these features rapidly weaken and the ray-tracing phase functions become more and more isotropic, in qualitative agreement with the results of laboratory measurements by McGuire and Hapke (1995). Similarly, the effect of inclusions on the phase function of hexagonal ice crystals is to wash out the primary and secondary halos and the backscattering peak (Macke *et al.* 1996a). These effects can be explained qualitatively by increased multiple scattering among the inclusions, which tends to randomize the directions of rays exiting the host. Accordingly, the total asymmetry parameter of the composite spherical particles decreases from approximately 0.815 for $\tau = 0$ to approximately 0.5 for $\tau = 25$ (Fig. 10.66).

When the size of the inclusions is much smaller than the wavelength, a widely used approach is to assume that the composite particle is homogeneous and has an "effective" permittivity obtained by combining in a certain way the permittivities of the host and the inclusions. Several effective-medium approximations and their ranges of applicability are reviewed by Sihvola (1999) and Chýlek *et al.* (2000).

10.11 Optical characterization of nonspherical particles

There are two basic reasons why the optical characterization of nonspherical particles is significantly more involved than that of spherical particles. First, solving the direct

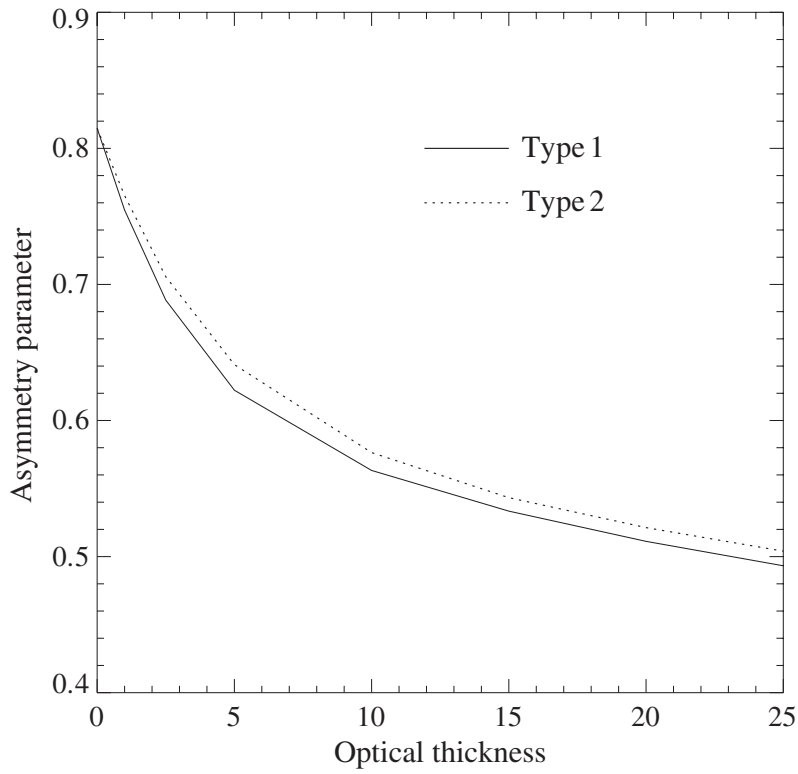

Figure 10.66. Total asymmetry parameter for 50-μm-diameter composite spherical particles containing type-1 and type-2 inclusions, with optical thickness varying from $\tau = 0$ (no inclusions) to $\tau = 25$ (after Mishchenko and Macke 1997).

scattering problem for nonspherical particles is more difficult than applying the standard Lorenz–Mie theory for spheres. Second, solving the inverse problem requires the introduction of at least two (and often many more) additional model parameters describing the particle shape and the orientation distribution function. These additional parameters are often unknown and must be retrieved from the experimental data, along with the particle size and the relative refractive index.

Apparently the simplest task is the detection of preferentially oriented nonspherical particles using the qualitative criteria summarized in Section 4.9. We have already mentioned in this regard observations of interstellar polarization and measurements of the depolarization of radio waves propagating through falling hydrometeors. Another technique involves directing the incident unpolarized beam along the z-axis of the laboratory reference frame and measuring the two-dimensional angular distribution of the scattered intensity. The lack of axial symmetry in this distribution will be an unequivocal indication of the presence of oriented nonspherical particles (see Figs. 10.1–10.5 and Section 10.1). This technique will fail, however, when axially symmetric particles are present whose rotation axes are also directed along the z-axis (note the upper left panels of Figs. 10.2–10.5). Also, it may be difficult to use such

measurements to say something specific about the particle microphysical characteristics. We have seen in Section 10.1 that the number of patches per unit solid angle in the scattering diagram may be indicative of the particle size parameter, while features such as the bright vertical bands in the upper right panels of Figs. 10.3 and 10.5 may suggest the presence of cylindrical particles with axes perpendicular to the scattering plane. However, more research is obviously needed in order to realize fully the potential information content of two-dimensional scattering measurements (e.g., Sachweh *et al.* 1995; Barthel *et al.* 1998; Dick *et al.* 1998; Kaye 1998; Braun and Krieger 2001; Crosta *et al.* 2001; Prabhu *et al.* 2001; Secker *et al.* 2001).

An interesting laboratory technique for detecting nonspherical aerosols is to subject the particles in question to a pulsed external electric field and look for accompanying changes in the particle optical properties (Kapustin *et al.* 1975, 1980). The amplitude of the field is chosen to be sufficient to cause a significant degree of particle alignment provided that the aerosols are nonspherical, while the duration of the pulse is long enough to allow an equilibrium orientation to be reached. After the electric field is turned off, the particles return to random orientation, owing to Brownian motion. Any differences in the elements of the phase and extinction matrices or the total optical cross sections between the states with the electric field turned on and off indicate the presence of nonspherical particles. Furthermore, the magnitude of the differences and the relaxation time for the disorientation process after the electric field is turned off may indicate a value for the average particle aspect ratio.

As we have seen previously (cf. Section 4.9), the only unequivocal indicator of nonsphericity for randomly oriented particles forming a macroscopically isotropic and mirror-symmetric medium is violation of the Lorenz–Mie identities $F_{22}(\Theta) \equiv F_{11}(\Theta)$ and $F_{44}(\Theta) \equiv F_{33}(\Theta)$. As a consequence, the linear and circular backscattering depolarization ratios defined by Eqs. (10.2) and (10.3) become non-zero. Backscattering depolarization measurements are widely used for detecting and characterizing nonspherical particles in lidar (Gobbi 1998; Sassen 2000) and radar (Aydin 2000; Bringi and Chandrasekar 2001) atmospheric remote sensing and biomedicine (Schmitt and Xiang 1998; de Boer *et al.* 1999). For example, Liu and Chandrasekar (2000) and Straka *et al.* (2000) reviewed the foundation of fuzzy logic systems for classification of hydrometeor type based on polarimetric radar observations. Sassen (1991) developed a depolarization classification of different cloud-particle types based on data collected by a helium–neon continuous-wave laser-lidar analog device in the laboratory and field during the early 1970s (Fig. 10.67). Browell *et al.* (1990) used lidar depolarization observations to differentiate between various types of polar stratospheric clouds. Although most lidars operating at visible wavelengths measure the linear depolarization ratio, measurements of the circular depolarization ratio are also gaining popularity (Woodard *et al.* 1998).

The strong depolarization of light by large transparent particles such as ice cloud crystals at visible wavelengths (Fig. 10.67) is traditionally attributed to refractions and multiple internal reflections (Fig. 7.2), which tend to randomize the polarization

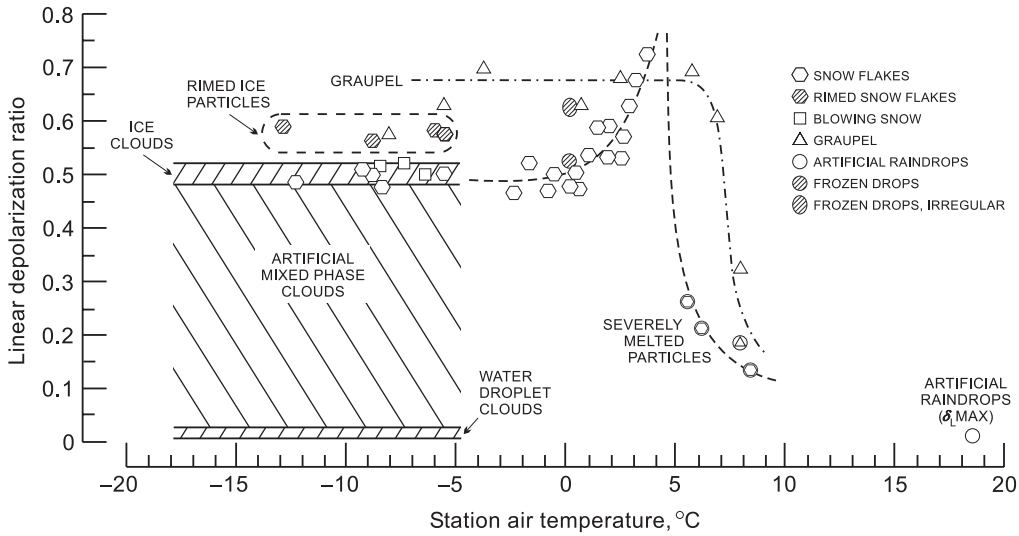

Figure 10.67. Results of early laboratory and field studies showing the wide range of linear depolarization ratios encountered from various types of hydrometeors at visible wavelengths (from Sassen 1991).

plane of rays exiting the particle (Liou and Lahore 1974). However, the geometrical optics concepts of rays, refractions, and reflections become inapplicable when the size of the particle is comparable to the wavelength. Yet wavelength-sized particles can produce even larger depolarization ratios, as demonstrated in Fig. 10.68. An interesting feature of essentially all the depolarization curves shown in this figure and computed with the exact *T*-matrix method is a rapid increase in δ_L as the effective size parameter increases from 0 to about 10. Moreover, maximal δ_L-values for most shapes are observed at size parameters close to and sometimes slightly smaller than 10. The *T*-matrix results show no obvious relationship between δ_L and the particle aspect ratio. Even spheroids with aspect ratio as small as 1.05 (a 2.5% deviation from the perfect spherical shape) produce strong depolarization. The largest δ_L-values are generated by prolate spheroids with aspect ratios as small as 1.2 (a 10% deviation from a sphere). Furthermore, δ_L for spheroids and, especially, cylinders tends to saturate with increasing aspect ratio.

The steep rise in δ_L with size parameter in the range $0 \lesssim x_{\text{eff}} \lesssim 10$ exhibited by the *T*-matrix results can explain the initial increase in lidar linear depolarization with time for very young, rapidly growing aircraft condensation-trail (contrail) particles observed by Freudenthaler *et al.* (1996). Figure 10.68 suggests that further growth of ice particles may lead to a decrease in δ_L with time, which was indeed observed by Sassen and Hsueh (1998). Furthermore, the *T*-matrix results seem to explain the occurrence of unusually large depolarization ratios for contrails ($\delta_L \sim 0.65$), which exceed significantly the values normal for most cirrus ($\delta_L \sim 0.35$–0.5). Similar *T*-matrix computations have been used by Carslaw *et al.* (1998), Toon *et al.* (2000), Beyerle *et al.* (2001), and Liu and Mishchenko (2001) to explain the results of lidar

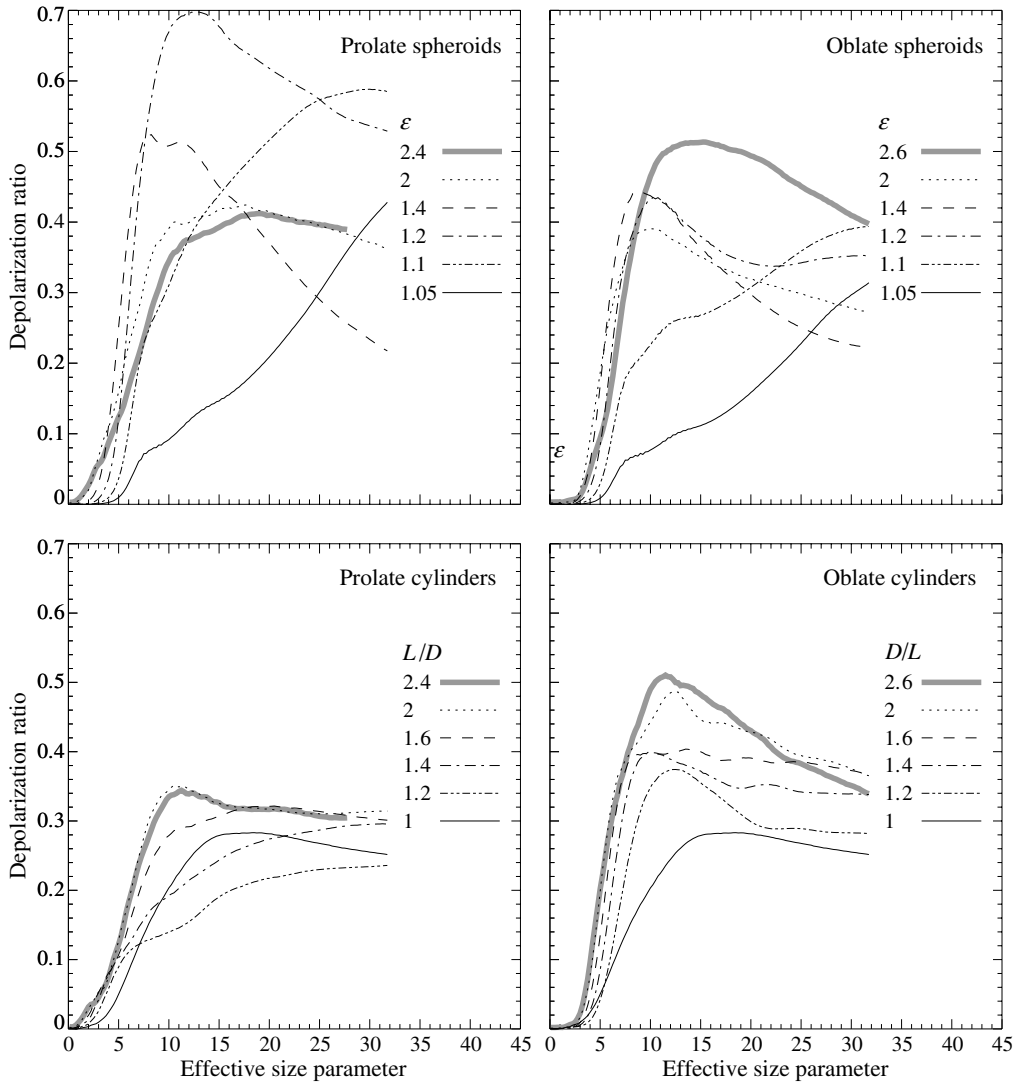

Figure 10.68. Linear backscattering depolarization ratio versus effective size parameter for polydisperse, randomly oriented ice spheroids with aspect ratios ranging from 1.05 to 2.6 and circular cylinders with various length-to-diameter or diameter-to-length ratios. The relative refractive index is 1.311 and the size distribution is given by Eq. (5.246) with $\alpha = -3$ and $v_{\text{eff}} = 0.1$. (After Mishchenko and Sassen 1998.)

observations of polar stratospheric cloud particles, which are another interesting example of natural wavelength-sized scatterers generating strong depolarization ratios.

In view of the apparent strong dependence of depolarization on size parameter for wavelength-sized particles, measuring depolarization at multiple wavelengths should be very useful for retrieving particle size and studying its temporal evolution. As an example, Plate 10.9 shows a variety of remote sensing observations of a mesoscale cirrus cloud band with contrails along its edges performed by Sassen *et al.* (2001) on 5 March 1999. It can be seen from the fish-eye images and the depolarization

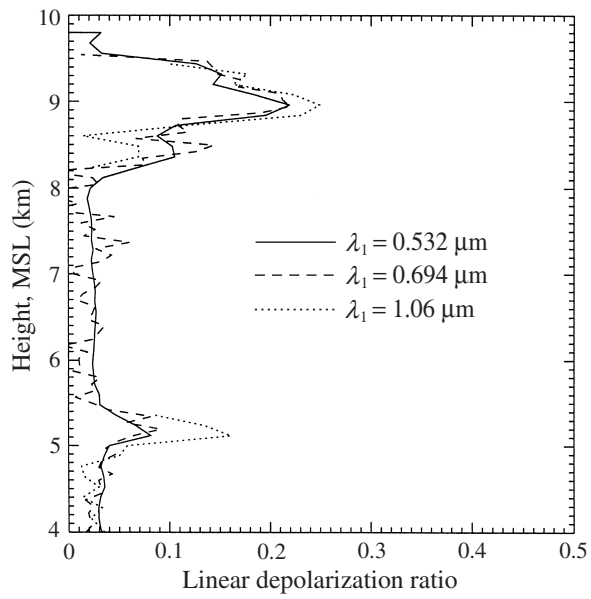

Figure 10.69. Comparison of 5-minute-averaged (1854–1859 UTC) linear depolarization profiles for three lidar wavelengths during a period when the backscattered intensity from the elevated aerosol layer was relatively strong. Table 10.5 gives the depolarization values at the ~5.25 km aerosol maximum in terms of the total molecular and aerosol and aerosol-only values. (From Sassen *et al.* 2001.)

displays that the contrails occurred just above the cirrus cloud top at the very beginning (missing the contrail leading edge) and at the end of the measurement period, when two contrails passed overhead in succession. Although the backscattered intensity displays at the $0.532\,\mu\text{m}$ (bottom left panel) and $1.06\,\mu\text{m}$ (bottom right) wavelengths are similar, there are large differences between the respective depolarization displays. The significantly smaller δ_L-values in the contrail at the longer wavelength imply the presence of $\sim 2\,\mu\text{m}$ diameter crystals (cf. Fig. 10.68), despite the fact that the contrails were probably of order one hour old when observed in the zenith. In contrast, the δ_L-values in the main cirrus cloud at the two wavelengths are quite similar, as can be expected of nonabsorbing particles with sizes much larger than a wavelength. It can, therefore, be concluded that contrails are unique among ice clouds in their ability to generate and maintain sufficiently tiny ice-particle sizes to manifest the depolarization dependence typical of the transition zone between the Rayleigh and the geometrical optics region of size parameters.

Another interesting feature of the lidar displays in Plate 10.9 is the significant depolarization caused by the elevated aerosol layer centered at about 5.3 km. This aerosol was almost certainly a product of the transport of dust from Asian dust storms. As more clearly seen in Fig. 10.69, the δ_L-values at the three lidar wavelengths reveal differences which may be attributed partly to significant noise in the weak aerosol backscattering and partly to the decreasing contribution of weakly depolarizing

Table 10.5. Linear depolarization ratio at the ~ 5.25 km aerosol maximum in terms of the total molecular and aerosol (δ_L) and aerosol-only ($\delta_{L,a}$) values at the three lidar wavelengths (after Sassen *et al*. 2001)

λ_1 (μm)	δ_L	$\delta_{L,a}$
0.532	0.08	0.21
0.694	0.09	0.23
1.06	0.16	0.25

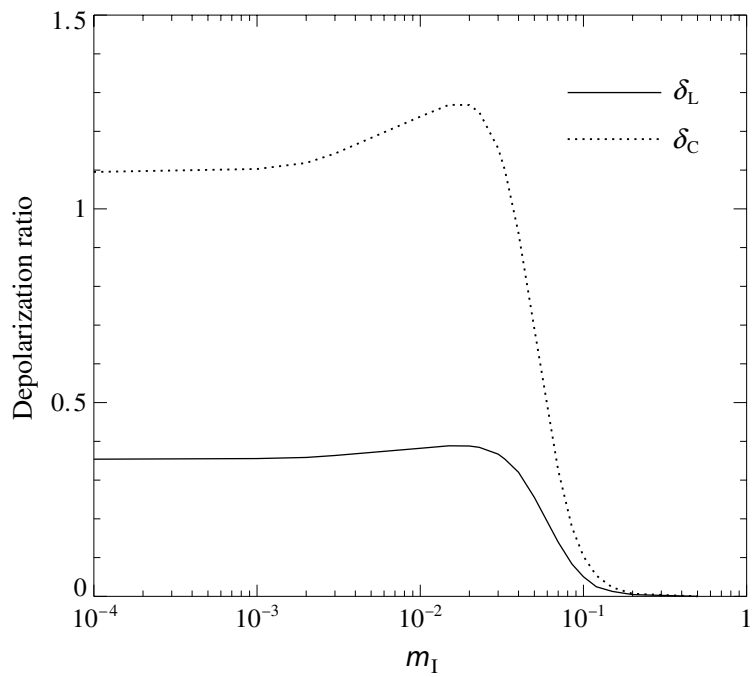

Figure 10.70. Linear and circular backscattering depolarization ratios versus imaginary part of the relative refractive index for polydisperse, randomly oriented oblate spheroids with $a/b = 1.7$. The size distribution is given by Eq. (5.246) with $\alpha = -3$ and $v_{eff} = 0.1$. The effective surface-equivalent-sphere size parameter is $x_{eff} = 15$ and the real part of the relative refractive index is 1.31.

molecular scattering to the total molecular plus aerosol depolarization with increasing wavelength (cf. Eq. (7.6), which indicates that the molecular contribution to the total molecular plus aerosol scattering matrix decreases as the inverse fourth power of wavelength). Table 10.5 shows that when the molecular backscattering contributions are approximately removed, the aerosol-only peak depolarization values are about 0.2–0.25, which is similar to the strong Kosa dust-dominated depolarization measured in Japan (Murayama *et al.* 1999; Sassen 2000). The spectral effect of molecular scattering on the total molecular plus cloud depolarization, the feature at about 9 km

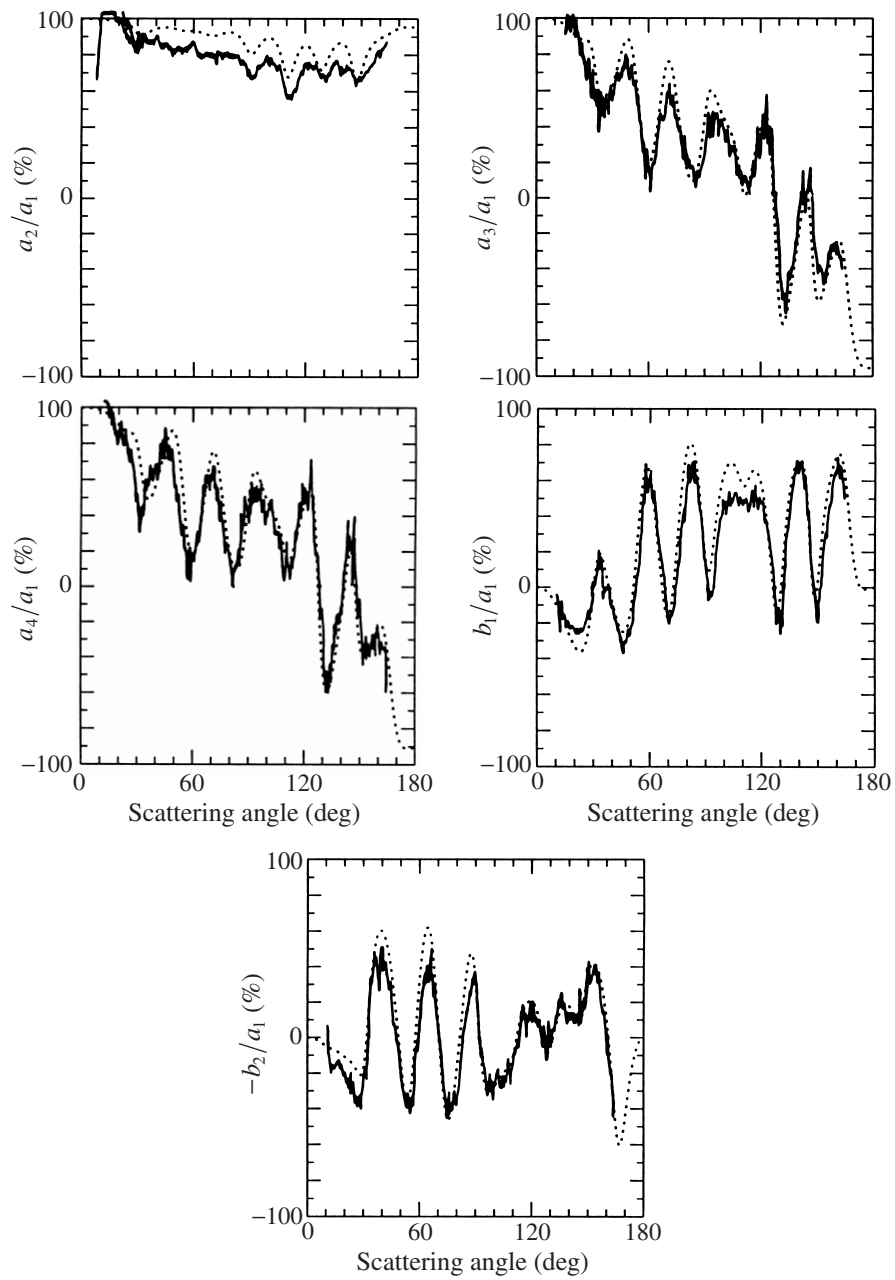

Figure 10.71. Ratios of the elements of the normalized Stokes scattering matrix for a latex two-sphere cluster in random orientation. The solid curves depict laboratory data of Bottiger *et al.* (1980) at a wavelength 441.6 nm, whereas the dotted curves show the results of *T*-matrix computations for a component-sphere diameter 1129 nm.

in Fig. 10.69, is significantly weaker because of the much stronger cloud backscattering.

We saw in Section 10.2 that increasing imaginary part of the relative refractive index m_{I} reduces and eventually eliminates the differences between the scattering pat-

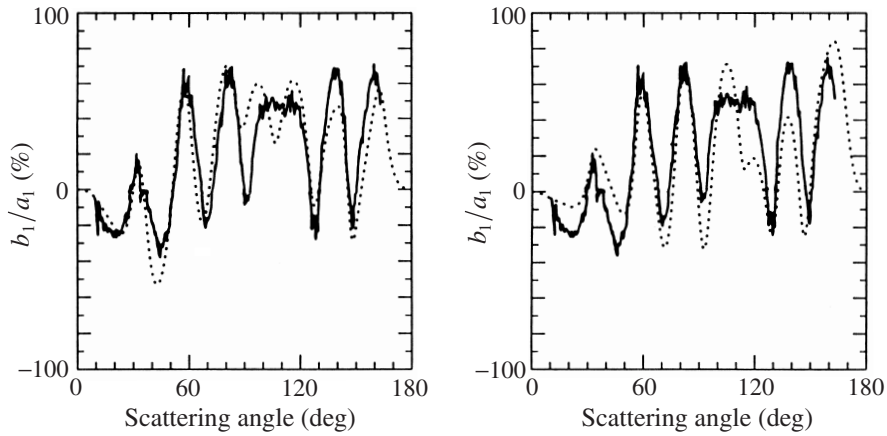

Figure 10.72. As in Fig. 10.71, but for component-sphere diameters 1108 nm (left-hand panel) and 1150 nm (right-hand panel).

terns of spherical and surface-equivalent convex nonspherical particles. Accordingly, increasing m_{I} leads to reduced and ultimately zero linear and circular depolarization ratios, as Fig. 10.70 illustrates. This factor limits the usefulness of depolarization observations of cirrus clouds and contrails at infrared wavelengths (Eberhard 1992), where water ice is strongly absorbing (Warren 1984).

A more detailed characterization of randomly oriented nonspherical particles can be achieved by exploiting multi-angle measurements of the full scattering matrix (e.g., Volten *et al.* 1999). The results can be especially precise when one or more particle microphysical parameters are known beforehand. As an example, Figs. 10.71 and 10.72 parallel Figs. 9.30 and 9.31 in showing the results of laboratory measurements (Bottiger *et al.* 1980) and *T*-matrix computations (Mishchenko and Mackowski 1996) for a two-sphere cluster with touching components. An electrostatically levitated latex bisphere was subject to Brownian motion and rapidly changed its orientation during the measurement. Therefore, although the sample was a single particle, the measurement of the scattering matrix was equivalent to that for randomly oriented monodisperse particles. According to Bottiger *et al.*, this was indeed corroborated by simultaneous measurements of the (1,3), (1,4), (2,3), (2,4), (3,1), (3,2), (4,1), and (4,2) elements of the scattering matrix, which were all found to be zero within the experimental accuracy (cf. Eq. (4.51)). Since the particle morphology and relative refractive index are known, the only free parameters are the diameters of the component spheres. Mishchenko and Mackowski have found that good agreement between the results of *T*-matrix computations and laboratory measurements can be obtained for component sphere diameters equal to 1129 nm (Fig. 10.71). Figure 10.72 shows the results for sphere diameters 1108 nm and 1150 nm, which give limits on the plausible range of diameters. This illustrates once again the potential accuracy of particle sizing techniques based on measurements of the scattering matrix.

Further reading

The book edited by Mishchenko *et al.* (2000a) is a major systematic source of information on calculations, measurements, and applications of electromagnetic scattering by nonspherical and heterogeneous particles. Further information can be found in the special journal issues edited by Shafai (1991), Barber *et al.* (1994), Hovenier (1996), Lumme (1998), Mishchenko *et al.* (1999a,b), and Videen *et al.* (2001) as well as in the conference proceedings edited by Schuerman (1980), Wriedt *et al.* (1996), Wriedt and Eremin (1998), Obelleiro *et al.* (1999), and Videen *et al.* (2000b). The book by Colton and Kress (1998) treats mathematical and numerical aspects of the inverse scattering problem for electromagnetic and acoustic waves.

Scattering by randomly and preferentially oriented spheroids and finite circular cylinders in the geometrical optics limit is discussed by Yang and Cai (1991), Arnott and Marston (1991), Macke and Mishchenko (1996), Kokhanovsky and Nakajima (1998), Langley and Marston (1998), and Marston (1999). Listed in Sassen and Arnott (1998) are several feature journal issues discussing optical phenomena associated with natural ice crystals.

Appendix A

Spherical wave expansion of a plane wave in the far-field zone

In this appendix we derive Eq. (2.57) following the approach described by Saxon (1955b). We begin with the well-known expansion of a plane wave in scalar spherical harmonics (Jackson 1998, page 471):

$$\exp(\mathrm{i}\mathbf{r}\cdot\mathbf{r}') = 4\pi \sum_{l=0}^{\infty} \mathrm{i}^l j_l(rr') \sum_{m=-l}^{l} Y_{lm}^*(\hat{\mathbf{r}}) Y_{lm}(\hat{\mathbf{r}}'), \tag{A.1}$$

where $\hat{\mathbf{r}} = \dfrac{\mathbf{r}}{r}$, $\hat{\mathbf{r}}' = \dfrac{\mathbf{r}'}{r'}$, the $j_l(y) = y^l \left(-\dfrac{1}{y}\dfrac{\mathrm{d}}{\mathrm{d}y}\right)^l \left(\dfrac{\sin y}{y}\right)$ are spherical Bessel functions of the first kind, and the $Y_{lm}(\hat{\mathbf{r}})$ are scalar spherical harmonics. The latter are defined as

$$Y_{lm}(\hat{\mathbf{r}}) = \sqrt{\frac{(2l+1)(l-m)!}{4\pi(l+m)!}}\, P_l^m(\cos\vartheta)\mathrm{e}^{\mathrm{i}m\varphi}, \tag{A.2}$$

where ϑ and φ are spherical angular coordinates of the unit vector $\hat{\mathbf{r}}$ and P_l^m are associated Legendre functions defined in terms of Legendre polynomials P_l as follows:

$$P_l^m(x) = (-1)^m (1-x^2)^{m/2} \frac{\mathrm{d}^m}{\mathrm{d}x^m} P_l(x), \quad P_l(x) = \frac{1}{2^l l!}\frac{\mathrm{d}^l}{\mathrm{d}x^l}(x^2-1)^l \tag{A.3}$$

with $x \in [-1, 1]$. Using the asymptotic form (Arfken and Weber 1995, p. 682)

$$j_l(y) \underset{y\to\infty}{=} \frac{1}{y}\sin\left(y - \frac{\pi l}{2}\right), \tag{A.4}$$

we have

$$j_l(rr') \underset{rr'\to\infty}{=} \frac{1}{rr'}\frac{\mathrm{i}}{2}\left[\exp\left(-\mathrm{i}rr'+\frac{1}{2}\mathrm{i}\pi l\right)-\exp\left(\mathrm{i}rr'-\frac{1}{2}\mathrm{i}\pi l\right)\right]. \tag{A.5}$$

Substituting this expression in Eq. (A.1) and making use of the completeness relation for spherical harmonics (Jackson 1998, p. 108)

$$\sum_{l=0}^{\infty}\sum_{m=-l}^{l} Y_{lm}^*(\hat{\mathbf{r}})Y_{lm}(\hat{\mathbf{r}}') = \delta(\cos\vartheta-\cos\vartheta')\,\delta(\varphi-\varphi') = \delta(\hat{\mathbf{r}}-\hat{\mathbf{r}}') \tag{A.6}$$

and the symmetry relation

$$Y_{lm}(-\hat{\mathbf{r}}') = (-1)^l\, Y_{lm}(\hat{\mathbf{r}}'), \tag{A.7}$$

we derive, after simple algebra,

$$\exp(\mathrm{i}rr'\,\hat{\mathbf{r}}\cdot\hat{\mathbf{r}}') \underset{rr'\to\infty}{=} \frac{\mathrm{i}2\pi}{r'}\left[\delta(\hat{\mathbf{r}}+\hat{\mathbf{r}}')\frac{\mathrm{e}^{-\mathrm{i}rr'}}{r} - \delta(\hat{\mathbf{r}}-\hat{\mathbf{r}}')\frac{\mathrm{e}^{\mathrm{i}rr'}}{r}\right]. \tag{A.8}$$

Appendix B

Wigner functions, Jacobi polynomials, and generalized spherical functions

Jacobi polynomials, Wigner functions, and generalized spherical functions are closely related special functions which were introduced in classical analysis, the quantum theory of angular momentum, and the theory of representations of the rotation group, respectively (Szegő 1959; Wigner 1959; Gelfand *et al.* 1963). Because differences in notational conventions in various publications may lead to confusion, we present in this appendix a short consistent summary of the main properties of these functions.

Wigner d-functions are defined as

$$d^s_{mn}(\vartheta) = \sqrt{(s+m)!(s-m)!(s+n)!(s-n)!} \times \sum_k (-1)^k \frac{(\cos\frac{1}{2}\vartheta)^{2s-2k+m-n}(\sin\frac{1}{2}\vartheta)^{2k-m+n}}{k!(s+m-k)!(s-n-k)!(n-m+k)!}, \tag{B.1}$$

where s, m, and n are integers, $0 \le \vartheta \le \pi$, and the sum is taken over all integer values of k that lead to non-negative factorials. Thus the summation index runs from $k_{\min} = \max(0, m-n)$ to $k_{\max} = \min(s+m, s-n)$. Therefore, $d^s_{mn}(\vartheta) = 0$ unless $k_{\max} \ge k_{\min}$, which is equivalent to requiring that $s \ge 0$ and $-s \le m, n \le s$. Making the substitutions $k \to s-n-k$, $k \to s+m-k$, and $k \to m-n+k$, respectively, we derive the following alternative expressions:

$$d^s_{mn}(\vartheta) = (-1)^{s-n}\sqrt{(s+m)!(s-m)!(s+n)!(s-n)!} \times \sum_k (-1)^k \frac{(\cos\frac{1}{2}\vartheta)^{m+n+2k}(\sin\frac{1}{2}\vartheta)^{2s-m-n-2k}}{k!(s-m-k)!(s-n-k)!(m+n+k)!}, \tag{B.2}$$

$$d^s_{mn}(\vartheta) = (-1)^{s+m}\sqrt{(s+m)!(s-m)!(s+n)!(s-n)!}$$
$$\times\sum_k (-1)^k \frac{(\cos\frac{1}{2}\vartheta)^{2k-m-n}(\sin\frac{1}{2}\vartheta)^{2s+m+n-2k}}{k!(s+m-k)!(s+n-k)!(k-m-n)!}, \tag{B.3}$$

$$d^s_{mn}(\vartheta) = (-1)^{m-n}\sqrt{(s+m)!(s-m)!(s+n)!(s-n)!}$$
$$\times\sum_k (-1)^k \frac{(\cos\frac{1}{2}\vartheta)^{2s-2k-m+n}(\sin\frac{1}{2}\vartheta)^{2k+m-n}}{k!(s-m-k)!(s+n-k)!(m-n+k)!}. \tag{B.4}$$

Equations (B.1)–(B.4) imply that the d-functions are real and have the following symmetry properties:

$$d^s_{mn}(\vartheta) = (-1)^{m-n} d^s_{-m,-n}(\vartheta) = (-1)^{m-n} d^s_{nm}(\vartheta) = d^s_{-n,-m}(\vartheta), \tag{B.5}$$

$$d^s_{mn}(-\vartheta) = (-1)^{m-n} d^s_{mn}(\vartheta) = d^s_{nm}(\vartheta), \qquad d^s_{mn}(0) = \delta_{mn}, \tag{B.6}$$

$$d^s_{mn}(\pi-\vartheta) = (-1)^{s-n} d^s_{-mn}(\vartheta) = (-1)^{s+m} d^s_{m,-n}(\vartheta), \qquad d^s_{mn}(\pi) = (-1)^{s-n}\delta_{-mn}, \tag{B.7}$$

where δ_{mn} is the Kronecker delta:

$$\delta_{mn} = \begin{cases} 1 \text{ if } m = n, \\ 0 \text{ if } m \neq n. \end{cases}$$

Denoting $x = \cos\vartheta$ and requiring that $\vartheta \in [0, \pi]$ yield

$$\cos\tfrac{1}{2}\vartheta = \sqrt{\tfrac{1}{2}(1+x)}, \qquad \sin\tfrac{1}{2}\vartheta = \sqrt{\tfrac{1}{2}(1-x)}. \tag{B.8}$$

Substituting Eq. (B.8) in Eq. (B.1) and modifying the resulting formula, we obtain

$$d^s_{mn}(\vartheta) = A^s_{mn}(1-x)^{(m-n)/2}(1+x)^{-(m+n)/2}\sum_k (-1)^{s-n-k}$$
$$\times\frac{(s+m)!(s-m)!(s-n)!}{k!(s+m-k)!(s-n-k)!(k-m+n)!}(1+x)^{s+m-k}(1-x)^{k-m+n}, \tag{B.9}$$

where

$$A^s_{mn} = \frac{(-1)^{s-n}}{2^s}\left[\frac{(s+n)!}{(s+m)!(s-m)!(s-n)!}\right]^{1/2}. \tag{B.10}$$

Finally, recalling the Leibniz rule,

$$\left(\frac{\mathrm{d}}{\mathrm{d}x}\right)^N [f(x)g(x)] = \sum_{k=0}^{N}\frac{N!}{k!(N-k)!}\left[\left(\frac{\mathrm{d}}{\mathrm{d}x}\right)^k f(x)\right]\left[\left(\frac{\mathrm{d}}{\mathrm{d}x}\right)^{N-k} g(x)\right], \tag{B.11}$$

and applying it to $f(x) = (1+x)^{s+m}$, $g(x) = (1-x)^{s-m}$, and $N = s-n$, we can rewrite Eq. (B.9) in the form

$$d^s_{mn}(\vartheta) = A^s_{mn}(1-x)^{(m-n)/2}(1+x)^{-(m+n)/2}\left(\frac{\mathrm{d}}{\mathrm{d}x}\right)^{s-n}[(1+x)^{s+m}(1-x)^{s-m}]. \tag{B.12}$$

The Jacobi polynomial of degree q is given by Eq. (4.3.1) of Szegő (1959):

$$P_q^{(a,b)}(x) = (1-x)^{-a}(1+x)^{-b}\frac{(-1)^q}{2^q q!}\left(\frac{\mathrm{d}}{\mathrm{d}x}\right)^q [(1+x)^{q+b}(1-x)^{q+a}], \tag{B.13}$$

where q is a non-negative integer and $a > -1$ and $b > -1$ are real. Comparing Eq. (B.12) with Eq. (B.13), we obtain the following expression of the Wigner d-functions in terms of the Jacobi polynomials for $n \geq |m|$:

$$d_{mn}^s(\vartheta) = \frac{\xi_{mn}}{2^{(a+b)/2}}\left[\frac{q!(q+a+b)!}{(q+a)!(q+b)!}\right]^{1/2}(1-x)^{a/2}(1+x)^{b/2}P_q^{(a,b)}(x), \tag{B.14}$$

where $a = n-m$, $b = n+m$, $q = s-n$, and $\xi_{mn} = 1$. The condition $n \geq |m|$ ensures that $a \geq 0$ and $b \geq 0$, thereby preventing singularities for $x = \pm 1$. Using the symmetry relations of Eq. (B.5), it is straightforward to show that Eq. (B.14) can be used for arbitrary m and n, provided that

$$a = |m-n|, \qquad b = |m+n|, \qquad q = s - \tfrac{1}{2}(a+b), \tag{B.15}$$

$$\xi_{mn} = \begin{cases} 1 & \text{for } n \geq m, \\ (-1)^{m-n} & \text{for } n < m. \end{cases} \tag{B.16}$$

The orthogonality property of the Jacobi polynomials (Eq. (4.3.3) of Szegő 1959) and Eqs. (B.14)–(B.16) lead to the following orthogonality property of the d-functions:

$$\int_0^\pi \mathrm{d}\vartheta \sin\vartheta\, d_{mn}^s(\vartheta) d_{mn}^{s'}(\vartheta) = \frac{2}{2s+1}\delta_{ss'}. \tag{B.17}$$

The completeness property of the Jacobi polynomials (Szegő 1959) and Eqs. (B.14) and (B.17) imply that functions $\sqrt{s+\frac{1}{2}}\, d_{mn}^s(\vartheta)$ with $s = s_{\min}, s_{\min}+1, \ldots$ form a complete orthonormal system of functions on $[0, \pi]$, where

$$s_{\min} = \max(|m|, |n|).$$

This means that if a real-valued function $f(\vartheta)$ defined on the closed interval $[0, \pi]$ is square integrable on this interval, i.e., if

$$\int_0^\pi \mathrm{d}\vartheta \sin\vartheta [f(\vartheta)]^2 < \infty, \tag{B.18}$$

then there exists a unique set of coefficients η_s $(s \geq s_{\min})$ such that the series expansion

$$f(\vartheta) = \sum_{s=s_{\min}}^{\infty} \eta_s d_{mn}^s(\vartheta), \qquad \vartheta \in [0, \pi] \tag{B.19}$$

holds in the following sense:

$$\lim_{S\to\infty} \int_0^\pi \mathrm{d}\vartheta \sin\vartheta \left| f(\vartheta) - \sum_{s=s_{\min}}^{S} \eta_s d_{mn}^s(\vartheta)\right|^2 = 0. \tag{B.20}$$

Conversely, if a real-valued function $f(\vartheta)$ on $[0,\pi]$ admits the expansion of Eq. (B.19) in the sense of Eq. (B.20), then it is square integrable on $[0,\pi]$ and the expansion coefficients are given by

$$\eta_s = (s+\tfrac{1}{2})\int_0^\pi \mathrm{d}\vartheta \sin\vartheta\, f(\vartheta) d^s_{mn}(\vartheta). \tag{B.21}$$

The latter formula follows directly from Eqs. (B.19) and (B.17).

Using Eq. (4.5.1) of Szegő (1959) and Eq. (B.14), we obtain the following recurrence relation for the Wigner *d*-functions:

$$\begin{aligned} d^{s+1}_{mn}(\vartheta) = {} & \frac{1}{s\sqrt{(s+1)^2-m^2}\sqrt{(s+1)^2-n^2}}\{(2s+1)[s(s+1)x-mn]d^s_{mn}(\vartheta) \\ & -(s+1)\sqrt{s^2-m^2}\sqrt{s^2-n^2}\, d^{s-1}_{mn}(\vartheta)\}, \qquad s \ge s_{\min}. \end{aligned} \tag{B.22}$$

The simplest way to derive this formula is to consider first the case $n \ge |m|$, which corresponds to $a = n-m$, $b = n+m$, $q = s-n$, and then to use the symmetry relations of Eq. (B.5) in order to verify that Eq. (B.22) is correct for arbitrary *m* and *n*. The initial values are given by

$$d^{s_{\min}-1}_{mn}(\vartheta) = 0, \tag{B.23}$$

$$d^{s_{\min}}_{mn}(\vartheta) = \xi_{mn}\, 2^{-s_{\min}}\left[\frac{(2s_{\min})!}{(|m-n|)!(|m+n|)!}\right]^{1/2}(1-x)^{|m-n|/2}(1+x)^{|m+n|/2}, \tag{B.24}$$

where ξ_{mn} is given by Eq. (B.16). Equation (B.24) follows directly from Eq. (B.12) if $n \ge |m|$, and it is extended to arbitrary *m* and *n* using Eq. (B.5). From Eq. (B.12), we easily derive

$$\begin{aligned} \frac{\mathrm{d}}{\mathrm{d}\vartheta} d^s_{mn}(\vartheta) &= \frac{m-n\cos\vartheta}{\sin\vartheta} d^s_{mn}(\vartheta) + \sqrt{(s+n)(s-n+1)}\, d^s_{mn-1}(\vartheta) \\ &= -\frac{m-n\cos\vartheta}{\sin\vartheta} d^s_{mn}(\vartheta) - \sqrt{(s-n)(s+n+1)}\, d^s_{mn+1}(\vartheta). \end{aligned} \tag{B.25}$$

Alternatively, we have from Eq. (4.5.5) of Szegő (1959) and Eq. (B.22)

$$\begin{aligned} \frac{\mathrm{d}}{\mathrm{d}\vartheta} d^s_{mn}(\vartheta) = \frac{1}{\sin\vartheta}\Bigg[& -\frac{(s+1)\sqrt{(s^2-m^2)(s^2-n^2)}}{s(2s+1)} d^{s-1}_{mn}(\vartheta) \\ & -\frac{mn}{s(s+1)} d^s_{mn}(\vartheta) + \frac{s\sqrt{(s+1)^2-m^2}\sqrt{(s+1)^2-n^2}}{(s+1)(2s+1)} d^{s+1}_{mn}(\vartheta)\Bigg]. \end{aligned} \tag{B.26}$$

The Wigner *d*-functions with $m=0$ and $n=0$ are equivalent to the usual Legendre polynomials (cf. Eqs. (B.12) and (A.3)):

$$d^s_{00}(\vartheta) = P_s(x). \tag{B.27}$$

For $n = 0$, we obtain

$$d^s_{m0}(\vartheta) = \sqrt{\frac{(s-m)!}{(s+m)!}}\, P^m_s(x), \tag{B.28}$$

where $P^m_s(x)$ are associated Legendre functions defined by Eq. (A.3). Equations (B.22) and (B.28) give a simple recurrence relation for the associated Legendre functions:

$$(s-m+1)P^m_{s+1}(x) = (2s+1)xP^m_s(x) - (s+m)P^m_{s-1}(x). \tag{B.29}$$

Despite its simplicity, the use of this relation in computer calculations for large s and $|m|$ results in overflows, whereas the original recurrence relation for the functions $d^s_{m0}(\vartheta)$ remains stable and accurate. Furthermore, the functions $d^s_{m0}(\vartheta)$ have simpler symmetry properties than the $P^m_s(x)$. It is, therefore, advisable to use the d-functions instead of the associated Legendre functions from both the analytical and the numerical standpoint.

The generalized spherical functions $P^s_{mn}(x)$ are complex-valued functions related to the Wigner d-functions by (Gelfand *et al.* 1963; Hovenier and van der Mee 1983)

$$P^s_{mn}(x) = \mathrm{i}^{m-n} d^s_{mn}(\vartheta). \tag{B.30}$$

Using Eqs. (B.5)–(B.7), we easily derive

$$P^s_{mn}(x) = P^s_{nm}(x) = P^s_{-m,-n}(x) = (-1)^{m+n}[P^s_{mn}(x)]^*, \tag{B.31}$$

$$P^s_{mn}(-x) = (-1)^{s+m-n} P^s_{-mn}(x). \tag{B.32}$$

The corresponding orthogonality and normalization condition follows directly from Eq. (B.17):

$$\begin{aligned}\int_{-1}^{+1} \mathrm{d}x\, P^s_{mn}(x)P^{s'}_{mn}(x) &= (-1)^{m+n} \int_{-1}^{+1} \mathrm{d}x\, P^s_{mn}(x)[P^{s'}_{mn}(x)]^* \\ &= (-1)^{m+n} \frac{2}{2s+1}\delta_{ss'}.\end{aligned} \tag{B.33}$$

It is straightforward to show that the generalized spherical functions form a complete set of complex functions on the interval $x \in [-1, +1]$. This means that any complex-valued function $f(x)$, defined and square-integrable on the interval $x \in [-1, +1]$, can be uniquely expanded in the functions $P^s_{mn}(x)$ with $s = s_{\min}, s_{\min}+1, \ldots$. In other words, if

$$\int_{-1}^{+1} \mathrm{d}x |f(x)|^2 < \infty \tag{B.34}$$

then there exists a unique set of coefficients η_s $(s \geq s_{\min})$ such that

$$\lim_{S\to\infty} \int_{-1}^{+1} \mathrm{d}x \left| f(x) - \sum_{s=s_{\min}}^{S} \eta_s P^s_{mn}(x) \right|^2 = 0. \tag{B.35}$$

Conversely, if a complex-valued function $f(x)$ on $[-1,+1]$ admits the expansion

$$f(x)=\sum_{s=s_{\min}}^{\infty}\eta_s P_{mn}^s(x) \tag{B.36}$$

in the sense of Eq. (B.35), then it is square integrable on $[-1,+1]$ and the expansion coefficients are given by

$$\eta_s=(-1)^{m+n}(s+\tfrac{1}{2})\int_{-1}^{+1}\mathrm{d}x\, f(x)P_{mn}^s(x) \tag{B.37}$$

(cf. Eqs. (B.33) and (B.36)).

The Wigner *D*-functions are defined as

$$D_{mm'}^n(\alpha,\beta,\gamma)=\mathrm{e}^{-\mathrm{i}m\alpha}d_{mm'}^n(\beta)\mathrm{e}^{-\mathrm{i}m'\gamma}, \tag{B.38}$$

where

$$0\le\alpha<2\pi,\quad 0\le\beta\le\pi,\quad 0\le\gamma<2\pi. \tag{B.39}$$

If the sets of Euler angles $(\alpha_1,\beta_1,\gamma_1)$ and $(\alpha_2,\beta_2,\gamma_2)$ (Section 2.4) describe two consecutive rotations of a coordinate system and the set (α,β,γ) describes the resulting rotation, then the addition theorem for the *D*-functions reads

$$D_{mm'}^n(\alpha,\beta,\gamma)=\sum_{m''=-n}^{n}D_{mm''}^n(\alpha_1,\beta_1,\gamma_1)D_{m''m'}^n(\alpha_2,\beta_2,\gamma_2) \tag{B.40}$$

(see Eq. (2) in Section 4.7 of Varshalovich *et al.* 1988). A direct consequence of the addition theorem is the unitarity condition

$$\sum_{m''=-n}^{n}D_{mm''}^n(\alpha,\beta,\gamma)D_{m''m'}^n(-\gamma,-\beta,-\alpha)=D_{mm'}^n(0,0,0)=\delta_{mm'} \tag{B.41}$$

(cf. Eq. (B.6)).

Using Eq. (B.40), we can derive the addition theorem for the Wigner *d*-functions. Consider the geometry shown in Fig. B.1, where the angles ϑ_1, ϑ_2, $\varphi_2-\varphi_1$, σ_1, σ_2, and Θ are non-negative and are related by

$$\cos\Theta=\cos\vartheta_2\cos\vartheta_1+\sin\vartheta_2\sin\vartheta_1\cos(\varphi_2-\varphi_1), \tag{B.42}$$

$$\cos\sigma_1=\frac{\cos\vartheta_2-\cos\vartheta_1\cos\Theta}{\sin\vartheta_1\sin\Theta}, \tag{B.43}$$

$$\cos\sigma_2=\frac{\cos\vartheta_1-\cos\vartheta_2\cos\Theta}{\sin\vartheta_2\sin\Theta} \tag{B.44}$$

(cf. Eqs. (4.17)–(4.19)). The reference frame formed by the unit vectors $(\hat{\mathbf{n}}_1,\hat{\boldsymbol{\vartheta}}_1,\hat{\boldsymbol{\varphi}}_1)$ can be transformed into the reference frame formed by the unit vectors $(\hat{\mathbf{n}}_2,\hat{\boldsymbol{\vartheta}}_2,\hat{\boldsymbol{\varphi}}_2)$ in two ways: (i) via a single rotation through Euler angles $(\pi-\sigma_1,\Theta,-\sigma_2)$, and (ii)

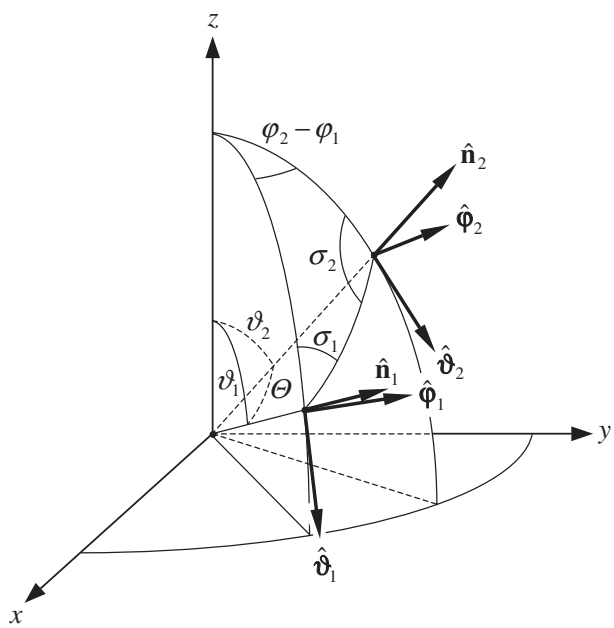

Figure B.1. Illustration of the addition theorem for Wigner *d*-functions.

via two consecutive rotations through Euler angles $(0, -\vartheta_1, \varphi_2 - \varphi_1)$ and $(0, \vartheta_2, 0)$. We, therefore, derive from Eqs. (B.38) and (B.40)

$$\mathrm{e}^{\mathrm{i}m\sigma_1} d^n_{mm'}(\Theta)\mathrm{e}^{\mathrm{i}m'\sigma_2} = \sum_{m''=-n}^{n} (-1)^{m''} d^n_{mm''}(\vartheta_1) d^n_{m''m'}(\vartheta_2)\mathrm{e}^{-\mathrm{i}m''(\varphi_2-\varphi_1)}. \tag{B.45}$$

Consider two special cases of Eq. (B.45). If $\varphi_2 - \varphi_1 = 0$ and $\vartheta_1 \geq \vartheta_2$ then $\sigma_1 = 0$, $\sigma_2 = \pi$, and $\Theta = \vartheta_1 - \vartheta_2$, and we obtain

$$d^n_{mm'}(\vartheta_1 - \vartheta_2) = \sum_{m''=-n}^{n} (-1)^{m''-m'} d^n_{mm''}(\vartheta_1) d^n_{m''m'}(\vartheta_2). \tag{B.46}$$

In particular, when $\vartheta_1 = \vartheta_2$, Eqs. (B.6) and (B.46) render the unitarity condition for the *d*-functions:

$$\begin{aligned}\sum_{m''=-n}^{n} (-1)^{m''-m'} d^n_{mm''}(\vartheta) d^n_{m''m'}(\vartheta) &= \sum_{m''=-n}^{n} d^n_{mm''}(\vartheta) d^n_{m''m'}(-\vartheta) \\ &= \sum_{m''=-n}^{n} d^n_{mm''}(\vartheta) d^n_{m'm''}(\vartheta) \\ &= \delta_{mm'}.\end{aligned} \tag{B.47}$$

This formula can also be derived directly from the unitarity condition for the *D*-functions, Eq. (B.41), by substituting $\alpha = \gamma = 0$. If $\varphi_2 - \varphi_1 = \pi$, then $\sigma_1 = \sigma_2 = 0$

and $\Theta = \vartheta_1 + \vartheta_2$, and we have

$$d^n_{mm'}(\vartheta_1 + \vartheta_2) = \sum_{m''=-n}^{n} d^n_{mm''}(\vartheta_1) d^n_{m''m'}(\vartheta_2). \tag{B.48}$$

The product of two D-functions can be expanded in the so-called Clebsch–Gordan series (Eq. (1) of Section 4.6 of Varshalovich *et al.* 1988):

$$D^{n_1}_{m_1 m_1'}(\alpha, \beta, \gamma) D^{n_2}_{m_2 m_2'}(\alpha, \beta, \gamma) = \sum_{n=|n_1-n_2|}^{n_1+n_2} C^{n, m_1+m_2}_{n_1 m_1\, n_2 m_2} D^n_{m_1+m_2, m_1'+m_2'}(\alpha, \beta, \gamma)\, C^{n, m_1'+m_2'}_{n_1 m_1'\, n_2 m_2'}, \tag{B.49}$$

where the $C^{nm}_{n_1 m_1\, n_2 m_2}$ are Clebsch–Gordan coefficients (Appendix D). Substituting $\alpha = \gamma = 0$ yields

$$d^{n_1}_{m_1 m_1'}(\beta) d^{n_2}_{m_2 m_2'}(\beta) = \sum_{n=|n_1-n_2|}^{n_1+n_2} C^{n, m_1+m_2}_{n_1 m_1\, n_2 m_2} d^n_{m_1+m_2, m_1'+m_2'}(\beta) C^{n, m_1'+m_2'}_{n_1 m_1'\, n_2 m_2'}. \tag{B.50}$$

Further reading

Detailed accounts of Jacobi polynomials, Wigner d-functions, and generalized spherical functions are given in Szegő (1959), Gelfand *et al.* (1963), Vilenkin (1968), Biedenharn and Louck (1981), Varshalovich *et al.* (1988), Brink and Satchler (1993), Rose (1995), and Edmonds (1996). Our definition of the d-functions is consistent with that of Biedenharn and Louck (1981), Hovenier and van der Mee (1983), Varshalovich *et al.* (1988), Brink and Satchler (1993), and Rose (1995). Vilenkin (1968) uses functions $P^s_{mn}(x)$ related to the Wigner d-functions by $P^s_{mn}(x) = \mathrm{i}^{n-m} d^s_{mn}(\vartheta)$. Edmonds (1996) uses a function $d^{(s)}_{mn}(\vartheta)$, which is related to $d^s_{mn}(\vartheta)$ by $d^{(s)}_{mn}(\vartheta) = (-1)^{m+n} d^s_{mn}(\vartheta)$.

Appendix C

Scalar and vector spherical wave functions

Real-valued spherical Bessel functions of the first kind,

$$j_n(x) = x^n \left(-\frac{1}{x}\frac{\mathrm{d}}{\mathrm{d}x} \right)^n \left(\frac{\sin x}{x} \right),$$

and of the second kind,

$$y_n(x) = -x^n \left(-\frac{1}{x}\frac{\mathrm{d}}{\mathrm{d}x} \right)^n \left(\frac{\cos x}{x} \right),$$

as well as their complex-valued combinations such as Hankel functions of the first kind,

$$h_n^{(1)}(x) = j_n(x) + \mathrm{i}y_n(x), \tag{C.1}$$

and of the second kind,

$$h_n^{(2)}(x) = j_n(x) - \mathrm{i}y_n(x), \tag{C.2}$$

are solutions of the same differential equation,

$$\frac{\mathrm{d}}{\mathrm{d}x}\left(x^2 \frac{\mathrm{d}z_n(x)}{\mathrm{d}x} \right) + [x^2 - n(n+1)]z_n(x) = 0, \tag{C.3}$$

where n is an integer (e.g., Abramowitz and Stegun 1964). Taking into account that

$$\frac{1}{\sin\vartheta}\frac{\mathrm{d}}{\mathrm{d}\vartheta}\left(\sin\vartheta \frac{\mathrm{d}P_n^m(\cos\vartheta)}{\mathrm{d}\vartheta} \right) + \left(n(n+1) - \frac{m^2}{\sin^2\vartheta} \right) P_n^m(\cos\vartheta) = 0, \tag{C.4}$$

we find that

$$\psi_{mn}(kr, \vartheta, \varphi) = h_n^{(1)}(kr)\, P_n^m(\cos\vartheta)\, \mathrm{e}^{\mathrm{i}m\varphi}, \qquad n = 0, 1, 2, ..., \qquad m = 0, \pm 1, \pm 2, ..., \pm n \tag{C.5}$$

is a solution of the scalar Helmholtz equation

$$(\nabla^2 + k^2)\psi_{mn}(kr, \vartheta, \varphi) = 0, \tag{C.6}$$

where, in spherical coordinates,

$$\nabla^2 = \frac{1}{r^2}\frac{\partial}{\partial r}\left(r^2 \frac{\partial}{\partial r}\right) + \frac{1}{r^2 \sin\vartheta}\frac{\partial}{\partial \vartheta}\left(\sin\vartheta \frac{\partial}{\partial \vartheta}\right) + \frac{1}{r^2 \sin^2\vartheta}\left(\frac{\partial}{\partial \varphi}\right)^2. \tag{C.7}$$

Since

$$h_n^{(1)}(kr) \underset{\substack{kr\to\infty \\ kr \gg n^2}}{=} \frac{(-\mathrm{i})^{n+1}\mathrm{e}^{\mathrm{i}kr}}{kr} \tag{C.8}$$

and

$$h_n^{(1)}(kr) \underset{kr\to 0}{=} \frac{(kr)^n}{(2n+1)!!} - \mathrm{i}(2n-1)!!(kr)^{-n-1},$$

the functions $\psi_{mn}(kr, \vartheta, \varphi)$ behave as *outgoing scalar spherical waves* at infinity and diverge at the origin. The functions

$$\mathrm{Rg}\,\psi_{mn}(kr, \vartheta, \varphi) = j_n(kr)P_n^m(\cos\vartheta)\mathrm{e}^{\mathrm{i}m\varphi}, \quad n = 0, 1, 2, ..., \quad m = 0, \pm 1, \pm 2, ..., \pm n \tag{C.9}$$

also satisfy the Helmholtz equation but, unlike $\psi_{mn}(kr, \vartheta, \varphi)$, are *regular* (finite) at the origin, owing to

$$j_n(kr) \underset{kr\to 0}{=} \frac{(kr)^n}{(2n+1)!!}.$$

Since numerical computation of the associated Legendre functions having large n and $|m|$ is problematic (see Appendix B), it is useful to rewrite Eqs. (C.5) and (C.9) in terms of Wigner d-functions:

$$\begin{matrix} \psi_{mn}(kr, \vartheta, \varphi) \\ \mathrm{Rg}\,\psi_{mn}(kr, \vartheta, \varphi) \end{matrix} = \begin{matrix} h_n^{(1)}(kr) \\ j_n(kr) \end{matrix} (-1)^m \sqrt{\frac{(n+m)!}{(n-m)!}}\, d_{0m}^n(\vartheta)\mathrm{e}^{\mathrm{i}m\varphi} \tag{C.10}$$

(cf. Eqs. (B.28) and (B.5)), where we have used a compact way to write two formulas (for ψ_{mn} and $\mathrm{Rg}\,\psi_{mn}$) as a single equation.

The functions $\psi_{mn}(kr, \vartheta, \varphi)$ and $\mathrm{Rg}\,\psi_{mn}(kr, \vartheta, \varphi)$ are called scalar spherical wave functions and form a complete set of expansion functions that can be used to represent any time-harmonic scalar wave. Furthermore, they can be used to create vector spherical wave functions suitable for expanding time-harmonic vector fields. According to Eq. (1.17), the electric field in a linear, isotropic, homogeneous medium is divergence-free:

$$\nabla \cdot \mathbf{E}(\mathbf{r}) = 0. \tag{C.11}$$

Therefore, it follows from Eqs. (2.3) and (2.4) and the vector identity

$$\nabla\times\nabla\times\mathbf{a}(\mathbf{r})=\nabla[\nabla\cdot\mathbf{a}(\mathbf{r})]-\nabla^2\mathbf{a}(\mathbf{r}) \tag{C.12}$$

that $\mathbf{E}(\mathbf{r})$ must satisfy the vector Helmholtz equation

$$\nabla^2\mathbf{E}(\mathbf{r})+k^2\,\mathbf{E}(\mathbf{r})=0. \tag{C.13}$$

Obviously, vector functions used to expand $\mathbf{E}(\mathbf{r})$ must also be divergence-free and must satisfy the vector Helmholtz equation. It can be shown (Stratton 1941; Morse and Feshbach 1953) that two sets of vector functions that meet these criteria are as follows:

$$\begin{aligned}\begin{matrix}\mathbf{M}_{mn}(kr,\vartheta,\varphi)\\ \mathrm{Rg}\mathbf{M}_{mn}(kr,\vartheta,\varphi)\end{matrix}&=\gamma_{mn}\nabla\times\left(\mathbf{r}\begin{matrix}\psi_{mn}(kr,\vartheta,\varphi)\\ \mathrm{Rg}\,\psi_{mn}(kr,\vartheta,\varphi)\end{matrix}\right)\\&=\gamma_{mn}\begin{matrix}h_n^{(1)}(kr)\\ j_n(kr)\end{matrix}\mathbf{C}_{mn}(\vartheta,\varphi)\\&=\frac{1}{k}\nabla\times\begin{matrix}\mathbf{N}_{mn}(kr,\vartheta,\varphi)\\ \mathrm{Rg}\mathbf{N}_{mn}(kr,\vartheta,\varphi)\end{matrix}\end{aligned} \tag{C.14}$$

and

$$\begin{aligned}\begin{matrix}\mathbf{N}_{mn}(kr,\vartheta,\varphi)\\ \mathrm{Rg}\mathbf{N}_{mn}(kr,\vartheta,\varphi)\end{matrix}&=\frac{1}{k}\nabla\times\begin{matrix}\mathbf{M}_{mn}(kr,\vartheta,\varphi)\\ \mathrm{Rg}\mathbf{M}_{mn}(kr,\vartheta,\varphi)\end{matrix}\\&=\gamma_{mn}\left\{\frac{n(n+1)}{kr}\begin{matrix}h_n^{(1)}(kr)\\ j_n(kr)\end{matrix}\mathbf{P}_{mn}(\vartheta,\varphi)+\frac{1}{kr}\frac{\mathrm{d}}{\mathrm{d}(kr)}\left(kr\begin{matrix}h_n^{(1)}(kr)\\ j_n(kr)\end{matrix}\right)\mathbf{B}_{mn}(\vartheta,\varphi)\right\},\end{aligned} \tag{C.15}$$

where

$$\begin{aligned}\mathbf{B}_{mn}(\vartheta,\varphi)&=r\nabla[P_n^m(\cos\vartheta)\mathrm{e}^{\mathrm{i}m\varphi}]\\&=\left[\hat{\boldsymbol{\vartheta}}\frac{\mathrm{d}}{\mathrm{d}\vartheta}P_n^m(\cos\vartheta)+\hat{\boldsymbol{\varphi}}\frac{\mathrm{i}m}{\sin\vartheta}P_n^m(\cos\vartheta)\right]\mathrm{e}^{\mathrm{i}m\varphi}\\&=(-1)^m\sqrt{\frac{(n+m)!}{(n-m)!}}\,\mathbf{B}_{mn}(\vartheta)\mathrm{e}^{\mathrm{i}m\varphi}\\&=\hat{\mathbf{r}}\times\mathbf{C}_{mn}(\vartheta,\varphi),\end{aligned} \tag{C.16}$$

$$\begin{aligned}\mathbf{C}_{mn}(\vartheta,\varphi)&=\nabla\times[\mathbf{r}P_n^m(\cos\vartheta)\mathrm{e}^{\mathrm{i}m\varphi}]\\&=\left[\hat{\boldsymbol{\vartheta}}\frac{\mathrm{i}m}{\sin\vartheta}P_n^m(\cos\vartheta)-\hat{\boldsymbol{\varphi}}\frac{\mathrm{d}}{\mathrm{d}\vartheta}P_n^m(\cos\vartheta)\right]\mathrm{e}^{\mathrm{i}m\varphi}\\&=(-1)^m\sqrt{\frac{(n+m)!}{(n-m)!}}\,\mathbf{C}_{mn}(\vartheta)\mathrm{e}^{\mathrm{i}m\varphi}\\&=\mathbf{B}_{mn}(\vartheta,\varphi)\times\hat{\mathbf{r}},\end{aligned} \tag{C.17}$$

$$\mathbf{P}_{mn}(\vartheta,\varphi)=\hat{\mathbf{r}}P_n^m(\cos\vartheta)\mathrm{e}^{\mathrm{i}m\varphi}$$

$$=(-1)^m\sqrt{\frac{(n+m)!}{(n-m)!}}\,\mathbf{P}_{mn}(\vartheta)\mathrm{e}^{\mathrm{i}m\varphi}, \tag{C.18}$$

$$\mathbf{B}_{mn}(\vartheta)=\hat{\boldsymbol{\vartheta}}\frac{\mathrm{d}}{\mathrm{d}\vartheta}d_{0m}^n(\vartheta)+\hat{\boldsymbol{\varphi}}\frac{\mathrm{i}m}{\sin\vartheta}d_{0m}^n(\vartheta)$$

$$=\hat{\boldsymbol{\vartheta}}\tau_{mn}(\vartheta)+\hat{\boldsymbol{\varphi}}\mathrm{i}\pi_{mn}(\vartheta), \tag{C.19}$$

$$\mathbf{C}_{mn}(\vartheta)=\hat{\boldsymbol{\vartheta}}\frac{\mathrm{i}m}{\sin\vartheta}d_{0m}^n(\vartheta)-\hat{\boldsymbol{\varphi}}\frac{\mathrm{d}}{\mathrm{d}\vartheta}d_{0m}^n(\vartheta)$$

$$=\hat{\boldsymbol{\vartheta}}\mathrm{i}\pi_{mn}(\vartheta)-\hat{\boldsymbol{\varphi}}\tau_{mn}(\vartheta), \tag{C.20}$$

$$\mathbf{P}_{mn}(\vartheta)=\hat{\mathbf{r}}d_{0m}^n(\vartheta), \tag{C.21}$$

$$\gamma_{mn}=\left[\frac{(2n+1)(n-m)!}{4\pi n(n+1)(n+m)!}\right]^{1/2}. \tag{C.22}$$

In Eqs. (C.19) and (C.20),

$$\pi_{mn}(\vartheta)=\frac{m}{\sin\vartheta}d_{0m}^n(\vartheta),$$

$$\tau_{mn}(\vartheta)=\frac{\mathrm{d}}{\mathrm{d}\vartheta}d_{0m}^n(\vartheta).$$

It is straightforward to verify that another class of solutions of the vector Helmholtz equation

$$\nabla^2\mathbf{E}(\mathbf{r})+k^2\,\mathbf{E}(\mathbf{r})=\nabla[\nabla\cdot\mathbf{E}(\mathbf{r})]-\nabla\times\nabla\times\mathbf{E}(\mathbf{r})+k^2\,\mathbf{E}(\mathbf{r})=0 \tag{C.23}$$

is the set of so-called longitudinal vector spherical wave functions

$$\begin{matrix}\mathbf{L}_{mn}(kr,\vartheta,\varphi)\\ \mathrm{Rg}\mathbf{L}_{mn}(kr,\vartheta,\varphi)\end{matrix}=\frac{\gamma'_{mn}}{k}\nabla\begin{matrix}\psi_{mn}(kr,\vartheta,\varphi)\\ \mathrm{Rg}\,\psi_{mn}(kr,\vartheta,\varphi)\end{matrix}$$

$$=\gamma'_{mn}\left\{\frac{\mathrm{d}}{\mathrm{d}(kr)}\frac{h_n^{(1)}(kr)}{j_n(kr)}\mathbf{P}_{mn}(\vartheta,\varphi)+\frac{1}{kr}\frac{h_n^{(1)}(kr)}{j_n(kr)}\mathbf{B}_{mn}(\vartheta,\varphi)\right\}, \tag{C.24}$$

where

$$\gamma'_{mn}=\left[\frac{(2n+1)(n-m)!}{4\pi(n+m)!}\right]^{1/2}. \tag{C.25}$$

These functions are not divergence-free. It is evident that the vector spherical harmonics $\mathbf{B}_{mn}(\vartheta,\varphi)$, $\mathbf{C}_{mn}(\vartheta,\varphi)$, and $\mathbf{P}_{mn}(\vartheta,\varphi)$ are mutually orthogonal:

$$\mathbf{B}_{mn}(\vartheta,\varphi)\cdot\mathbf{C}_{mn}(\vartheta,\varphi)=\mathbf{B}_{mn}(\vartheta,\varphi)\cdot\mathbf{P}_{mn}(\vartheta,\varphi)=\mathbf{C}_{mn}(\vartheta,\varphi)\cdot\mathbf{P}_{mn}(\vartheta,\varphi)=0. \tag{C.26}$$

Furthermore, **M** and Rg**M** are perpendicular to **N,** Rg**N**, **L**, Rg**L**, and the position

vector **r**. Recalling the symmetry relation (B.5), we derive the following symmetry property of the vector spherical harmonics:

$$\mathbf{B}_{-mn}(\vartheta, \varphi) = (-1)^m \frac{(n-m)!}{(n+m)!} \mathbf{B}^*_{mn}(\vartheta, \varphi), \tag{C.27}$$

and analogous relations hold for $\mathbf{C}_{mn}(\vartheta, \varphi)$ and $\mathbf{P}_{mn}(\vartheta, \varphi)$. The regular vector spherical wave functions obey a similar symmetry relation:

$$\mathrm{Rg}\mathbf{M}_{-mn}(kr, \vartheta, \varphi) = (-1)^m \mathrm{Rg}\mathbf{M}^*_{mn}(kr, \vartheta, \varphi), \tag{C.28}$$

and analogous relations again hold for Rg**N** and Rg**L**.

As follows from Eqs. (C.14), (C.15), and (C.24), the functions Rg**M**, Rg**N**, and Rg**L** are regular at the origin $(r = 0)$. On the other hand, using Eq. (C.8) and the formula

$$\frac{\mathrm{d}h_n^{(1)}(x)}{\mathrm{d}x} = \frac{1}{2n+1}[n h_{n-1}^{(1)}(x) - (n+1)h_{n+1}^{(1)}(x)], \tag{C.29}$$

we find that at infinity, the functions **M** and **N** behave as outgoing transverse vector spherical waves:

$$\mathbf{M}_{mn}(kr, \vartheta, \varphi) \underset{\substack{kr\to\infty \\ kr \gg n^2}}{=} \frac{(-\mathrm{i})^{n+1}\mathrm{e}^{\mathrm{i}kr}}{kr} \gamma_{mn} \mathbf{C}_{mn}(\vartheta, \varphi), \tag{C.30}$$

$$\mathbf{N}_{mn}(kr, \vartheta, \varphi) \underset{\substack{kr\to\infty \\ kr \gg n^2}}{=} \frac{(-\mathrm{i})^{n}\mathrm{e}^{\mathrm{i}kr}}{kr} \gamma_{mn} \mathbf{B}_{mn}(\vartheta, \varphi), \tag{C.31}$$

whereas **L** behaves as an outgoing longitudinal vector spherical wave:

$$\mathbf{L}_{mn}(kr, \vartheta, \varphi) \underset{\substack{kr\to\infty \\ kr \gg n^2}}{=} \frac{(-\mathrm{i})^{n}\mathrm{e}^{\mathrm{i}kr}}{kr} \gamma'_{mn} \mathbf{P}_{mn}(\vartheta, \varphi). \tag{C.32}$$

The vector spherical wave functions defined by Eqs. (C.14), (C.15), and (C.24) and the vector spherical harmonics defined by Eqs. (C.16)–(C.18) are identical to those used by Tsang *et al.* (1985, 2000) and are directly related to the functions $\mathbf{M}^{1,3}_{\sigma mn}$, $\mathbf{N}^{1,3}_{\sigma mn}$, $\mathbf{L}^{1,3}_{\sigma mn}$, $\mathbf{B}^{\sigma}_{mn}$, $\mathbf{C}^{\sigma}_{mn}$, and $\mathbf{P}^{\sigma}_{mn}$ $(\sigma = e, o)$, where *e* and *o* stand for even and odd, introduced by Morse and Feshbach (1953). Taking into account that the definition of associated Legendre functions on p. 1325 of Morse and Feshbach (1953) lacks the factor $(-1)^m$ (cf. Eq. (A.3)) and using their Eqs. (13.3.67)–(13.3.69) as well as their table of vector spherical harmonics on pp. 1898 and 1899, we find for $m \geq 0$

$$\mathbf{B}_{mn}(\vartheta, \varphi) = (-1)^m \sqrt{n(n+1)}\,[\mathbf{B}^e_{mn}(\vartheta, \varphi) + \mathrm{i}\mathbf{B}^o_{mn}(\vartheta, \varphi)], \tag{C.33}$$

$$\mathbf{C}_{mn}(\vartheta, \varphi) = (-1)^m \sqrt{n(n+1)}\,[\mathbf{C}^e_{mn}(\vartheta, \varphi) + \mathrm{i}\mathbf{C}^o_{mn}(\vartheta, \varphi)], \tag{C.34}$$

$$\mathbf{P}_{mn}(\vartheta, \varphi) = (-1)^m [\mathbf{P}^e_{mn}(\vartheta, \varphi) + \mathrm{i}\mathbf{P}^o_{mn}(\vartheta, \varphi)], \tag{C.35}$$

$$\mathbf{M}_{mn}(kr, \vartheta, \varphi) = (-1)^m \gamma_{mn}\,[\mathbf{M}^3_{emn}(kr, \vartheta, \varphi) + \mathrm{i}\mathbf{M}^3_{omn}(kr, \vartheta, \varphi)], \tag{C.36}$$

$$\mathbf{N}_{mn}(kr, \vartheta, \varphi) = (-1)^m \gamma_{mn}[\mathbf{N}^3_{emn}(kr, \vartheta, \varphi) + \mathrm{i}\mathbf{N}^3_{omn}(kr, \vartheta, \varphi)], \tag{C.37}$$

$$\mathbf{L}_{mn}(kr, \vartheta, \varphi) = (-1)^m \gamma'_{mn}[\mathbf{L}^3_{emn}(kr, \vartheta, \varphi) + \mathrm{i}\mathbf{L}^3_{omn}(kr, \vartheta, \varphi)], \tag{C.38}$$

$$\mathrm{Rg}\mathbf{M}_{mn}(kr, \vartheta, \varphi) = (-1)^m \gamma_{mn}[\mathbf{M}^1_{emn}(kr, \vartheta, \varphi) + \mathrm{i}\mathbf{M}^1_{omn}(kr, \vartheta, \varphi)], \tag{C.39}$$

$$\mathrm{Rg}\mathbf{N}_{mn}(kr, \vartheta, \varphi) = (-1)^m \gamma_{mn}[\mathbf{N}^1_{emn}(kr, \vartheta, \varphi) + \mathrm{i}\mathbf{N}^1_{omn}(kr, \vartheta, \varphi)], \tag{C.40}$$

$$\mathrm{Rg}\mathbf{L}_{mn}(kr, \vartheta, \varphi) = (-1)^m \gamma'_{mn}[\mathbf{L}^1_{emn}(kr, \vartheta, \varphi) + \mathrm{i}\mathbf{L}^1_{omn}(kr, \vartheta, \varphi)]. \tag{C.41}$$

Conversely,

$$\begin{aligned}\mathbf{B}^{\substack{e\\o}}_{mn}(\vartheta, \varphi) &= \frac{1}{-\mathrm{i}} \frac{(-1)^m}{2\sqrt{n(n+1)}}[\mathbf{B}_{mn}(\vartheta, \varphi) \pm \mathbf{B}^*_{mn}(\vartheta, \varphi)] \\ &= \frac{1}{-\mathrm{i}} \frac{1}{2\sqrt{n(n+1)}}[(-1)^m \mathbf{B}_{mn}(\vartheta, \varphi) \pm \frac{(n+m)!}{(n-m)!}\mathbf{B}_{-mn}(\vartheta, \varphi)],\end{aligned} \tag{C.42}$$

$$\begin{aligned}\mathbf{C}^{\substack{e\\o}}_{mn}(\vartheta, \varphi) &= \frac{1}{-\mathrm{i}} \frac{(-1)^m}{2\sqrt{n(n+1)}}[\mathbf{C}_{mn}(\vartheta, \varphi) \pm \mathbf{C}^*_{mn}(\vartheta, \varphi)] \\ &= \frac{1}{-\mathrm{i}} \frac{1}{2\sqrt{n(n+1)}}[(-1)^m \mathbf{C}_{mn}(\vartheta, \varphi) \pm \frac{(n+m)!}{(n-m)!}\mathbf{C}_{-mn}(\vartheta, \varphi)],\end{aligned} \tag{C.43}$$

$$\begin{aligned}\mathbf{P}^{\substack{e\\o}}_{mn}(\vartheta, \varphi) &= \frac{1}{-\mathrm{i}} \frac{(-1)^m}{2}[\mathbf{P}_{mn}(\vartheta, \varphi) \pm \mathbf{P}^*_{mn}(\vartheta, \varphi)] \\ &= \frac{1}{-\mathrm{i}} \frac{1}{2}[(-1)^m \mathbf{P}_{mn}(\vartheta, \varphi) \pm \frac{(n+m)!}{(n-m)!}\mathbf{P}_{-mn}(\vartheta, \varphi)],\end{aligned} \tag{C.44}$$

$$\begin{aligned}\mathbf{M}^1_{\substack{e\\o}mn}(kr, \vartheta, \varphi) &= \frac{1}{-\mathrm{i}} \frac{(-1)^m}{2\gamma_{mn}}[\mathrm{Rg}\mathbf{M}_{mn}(kr, \vartheta, \varphi) \pm \mathrm{Rg}\mathbf{M}^*_{mn}(kr, \vartheta, \varphi)] \\ &= \frac{1}{-\mathrm{i}} \frac{1}{2\gamma_{mn}}[(-1)^m \mathrm{Rg}\mathbf{M}_{mn}(kr, \vartheta, \varphi) \pm \mathrm{Rg}\mathbf{M}_{-mn}(kr, \vartheta, \varphi)],\end{aligned} \tag{C.45}$$

$$\mathbf{M}^3_{\substack{e\\o}mn}(kr, \vartheta, \varphi) = \frac{1}{-\mathrm{i}} \frac{(-1)^m}{2\gamma_{mn}}[\mathbf{M}_{mn}(kr, \vartheta, \varphi) \pm \mathbf{M}^*_{mn}(kr, \vartheta, \varphi)], \tag{C.46}$$

$$\begin{aligned}\mathbf{N}^1_{\substack{e\\o}mn}(kr, \vartheta, \varphi) &= \frac{1}{-\mathrm{i}} \frac{(-1)^m}{2\gamma_{mn}}[\mathrm{Rg}\mathbf{N}_{mn}(kr, \vartheta, \varphi) \pm \mathrm{Rg}\mathbf{N}^*_{mn}(kr, \vartheta, \varphi)] \\ &= \frac{1}{-\mathrm{i}} \frac{1}{2\gamma_{mn}}[(-1)^m \mathrm{Rg}\mathbf{N}_{mn}(kr, \vartheta, \varphi) \pm \mathrm{Rg}\mathbf{N}_{-mn}(kr, \vartheta, \varphi)],\end{aligned} \tag{C.47}$$

$$\mathbf{N}^3_{\substack{e\\o}mn}(kr, \vartheta, \varphi) = \frac{1}{-\mathrm{i}} \frac{(-1)^m}{2\gamma_{mn}}[\mathbf{N}_{mn}(kr, \vartheta, \varphi) \pm \mathbf{N}^*_{mn}(kr, \vartheta, \varphi)], \tag{C.48}$$

$$\mathbf{L}^1_{\substack{e\\o}mn}(kr,\vartheta,\varphi)=\frac{1}{-\mathrm{i}}\frac{(-1)^m}{2\gamma'_{mn}}[\mathrm{Rg}\mathbf{L}_{mn}(kr,\vartheta,\varphi)\pm\mathrm{Rg}\mathbf{L}^*_{mn}(kr,\vartheta,\varphi)]$$

$$=\frac{1}{-\mathrm{i}}\frac{1}{2\gamma'_{mn}}[(-1)^m\,\mathrm{Rg}\mathbf{L}_{mn}(kr,\vartheta,\varphi)\pm\mathrm{Rg}\mathbf{L}_{-mn}(kr,\vartheta,\varphi)], \tag{C.49}$$

$$\mathbf{L}^3_{\substack{e\\o}mn}(kr,\vartheta,\varphi)=\frac{1}{-\mathrm{i}}\frac{(-1)^m}{2\gamma'_{mn}}[\mathbf{L}_{mn}(kr,\vartheta,\varphi)\pm\mathbf{L}^*_{mn}(kr,\vartheta,\varphi)]. \tag{C.50}$$

The equations on p. 1900 of Morse and Feshbach (1953) and Eqs. (C.33)–(C.35) yield the following orthogonality relations for the vector spherical harmonics:

$$\int_0^{2\pi}\mathrm{d}\varphi\int_0^{\pi}\mathrm{d}\vartheta\sin\vartheta\,\mathbf{B}_{mn}(\vartheta,\varphi)\mathbf{C}^*_{m'n'}(\vartheta,\varphi)$$

$$=\int_0^{2\pi}\mathrm{d}\varphi\int_0^{\pi}\mathrm{d}\vartheta\sin\vartheta\,\mathbf{B}_{mn}(\vartheta,\varphi)\mathbf{P}^*_{m'n'}(\vartheta,\varphi)$$

$$=\int_0^{2\pi}\mathrm{d}\varphi\int_0^{\pi}\mathrm{d}\vartheta\sin\vartheta\,\mathbf{C}_{mn}(\vartheta,\varphi)\mathbf{P}^*_{m'n'}(\vartheta,\varphi)$$

$$=0, \tag{C.51}$$

$$\int_0^{2\pi}\mathrm{d}\varphi\int_0^{\pi}\mathrm{d}\vartheta\sin\vartheta\,\mathbf{B}_{mn}(\vartheta,\varphi)\mathbf{B}^*_{m'n'}(\vartheta,\varphi)$$

$$=\int_0^{2\pi}\mathrm{d}\varphi\int_0^{\pi}\mathrm{d}\vartheta\sin\vartheta\,\mathbf{C}_{mn}(\vartheta,\varphi)\mathbf{C}^*_{m'n'}(\vartheta,\varphi)$$

$$=\frac{1}{(\gamma_{mn})^2}\delta_{mm'}\delta_{nn'}, \tag{C.52}$$

$$\int_0^{2\pi}\mathrm{d}\varphi\int_0^{\pi}\mathrm{d}\vartheta\sin\vartheta\,\mathbf{P}_{mn}(\vartheta,\varphi)\mathbf{P}^*_{m'n'}(\vartheta,\varphi)=\frac{1}{(\gamma'_{mn})^2}\delta_{mm'}\delta_{nn'}. \tag{C.53}$$

Using Eqs. (C.42)–(C.50), we can rewrite the series expansion of the dyadic $\overleftrightarrow{I}\mathrm{e}^{\mathrm{i}\mathbf{r}'\cdot\mathbf{r}}$ on p. 1866 of Morse and Feshbach (1953) as follows (Tsang *et al.* 1985, 2000):

$$\overleftrightarrow{I}\mathrm{e}^{\mathrm{i}\mathbf{r}'\cdot\mathbf{r}}=\sum_{n=0}^{\infty}\sum_{m=-n}^{n}(-1)^m\mathrm{i}^n\frac{2n+1}{n(n+1)}\left\{\frac{n(n+1)}{\mathrm{i}\gamma'_{mn}}\mathbf{P}_{-mn}(\vartheta',\varphi')\otimes\mathrm{Rg}\mathbf{L}_{mn}(r'r,\vartheta,\varphi)\right.$$

$$+\frac{1}{\gamma_{mn}}\mathbf{C}_{-mn}(\vartheta',\varphi')\otimes\mathrm{Rg}\mathbf{M}_{mn}(r'r,\vartheta,\varphi)$$

$$\left.+\frac{1}{\mathrm{i}\gamma_{mn}}\mathbf{B}_{-mn}(\vartheta',\varphi')\otimes\mathrm{Rg}\mathbf{N}_{mn}(r'r,\vartheta,\varphi)\right\}. \tag{C.54}$$

The expansion of the plane electromagnetic wave

$$\mathbf{E}(\mathbf{r}) = \mathbf{E}_0\, \mathrm{e}^{\mathrm{i}k\hat{\mathbf{r}}'\cdot\mathbf{r}}, \qquad \mathbf{E}_0 \cdot \hat{\mathbf{r}}' = 0, \tag{C.55}$$

in vector spherical wave functions is obtained by taking the dot product of $\mathbf{E}_0$ and $\overleftrightarrow{I}\mathrm{e}^{\mathrm{i}k\hat{\mathbf{r}}'\cdot\mathbf{r}}$:

$$\mathbf{E}_0\, \mathrm{e}^{\mathrm{i}k\hat{\mathbf{r}}'\cdot\mathbf{r}} = \sum_{n=1}^{\infty}\sum_{m=-n}^{n} [a_{mn}\mathrm{Rg}\mathbf{M}_{mn}(kr, \vartheta, \varphi) + b_{mn}\mathrm{Rg}\mathbf{N}_{mn}(kr, \vartheta, \varphi)], \tag{C.56}$$

where

$$a_{mn} = 4\pi(-1)^m \mathrm{i}^n d_n \mathbf{E}_0 \cdot \mathbf{C}^*_{mn}(\vartheta')\exp(-\mathrm{i}m\varphi'), \tag{C.57}$$

$$b_{mn} = 4\pi(-1)^m \mathrm{i}^{n-1} d_n \mathbf{E}_0 \cdot \mathbf{B}^*_{mn}(\vartheta')\exp(-\mathrm{i}m\varphi'), \tag{C.58}$$

$$d_n = \left[\frac{2n+1}{4\pi n(n+1)}\right]^{1/2}, \tag{C.59}$$

and we have taken into account that a_{mn} and b_{mn} vanish for $n = 0$. The free space dyadic Green's function given by

$$\overleftrightarrow{G}(\mathbf{r}, \mathbf{r}') = \left(\overleftrightarrow{I} + \frac{1}{k^2}\nabla\otimes\nabla\right)\frac{\exp(\mathrm{i}k|\mathbf{r}-\mathbf{r}'|)}{4\pi|\mathbf{r}-\mathbf{r}'|} \tag{C.60}$$

(cf. Eqs. (2.13) and (2.15)) can also be expressed in terms of vector spherical wave functions:

$$\overleftrightarrow{G}(\mathbf{r}, \mathbf{r}') = \mathrm{i}k\sum_{n=1}^{\infty}\sum_{m=-n}^{n}(-1)^m \begin{cases} \mathbf{M}_{-mn}(kr, \vartheta, \varphi)\otimes\mathrm{Rg}\mathbf{M}_{mn}(kr', \vartheta', \varphi') \\ +\mathbf{N}_{-mn}(kr, \vartheta, \varphi)\otimes\mathrm{Rg}\mathbf{N}_{mn}(kr', \vartheta', \varphi') \quad \text{for } r > r', \\ \\ \mathrm{Rg}\mathbf{M}_{-mn}(kr, \vartheta, \varphi)\otimes\mathbf{M}_{mn}(kr', \vartheta', \varphi') \\ +\mathrm{Rg}\mathbf{N}_{-mn}(kr, \vartheta, \varphi)\otimes\mathbf{N}_{mn}(kr', \vartheta', \varphi') \quad \text{for } r' > r, \end{cases} \tag{C.61}$$

where $\mathbf{r} \neq \mathbf{r}'$ (Tsang *et al.* 1985, p. 183).

Let (ϑ_1, φ_1) and (ϑ_2, φ_2) be the spherical angles of the same position vector $\mathbf{r}$ in coordinate systems 1 and 2, respectively. Both coordinate systems have the same origin. Coordinate system 2 is obtained by rotating coordinate system 1 though Euler angles (α, β, γ) (Section 2.4). From Eq. (1) of Section 5.2 and Eq. (1) of Section 5.5 of Varshalovich *et al.* (1988) and Eqs. (C.5) and (C.9) above we have

$$\gamma_{mn}\begin{matrix}\psi_{mn}(kr, \vartheta_2, \varphi_2) \\ \mathrm{Rg}\,\psi_{mn}(kr, \vartheta_2, \varphi_2)\end{matrix} = \sum_{m'=-n}^{n}\gamma_{m'n}\begin{matrix}\psi_{m'n}(kr, \vartheta_1, \varphi_1) \\ \mathrm{Rg}\,\psi_{m'n}(kr, \vartheta_1, \varphi_1)\end{matrix} D^n_{m'm}(\alpha, \beta, \gamma), \tag{C.62}$$

where

$$D^n_{m'm}(\alpha, \beta, \gamma) = \mathrm{e}^{-\mathrm{i}m'\alpha} d^n_{m'm}(\beta)\mathrm{e}^{-\mathrm{i}m\gamma} \tag{C.63}$$

are Wigner D-functions and $d^n_{m'm}(\beta)$ are Wigner d-functions (Appendix B). Substituting Eq. (C.62) in Eqs. (C.14) and (C.15) yields

$$\begin{matrix}\mathbf{M}_{mn}(kr, \vartheta_2, \varphi_2)\\ \mathrm{Rg}\mathbf{M}_{mn}(kr, \vartheta_2, \varphi_2)\end{matrix} = \sum_{m'=-n}^{n} \begin{matrix}\mathbf{M}_{m'n}(kr, \vartheta_1, \varphi_1)\\ \mathrm{Rg}\mathbf{M}_{m'n}(kr, \vartheta_1, \varphi_1)\end{matrix} D^n_{m'm}(\alpha, \beta, \gamma), \tag{C.64}$$

and analogously for $\mathbf{N}$ and $\mathrm{Rg}\mathbf{N}$. Conversely,

$$\begin{matrix}\mathbf{M}_{mn}(kr, \vartheta_1, \varphi_1)\\ \mathrm{Rg}\mathbf{M}_{mn}(kr, \vartheta_1, \varphi_1)\end{matrix} = \sum_{m'=-n}^{n} \begin{matrix}\mathbf{M}_{m'n}(kr, \vartheta_2, \varphi_2)\\ \mathrm{Rg}\mathbf{M}_{m'n}(kr, \vartheta_2, \varphi_2)\end{matrix} D^n_{m'm}(-\gamma, -\beta, -\alpha). \tag{C.65}$$

Consider now coordinate systems 1 and 2 having the same spatial orientation and denote by $\mathbf{r}_{12}$ the vector connecting the origin of coordinate system 1 with the origin of coordinate system 2 (cf. Fig. 5.2). The translation addition theorem allows one to expand the vector spherical wave functions centered at the origin of coordinate system 1 in terms of the vector spherical wave functions centered at the origin of coordinate system 2 (Tsang *et al.* 1985; Boström *et al.* 1991). Specifically, if vectors $\mathbf{r}_1$, $\mathbf{r}_2$, and $\mathbf{r}_{12}$ form a triangle such that $\mathbf{r}_1 = \mathbf{r}_{12} + \mathbf{r}_2$ (Fig. 5.2) and $(r_1, \vartheta_1, \varphi_1)$, $(r_2, \vartheta_2, \varphi_2)$, and $(r_{12}, \vartheta_{12}, \varphi_{12})$ are their respective spherical coordinates, then

$$\mathrm{Rg}\begin{matrix}\mathbf{M}_{mn}\\ \mathbf{N}_{mn}\end{matrix}(kr_1, \vartheta_1, \varphi_1) = \sum_{\nu=1}^{\infty}\sum_{\mu=-\nu}^{\nu}\left[\mathrm{Rg}\begin{matrix}A_{\mu\nu mn}\\ B_{\mu\nu mn}\end{matrix}(kr_{12}, \vartheta_{12}, \varphi_{12})\mathrm{Rg}\mathbf{M}_{\mu\nu}(kr_2, \vartheta_2, \varphi_2)\right.$$
$$\left. + \mathrm{Rg}\begin{matrix}B_{\mu\nu mn}\\ A_{\mu\nu mn}\end{matrix}(kr_{12}, \vartheta_{12}, \varphi_{12})\mathrm{Rg}\mathbf{N}_{\mu\nu}(kr_2, \vartheta_2, \varphi_2)\right], \tag{C.66}$$

$$\begin{matrix}\mathbf{M}_{mn}\\ \mathbf{N}_{mn}\end{matrix}(kr_1, \vartheta_1, \varphi_1) = \sum_{\nu=1}^{\infty}\sum_{\mu=-\nu}^{\nu}\left[\mathrm{Rg}\begin{matrix}A_{\mu\nu mn}\\ B_{\mu\nu mn}\end{matrix}(kr_{12}, \vartheta_{12}, \varphi_{12})\mathbf{M}_{\mu\nu}(kr_2, \vartheta_2, \varphi_2)\right.$$
$$\left. + \mathrm{Rg}\begin{matrix}B_{\mu\nu mn}\\ A_{\mu\nu mn}\end{matrix}(kr_{12}, \vartheta_{12}, \varphi_{12})\mathbf{N}_{\mu\nu}(kr_2, \vartheta_2, \varphi_2)\right], \quad r_2 > r_{12}, \tag{C.67}$$

$$\begin{matrix}\mathbf{M}_{mn}\\ \mathbf{N}_{mn}\end{matrix}(kr_1, \vartheta_1, \varphi_1) = \sum_{\nu=1}^{\infty}\sum_{\mu=-\nu}^{\nu}\left[\begin{matrix}A_{\mu\nu mn}\\ B_{\mu\nu mn}\end{matrix}(kr_{12}, \vartheta_{12}, \varphi_{12})\mathrm{Rg}\mathbf{M}_{\mu\nu}(kr_2, \vartheta_2, \varphi_2)\right.$$
$$\left. + \begin{matrix}B_{\mu\nu mn}\\ A_{\mu\nu mn}\end{matrix}(kr_{12}, \vartheta_{12}, \varphi_{12})\mathrm{Rg}\mathbf{N}_{\mu\nu}(kr_2, \vartheta_2, \varphi_2)\right], \quad r_2 < r_{12}, \tag{C.68}$$

where

$$A_{\mu\nu mn}(kr_{12}, \vartheta_{12}, \varphi_{12}) = \frac{\gamma_{mn}}{\gamma_{\mu\nu}}(-1)^{\mu}\sum_{p=|n-\nu|}^{n+\nu} a(m, n|-\mu, \nu|p)a(n, \nu, p)h_p^{(1)}(kr_{12})$$
$$\times P_p^{m-\mu}(\cos\vartheta_{12})\exp[\mathrm{i}(m-\mu)\varphi_{12}], \tag{C.69}$$

$$B_{\mu\nu mn}(kr_{12}, \vartheta_{12}, \varphi_{12}) = \frac{\gamma_{mn}}{\gamma_{\mu\nu}}(-1)^{\mu+1} \sum_{p=|n-\nu|}^{n+\nu} a(m, n|-\mu, \nu|p, p-1) b(n, \nu, p) h_p^{(1)}(kr_{12})$$
$$\times P_p^{m-\mu}(\cos\vartheta_{12}) \exp[\mathrm{i}(m-\mu)\varphi_{12}] \tag{C.70}$$

are translation coefficients. Here

$$a(m, n|\mu, \nu|p) = (-1)^{m+\mu}(2p+1)\left[\frac{(n+m)!(\nu+\mu)!(p-m-\mu)!}{(n-m)!(\nu-\mu)!(p+m+\mu)!}\right]^{1/2}$$
$$\times \begin{pmatrix} n & \nu & p \\ m & \mu & -(m+\mu) \end{pmatrix} \begin{pmatrix} n & \nu & p \\ 0 & 0 & 0 \end{pmatrix}, \tag{C.71}$$

$$a(m, n|\mu, \nu|p, q) = (-1)^{m+\mu}(2p+1)\left[\frac{(n+m)!(\nu+\mu)!(p-m-\mu)!}{(n-m)!(\nu-\mu)!(p+m+\mu)!}\right]^{1/2}$$
$$\times \begin{pmatrix} n & \nu & p \\ m & \mu & -(m+\mu) \end{pmatrix} \begin{pmatrix} n & \nu & q \\ 0 & 0 & 0 \end{pmatrix}, \tag{C.72}$$

$$a(n, \nu, p) = \frac{\mathrm{i}^{\nu-n+p}(2\nu+1)}{2\nu(\nu+1)}[n(n+1)+\nu(\nu+1)-p(p+1)], \tag{C.73}$$

$$b(n, \nu, p) = -\frac{\mathrm{i}^{\nu-n+p}(2\nu+1)}{2\nu(\nu+1)}[(n+\nu+1+p)(n+\nu+1-p)$$
$$\times (p+n-\nu)(p-n+\nu)]^{1/2}, \tag{C.74}$$

and the coefficients

$$\begin{pmatrix} n & \nu & p \\ m & \mu & -(m+\mu) \end{pmatrix}$$

are Wigner 3j symbols (Appendix D). As usual, the formulas for $\mathrm{Rg}A_{\mu\nu mn}$ and $\mathrm{Rg}B_{\mu\nu mn}$ are obtained by replacing $h_p^{(1)}$ by j_p in Eqs. (C.69) and (C.70). Efficient numerical computation of the translation coefficients $A_{\mu\nu mn}$, $B_{\mu\nu mn}$, $\mathrm{Rg}A_{\mu\nu mn}$, and $\mathrm{Rg}B_{\mu\nu mn}$ is discussed by Fuller and Mackowski (2000).

Appendix D

Clebsch–Gordan coefficients and Wigner 3*j* symbols

The real-valued coefficients appearing in the Clebsch–Gordan expansion, Eq. (B.49), are defined as an algebraic sum (Varshalovich *et al.* 1988; Rose 1995):

$$
\begin{aligned}
&C^{nm}_{n_1m_1\,n_2m_2} \\
&= \delta_{m,m_1+m_2}\left[\frac{(n_1+n_2-n)!(n_1-n_2+n)!(-n_1+n_2+n)!}{(n_1+n_2+n+1)!}\right]^{1/2} \\
&\times[(n_1+m_1)!(n_1-m_1)!(n_2+m_2)!(n_2-m_2)!(n+m)!(n-m)!(2n+1)]^{1/2} \\
&\times\sum_p \frac{(-1)^p}{p!(n_1+n_2-n-p)!(n_1-m_1-p)!(n_2+m_2-p)!(n-n_2+m_1+p)!(n-n_1-m_2+p)!},
\end{aligned}
\tag{D.1}
$$

where

- n_1, n_2, and n are non-negative integers or half-integers;
- m_1, m_2, and m are integers or half-integers;
- $|m_1| \le n_1$, $|m_2| \le n_2$, and $|m| \le n$;
- m_1+n_1, m_2+n_2, $m+n$, and n_1+n_2+n are non-negative integers.

The Clebsch–Gordan coefficients are nonzero only when

$$|n_1-n_2| \le n \le n_1+n_2 \tag{D.2}$$

and

$$m = m_1+m_2. \tag{D.3}$$

The so-called unitarity relations for the Clebsch–Gordan coefficients read as

$$\sum_{m_1m_2} C^{nm}_{n_1m_1\,n_2m_2} C^{n'm'}_{n_1m_1\,n_2m_2} = \delta_{nn'}\delta_{mm'}, \tag{D.4}$$

$$\sum_{nm} C^{nm}_{n_1m_1\,n_2m_2} C^{nm}_{n_1m_1'\,n_2m_2'} = \delta_{m_1m_1'}\,\delta_{m_2m_2'}. \tag{D.5}$$

The Clebsch–Gordan coefficients have the following symmetry properties:

$$\begin{aligned} C^{nm}_{n_1m_1\,n_2m_2} &= (-1)^{n_1+n_2-n} C^{nm}_{n_2m_2\,n_1m_1} = (-1)^{n_1-m_1}\sqrt{\frac{2n+1}{2n_2+1}}\, C^{n_2,-m_2}_{n_1m_1\,n,-m} \\ &= (-1)^{n_1-m_1}\sqrt{\frac{2n+1}{2n_2+1}}\, C^{n_2m_2}_{nm\,n_1,-m_1} = (-1)^{n_2+m_2}\sqrt{\frac{2n+1}{2n_1+1}}\, C^{n_1,-m_1}_{n,-m\,n_2m_2} \\ &= (-1)^{n_2+m_2}\sqrt{\frac{2n+1}{2n_1+1}}\, C^{n_1m_1}_{n_2,-m_2\,nm}, \end{aligned} \tag{D.6}$$

$$C^{nm}_{n_1m_1\,n_2m_2} = (-1)^{n_1+n_2-n} C^{n,-m}_{n_1,-m_1\,n_2,-m_2}. \tag{D.7}$$

The so-called Wigner 3*j* symbols are defined in terms of the Clebsch–Gordan coefficients as

$$\begin{pmatrix} n_1 & n_2 & n \\ m_1 & m_2 & m \end{pmatrix} = (-1)^{n+m+2n_1}\frac{1}{\sqrt{2n+1}} C^{nm}_{n_1,-m_1\,n_2,-m_2}. \tag{D.8}$$

Conversely,

$$C^{nm}_{n_1m_1\,n_2m_2} = (-1)^{n_1-n_2+m}\sqrt{2n+1}\begin{pmatrix} n_1 & n_2 & n \\ m_1 & m_2 & -m \end{pmatrix}. \tag{D.9}$$

The symmetry properties of the 3*j* symbols follow from Eqs. (D.6)–(D.9) and are simpler than those for the Clebsch–Gordan coefficients:

$$\begin{aligned} &\begin{pmatrix} n_1 & n_2 & n \\ m_1 & m_2 & m \end{pmatrix} = \begin{pmatrix} n_2 & n & n_1 \\ m_2 & m & m_1 \end{pmatrix} = \begin{pmatrix} n & n_1 & n_2 \\ m & m_1 & m_2 \end{pmatrix} \\ &= (-1)^{n_1+n_2+n}\begin{pmatrix} n_1 & n & n_2 \\ m_1 & m & m_2 \end{pmatrix} = (-1)^{n_1+n_2+n}\begin{pmatrix} n_2 & n_1 & n \\ m_2 & m_1 & m \end{pmatrix} \\ &= (-1)^{n_1+n_2+n}\begin{pmatrix} n & n_2 & n_1 \\ m & m_2 & m_1 \end{pmatrix}, \end{aligned} \tag{D.10}$$

$$\begin{pmatrix} n_1 & n_2 & n \\ m_1 & m_2 & m \end{pmatrix} = (-1)^{n_1+n_2+n}\begin{pmatrix} n_1 & n_2 & n \\ -m_1 & -m_2 & -m \end{pmatrix}. \tag{D.11}$$

The numerical computation of the Clebsch–Gordan coefficients is based on the following formulas, which are either listed by Varshalovich *et al.* (1988) or can be easily derived from equations therein (Mishchenko 1991a).

- For $n' < N_{\min} = \max(|n-n_1|, |m'|)$,

$$C^{n'm'}_{nm\,n_1,m'-m} = 0. \tag{D.12}$$

- For $n' > N_{\min}$,

$$C^{n'm'}_{nm\,n_1,m'-m} = A(BC^{n'-1,m'}_{nm\,n_1,m'-m} - CC^{n'-2,m'}_{nm\,n_1,m'-m}), \tag{D.13}$$

where

$$A = \left[\frac{4n'^2(2n'+1)(2n'-1)}{(n'+m')(n'-m')(n_1-n+n')(n-n_1+n')(n+n_1-n'+1)(n+n_1+n'+1)}\right]^{1/2}, \tag{D.14}$$

$$B = \frac{(2m-m')n'(n'-1)-m'n(n+1)+m'n_1(n_1+1)}{2n'(n'-1)}, \tag{D.15}$$

$$C = \left[\frac{(n'-m'-1)(n'+m'-1)(n_1-n+n'-1)(n-n_1+n'-1)(n+n_1-n'+2)(n+n_1+n')}{4(n'-1)^2(2n'-3)(2n'-1)}\right]^{1/2}. \tag{D.16}$$

- For $n' = N_{\min}$, the following four particular cases must be considered.

(1) For $|n-n_1| \geq |m'|$ and $n \geq n_1$,

$$C^{n-n_1,m'}_{nm\,n_1,m'-m} = (-1)^{n_1+m'+m}\left[\frac{(n+m)!(n-m)!(2n_1)!(2n-2n_1+1)!}{(2n+1)!(n_1+m'-m)!(n_1-m'+m)!(n-n_1+m')!(n-n_1-m')!}\right]^{1/2}. \tag{D.17}$$

(2) For $|n-n_1| \geq |m'|$ and $n < n_1$, we use the symmetry relation (cf. Eq. (D.6))

$$C^{n_1-n,m'}_{nm\,n_1,m'-m} = C^{n_1-n,m'}_{n_1,m'-m\,nm} \tag{D.18}$$

along with Eq. (D.17).

(3) For $|n-n_1| < |m'|$ and $m' \geq 0$,

$$C^{m'm'}_{nm\,n_1,m'-m} = (-1)^{n+m}\left[\frac{(2m'+1)!(n+n_1-m')!(n+m)!(n_1+m'-m)!}{(n+n_1+m'+1)!(n-n_1+m')!(n_1-n+m')!(n-m)!(n_1-m'+m)!}\right]^{1/2}. \tag{D.19}$$

(4) For $|n-n_1| < |m'|$ and $m' < 0$, we use the formula (cf. Eq. (D.7))

$$C^{-m',m'}_{nm\,n_1,m'-m} = (-1)^{n+n_1+m'}C^{-m',-m'}_{n,-m\,n_1,m-m'} \tag{D.20}$$

along with Eq. (D.19).

We have found that the numerical scheme based on the upward recursion (D.13) produces stable results only for n' smaller than approximately 60 if double-precision (REAL*8) floating-point FORTRAN variables are used and smaller than approximately 105 if the scheme is implemented using extended-precision (REAL*16) variables. The instability occurs in those cases when the use of the upward recursion causes n' to reach what Schulten and Gordon (1975) call the classical domain of

n' - values centered at $n' \approx N = (N_{\min} + N_{\max})/2$, where $N_{\max} = n + n_1$, and then the non-classical domain with $n' \gg N$. Clebsch–Gordan coefficients first increase in absolute value with increasing n', then oscillate with a slowly varying amplitude in the classical domain, and finally rapidly decay in absolute value as n' reaches the non-classical domain. This behavior results in catastrophic loss of numerical accuracy in the classical domain followed by overflows in the non-classical domain.

To stabilize the computation of the Clebsch–Gordan coefficients, we have implemented a modified version of the procedure proposed by Schulten and Gordon (1975). Specifically, the upward recursion of Eq. (13) is used only for $n' \le N$, whereas the Clebsch–Gordan coefficients with $n' > N$ are computed using the downward analog of Eq. (13),

$$C^{n'm'}_{nm\,n_1,m'-m} = D(EC^{n'+1,m'}_{nm\,n_1,m'-m} - FC^{n'+2,m'}_{nm\,n_1,m'-m}), \tag{D.21}$$

where

$$D = \left[\frac{4(n'+1)^2(2n'+1)(2n'+3)}{(n'+m'+1)(n'-m'+1)(n_1-n+n'+1)(n-n_1+n'+1)(n+n_1-n')(n+n_1+n'+2)}\right]^{1/2}, \tag{D.22}$$

$$E = \frac{(2m-m')(n'+2)(n'+1) - m'n(n+1) + m'n_1(n_1+1)}{2(n'+2)(n'+1)}, \tag{D.23}$$

$$F = \left[\frac{(n'-m'+2)(n'+m'+2)(n_1-n+n'+2)(n-n_1+n'+2)(n+n_1-n'-1)(n+n_1+n'+3)}{4(n'+2)^2(2n'+5)(2n'+3)}\right]^{1/2}, \tag{D.24}$$

supplemented by the initial values

$$C^{N_{\max}+1,m'}_{nm\,n_1,m'-m} = 0, \tag{D.25}$$

$$C^{N_{\max},m'}_{nm\,n_1,m'-m} = \left[\frac{(2n)!(2n_1)!(n+n_1+m')!(n+n_1-m')!}{(2n+2n_1)!(n+m)!(n-m)!(n_1+m'-m)!(n_1-m'+m)!}\right]^{1/2}. \tag{D.26}$$

Since the two-directional recursion scheme always works towards the center of the classical domain $(n' \cong N)$, it produces highly accurate and stable results. We have found that it works well for n' exceeding 150 even when the numerical procedure is implemented using double-precision variables (Wielaard *et al.* 1997).

Equations (D.17), (D.19), and (D.26) involve ratios of products of several factorials. Although these ratios are finite numbers with quite limited values, the factorials themselves can cause computer overflows in actual computer calculations. In order to avoid overflows, a useful approach is to store an array of natural logarithms of factorials of integers ranging from 0 to an appropriate maximal value. Then the ratio of two factorials is computed as $m!/n! = \exp[\ln(m!) - \ln(n!)]$. The logarithms of the factorials should be computed using the upward recursion $\ln[(m+1)!] = \ln(m!) + \ln(m+1)$.

Appendix E

Système International units

The system of physical units adopted in this book is the internationally accepted form of the metric system known as the Système International (SI). The SI is formed by base units, supplementary units, and units derived from the base units. The table below lists only those derived SI units that are used in this book.

Quantity	Unit	Symbol	Definition
Base units			
length	meter	m	
time	second	s	
mass	kilogram	kg	
electric current	ampere	A	
temperature	kelvin	K	
amount of substance	mole	mol	
Supplementary units			
plane angle	radian	rad	
solid angle	steradian	sr	
Derived units			
energy	joule	J	$\mathrm{N\,m = kg\,m^2\,s^{-2}}$
electric charge	coulomb	C	$\mathrm{A\,s}$
electric potential	volt	V	$\mathrm{W\,A^{-1} = kg\,m^2\,s^{-3}\,A^{-1}}$
electric capacitance	farad	F	$\mathrm{C\,V^{-1} = kg^{-1}\,m^{-2}\,s^4\,A^2}$
electric resistance	ohm	Ω	$\mathrm{V\,A^{-1} = kg\,m^2\,s^{-3}\,A^{-2}}$
magnetic flux	weber	Wb	$\mathrm{V\,s = kg\,m^2\,s^{-2}\,A^{-1}}$
inductance	henry	H	$\mathrm{Wb\,A^{-1} = kg\,m^2\,s^{-2}\,A^{-2}}$
frequency	hertz	Hz	$\mathrm{s^{-1}}$
power	watt	W	$\mathrm{J\,s^{-1} = kg\,m^2\,s^{-3}}$
force	newton	N	$\mathrm{kg\,m\,s^{-2}}$

Abbreviations and symbols

The list includes only those abbreviations and symbols that are encountered in two or more sections or are used to denote two or more quantities.

Abbreviation or symbol	Definition and dimension in SI units	Introduced in Section
English abbreviations and symbols		
a	semi-axis of an ellipsoid [m]	3.2
a	equivalent-sphere radius [m]	3.2
a	radius of a sphere [m]	3.3
a	typical particle dimension [m]	5.8.2
a	parameter of the gamma size distribution [m]	5.10.1
a	horizontal semi-axis of a spheroid [m]	5.11.2
a	semi-major particle dimension [m]	7.1
$\mathbf{a}$	column vector of expansion coefficients of the incident electric field [V m^{-1}]	5.1
a_n	Lorenz–Mie coefficients [–]	5.2.2
a_{mn}	expansion coefficients of the incident electric field [V m^{-1}]	5.1
$a_j(\Theta)$	diagonal elements of the normalized Stokes scattering matrix [–]	4.10
$\mathbf{A}$	4×4 transformation matrix [–]	1.3
$\mathbf{A}$	matrix formed by the translation coefficients $A_{\mu\nu mn}$ [–]	5.2.4
$\mathbf{A}$	Mueller matrix of the analyzer [–]	8.1
$A_{\mu\nu mn}$	translation coefficients [–]	Appendix C
$\overleftrightarrow{A}$	scattering dyadic [m]	2.2
b	semi-axis of an ellipsoid [m]	3.2
b	parameter of the gamma size distribution [–]	5.10.1

Abbreviation or symbol	Definition and dimension in SI units	Introduced in Section
b	vertical (rotational) semi-axis of a spheroid [m]	5.11.2
$\mathbf{b}$	column vector of the expansion coefficients of the incident electric field [V m^{-1}]	5.1
b_n	Lorenz–Mie coefficients [–]	5.2.2
b_{mn}	expansion coefficients of the incident electric field [V m^{-1}]	5.1
$b_j(\Theta)$	off-diagonal elements of the normalized Stokes scattering matrix [–]	4.10
$\mathbf{B}$	magnetic induction [Wb m^{-2}]	1.1
$\mathbf{B}$	4×4 transformation matrix [–]	1.3
$\mathbf{B}$	matrix formed by the translation coefficients $B_{\mu\nu mn}$ [–]	5.2.4
BCGM	bi-conjugate gradient method	6.5
$B_{\mu\nu mn}$	translation coefficients [–]	Appendix C
$\mathbf{B}_{mn}(\vartheta)$	vector angular functions [–]	Appendix C
$\mathbf{B}_{mn}(\vartheta, \varphi)$	vector angular functions [–]	Appendix C
c	speed of light in a vacuum [m s^{-1}]	1.2
c	semi-axis of an ellipsoid [m]	3.2
$\langle\cos\Theta\rangle$	asymmetry parameter [–]	2.8
$\mathbf{C}$	circular-polarization amplitude scattering matrix [m]	4.12
CGM	conjugate gradient method	6.2
$C_{++}, C_{+-}, C_{-+}, C_{--}$	elements of the circular-polarization amplitude scattering matrix [m]	4.12
C_{abs}	absorption cross section [m^2]	2.8
C_{ext}	extinction cross section [m^2]	2.8
C_{pr}	radiation-pressure cross section [m^2]	2.9
C_{sca}	scattering cross section [m^2]	2.8
$C^{nm}_{n_1m_1\,n_2m_2}$	Clebsch–Gordan coefficients [–]	Appendix D
$\mathbf{C}_{mn}(\vartheta)$	vector angular functions [–]	Appendix C
$\mathbf{C}_{mn}(\vartheta, \varphi)$	vector angular functions [–]	Appendix C
$\langle C_{\mathrm{abs}}\rangle$	average absorption cross section per particle [m^2]	3.1
$\langle C_{\mathrm{b}}\rangle$	average backscattering cross section per particle [m^2]	9.5
$\langle C_{\mathrm{ext}}\rangle$	average extinction cross section per particle [m^2]	3.1
$\langle C_{\mathrm{pr}}\rangle$	average radiation-pressure cross section per particle [m^2]	3.1

Abbreviation or symbol	Definition and dimension in SI units	Introduced in Section
$\langle C_{\text{sca}} \rangle$	average scattering cross section per particle [m^2]	3.1
$\dfrac{\mathrm{d}C_{\text{sca}}}{\mathrm{d}\Omega}$	differential scattering cross section [m^2]	2.8
d_n	coefficient [–]	Appendix C
$d^s_{mn}(\vartheta)$	Wigner d-functions [–]	Appendix B
D	diameter of a circular cylinder [m]	5.11.2
D	diameter of the host sphere [m]	10.10
$\mathbf{D}$	electric displacement [C m^{-2}]	1.1
D	4×4 transformation matrix [–]	1.3
DDA	discrete dipole approximation	6.5
$D^s_{mn}(\vartheta)$	Wigner D-functions [–]	Appendix B
e	base of natural logarithms [–]	
$\mathbf{E}$	electric field [V m^{-1}]	1.1
E	unit matrix [–]	5.2.3
EBCM	extended boundary condition method	5.8.1
E_ϑ, E_φ	spherical coordinate components of the electric field vector [V m^{-1}]	1.3
E_+, E_-	circular components of the electric field vector [V m^{-1}]	4.12
$\mathbf{F}$	radiation force [N]	2.9
F	Stokes scattering matrix [m^2]	Introduction to Chapter 4
FDM	finite-difference method	6.2
FDTDM	finite-difference time-domain method	6.3
FEM	finite-element method	6.2
FFT	fast Fourier transform	6.5
FIEM	Fredholm integral equation method	6.5
F_{ij}	elements of the Stokes scattering matrix [m^2]	4.1
$\tilde{\mathsf{F}}$	normalized Stokes scattering matrix [–]	4.10
$\tilde{\mathsf{F}}^{\text{CP}}$	normalized circular-polarization scattering matrix [–]	4.12
$\langle \mathbf{F} \rangle$	average radiation force per particle [N]	4.6
$\langle \mathsf{F} \rangle$	average Stokes scattering matrix per particle [m^2]	4.2
$g(\mathbf{r}, \mathbf{r}')$	scalar Green's function [m^{-1}]	2.1
g^s_{pq}	expansion coefficients [–]	4.12
G	area of the particle geometrical projection [m^2]	2.8
GE	Gaussian elimination	6.2

Abbreviation or symbol	Definition and dimension in SI units	Introduced in Section
GPMM	generalized PMM	6.4
$\overleftrightarrow{G}$	free space dyadic Green's function [m^{-1}]	2.1
$\langle G \rangle$	average area of the geometrical projection per particle [m^2]	4.6
$h_n^{(1)}$	Hankel functions of the first kind [–]	Appendix C
$h_n^{(2)}$	Hankel functions of the second kind [–]	Appendix C
$\mathbf{H}$	magnetic field [A m^{-1}]	1.1
i	$\sqrt{-1}$ [–]	1.1
I	intensity (irradiance) [W m^{-2}]	1.2
I	monochromatic specific intensity (radiance) [W rad^{-1} s m^{-2} sr^{-1}]	3.4
I	first Stokes parameter [W m^{-2}]	1.3
$\mathbf{I}$	4×1 Stokes column vector [W m^{-2}]	1.3
$\mathbf{I}$	4×1 monochromatic specific intensity column vector [W rad^{-1} s m^{-2} sr^{-1}]	3.4
Im	imaginary part	
I_2, I_0, I_{-0}, I_2	elements of the circular-polarization column vector [W m^{-2}]	1.3
I_b	Planck blackbody energy distribution [W rad^{-1} s m^{-2} sr^{-1}]	2.10
$\mathbf{I}_\mathrm{b}$	4×1 blackbody Stokes column vector [W rad^{-1} s m^{-2} sr^{-1}]	2.10
$I_\mathrm{v}, I_\mathrm{h}$	first and second elements of the modified Stokes column vector [W m^{-2}]	1.3
$\mathbf{I}^\mathrm{CP}$	4×1 circular-polarization column vector [W m^{-2}]	1.3
$\mathbf{I}^\mathrm{MS}$	4×1 modified Stokes column vector [W m^{-2}]	1.3
$\overleftrightarrow{I}$	identity dyadic [–]	2.1
j_l	spherical Bessel functions of the first kind [–]	Appendix A
$\mathbf{J}$	current density [A m^{-2}]	1.1
$\mathbf{J}$	4×1 coherency column vector [W m^{-2}]	1.3
$\mathbf{J}_S$	surface current density [A m^{-1}]	1.1
$k = k_\mathrm{R} + \mathrm{i}k_\mathrm{I}$	(complex) wave number [m^{-1}]	1.2
$\mathbf{k} = \mathbf{k}_\mathrm{R} + \mathrm{i}\mathbf{k}_\mathrm{I}$	(complex) wave vector [m^{-1}]	1.2
k_1	wave number in the exterior region [m^{-1}]	2.1
k_2	wave number in the interior region [m^{-1}]	2.1
L	length of a cylinder [m]	5.11.2
$\mathbf{L}, \mathbf{L}^\mathrm{MS}, \mathbf{L}^\mathrm{CP}$	4×4 rotation matrices [–]	1.5
$m = m_\mathrm{R} + \mathrm{i}m_\mathrm{I}$	(complex) refractive index relative to vacuum or surrounding medium [–]	1.2, 2.1

Abbreviation or symbol	Definition and dimension in SI units	Introduced in Section
$\mathbf{M}$	magnetization [A m^{-1}]	1.1
M	Mueller matrix of the modulator [–]	8.1
ME-GPMM	multiple-expansion GPMM	6.4
MOM	method of moments	6.5
$\mathbf{M}_{mn}$	vector spherical wave functions [–]	Appendix C
$n(a)$	size distribution function [m^{-1}]	3.2
n_0	particle number density [m^{-3}]	3.4
$n_{\max}$	parameter specifying the size of the T matrix [–]	5.8.4
$n_{\max}$	maximal order of Lorenz–Mie coefficients [–]	5.10.1
$\hat{\mathbf{n}}$	unit vector [–]	1.1
$\hat{\mathbf{n}}^{\text{inc}}$	unit vector in the incidence direction [–]	2.2
$\hat{\mathbf{n}}^{\text{sca}}$	unit vector in the scattering direction [–]	2.2
N	number of particles [–]	3.1
N_{G}	number of Gaussian division points in Eq. (5.202) [–]	5.8.3
$\mathbf{N}_{mn}$	vector spherical wave functions [–]	Appendix C
p	phase function [–]	2.8
$p(x)$	probability density function [dimension is that of x^{-1}]	3.2
p	column vector of the expansion coefficients of the scattered electric field [V m^{-1}]	5.1
p_{mn}	expansion coefficients of the scattered electric field [V m^{-1}]	5.1
P	degree of (elliptical) polarization [–]	1.6
$\mathbf{P}$	electric polarization [C m^{-2}]	1.1
P	Mueller matrix of the polarizer [–]	8.1
PMM	point-matching method	6.4
P_{C}	degree of circular polarization [–]	1.6
P_{L}	degree of linear polarization [–]	1.6
P_Q	degree of linear polarization [–]	1.6
$P_l(x)$	Legendre polynomials [–]	Appendix A
$P_l^m(x)$	associated Legendre functions [–]	Appendix A
$P_{mn}^s(x)$	generalized spherical functions [–]	Appendix B
$P_q^{(a,b)}(x)$	Jacobi polynomials [–]	Appendix B
$\mathbf{P}_{mn}(\vartheta)$	vector angular functions [–]	Appendix C
$\mathbf{P}_{mn}(\vartheta, \varphi)$	vector angular functions [–]	Appendix C
q	2×2 transformation matrix [–]	4.12
q	column vector of the expansion coefficients of the scattered electric field [V m^{-1}]	5.1

Abbreviation or symbol	Definition and dimension in SI units	Introduced in Section
q_{mn}	expansion coefficients of the scattered electric field [V m^{-1}]	5.1
Q	second Stokes parameter [W m^{-2}]	1.3
Q	second element of the monochromatic specific intensity column vector [W rad^{-1} s m^{-2} sr^{-1}]	3.4
$\mathbf{Q}$	Q matrix [–]	5.8.1
$\mathbf{Q}$	Mueller matrix of the quarter-wave plate [–]	8.1
Q_{abs}	efficiency factor for absorption [–]	2.8
Q_{b}	backscattering efficiency factor [–]	9.5
Q_{ext}	efficiency factor for extinction [–]	2.8
Q_{pr}	efficiency factor for radiation pressure [–]	2.9
Q_{sca}	efficiency factor for scattering [–]	2.8
r	distance from the origin of a coordinate system [m]	2.2
r	radius of a spherical particle [m]	5.10.1
$\mathbf{r}$	radius (position) vector [m]	1.1
r_0	parameter specifying the size of Chebyshev and generalized Chebyshev particles [m]	5.11.2, 5.12
r_1, r_2	parameters of the power law and modified power law size distributions [m]	5.10.1
r_{12}	distance between two coordinate system origins [m]	2.11
r_{12}	distance between the components of a two-sphere cluster [m]	5.13
r_c	parameter of the modified gamma size distribution [m]	5.10.1
r_{eff}	effective radius of a size distribution [m]	5.10.1
r_g	parameter of the log normal size distribution [m]	5.10.1
r_{g1}, r_{g2}	parameters of the modified bimodal log normal size distribution [m]	5.10.1
r_{max}	maximal radius of a size distribution [m]	5.10.1
r_{min}	minimal radius of a size distribution [m]	5.10.1
r_{s}	surface-equivalent-sphere radius [m]	5.8.4
r_{v}	volume-equivalent-sphere radius [m]	5.11.2
$r_>$	radius of the smallest sphere circumscribing a particle [m]	5.1
$r_<$	radius of the largest inscribed sphere of a nonspherical particle [m]	5.8.1

Abbreviation or symbol	Definition and dimension in SI units	Introduced in Section
$\hat{\mathbf{r}}$	unit vector in the direction of **r** [–]	2.2
Re	real part	
Rg	stands for "regular"	Appendix C
RH	Rayleigh hypothesis	6.4
R_{be}	backscatter-to-extinction ratio [–]	9.5
R_{eb}	extinction-to-backscatter ratio [–]	9.5
S	surface area [m^2]	1.1
$\mathbf{S}$	Poynting vector [W m^{-2}]	1.1
S	amplitude scattering matrix [m]	2.2
S	S matrix [–]	5.2.3
S_{ij}	elements of the amplitude scattering matrix [m]	2.2
SIEM	surface integral equation method	6.5
SVM	separation of variables method	6.1
$\overleftrightarrow{S}$	scattering tensor [–]	2.3
$\langle\mathbf{S}\rangle$	time-averaged Poynting vector [W m^{-2}]	1.1
t	time [s]	1.1
t	crystal distortion parameter [–]	10.7
t	2×2 transformation matrix [–]	2.4
T	absolute temperature [K]	2.10
T	T matrix [–]	5.1
$T^{kl}_{mnm'n'}$	elements of the T matrix [–]	5.1
$T_n(\cos\vartheta)$	Chebyshev polynomial of degree n [–]	5.11.2
$\overleftrightarrow{T}$	dyadic transition operator [m^{-5}]	2.1
$\overleftrightarrow{T}_{\mathrm{M}}$	Maxwell stress tensor [N m^{-2}]	2.9
U	third Stokes parameter [W m^{-2}]	1.3
U	third element of the monochromatic specific intensity column vector [W rad^{-1} s m^{-2} sr^{-1}]	3.4
v	phase velocity [m s^{-1}]	1.2
$\mathbf{v}$	velocity vector [m s^{-1}]	1.1
v_{eff}	effective variance of a size distribution [–]	5.10.1
V	volume [m^3]	1.1
V	fourth Stokes parameter [W m^{-2}]	1.3
V	fourth element of the monochromatic specific Intensity column vector [W rad^{-1} s m^{-2} sr^{-1}]	3.4
VIEM	volume integral equation method	6.5
V_{EXT}	exterior region [m^3]	2.1
V_{INT}	interior region [m^3]	2.1
W	power [W]	1.1

Abbreviation or symbol	Definition and dimension in SI units	Introduced in Section
x	size parameter [–]	5.8.2
x_a, x_b	size parameters along spheroid semi-axes [m]	5.11.7
x_{eff}	effective size parameter of a size distribution [–]	9.2
x_{s}	surface-equivalent-sphere size parameter [–]	5.8.4
x_{v}	volume-equivalent-sphere size parameter [–]	10.4
y_l	spherical Bessel functions of the second kind [–]	Appendix C
$Y_{lm}(\hat{\mathbf{r}})$	spherical harmonics [–]	Appendix A
$\mathbf{Z}$	Stokes phase matrix [m^2]	2.6
Z_{ij}	elements of the Stokes phase matrix [m^2]	2.6
$\mathbf{Z}^{\text{CP}}$	circular-polarization phase matrix [m^2]	2.6
$\mathbf{Z}^{J}$	coherency phase matrix [m^2]	2.6
$\mathbf{Z}^{\text{MS}}$	modified Stokes phase matrix [m^2]	2.6
$\tilde{\mathbf{Z}}$	normalized Stokes phase matrix [–]	4.10
$\tilde{\mathbf{Z}}^{\text{CP}}$	normalized circular-polarization phase matrix [–]	4.12
$\langle\mathbf{Z}\rangle$	average Stokes phase matrix per particle [m^2]	3.1
Greek symbols		
α	absorption coefficient [m^{-1}]	1.2
α	first Euler angle [rad]	2.4
α	parameter of the modified gamma size distribution [–]	5.10.1
α	exponent of the modified power law size distribution [–]	5.10.1
α	local incidence angle [rad]	9.4
$\boldsymbol{\alpha}$	3×2 transformation matrix [–]	2.4
α_j^s	expansion coefficients [–]	4.11
β	ellipticity angle of the polarization ellipse [rad]	1.4
β	second Euler angle [rad]	2.4
$\boldsymbol{\beta}$	3×3 transformation matrix [–]	2.4
β_j^s	expansion coefficients [–]	4.11
$\overline{\beta}$	backscattered fraction for isotropically incident radiation [–]	10.3
γ	third Euler angle [rad]	2.4
γ	parameter of the modified gamma size distribution [–]	5.10.1
γ	parameter of the modified bimodal log normal size distribution [–]	5.10.1

Abbreviation or symbol	Definition and dimension in SI units	Introduced in Section
γ_{mn}	coefficient [–]	Appendix C
γ'_{mn}	coefficient [–]	Appendix C
$\mathbf{\Gamma}$	radiation torque [N m]	2.9
$\delta(x)$	Dirac delta function [dimension is that of x^{-1}]	2.1
$\delta(\mathbf{r})$	three-dimensional Dirac delta function [m^{-3}]	2.1
$\delta(\hat{\mathbf{n}})$	solid-angle Dirac delta function [–]	2.3
δ_{C}	circular backscattering depolarization ratio [–]	10.2
δ_{L}	linear backscattering depolarization ratio [–]	4.9
δ_{mn}	Kronecker delta [–]	Appendix B
$\mathbf{\Delta}$	4×4 unit matrix [–]	4.4
$\mathbf{\Delta}_3$	4×4 transformation matrix [–]	2.6
$\mathbf{\Delta}_{23}$	4×4 transformation matrix [–]	2.6
$\mathbf{\Delta}_{34}$	4×4 transformation matrix [–]	4.3
$\mathbf{\Delta}^{\mathrm{CP}}$	4×4 transformation matrix [–]	4.12
$\mathbf{\Delta}^{\mathrm{MS}}$	4×4 transformation matrix [–]	2.6
ε	electric permittivity [$\mathrm{F\ m^{-1}}$]	1.1
ε	aspect ratio of a nonspherical particle [–]	3.2
ε_0	electric permittivity of free space [$\mathrm{F\ m^{-1}}$]	1.1
ε_1	electric permittivity of the surrounding medium [$\mathrm{F\ m^{-1}}$]	2.1
ζ	orientation angle of the polarization ellipse [rad]	1.4
η	rotation angle [rad]	1.5
ϑ	polar (zenith) angle [rad]	1.3
$\hat{\boldsymbol{\vartheta}}$	unit vector in the ϑ direction [–]	1.3
Θ	scattering angle [rad]	2.8
$\mathbf{K}$	Stokes extinction matrix [m^2]	2.7
K_{ij}	elements of the Stokes extinction matrix [m^2]	2.7
$\mathbf{K}^{\mathrm{CP}}$	circular-polarization extinction matrix [m^2]	2.7
$\mathbf{K}_{\mathrm{e}}$	4×1 Stokes emission column vector [$\mathrm{W\ rad^{-1}\ s\ sr^{-1}}$]	2.10
$\mathbf{K}^J$	coherency extinction matrix [m^2]	2.7
$\mathbf{K}^{\mathrm{MS}}$	modified Stokes extinction matrix [m^2]	2.7
$\langle\mathbf{K}\rangle$	average Stokes extinction matrix per particle [m^2]	3.1
$\langle\mathbf{K}_{\mathrm{e}}\rangle$	average Stokes emission column vector per particle [$\mathrm{W\ rad^{-1}\ s\ sr^{-1}}$]	3.1
λ	free-space wavelength [m]	1.2
λ_1	wavelength in the surrounding medium [m]	3.4

Abbreviation or symbol	Definition and dimension in SI units	Introduced in Section
μ	magnetic permeability [H m^{-1}]	1.1
μ_0	magnetic permeability of free space [H m^{-1}]	1.1
ξ	deformation parameter for Chebyshev particles [–]	5.11.2
ξ_{mn}	coefficient [–]	Appendix B
π	pi [–]	
ϖ	single-scattering albedo [–]	2.8
$\pi_n(\vartheta)$	angular functions [–]	5.7
$\pi_{mn}(\vartheta)$	angular functions [–]	5.1
ρ	charge density [C m^{-3}]	1.1
ρ	phase shift [–]	9.1
ρ	phase function ratio [–]	10.2
$\boldsymbol{\rho}$	2×2 coherency (density) matrix [W m^{-2}]	1.3
ρ_S	surface charge density [C m^{-2}]	1.1
σ	conductivity [Ω^{-1} m^{-1}]	1.1
σ	surface roughness parameter [–]	10.7
σ_1, σ_2	rotation angles [rad]	4.3
σ_g	parameter of the log normal size distribution [–]	5.10.1
σ_{g1}, σ_{g2}	parameters of the modified bimodal log normal size distribution [–]	5.10.1
$\langle\sigma_\mathrm{b}\rangle$	average radar backscattering cross section per particle [m^2]	9.5
τ	optical path length [–]	4.13
τ	optical thickness of the host particle [–]	10.10
$\tau_n(\vartheta)$	angular functions [–]	5.7
$\tau_{mn}(\vartheta)$	angular functions [–]	5.1
φ	azimuth angle [rad]	1.3
$\hat{\boldsymbol{\varphi}}$	unit vector in the φ direction [–]	1.3
χ	electric susceptibility [–]	1.1
ω	angular frequency [rad s^{-1}]	1.1
Ω	solid angle [sr]	2.10

Miscellaneous symbols

x^*	complex-conjugate value of x	1.1
$\langle x\rangle$	average of x	1.1
$\lvert x\rvert$	absolute value of x	
$\mathbf{a}\cdot\mathbf{b}$	dot (scalar) product of vectors **a** and **b**	
$\mathbf{a}\times\mathbf{b}$	vector product of vectors **a** and **b**	
$\mathbf{a}\otimes\mathbf{b}$	dyadic product of vectors **a** and **b**	2.1

Abbreviation or symbol	Definition and dimension in SI units	Introduced in Section
$\begin{pmatrix} l & m & n \\ p & q & r \end{pmatrix}$	Wigner $3j$ symbols	Appendix D
$\begin{bmatrix} a & \dots & b \\ \vdots & \ddots & \vdots \\ c & \cdots & d \end{bmatrix}$	matrix	
$\mathbf{A}^{-1}$	inverse of $\mathbf{A}$	1.3
$\mathbf{A}^{\mathrm{T}}$	transpose of $\mathbf{A}$	1.4
$\mathrm{diag}[a, b]$	$\begin{bmatrix} a & 0 \\ 0 & b \end{bmatrix}$	
$\ddot{\tilde{S}}^{\mathrm{T}}$	transpose of $\ddot{\tilde{S}}$	2.3
∇	gradient [m^{-1}]	
$\in$	element of	
$\cup$	union of sets	

References

Abramowitz, M., and Stegun, I. A., eds. (1964). *Handbook of Mathematical Functions with Formulas, Graphs and Mathematical Tables* (National Bureau of Standards, Washington, D. C.).

Acquista, C. (1976). Light scattering by tenuous particles: A generalization of the Rayleigh–Gans–Rocard approach. *Appl. Opt.* **15**, 2932–2936.

Aden, A. L., and Kerker, M. (1951). Scattering of electromagnetic waves from two concentric spheres. *J. Appl. Phys.* **22**, 1242–1246.

Agarwal, G. S. (1976). Relation between Waterman's extended boundary condition and the generalized extinction theorem. *Phys. Rev. D* **14**, 1168–1171.

Alpers, M., Gerding, M., Höffner, J., and Schneider, J. (2001). Multiwavelength lidar observation of a strange noctilucent cloud at Kühlungsborn, Germany (54° N). *J. Geophys. Res.* **106**, 7945–7953.

Al-Rizzo, H. M., and Tranquilla, J. M. (1995a). Electromagnetic scattering from dielectrically coated axisymmetric objects using the generalized point-matching technique. I. Theoretical formulation. *J. Comput. Phys.* **119**, 342–355.

Al-Rizzo, H. M., and Tranquilla, J. M. (1995b). Electromagnetic scattering from dielectrically coated axisymmetric objects using the generalized point-matching technique (GPMT). II. Numerical results and comparisons. *J. Comput. Phys.* **119**, 356–373.

Al-Rizzo, H. M., and Tranquilla, J. M. (1995c). Electromagnetic wave scattering by highly elongated and geometrically composite objects of large size parameters: The generalized multipole technique. *Appl. Opt.* **34**, 3502–3521.

Amic, E., Luck, J. M., and Nieuwenhuizen, Th. M. (1997). Multiple Rayleigh scattering of electromagnetic waves. *J. Phys. I (Paris)* **7**, 445–483.

Anderson, R. (1992). Measurement of Mueller matrices. *Appl. Opt.* **31**, 11–13.

Anderson, T. L., Covert, D. S., Marshall, S. F., *et al*. (1996). Performance characteristics of a

high-sensitivity, three-wavelength, total scatter/backscatter nephelometer. *J. Atmos. Oceanic Technol.* **13**, 967–986.

Apresyan, L. A., and Kravtsov, Yu. A. (1996). *Radiation Transfer. Statistical and Wave Aspects* (Gordon and Breach, Basel).

Arfken, G. B., and Weber, H. J. (1995). *Mathematical Methods for Physicists* (Academic Press, San Diego).

Arnott, W. P., and Marston, P. L. (1991). Unfolded optical glory of spheroids: backscattering of laser light from freely rising spheroidal air bubbles in water. *Appl. Opt.* **30**, 3429–3442.

Asano, S. (1979). Light scattering properties of spheroidal particles. *Appl. Opt.* **18**, 712–723.

Asano, S. (1983). Light scattering by horizontally oriented spheroidal particles. *Appl. Opt.* **22**, 1390–1396.

Asano, S., and Sato, M. (1980). Light scattering by randomly oriented spheroidal particles. *Appl. Opt.* **19**, 962–974.

Asano, S., and Yamamoto, G. (1975). Light scattering by a spheroidal particle. *Appl. Opt.* **14**, 29–49.

Ashkin, A. (2000). History of optical trapping and manipulation of small-neutral particle, atoms, and molecules. *IEEE J. Select. Topics Quant. Electron.* **6**, 841–856.

Ashkin, A., and Dziedzic, J. (1980). Observation of light scattering from nonspherical particles using optical levitation. *Appl. Opt.* **19**, 660–668.

Astafieva, L. G., and Babenko, V. A. (1999). Heating of a spheroidal particle by intense laser radiation. *J. Quant. Spectrosc. Radiat. Transfer* **63**, 459–468.

Auger, J.-C., Stout, B., Barrera, R. G., and Curiel, F. (2001). Scattering properties of rutile pigments located eccentrically within microvoids. *J. Quant. Spectrosc. Radiat. Transfer* **70**, 675–695.

Aydin, K. (2000). Centimeter and millimeter wave scattering from nonspherical hydrometeors. In *Light Scattering by Nonspherical Particles: Theory, Measurements, and Applications*, eds. M. I. Mishchenko, J. W. Hovenier, and L. D. Travis, pp. 451–479 (Academic Press, San Diego).

Aydin, K., and Tang, C. (1997a). Millimeter wave radar scattering from model ice crystal distributions. *IEEE Trans. Geosci. Remote Sens.* **35**, 140–146.

Aydin, K., and Tang, C. (1997b). Relationships between IWC and polarimetric radar measurands at 94 and 220 GHz for hexagonal columns and plates. *J. Atmos. Oceanic Technol.* **14**, 1055–1063.

Aydin, K., and Walsh, T. M. (1999). Millimeter wave scattering from spatial and planar bullet rosettes. *IEEE Trans. Geosci. Remote Sens.* **37**, 1138–1150.

Azzam, R. M. A., and Bashara, N. M. (1977). *Ellipsometry and Polarized Light* (North-Holland, Amsterdam).

Babenko, V. A., Astafyeva, L. G., and Kuzmin, V. N. (2003). *Electromagnetic Scattering in Disperse Media. Inhomogeneous and Anisotropic Particles* (Praxis, Chichester, UK).

Bacon, N. J., and Swanson, B. D. (2000). Laboratory measurements of light scattering by single levitated ice crystals. *J. Atmos. Sci.* **57**, 2094–2104.

Bantges, R. J., Russell, J. E., and Haigh, J. D. (1999). Cirrus cloud top-of-atmosphere radiance spectra in the thermal infrared. *J. Quant. Spectrosc. Radiat. Transfer* **63**, 487–498.

Barabanenkov, Yu. N., Kravtsov, Yu. A., Ozrin, V. D., and Saichev, A. I. (1991). Enhanced backscattering in optics. In *Progress in Optics XXIX*, ed. E. Wolf, pp. 65–197 (Elsevier, Amsterdam).

Baran, A. J., Foot, J. S., and Mitchell, D. L. (1998). Ice-crystal absorption: a comparison between theory and implications for remote sensing. *Appl. Opt.* **37**, 2207–2215.

Baran, A. J., Francis, P. N., Havemann, S., and Yang, P. (2001a). A study of the absorption and extinction properties of hexagonal ice columns and plates in random and preferred orientations, using exact *T*-matrix theory and aircraft observations of cirrus. *J. Quant. Spectrosc. Radiat. Transfer* **70**, 505–518.

Baran, A. J., Yang, P., and Havemann, S. (2001b). Calculation of the single-scattering properties of randomly oriented hexagonal ice columns: a comparison of the *T*-matrix and the finite-difference time-domain methods. *Appl. Opt.* **40**, 4376–4386.

Barber, P. W. (1977). Resonance electromagnetic absorption by nonspherical dielectric objects. *IEEE Trans. Microwave Theory Tech.* **25**, 373–381.

Barber, P. W., and Hill, S. C. (1990). *Light Scattering by Particles: Computational Methods* (World Scientific, Singapore).

Barber, P. W., and Wang, D.-S. (1978). Rayleigh–Gans–Debye applicability to scattering by nonspherical particles. *Appl. Opt.* **17**, 797–803.

Barber, P., and Yeh, C. (1975). Scattering of electromagnetic waves by arbitrarily shaped dielectric bodies. *Appl. Opt.* **14**, 2864–2872.

Barber, P. W., Miller, E. K., and Sarkar, T. K., eds. (1994). Feature issue on Scattering by Three-Dimensional Objects. *J. Opt. Soc. Am. A* **11**, 1379–1545.

Barkey, B., and Liou, K. N. (2001). Polar nephelometer for light-scattering measurements of ice crystals. *Opt. Lett.* **26**, 232–234.

Barthel, H., Sachweh, B., and Ebert, F. (1998). Measurement of airborne mineral fibers using a new differential light scattering device. *Meas. Sci. Technol.* **9**, 210–220.

Barton, J. P., and Alexander, D. R. (1991). Electromagnetic fields for an irregularly shaped, near-spherical particle illuminated by a focused laser beam. *J. Appl. Phys.* **69**, 7973–7986.

Barton, J. P., Alexander, D. R., and Schaub, S. A. (1989). Theoretical determination of net radiation force and torque for a spherical particle illuminated by a focused laser beam. *J. Appl. Phys.* **66**, 4594–4602.

Bates, R. H. T. (1975). Analytic constraints on electromagnetic field computations. *IEEE Trans. Microwave Theory Tech.* **23**, 605–623.

Bates, R. H. T., and Wall, D. J. N. (1977). Null field approach to scalar diffraction. *Phil. Trans. Roy. Soc. London A* **287**, 45–114.

Battaglia, A., Muinonen, K., Nousiainen, T., and Peltoniemi, J. I. (1999). Light scattering by Gaussian particles: Rayleigh-ellipsoid approximation. *J. Quant. Spectrosc. Radiat. Transfer* **63**, 277–303.

Battaglia, A., Prodi, F., and Sturniolo, O. (2001). Radar and scattering parameters through falling hydrometeors with axisymmetric shapes. *Appl. Opt.* **40**, 3092–3100.

Battan, L. J. (1973). *Radar Observation of the Atmosphere* (University of Chicago Press, Chicago).

Bayvel, L. P., and Jones, A. R. (1981). *Electromagnetic Scattering and its Applications* (Applied Science Publishers, London).

Beardsley, G. F. (1968). Mueller scattering matrix of sea water. *J. Opt. Soc. Am.* **58**, 52–57.

Berenger, J.-P. (1996). Three-dimensional perfectly matched layer for the absorption of electromagnetic waves. *J. Comput. Phys.* **127**, 363–379.

Berne, B. J., and Pecora, R. (2000). *Dynamic Light Scattering with Applications to Chemistry, Biology, and Physics* (Dover Publications, Mineola, NY).

Beyerle, G., Deckelmann, H., Neuber, R., *et al.* (2001). Occurrence of solid particles in the winter polar stratosphere above the nitric acid trihydrate coexistence temperature inferred from ground-based polarization lidar observations at Ny-Ålesund, Spitsbergen. *J. Geophys. Res.* **106**, 2979–2992.

Bhandari, R. (1985). Scattering coefficients for a multilayered sphere: analytic expressions and algorithms. *Appl. Opt.* **24**, 1960–1967.

Bickel, W. S., Davidson, J. F., Huffman, D. R., and Kilkson, R. (1976). Application of polarization effects in light scattering: a new biophysical tool. *Proc. Nat. Acad. Sci. USA* **73**, 486–490.

Biedenharn, L. C., and Louck, J. D. (1981). *Angular Momentum in Quantum Physics: Theory and Application* (Addison-Wesley, Reading, MA).

Bohren, C. F. (1974). Light scattering by an optically active sphere. *Chem. Phys. Lett.* **29**, 458–462.

Bohren, C. F., and Gilra, D. P. (1979). Extinction by a spherical particle in an absorbing medium. *J. Colloid Interface Sci.* **72**, 215–221.

Bohren, C. F., and Huffman, D. R. (1983). *Absorption and Scattering of Light by Small Particles* (John Wiley & Sons, New York).

Bohren, C. F., and Singham, S. B. (1991). Backscattering by nonspherical particles: a review of methods and suggested new approaches. *J. Geophys. Res.* **96**, 5269–5277.

Borghese, F., Denti, P., Toscano, G., and Sindoni, O. I. (1979). Electromagnetic scattering by a cluster of spheres. *Appl. Opt.* **18**, 116–120.

Borghese, F., Denti, P., Saija, R., *et al*. (1984). Multiple electromagnetic scattering from a cluster of spheres. I. Theory. *Aerosol Sci. Technol.* **3**, 227–235.

Borghese, F., Denti, P., Saija, R., and Sindoni, O. I. (1992). Optical properties of spheres containing a spherical eccentric inclusion. *J. Opt. Soc. Am. A* **9**, 1327–1335.

Borghese, F., Denti, P., and Saija, R. (1994). Optical properties of spheres containing several spherical inclusions. *Appl. Opt.* **33**, 484–493. (Errata: **34**, 5556 (1995).)

Borghese, F., Denti, P., Saija, R., *et al*. (2001). Optical properties of a dispersion of anisotropic particles with non-randomly distributed orientations. The case of atmospheric ice crystals. *J. Quant. Spectrosc. Radiat. Transfer* **70**, 237–251.

Borghese, F., Denti, P., and Saija, R. (2003). *Scattering from Model Nonspherical Particles. Theory and Applications to Environmental Physics* (Springer-Verlag, Berlin).

Born, M., and Wolf, E. (1999). *Principles of Optics* (Cambridge University Press, Cambridge).

Borovoi, A., Naats, E., Oppel, U., and Grishin, I. (2000). Shape characterization of a large nonspherical particle by use of its Fraunhofer diffraction pattern. *Appl. Opt.* **39**, 1989–1997.

Borrmann, S., Solomon, S., Dye, J. E., and Luo, B. (1996). The potential of cirrus clouds for heterogeneous chlorine activation. *Geophys. Res. Lett.* **23**, 2133–2136.

Borrmann, S., Luo, B., and Mishchenko, M. (2000). Application of the T-matrix method to the measurement of aspherical (ellipsoidal) particles with forward scattering optical particle counters. *J. Aerosol Sci.* **31**, 789–799.

Boström, A., Kristensson, G., and Ström, S. (1991). Transformation properties of plane, spherical and cylindrical scalar and vector wave functions. In *Field Representations and Introduction to Scattering*, eds. V. V. Varadan, A. Lakhtakia, and V. K. Varadan, pp. 165–210 (North-Holland, Amsterdam).

Botet, R., Rannou, P., and Cabane, M. (1997). Mean-field approximation of Mie scattering by fractal aggregates of identical spheres. *Appl. Opt.* **36**, 8791–8797.

Bottiger, J. R., Fry, E. S., and Thompson, R. C. (1980). Phase matrix measurements for electromagnetic scattering by sphere aggregates. In *Light Scattering by Irregularly Shaped Particles*, ed. D. W. Schuerman, pp. 283–290 (Plenum Press, New York).

Boucher, O., Schwartz, S. E., Ackerman, T. P., *et al*. (1998). Intercomparison of models representing direct shortwave radiative forcing by sulfate aerosols. *J. Geophys. Res.* **103**, 16 979–16 998.

Bourrely, C., Chiappetta, P., and Lemaire, T. (1989). Electromagnetic scattering by large rotating particles in the eikonal formalism. *Opt. Commun.* **70**, 173–176.

Braak, C. J., de Haan, J. F., van der Mee, C. V. M., *et al.* (2001). Parameterized scattering matrices for small particles in planetary atmospheres. *J. Quant. Spectrosc. Radiat. Transfer* **69**, 585–604.

Braun, C., and Krieger, U. K. (2001). Two-dimensional angular light-scattering in aqueous NaCl single aerosol particles during deliquescence and efflorescence. *Opt. Express* **8**, 314–321.

Bringi, V. N., and Chandrasekar, V. (2001). *Polarimetric Doppler Weather Radar: Principles and Applications* (Cambridge University Press, Cambridge).

Bringi, V. N., and Seliga, T. A. (1977). Scattering from axisymmetric dielectrics or perfect conductors imbedded in an axisymmetric dielectric. *IEEE Trans. Antennas Propag.* **25**, 575–580.

Brink, D. M., and Satchler, G. R. (1993). *Angular Momentum* (Oxford University Press, Oxford).

Brogniez, C., Santer, R., Diallo, B. S., *et al*. (1992). Comparative observations of stratospheric aerosols by ground-based lidar, balloon-borne polarimeter, and satellite solar occultation. *J. Geophys. Res.* **97**, 20 805–20 823.

Brosseau, C. (1998). *Polarized Light: A Statistical Optics Approach* (John Wiley & Sons, New York).

Browell, E. V., Butler, C. F., Ismail, S., *et al.* (1990). Airborne lidar observations in the wintertime Arctic stratosphere: polar stratospheric clouds. *Geophys. Res. Lett*. **17**, 385–388.

Brown, W., ed. (1993). *Dynamic Light Scattering: The Method and Some Applications* (Oxford University Press, Oxford).

Bruning, J. H., and Lo, Y. T. (1971a). Multiple scattering of EM waves by spheres. I. Multipole expansion and ray-optical solutions. *IEEE Trans. Antennas Propag.* **19**, 378–390.

Bruning, J. H., and Lo, Y. T. (1971b). Multiple scattering of EM waves by spheres. II. Numerical and experimental results. *IEEE Trans. Antennas Propag.* **19**, 391–400.

Bruscaglioni, P., Ismaelli, A., and Zaccanti, G. (1993). A note on the definition of scattering cross sections and phase functions for spheres immersed in an absorbing medium. *Waves in Random Media* **3**, 147–156.

Bugaenko, O. I. (1976). Generalized spherical functions in the Mie problem. *Izv. Acad. Sci. USSR, Atmos. Oceanic Phys.* (Engl. transl.) **12**, 366–370.

Buriez, J. C., Vanbauce, C., Parol, F., *et al*. (1997). Cloud detection and derivation of cloud properties from POLDER. *Int. J. Remote Sens.* **18**, 2785–2813.

Burrows, M. L. (1969). Equivalence of the Rayleigh solution and the extended-boundary-condition solution for scattering problems. *Electron. Lett.* **5**, 277–278.

Cai, Q., and Liou, K.-N. (1982). Polarized light scattering by hexagonal ice crystals: theory. *Appl. Opt.* **21**, 3569–3580.

Card, J. B. A., and Jones, A. R. (1999a). An investigation of the use of a CCD camera for the characterisation of irregular particles. *Part. Part. Syst. Charact.* **16**, 135–142.

Card, J. B. A., and Jones, A. R. (1999b). An investigation of the potential of polarized light scattering for the characterization of irregular particles. *J. Phys. D: Appl. Phys.* **32**, 2467–2474.

Carey, L. D., Rutledge, S. A., Ahijevych, D. A., and Keenan, T. D. (2000). Correcting propagation effects in C-band polarimetric radar observations of tropical convection using differential propagation phase. *J. Appl. Meteorol.* **39**, 1405–1433.

Carslaw, K. S., Wirth, M., Tsias, A., *et al.* (1998). Particle microphysics and chemistry in remotely observed mountain polar stratospheric clouds. *J. Geophys. Res.* **103**, 5785–5796.

Chamaillard, K., and Lafon, J.-P. J. (2000). Statistical study of polarization of light scattered by rough grains. I. The method with preliminary results. *Astron. Astrophys.* **363**, 1155–1165.

Chamaillard, K., and Lafon, J.-P. J. (2001). Statistical approach of the effects of roughness on the polarization of light scattered by dust grains. *J. Quant. Spectrosc. Radiat. Transfer* **70**, 519–528.

Chandrasekhar, S. (1960). *Radiative Transfer* (Dover Publications, New York).

Chepfer, H., Brogniez, G., Goloub, P., *et al*. (1999). Observations of horizontally oriented ice crystals in cirrus clouds with POLDER-1/ADEOS-1. *J. Quant. Spectrosc. Radiat. Transfer* **63**, 521–543.

Chew, W. C. (1995). *Waves and Fields in Inhomogeneous Media* (IEEE Press, New York).

Chiappetta, P. (1980). Multiple scattering approach to light scattering by arbitrarily shaped particles. *J. Phys. A: Math. Gen.* **13**, 2101–2108.

Cho, S. K. (1990). *Electromagnetic Scattering* (Springer-Verlag, New York).

Chowdhary, J., Cairns, B., Mishchenko, M., and Travis, L. (2001). Retrieval of aerosol properties over the ocean using multispectral and multiangle photopolarimetric measurements from the Research Scanning Polarimeter. *Geophys. Res. Lett*. **28**, 243–246.

Chuang, C., and Beard, K. V. (1990). A numerical model for the equilibrium shape of electrified raindrops. *J. Atmos. Sci.* **47**, 1374–1389.

Chýlek, P. (1973). Large-sphere limits of the Mie-scattering functions. *J. Opt. Soc. Am.* **63**, 699–706.

Chýlek, P. (1976). Partial-wave resonances and the ripple structure in the Mie normalized extinction cross section. *J. Opt. Soc. Am.* **66**, 285–287.

Chýlek, P. (1977). Light scattering by small particles in an absorbing medium. *J. Opt. Soc. Am.* **67**, 561–563.

Chýlek, P., and Klett, J. D. (1991a). Extinction cross sections of nonspherical particles in the anomalous diffraction approximation. *J. Opt. Soc. Am. A* **8**, 274–281.

Chýlek, P., and Klett, J. D. (1991b). Absorption and scattering of electromagnetic radiation by prismatic columns: anomalous diffraction approximation. *J. Opt. Soc. Am. A* **8**, 1713–1720.

Chýlek, P., and Videen, G. (1994). Longwave radiative properties of polydispersed hexagonal ice crystals. *J. Atmos. Sci.* **51**, 175–190.

Chýlek, P., and Zhan, J. (1989). Interference structure of the Mie extinction cross section. *J. Opt. Soc. Am. A* **6**, 1846–1851.

Chýlek, P., Kiehl, J. T., and Ko, M. K. W. (1978). Narrow resonance structure in the Mie scattering characteristics. *Appl. Opt.* **17**, 3019–3021.

Chýlek, P., Ramaswamy, V., Ashkin, A., and Dziedzic, J. M. (1983). Simultaneous determination of refractive index and size of spherical dielectric particles from light scattering data. *Appl. Opt.* **22**, 2302–2307.

Chýlek, P., Ngo, D., and Pinnick, R. G. (1992). Resonance structure of composite and slightly absorbing spheres. *J. Opt. Soc. Am. A* **9**, 775–780.

Chýlek, P., Videen, G., Ngo, D., *et al*. (1995). Effect of black carbon on the optical properties and climate forcing of sulfate aerosols. *J. Geophys. Res.* **100**, 16 325–16 332.

Chýlek, P., Lesins, G. B., Videen, G., *et al.* (1996). Black carbon and absorption of solar radiation by clouds. *J. Geophys. Res.* **101**, 23 365–23 371.

Chýlek, P., Videen, G., Geldart, D. J. W., *et al*. (2000). Effective medium approximations for heterogeneous particles. In *Light Scattering by Nonspherical Particles: Theory, Measurements, and Applications*, eds. M. I. Mishchenko, J. W. Hovenier, and L. D. Travis, pp. 273–308 (Academic Press, San Diego).

Ciric, I. R., and Cooray, F. R. (1999). Benchmark solutions for electromagnetic scattering by systems of randomly oriented spheroids. *J. Quant. Spectrosc. Radiat. Transfer* **63**, 131–148.

Ciric, I. R., and Cooray, F. R. (2000). Separation of variables for electromagnetic scattering by spheroidal particles. In *Light Scattering by Nonspherical Particles: Theory, Measurements, and Applications*, eds. M. I. Mishchenko, J. W. Hovenier, and L. D. Travis, pp. 89–130 (Academic Press, San Diego).

C.-Labonnote, L., Brogniez, G., Doutriaux-Boucher, M., *et al.* (2000). Modeling of light scattering in cirrus clouds with inhomogeneous hexagonal monocrystals. Comparison with in-situ and ADEOS-POLDER measurements. *Geophys. Res. Lett.* **27**, 113–116.

C.-Labonnote, L., Brogniez, G., Buriez, J.-C., *et al.* (2001). Polarized light scattering by inhomogeneous hexagonal monocrystals. Validation with ADEOS-POLDER measurements. *J. Geophys. Res.* **106**, 12 139–12 153.

Clarke, D., and Grainger, J. F. (1971). *Polarized Light and Optical Measurement* (Pergamon Press, Oxford).

Cloude, S. R., and Pottier, E. (1996). A review of target decomposition theorems in radar polarimetry. *IEEE Trans. Geosci. Remote Sens.* **34**, 498–518.

Coakley, J. A., Jr., and Chýlek, P. (1975). The two-stream approximation in radiative transfer: including the angle of the incident radiation. *J. Atmos. Sci.* **32**, 409–418.

Coletti, A. (1984). Light scattering by nonspherical particles: a laboratory study. *Aerosol Sci. Technol.* **3**, 39–52.

Collett, E. (1992). *Polarized Light: Fundamentals and Applications* (Marcel Dekker, New York).

Colton, D., and Kress, R. (1983). *Integral Equation Methods in Scattering Theory* (John Wiley & Sons, New York).

Colton, D., and Kress, R. (1998). *Inverse Acoustic and Electromagnetic Scattering Theory* (Springer-Verlag, Berlin).

Comberg, U., and Wriedt, T. (1999). Comparison of scattering calculations for aggregated particles based on different models. *J. Quant. Spectrosc. Radiat. Transfer* **63**, 149–162.

Conwell, P. R., Barber, P. W., and Rushforth, C. K. (1984). Resonant spectra of dielectric spheres. *J. Opt. Soc. Am. A* **1**, 62–67.

Cooper, J., Hombach, V., and Schiavoni, A. (1996). Comparison of computational electromagnetic codes applied to a sphere canonical problem. *IEE Proc. Microwave Antennas Propag.* **143**, 309–316.

Cooray, M. F. R., and Ciric, I. R. (1989). Rotational–translational addition theorems for vector spheroidal wave functions. *COMPEL* **8**, 151–166.

Cooray, M. F. R., and Ciric, I. R. (1991). Scattering by systems of spheroids in arbitrary configurations. *Comput. Phys. Commun.* **68**, 279–305.

Cooray, M. F. R., and Ciric, I. R. (1992). Scattering of electromagnetic waves by a coated dielectric spheroid. *J. Electromagn. Waves Appl.* **6**, 1491–1507.

Cooray, M. F. R., and Ciric, I. R. (1993). Wave scattering by a chiral spheroid. *J. Opt. Soc. Am. A* **10**, 1197–1203.

Crosta, G. F., Camatini, M. C., Zomer, S., *et al*. (2001). Optical scattering (TAOS) by tire debris particles: preliminary results. *Opt. Express* **8**, 302–307.

Cummins, H. Z., and Pike, E. R., eds. (1974). *Photon Correlation and Light Beating Spectroscopy* (Plenum Press, New York).

Cummins, H. Z., and Pike, E. R., eds. (1977). *Photon Correlation Spectroscopy and Velocimetry* (Plenum Press, New York).

Czekala, H., Havemann, S., Schmidt, K., *et al*. (1999). Comparison of microwave radiative transfer calculations obtained with three different approximations of hydrometeor shape. *J. Quant. Spectrosc. Radiat. Transfer* **63**, 545–558.

Czekala, H., Crewell, S., Simmer, C., and Thiele, A. (2001). Discrimination of cloud and rain liquid water path by groundbased polarized microwave radiometry. *Geophys. Res. Lett.* **28**, 267–270.

D'Almeida, G. A., Koepke, P., and Shettle, E. P. (1991). *Atmospheric Aerosols:Global Climatology and Radiative Characteristics* (A. Deepak Publishing, Hampton, VA).

Debye, P. (1909). Der Lichtdruk auf Kugeln von beliebigem Material. *Ann. Physik* **30**, 57–136.

de Boer, J. F., Srinivas, S. M., Park, B. H., *et al*. (1999). Polarization effects in optical coherence tomography of various biological tissues. *IEEE J. Select. Topics Quant. Electron.* **5**, 1200–1204.

de Haan, J. F. (1987). Effects of aerosols on the brightness and polarization of cloudless planetary atmospheres. Ph. D. dissertation, Free University, Amsterdam.

de Haan, J. F., Bosma, P. B., and Hovenier, J. W. (1987). The adding method for multiple scattering calculations of polarized light. *Astron. Astrophys.* **183**, 371–391.

de Hoop, A. T. (1995). *Handbook of Radiation and Scattering of Waves* (Academic Press, London).

Deirmendjian, D. (1969). *Electromagnetic Scattering on Spherical Polydispersions* (Elsevier, New York).

Denti, P., Borghese, F., Saija, R., *et al.* (1999a). Optical properties of aggregated spheres in the vicinity of a plane surface. *J. Opt. Soc. Am. A* **16**, 167–175.

Denti, P., Borghese, F., Saija, R., *et al*. (1999b). Optical properties of a dispersion of randomly oriented identical aggregates of spheres deposited on a plane surface. *Appl. Opt.* **38**, 6421–6430.

de Rooij, W. A. (1985). Reflection and transmission of polarized light by planetary atmospheres. Ph. D. dissertation, Free University, Amsterdam.

de Rooij, W. A., and van der Stap, C. C. A. H. (1984). Expansion of Mie scattering matrices in generalized spherical functions. *Astron. Astrophys.* **131**, 237–248.

Deuzé, J. L., Goloub, P., Herman, M., *et al*. (2000). Estimate of the aerosol properties over the ocean with POLDER. *J. Geophys. Res.* **105**, 15 329–15 346.

Dick, W. D., Zeimann, P. J., Huang, P.-F., and McMurry, P. H. (1998). Optical shape fraction measurements of submicrometre laboratory and atmospheric aerosols. *Meas. Sci. Technol.* **9**, 183–196.

Ding, J., and Xu, L. (1999). Convergence of the T-matrix approach for randomly oriented, nonabsorbing, nonspherical Chebyshev particles. *J. Quant. Spectrosc. Radiat. Transfer* **63**, 163–174.

Doicu, A. (1999). Null-field method with discrete sources. In *Generalized Multipole Techniques for Electromagnetic and Light Scattering*, ed. T. Wriedt, pp. 229–253 (Elsevier, Amsterdam).

Doicu, A., and Wriedt, T. (1997a). Multiple multipole extended boundary condition method. *Optik* **105**, 57–60.

Doicu, A., and Wriedt, T. (1997b). Extended boundary condition method with multipole sources located in the complex plane. *Opt. Commun.* **139**, 85–91.

Doicu, A., and Wriedt, T. (1999). Calculation of the T matrix in the null-field method with discrete sources. *J. Opt. Soc. Am. A* **16**, 2539–2544.

Doicu, A., Wriedt, T., and Bauckhage, K. (1997). Light scattering by homogeneous axisymmetric particles for PDA calculations to measure both axes of spheroidal particles. *Part. Part. Syst. Charact.* **14**, 3–11.

Doicu, A., Köser, J., Wriedt, T., and Bauckhage, K. (1998). Light scattering simulation and measurement of monodisperse spheroids using a phase Doppler anemometer. *Part. Part. Syst. Charact.* **15**, 257–262.

Doicu, A., Eremin, Yu. A., and Wriedt, T. (1999). Convergence of the T-matrix method for light scattering from a particle on or near a surface. *Opt. Commun.* **159**, 266–277.

Doicu, A., Eremin, Yu., and Wriedt, T. (2000). *Acoustic and Electromagnetic Scattering Analysis Using Discrete Sources* (Academic Press, San Diego).

Dolginov, A. Z., Gnedin, Yu. N., and Silant'ev, N. A. (1995). *Propagation and Polarization of Radiation in Cosmic Media* (Gordon and Breach, Basel). (Original Russian edi-

tion: Nauka, Moscow, 1979.)

Domke, H. (1974). The expansion of scattering matrices for an isotropic medium in generalized spherical functions. *Astrophys. Space Sci.* **29**, 379–386.

Domke, H. (1975). Fourier expansion of the phase matrix for Mie scattering. *Z. Meteorol.* **25**, 357–361.

Do-Nhat, T., and MacPhie, R. H. (1997). Accurate values of prolate spheroidal radial functions of the second kind. *Can. J. Phys.* **75**, 671–675.

Draine, B. T. (1988). The discrete-dipole approximation and its application to interstellar graphite grains. *Astrophys. J.* **333**, 848–872.

Draine, B. T. (2000). The discrete dipole approximation for light scattering by irregular targets. In *Light Scattering by Nonspherical Particles: Theory, Measurements, and Applications*, eds. M. I. Mishchenko, J. W. Hovenier, and L. D. Travis, pp. 131–145 (Academic Press, San Diego).

Draine, B. T., and Flatau, P. J. (1994). Discrete-dipole approximation for scattering calculations. *J. Opt. Soc. Am. A* **11**, 1491–1499.

Draine, B. T., and Flatau, P. J. (1997). User guide for the discrete dipole approximation code DDSCAT (Version 5a). Princeton Observatory Preprint POPe-695 (http://www.astro. princeton.edu/~draine/UserGuide/UserGuide.html).

Draine, B. T., and Goodman, J. (1993). Beyond Clausius–Mossotti: wave propagation on a polarizable point lattice and the discrete dipole approximation. *Astrophys. J.* **405**, 685–697.

Draine, B. T., and Weingartner, J. C. (1996). Radiative torques on interstellar grains. I. Superthermal spin-up. *Astrophys. J.* **470**, 551–565.

Drezek, R., Dunn, A., and Richards-Kortum, R. (1999). Light scattering from cells: finite-difference time-domain simulations and goniometric measurements. *Appl. Opt.* **38**, 3651–3661.

Drossart, P. (1990). A statistical model for the scattering by irregular particles. *Astrophys. J. Lett.* **361**, 29–32.

Dubovik, O., and King, M. D. (2000). A flexible inversion algorithm for retrieval of aerosol optical properties from Sun and sky radiance measurements. *J. Geophys. Res.* **105**, 20 673–20 696.

Dungey, C. E., and Bohren, C. F. (1991). Light scattering by nonspherical particles: a refinement to the coupled-dipole method. *J. Opt. Soc. Am. A* **8**, 81–87.

Eberhard, W. L. (1992). Ice-cloud depolarization of backscatter for CO_2 and other infrared lidars. *Appl. Opt.* **31**, 6485–6490.

Edmonds, A. R. (1996). *Angular Momentum in Quantum Mechanics* (Princeton University Press, Princeton, NJ).

Eide, H., Stamnes, J. J., Stamnes, K., and Schulz, F. M. (1999). New method for computing expansion coefficients for spheroidal functions. *J. Quant. Spectrosc. Radiat. Transfer* **63**, 191–203.

Eide, H. A., Stamnes, K., Hu, Y., and Stamnes, J. J. (2000). Determination of ice particle characteristics from depolarization lidar backscatter returns. In *Light Scattering by Nonspherical Particles: Halifax Contributions*, eds. G. Videen, Q. Fu, and P. Chýlek, pp. 173–176 (Army Research Laboratory, Adelphi, MD).

Eremin, Yu., and Orlov, N. (1998). Modeling of light scattering by non-spherical particles

based on discrete sources method. *J. Quant. Spectrosc. Radiat. Transfer* **60**, 451–62.

Erma, V. A. (1969). Exact solution for the scattering of electromagnetic waves from bodies of arbitrary shape. III. Obstacles with arbitrary electromagnetic properties. *Phys. Rev.* **179**, 1238–1246.

Evans, B. T. N., and Fournier, G. R. (1994). Analytic approximation to randomly oriented spheroid extinction. *Appl. Opt.* **33**, 5796–5804.

Evans, B. G., and Holt, A. R. (1977). Scattering amplitudes and cross-polarisation of ice particles. *Electron. Lett.* **13**, 342–344.

Evans, K. F., and Stephens, G. L. (1995). Microwave radiative transfer through clouds composed of realistically shaped ice crystals. I. Single scattering properties. *J. Atmos. Sci.* **52**, 2041–2057.

Farafonov, V. G. (1983). The scattering of a plane electromagnetic wave by a dielectric spheroid. *Differential Equations (Sov.)* **19**, 1765–1777.

Farafonov, V. G. (2000). Light scattering by multilayer ellipsoids in the Rayleigh approximation. *Opt. Spectrosc.* **88**, 441–443.

Farafonov, V. G., Voshchinnikov, N. V., and Somsikov, V. V. (1996). Light scattering by a core-mantle spheroidal particle. *Appl. Opt.* **35**, 5412–5426.

Farafonov, V. G., Il'in, V. B., and Henning, T. (1999). A new solution of the light scattering problem for axisymmetric particles. *J. Quant. Spectrosc. Radiat. Transfer* **63**, 205–215.

Fikioris, J. G., and Uzunoglu, N. K. (1979). Scattering from an eccentrically stratified dielectric sphere. *J. Opt. Soc. Am.* **69**, 1359–1366.

Flammer, C. (1957). *Spheroidal Wave Functions* (Stanford University Press, Stanford, CA).

Flatau, P. J. (1997). Improvements in the discrete-dipole approximation method of computing scattering and absorption. *Opt. Lett.* **22**, 1205–1207.

Flatau, P. J. (2000). SCATTERLIB: Light Scattering Codes Library. URL: atol.ucsd.edu/~pflatau/scatlib/.

Flatau, P. J., Fuller, K. A., and Mackowski, D. W. (1993). Scattering by two spheres in contact: comparisons between the discrete dipole approximation and modal analysis. *Appl. Opt.* **32**, 3302–3305.

Forsythe, G. E., Malcolm, M. A., and Moler, C. B. (1977). *Computer Methods for Mathematical Computations* (Prentice-Hall, Englewood Cliffs, NJ).

Francis, P. N. (1995). Some aircraft observations of the scattering properties of ice crystals. *J. Atmos. Sci.* **52**, 1142–1154.

Francis, P. N., Hignett, P., and Macke, A. (1998). The retrieval of cirrus cloud properties from aircraft multi-spectral reflectance measurements during EUCREX'93. *Q. J. R. Meteorol. Soc.* **124**, 1273–1291.

Francis, P. N., Foot, J. S., and Baran, A. J. (1999). Aircraft measurements of the solar and infrared radiative properties of cirrus and their dependence on ice crystal shape. *J. Geophys. Res.* **104**, 31 685–31 695.

Freudenthaler, V., Homburg, F., and Jäger, H. (1996). Optical parameters of contrails from lidar measurements: linear depolarization. *Geophys. Res. Lett.* **23**, 3715–3718.

Fu, Q., and Sun, W. (2001). Mie theory for light scattering by a spherical particle in an absorbing medium. *Appl. Opt.* **40**, 1354–1361.

Fu, Q., Sun, W. B., and Yang, P. (1999). Modeling of scattering and absorption by nonspheri-

cal cirrus ice particles at thermal infrared wavelengths. *J. Atmos. Sci.* **56**, 2937–2947.

Fucile, E., Borghese, F., Denti, P., and Saija, R. (1993). Theoretical description of dynamic light scattering from an assembly of large axially symmetric particles. *J. Opt. Soc. Am. A* **10**, 2611–2617.

Fucile, E., Borghese, F., Denti, P., and Saija, R. (1995). Effect of an electrostatic field on the optical properties of a cloud of dielectric particles. *Appl. Opt.* **34**, 4552–4562.

Fuller, K. A. (1991). Optical resonances and two-sphere systems. *Appl. Opt.* **30**, 4716–4731.

Fuller, K. A. (1993). Scattering of light by coated spheres. *Opt. Lett.* **18**, 257–259.

Fuller, K. A. (1994). Scattering and absorption cross sections of compounded spheres. I. Theory for external aggregation. *J. Opt. Soc. Am. A* **11**, 3251–3260.

Fuller, K. A. (1995a). Scattering and absorption cross sections of compounded spheres. II. Calculations for external aggregation. *J. Opt. Soc. Am. A* **12**, 881–892.

Fuller, K. A. (1995b). Scattering and absorption cross sections of compounded spheres. III. Spheres containing arbitrarily located spherical inhomogeneities. *J. Opt. Soc. Am. A* **12**, 893–904.

Fuller, K. A., and Mackowski, D. W. (2000). Electromagnetic scattering by compounded spherical particles. In *Light Scattering by Nonspherical Particles: Theory, Measurements, and Applications*, eds. M. I. Mishchenko, J. W. Hovenier, and L. D. Travis, pp. 225–272 (Academic Press, San Diego).

Fung, A. K. (1994). *Microwave Scattering and Emission Models and Their Applications* (Artech House, Boston, MA).

Gan, H., and Chew, W. C. (1995). A discrete BCG-FFT algorithm for solving 3D inhomogeneous scatterer problems. *J. Electromagn. Waves Appl.* **9**, 1339–1357.

Garrett, T. J., Hobbs, P. V., and Gerber, H. (2001). Shortwave, single-scattering properties of arctic ice clouds. *J. Geophys. Res.* **106**, 15 155–15 172.

Gayet, J.-F., Auriol, F., Oshchepkov, S., *et al*. (1998). In situ measurements of the scattering phase function of stratocumulus, contrails and cirrus. *Geophys. Res. Lett.* **25**, 971–974.

Gehrels, T., ed. (1974). *Planets, Stars and Nebulae Studied with Photopolarimetry* (University of Arizona Press, Tucson, AZ).

Gelfand, I. M., Minlos, R. A., and Shapiro, Z. Ya. (1963). *Representations of the Rotation and Lorentz Groups and their Applications* (Pergamon Press, New York). (Original Russian edition: Fizmatgiz, Moscow, 1958.)

Gerber, H., Takano, Y., Garrett, T. J., and Hobbs, P. V. (2000). Nephelometer measurements of the asymmetry parameter, volume extinction coefficient, and backscatter ratio in Arctic clouds. *J. Atmos. Sci.* **57**, 3021–3034.

Gledhill, T. M., and McCall, A. (2000). Circular polarization by scattering from spheroidal dust grains. *Mon. Not. R. Astron. Soc.* **314**, 123–137.

Gobbi, G. P. (1998). Polarization lidar returns from aerosols and thin clouds: a framework for the analysis. *Appl. Opt*. **37**, 5505–5508.

Göbel, G., Lippek, A., Wriedt, T., and Bauckhage, K. (1998). Monte Carlo simulation of light scattering by inhomogeneous spheres. In *Radiative Transfer II*, ed. M. P. Mengüc, pp. 367–376 (Begel House, New York).

Goedecke, G. H., and O'Brien, S. G. (1988). Scattering by irregular inhomogeneous particles via the digitized Green's function algorithm. *Appl. Opt.* **27**, 2431–2438.

Goncharenko, A. V., Semenov, Yu. G., and Venger, E. F. (1999). Effective scattering cross section of an assembly of small ellipsoidal particles. *J. Opt. Soc. Am. A* **16**, 517–522.

Goodman, J. J., Draine, B. T., and Flatau, P. J. (1991). Application of fast-Fourier-transform techniques to the discrete-dipole approximation. *Opt. Lett.* **16**, 1198–1200.

Gouesbet, G., and Gréhan, G., eds. (1988). *Optical Particle Sizing: Theory and Practice* (Plenum Press, New York).

Gouesbet, G., Maheu, B., and Gréhan, G. (1988). Light scattering from a sphere arbitrarily located in a Gaussian beam, using a Bromwich formulation. *J. Opt. Soc. Am. A* **5**, 1427–1443.

Gouesbet, G., Gréhan, G., and Maheu, B. (1991). Generalized Lorenz–Mie theory and applications to optical sizing. In *Combustion Measurements*, ed. N. Chigier, pp. 339–384 (Hemisphere Publishing Corporation, New York).

Grandy, W. T., Jr. (2000). *Scattering of Waves from Large Spheres* (Cambridge University Press, Cambridge).

Greenberg, J. M., Pedersen, N. E., and Pedersen, J. C. (1961). Microwave analog to the scattering of light by nonspherical particles. *J. Appl. Phys.* **32**, 233–242.

Greenler, R. (1980). *Rainbows, Halos, and Glories* (Cambridge University Press, Cambridge).

Grenfell, T. C., and Warren, S. G. (1999). Representation of a nonspherical ice particle by a collection of independent spheres for scattering and absorption of radiation. *J. Geophys. Res.* **104**, 31 697–31 709.

Grote, M. J., and Keller, J. B. (1998). Nonreflecting boundary conditions for Maxwell's equations. *J. Comput. Phys.* **139**, 327–342.

Grundy, W. M., Douté, S., and Schmitt, B. (2000). A Monte Carlo ray-tracing model for scattering and polarization by large particles with complex shapes. *J. Geophys. Res.* **105**, 29 291–29 314.

Guggenheimer, H. W. (1977). *Differential Geometry* (Dover Publications, New York).

Gurwich, I., Kleiman, M., Shiloah, N., and Cohen, A. (2000). Scattering of electromagnetic radiation by multilayered spheroidal particles: recursive procedure. *Appl. Opt.* **39**, 470–477.

Gustafson, B. Å. S. (1996). Microwave analog to light scattering measurements: a modern implementation of a proven method to achieve precise control. *J. Quant. Spectrosc. Radiat. Transfer* **55**, 663–672.

Gustafson, B. Å. S. (2000). Microwave analog to light-scattering measurements. In *Light Scattering by Nonspherical Particles: Theory, Measurements, and Applications*, eds. M. I. Mishchenko, J. W. Hovenier, and L. D. Travis, pp. 367–390 (Academic Press, San Diego).

Gustafson, B. Å. S., and Kolokolova, L. (1999). A systematic study of light scattering by aggregate particles using the microwave analog technique: angular and wavelength dependence of intensity and polarization. *J. Geophys. Res.* **104**, 31 711–31 720.

Haferman, J. L. (2000). Microwave scattering by precipitation. In *Light Scattering by Nonspherical Particles: Theory, Measurements, and Applications*, eds. M. I. Mishchenko, J. W. Hovenier, and L. D. Travis, pp. 481–524 (Academic Press, San Diego).

Hafner, C. (1990). *The Generalized Multipole Technique for Computational Electromagnetics* (Artech House, Boston, MA).

Hage, J. I., Greenberg, J. M., and Wang, R. T. (1991). Scattering from arbitrarily shaped particles: theory and experiment. *Appl. Opt.* **30**, 1141–1152.

Hamid, A.-K. (1996). Modeling the scattering from a dielectric spheroid by a system of dielectric spheres. *J. Electromagn. Waves Appl.* **10**, 723–729.

Hamid, A.-K., Ciric, I. R., and Hamid, M. (1990). Electromagnetic scattering by an arbitrary configuration of dielectric spheres. *Can. J. Phys.* **68**, 1419–1428.

Hamid, A.-K., Ciric, I. R., and Hamid, M. (1991). Iterative solution of the scattering by an arbitrary configuration of conducting or dielectric spheres. *IEE Proc. H* **138**, 565–572.

Hamid, A.-K., Ciric, I. R., and Hamid, M. (1992). Analytic solutions of the scattering by two multilayered dielectric spheres. *Can. J. Phys.* **70**, 696–705.

Han, Q., Rossow, W. B., Chou, J., *et al*. (1999). The effects of aspect ratio and surface roughness on satellite retrievals of ice-cloud properties. *J. Quant. Spectrosc. Radiat. Transfer* **63**, 559–583.

Hansen, J. E. (1971). Multiple scattering of polarized light in planetary atmospheres. II. Sunlight reflected by terrestrial water clouds. *J. Atmos. Sci.* **28**, 1400–1426.

Hansen, J. E., and Hovenier, J. W. (1974). Interpretation of the polarization of Venus. *J. Atmos. Sci.* **31**, 1137–1160.

Hansen, J. E., and Travis, L. D. (1974). Light scattering in planetary atmospheres. *Space Sci. Rev.* **16**, 527–610.

Haracz, R. D., Cohen, L. D., and Cohen, A. (1984). Perturbation theory for scattering from dielectric spheroids and short cylinders. *Appl. Opt.* **23**, 436–441.

Haracz, R. D., Cohen, L. D., and Cohen, A. (1985). Scattering of linearly polarized light from randomly oriented cylinders and spheroids. *J. Appl. Phys.* **58**, 3322–3327.

Haracz, R. D., Cohen, L. D., Cohen, A., and Acquista, C. (1986). Light scattering from dielectric targets composed of a continuous assembly of circular disks. *Appl. Opt.* **25**, 4386–4395.

Havemann, S., and Baran, A. J. (2001). Extension of *T*-matrix to scattering of electromagnetic plane waves by non-axisymmetric dielectric particles: application to hexagonal ice cylinders. *J. Quant. Spectrosc. Radiat. Transfer* **70**, 139–158.

He, S., and Cao, J. (1998). Scattering from a bi-isotropic object of arbitrary shape. *J. Electromagn. Waves Appl.* **12**, 1547–1574.

Heintzenberg, J., and Charlson, R. J. (1996). Design and application of the integrating nephelometer: a review. *J. Atmos. Oceanic Technol.* **13**, 987–1000.

Hess, M., Koelemeijer, R. B. A., and Stammes, P. (1998). Scattering matrices of imperfect hexagonal ice crystals. *J. Quant. Spectrosc. Radiat. Transfer* **60**, 301–308.

Heymsfield, A. J., and Iaquinta, J. (2000). Cirrus crystal terminal velocities. *J. Atmos. Sci.* **57**, 916–938.

Hill, S. C., and Benner, R. E. (1988). Morphology-dependent resonances. In *Optical Effects Associated with Small Particles*, eds. P. W. Barber and R. K. Chang, pp. 3–61 (World Scientific, Singapore).

Hill, S. C., Hill, A. C., and Barber, P. W. (1984). Light scattering by size/shape distributions of soil particles and spheroids. *Appl. Opt.* **23**, 1025–1031.

Hillier, J. K., and Buratti, B. J. (2001). Monte Carlo simulations of light scattering by composite particles in a planetary surface. *Icarus* **149**, 251–261.

Hirleman, E. D., and Bohren, C. F., eds. (1991). Special feature on optical particle sizing. *Appl. Opt.* **30**, 4685–4986.

Hirst, E., and Kaye, P. H. (1996). Experimental and theoretical light scattering profiles from spherical and nonspherical particles. *J. Geophys. Res.* **101**, 19 231–19 235.

Hirst, E., Kaye, P. H., and Guppy, J. R. (1994). Light scattering from nonspherical airborne particles: experimental and theoretical comparisons. *Appl. Opt.* **33**, 7180–7186.

Hirst, E., Kaye, P. H., Greenaway, R. S., *et al*. (2001). Discrimination of micrometre-sized ice and super-cooled droplets in mixed-phase cloud. *Atmos. Environ.* **35**, 33–47.

Hodkinson, J. R. (1963). Light scattering and extinction by irregular particles larger than the wavelength. In *ICES Electromagnetic Scattering*, ed. M. Kerker, pp. 87–100 (Pergamon Press, New York).

Hoekstra, A. G., and Sloot, P. M. A. (2000). Biophysical and biomedical applications of nonspherical scattering. In *Light Scattering by Nonspherical Particles: Theory, Measurements, and Applications*, eds. M. I. Mishchenko, J. W. Hovenier, and L. D. Travis, pp. 585–602 (Academic Press, San Diego).

Hoekstra, A. G., Grimminck, M., and Sloot, P. M. A. (1998). Large scale simulations of elastic light scattering by a fast discrete dipole approximation. *Int. J. Mod. Phys. C* **9**, 87–102.

Hoekstra, A., Frijlink, M., and Sloot, P. (2000). Calculation of the radiation forces on each dipole in the discrete dipole approximation. In *Light Scattering by Nonspherical Particles: Halifax Contributions*, eds. G. Videen, Q. Fu, and P. Chýlek, pp. 237–240 (Army Research Laboratory, Adelphi, MD).

Hogan, R. J., Illingworth, A. J., and Sauvageot, H. (2000). Measuring crystal size in cirrus using 35- and 84-GHz radars. *J. Atmos. Oceanic Technol.* **17**, 27–37.

Holler, S., Pan, Y., Chang, R. K., *et al*. (1998). Two-dimensional angular optical scattering for the characterization of airborne microparticles. *Opt. Lett.* **23**, 1489–1491.

Holler, S., Surbek, M., Chang, R. K., and Pan, Y.-L. (1999). Two-dimensional angular optical scattering patterns as droplets evolve into clusters. *Opt. Lett.* **24**, 1185–1187.

Holler, S., Auger, J.-C., Stout, B., *et al*. (2000). Observations and calculations of light scattering from clusters of spheres. *Appl. Opt.* **39**, 6873–6887.

Holt, A. R. (1982). The scattering of electromagnetic waves by single hydrometeors. *Radio Sci.* **17**, 929–945.

Holt, A. R., and Shepherd, J. W. (1979). Electromagnetic scattering by dielectric spheroids in the forward and backward directions. *J. Phys. A: Math. Gen.* **12**, 159–166.

Holt, A. R., Uzunoglu, N. K., and Evans, B. G. (1978). An integral equation solution to the scattering of electromagnetic radiation by dielectric spheroids and ellipsoids. *IEEE Trans. Antennas Propag.* **26**, 706–712.

Hovenier, J. W. (1969). Symmetry relationships for scattering of polarized light in a slab of randomly oriented particles. *J. Atmos. Sci.* **26**, 488–499.

Hovenier, J. W. (1971). Multiple scattering of polarized light in planetary atmospheres. *Astron. Astrophys.* **13**, 7–29.

Hovenier, J. W., ed. (1996). Special issue on light scattering by non-spherical particles. *J. Quant. Spectrosc. Radiat. Transfer* **55**, 535–694.

Hovenier, J. W. (2000). Measuring scattering matrices of small particles at optical wavelengths. In *Light Scattering by Nonspherical Particles: Theory, Measurements, and Appli-*

cations, eds. M. I. Mishchenko, J. W. Hovenier, and L. D. Travis, pp. 355–365 (Academic Press, San Diego).

Hovenier, J. W., and Mackowski, D. W. (1998). Symmetry relations for forward and backward scattering by randomly oriented particles. *J. Quant. Spectrosc. Radiat. Transfer* **60**, 483–492.

Hovenier, J. W., and van der Mee, C. V. M. (1983). Fundamental relationships relevant to the transfer of polarized light in a scattering atmosphere. *Astron. Astrophys.* **128**, 1–16.

Hovenier, J. W., and van der Mee, C. V. M. (1996). Testing scattering matrices: a compendium of recipes. *J. Quant. Spectrosc. Radiat. Transfer* **55**, 649–661.

Hovenier, J. W., and van der Mee, C. V. M. (2000). Basic relationships for matrices describing scattering by small particles. In *Light Scattering by Nonspherical Particles: Theory, Measurements, and Applications*, eds. M. I. Mishchenko, J. W. Hovenier, and L. D. Travis, pp. 61–85 (Academic Press, San Diego).

Hovenier, J. W., van de Hulst, H. C., and van der Mee, C. V. M. (1986). Conditions for the elements of the scattering matrix. *Astron. Astrophys.* **157**, 301–310.

Hovenier, J. W., Lumme, K., Mishchenko, M. I., *et al.* (1996). Computations of scattering matrices of four types of non-spherical particles using diverse methods. *J. Quant. Spectrosc. Radiat. Transfer* **55**, 695–705.

Hovenier, J. W., van der Mee, C., and Domke, H. (2004). *Transfer of Polarized Light in Planetary Atmospheres* (Kluwer Academic Publishers, Dordrecht, The Netherlands).

Huang, X., and Jin, Y.-Q. (1998). Numerical simulations of polarized scattering from random clusters of spatially-oriented, nonspherical scatterers. *J. Electron.* **15**, 267–273.

Huckaby, J. L., Ray, A. K., and Das, B. (1994). Determination of size, refractive index, and dispersion of single droplets from wavelength-dependent scattering spectra. *Appl. Opt.* **33**, 7112–7125.

Huffman, D. R. (1988). The applicability of bulk optical constants to small particles. In *Optical Effects Associated with Small Particles*, eds. P. W. Barber and R. K. Chang, pp. 279–324 (World Scientific, Singapore).

Hunt, A. J., and Huffman, D. R. (1973). A new polarization-modulated light scattering instrument. *Rev. Sci. Instrum.* **44**, 1753–1762.

Hunter, B. A., Box, M. A., and Maier, B. (1988). Resonance structure in weakly absorbing spheres. *J. Opt. Soc. Am. A* **5**, 1281–1286.

Iaquinta, J., Isaka, H., and Personne, P. (1995). Scattering phase function of bullet rosette ice crystals. *J. Atmos. Sci.* **52**, 1401–1413.

Il'in, V. B., and Voshchinnikov, N. V. (1998). Radiation pressure on non-spherical dust grains in envelopes of late-type giants. *Astron. Astrophys. Suppl.* **128**, 187–196.

Irvine, W. M. (1963). The asymmetry of the scattering diagram of a spherical particle. *Bull. Astron. Inst. Neth.* **17**, 176–184.

Ishimaru, A. (1997). *Wave Propagation and Scattering in Random Media* (IEEE Press, New York).

Iskander, M. F., Lakhtakia, A., and Durney, C. H. (1983). A new procedure for improving the solution stability and extending the frequency range of EBCM. *IEEE Trans. Antennas Propag.* **31**, 317–324.

Iskander, M. F., Chen, H. Y., and Penner, J. E. (1989a). Optical scattering and absorption by

branched chains of aerosols. *Appl. Opt.* **28**, 3083–3091.

Iskander, M. F., Chen, H. Y., and Duong, T. V. (1989b). A new sectioning procedure for calculating scattering and absorption by elongated dielectric objects. *IEEE Trans. Electromagn. Compat.* **31**, 157–163.

Ismagilov, F. M., and Kravtsov, Yu. A. (1993). Backscattering enhancement polarization effects on a system of two small randomly oriented scatterers. *Waves in Random Media* **3**, 17–24.

Iwai, T., Furukawa, H., and Asakura, T. (1995). Numerical analysis of enhanced backscattering of light based on Rayleigh–Debye scattering theory. *Opt. Rev.* **2**, 413–419.

Jackson, J. D. (1998). *Classical Electrodynamics* (John Wiley & Sons, New York).

Jaggard, D. L., Hill, C., Shorthill, R. W., *et al*. (1981). Light scattering from particles of regular and irregular shape. *Atmos. Environ.* **15**, 2511–2519.

Jakeman, E. (2000). Polarization fluctuations in light scattered by small particles. In *Light Scattering from Microstructures*, eds. F. Moreno and F. González, pp. 179–189 (Springer-Verlag, Berlin).

Jin, Y.-Q., and Huang, X. (1996a). Numerical simulations of *T*-matrix solution for polarized bistatic scattering from a cluster of scatterers. *Opt. Commun.* **124**, 27–32.

Jin, Y.-Q., and Huang, X. (1996b). Numerical *T*-matrix solution for polarized scattering from a cluster of spatially oriented, nonspherical scatterers. *Microwave Opt. Technol. Lett.* **12**, 154–158.

Jones, A. R. (1979). Electromagnetic wave scattering by assemblies of particles in the Rayleigh approximation. *Proc. Roy. Soc. London A* **366**, 111–127. (Errata: **375**, 453–454 (1981).)

Jones, A. R. (1999). Light scattering for particle characterization. *Progr. Energy Combust. Sci.* **25**, 1–53.

Joo, K., and Iskander, M. F. (1990). A new procedure of point-matching method for calculating the absorption and scattering of lossy dielectric objects. *IEEE Trans. Antennas Propag.* **38**, 1483–1490.

Kahnert, F. M. (2003). Numerical methods in electromagnetic scattering theory. *J. Quant. Spectrosc. Radiat. Transfer* **79–80**, 775–824.

Kahnert, F. M., Stamnes, J. J., and Stamnes, K. (2001a). Application of the extended boundary condition method to homogeneous particles with point-group symmetries. *Appl. Opt.* **40**, 3110–3123.

Kahnert, F. M., Stamnes, J. J., and Stamnes, K. (2001b). Application of the extended boundary condition method to particles with sharp edges: a comparison of two surface integration approaches. *Appl. Opt.* **40**, 3101–3109.

Kaiser, T., and Schweiger, G. (1993). Stable algorithm for the computation of Mie coefficients for scattered and transmitted fields of a coated sphere. *Computers in Physics* **7**, 682–686.

Kang, X. K., Li, L. W., Leong, M. S., and Kooi, P. S. (2000). Specific absorption rate distributions in a multilayered spheroidal human head model exposed to mobile dipoles. *Radio Sci.* **35**, 247–256.

Kaplan, B., Compain, E., Drevillon, B., and Chaput, F. (1999). Phase modulated Mueller ellipsometry characterization of the scattering by particle suspensions. In *4th Conference on*

Electromagnetic and Light Scattering by Nonspherical Particles:Theory and Applications, eds. F. Obelleiro, J. L. Rodríguez, and T. Wriedt, pp. 13–20 (University of Vigo, Vigo, Spain).

Kaplan, B., Compain, E., and Drevillon, B. (2000). Phase-modulated Mueller ellipsometry characterization of scattering by latex sphere suspensions. *Appl. Opt.* **39**, 629–636.

Kapustin, V. N., Lyubovtseva, Yu. S., and Rozenberg, G. V. (1975). An experiment in electro-optical investigation of aerosols. *Izv. Acad. Sci. USSR, Atmos. Oceanic Phys.* (Engl. transl.) **11**, 636–639.

Kapustin, V. N., Rozenberg, G. V., Ahlquist, N. C., *et al*. (1980). Characterization of nonspherical atmospheric aerosol particles with electrooptical nephelometry. *Appl. Opt.* **19**, 1345–1348.

Karam, M. A., and Fung, A. K. (1988). Electromagnetic scattering from a layer of finite length, randomly oriented, dielectric, circular cylinders over a rough interface with application to vegetation. *Int. J. Remote Sens.* **9**, 1109–1134.

Karonis, G. J., Kaklamani, D. I., and Uzunoglu, N. K. (1999). Scattering of electromagnetic waves by a chiral object of ellipsoidal shape. *J. Electromagn. Waves Appl.* **13**, 817–845.

Kattawar, G. W., Hu, C.-R., Parkin, M. E., and Herb, P. (1987). Mueller matrix calculations for dielectric cubes: Comparison with experiments. *Appl. Opt.* **26**, 4174–4180.

Kaye, P. H. (1998). Spatial light-scattering analysis as a means of characterizing and classifying non-spherical particles. *Meas. Sci. Technol.* **9**, 141–149.

Kaye, P. H., Alexander-Buckley, K., Hirst, E., *et al*. (1996). A real-time monitoring system for airborne particle shape and size analysis. *J. Geophys. Res.* **101**, 19 215–19 221.

Kaye, P., Hirst, E., and Wang-Thomas, Z. (1997). Neural-network-based spatial light-scattering instrument for hazardous airborne fiber detection. *Appl. Opt.* **36**, 6149–6156.

Keenan, T. D., Carey, L. D., Zrnić, D. S., and May, P. T. (2001). Sensitivity of 5-cm wavelength polarimetric radar variables to raindrop axial ratio and drop size distribution. *J. Appl. Meteorol.* **40**, 526–545.

Kerker, M. (1969). *The Scattering of Light and Other Electromagnetic Radiation* (Academic Press, New York).

Kerker, M., ed. (1988). *Selected Papers on Light Scattering* (SPIE Press, Bellingham, WA).

Kerker, M., Scheiner, P., and Cooke, D. D. (1978). The range of validity of the Rayleigh and Thomson limits for Lorenz–Mie scattering. *J. Opt. Soc. Am.* **68**, 135–137.

Kerola, D. X., and Larson, S. M. (2001). Analysis of coma dust optical properties in comet C/1995 O1 (Hale-Bopp). II. Effects of polarization. *Icarus* **149**, 351–356.

Khlebtsov, N. G. (1979). Analysis and numerical calculation of the scattering matrix for soft spheroids comparable in size with the wavelength of light. *Opt. Spectrosc.* **46**, 292–295.

Khlebtsov, N. G. (1984). Integral equation for problems of light scattering by particles of the medium. *Opt. Spectrosc.* **57**, 399–401.

Khlebtsov, N. G. (1992). Orientational averaging of light-scattering observables in the *T*-matrix approach. *Appl. Opt.* **31**, 5359–5365.

Khlebtsov, N. G. (1993). Optics of fractal clusters in the anomalous diffraction approximation. *J. Mod. Opt.* **40**, 2221–2235.

Khlebtsov, N. G. (2001). Orientational averaging of integrated cross sections in the discrete dipole method. *Opt. Spectrosc.* **90**, 408–415.

Khlebtsov, N. G., and Melnikov, A. G. (1991). Integral equation for light scattering problems: application to the orientationally induced birefringence of colloidal dispersions. *J. Colloid Interface Sci.* **142**, 396–408.

Khlebtsov, N. G., Melnikov, A. G., and Bogatyrev, V. A. (1991). The linear dichroism and birefringence of colloidal dispersions: approximate and exact approaches. *J. Colloid Interface Sci.* **146**, 463–478.

Khlebtsov, N. G., Melnikov, A. G., Bogatyrev, V. A., and Sirota, A. I. (1999). Electrooptics effects in dilute suspensions of bacterial cells and fractal aggregates. *J. Quant. Spectrosc. Radiat. Transfer* **63**, 469–478.

Kiehl, J. T., Ko, M. W., Mugnai, A., and Chýlek, P. (1980). Perturbation approach to light scattering by nonspherical particles. In *Light Scattering by Irregularly Shaped Particles*, ed. D. Schuerman, pp. 135–140 (Plenum Press, New York).

Kim, S.-H., and Martin, P. G. (1995). The size distribution of interstellar dust particles as determined from polarization: Spheroids. *Astrophys. J.* **444**, 293–305.

Kim, C. S., and Yeh, C. (1991). Scattering of an obliquely incident wave by a multilayered elliptical lossy dielectric cylinder. *Radio Sci.* **26**, 1165–1176.

Kimura, H. (2001). Light-scattering properties of fractal aggregates: numerical calculations by a superposition technique and the discrete-dipole approximation. *J. Quant. Spectrosc. Radiat. Transfer* **70**, 581–594.

Kimura, H., and Mann, I. (1998). Radiation pressure cross section for fluffy aggregates. *J. Quant. Spectrosc. Radiat. Transfer* **60**, 425–438.

King, M. D., Kaufman, Y. J., Tanré, D., and Nakajima, T. (1999). Remote sensing of tropospheric aerosols from space: past, present, and future. *Bull. Am. Meteorol. Soc.* **80**, 2229–2259.

Kleinman, R. E., and Senior, T. B. A. (1986). Rayleigh scattering. In *Low and High Frequency Asymptotics*, eds. V. K. Varadan and V. V. Varadan, pp. 1–70 (Elsevier, Amsterdam).

Klett, J. D., and Sutherland, R. A. (1992). Approximate methods for modeling the scattering properties of non-spherical particles: evaluation of the Wentzel–Kramers–Brillouin method. *Appl. Opt.* **31**, 373–386.

Kliger, D. S., Lewis, J. W., and Randall, C. E. (1990). *Polarized Light in Optics and Spectroscopy* (Academic Press, San Diego).

Kokhanovsky, A. (2001). *Optics of Light Scattering Media: Problems and Solutions* (Praxis, Chichester).

Kokhanovsky, A. A., and Nakajima, T. Y. (1998). The dependence of phase functions of large transparent particles on their refractive index and shape. *J. Phys. D: Appl. Phys.* **31**, 1329–1335.

Kolokolova, L., and Gustafson, B. Å. S. (2001). Scattering by inhomogeneous particles: microwave analog experiments and comparison to effective medium theories. *J. Quant. Spectrosc. Radiat. Transfer* **70**, 611–625.

Kong, J. A. (1990). *Electromagnetic Wave Theory* (John Wiley & Sons, New York).

Korolev, A. V., Isaac, G. A., and Hallett, J. (1999). Ice particle habits in Arctic clouds. *Geophys. Res. Lett.* **26**, 1299–1302.

Korolev, A. V., Isaac, G. A., and Hallett, J. (2000). Ice particle habits in stratiform clouds.

Q. J. R. Meteorol. Soc. **126**, 2873–2902.

Kouzoubov, A., Brennan, M. J., Thomas, J. C., and Abbot, R. H. (1999). Monte Carlo simulations of the influence of particle nonsphericity on remote sensing of ocean water. *J. Geophys. Res.* **104**, 31 731–31 737.

Kravtsov, Yu. A., and Orlov, Yu. I. (1990). *Geometrical Optics of Inhomogeneous Media* (Springer-Verlag, Berlin). (Original Russian edition: Nauka, Moscow, 1980).

Kravtsov, Yu. A., and Orlov, Yu. I. (1999). *Caustics, Catastrophes and Wave Fields* (Springer-Verlag, Berlin).

Kristensson, G. (1980). Electromagnetic scattering from buried inhomogeneities – a general three-dimensional approach. *J. Appl. Phys.* **51**, 3486–3500.

Krotkov, N. A., Flittner, D. E., Krueger, A. J., *et al*. (1999). Effect of particle nonsphericity on satellite monitoring of drifting volcanic ash clouds. *J. Quant. Spectrosc. Radiat. Transfer* **63**, 613–630.

Krylov, V. I. (1962). *Approximate Calculation of Integrals* (Macmillan, New York).

Ku, J. C. (1993). Comparisons of coupled-dipole solutions and dipole refractive indices for light scattering and absorption by arbitrarily shaped or agglomerated particles. *J. Opt. Soc. Am. A* **10**, 336–342.

Ku, J. C., and Felske, J. D. (1984). The range of validity of the Rayleigh limit for computing Mie scattering and extinction efficiencies. *J. Quant. Spectrosc. Radiat. Transfer* **31**, 569–574.

Kuga, Y., and Ishimaru, A. (1984). Retroreflectance from a dense distribution of spherical particles. *J. Opt. Soc. Am. A* **1**, 831–835.

Kuik, F. (1992). Single scattering of light by ensembles of particles with various shapes. Ph. D. dissertation, Free University, Amsterdam.

Kuik, F., Stammes, P., and Hovenier, J. W. (1991). Experimental determination of scattering matrices of water droplets and quartz particles. *Appl. Opt.* **30**, 4872–4881.

Kuik, F., de Haan, J. F., and Hovenier, J. W. (1992). Benchmark results for single scattering by spheroids. *J. Quant. Spectrosc. Radiat. Transfer* **47**, 477–489.

Kuik, F., de Haan, J. F., and Hovenier, J. W. (1994). Single scattering of light by circular cylinders. *Appl. Opt.* **33**, 4906–4918.

Kunz, K. S., and Luebbers, R. J. (1993). *Finite Difference Time Domain Method for Electromagnetics* (CRC Press, Boca Raton, FL).

Kurtz, V., and Salib, S. (1993). Scattering and absorption of electromagnetic radiation by spheroidally shaped particles: computation of the scattering properties. *J. Imaging Sci. Technol.* **37**, 43–60.

Kuščer, I., and Ribarič, M. (1959). Matrix formalism in the theory of diffusion of light. *Opt. Acta* **6**, 42–51 (1959).

Kuzmin, V. N., and Babenko, V. A. (1981). Light scattering by a weakly anisotropic spherical particle. *Opt. Spectrosc.* **50**, 269–273.

Labeyrie, G., Müller, C. A., Wiersma, D. S., *et al*. (2000). Observation of coherent backscattering of light by cold atoms. *J. Opt. B: Quantum Semiclass. Opt.* **2**, 672–685.

Lacis, A. A., Carlson, B. E., and Hansen, J. E. (2000). Retrieval of atmospheric NO_2, O_3, aerosol optical depth, effective radius and variance information from SAGE II multispectral extinction measurements. *Appl. Math. Comput.* **116**, 133–151.

Lacoste, D., and van Tiggelen, B. A. (1999). Stokes parameters for light scattering from a Faraday-active sphere. *J. Quant. Spectrosc. Radiat. Transfer* **63**, 305–319.

Lacoste, D., van Tiggelen, B. A., Rikken, G. L. J. A., and Sparenberg, A. (1998). Optics of a Faraday-active Mie sphere. *J. Opt. Soc. Am. A* **15**, 1636–1642.

Lagendijk, A., and van Tiggelen, B. A. (1996). Resonant multiple scattering of light. *Phys. Rep.* **270**, 143–215.

Laitinen, H., and Lumme, K. (1998). *T*-matrix method for general star-shaped particles: first results. *J. Quant. Spectrosc. Radiat. Transfer* **60**, 325–334.

Lakhtakia, A. (1991). The extended boundary condition method for scattering by a chiral scatterer in a chiral medium: formulation and analysis. *Optik* **86**, 155–161.

Lakhtakia, A. (1992). General theory of the Purcell–Pennypacker scattering approach and its extension to bianisotropic scatterers. *Astrophys. J.* **394**, 494–499.

Lakhtakia, A., and Mulholland, G. W. (1993). On two numerical techniques for light scattering by dielectric agglomerated structures. *J. Res. Natl. Inst. Stand. Technol.* **98**, 699–716.

Lakhtakia, A., Varadan, V. K., and Varadan, V. V. (1984). Scattering by highly aspherical targets: EBCM coupled with reinforced orthogonalization. *Appl. Opt.* **23**, 3502–3504.

Lakhtakia, A., Varadan, V. V., and Varadan, V. K. (1985a). Scattering of ultrasonic waves by oblate spheroidal voids of high aspect ratio. *J. Appl. Phys.* **58**, 4525–4530.

Lakhtakia, A., Varadan, V. K., and Varadan, V. V. (1985b). Scattering and absorption characteristics of lossy dielectric, chiral, nonspherical objects. *Appl. Opt.* **24**, 4146–4154.

Landgraf, M., Augustsson, K., Grün, E., and Gustafson, B. Å. S. (1999). Deflection of the local interstellar dust flow by solar radiation pressure. *Science* **286**, 2319–2322.

Langley, D. S., and Marston, P. L. (1998). Generalized tertiary rainbow of slightly oblate drops: observations with laser illumination. *Appl. Opt.* **37**, 1520–1526.

Latimer, P. (1975). Light scattering by ellipsoids. *J. Colloid. Interface Sci.* **53**, 102–109.

Latimer, P., and Barber, P. (1978). Scattering by ellipsoids of revolution: a comparison of theoretical methods. *J. Colloid Interface Sci.* **63**, 310–316.

Lawson, R. P., Heymsfield, A. J., Aulenbach, S. M., and Jensen, T. L. (1998). Shapes, sizes and light scattering properties of ice crystals in cirrus and a persistent contrail during SUCCESS. *Geophys. Res. Lett.* **25**, 1331–1334.

Lebedev, A. N., Gartz, M., Kreibig, U., and Stenzel, O. (1999). Optical extinction by spherical particles in an absorbing medium: application to composite absorbing films. *Eur. Phys. J. D* **6**, 365–373.

Lemaire, T. (1997). Coupled-dipole formulation for the treatment of electromagnetic scattering by a small dielectric particle of arbitrary shape. *J. Opt. Soc. Am. A* **14**, 470–474.

Lemke, H. M., and Quante, M. (1999). Backscatter characteristics of nonspherical ice crystals: assessing the potential of polarimetric radar measurements. *J. Geophys. Res.* **104**, 31 739–31 751.

Lemke, H., Okamoto, H., and Quante, M. (1998). Comment on error analysis of backscatter from discrete dipole approximation for different ice particle shapes. *Atmos. Res.* **49**, 189–197.

Lenke, R., and Maret, G. (2000). Multiple scattering of light: coherent backscattering and transmission. In *Scattering in Polymeric and Colloidal Systems*, eds. W. Brown and K. Mortensen, pp. 1–73 (Gordon and Breach Science Publishers, Amsterdam).

Lenoble, J., ed. (1985). *Radiative Transfer in Scattering and Absorbing Atmospheres: Standard Computational Procedures* (A. Deepak Publishing, Hampton, VA).

Le Vine, D. M., Schneider, A., Lang, R. H., and Carter, H. G. (1985). Scattering from thin dielectric disks. *IEEE Trans. Antennas Propag.* **33**, 1410–1413.

Lewin, L. (1970). On the restricted validity of point-matching techniques. *IEEE Trans. Microwave Theory Tech.* **18**, 1041–1047.

Li, L.-W., Leong, M.-S., Yeo, T.-S., *et al*. (1998a). Computations of spheroidal harmonics with complex arguments: a review with an algorithm. *Phys. Rev. E* **58**, 6792–6806.

Li, L. W., Yeo, T. S., Kooi, P. S., and Leong, M. S. (1998b). Microwave specific attenuation by oblate spheroidal raindrops: an exact analysis of TCS's in terms of spheroidal wave functions. *Progr. Electromagn. Res. (PIER)* **18**, 127–150.

Li, L.-W., Leong, M.-S., Kooi, P.-S., and Yeo, T.-S. (2001). Spheroidal vector wave eigenfunction expansion of dyadic Green's functions for a dielectric spheroid. *IEEE Trans. Antennas Propag.* **49**, 645–659.

Lin, Y.-C., and Sarabandi, K. (1995). Electromagnetic scattering model for a tree trunk above a tilted ground plane. *IEEE Trans. Geosci. Remote Sens.* **33**, 1063–1070.

Lind, A. C., Wang, R. T., and Greenberg, J. M. (1965). Microwave scattering by nonspherical particles. *Appl. Opt.* **4**, 1555–1561.

Liou, K.-N. (1980). *An Introduction to Atmospheric Radiation* (Academic Press, New York).

Liou, K. N. (1992). *Radiation and Cloud Processes in the Atmosphere: Theory, Observation, and Modeling* (Oxford University Press, New York).

Liou, K.-N., and Hansen, J. E. (1971). Intensity and polarization for single scattering by polydisperse spheres: a comparison of ray optics and Mie theory. *J. Atmos. Sci.* **28**, 995–1004.

Liou, K.-N., and Lahore, H. (1974). Laser sensing of cloud composition: a backscattered depolarization technique. *J. Appl. Meteorol.* **13**, 257–263.

Liou, K. N., Cai, Q., Pollack, J. B., and Cuzzi, J. N. (1983). Light scattering by randomly oriented cubes and parallelepipeds. *Appl. Opt.* **22**, 3001–3008.

Liou, K. N., Yang, P., Takano, Y., *et al*. (1998). On the radiative properties of contrail cirrus. *Geophys. Res. Lett.* **25**, 1161–1164.

Liou, K. N., Takano, Y., and Yang, P. (2000). Light scattering and radiative transfer in ice crystal clouds: aplications to climate research. In *Light Scattering by Nonspherical Particles: Theory, Measurements, and Applications*, eds. M. I. Mishchenko, J. W. Hovenier, and L. D. Travis, pp. 3–27 (Academic Press, San Diego).

Lippmann, B. A., and Schwinger, J. (1950). Variational principles for scattering processes. *Phys. Rev.* **79**, 469–480.

Liu, H., and Chandrasekar, V. (2000). Classification of hydrometeors based on polarimetric radar measurements: development of fuzzy logic and neuro-fuzzy systems, and in situ verification. *J. Atmos. Oceanic Technol.* **17**, 140–164.

Liu, L., and Mishchenko, M. I. (2001). Constraints on PSC particle microphysics derived from lidar observations. *J. Quant. Spectrosc. Radiat. Transfer* **70**, 817–831.

Liu, C., Jonas, P. R., and Saunders, C. P. R. (1996). Pyramidal ice crystal scattering phase functions and concentric halos. *Ann. Geophys.* **14**, 1192–1197.

Liu, Y., Arnott, W. P., and Hallett, J. (1998). Anomalous diffraction theory for arbitrarily oriented finite circular cylinders and comparison with exact *T*-matrix results. *Appl. Opt.* **37**,

5019–5030.

Liu, Y., Arnott, W. P., and Hallett, J. (1999). Particle size distribution retrieval from multispectral optical depth: influences of particle nonsphericity and refractive index. *J. Geophys. Res.* **104**, 31 753–31 762.

Lock, J. A. (1995). Improved Gaussian beam-scattering algorithm. *Appl. Opt.* **34**, 559–570.

Lock, J. A., and Yang, L. (1991). Interference between diffraction and transmission in the Mie extinction efficiency. *J. Opt. Soc. Am. A* **8**, 1132–1134.

Lopatin, V. N., and Sid'ko, F. Ya. (1988). *Introduction to Optics of Cell Suspensions* (Nauka, Novosibirsk) (in Russian).

Love, A. E. H. (1899). The scattering of electric waves by a dielectric sphere. *Proc. London Math. Soc.* **30**, 308–321.

Ludwig, A. C. (1991). The generalized multipole technique. *Comput. Phys. Commun.* **68**, 306–314.

Lumme, K., ed. (1998). Special issue on light scattering by non-spherical particles. *J. Quant. Spectrosc. Radiat. Transfer* **60**, 301–500.

Lumme, K. (2000). Scattering properties of interplanetary dust particles. In *Light Scattering by Nonspherical Particles: Theory, Measurements, and Applications*, eds. M. I. Mishchenko, J. W. Hovenier, and L. D. Travis, pp. 555–583 (Academic Press, San Diego).

Lumme, K., and Rahola, J. (1994). Light scattering by porous dust particles in the discrete-dipole approximation. *Astrophys. J.* **425**, 653–667.

Lumme, K., and Rahola, J. (1998). Comparison of light scattering by stochastically rough spheres, best-fit spheroids and spheres. *J. Quant. Spectrosc. Radiat. Transfer* **60**, 439–450.

Lumme, K., Rahola, J., and Hovenier, J. W. (1997). Light scattering by dense clusters of spheres. *Icarus* **126**, 455–469.

Lynch, D. K., and Livingston, W. (1995). *Color and Light in Nature* (Cambridge University Press, Cambridge).

Lyot, B. (1929). Recherches sur la polarisation de la lumière des planetes et de quelques substances terrestres. *Ann. Observ. Paris, Sect. Meudon* **8**, No. 1. (English translation: Research on the polarization of light from planets and from some terrestrial substances, NASA Tech. Transl. NASA TT F-187, Washington, DC, 1964.)

Macke, A. (1993). Scattering of light by polyhedral ice crystals. *Appl. Opt.* **32**, 2780–2788.

Macke, A. (2000). Monte Carlo calculations of light scattering by large particles with multiple internal inclusions. In *Light Scattering by Nonspherical Particles: Theory, Measurements, and Applications*, eds. M. I. Mishchenko, J. W. Hovenier, and L. D. Travis, pp. 309–322 (Academic Press, San Diego).

Macke, A., and Großklaus, M. (1998). Light scattering by nonspherical raindrops: implications for lidar remote sensing of rainrates. *J. Quant. Spectrosc. Radiat. Transfer* **60**, 355–363.

Macke, A., and Mishchenko, M. I. (1996). Applicability of regular particle shapes in light scattering calculations for atmospheric ice particles. *Appl. Opt.* **35**, 4291–4296.

Macke, A., Mishchenko, M. I., Muinonen, K., and Carlson, B. E. (1995). Scattering of light by large nonspherical particles: ray tracing approximation versus *T*-matrix method. *Opt. Lett.* **20**, 1934–1936.

Macke, A., Mishchenko, M. I., and Cairns, B. (1996a). The influence of inclusions on light

scattering by large ice particles. *J. Geophys. Res.* **101**, 23 311–23 316.

Macke, A., Mueller, J., and Raschke, E. (1996b). Scattering properties of atmospheric ice crystals. *J. Atmos. Sci.* **53**, 2813–2825.

Mackowski, D. W. (1991). Analysis of radiative scattering for multiple sphere configurations. *Proc. Roy. Soc. London A* **433**, 599–614.

Mackowski, D. W. (1994). Calculation of total cross sections of multiple-sphere clusters. *J. Opt. Soc. Am. A* **11**, 2851–2861.

Mackowski, D. W. (1995). Electrostatic analysis of radiative absorption by sphere clusters in the Rayleigh limit: application to soot. *Appl. Opt.* **34**, 3535–3545.

Mackowski, D. W. (2001). An effective medium method for calculation of the *T* matrix of aggregated spheres. *J. Quant. Spectrosc. Radiat. Transfer* **70**, 441–464.

Mackowski, D. W., and Jones, P. D. (1995). Theoretical investigation of particles having directionally dependent absorption cross section. *J. Thermophys. Heat Transfer* **9**, 193–201.

Mackowski, D. W., and Mishchenko, M. I. (1996). Calculation of the *T* matrix and the scattering matrix for ensembles of spheres. *J. Opt. Soc. Am. A* **13**, 2266–2278.

Mackowski, D. W., Altenkirch, R. A., Menguc, M. P. (1990). Internal absorption cross sections in a stratified sphere. *Appl. Opt.* **29**, 1551–1559.

Maltsev, V. P., Chernyshev, A. V., Sem'yanov, K. A., and Soini, E. (1997). Absolute real-time determination of size and refractive index of individual microspheres. *Meas. Sci. Technol.* **8**, 1023–1027.

Mandel, L., and Wolf, E. (1995). *Optical Coherence and Quantum Optics* (Cambridge University Press, Cambridge).

Markel, V. A., and George, T. F., eds. (2001). *Optics of Nanostructured Materials* (John Wiley & Sons, New York).

Markel, V. A., Shalaev, V. M., and George, T. F. (2000). Some theoretical and numerical approaches to the optics of fractal smoke. In *Optics of Nanostructured Materials*, eds. V. A. Markel and T. F. George, pp. 355–411 (John Wiley & Sons, New York).

Marshall, S. F., Covert. D. S., and Charlson, R. J. (1995). Relationship between asymmetry parameter and hemispheric backscatter ratio: implications for climate forcing by aerosols. *Appl. Opt.* **34**, 6306–6311.

Marston, P. L. (1992). Geometrical and catastrophe optics methods in scattering. In *High Frequency and Pulse Scattering*, eds. A. D. Pierce and R. N. Thurston, pp. 1–234 (Academic Press, San Diego).

Marston, P. L., ed. (1994). *Geometrical Aspects of Scattering* (SPIE Press, Bellingham, WA).

Marston, P. L. (1999). Catastrophe optics of spheroidal drops and generalized rainbows. *J. Quant. Spectrosc. Radiat. Transfer* **63**, 341–351.

Marston, P. L., and Crichton, J. H. (1984). Radiation torque on a sphere caused by a circularly-polarized electromagnetic wave. *Phys. Rev. A* **30**, 2508–2516.

Martin, P. G. (1978). *Cosmic Dust* (Oxford University Press, Oxford).

Martin, R. J. (1993). Mie scattering formulae for non-spherical particles. *J. Mod. Opt.* **40**, 2467–2494.

Martin, T. (1998). An improved near- to far-zone transformation for the finite-difference time-domain method. *IEEE Trans. Antennas Propag.* **46**, 1263–1271.

Martinez, A. S., and Maynard, R. (1994). Faraday effect and multiple scattering of light.

Phys. Rev. B **50**, 3714–3732.

Masłowska, A., Flatau, P. J., and Stephens, G. L. (1994). On the validity of the anomalous diffraction theory to light scattering by cubes. *Opt. Commun.* **107**, 35–40.

Masuda, K., and Takashima, T. (1992). Feasibility study of derivation of cirrus information using polarimetric measurements from satellite. *Remote Sens. Environ.* **39**, 45–59.

Masuda, K., Takashima, T., Kawata, Y., *et al*. (2000). Retrieval of aerosol optical properties over the ocean using multispectral polarization measurements from space. *Appl. Math. Comput.* **116**, 103–114.

Matsumura, M., and Seki, M. (1991). Light scattering calculations by the Fredholm integral equation method. *Astrophys. Space Sci.* **176**, 283–295.

Matsumura, M., and Seki, M. (1996). Extinction and polarization by ellipsoidal particles in the infrared. *Astrophys. J.* **456**, 557–565.

Mazeron, P., and Muller, S. (1996). Light scattering by ellipsoids in a physical optics approximation. *Appl. Opt.* **35**, 3726–3735.

Mazin, I. P., and Khrgian, A. Kh., eds. (1989). *Handbook of Clouds and Cloudy Atmosphere* (Gidrometeoizdat, Leningrad) (in Russian).

McClain, W. M., and Ghoul, W. A. (1986). Elastic light scattering by randomly oriented macromolecules: computation of the complete set of observables. *J. Chem. Phys.* **84**, 6609–6622.

McGuire, A. F., and Hapke, B. W. (1995). An experimental study of light scattering by large, irregular particles. *Icarus* **113**, 134–155.

Medgyesi-Mitschang, L. N., Putnam, J. M., and Gedera, M. B. (1994). Generalized method of moments for three-dimensional penetrable scatterers. *J. Opt. Soc. Am. A* **11**, 1383–1398.

Meeten, G. H. (1982). An anomalous diffraction theory of linear birefringence and dichroism in colloidal dispersions. *J. Colloid. Interface Sci.* **87**, 407–415.

Mei, K. K. (1974). Unimoment method of solving antenna and scattering problems. *IEEE Trans. Antennas Propag.* **22**, 760–766.

Meyer, W. V., Smart, A. E., Brown, R. G. W., and Anisimov, M. A., eds. (1997). Feature issue on photon correlation and scattering. *Appl. Opt.* **36**, 7477–7677.

Meyer, W. V., Smart, A. E., and Brown, R. G. W., eds. (2001). Feature issue on photon correlation and scattering. *Appl. Opt.* **40**, 3965–4242.

Mie, G. (1908). Beiträge zur Optik trüber Medien, speziell kolloidaler Metallösungen. *Ann. Physik* **25**, 377–445.

Mikulski, J. J., and Murphy, E. L. (1963). The computation of electromagnetic scattering from concentric spherical structures. *IEEE Trans. Antennas Propag.* **11**, 169–177.

Millar, R. F. (1969). Rayleigh hypothesis in scattering problems. *Electron. Lett.* **5**, 416–417.

Miller, E. K., Medgyesi-Mitschang, L. N., and Newman, E. H. (1991). *Computational Electromagnetics: Frequency Domain Method of Moments* (IEEE Press, New York).

Mishchenko, M. I. (1990a). Multiple scattering of polarized light in anisotropic plane-parallel media. *Transp. Theory Statist. Phys.* **19**, 293–316.

Mishchenko, M. I. (1990b). Extinction of light by randomly-oriented non-spherical grains. *Astrophys. Space Sci.* **164**, 1–13.

Mishchenko, M. I. (1990c). Expansion of scattering matrix in generalized spherical functions for radially inhomogeneous spherical particles. *Kinem. Phys. Celest. Bodies* **6**(1), 93–95.

Mishchenko, M. I. (1991a). Light scattering by randomly oriented axially symmetric particles. *J. Opt. Soc. Am. A* **8**, 871–882. (Errata: **9**, 497 (1992).)

Mishchenko, M. I. (1991b). Extinction and polarization of transmitted light by partially aligned nonspherical grains. *Astrophys. J.* **367**, 561–574.

Mishchenko, M. I. (1991c). Scattering cross section for randomly oriented particles of arbitrary shape. *Kinem. Phys. Celest. Bodies* **7**(5), 83–86.

Mishchenko, M. I. (1992a). Coherent propagation of polarized millimeter waves through falling hydrometeors. *J. Electromagn. Waves Appl.* **6**, 1341–1351.

Mishchenko, M. I. (1992b). Enhanced backscattering of polarized light from discrete random media: calculations in exactly the backscattering direction. *J. Opt. Soc. Am. A* **9**, 978–982.

Mishchenko, M. I. (1993). Light scattering by size-shape distributions of randomly oriented axially symmetric particles of a size comparable to a wavelength. *Appl. Opt.* **32**, 4652–4666.

Mishchenko, M. I. (1996a). Coherent backscattering by two-sphere clusters. *Opt. Lett.* **21**, 623–625.

Mishchenko, M. I. (1996b). Diffuse and coherent backscattering by discrete random media. I. Radar reflectivity, polarization ratios, and enhancement factors for a half-space of polydisperse, nonabsorbing and absorbing spherical particles. *J. Quant. Spectrosc. Radiat. Transfer* **56**, 673–702.

Mishchenko, M. I. (2000). Calculation of the amplitude matrix for a nonspherical particle in a fixed orientation. *Appl. Opt.* **39**, 1026–1031.

Mishchenko, M. I. (2001). Radiation force caused by scattering, absorption, and emission of light by nonspherical particles. *J. Quant. Spectrosc. Radiat. Transfer* **70**, 811–816.

Mishchenko, M. I. (2002). Vector radiative transfer equation for arbitrarily shaped and arbitrarily oriented particles: a microphysical derivation from statistical electromagnetics. *Appl. Opt.* **41**, 7114–7134.

Mishchenko, M. I. (2003). Microphysical approach to polarized radiative transfer: extension to the case of an external observation point. *Appl. Opt.* **42**, 4963–4967.

Mishchenko, M. I. (2005). Scale invariance rule in electromagnetic scattering. *J. Quant. Spectrosc. Radiat. Transfer* (in press).

Mishchenko, M. I., and Hovenier, J. W. (1995). Depolarization of light backscattered by randomly oriented nonspherical particles. *Opt. Lett.* **20**, 1356–1358.

Mishchenko, M. I., and Lacis, A. A. (2000). Manifestations of morphology-dependent resonances in Mie scattering matrices. *Appl. Math. Comput.* **116**, 167–179.

Mishchenko, M. I., and Macke, A. (1997). Asymmetry parameters of the phase function for isolated and densely packed spherical particles with multiple internal inclusions in the geometric optics limit. *J. Quant. Spectrosc. Radiat. Transfer* **57**, 767–794.

Mishchenko, M. I., and Macke, A. (1998). Incorporation of physical optics effects and computation of the Legendre expansion for ray-tracing phase functions involving δ-function transmission. *J. Geophys. Res.* **103**, 1799–1805.

Mishchenko, M. I., and Macke, A. (1999). How big should hexagonal ice crystals be to produce halos? *Appl. Opt.* **38**, 1626–1629.

Mishchenko, M. I., and Mackowski, D. W. (1994). Light scattering by randomly oriented bispheres. *Opt. Lett.* **19**, 1604–1606.

Mishchenko, M. I., and Mackowski, D. W. (1996). Electromagnetic scattering by randomly oriented bispheres: comparison of theory and experiment and benchmark calculations. *J. Quant. Spectrosc. Radiat. Transfer* **55**, 683–694.

Mishchenko, M. I., and Sassen, K. (1998). Depolarization of lidar returns by small ice crystals: an application to contrails. *Geophys. Res. Lett.* **25**, 309–312.

Mishchenko, M. I., and Travis, L. D. (1994a). T-matrix computations of light scattering by large spheroidal particles. *Opt. Commun.* **109**, 16–21.

Mishchenko, M. I., and Travis, L. D. (1994b). Light scattering by polydisperse, rotationally symmetric nonspherical particles: linear polarization. *J. Quant. Spectrosc. Radiat. Transfer* **51**, 759–778.

Mishchenko, M. I., and Travis, L. D. (1994c). Light scattering by polydispersions of randomly oriented spheroids with sizes comparable to wavelengths of observation. *Appl. Opt.* **33**, 7206–7225.

Mishchenko, M. I., and Travis, D. L. (1997). Satellite retrieval of aerosol properties over the ocean using polarization as well as intensity of reflected sunlight. *J. Geophys. Res.* **102**, 16 989–17 013.

Mishchenko, M. I., and Travis, L. D. (1998). Capabilities and limitations of a current FORTRAN implementation of the *T*-matrix method for randomly oriented, rotationally symmetric scatterers. *J. Quant. Spectrosc. Radiat. Transfer* **60**, 309–324.

Mishchenko, M. I., and Videen, G. (1999). Single-expansion EBCM computations for osculating spheres. *J. Quant. Spectrosc. Radiat. Transfer* **63**, 231–236.

Mishchenko, M. I., Lacis, A. A., and Travis, L. D. (1994). Errors introduced by the neglect of polarization in radiance calculations for Rayleigh-scattering atmospheres. *J. Quant. Spectrosc. Radiat. Transfer* **51**, 491–510.

Mishchenko, M. I., Mackowski, D. W., and Travis, L. D. (1995). Scattering of light by bispheres with touching and separated components. *Appl. Opt.* **34**, 4589–4599.

Mishchenko, M. I., Travis, L. D., and Macke, A. (1996a). Scattering of light by polydisperse, randomly oriented, finite circular cylinders. *Appl. Opt.* **35**, 4927–4940.

Mishchenko, M. I., Travis, L. D., and Mackowski, D. W. (1996b). *T*-matrix computations of light scattering by nonspherical particles: a review. *J. Quant. Spectrosc. Radiat. Transfer* **55**, 535–575.

Mishchenko, M. I., Rossow, W. B., Macke, A., and Lacis, A. A. (1996c). Sensitivity of cirrus cloud albedo, bidirectional reflectance and optical thickness retrieval accuracy to ice particle shape. *J. Geophys. Res.* **101**, 16 973–16 985.

Mishchenko, M. I., Travis, L. D., Kahn, R. A., and West, R. A. (1997a). Modeling phase functions for dustlike tropospheric aerosols using a shape mixture of randomly oriented polydisperse spheroids. *J. Geophys. Res.* **102**, 16 831–16 847.

Mishchenko, M. I., Wielaard, D. J., and Carlson, B. E. (1997b). *T*-matrix computations of zenith-enhanced lidar backscatter from horizontally oriented ice plates. *Geophys. Res. Lett.* **24**, 771–774.

Mishchenko, M. I., Hovenier, J. W., and Travis, L. D., eds. (1999a). Special issue on light scattering by nonspherical particles'98. *J. Quant. Spectrosc. Radiat. Transfer* **63**, 127–738.

Mishchenko, M. I., Travis, L. D., and Hovenier, J. W., coordinators (1999b). Special sec-

tion on electromagnetic scattering by nonspherical particles. *J. Geophys. Res.* **104**, 31 671–31 808.

Mishchenko, M. I., Hovenier, J. W., and Travis, L. D., eds. (2000a). *Light Scattering by Nonspherical Particles: Theory, Measurements, and Applications* (Academic Press, San Diego).

Mishchenko, M. I., Hovenier, J. W., and Travis, L. D. (2000b). Concepts, terms, notation. In *Light Scattering by Nonspherical Particles: Theory, Measurements, and Applications*, eds. M. I. Mishchenko, J. W. Hovenier, and L. D. Travis, pp. 3–27 (Academic Press, San Diego).

Mishchenko, M. I., Hovenier, J. W., Wiscombe, W. J., and Travis, L. D. (2000c). Overview of scattering by nonspherical particles. In *Light Scattering by Nonspherical Particles: Theory, Measurements, and Applications*, eds. M. I. Mishchenko, J. W. Hovenier, and L. D. Travis, pp. 29–60 (Academic Press, San Diego).

Mishchenko, M. I., Travis, L. D., and Macke, A. (2000d). *T*-matrix method and its applications. In *Light Scattering by Nonspherical Particles: Theory, Measurements, and Applications*, eds. M. I. Mishchenko, J. W. Hovenier, and L. D. Travis, pp. 147–172 (Academic Press, San Diego).

Mishchenko, M. I., Luck, J.-M., and Nieuwenhuizen, Th. M. (2000e). Full angular profile of the coherent polarization opposition effect. *J. Opt. Soc. Am. A* **17**, 888–891.

Mishchenko, M. I., Hovenier, J. W., and Mackowski, D. W. (2004a). Singe scattering by a small volume element. *J. Opt. Soc. Am. A* **21**, 71–87.

Mishchenko, M. I., Videen, G., Babenko, V. A., *et al*. (2004b). *T*-matrix theory of electromagnetic scattering by particles and its applications: a comprehensive reference database. *J. Quant. Spectrosc. Radiat. Transfer* **88**, 357–406 (updated version available at http://www.giss.nasa.gov/~crmim/publications).

Mittra, R., and Ramahi, O. (1990). Absorbing boundary conditions for the direct solution of partial differential equations arising in electromagnetic scattering problems. In *Finite Element and Finite Difference Methods in Electromagnetic Scattering*, ed. M. A. Morgan, pp. 133–173 (Elsevier, New York).

Moreno, F., and González, F., eds. (2000). *Light Scattering from Microstructures* (Springer-Verlag, Berlin).

Morgan, M. A. (1980). Finite element computation of microwave scattering by raindrops. *Radio Sci.* **15**, 1109–1119.

Morgan, M. A., ed. (1990). *Finite Element and Finite Difference Methods in Electromagnetic Scattering* (Elsevier, New York).

Morgan, M. A., and Mei, K. K. (1979). Finite-element computation of scattering by inhomogeneous penetrable bodies of revolution. *IEEE Trans. Antennas Propag.* **27**, 202–214.

Morita, N. (1979). Another method of extending the boundary condition for the problem of scattering by dielectric cylinders. *IEEE Trans. Antennas Propag.* **27**, 97–99.

Morrison, J. A., and Cross, M.-J. (1974). Scattering of a plane electromagnetic wave by axisymmetric raindrops. *Bell Syst. Tech. J.* **53**, 955–1019.

Morse, P. M., and Feshbach, H. (1953). *Methods of Theoretical Physics* (McGraw-Hill, New York).

Mugnai, A., and Wiscombe, W. J. (1980). Scattering of radiation by moderately nonspherical

particles. *J. Atmos. Sci.* **37**, 1291–1307.

Mugnai, A., and Wiscombe, W. J. (1986). Scattering from nonspherical Chebyshev particles. 1. Cross sections, single-scattering albedo, asymmetry factor, and backscattered fraction. *Appl. Opt.* **25**, 1235–1244.

Mugnai, A., and Wiscombe, W. J. (1989). Scattering from nonspherical Chebyshev particles. 3. Variability in angular scattering patterns. *Appl. Opt.* **28**, 3061–3073.

Muinonen, K. (1989). Scattering of light by crystals: a modified Kirchhoff approximation. *Appl. Opt.* **28**, 3044–3050.

Muinonen, K. (1993). Coherent backscattering by solar system dust particles. In *Asteroids, Comets, Meteors*, eds. A. Milani *et al*., pp. 271–296 (Kluwer Academic Publishers, Dordrecht, The Netherlands).

Muinonen, K. (1996). Light scattering by Gaussian random particles: Rayleigh and Rayleigh–Gans approximations. *J. Quant. Spectrosc. Radiat. Transfer* **55**, 603–613.

Muinonen, K. (2000). Light scattering by stochastically shaped particles. In *Light Scattering by Nonspherical Particles: Theory, Measurements, and Applications*, eds. M. I. Mishchenko, J. W. Hovenier, and L. D. Travis, pp. 323–352 (Academic Press, San Diego).

Muinonen, K., Lumme, K., Peltoniemi, J., and Irvine, W. M. (1989). Light scattering by randomly oriented crystals. *Appl. Opt.* **28**, 3051–3060.

Muinonen, K., Nousiainen, T., Fast, P., *et al*. (1996). Light scattering by Gaussian random particles: ray optics approximation. *J. Quant. Spectrosc. Radiat. Transfer* **55**, 577–601.

Mulholland, G. W., Bohren, C. F., and Fuller, K. A. (1994). Light scattering by agglomerates: coupled electric and magnetic dipole method. *Langmuir* **10**, 2533–2546.

Muñoz, O., Volten, H., de Haan, J. F., *et al*. (2000a). Experimental determination of scattering matrices of olivine and Allende meteorite particles. *Astron. Astrophys.* **360**, 777–788.

Muñoz, O., Volten, H., Vermeulen, K., *et al*. (2000b). Scattering matrices of fly-ash and green clay particles. In *Light Scattering by Nonspherical Particles: Halifax Contributions*, eds. G. Videen, Q. Fu, and P. Chýlek, pp. 45–48 (Army Research Laboratory, Adelphi, MD).

Muñoz, O., Volten, H., de Haan, J. F., *et al*. (2001). Experimental determination of scattering matrices of randomly oriented fly ash and clay particles at 442 and 633 nm. *J. Geophys. Res.* **106**, 22 833–22 844.

Murayama, T., Okamoto, H., Kaneyasu, N., *et al*. (1999). Application of lidar depolarization measurement in the atmospheric boundary layer: effects of dust and sea-salt particles. *J. Geophys. Res.* **104**, 31 781–31 792.

Nag, S., and Sinha, B. P. (1995). Electromagnetic plane wave scattering by a system of two uniformly lossy dielectric prolate spheroids in arbitrary orientation. *IEEE Trans. Antennas Propag.* **43**, 322–327.

Nakajima, T., and King, M. D. (1990). Determination of optical thickness and effective particle radius of clouds from reflected solar radiation measurements. I. Theory. *J. Atmos. Sci.* **47**, 1878–1893.

Nakajima, T., Tanaka, M., Yamano, M., *et al*. (1989). Aerosol optical characteristics in the yellow sand events observed in May, 1982 at Nagasaki. II. Models. *J. Meteorol. Soc. Japan* **67**, 279–291.

Napper, D. H., and Ottewill, R. H. (1963). Light scattering studies on monodisperse silver bromide sols. In *ICES Electromagnetic Scattering*, ed. M. Kerker, pp. 377–386 (Pergamon

Press, New York).

Nevitt, T. J., and Bohren, C. F. (1984). Infrared backscattering by irregularly shaped particles: a statistical approach. *J. Climate Appl. Meteorol.* **23**, 1342–1349.

Newton, R. G. (1966). *Scattering Theory of Waves and Particles* (McGraw-Hill, New York).

Ngo, D., Videen, G., and Dalling, R. (1997). Chaotic light scattering from a system of osculating, conducting spheres. *Phys. Lett. A* **227**, 197–202.

Nieminen, T. A., Rubinsztein-Dunlop, H., and Heckenberg, N. R. (2001). Calculation and optical measurement of laser trapping forces on non-spherical particles. *J. Quant. Spectrosc. Radiat. Transfer* **70**, 627–637.

Nousiainen, T. (2000). Scattering of light by raindrops with single-mode oscillations. *J. Atmos. Sci.* **57**, 789–802.

Nousiainen, T., and Muinonen, K. (1999). Light scattering by Gaussian, randomly oriented raindrops. *J. Quant. Spectrosc. Radiat. Transfer* **63**, 643–666.

Nousiainen, T., Muinonen, K., Avelin, J., and Sihvola, A. (2001). Microwave backscattering by nonspherical ice particles at 5.6 GHz using second-order perturbation series. *J. Quant. Spectrosc. Radiat. Transfer* **70**, 639–661.

Nussenzveig, H. M. (1992). *Diffraction Effects in Semiclassical Scattering* (Cambridge University Press, Cambridge).

Obelleiro, F., Rodríguez, J. L., and Wriedt, T., eds. (1999). *4th Conference on Electromagnetic and Light Scattering by Nonspherical Particles: Theory and Applications* (University of Vigo, Vigo, Spain).

Oguchi, T. (1960). Attenuation of electromagnetic waves due to rain with distorted raindrops. *J. Radio Res. Lab. Japan* **7**, 467–485.

Oguchi, T. (1973). Scattering properties of oblate raindrops and cross polarization of radio waves due to rain: calculations at 19.3 and 34.8 GHz. *J. Radio Res. Lab. Japan* **20**, 79–118.

Oguchi, T. (1981). Scattering from hydrometeors: a survey. *Radio Sci.* **16**, 691–730.

Oguchi, T. (1983). Electromagnetic wave propagation and scattering in rain and other hydrometeors. *Proc. IEEE* **71**, 1029–1078.

Oguchi, T., and Hosoya, Y. (1974). Scattering properties of oblate raindrops and cross polarization of radio waves due to rain. II. Calculations at microwave and millimeter wave regions. *J. Radio Res. Lab. Japan* **21**, 191–259.

Ogura, H., and Takahashi, N. (1990). Scattering of waves from a random spherical surface – Mie scattering. *J. Math. Phys.* **31**, 61–75.

Okamoto, H. (1995). Light scattering by clusters: the a_1-term method. *Opt. Rev.* **2**, 407–412.

Okamoto, H., Macke, A., Quante, M., and Raschke, E. (1995). Modeling of backscattering by nonspherical ice particles for the interpretation of cloud radar signals at 94 GHz. An error analysis. *Beitr. Phys. Atmos.* **68**, 319–334.

Onaka, T. (1980). Light scattering by spheroidal grains. *Ann. Tokyo Astron. Observ.* **18**, 1–54.

O'Neill, E. L. (1992). *Introduction to Statistical Optics* (Dover Publications, New York).

Ozrin, V. D. (1992). Exact solution for coherent backscattering of polarized light from a random medium of Rayleigh scatterers. *Waves in Random Media* **2**, 141–164.

Palik, E. D., and Ghosh, G. (1997). *Handbook of Optical Constants of Solids* (Academic Press, San Diego).

Papadakis, S. N., Uzunoglu, N. K., and Capsalis, C. N. (1990). Scattering of a plane wave by

a general anisotropic dielectric ellipsoid. *J. Opt. Soc. Am. A* **7**, 991–997.

Paramonov, L. E. (1995). *T*-matrix approach and the angular momentum theory in light scattering problems by ensembles of arbitrarily shaped particles. *J. Opt. Soc. Am. A* **12**, 2698–2707.

Paulick, T. C. (1990). Applicability of the Rayleigh hypothesis to real materials. *Phys. Rev. B* **42**, 2801–2824.

Pecora, R., ed. (1985). *Dynamic Light Scattering: Applications of Photon Correlation Spectroscopy* (Plenum Press, New York).

Peltoniemi, J. I. (1996). Variational volume integral equation method for electromagnetic scattering by irregular grains. *J. Quant. Spectrosc. Radiat. Transfer* **55**, 637–647.

Peltoniemi, J. I., Lumme, K., Muinonen, K., and Irvine, W. M. (1989). Scattering of light by stochastically rough particles. *Appl. Opt.* **28**, 4088–4095.

Perelman, A. Y. (1996). Scattering by particles with radially variable refractive index. *Appl. Opt.* **35**, 5452–5460.

Perrin, J.-M., and Lamy, P. L. (1986). Light scattering by large particles. II. A vectorial description in the eikonal picture. *Opt. Acta* **33**, 1001–1022.

Perry, R. J., Hunt, A. J., and Huffman, D. R. (1978). Experimental determination of Mueller scattering matrices for nonspherical particles. *Appl. Opt.* **17**, 2700–2710.

Peterson, B., and Ström, S. (1973). *T* matrix for electromagnetic scattering from an arbitrary number of scatterers and representations of E(3)*. *Phys. Rev. D* **8**, 3661–3678.

Peterson, B., and Ström, S. (1974). *T*-matrix formulation of electromagnetic scattering from multilayered scatterers. *Phys. Rev. D* **10**, 2670–2684.

Peterson, A. F., Ray, S. L., and Mittra, R. (1998). *Computational Methods for Electromagnetics* (IEEE Press, New York).

Petrova, E. V. (1999). Mars aerosol optical thickness retrieved from measurements of the polarization inversion angle and the shape of dust particles. *J. Quant. Spectrosc. Radiat. Transfer* **63**, 667–676.

Petrova, E. V., Jockers, K., and Kiselev, N. N. (2000). Light scattering by aggregates with sizes comparable to the wavelength: an application to cometary dust. *Icarus* **148**, 526–536.

Petrushin, A. G. (1994). Light scattering by hexagonal ice prisms. I. Small scattering angles. *Izv., Atmos. Oceanic Phys.* (Engl. transl.) **30**, 291–299.

Pike, E. R., and Abbiss, J. B., eds. (1997). *Light Scattering and Photon Correlation Spectroscopy* (Kluwer Academic Publishers, Dordrecht, The Netherlands).

Piller, N. B. (1999). Coupled-dipole approximation for high permittivity materials. *Opt. Commun.* **160**, 10–14.

Piller, N. B., and Martin, O. J. F. (1998a). Extension of the generalized multipole technique to three-dimensional anisotropic scatterers. *Opt. Lett.* **23**, 579–581.

Piller, N. B., and Martin, O. J. F. (1998b). Increasing the performance of the coupled-dipole approximation: a spectral approach. *IEEE Trans. Antennas Propag.* **46**, 1126–1137.

Pitter, M. C., Hopcraft, K. I., Jakeman, E., and Walker, J. G. (1999). Structure of polarization fluctuations and their relation to particle shape. *J. Quant. Spectrosc. Radiat. Transfer* **63**, 433–444.

Platt, C. M. R. (1978). Lidar backscattering from horizontally oriented ice crystal plates. *J.*

Appl. Meteorol. **17**, 482–488.

POAN Research Group, ed. (1998). *New Aspects of Electromagnetic and Acoustic Wave Diffusion* (Springer-Verlag, Berlin).

Pocock, M. D., Bluck, M. J., and Walker, S. P. (1998). Electromagnetic scattering from 3-D curved dielectric bodies using time-domain integral equations. *IEEE Trans. Antennas Propag.* **46**, 1212–1219.

Poggio, A. J., and Miller, E. K. (1973). Integral equation sol utions of three-dimensional scattering problems. In *Computer Techniques for Electromagnetics*, ed. R. Mittra, pp. 159–264 (Pergamon, Oxford).

Pollack, J. B., and Cuzzi, J. N. (1980). Scattering by nonspherical particles of size comparable to a wavelength: a new semi-empirical theory and its application to tropospheric aerosols. *J. Atmos. Sci.* **37**, 868–881.

Porstendorfer, J., Berg, K.-J., and Berg, G. (1999). Calculation of extinction and scattering spectra of large spheroidal gold particles embedded in a glass matrix. *J. Quant. Spectrosc. Radiat. Transfer* **63**, 479–486.

Prabhu, D. R., Davies, M., and Videen, G. (2001). Light scattering calculations from oleic-acid droplets with water inclusions. *Opt. Express* **8**, 308–313.

Prigent, C., Pardo, J. R., Mishchenko, M. I., and Rossow, W. B. (2001). Microwave polarized signatures generated within cloud systems: Special Sensor Microwave Imager (SSM/I) observations interpreted with radiative transfer simulations. *J. Geophys. Res.* **106**, 28 243–28 258.

Prishivalko, A. P., Babenko, V. A., and Kuzmin, V. N. (1984). *Scattering and Absorption of Light by Inhomogeneous and Anisotropic Spherical Particles* (Nauka i Tekhnika, Minsk, USSR) (in Russian).

Pritchard, B. S., and Elliott, W. G. (1960). Two instruments for atmospheric optics measurements. *J. Opt. Soc. Am.* **50**, 191–202.

Probert-Jones, J. R. (1984). Resonance component of backscattering by large dielectric spheres. *J. Opt. Soc. Am. A* **1**, 822–830.

Prodi, F., Sturniolo, O., Battaglia, A., and Medini, R. (1999). Radar parameters simulation for populations of spherical and non-spherical hydrometeors: dependence on size distributions, shapes and composition. *J. Quant. Spectrosc. Radiat. Transfer* **63**, 677–699.

Purcell, E. M., and Pennypacker, C. R. (1973). Scattering and absorption of light by nonspherical dielectric grains. *Astrophys. J.* **186**, 705–714.

Pye, D. (2001). *Polarised Light in Science and Nature* (Institute of Physics Publishing, Bristol, UK).

Qingan, W., Zixiang, O., Liping, L., and Zengming, C. (1998). A comparative study on the backscattering ability of raindrops and ice particles (hail). *Contr. Atmos. Phys.* **71**, 377–386.

Qingan, W., Kang, C., and Xiang, O. Y. Z. (1999). Discussion of key algorithms for computing scattering cross sections using the separation of variables method for spheroids. *J. Quant. Spectrosc. Radiat. Transfer* **63**, 251–261.

Quinby-Hunt, M. S., Hull, P. G., and Hunt, A. (2000). Polarized light scattering in the marine environment. In *Light Scattering by Nonspherical Particles: Theory, Measurements, and Applications*, eds. M. I. Mishchenko, J. W. Hovenier, and L. D. Travis, pp. 525–554 (Aca-

demic Press, San Diego).

Quinten, M. (1999). Optical effects associated with aggregates of clusters. *J. Cluster Sci.* **10**, 319–358.

Quinten, M., and Kreibig, U. (1993). Absorption and elastic scattering of light by particle aggregates. *Appl. Opt.* **32**, 6173–6182.

Quinten, M., and Rostalski, J. (1996). Lorenz–Mie theory for spheres immersed in an absorbing host medium. *Part. Part. Syst. Charact.* **13**, 89–96.

Quirantes, A. (1999). Light scattering properties of spheroidal coated particles in random orientation. *J. Quant. Spectrosc. Radiat. Transfer* **63**, 263–275.

Quirantes, A., and Delgado, A. V. (1995). Particle size determinations in colloidal suspensions of randomly oriented ellipsoids. *Progr. Colloid Polymer Sci.* **98**, 145–150.

Quirantes, A., and Delgado, A. V. (2001). Scattering cross sections of randomly orientated coated spheroids. *J. Quant. Spectrosc. Radiat. Transfer* **70**, 261–272.

Ravey, J.-C., and Mazeron, P. (1982). Light scattering in the physical optics approximation: application to large spheroids. *J. Opt. (Paris)* **13**, 273–282.

Ravey, J.-C., and Mazeron, P. (1983). Light scattering by large spheroids in the physical optics approximation: numerical comparison with other approximate and exact results. *J. Opt. (Paris)* **14**, 29–41.

Ray, A. K., and Nandakumar, R. (1995). Simultaneous determination of size and wavelength-dependent refractive indices of thin-layered droplets from optical resonances. *Appl. Opt.* **34**, 7759–7770.

Rayleigh, Lord (1897). On the incidence of aerial and electric waves upon small obstacles in the form of ellipsoids or elliptic cylinders, and on the passage of electric waves through a circular aperture in a conducting screen. *Phil. Mag.* **44**, 28–52.

Reagan, J. A., McCormick, M. P., and Spinhirne, J. D. (1989). Lidar sensing of aerosols and clouds in the troposphere and stratosphere. *Proc. IEEE* **77**, 433–448.

Reichardt, J., Tsias, A., and Behrendt, A. (2000a). Optical properties of PSC Ia-enhanced at UV and visible wavelengths: Model and observations. *Geophys. Res. Lett.* **27**, 201–204.

Reichardt, J., Hess, M., and Macke, A. (2000b). Lidar inelastic multiple-scattering parameters of cirrus particle ensembles determined with geometrical-optics crystal phase functions. *Appl. Opt.* **39**, 1895–1910.

Rockwitz, K.-D. (1989). Scattering properties of horizontally oriented ice crystal columns in cirrus clouds. *Appl. Opt.* **28**, 4103–4110.

Rogers, C., and Martin, P. G. (1979). On the shape of interstellar grains. *Astrophys. J.* **228**, 450–464.

Rojas, R. G. (1992). Integral equations for the scattering by a three dimensional inhomogeneous chiral body. *J. Electromagn. Waves Appl.* **6**, 733–750.

Roll, G., and Schweiger, G. (2000). Geometrical optics model of Mie resonances. *J. Opt. Soc. Am. A* **17**, 1301–1311.

Rose, M. E. (1995). *Elementary Theory of Angular Momentum* (Dover Publications, New York).

Rosen, J. M., Pinnick, R. G., and Garvey, D. M. (1997). Nephelometer optical response model for the interpretation of atmospheric aerosol measurements. *Appl. Opt.* **36**, 2642–2649.

Rossow, W. B., and Schiffer, R. A. (1999). Advances in understanding clouds from ISCCP.

Bull. Am. Meteorol. Soc. **80**, 2261–2287.

Rother, T. (1998). Generalization of the separation of variables method for non-spherical scattering of dielectric objects. *J. Quant. Spectrosc. Radiat. Transfer* **60**, 335–353.

Rother, T., and Schmidt, K. (1996). The discretized Mie-formalism for plane wave scattering on dielectric objects with non-separable geometries. *J. Quant. Spectrosc. Radiat. Transfer* **55**, 615–625.

Rother, T., Havemann, S., and Schmidt, K. (1999). Scattering of plane waves on finite cylinders with non-circular cross-sections. *Progr. Electromagn. Res. (PIER)* **23**, 79–105.

Rozenberg, G. V. (1977). The light ray (contribution to the theory of the light field). *Sov. Phys. Usp.* **20**, 55–79.

Rozenberg, G. V., Lyubovtseva, Yu. S., Kadyshevich, Ye. A., and Amnuil, N. R. (1970). Measurement of the light scattering matrix of a hydrosol. *Izv. Acad. Sci. USSR, Atmos. Oceanic Phys.* (Engl. transl.) **6**, 747–750.

Ruppin, R. (1999). Effects of high-order multipoles on the extinction spectra of dispersive bispheres. *Opt. Commun.* **168**, 35–38.

Sachweh, B. A., Dick, W. D., and McMurry, P. H. (1995). Distinguishing between spherical and nonspherical particles by measuring the variability in azimuthal light scattering. *Aerosol Sci. Technol.* **23**, 373–391.

Sachweh, B., Barthel, H., Polke, R., *et al*. (1999). Particle shape and structure analysis from the spatial intensity pattern of scattered light using different measuring devices. *J. Aerosol Sci.* **30**, 1257–1270.

Saija, R., Iatì, M. A., Denti, P., *et al*. (2001). Backscattered intensity from model atmospheric ice crystals in the millimeter-wave range. *Appl. Opt.* **40**, 5337–5342.

Sano, I., and Mukai, S. (2000). Algorithm description of system flow for global aerosol distribution. *Appl. Math. Comput.* **116**, 79–91.

Sarkar, D., and Halas, N. J. (1997). General vector basis function solution of Maxwell's equations. *Phys. Rev. E* **56**, 1102–1112.

Sassen, K. (1991). The polarization lidar technique for cloud research: a review and current assessment. *Bull. Am. Meteorol. Soc.* **72**, 1848–1866.

Sassen, K. (2000). Lidar backscatter depolarization technique for cloud and aerosol research. In *Light Scattering by Nonspherical Particles: Theory, Measurements, and Applications*, eds. M. I. Mishchenko, J. W. Hovenier, and L. D. Travis, pp. 393–416 (Academic Press, San Diego).

Sassen, K., and Arnott, W. P. (1998). Light and color in the open air: introduction to the feature issue. *Appl. Opt.* **37**, 1425–1426.

Sassen, K., and Hsueh, C.-y. (1998). Contrail properties derived from high-resolution polarization lidar studies during SUCCESS. *Geophys. Res. Lett.* **25**, 1165–1168.

Sassen, K., and Liou, K.-N. (1979). Scattering of polarized laser light by water droplet, mixed-phase and ice crystal clouds. I. Angular scattering patterns. *J. Atmos. Sci.* **36**, 838–851.

Sassen, K., Knight, N. C., Takano, Y., and Heymsfield, A. J. (1994). Effects of ice-crystal structure on halo formation: cirrus cloud experimental and ray-tracing modeling studies. *Appl. Opt.* **33**, 4590–4601.

Sassen, K., Comstock, J. M., Wang, Zh., and Mace, G. G. (2001). Cloud and aerosol research

capabilities at FARS: the Facility for Atmospheric Remote Sensing. *Bull. Am. Meteorol. Soc.* **82**, 1119–1138.

Sato, M., Travis, L. D., and Kawabata, K. (1996). Photopolarimetry analysis of the Venus atmosphere in polar regions. *Icarus* **124**, 569–585.

Saxon, D. S. (1955a). Tensor scattering matrix for the electromagnetic field. *Phys. Rev.* **100**, 1771–1775.

Saxon, D. S. (1955b). Lectures on the scattering of light (scientific report No. 9, Department of Meteorology, University of California at Los Angeles).

Schaefer, R. W. (1980). Calculations of the light scattered by randomly oriented ensembles of spheroids of size comparable to the wavelength. Ph. D. dissertation, State University of New York at Albany.

Schiffer, R. (1989). Light scattering by perfectly conducting statistically irregular particles. *J. Opt. Soc. Am. A* **6**, 385–402.

Schiffer, R. (1990). Perturbation approach for light scattering by an ensemble of irregular particles of arbitrary material. *Appl. Opt.* **29**, 1536–1550.

Schiffer, R., and Thielheim, K. O. (1979). Light scattering by dielectric needles and disks. *J. Appl. Phys.* **50**, 2476–2483.

Schmidt, K., Rother, T., and Wauer, J. (1998). The equivalence of applying the Extended Boundary Condition and the continuity conditions for solving electromagnetic scattering problems. *Opt. Commun.* **150**, 1–4.

Schmitt, J. M., and Xiang, S. H. (1998). Cross-polarized backscatter in optical coherence tomography of biological tissue. *Opt. Lett.* **23**, 1060–1062.

Schneider, J. B., and Peden, I. C. (1988). Differential cross section of a dielectric ellipsoid by the *T*-matrix extended boundary condition method. *IEEE Trans. Antennas Propag.* **36**, 1317–1321.

Schneider, J., Brew, J., and Peden, I. C. (1991). Electromagnetic detection of buried dielectric targets. *IEEE Trans. Geosci. Remote Sens.* **29**, 555–562.

Schuerman, D. W., ed. (1980). *Light Scattering by Irregularly Shaped Particles* (Plenum Press, New York).

Schuh, R., and Wriedt, T. (2001). Computer programs for light scattering by particles with inclusions. *J. Quant. Spectrosc. Radiat. Transfer* **70**, 715–723.

Schulten, K., and Gordon, R. G. (1975). Exact recursive evaluation of 3*j*- and 6*j*-coefficients for quantum-mechanical coupling of angular momenta. *J. Math. Phys.* **16**, 1961–1970.

Schulz, F. M., Stamnes, K., and Stamnes, J. J. (1998a). Scattering of electromagnetic waves by spheroidal particles: a novel approach exploiting the *T* matrix computed in spheroidal coordinates. *Appl. Opt.* **37**, 7875–7896.

Schulz, F. M., Stamnes, K., and Stamnes, J. J. (1998b). Modeling the radiative transfer properties of media containing particles of moderately and highly elongated shape. *Geophys. Res. Lett.* **25**, 4481–4484.

Schulz, F. M., Stamnes, K., and Stamnes, J. J. (1999a). Point-group symmetries in electromagnetic scattering. *J. Opt. Soc. Am. A* **16**, 853–865.

Schulz, F. M., Stamnes, K., and Stamnes, J. J. (1999b). Shape dependence of the optical properties in size-shape distributions of randomly oriented prolate spheroids, including highly

elongated shapes. *J. Geophys. Res.* **104**, 9413–9421.

Sebak, A. R., and Sinha, B. P. (1992). Scattering by a conducting spheroidal object with dielectric coating at axial incidence. *IEEE Trans. Antennas Propag.* **40**, 268–274.

Secker, D. R., Kaye, P. H., Greenaway, R. S., *et al*. (2000). Light scattering from deformed droplets and droplets with inclusions. I. Experimental results. *Appl. Opt.* **39**, 5023–5030.

Secker, D. R., Kaye, P. H., and Hirst, E. (2001). Real-time observation of the change in light scattering from droplets with increasing deformity. *Opt. Express* **8**, 290–295.

Seker, S. S., and Schneider, A. (1988). Electromagnetic scattering from a dielectric cylinder of finite length. *IEEE Trans. Antennas Propag.* **36**, 303–307.

Senior, T. B. A., and Weil, H. (1977). Electromagnetic scattering and absorption by thin walled dielectric cylinders with application to ice crystals. *Appl. Opt.* **16**, 2979–2985.

Shafai, L., ed. (1991). Thematic issue on computational electromagnetics. *Comput. Phys. Commun.* **68**, 1–498.

Sharma, S. K., and Somerford, D. J. (1999). Scattering of light in the eikonal approximation. *Progr. Opt.* **39**, 213–290.

Sheng, P. (1995). *Introduction to Wave Scattering, Localization, and Mesoscopic Phenomena* (Academic Press, San Diego).

Sheng, X.-Q., Jin, J.-M., Song, J., *et al*. (1998). On the formulation of hybrid finite-element and boundary-integral methods for 3-D scattering. *IEEE Trans. Antennas Propag.* **46**, 303–311.

Shepelevich, N. V., Prostakova, I. V., and Lopatin, V. N. (1999). Extrema in the light-scattering indicatrix of a homogeneous spheroid. *J. Quant. Spectrosc. Radiat. Transfer* **63**, 353–367.

Shepherd, J. W., and Holt, A. R. (1983). The scattering of electromagnetic radiation from finite dielectric circular cylinders. *J. Phys. A: Math. Gen.* **16**, 651–662.

Shifrin, K. S. (1968). *Scattering of Light in a Turbid Medium* (NASA Technical Translation NASA TT F-477). (Original Russian edition: Gostehteorizdat, Moscow, 1951.)

Shifrin, K. S., and Mikulinsky, I. A. (1987). Ensemble approach to the problem of light scattering by a system of tenuous particles. *Appl. Opt.* **26**, 3012–3017.

Shkuratov, Yu. G. (1994). Light backscattering by the solid surfaces of celestial bodies: theoretical models of the opposition effect. *Solar Syst. Res.* **28**, 418–431.

Shurcliff, W. A. (1962). *Polarized Light: Production and Use* (Harvard University Press, Cambridge, MA).

Shvalov, A. N., Soini, J. T., Surovtsev, I. V., *et al*. (2000). Individual *Escherichia coli* cells studied from light scattering with the scanning flow cytometer. *Cytometry* **41**, 41–45.

Siewert, C. E. (1981). On the equation of transfer relevant to the scattering of polarized light. *Astrophys. J.* **245**, 1080–1086.

Sihvola, A. (1999). *Electromagnetic Mixing Formulas and Applications* (IEE Press, London).

Silvester, P. P., and Ferrari, R. L. (1996). *Finite Elements for Electrical Engineers* (Cambridge University Press, New York).

Singham, S. B. (1989). Theoretical factors in modeling polarized light scattering by arbitrary particles. *Appl. Opt.* **28**, 5058–5064.

Singham, S. B., and Bohren, C. F. (1987). Light scattering by an arbitrary particle: a physical

reformulation of the coupled dipole method. *Opt. Lett.* **12**, 10–12.

Singham, S. B., and Bohren, C. F. (1988). Light scattering by an arbitrary particle: the scattering-order formulation of the coupled-dipole method. *J. Opt. Soc. Am. A* **5**, 1867–1872.

Singham, M. K., Singham, S. B., and Salzman, G. C. (1986). The scattering matrix for randomly oriented particles. *J. Chem. Phys.* **85**, 3807–3815.

Sinha, B. P., and MacPhie, R. H. (1977). Electromagnetic scattering by prolate spheroids for plane waves with arbitrary polarization and angle of incidence. *Radio Sci.* **12**, 171–184.

Siqueira, P. R., and Sarabandi, K. (2000). T-matrix determination of effective permittivity for three-dimensional dense random media. *IEEE Trans. Antennas Propag.* **48**, 317–327.

Skaropoulos, N. C., Ioannidou, M. P., and Chrissoulidis, D. P. (1994). Indirect mode-matching solution to scattering from a dielectric sphere with an eccentric inclusion. *J. Opt. Soc. Am. A* **11**, 1859–1866.

Sobolev, V. V. (1975). *Light Scattering in Planetary Atmospheres* (Pergamon Press, Oxford).

Somsikov, V. V. (1996). Optical properties of two-layered spheroidal dust grains. *Astron. Lett.* **22**, 696–703.

Sorensen, C. M. (2001). Light scattering by fractal aggregates: a review. *Aerosol Sci. Technol.* **35**, 648–687.

Stamatakos, G. S., and Uzunoglu, N. K. (1997). An integral equation solution to the scattering of electromagnetic radiation by a linear chain of interacting triaxial dielectric ellipsoids. The case of a red blood cell rouleau. *J. Electromagn. Waves Appl.* **11**, 949–980.

Stamatakos, G. S., Yova, D., and Uzunoglu, N. K. (1997). Integral equation model of light scattering by an oriented monodisperse system of triaxial dielectric ellipsoids: application in ectacytometry. *Appl. Opt.* **36**, 6503–6512.

Stammes, P. (1989). Light scattering properties of aerosols and the radiation inside a planetary atmosphere. Ph. D. dissertation, Free University, Amsterdam.

Stephen, M. J., and Cwilich, G. (1986). Rayleigh scattering and weak localization: effect of polarization. *Phys. Rev. B* **34**, 7564–7572.

Stephens, G. L. (1994). *Remote Sensing of the Lower Atmosphere* (Oxford University Press, New York).

Stephens, G. L., Tsay, S.-C., Stackhouse, P. W., Jr., and Flatau, P. J. (1990). The relevance of the microphysical and radiative properties of cirrus clouds to climate and climatic feedback. *J. Atmos. Sci.* **47**, 1742–1753.

Stevenson, A. F. (1953). Solution of electromagnetic scattering problems as power series in the ratio (dimension of scatterer/wavelength). *J. Appl. Phys.* **24**, 1134–1142.

Stevenson, A. F. (1968). Light scattering by spheroidal particles oriented by streaming. *J. Chem. Phys.* **49**, 4545–4550.

Straka, J. M., Zrnić, D. S., and Ryzhkov, A. V. (2000). Bulk hydrometeor classification and quantification using polarimetric radar data: synthesis of relations. *J. Appl. Meteorol.* **39**, 1341–1372.

Stratton, J. A. (1941). *Electromagnetic Theory* (McGraw Hill, New York).

Streekstra, G. J., Hoekstra, A. G., and Heethaar, R. M. (1994). Anomalous diffraction by arbitrarily oriented ellipsoids: applications in ektacytometry. *Appl. Opt.* **33**, 7288–7296.

Ström, S. (1975). On the integral equations for electromagnetic scattering. *Am. J. Phys.* **43**, 1060–1069.

Ström, S., and Zheng, W. (1987). Basic features of the null field method for dielectric scatterers. *Radio Sci.* **22**, 1273–1281.

Ström, S., and Zheng, W. (1988). The null field approach to electromagnetic scattering from composite objects. *IEEE Trans. Antennas Propag.* **36**, 376–382.

Stubenrauch, C. J., Holz, R., Chédin, A., *et al.* (1999). Retrieval of cirrus ice crystal sizes from 8.3 and 11.1 μm emissivities determined by the improved initialization inversion of TIROS-N Operational Vertical Sounder observations. *J. Geophys. Res.* **104**, 31 793–31 808.

Su, C.-C. (1989). Electromagnetic scattering by a dielectric body with arbitrary inhomogeneity and anisotropy. *IEEE Trans. Antennas Propag.* **37**, 384–389.

Sudiarta, I. W., and Chýlek, P. (2001). Mie-scattering formalism for spherical particles embedded in an absorbing medium. *J. Opt. Soc. Am. A* **18**, 1275–1278.

Sun, W., and Fu, Q. (1999). Anomalous diffraction theory for arbitrarily oriented hexagonal crystals. *J. Quant. Spectrosc. Radiat. Transfer* **63**, 727–737.

Sun, W., and Fu, Q. (2000). Finite-difference time-domain solution of light scattering by dielectric particles with large complex refractive indices. *Appl. Opt.* **39**, 5569–5578.

Sun, W., Fu, Q., and Chen, Z. (1999). Finite-difference time-domain solution of light scattering by dielectric particles with a perfectly matched layer absorbing boundary condition. *Appl. Opt.* **38**, 3141–3151.

Swatek, D. R., and Ciric, I. R. (2000a). Reduction of multiply-nested dielectric bodies for wave scattering analysis by single source surface integral equations. *J. Electromagn. Waves Appl.* **14**, 405–422.

Swatek, D. R., and Ciric, I. R. (2000b). A recursive single-source surface integral equation analysis for wave scattering by heterogeneous dielectric bodies. *IEEE Trans. Antennas Propag.* **48**, 1175–1185.

Szegő, G. (1959). *Orthogonal Polynomials* (American Mathematical Society, New York).

Taflove, A. (1995). *Computational Electrodynamics: The Finite-difference Time-domain Method* (Artech House, Boston, MA).

Taflove, A., ed. (1998). *Advances in Computational Electrodynamics: The Finite-difference Time-domain Method* (Artech House, Boston, MA).

Tai, C.-T. (1993). *Dyadic Green Functions in Electromagnetic Theory* (IEEE Press, New York).

Takano, Y., and Asano, S. (1983). Fraunhofer diffraction by ice crystals suspended in the atmosphere. *J. Meteorol. Soc. Japan* **61**, 289–300.

Takano, Y., and Jayaweera, K. (1985). Scattering phase matrix for hexagonal ice crystals computed from ray optics. *Appl. Opt.* **24**, 3254–3263.

Takano, Y., and Liou, K. N. (1989a). Solar radiative transfer in cirrus clouds. I. Single-scattering and optical properties of hexagonal ice crystals. *J. Atmos. Sci.* **46**, 3–19.

Takano, Y., and Liou, K.N. (1989b). Radiative transfer in cirrus clouds. II. Theory and computation of multiple scattering in an anisotropic medium. *J. Atmos. Sci.* **46**, 20–36.

Takano, Y., and Liou, K. N. (1995). Solar radiative transfer in cirrus clouds. III. Light scattering by irregular ice crystals. *J. Atmos. Sci.* **52**, 818–837.

Tang, C., and Aydin, K. (1995). Scattering from ice crystals at 94 and 220 GHz millimeter wave frequencies. *IEEE Trans. Geosci. Remote Sens.* **33**, 93–99.

Tavker, S., and Kumar, P. P. (2000). Laser depolarization studies of simulated crystallized H_2O/H_2SO_4 clouds. *Atmos. Res.* **53**, 219–230.

Tazaki, T., Tabuchi, H., Ikeda, K., *et al*. (2000). Laboratory measurements of polarimetric radar signatures of randomly distributed spherical and spheroidal scatterers at 30 GHz. *IEE Proc. Microwave Antennas Propag.* **147**, 8–12.

Thomas, G. E., and Stamnes, K. (1999). *Radiative Transfer in the Atmosphere and Ocean* (Cambridge University Press, New York).

Thompson, R. C. (1978). An electro-optic light scattering photometric polarimeter. Ph. D. dissertation, Texas A&M University, College Station, Texas.

Thompson, R. C., Bottiger, J. R,. and Fry, E. S. (1980). Measurement of polarized light interactions via the Mueller matrix. *Appl. Opt.* **19**, 1323–1332. (Errata: **19**, 2657 (1980).)

Tishkovets, V. P. (1994). Light scattering by clusters of spherical particles. Cooperative effects under chaotic orientation. *Kinem. Phys. Celest. Bodies* **10**(2), 50–54.

Tomasko, M. G., West, R. A., and Castillo, N. D. (1978). Photometry and polarimetry of Jupiter at large phase angles. I. Analysis of imaging data of a prominent belt and a zone from Pioneer 10. *Icarus* **33**, 558–592.

Toon, O. B., and Ackerman, T. P. (1981). Algorithms for the calculation of scattering by stratified spheres. *Appl. Opt.* **20**, 3657–3660.

Toon, O. B., Tabazadeh, A., Browell, E. V., and Jordan, J. (2000). Analysis of lidar observations of Arctic polar stratospheric clouds during January 1989. *J. Geophys. Res*. **105**, 20 589–20 615.

Tozer, W. F., and Beeson, D. E. (1974). Optical model of noctilucent clouds based on polarimetric measurements from two sounding rocket campaigns. *J. Geophys. Res.* **79**, 5607–5612.

Tsang, L., Kong, J. A., and Shin, R. T. (1985). *Theory of Microwave Remote Sensing* (John Wiley & Sons, New York).

Tsang, L., Mandt, C. E., and Ding, K. H. (1992). Monte Carlo simulations of the extinction rate of dense media with randomly distributed dielectric spheres based on solution of Maxwell's equations. *Opt. Lett.* **17**, 314–316.

Tsang, L., Kong, J. A., and Ding, K.-H. (2000). *Scattering of Electromagnetic Waves: Theories and Applications* (John Wiley & Sons, New York).

Tsias, A., Wirth, M., Carslaw, K. S., *et al*. (1999). Aircraft observations of an enhanced type Ia polar stratospheric cloud during APE-POLECAT. *J. Geophys. Res.* **104**, 23 961–23 969.

Tu, H., and Ray, A. K. (2001). Analysis of time-dependent scattering spectra for studying processes associated with microdroplets. *Appl. Opt.* **40**, 2522–2534.

Ulaby, F. T., and Elachi, C., eds. (1990). *Radar Polarimetry for Geoscience Applications* (Artech House, Norwood, MA).

Ulaby, F. T., Moore, R. K., and Fung, A. K. (1981). *Microwave Remote Sensing: Active and Passive*, Vol. 1 (Artech House, Boston, MA).

Umashankar, K., Taflove, A., and Rao, S. M. (1986). Electromagnetic scattering by arbitrarily shaped three-dimensional homogeneous lossy dielectric objects. *IEEE Trans. Antennas Propag.* **34**, 758–766.

Uzunoglu, N. K., Alexopoulos, N. G., and Fikioris, J. G. (1978). Scattering from thin and

finite dielectric fibers. *J. Opt. Soc. Am.* **68**, 194–197.

van Albada, M. P., and Lagendijk, A. (1985). Observation of weak localization of light in a random medium. *Phys. Rev. Lett.* **55**, 2692–2695.

van Albada, M. P., and Lagendijk, A. (1987). Vector character of light in weak localization: spatial anisotropy in coherent backscattering from a random medium. *Phys. Rev. B* **36**, 2353–2356.

van Albada, M. P., van der Mark, M. B., and Lagendijk, A. (1987). Observation of weak localization of light in a finite slab: anisotropy effects and light-path classification. *Phys. Rev. Lett.* **58**, 361–364.

Van Bladel, J. (1964). *Electromagnetic Fields* (McGraw Hill, New York).

van de Hulst, H. C. (1957). *Light Scattering by Small Particles* (John Wiley & Sons, New York).

van de Hulst, H. C. (1980). *Multiple Light Scattering. Tables, Formulas, and Applications*, Vols. 1 and 2 (Academic Press, San Diego).

van der Mee, C. V. M., and Hovenier, J. W. (1990). Expansion coefficients in polarized light transfer. *Astron. Astrophys.* **228**, 559–568.

van Tiggelen, B. A., and Maynard, R. (1997). Reciprocity and coherent backscattering of light. In *Wave Propagation in Complex Media*, ed. G. Papanicolaou, pp. 247–271 (Springer-Verlag, Berlin).

Varadan, V. K., and Varadan, V. V., eds. (1980). *Acoustic, Electromagnetic and Elastic Wave Scattering – Focus on the T-matrix Approach* (Pergamon Press, New York).

Varadan, V. V., Lakhtakia, A., and Varadan, V. K. (1989). Scattering by three-dimensional anisotropic scatterers. *IEEE Trans. Antennas Propag.* **37**, 800–802.

Varadan, V. V., Lakhtakia, A., and Varadan, V. K. (1991). *Field Representations and Introduction to Scattering* (North-Holland, Amsterdam).

Vargas, W. E., and Niklasson, G. A. (2001). Reflectance of pigmented polymer coatings: comparisons between measurements and radiative transfer calculations. *Appl. Opt.* **40**, 85–94.

Varshalovich, D. A., Moskalev, A. N., and Khersonskii, V. K. (1988). *Quantum Theory of Angular Momentum* (World Scientific, Singapore). (Original Russian edition: Nauka, Leningrad, 1975.)

Vechinski, D. A., Rao, S. M., and Sarkar, T. K. (1994). Transient scattering from three-dimensional arbitrarily shaped dielectric bodies. *J. Opt. Soc. Am. A* **11**, 1458–1470.

Vermeulen, K. (1999). Calculated scattering matrices of randomly oriented spheroids distributed over size and shape: a comparison with laboratory measurements for feldspar. Graduation report, Free University, Amsterdam.

Videen, G. (1996). Light scattering from an irregular particle behind a plane interface. *Opt. Commun.* **128**, 81–90.

Videen, G., Ngo, D., Chýlek, P., and Pinnick, R. G. (1995). Light scattering from a sphere with an irregular inclusion. *J. Opt. Soc. Am. A* **12**, 922–928.

Videen, G., Ngo, D., and Hart, M. B. (1996). Light scattering from a pair of conducting, osculating spheres. *Opt. Commun.* **125**, 275–287.

Videen, G., Pinnick, R. G., Ngo, D., *et al.* (1998a). Asymmetry parameter and aggregate particles. *Appl. Opt.* **37**, 1104–1109.

Videen, G., Sun, W., and Fu, Q. (1998b). Light scattering from irregular tetrahedral aggregates. *Opt. Commun.* **156**, 5–9.

Videen, G., Sun, W., Fu, Q., *et al.* (2000a). Light scattering from deformed droplets and droplets with inclusions. II. Theoretical treatment. *Appl. Opt.* **39**, 5031–5039.

Videen, G., Fu, Q., and Chýlek, P., eds. (2000b). *Light Scattering by Nonspherical Particles: Halifax Contributions* (Army Research Laboratory, Adelphi, MD).

Videen, G., Fu, Q., and Chýlek, P., eds. (2001). Special issue on light scattering by nonspherical particles. *J. Quant. Spectrosc. Radiat. Transfer* **70**, 373–831.

Vilenkin, N. Ja. (1968). *Special Functions and the Theory of Group Representations* (American Mathematical Society, New York). (Original Russian edition: Nauka, Moscow, 1965.)

Volakis, J. L., Chatterjee, A., and Kempel, L. C. (1998). *Finite Element Method for Electromagnetics* (IEEE Press, New York).

Volkovitsky, O. A., Pavlova, L. N., and Petrushin, A. G. (1984). *Optical Properties of Ice Clouds* (Gidrometeoizdat, Leningrad) (in Russian).

Volten, H. (2001). Light scattering by small planetary particles: an experimental study. Ph. D. dissertation, Free University, Amsterdam.

Volten, H., de Haan, J. F., Hovenier, J. W., *et al*. (1998). Laboratory measurements of angular distributions of light scattered by phytoplancton and slit. *Limnol. Oceanogr.* **43**, 1180–1197.

Volten, H., Jalava, J.-P., Lumme, K., *et al*. (1999). Laboratory measurements and T-matrix calculations of the scattering matrix of rutile particles in water. *Appl. Opt.* **38**, 5232–5240.

Volten, H., Muñoz, O., Rol, E., *et al*. (2001). Scattering matrices of mineral aerosol particles at 441.6 nm and 632.8 nm. *J. Geophys. Res.* **106**, 17 375–17 402.

von Ross, O. (1971). Method for the solution of electromagnetic scattering problems for inhomogeneous dielectrics as a power series in the ratio (dimension of scatterer)/wavelength. *J. Appl. Phys.* **42**, 4197–4201.

Voshchinnikov, N. V. (1996). Electromagnetic scattering by homogeneous and coated spheroids: calculations using the separation of variables method. *J. Quant. Spectrosc. Radiat. Transfer* **55**, 627–636.

Voshchinnikov, N. V., and Farafonov, V. G. (1993). Optical properties of spheroidal particles. *Astrophys. Space Sci.* **204**, 19–86.

Voshchinnikov, N. G., and Farafonov, V. G. (1994). Peculiarities of scattering of radiation by the nonspherical particles of atmospheric aerosol. *Izv., Atmos. Oceanic Phys.* (Engl. transl.) **30**, 43–49.

Voshchinnikov, N. V., and Farafonov, V. G. (2000). Applicability of quasi-static and Rayleigh approximations for spheroidal particles. *Opt. Spectrosc.* **88**, 71–75.

Voshchinnikov, N. V., Il'in, V. B., Henning, Th., *et al*. (2000). Extinction and polarization of radiation by absorbing spheroids: shape/size effects and benchmark results. *J. Quant. Spectrosc. Radiat. Transfer* **65**, 877–893.

Vouk, V. (1948). Projected area of convex bodies. *Nature (London)* **162**, 330–331.

Wait, J. R. (1955). Scattering of a plane wave from a circular dielectric cylinder at oblique incidence. *Can. J. Phys.* **33**, 189–195.

Wait, J. R. (1963). Electromagnetic scattering from a radially inhomogeneous sphere. *Appl.*

Sci. Res. Sect. B **10**, 441–450.

Waldemarsson, K. W. T., and Gustafson, B. Å. S. (2000). Light scattering by thin flakes. In *Light Scattering by Nonspherical Particles: Halifax Contributions*, eds. G. Videen, Q. Fu, and P. Chýlek, pp. 34–37 (Army Research Laboratory, Adelphi, MD).

Wang, J. J. H. (1991). *Generalized Moment Methods in Electromagnetics: Formulation and Computer Solution of Integral Equations* (John Wiley & Sons, New York).

Wang, D.-S., and Barber, P. W. (1979). Scattering by inhomogeneous nonspherical objects. *Appl. Opt.* **18**, 1190–1197.

Wang, Y. M., and Chew, W. C. (1993). A recursive T-matrix approach for the solution of electromagnetic scattering by many spheres. *IEEE Trans. Antennas Propag.* **41**, 1633–1639.

Warren, S. G. (1984). Optical constants of ice from the ultraviolet to the microwave. *Appl. Opt.* **23**, 1206–1225.

Waterman, P. C. (1965). Matrix formulation of electromagnetic scattering. *Proc. IEEE* **53**, 805–812.

Waterman, P. C. (1971). Symmetry, unitarity, and geometry in electromagnetic scattering. *Phys. Rev. D* **3**, 825–839.

Waterman, P. C. (1973). Numerical solution of electromagnetic scattering problems. In *Computer Techniques for Electromagnetics*, ed. R. Mittra, pp. 97–157 (Pergamon, Oxford).

Waterman, P. C. (1979). Matrix methods in potential theory and electromagnetic scattering. *J. Appl. Phys.* **50**, 4550–4566.

Watson, K. M. (1969). Multiple scattering of electromagnetic waves in an underdense plasma. *J. Math. Phys.* **10**, 688–702.

Weil, H., and Chu, C. M. (1976). Scattering and absorption of electromagnetic radiation by thin dielectric disks. *Appl. Opt*. **15**, 1832–1836.

Weil, H., and Chu, C. M. (1980). Scattering and absorption by thin flat aerosols. *Appl. Opt.* **19**, 2066–2071.

Wendling, P., Wendling, R., and Weickmann, H. K. (1979). Scattering of solar radiation by hexagonal ice crystals. *Appl. Opt.* **18**, 2663–2671.

West, R. A. (1991). Optical properties of aggregate particles whose outer diameter is comparable to the wavelength. *Appl. Opt.* **30**, 5316–5324.

West, R. A., and Smith, P. H. (1991). Evidence for aggregate particles in the atmospheres of Titan and Jupiter. *Icarus* **90**, 330–333.

West, R. A., Lane, A. L., Hart, H., *et al*. (1983). Voyager 2 photopolarimeter observations of Titan. *J. Geophys. Res*. **88**, 8699–8707.

Wielaard, D. J., Mishchenko, M. I., Macke, A., and Carlson, B. E. (1997). Improved **T**-matrix computations for large, nonabsorbing and weakly absorbing nonspherical particles and comparison with geometrical-optics approximation. *Appl. Opt.* **36**, 4305–4313.

Wigner, E. P. (1959). *Group Theory and its Application to the Quantum Mechanics of Atomic Spectra* (Academic Press, New York).

Wirth, M., Tsias, A., Dörnbrack, A., *et al*. (1999). Model-guided Lagrangian observation and simulation of mountain polar stratospheric clouds. *J. Geophys. Res.* **104**, 23 971–23 981.

Wiscombe, W. J. (1980). Improved Mie scattering algorithms. *Appl. Opt.* **19**, 1505–1509.

Wiscombe, W. J., and Grams, G. W. (1976). The backscattered fraction in two-stream ap-

proximations. *J. Atmos. Sci.* **33**, 2440–2451.

Wiscombe, W. J., and Mugnai, A. (1986). Single scattering from nonspherical Chebyshev particles: a compendium of calculations (NASA Ref. Publ. NASA RP-1157).

Wiscombe, W. J., and Mugnai, A. (1988). Scattering from nonspherical Chebyshev particles. 2. Means of angular scattering patterns. *Appl. Opt.* **27**, 2405–2421.

Witt, G., Dye, J. E., and Wilhelm, N. (1976). Rocket-borne measurements of scattered sunlight in the mesosphere. *J. Atmos. Terrestrial Phys*. **38**, 223–238.

Wolf, P. E., Maret, G., Akkermans, E., and Maynard, R. (1988). Optical coherent backscattering by random media: an experimental study. *J. Phys. (Paris)* **49**, 63–75.

Woodard, R., Collins, R. L., Disselkamp, R. S., *et al.* (1998). Circular depolarization lidar measurements of cirrus clouds. In *Proc. 19th Int. Laser Radar Conf.*, NASA Conf. Publ. NASA/CP-1998-207671/PT1, pp. 47–50.

Worms, J.-C., Renard, J.-B., Hadamcik, E., *et al*. (2000). Light scattering by dust particles with the PROGRA^2 instrument – comparative measurements between clouds under microgravity and layers on the ground. *Planet. Space Sci.* **48**, 493–505.

Wriedt, T., ed. (1999). *Generalized Multipole Techniques for Electromagnetic and Light Scattering* (Elsevier, Amsterdam).

Wriedt, T. (2000). Electromagnetic scattering programs. URL: http://www.t-matrix.de/.

Wriedt, T., and Comberg, U. (1998). Comparison of computational scattering methods. *J. Quant. Spectrosc. Radiat. Transfer* **60**, 411–423.

Wriedt, T., and Eremin, Yu., eds. (1998). *Electromagnetic and Light Scattering: Theory and Applications III* (University of Bremen, Bremen).

Wriedt, T., and Doicu, A. (1998a). Formulations of the extended boundary condition method for three-dimensional scattering using the method of discrete sources. *J. Mod. Opt.* **45**, 199–213.

Wriedt, T., and Doicu, A. (1998b). Light scattering from a particle on or near a surface. *Opt. Commun.* **152**, 376–384.

Wriedt, T., Quinten, M., and Bauckhage, K., eds. (1996). *Electromagnetic and Light Scattering: Theory and Applications* (University of Bremen, Bremen).

Wurm, G., Heim, L.-O., and Göhzold, T. (2000). Light scattering experiments on CCA dust aggregates and applications to astrophysics. In *Light Scattering by Nonspherical Particles: Halifax Contributions*, eds. G. Videen, Q. Fu, and P. Chýlek, pp. 226–229 (Army Research Laboratory, Adelphi, MD).

Wyatt, P. J. (1962). Scattering of electromagnetic plane waves from inhomogeneous spherically symmetric objects. *Phys. Rev.* **127**, 1837–1843.

Xu, Y.-l. (1995). Electromagnetic scattering by an aggregate of spheres. *Appl. Opt.* **34**, 4573–4588.

Xu, R. (2000). *Particle Characterization: Light Scattering Methods* (Kluwer Academic Publishers, Dordrecht, The Netherlands).

Xu, L., Zhang, G., Ding, J., and Chen, H. (1997). Light scattering by polydispersions of randomly oriented hexagonal ice crystals: phase function analysis. *Optik* **106**, 103–114.

Yang, P., and Cai, Q. (1991). Light scattering phase matrices for spheroidal and cylindric large particles. *Chinese J. Atmos. Sci.* **14**, 345–358.

Yang, P., and Liou, K. N. (1995). Light scattering by hexagonal ice crystals: comparison of

finite-difference time domain and geometric optics models. *J. Opt. Soc. Am. A* **12**, 162–176.

Yang, P., and Liou, K. N. (1996a). Finite-difference time domain method for light scattering by small ice crystals in three-dimensional space. *J. Opt. Soc. Am. A* **13**, 2072–2085.

Yang, P., and Liou, K. N. (1996b). Geometric-optics–integral-equation method for light scattering by nonspherical ice crystals. *Appl. Opt.* **35**, 6568–6584.

Yang, P., and Liou, K. N. (1998a). Single-scattering properties of complex ice crystals in terrestrial atmosphere. *Contr. Atmos. Phys.* **71**, 223–248.

Yang, P., and Liou, K. N. (1998b). An efficient algorithm for truncating spatial domain in modeling light scattering by finite-difference technique. *J. Comput. Phys.* **140**, 346–369.

Yang, P., and Liou, K. N. (2000). Finite difference time domain method for light scattering by nonspherical and inhomogeneous particles. In *Light Scattering by Nonspherical Particles: Theory, Measurements, and Applications*, eds. M. I. Mishchenko, J. W. Hovenier, and L. D. Travis, pp. 173–221 (Academic Press, San Diego).

Yang, P., Liou, K. N., and Arnott, W. P. (1997). Extinction efficiency and single-scattering albedo for laboratory and natural cirrus clouds. *J. Geophys. Res.* **102**, 21 825–21 835.

Yang, P., Liou, K. N., Wyser, K., and Mitchell, D. (2000a). Parameterization of the scattering and absorption properties of individual ice crystals. *J. Geophys. Res.* **105**, 4699–4718.

Yang, P., Liou, K. N., Mishchenko, M. I., and Gao, B.-C. (2000b). Efficient finite-difference time-domain scheme for light scattering by dielectric particles: application to aerosols. *Appl. Opt.* **39**, 3727–3737.

Yang, P., Gao, B.-C., Baum, B. A., *et al*. (2001a). Asymptotic solutions for optical properties of large particles with strong absorption. *Appl. Opt.* **40**, 1532–1547.

Yang, P., Gao, B.-C., Baum, B. A., *et al.* (2001b). Sensitivity of cirrus bidirectional reflectance to vertical inhomogeneity of ice crystal habits and size distributions for two MODIS bands. *J. Geophys. Res.* **106**, 17 267–17 292.

Yanovitskij, E. G. (1997). *Light Scattering in Inhomogeneous Atmospheres* (Springer-Verlag, Berlin).

Yee, K. S. (1966). Numerical solution of initial boundary value problems involving Maxwell's equations in isotropic media. *IEEE Trans. Antennas Propag.* **14**, 302–307.

Yeh, C. (1964). Perturbation approach to the diffraction of electromagnetic waves by arbitrarily shaped dielectric obstacles. *Phys. Rev. A* **135**, 1193–1201.

Zakharova, N. T., and Mishchenko, M. I. (2000). Scattering properties of needlelike and platelike ice spheroids with moderate size parameters. *Appl. Opt.* **39**, 5052–5057.

Zakharova, N. T., and Mishchenko, M. I. (2001) Scattering by randomly oriented thin ice disks with moderate equivalent-sphere size parameters. *J. Quant. Spectrosc. Radiat. Transfer* **70**, 465–471.

Zerull, R. H. (1976). Scattering measurements of dielectric and absorbing nonspherical particles. *Beitr. Phys. Atmos.* **49**, 168–188.

Zhang, J., and Xu, L. (1995). Light scattering by absorbing hexagonal ice crystals in cirrus clouds. *Appl. Opt.* **34**, 5867–5874.

Zheng, W., and Ström. S. (1989). The null field approach to electromagnetic scattering from composite objects: the case of concavo-convex constituents. *IEEE Trans. Antennas Propag.* **37**, 373–383.

Zrnić, D. S., Keenan, T. D., Carey, L. D., and May, P. (2000). Sensitivity analysis of polarimetric variables at a 5-cm wavelength in rain. *J. Appl. Meteorol.* **39**, 1514–1526.

Zuffada, C., and Crisp, D. (1997). Particle scattering in the resonance regime: full-wave solution for axisymmetric particles with large aspect ratios. *J. Opt. Soc. Am. A* **14**, 459–469.

Zurk, L. M., Tsang, L., Ding, K. H., and Winebrenner, D. P. (1995). Monte Carlo simulations of the extinction rate of densely packed spheres with clustered and nonclustered geometries. *J. Opt. Soc. Am. A* **12**, 1772–1781.

Zurk, L. M., Tsang, L., and Winebrenner, D. P. (1996). Scattering properties of dense media from Monte Carlo simulations with application to active remote sensing of snow. *Radio Sci.* **31**, 803–819.

Index

absorption, 3, 11, 58
absorption coefficient, 15
aggregated particles, *see* particles, aggregated
Alexander's dark band, 259
amplitude scattering matrix, 37–8, 118
  backscattering, 94
  backscattering theorem for, 41–2
  circular-polarization, 106
    for spherically symmetric particles, 141
  for rotationally symmetric particles, 183
  for spherically symmetric particles, 139–40
  forward-scattering, 91–3
  reciprocity relation for, 41, 84
  rotation transformation law for, 46
  symmetry properties of, 84–5
  translation transformation law for, 66–7
angle
  azimuth, 16
  polar, 16
  scattering, 60, 83, 87
  zenith, *see* angle, polar
angular frequency, 5, 10
anomalous diffraction approximation, *see* approximation, anomalous diffraction
approximation
  anomalous diffraction, 210
  Born, *see* approximation, Rayleigh–Gans
  effective-medium, 350
  eikonal, 210
  geometrical optics, 210–21, 258–60, 264–5, 320–5
  high-energy, 210
  Kirchhoff, 212, 220
  ray optics, *see* approximation, geometrical optics
  ray-tracing, *see* approximation, geometrical optics
  Rayleigh, 206–9, 264
  Rayleigh–Debye, *see* approximation, Rayleigh–Gans
  Rayleigh–Gans, 35, 209–10, 256, 264, 271
  Rayleigh–Gans–Stevenson, 207
  scalar, 109
  single-scattering, 6
  Wentzel–Kramers–Brillouin, 210
aspect ratio, 73, 192, 290
asymmetry parameter, 60, 96, 101, 105, 295, 299–300, 304, 309, 327, 340, 344, 350–1
  for spherically symmetric particles, 142, 239, 242–3, 245, 256–7
averaging
  ensemble, 72–3, 159–60, 334–7
  orientation, 72–3, 172–3, 334–7, 338, 344

analytical, 121, 127, 131, 134, 186, 199, 201
effects of, 279–82
numerical, 134, 137, 186
shape, 72–3, 334–7
size, 72–3, 159–61, 172–3, 335
effects of, 250–2, 279–82, 341
axis ratio for spheroids, 171
azimuth angle, 16

backscatter-to-extinction ratio, 267, 270, 292, 295, 303, 308
backscattered fraction, 299–300, 305
backscattering, 7, 94–5, 99, 267–71, 320–1
backscattering depolarization ratio
circular, 100, 228, 295–6, 307, 310, 339, 342, 352, 356–8
linear, 100, 228, 295–7, 307, 309, 339, 342, 352–8
backscattering theorem, 41–2, 54
benchmark results, 180–2, 189, 203–4
Bessel functions, spherical, 167–9, 360, 370
asymptotic form for, 360
bispheres, *see* clusters, two-sphere
blackbody
energy distribution, 63
Stokes column vector, 65, 98
blue moon, 250
Born approximation, *see* approximation, Rayleigh–Gans
boundary conditions, 5, 7, 9–10, 78, 113, 145, 191, 192, 196
absorbing, 194, 195
boundary-matching method, 196–7
Brewster angle, 272
bulk matter, 32
optical constants of, 32

charge density, 9
surface, 10
Chebyshev particles, 171–2, 182, 185, 319
generalized, 182, 185
cirrus clouds, *see* ice clouds
Clebsch–Gordan coefficients, 128, 131, 141, 369, 380–3
Clebsch–Gordan expansion, 128, 141, 368
clusters, 5, 80, 154
of spheres, 156, 190, 201, 337–47
of spheroids, 201
two-sphere, 74–6, 80–1, 186–9, 203–4, 337–45, 357–8
coherency matrix, 17
additivity of, 28
coherency column vector, 17, 50, 54–5
coherent backscattering, 7, 42, 79–82, 220
completely polarized light, *see* fully polarized light
composite particles, 154–8
computer codes, 158–90, 193, 195, 199, 205, 214
condensation trails (contrails), 353–5
conductivity, 9
constitutive relations, 9, 117
continuity equation, 9
coordinate system
Cartesian, 15
device, 130
laboratory, 42–6, 119, 130
particle, 42–6, 119
right-handed, 15–6
spherical, 15–6
coupled dipole method, *see* discrete dipole approximation
cross section
absorption, 57–8, 227–8, 254–5, 294, 299, 302, 340, 343
average, 71, 97
backscattering, 267
differential scattering, 59
extinction, 57–9, 119, 227, 294–5, 299, 300, 339–40, 343
average, 70, 93
for randomly oriented particles, 132–3
for spherically symmetric particles, 140
geometrical, 59
radar backscattering, 267
radiation-pressure, 62
average, 71, 97
scattering, 57–8, 119, 294, 299, 301, 340, 343
average, 69, 71, 96
for macroscopically isotropic and mirror-symmetric media, 95–6
for randomly oriented particles,

138–9
for spherically symmetric particles, 140
current density, 9
surface, 10
cylinders
circular, 171–2, 185, 203–4, 210, 213, 215–20, 299–310
with extreme aspect ratios, 221–2, 315–8
hexagonal, 146, 210, 213, 320–2, 350

delta-function transmission, 218–20
density matrix, *see* coherency matrix
depolarization, 54, 100, 295–7, 307, 339
in remote sensing, 352–6
dichroism, 3, 56, 78
differential equation methods, 191
diffraction, *see* Fraunhofer diffraction
Dirac delta function
solid-angle, 41
three-dimensional, 33
direct scattering problem, 237, 351
discrete dipole approximation, 198–9, 203, 205
discretized Mie formalism, 205, 222
dyad, 34
dyadic, 33–34
dyadic transition operator, 35
integral equation for, 35

effective-medium approximation, 350
effective radius, 161, 285–7
effective size parameter, 250, 286
effective variance, 161, 251–2, 285–7
efficiency factor
for absorption, 59, 97, 254–5
for backscattering, 267, 269, 292, 295
for extinction, 59, 97, 238–47, 253–4, 309, 312
for radiation pressure, 62, 97, 257–8, 309, 312
for scattering, 59, 97, 253–4
eikonal approximation, 210
electric displacement, 9
electric field, 9
electric permittivity, 9
electric polarization, 9
electric susceptibility, 9
electromagnetic wave, 3, 12
circular components of, 105
emission column vector, Stokes, 63–5
average, 71, 78, 98
emission, thermal, 3, 63–6, 97–8
energy conservation law, 11, 37, 122
ensemble averaging, 72–3, 159–60, 334–7
equilibrium, thermal, 63–5
Euler angles, 42, 119–20, 367
Ewald–Oseen extinction theorem, 115
extended boundary condition, 144
extended boundary condition method, 115, 142–7, 196
convergence of, 150–3, 170–1, 178–80
for rotationally symmetric particles, 148–50
iterative, 152, 205
multiple-multipole, 152
extinction, 3, 58, 78
extinction matrix
circular-polarization, 56
reciprocity relation for, 56
coherency, 55
reciprocity relation for, 56
modified Stokes, 56
reciprocity relation for, 56
Stokes, 55–6
average, 70, 78
for axially oriented particles, 127–32
for macroscopically isotropic and mirror-symmetric media, 91–3
reciprocity relation for, 56, 71
symmetry property of, 56
extinction-to-backscatter ratio, 267

far-field zone, 5, 35–8
finite-difference method, 194, 205
finite-difference time-domain method, 195–6, 205, 321
finite-element method, 193–5, 205
Fraunhofer diffraction, 212–3, 220, 227, 258–9
Fredholm integral equation method, 200, 205
fully polarized light, 27, 54

Gaussian random spheres, 328
generalized spherical functions, 103, 107,

366–7
geometrical optics approximation, 210–21, 258–60, 264–5, 320–5
glory, 260, 264
Green's function
dyadic, free space, 33–6, 377
scalar, 34–6
Green's vector theorem, 142

halos, 320–2, 350
Hankel functions, 169, 370
Helmholtz equation
scalar, 371
vector, 193, 205, 372–3
homogeneous wave, 13
Huygens' principle, 115
hydrometeors
nonspherical, 100, 127, 352
partially aligned, 100

ice clouds, 321, 322, 352, 354–5, 358
identity dyadic, 33, 36
incident field, 31, 33, 47, 116
independently scattering particles, 6, 74
inhomogeneous wave, 13
integral equation methods, 191, 197–200
intensity of light, 15, 18
interference of light, 7, 58, 79, 343, 344
interference structure, 240, 250–1, 279–82
interstellar dust grains, 100, 127
interstellar polarization, 99, 351
inverse scattering problem, 237, 351
irradiance, *see* intensity
irregular particles, 322–34

Jacobi polynomials, 364

Kirchhoff approximation, 212, 220
Koch fractals, 325, 327
random, 325–8
Kronecker delta, 363

Legendre functions, associated, 140, 360, 366, 374
Legendre polynomials, 360, 365
levitation
electrostatic, 273, 358
optical, 60, 228, 273
lidars, 228, 352, 355
Lippmann–Schwinger equations, 35
Lorenz–Mie
coefficients, 122, 153–4
computer code, 158–65, 238
identities, 100, 352
scattering matrix, 99
theory, 99, 114, 115, 139–42, 238

magnetic field, 9
magnetic induction, 9
magnetic permeability, 9
magnetization, 9
Maxwell equations, 5, 8–9, 32, 77, 78, 113, 191, 195
linearity of, 37, 39, 117
plane-wave solution of, 12–15
Maxwell stress tensor, 60
measurement techniques for scattering, 224–33
using microwaves, 224, 230–3
using visible and infrared light, 113, 224–30, 273–4, 329–34, 345, 351–8
two-dimensional angular, 230, 351–2
meridional plane, 16, 23, 38, 83, 88
method of moments, 198–9, 205
microwave analog technique, 113, 147, 230–3
microwave measurement techniques, 224, 230–3
mineral particles, 329–39
monochromatic light, 3, 12
monodisperse particles, 165, 177, 238–50, 279–82, 335, 341

natural light, *see* unpolarized light
near-field effects, 80
nonsphericity, effects of, 99–100, 279–82
null-field method, 115
with discrete sources, 152

optical equivalence principle, 18, 28
optical theorem, 49, 56, 58, 207
orientation angle of the polarization ellipse, 20
orientation averaging, *see* averaging,

orientation
orientation distribution, 72–3
axially symmetric, 73, 127
random, 73
orientation of the scattering object, *see* particle orientation
outgoing wave, 34, 36, 371, 374

parallel beam of light, 3, 12
particle characterization, optical, 7, 82, 229–30, 249, 273–8, 350–8
particle collection, 5, 68
tenuous, 7
particle orientation, 42
effects of, 99–100, 279–82
particle shapes, 171–2, 182, 283, 322, 325, 330
particles
absorbing, 124, 216
aggregated, 154–8
Chebyshev, 171–2, 182, 185, 319
generalized, 182, 185
clay, 329–32
composite, 154–8
dust, 355–6
feldspar, 329–31
fly ash, 345, 348
independently scattering, 6, 74
irregular, 322–34
loess, 329–31, 335
mineral, 329–39
monodisperse, 165, 177, 238–50, 279–82, 335, 341
nonabsorbing, 122–5, 139, 152
polydisperse, 158, 165, 250–73, 282–310, 345, 354, 356
polyhedral, 146, 213, 320–3
quartz, 329–31, 333
randomly and sparsely distributed, 68–71, 75, 77
randomly oriented, 73, 87, 100, 132–9
randomly shaped, 322
rotationally symmetric, 46, 93, 102, 121, 125, 129, 133, 135, 138, 148–50, 165, 169, 171–2, 180
Sahara sand, 329–31, 337
spherical, 98–9, 102, 122, 139–42, 158, 214–6, 238–78
anisotropic, 222
Faraday-active, 221
monodisperse, 238–50
polydisperse, 250–73
stochastically shaped, *see* particles, randomly shaped
volcanic, 329–31, 334, 336
with inclusions, 156–7, 201, 213–14, 347–51
with rough surfaces, 325–6, 328
perturbation theories, 221
phase, 13, 18, 20
phase function, 59–60, 101
for irregular particles, 322–8
for monodisperse spherical particles, 248
for polydisperse spherical particles, 258–67
for randomly oriented circular cylinders, 301–2, 306, 315–6
for randomly oriented spheroids, 286–91, 297, 309
normalization condition for, 60, 101
Rayleigh, 208–9, 264
Rayleigh–Gans, 264
phase matrix, 49–54
circular-polarization, 52, 106
average, 107
normalized, 106–7
reciprocity relation for, 53
coherency, 50–1
reciprocity relation for, 53
modified Stokes, 52
reciprocity relation for, 53
normalized Stokes, 100–2
Fourier decomposition in azimuth for, 105
symmetry properties of, 102
Stokes, 51–2, 83
average, 70, 72, 78
backscattering, 54
expression in terms of the scattering matrix, 88–91
for macroscopically isotropic and mirror-symmetric media, 88–91
inequalities for, 52, 71
reciprocity relation for, 52–3, 71
symmetry relations for, 90–1
phase velocity, 13, 14

photon correlation spectroscopy, 7
physical optics approximation, 220
plane wave, 3, 12, 16–7, 37, 116
  expansion in spherical waves, 360–1
  expansion in vector spherical wave functions, 117, 376–7
point matching method, 196–7
  generalized, 197, 204
    multiple-expansion, 197, 204–5
polar angle, 16
polar stratospheric clouds, 352, 354
polarization, 54
  circular, 21, 23, 54
    degree of, 28
  complete, *see* polarization, full
  degree of, 28
  elliptical, 21, 23
    degree of, 28, 54
  full, 27, 54
  left-handed, 20
  linear, 21, 23, 54
    degree of, 28, 29, 271
  natural, 27
  right-handed, 20
polarization analyzer, 225
polarization ellipse, 20–4
  ellipticity of, 20
  orientation of, 20
polarization modulation technique, 226, 228
polarization modulator, 225
polarizer, 225
polydisperse particles, 158, 165, 250–73, 282–310, 345, 354, 356
polyhedral particles, 146, 213, 320–3
position vector, 10
Poynting vector, 11
  complex, 12
  time-averaged, 12, 14–5, 47, 123–4
probability density function, 72
  normalization condition for, 72

quarter-wave plate, 225
quasi-monochromatic light, 5, 26–9, 52, 56, 58, 63, 71, 77

radars, 233, 352
radiance, *see* specific intensity
radiation condition, 116–7, 194, 199
radiation force, 60–2, 96–7
  emission component of, 62, 65, 98
radiation pressure, 60
radiation torque, 62–3
  emission component of, 66
radiative transfer equation, 6–7, 76, 78
  for macroscopically isotropic and mirror-symmetric media, 105, 108–9
radius
  effective, 161, 285–7
  equivalent-sphere, 73, 172
  surface-equivalent-sphere, 171–2
  volume-equivalent-sphere, 172
radius vector, 10
rainbows, 258–60, 264
randomly and sparsely distributed particles, 68–71, 75, 77
randomly oriented particles, 73, 87, 100, 132–9
randomly shaped particles, 322
ray optics approximation, *see* approximation, geometrical optics
ray-tracing approximation, *see* approximation, geometrical optics
Rayleigh approximation, 206–9, 264
Rayleigh–Debye approximation, *see* approximation, Rayleigh–Gans
Rayleigh–Gans approximation, 35, 209–10, 256, 264, 271
Rayleigh–Gans scattering, 264, 271–3
Rayleigh hypothesis, 117, 146, 196, 221
Rayleigh scattering, 247, 250, 264, 271–3, 309, 310
reciprocity relation, 41, 52–3, 71, 84
reference plane, 24
  rotations of, 24–5
refractive index, 5, 14
  relative, 33
resonance structure, 241–50, 279–82, 338
resonances, 241–50, 273
ripple structure, 239, 241, 245, 250–1
rotation matrix
  for circular-polarization representation, 25–6
  for modified Stokes column vector, 25
  Stokes, 25
rotationally symmetric particles, 46, 93, 102, 121, 125, 129, 133, 135, 138,

148–50, 165, 169, 171–2, 180

S matrix, 122–5
unitarity condition for, 124–5
scale invariance rule, 147, 230
scattered field, 3, 31, 33, 36–7, 47, 116–7
scattering, 3
diffuse, 6
dynamic, 7
elastic, 3
electromagnetic, 3
far-field, 5, 35–8, 66–7
forward, 6, 49, 54, 91–4, 99
incoherent, 6, 74
independent, 6, 74, 75
condition for, 74
multiple, 6, 75, 344
single, 68–71
static, 7
scattering angle, 60, 83, 87
scattering dyadic, 37, 41, 117–8
reciprocity relation for, 41
scattering matrix, circular-polarization, normalized, 106–7
expansion in generalized spherical functions, 107–8, 136, 141
symmetry properties of, 107
scattering matrix, Stokes, 83, 85–6, 94
average, 87
effects of nonsphericity on, 99–100
for backward scattering, 94–5
for forward scattering, 93–4
for macroscopically isotropic and mirror-symmetric media, 87
for randomly oriented particles, 133–7
for rotationally symmetric particles, 93–4
for spherically symmetric particles, 98–9
inequalities for, 87–8
normalized, 100–3
expansion in generalized spherical functions, 103–5, 136–7, 141, 166, 172–3, 180–1
expansion in Wigner *d*-functions, 103–5
for clusters of spheres, 341–7
for irregular particles, 323–39
for randomly oriented circular cylinders, 215–8, 301–7, 315–8
for randomly oriented spheroids, 180, 182, 285–94, 297–8, 309–11, 313–4
for rotationally symmetric particles, 102
for spherically symmetric particles, 102, 140, 160, 167, 229–30, 245–9, 258–67, 271–6
properties of, 101–3
symmetries of, 85–6
scattering medium
macroscopically isotropic, 87
macroscopically isotropic and mirror-symmetric, 87, 100
macroscopically mirror-symmetric, 87
scattering plane, 83, 88
scattering tensor, 39
reciprocity condition for, 40
Schelkunoff equivalent current method, 115
secondary wave, 3
separation of variables method, 113–4, 179, 192–3, 202–5
multi-sphere, 156, 201
shape averaging, 72–3, 334–7
shape distribution, 72–3
single-scattering albedo, 58, 228, 255–6, 284, 293–6, 299, 303, 340, 344
average, 97
single-scattering approximation, 6
size averaging, 72–3, 159–61, 172–3, 335
effects of, 250–2, 279–82, 341
size distribution, 72–3, 160–1, 173, 177, 250–2, 283–6
gamma, 160, 252, 283–6
log normal, 160, 283–6
modified bimodal log normal, 161
modified gamma, 160, 283
modified power law, 161, 283–7
power law, 160, 285
size parameter, 74, 147, 192
effective, 250, 286
major-axis, 178
surface-equivalent-sphere, 178, 308
volume-equivalent-sphere, 308
specific intensity, 77
column vector, 77–8
speed of light, 14
spherical harmonics

scalar, 360
vector, 373–6
spherical particles, 98–9, 102, 122, 139–42, 158, 214–6, 238–78
anisotropic, 222
Faraday-active, 221
monodisperse, 238–50
polydisperse, 250–73
spherical wave, 36
spherical wave functions
scalar, 371
vector, 115, 116, 372–8
spheroids, 171–2
optical properties of, 180–2, 185, 203–4, 210, 213, 280–98
with extreme aspect ratios, 307–14
statistical approach, 334–7
stochastically shaped particles, 322
Stokes column vector, 17, 51
circular-polarization, 19, 23, 105–6
additivity of, 28
rotation transformation rule for, 25–6
for quasi-monochromatic light, 27
additivity of, 27, 28
modified, 18, 23
additivity of, 28
rotation transformation rule for, 25
rotation transformation rule for, 24–5
Stokes parameters, 6, 7, 15, 17–8
ellipsometric interpretation of, 19–24
for quasi-monochromatic light, 26
additivity of, 27–8
quadratic inequality for, 27
quadratic identity for, 18
rotation transformation rule for, 24–5
subtraction method, 226, 228
superposition method, 156, 201–2, 204
superposition principle, 37
surface integral equation methods, 200, 205
time-domain, 205
Système International, 384

T matrix, 115, 117, 146
for aggregated particles, 154–8, 201
for rotationally symmetric particles, 148–50, 167–71
orientation-averaged, 127–9, 131
rotation transformation rule for, 119–21
symmetry relations for, 121–2
translation transformation rule for, 125–7
unitarity property of, 122–5, 152
T-matrix computer code
for randomly oriented, rotationally symmetric particles, 165–80
for randomly oriented two-sphere clusters, 186–9
for a rotationally symmetric particle in an arbitrary orientation, 180–6
multi-sphere superposition, 190
T-matrix method, 114, 115–90, 202–5
superposition, 154–8, 201
recursive, 158
temperature, absolute, 3, 63
time, 5, 9
time factor, 5, 15
time-harmonic field, 10
total field, 31, 35, 54–5, 197
transition matrix, *see T* matrix
translation addition theorem, 126, 156, 157, 201, 378–9
transverse wave, 13, 36

unimoment method, 194
unitarity condition, 124
unpolarized light, 27

Venus clouds, 274–8
volume integral equation, 31–5, 197
volume integral equation method, 197–9

wave equation, vector, 33, 113
wave number, 14
wave vector, 12
wavelength, 15
weak photon localization, *see* coherent backscattering
Wentzel–Kramers–Brillouin approximation, 210
Wigner *d*-functions, 103–4, 362–9, 371, 377
Wigner *D*-functions, 367–8, 377
Wigner 3*j* symbols, 141, 379, 381

zenith angle, *see* angle, polar

Color plate section

M. I. Mishchenko, L. D. Travis, and A. A. Lacis
Scattering, Absorption, and Emission of Light by Small Particles
Cambridge University Press, Cambridge (2002)
http://www.giss.nasa.gov/~crmim/books.html © NASA

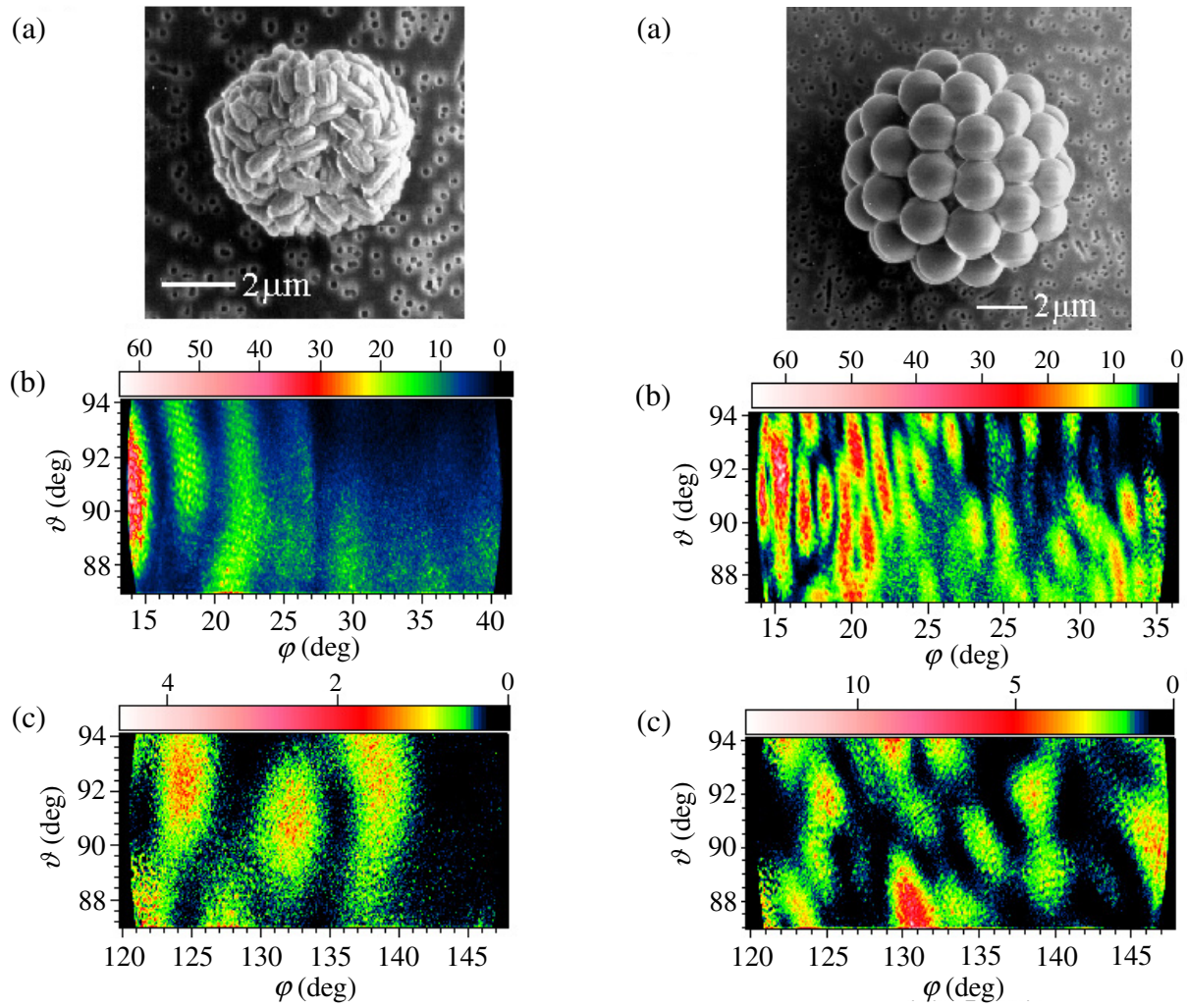

Plate 8.1. On the left: (a) scanning electron microscope image of a cluster of *Bacillus subtilis* spores and two-dimensional angular patterns of scattered intensity (in arbitrary units) in (b) the near-forward direction and (c) the near-backward direction. The particle was illuminated by a laser beam incident along the positive direction of the *x*-axis of the laboratory reference frame. The horizontal and vertical axes of each diagram show the azimuth and zenith angles of the scattering direction, respectively. On the right: as on the left, but for a cluster of polystyrene latex micro-spheres. (From Holler *et al.* 1998.)

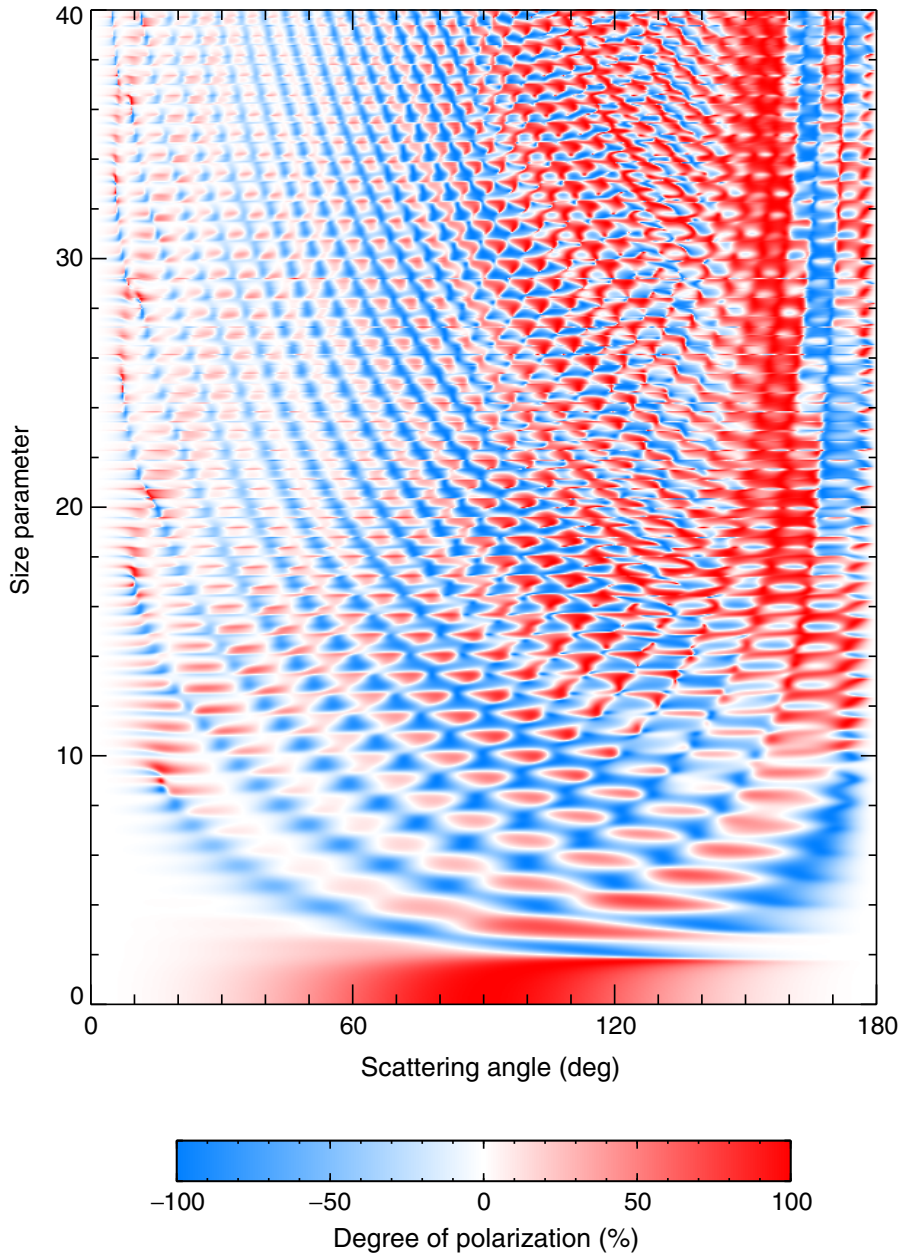

Plate 9.1. Low-resolution color image of the degree of linear polarization $P_Q = -b_1/a_1$ for monodisperse spherical particles with relative refractive index $m = 1.4$.

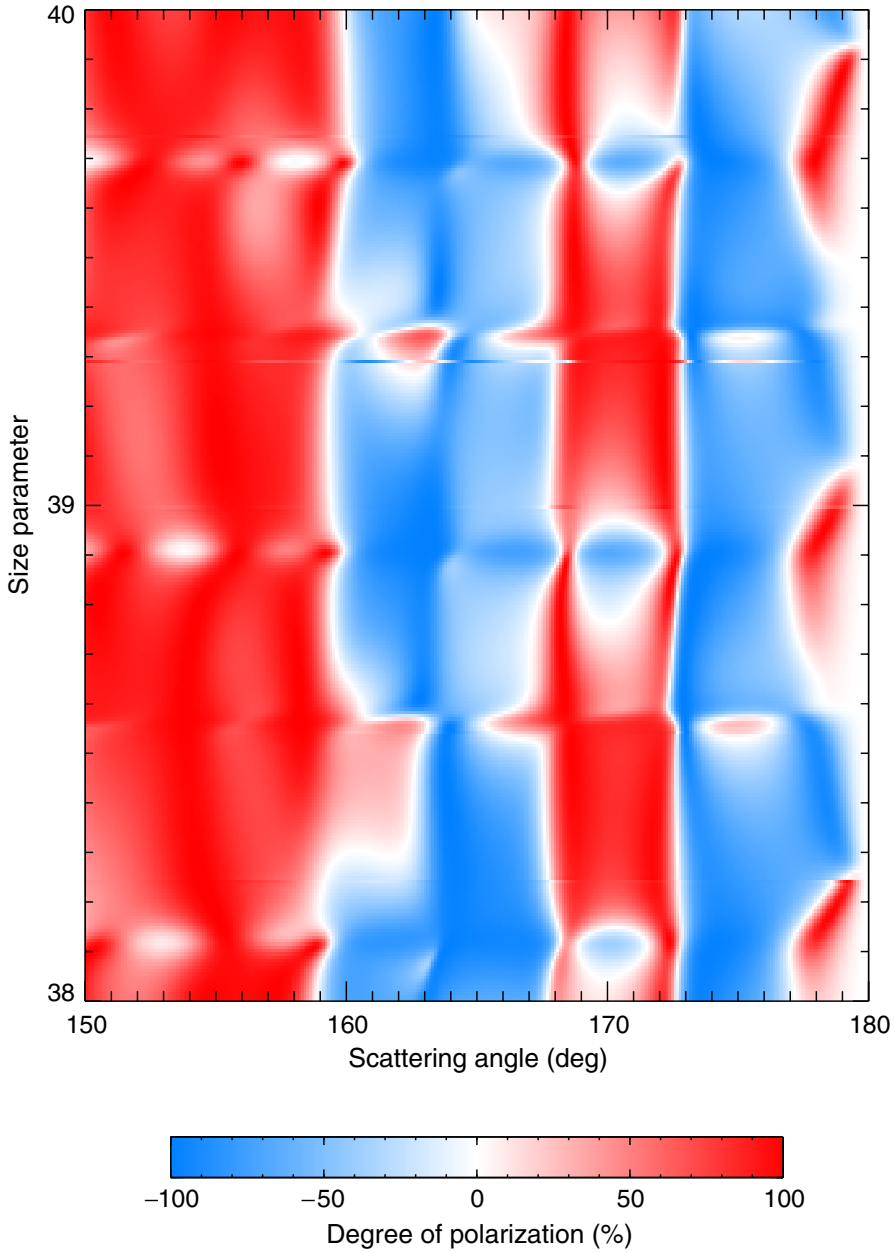

Plate 9.2. As in Plate 9.1, but using a finer sampling resolution.

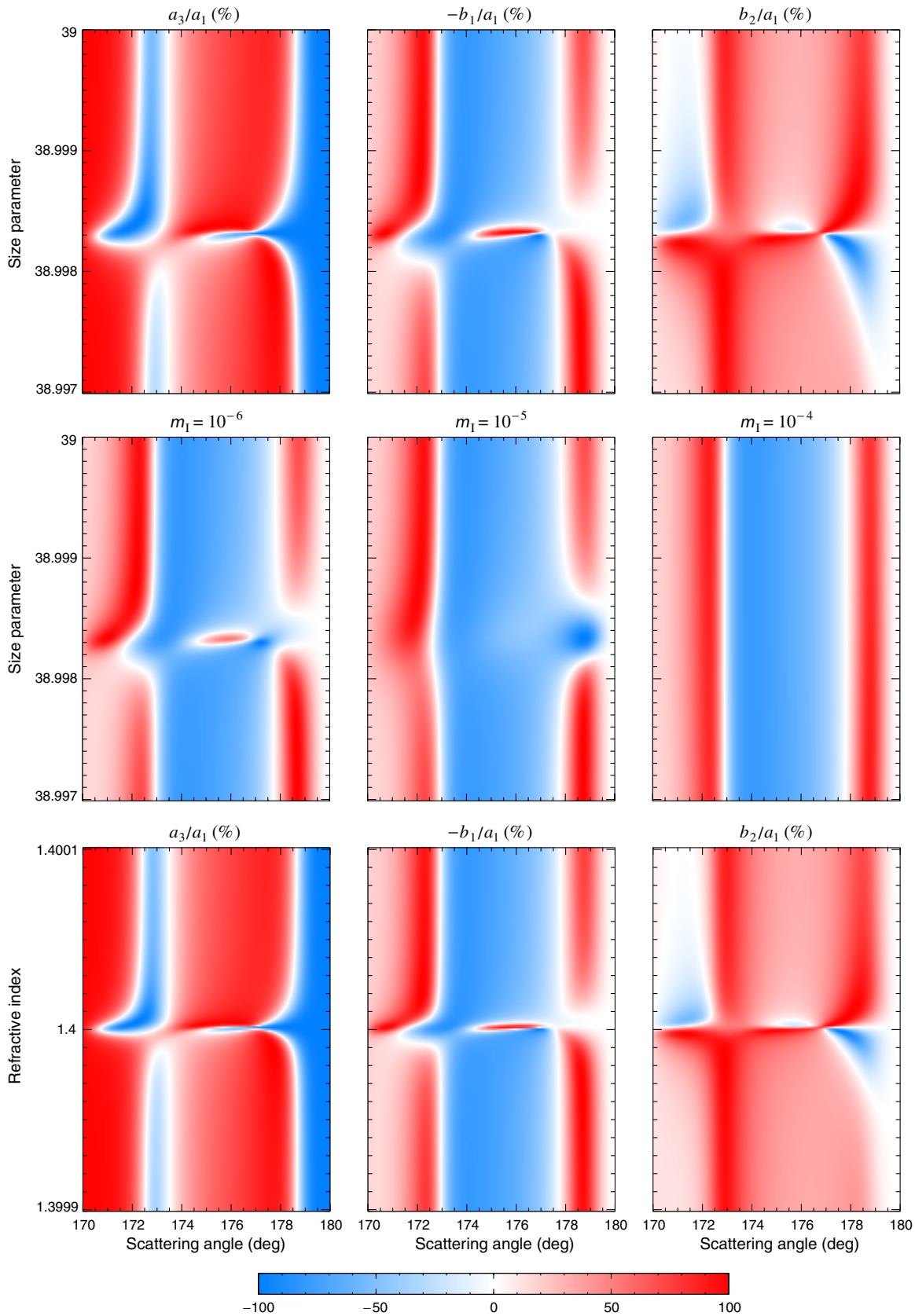

Plate 9.3. Top three panels: high-resolution images of Stokes-scattering-matrix-element ratios a_3/a_1, $-b_1/a_1$, and b_2/a_1 within the super-narrow resonance centered at $x \approx 38.9983$, for $m = 1.4$. Middle three panels: as in the top panels, but for the ratio $-b_1/a_1$ with $m_I = 10^{-6}$, 10^{-5}, and 10^{-4}. Bottom three panels: the ratios a_3/a_1, $-b_1/a_1$, and b_2/a_1 versus Θ and m_R for $x = 38.9983$ and $m_I = 0$.

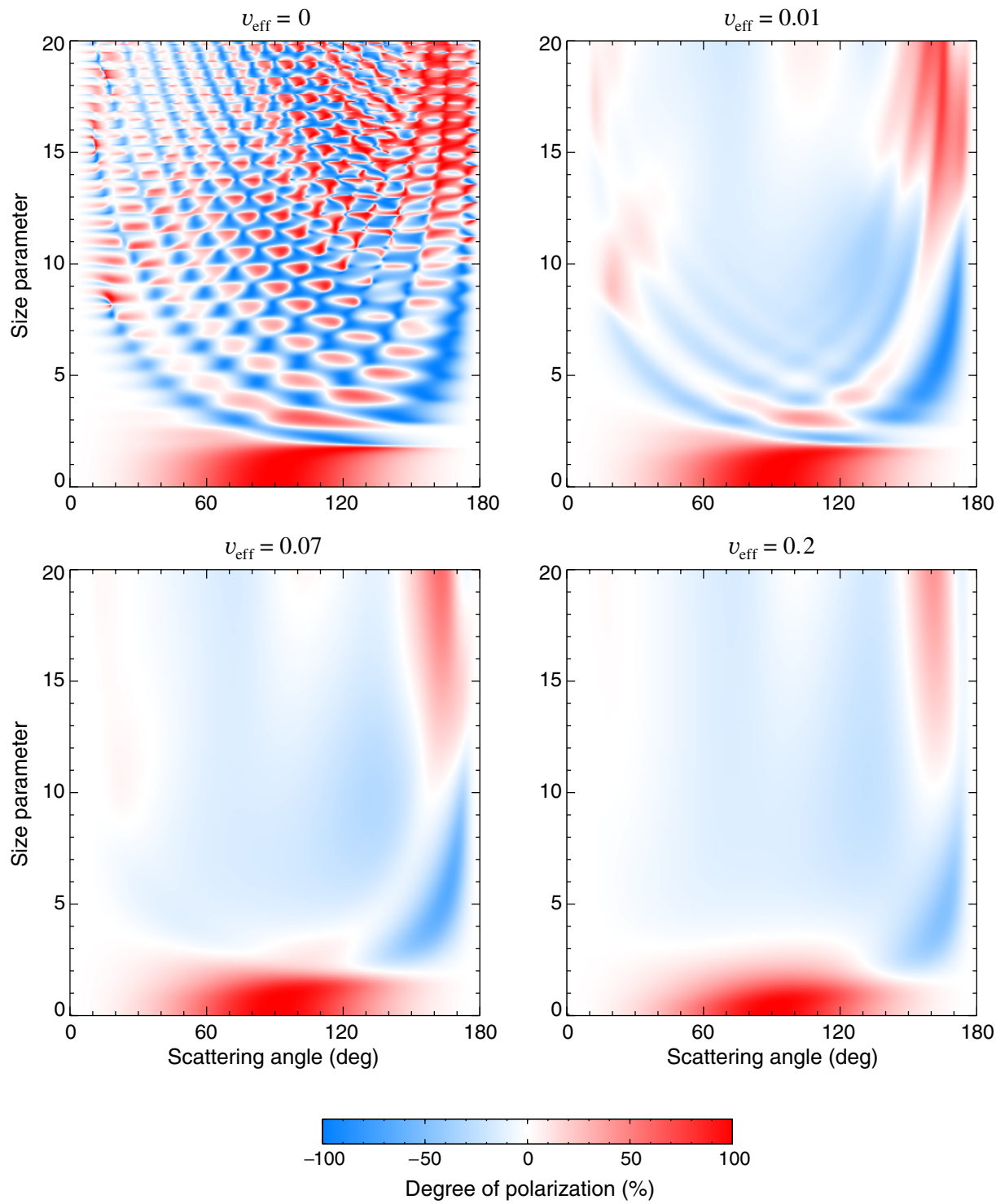

Plate 9.4. Images of the degree of linear polarization $P_Q = -b_1/a_1$ versus effective size parameter and scattering angle, for spherical particles with $m = 1.44$ and $v_{\mathrm{eff}} = 0$ (the value for monodisperse particles), 0.01, 0.07, and 0.2.

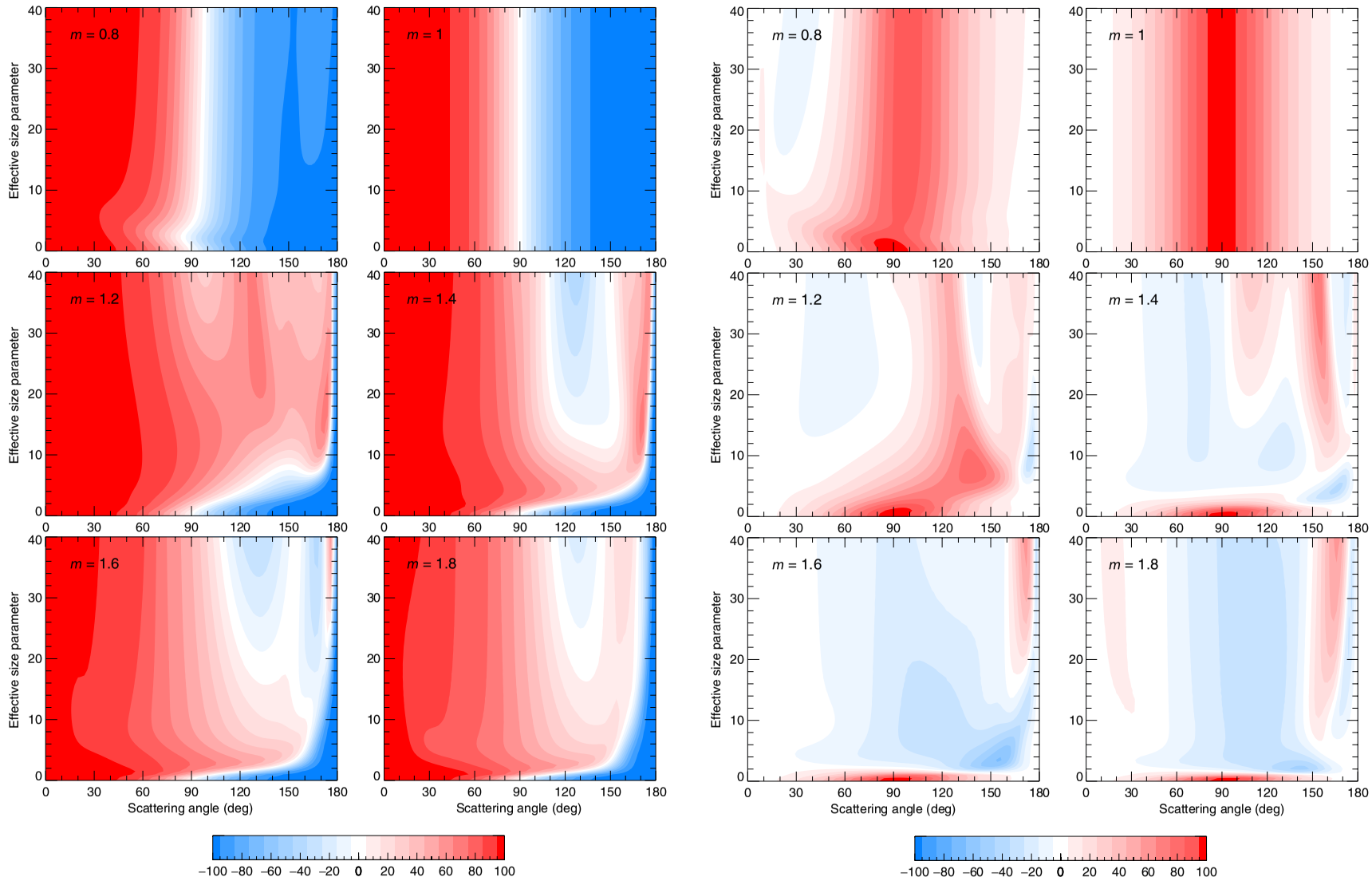

Plate 9.5. Two left-hand columns: color-contour plots of the ratio a_3/a_1 (%) versus effective size parameter and scattering angle for polydisperse spherical particles with relative refractive indices m = 0.8, 1, 1.2, 1.4, 1.6, and 1.8. Two right-hand columns: as in the two left-hand columns, but for the ratio $-b_1/a_1$ (%).

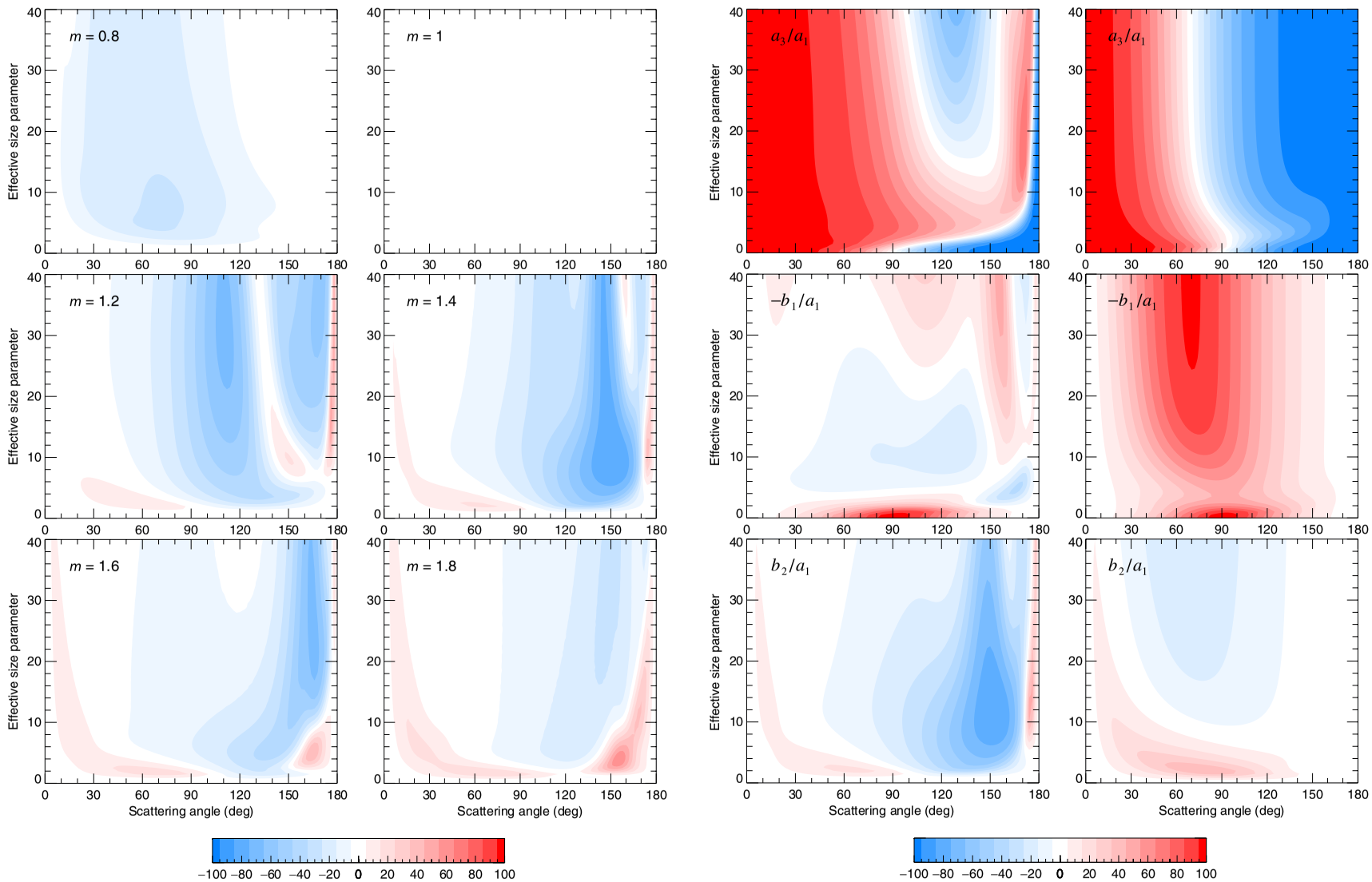

Plate 9.6. Two left-hand columns: as in Plate 9.5, but for the ratio b_2/a_1 (%). Two right-hand columns: the ratios a_3/a_1, $-b_1/a_1$, and b_2/a_1 (%) versus effective size parameter and scattering angle for polydisperse spherical particles with relative refractive indices $m = 1.4 + i0.01$ and $1.4 + i0.3$.

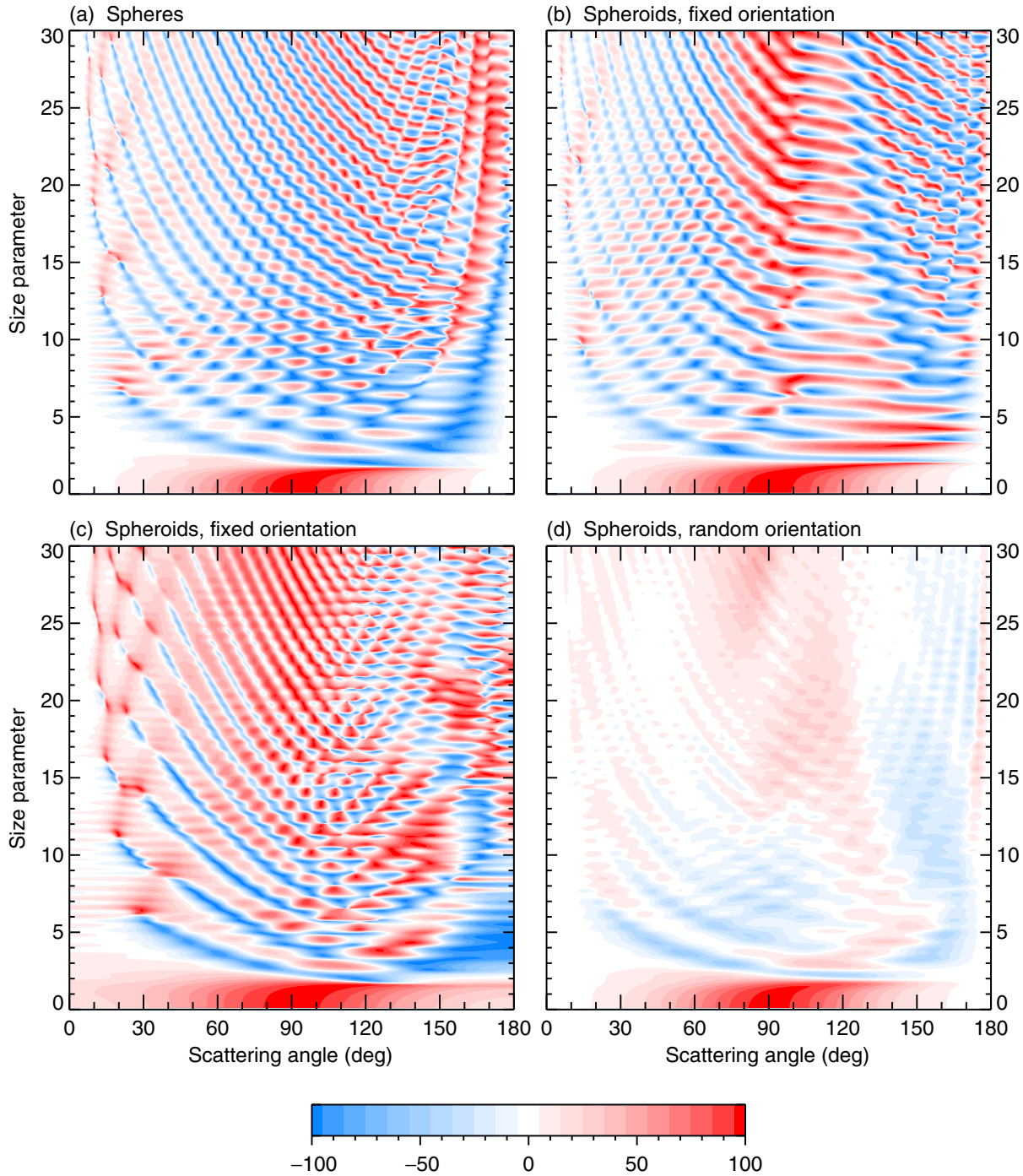

Plate 10.1. The ratio $-Z_{21}(\vartheta^{\rm sca}, \varphi^{\rm sca}=0; \vartheta^{\rm inc}=0, \varphi^{\rm inc}=0)/Z_{11}(\vartheta^{\rm sca}, \varphi^{\rm sca}=0; \vartheta^{\rm inc}=0, \varphi^{\rm inc}=0)$ in % versus $\vartheta^{\rm sca}$ and size parameter for monodisperse spheres and surface-equivalent oblate spheroids in fixed and random orientations. In panels (b) and (c), the rotation axis of the spheroids is oriented respectively along the z-axis and along the x-axis of the laboratory reference frame. The relative refractive index is 1.53 + i0.008 and the spheroid axis ratio $a/b = 1.7$.

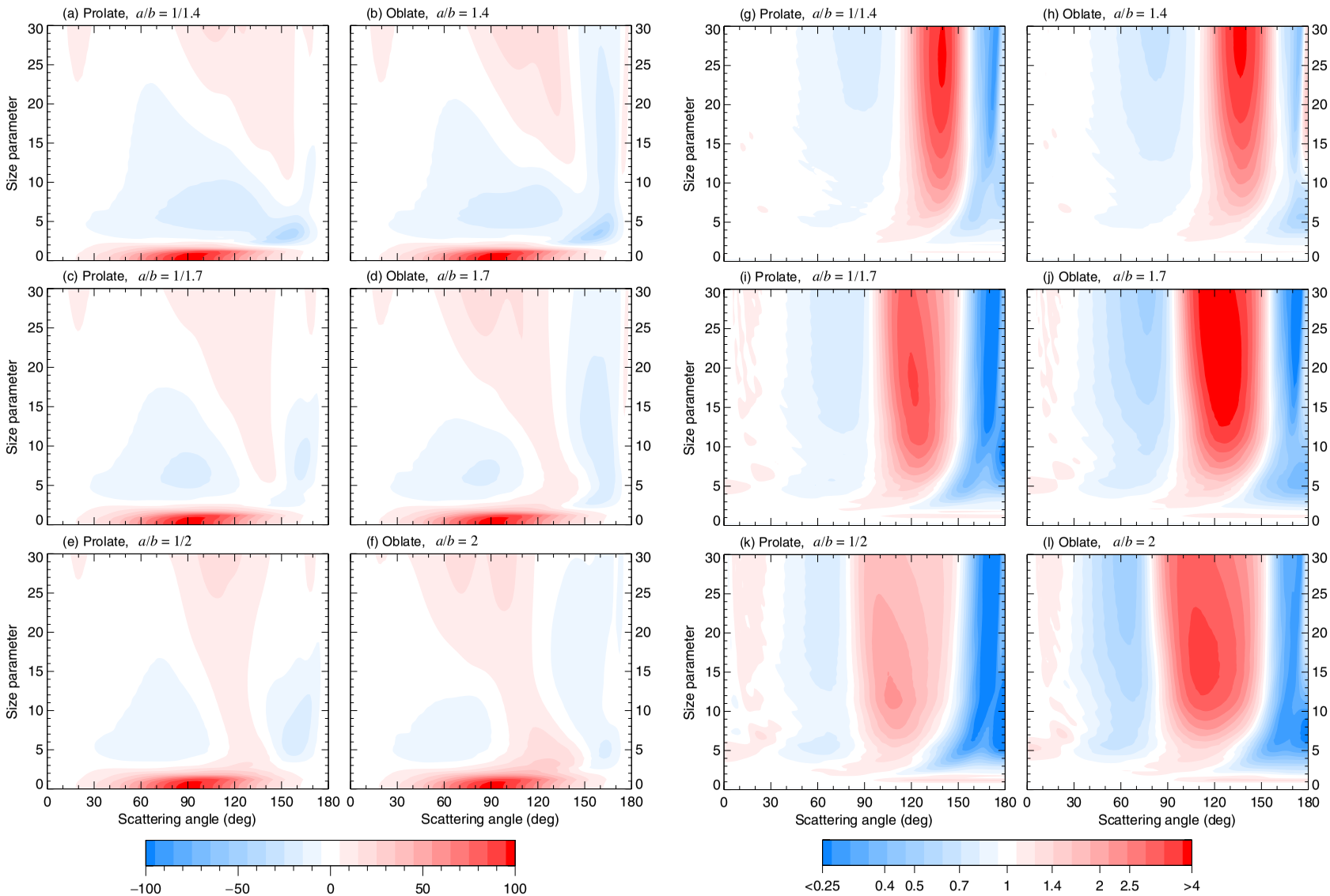

Plate 10.2. Two left-hand columns: $-b_1/a_1$ (in %) versus scattering angle and effective size parameter for polydisperse randomly oriented spheroids with various axis ratios and a fixed relative refractive index $m = 1.53 + i0.008$. The distribution of surface-equivalent-sphere radii is given by Eq. (5.246) with $\alpha = -3$ and $v_{\text{eff}} = 0.1$. Two right-hand columns: as in the two left-hand columns, but for the ratio of the phase function a_1 for randomly oriented polydisperse spheroids and that for surface-equivalent spheres.

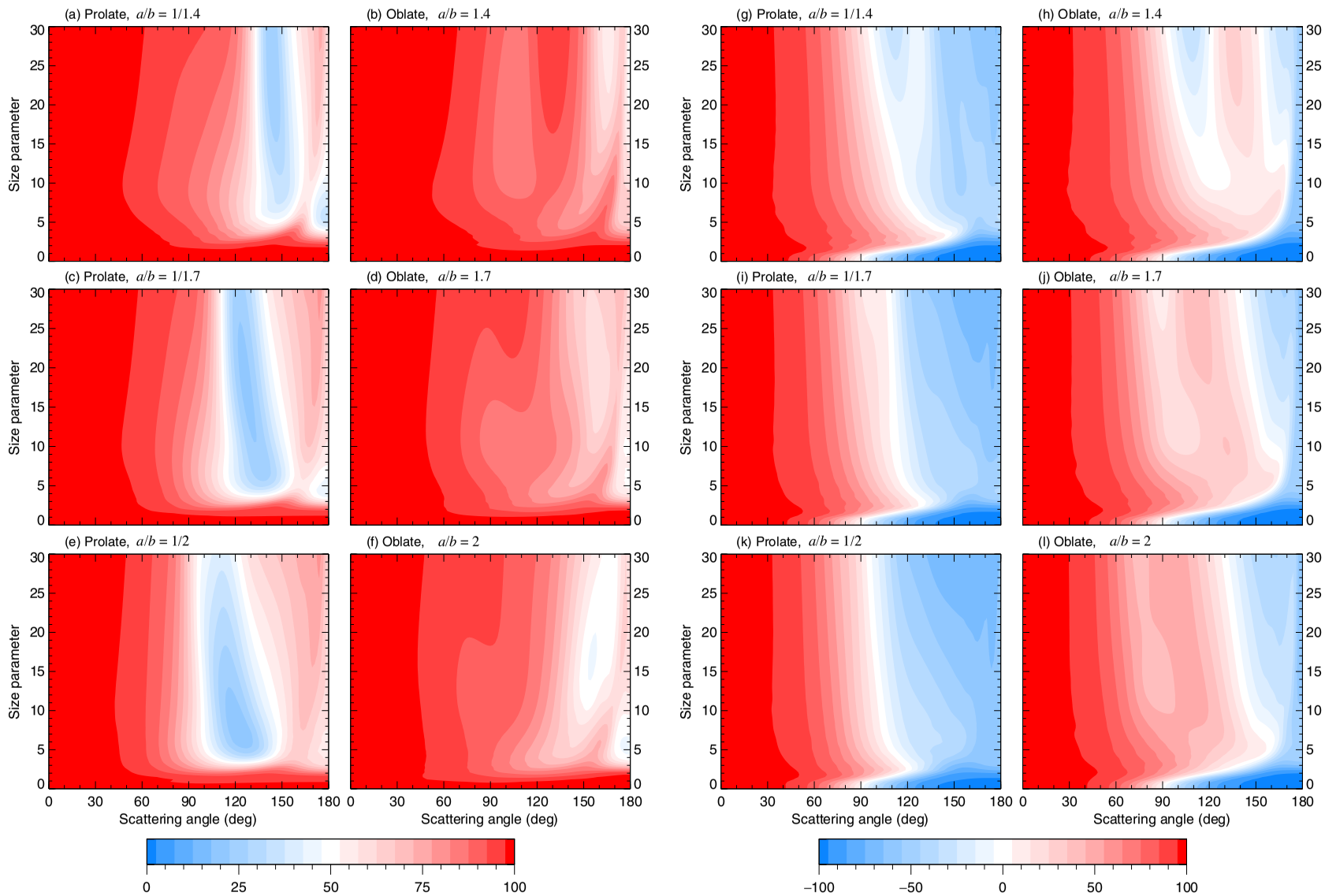

Plate 10.3. As in the two left-hand columns of Plate 10.2, but for a_2/a_1 (the two left-hand columns) and a_3/a_1 (the two right-hand columns).

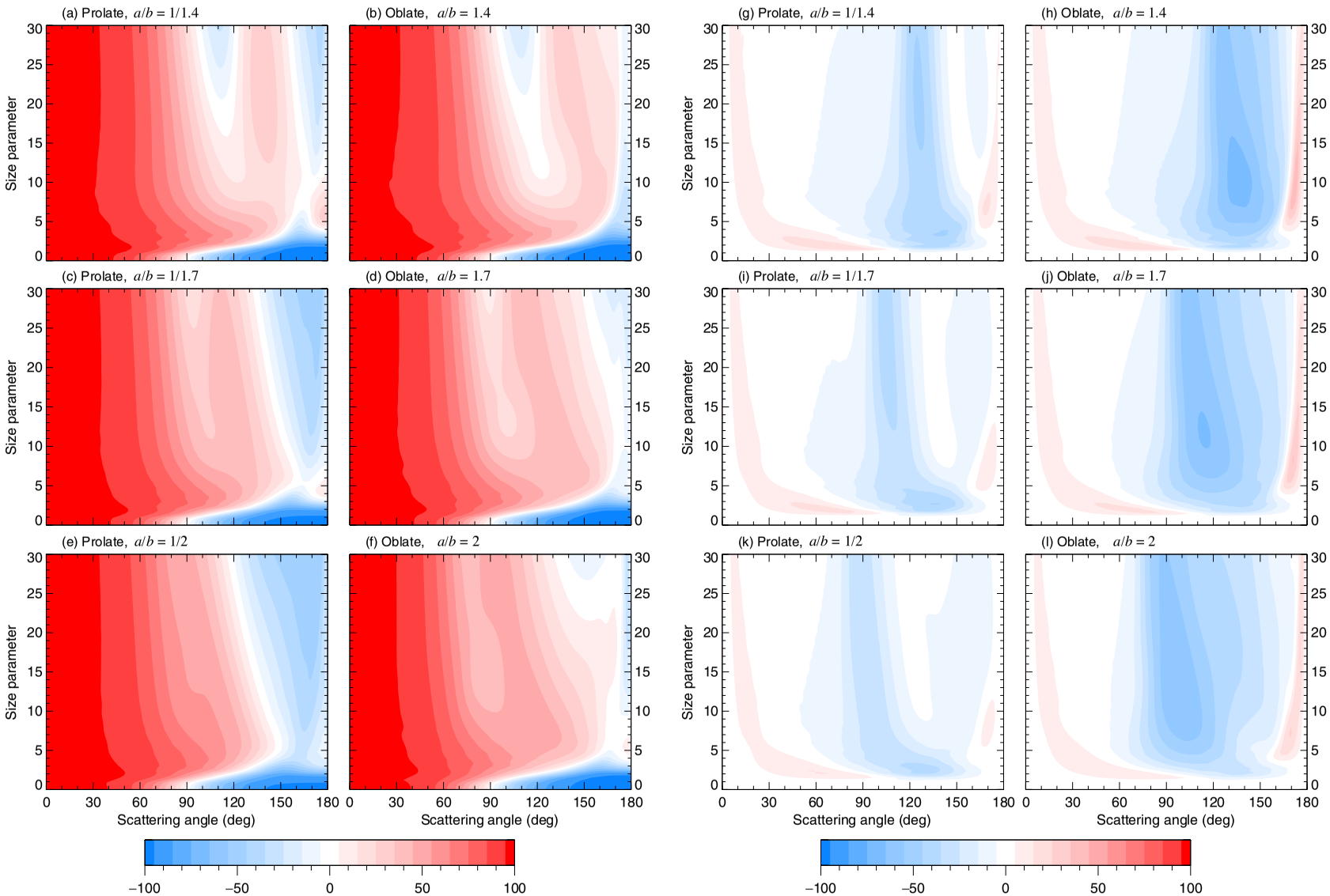

Plate 10.4. As in the two left columns of Plate 10.2, but for a_4/a_1 (the two left-hand columns) and b_2/a_1 (the two right-hand columns).

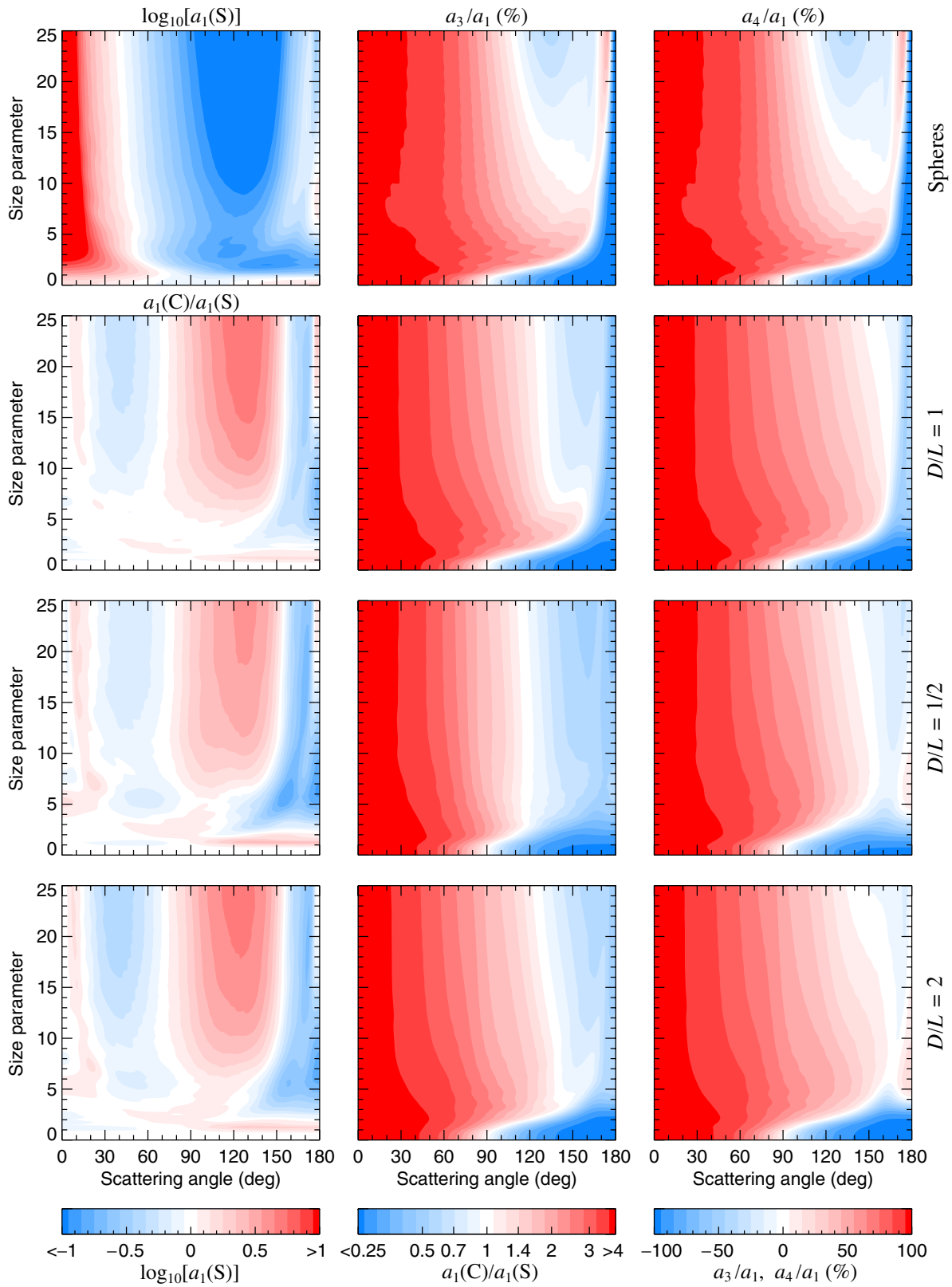

Plate 10.5. The top left panel shows the logarithm of the phase function versus scattering angle and effective size parameter for polydisperse spheres. The three lower diagrams in the left-hand column show the ratio of the phase function $a_1(\mathrm{C})$ for polydisperse randomly oriented cylinders with $D/L = 1$, 1/2, and 2 and the phase function $a_1(\mathrm{S})$ for surface-equivalent spheres. The middle and right-hand columns show a_3/a_1 and a_4/a_1 for spheres (top panels) and for surface-equivalent cylinders (lower three pairs of panels). Each diagram is quantified by the corresponding color bar at the bottom of the plate. All particles have the same relative refractive index, 1.53 + i0.008. The distribution of surface-equivalent-sphere radii is given by Eq. (5.246) with $\alpha = -3$ and $v_{\mathrm{eff}} = 0.1$.

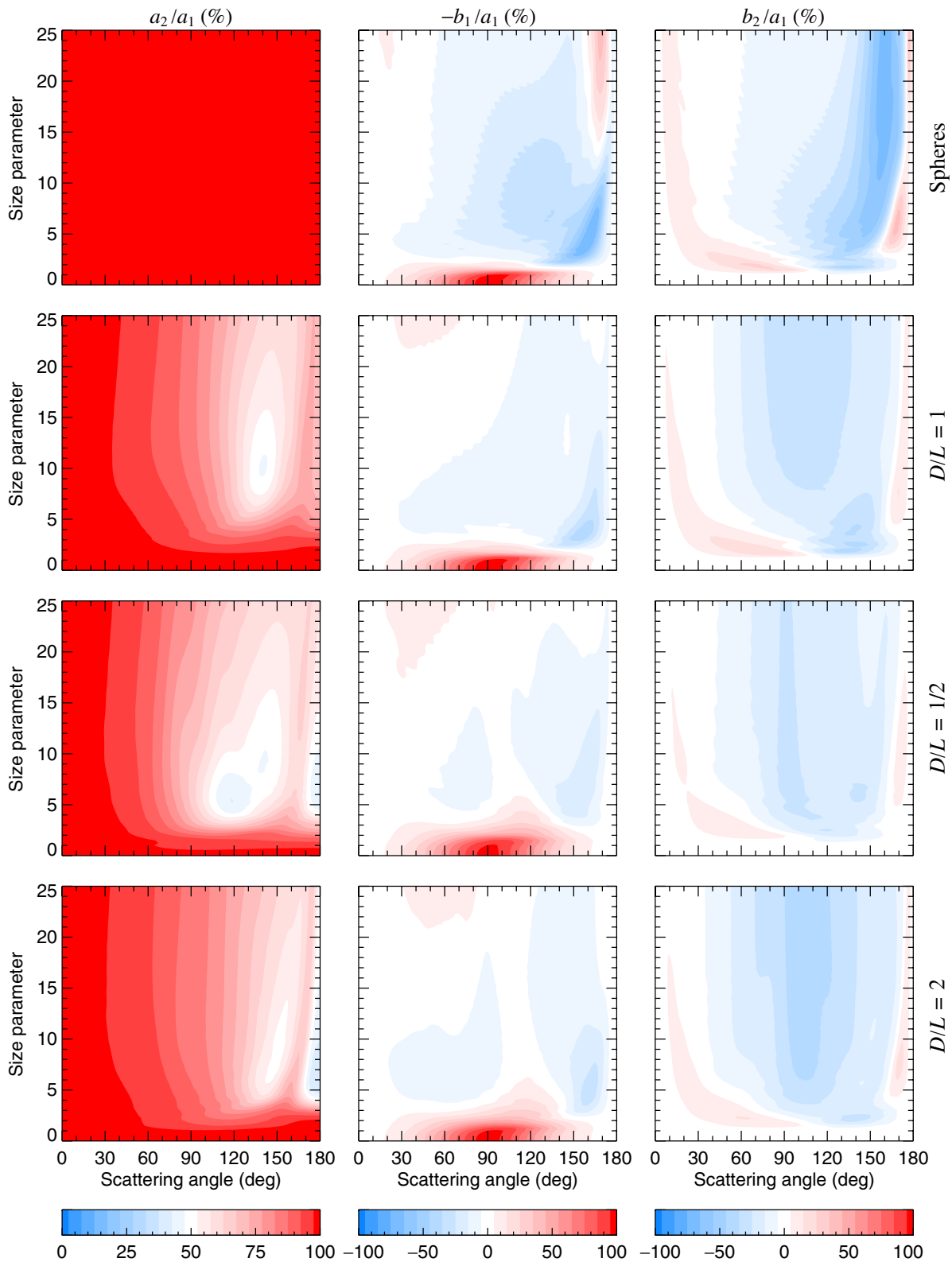

Plate 10.6. The ratios a_2/a_1, $-b_1/a_1$, and b_2/a_1 for polydisperse spheres and for surface-equivalent randomly oriented cylinders with $D/L = 1$, 1/2, and 2. The diagrams in each column are quantified using the color bar below the column. All particles have the same relative refractive index, 1.53 + i0.008. The distribution of surface-equivalent-sphere radii is given by Eq. (5.246) with $\alpha = -3$ and $v_{\text{eff}} = 0.1$.

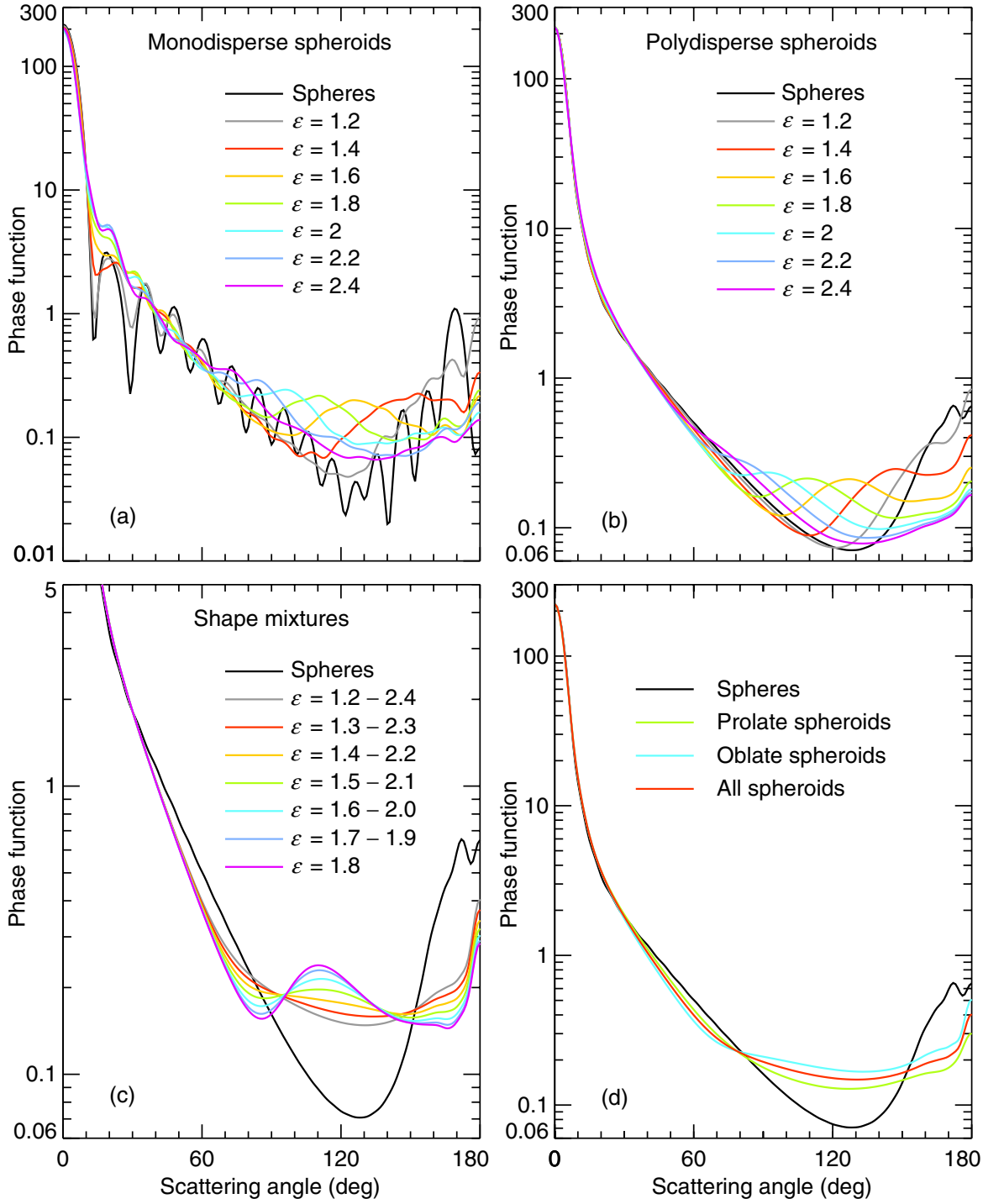

Plate 10.7. *T*-matrix computations of phase function versus scattering angle for monodisperse and polydisperse spheres and randomly oriented spheroids with a relative refractive index 1.53 + i0.008 at a wavelength 443 nm. Panel (a) shows results for a monodisperse sphere with a radius 1.163 μm and for surface-equivalent prolate spheroids with aspect ratios ranging from 1.2 to 2.4. Panel (b) shows similar computations but for a log normal size distribution with an effective radius 1.163 μm and an effective variance 0.168. Panel (c) demonstrates the effect of using a spheroid aspect-ratio distribution of finite width; it shows the ensemble-averaged phase functions for equiprobable shape mixtures of polydisperse prolate spheroids with different aspect-ratio ranges, all centered on $\varepsilon = 1.8$. Panel (d) shows the phase functions for polydisperse spheres and ensemble-averaged phase functions for equiprobable shape mixtures of prolate spheroids (green curve), oblate spheroids (blue curve), and prolate and oblate spheroids together (red curve) with aspect ratios ranging from 1.2 to 2.4 in steps of 0.1. (After Mishchenko *et al.* 1997a.)

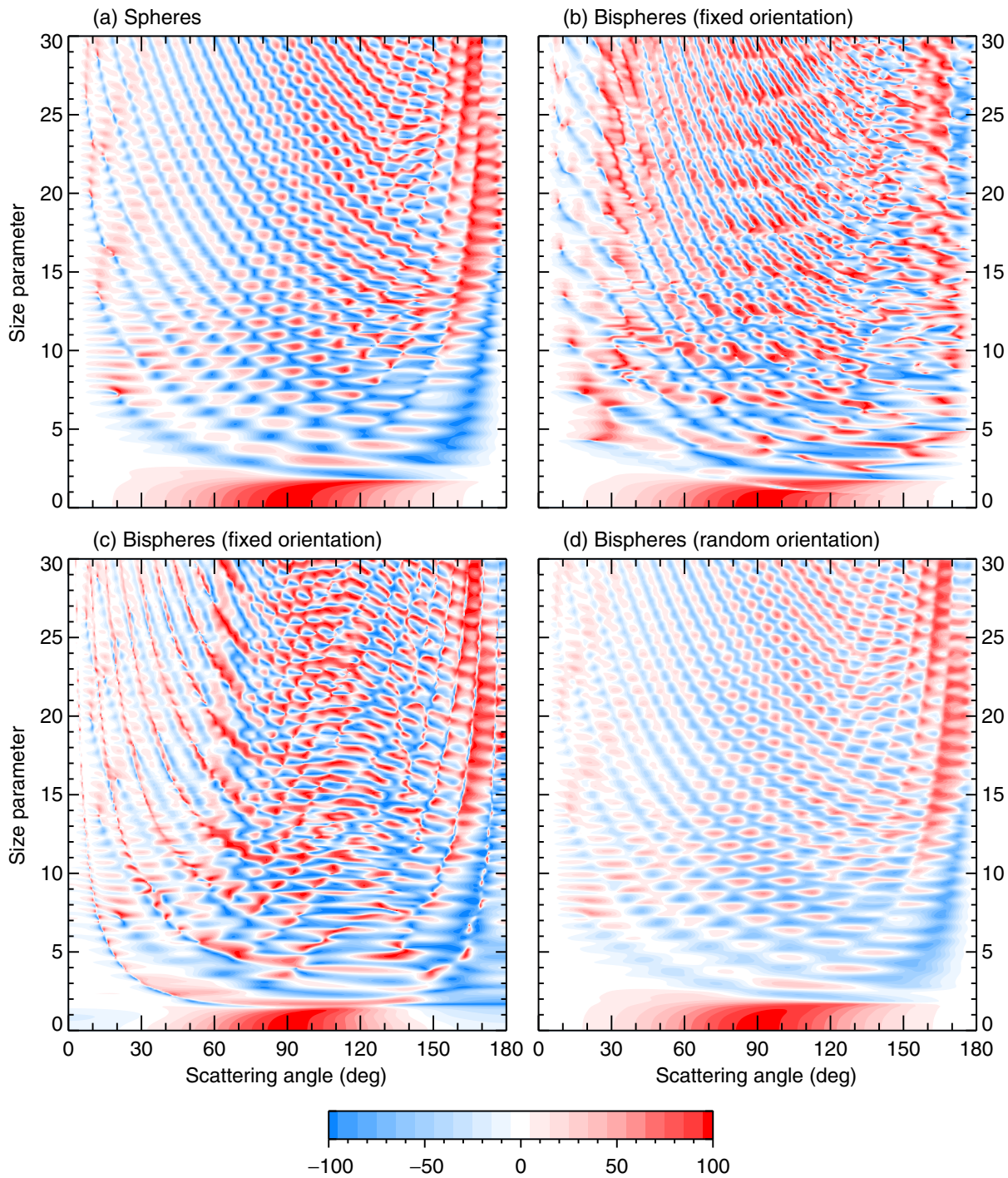

Plate 10.8. Panel (a): the ratio $-Z_{21}(\vartheta^{\rm sca}, \varphi^{\rm sca}=0; \vartheta^{\rm inc}=0, \varphi^{\rm inc}=0)/Z_{11}(\vartheta^{\rm sca}, \varphi^{\rm sca}=0; \vartheta^{\rm inc}=0, \varphi^{\rm inc}=0)$ in % versus $\vartheta^{\rm sca}$ and size parameter for monodisperse single spheres. Panels (b)–(d): the same ratio versus $\vartheta^{\rm sca}$ and constituent-sphere size parameter for monodisperse bispheres with equal touching components in fixed and random orientations. In panels (b) and (c) the bisphere axis is oriented respectively along the *z*-axis and along the *x*-axis of the laboratory reference frame. The relative refractive index is 1.5 + i0.005.

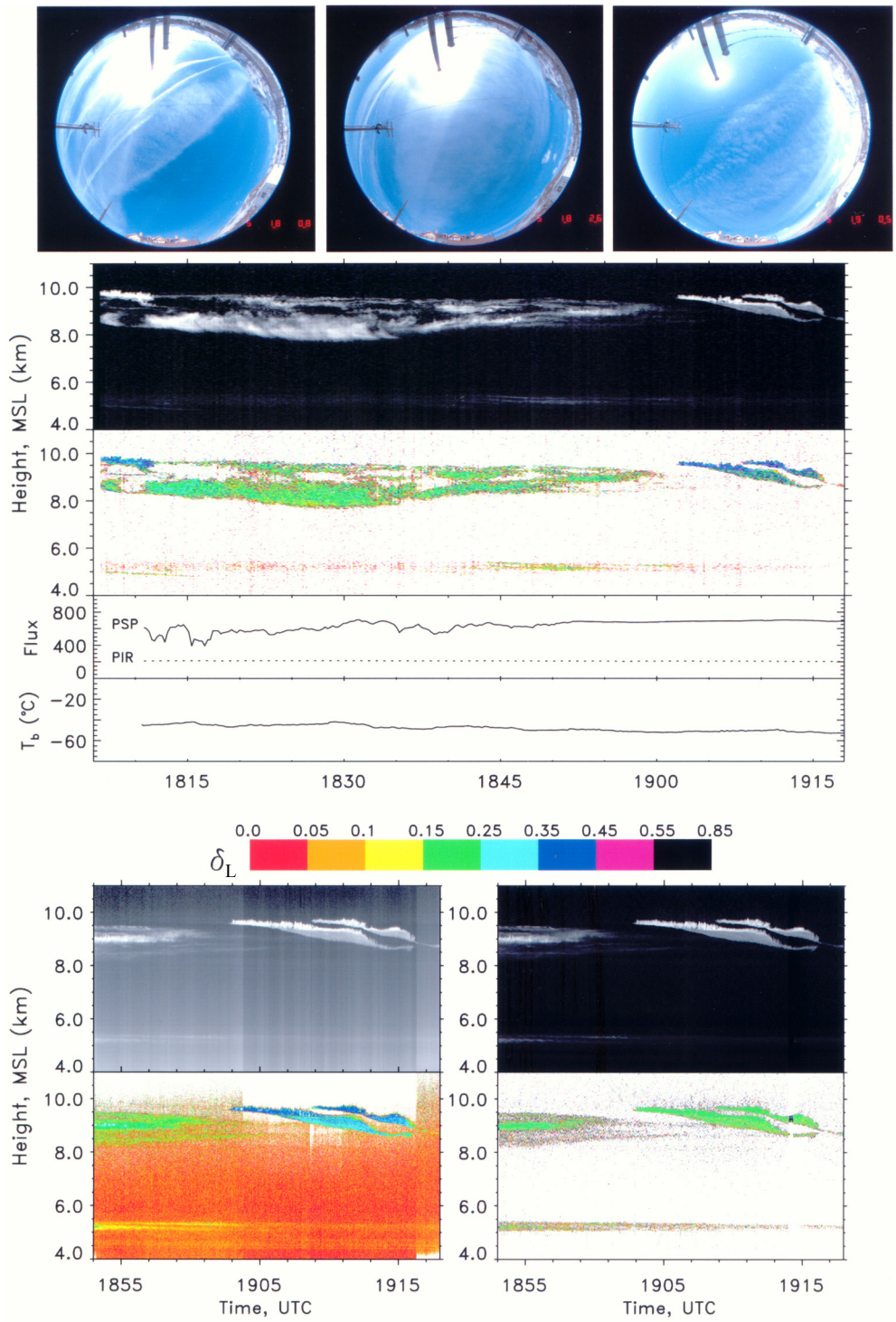

Plate 10.9. Compilation of data for the case study on 5 March 1999 of cirrus, contrails, and an Asian dust layer above Salt Lake City, Utah. Shown from top to bottom are: three fish-eye photographs of all-sky cloud conditions, obtained at 1808, 1826, and 1905 UTC (from left to right); backscattered intensity and linear depolarization time-height displays measured by an upward-looking lidar at a wavelength 0.694 μm, the broadband visible and infrared hemispherical fluxes, and the mid-infrared column brightness temperatures T_b; and, at the bottom, expanded views of backscattered intensity (black and white images) and linear depolarization (colored images) at wavelengths 0.532 μm (bottom left panel) and 1.06 μm (bottom right panel) for a time range near the end of the measurement period. The depolarization displays can be quantified using the inserted color bar. (From Sassen *et al.* 2001.)